



**ANA RUTE MARQUES
FERREIRA**

**EXTRAÇÃO DE MERCAPTANOS DE CORRENTES
DE JET-FUEL COM LÍQUIDOS IÓNICOS**

**MERCAPTANS EXTRACTION FROM JET-FUEL
STREAMS USING IONIC LIQUIDS**



**ANA RUTE MARQUES
FERREIRA**

**EXTRAÇÃO DE MERCAPTANOS DE CORRENTES DE
JET-FUEL COM LÍQUIDOS IÓNICOS**

**MERCAPTANS EXTRACTION FROM JET-FUEL
STREAMS USING IONIC LIQUIDS**

Tese apresentada à Universidade de Aveiro para cumprimento dos requisitos necessários à obtenção do grau de Doutor em Engenharia da Refinação, Petroquímica e Química, realizada sob a orientação científica do Doutor João Araújo Pereira Coutinho, Professor Catedrático do Departamento de Química da Universidade de Aveiro e do Doutor João Paulo Serejo Goulão Crespo, Professor Catedrático da Faculdade de Ciências e Tecnologia da Universidade Nova de Lisboa.

Apoio financeiro do POCTI no âmbito
do III Quadro Comunitário de Apoio.

Apoio financeiro da FCT e do FSE no
âmbito do III Quadro Comunitário de
Apoio.

Aos meus queridos pais e irmã.

o júri

presidente

Professor Doutor Helmuth Robert Malonek
Professor Catedrático da Universidade de Aveiro

Professor Doutor João Manuel da Costa Araújo Pereira Coutinho
Professor Catedrático da Universidade de Aveiro

Professor Doutor João Paulo Serejo Goulão Crespo
Professor Catedrático da Faculdade de Ciências e Tecnologia da Universidade Nova de Lisboa

Professora Doutora Alexandra Maria Pinheiro da Silva Ferreira Rodrigues Pinto
Professor Associada da Faculdade de Engenharia da Universidade de Porto

Professor Doutor Carlos Manuel Santos da Silva
Professor Auxiliar da Universidade de Aveiro

Professora Doutora Isabel Maria Rôla Coelho
Professora Auxiliar da Faculdade de Ciências e Tecnologia da Universidade Nova de Lisboa

Doutora Mara Guadalupe Freire Martins
Investigadora Coordenadora da Universidade de Aveiro

Engenheiro Fernando Morgado Lopes
Director de Operações, Refinaria de Sines, Galp Energia

Doutor Jorge Correia Ribeiro
Chefe de Laboratório, Refinaria de Matosinhos, Galp Energia

agradecimentos

Em primeiro lugar gostaria de agradecer, à Fundação para a Ciência e a Tecnologia e à Galp Energia, a bolsa de doutoramento atribuída e os subsídios para participação em congressos, que permitiram o desenvolvimento deste trabalho.

Agradeço ainda ao Professor João Coutinho e ao Professor João Crespo por toda a orientação científica e ajuda crucial no desenvolvimento deste projecto, bem como toda a disponibilidade, interesse e sugestões, que permitiram ultrapassar as dificuldades encontradas.

À Professora Isabel Coelho, à Doutora Luísa Neves, ao Doutor Pedro Carvalho e à Doutora Mara Freire, um muito obrigada pelas longas sessões de discussão que foram contributos indispensáveis para a realização deste trabalho.

Ao Engenheiro Fernando Lopes e ao Doutor Jorge Ribeiro, que tão bem me receberam e integraram durante a minha estadia na Refinaria de Matosinhos, além de todo o incentivo e entusiasmo que sempre demonstraram por este projeto.

São tantas as pessoas que nestes quatro anos conheci e as quais me proporcionam ótimos momentos, que o espaço que tenho não chegaria para as nomear. Assim, obrigada ao PATH pelo apoio e tardes de doce convívio, e ao BPEG pelas aventuras laboratoriais e convívios extracurriculares. Ao EngIQ, pelas longas horas de estudo, apoio e motivação, reconhecimento e avaliação da gastronomia do Porto. Ao Laboratório da Refinaria de Matosinhos, por tão bem me integrarem no meio e pelos dias divertidos de intenso trabalho.

Obrigada por todos os bons amigos e amigas que fiz.

Ao Joel e aos amigos de longa data, obrigada por não desistirem de mim, mesmo nos momentos mais difíceis e de ausência prolongada, e por estarem perto, mesmo estando longe.

Para a mãe São, para o pai Abel e para a mana Cátia, um agradecimento muito especial por todos os sacrifícios e pelo apoio incondicional que me permitiram chegar aqui hoje. Nada seria possível sem vocês. Obrigada por tudo.

A todos, o meu muito obrigada do fundo do coração, foram quatro anos inesquecíveis.

palavras-chave

Dessulfuração, mercaptano, “jet-fuel”, líquido iónico, equilíbrio de fase, COSMO-RS, extração com líquido iónicos, processo de separação por membrana.

resumo

A dessulfuração é um dos processos mais importantes na indústria da refinação. Devido a uma preocupação crescente com os riscos para a saúde humana e ambiente associados às emissões de compostos de enxofre, a legislação tem vindo a tornar-se mais rigorosa, exigindo uma redução drástica do teor de enxofre nos combustíveis para níveis próximos de zero (< 10 ppm S). No entanto, os processos convencionais de dessulfuração são ineficientes e apresentam custos operacionais elevados, o que tem impulsionado a melhoria dos processos existentes e o desenvolvimento de novas tecnologias com maior eficiência. Com o objetivo de colmatar as lacunas referidas, este projeto de doutoramento investiga um processo alternativo de dessulfuração com a utilização de líquidos iónicos para a remoção de mercaptanos de correntes de “jet-fuel”.

A triagem e a seleção do líquido iónico mais adequado foram realizadas com base em dados experimentais e previstos, utilizando o modelo termodinâmico COSMO-RS, de equilíbrio líquido-líquido. Foi seleccionada uma alimentação modelo de 1-hexanotiol e *n*-dodecano para representar a corrente de “jet-fuel”. Foram observadas seletividades elevadas, como resultado da baixa solubilidade mútua entre o líquido iónico e o hidrocarboneto, o que demonstra o potencial de utilização dos líquidos iónicos, uma vez que a contaminação e a perda do combustível para o solvente são evitadas. Os coeficientes de distribuição dos mercaptanos em relação aos líquidos iónicos são desfavoráveis, o que torna os processos tradicionais de extração líquido-líquido inadequados para a remoção de compostos alifáticos com enxofre, devido ao volume elevado de solvente que seria necessário utilizar. Este trabalho explora métodos alternativos e propõe a utilização dos líquidos iónicos num processo de separação assistido por membranas. No processo desenvolvido, o líquido iónico é utilizado como solvente na extração do mercaptano da alimentação, realizada num contactor de membrana de fibra oca, sem a co-extração do hidrocarboneto do “jet-fuel” modelo. Recorrendo a um segundo contactor, o líquido iónico é regenerado através de uma corrente de gás de arraste, o que permite a sua reciclagem e reutilização em circuito fechado entre os dois contactores. Este processo integrado de extração/regeneração produziu um “jet-fuel” modelo com teor de enxofre inferior a 2 ppm, atingindo-se assim valores inferiores aos estabelecidos pela actual legislação. Demonstra-se assim que este processo tem um potencial de desenvolvimento elevado para aplicação em processos industriais de dessulfuração profunda.

keywords

Desulfurization; mercaptan removal; jet-fuel; phase equilibria; COSMO-RS; ionic liquid extraction, membrane separation process.

abstract

Desulfurization is one of the most important processes in the refining industry. Due to a growing concern about the risks to human health and environment, associated with the emissions of sulfur compounds, legislation has become more stringent, requiring a drastic reduction in the sulfur content of fuel to levels close to zero (< 10 ppm S). However, conventional desulfurization processes are inefficient and have high operating costs. This scenario stimulates the improvement of existing processes and the development of new and more efficient technologies. Aiming at overcoming these shortcomings, this work investigates an alternative desulfurization process using ionic liquids for the removal of mercaptans from "jet fuel" streams.

The screening and selection of the most suitable ionic liquid were performed based on experimental and COSMO-RS predicted liquid-liquid equilibrium data. A model feed of 1-hexanethiol and n-dodecane was selected to represent a jet-fuel stream. High selectivities were determined, as a result of the low mutual solubility between the ionic liquid and the hydrocarbon matrix, proving the potential use of the ionic liquid, which prevents the loss of fuel for the solvent. The distribution ratios of mercaptans towards the ionic liquids were not as favorable, making the traditional liquid-liquid extraction processes not suitable for the removal of aliphatic S-compounds due to the high volume of extractant required. This work explores alternative methods and proposes the use of ionic liquids in a separation process assisted by membranes. In the process proposed the ionic liquid is used as extracting solvent of the sulfur species, in a hollow fiber membrane contactor, without co-extracting the other jet-fuel compound. In a second contactor, the ionic liquid is regenerated applying a sweep gas stripping, which allows for its reuse in a closed loop between the two membrane contactors. This integrated extraction/regeneration process of desulfurization produced a jet-fuel model with sulfur content lower than 2 ppm of S, as envisaged by legislation for the use of ultra-low sulfur jet-fuel. This result confirms the high potential for development of ultra-deep desulfurization application.

Table of Contents

List of Abbreviations	vii
List of Symbols	vii
List of Tables	xi
List of Figures	xiii
Chapter 1 – General Introduction.....	1
1.1. General Context.....	3
1.2. Scope and objectives	6
1.3. References.....	8
Chapter 2 - CONductor-like Screening Model for Real Solvents (COSMO-RS)	13
2.1. Theory.....	15
2.2. References.....	17
Chapter 3 – An Overview of the Liquid-Liquid Equilibria of (Ionic Liquid + Hydrocarbon) Binary Systems and their Modeling by COSMO-RS	19
3.1. Introduction	21
3.2. Ionic liquid + hydrocarbon liquid-liquid equilibria.....	23
3.3. Results and Discussion	23
3.3.1. Hydrocarbons + ILs binary systems	24
3.3.2. N-alkanes + ILs binary systems	25
3.3.2.1. Effect of the n-alkane chain length upon the phase behavior.....	26
3.3.2.2. Effect of the ionic liquid cation core upon the phase behavior.....	27
3.3.2.3. Effect of the ionic liquid cation alkyl chain length upon the phase behavior	29
3.3.2.4. Effect of the ionic liquid anion upon the phase behavior	30
3.3.2.5. Effect of the ionic liquid anion alkyl chain length upon the phase behavior	31
3.3.3. Aromatics + ILs binary systems	32
3.3.3.1. Effect of the aromatics structure on the phase behavior	33
3.3.3.2. Effect of the ionic liquid cation core upon the phase behavior.....	34

3.3.3.3.	Effect of the ionic liquid cation alkyl chain length upon the phase behavior	36
3.3.3.4.	Effect of the ionic liquid anion upon the phase behavior	38
3.3.4.	Cycloalkanes + ILs binary systems.....	39
3.3.4.1.	Effect of the cycloalkanes structure upon the phase behavior	39
3.3.4.2.	Effect of the ionic liquid cation core upon the phase behavior	40
3.3.4.3.	Effect of the ionic liquid cation alkyl chain length upon the phase behavior	41
3.3.4.4.	Effect of the ionic liquid anion upon the phase behavior	42
3.3.5.	Summary of the various effects studied upon the phase behavior	43
3.4.	Conclusions	45
3.5.	References	46
Chapter 4 – An Overview of the Liquid-Liquid Equilibria of Ternary Systems composed of Ionic Liquid, Aromatic and Aliphatic Hydrocarbons, and its Modeling by COSMO-RS.....		53
4.1.	Introduction.....	55
4.2.	Ionic Liquid + Hydrocarbons Liquid–Liquid Equilibria	56
4.3.	Results and Discussion.....	56
4.3.1.	Effect of the structural characteristics of the aliphatic hydrocarbons upon the phase behavior.....	59
4.3.1.1.	Effect of cyclization.....	59
4.3.1.2.	Effect of the alkane chain length.....	61
4.3.1.3.	Effect of the aromatic structural characteristics upon the phase behavior.	64
4.3.2.	Effect of the ionic liquid cation family upon the phase behavior	68
4.3.3.	Effect of the ionic liquid cation alkyl chain length upon the phase behavior .	73
4.3.4.	Effect of the ionic liquid anion upon the phase behavior	76
4.3.5.	Effect of the temperature upon the phase behavior	82
4.3.6.	Summary.....	84
4.4.	Conclusions	88

4.5. References.....	89
Chapter 5 – Ionic Liquids for Mercaptans Desulfurization: Experimental Liquid-Liquid Equilibrium and COSMO-RS Description.....	99
5.1. Introduction	101
5.2. Materials and methods.....	102
5.2.1. Liquid-liquid equilibrium	102
5.3. Results and Discussion.....	104
5.3.1. Ternary liquid-liquid equilibrium (tie-lines data).....	105
5.3.2. Selectivity and distribution ratio	110
5.3.2.1. Effect of the ionic liquid cation core	111
5.3.2.2. Effect of cation alkyl side chain length	112
5.3.2.3. Effect of the ionic liquid anion nature	113
5.3.2.4. Effect of the temperature	115
5.3.2.5. Effect of the ionic liquid water content.....	115
5.3.3. Evaluation of the COSMO-RS prediction capability	116
5.4. Ionic liquid screening.....	119
5.4.1. Tested ionic liquids	119
5.4.2. Selectivity, distribution ratio and σ -profiles.....	119
5.4.2.1. Predicted effect of the ionic liquid cation core.....	121
5.4.2.2. Predicted effect of the ionic liquid anion.....	123
5.4.2.3. Predicted effect of the alkyl side chain length and symmetry	124
5.4.3. Potential ionic liquids candidates	125
Comparison between the selection of ionic liquids for aliphatic or for aromatic sulfur compounds removal from fuels	126
5.5. Conclusions	127
5.6. References.....	128
Chapter 6 – Removal of Mercaptans from “Jet-Fuel” Streams assisted by Ionic Liquid Membrane Extraction	137
6.1. Introduction	139
6.2. Mass transfer model.....	141

6.3.	Materials and methods.....	144
6.3.1.	Materials.....	144
6.3.2.	Liquid-liquid extraction kinetic experiments.....	144
	Analytical methods.....	145
	Calculation methods	145
6.3.3.	Supported ionic liquid membranes (SILMs) experiments.....	145
6.3.3.1.	SILMs preparation.....	148
6.3.3.2.	SILMs characterization.....	148
6.3.3.3.	SILMs stability.....	148
6.3.3.4.	Permeation through the SILMs.....	149
6.4.	Results and discussion	149
6.4.1.	Liquid-liquid extraction kinetics.....	150
6.4.1.1.	Mass transfer kinetics.....	151
6.4.1.2.	Mass transfer correlations	153
6.4.2.	Supported ionic liquid membrane experiments.....	157
6.4.2.1.	Membrane support.....	157
6.4.2.2.	Ionic liquid losses	158
6.4.2.3.	Permeation through SILMs.....	160
6.5.	Conclusions	165
6.6.	References	166
Chapter 7 – Mercaptans Extraction from “Jet-Fuel” assisted by Ionic Liquids in Hollow Fiber Membrane Contactors		173
7.1.	Introduction.....	175
7.2.	Experimental Section.....	176
7.3.	Materials.....	177
7.3.1.	Experimental procedure	178
7.3.2.	Operating conditions	180
7.3.3.	Analytical methods	182
7.4.	Mass transfer model	183

Calculation methods.....	186
7.5. Results and discussion	186
7.5.1. Single extraction in a membrane contactor	187
7.5.2. Simultaneous extraction and regeneration in membrane contactors	188
7.5.2.1. Vacuum-based regeneration	188
7.5.2.2. Sweep-gas based regeneration	189
Mass transfer kinetics.....	191
Simulation of mercaptan transport.....	192
7.6. Conclusions	196
7.7. References.....	197
Chapter 8 – General Conclusions and Future Work	201
8.1. General conclusions.....	203
8.2. Future work	205
8.3. References.....	207
Appendix A	209
Appendix B	217
Appendix C	293
Appendix D	349

List of Abbreviations

ASTM D3227	Standard Test Method for (Thiol Mercaptan) Sulfur in Gasoline, Kerosine, Aviation Turbine, and Distillate Fuels
BASIL	Biphasic Acid Scavenging utilizing Ionic Liquids
CA	cellulose acetate
COSMO-RS	COnductor-like Screening MOdel for Real Solvents
H ₂ S	hydrogen sulfide
hb-PVDF	hydrophobic polyvinylidene fluoride
HDS	hydrodesulfurization
hl-PVDF	hydrophilic polyvinylidene fluoride
IFP	Institut Français du Pétrole
IL	ionic liquid
LLE	liquid-liquid equilibria
NRTL	Non-Random Two Liquid
PES	polyethersulfone
PP	polypropylene
PTFE	teflon
PVDF	polyvinylidene fluoride
RMSD	root mean square deviation
RSH	mercaptan
SILMs	supported ionic liquid membranes
SO _x	sulfur oxides
UCST	upper critical solution temperature
UNIQUAC	UNIversal QUAsiChemical Equation of State

List of Symbols

A_E	membrane area of the module of extraction (m ²)
A_M	module membrane area (m ²)
A_R	membrane area of the module of regeneration (m ²)
A_i	interfacial area of the cell (m ²)
C_{IL}	1-hexanethiol concentration in the ionic liquid rich phase (mol.m ⁻³)
C_{IL}^0	concentration of 1-hexanethiol in the ionic liquid phase, at the initial time (mol.m ⁻³)
C_f	1-hexanethiol concentration (mol.m ⁻³)
C_f^*	1-hexanethiol concentration in equilibrium with the 1-hexanethiol concentration in the ionic liquid phase (mol.m ⁻³)

C_f^0	concentration of 1-hexanethiol in the feed phase, at the initial time
C_f^{in}	inlet feed concentration in the membrane contactor (mol.m^{-3})
C_f^{out}	outlet feed concentration in the membrane contactor (mol.m^{-3})
C_g	concentration in the gaseous phase (mol.m^{-3})
C_g^0	concentration of 1-hexanethiol in the gaseous phase, at the initial time (mol.m^{-3})
C_{RSH}	1-hexanethiol concentration (mol.m^{-3})
D	distribution ratio
\mathcal{D}	diffusion coefficient ($\text{m}^2.\text{s}^{-1}$)
d_{fi}	internal fiber diameter (m)
d_{flm}	logarithmic mean fiber diameter (m)
d_{fo}	outer fiber diameter (m)
d_i	impeller diameter (m)
$\mathcal{D}_{Scheibel}$	diffusion coefficient by the Scheibel correlation ($\text{cm}^2.\text{s}^{-1}$)
$\mathcal{D}_{Wilke-Chang}$	diffusion coefficient by the Wilke-Chang correlation ($\text{cm}^2.\text{s}^{-1}$)
E_{HB}	hydrogen bounding energy (kcal.mol^{-1})
E_{misfit}	electrostatic misfit energy (kcal.mol^{-1})
E_{vdW}	van der Waals energy (kcal.mol^{-1})
H	Henry's constant
K_E	overall mass transfer coefficient associated with the module of extraction (m.s^{-1})
K_R	overall mass transfer coefficient associated with the module of regeneration (m.s^{-1})
K_f	overall mass transfer coefficient (m.s^{-1})
k_{IL}	individual mass transfer coefficients of ionic liquid boundary film (m.s^{-1})
k_M	membrane mass transfer coefficients (m.s^{-1})
k_f	individual mass transfer coefficients of feed boundary film (m.s^{-1})
k_g	individual mass transfer coefficients of gas boundary film (m.s^{-1})
L_f	fiber length (m)
$M_{solv.}$	molecular weight of solvent (g.mol^{-1})
N_f	number of fibers in the membrane contactor
N	impeller speed (rad.s^{-1})
Q_f	feed flow rate ($\text{m}^3.\text{s}^{-1}$)
Re	Reynolds number
r_{pore}	pore radius (m)
S	selectivity

Sh	Sherwood number
Sc	Schmidt number
T	temperature (K)
t	extraction time (s)
V_f	feed phase volume (m ³)
$V_{solv.}$	molar volume (cm ³ .mol ⁻¹) of the solvent at their normal boiling temperature (K).
v_{IL}	Ionic liquid velocity (cm.s ⁻¹)
v_g	sweep gas velocity (cm.s ⁻¹)
w_{H_2O}	content in water (ppm)
x	mole fraction
$\mu_{solv.}$	viscosity of solvent (mPa.s)
\emptyset	association factor of solvent
Δm	weight increase (%)
$\Delta \delta$	thickness increase (%)
β	solvatochromic parameter – hydrogen bond basicity
ΔP	pressure drop (bar)
ΔP_{cr}	critical breakthrough pressure
π^*	solvatochromic parameter – dipolarity/polarisability
σ	surface polarity charge
γ	interfacial tension (N.m ⁻¹)
δ	thickness (m)
ε	porosity
θ	contact angle (° or rad)
μ	dynamic viscosity (Pa.s)
ρ	density (kg.m ⁻³)
τ	tortuosity

List of Tables

Table 3.1 Summary of the factors that influence the solubility and the performance of COSMO-RS.	44
Table 4.1 Summary of the different factors that influence the solubility, selectivity and distribution ratio, and the performance of COSMO-RS in describing these factors.	86
Table 4.2 COSMO-RS predicted selectivity and distribution ratio for several <i>n</i> -hexane + benzene + ionic liquid systems at 298.15K.	87
Table 5.1 Root mean square deviation (RMSD) between the compositions predicted by the COSMO-RS model and the experimental data for the ternary phase diagrams studied.	118
Table 6.1 Solvents (<i>n</i> -dodecane and ionic liquids) physical properties, at 298.2 K.	144
Table 6.2 Membrane support specifications and properties.	147
Table 6.3 Overall mass transfer and coefficient distribution ratio for the systems ionic liquid + 1-hexanethiol + <i>n</i> -dodecane, at 298.2 K and atmospheric pressure.	152
Table 6.4 Estimated diffusion of 1-hexanethiol in the <i>n</i> -dodecane and several ionic liquids, by the Scheibel ($\mathcal{D}_{Scheibel}$) and the Wilke-Chang ($\mathcal{D}_{Wilke - Chang}$) correlations, with the molar volume at the boiling point temperature calculated by the Schroeder correlation.	154
Table 6.5 a) Estimated individual mass transfer coefficients for the several tested ionic liquids, with the respective Reynolds, Schmidt and Sherwood numbers determined. ..	156
Table 6.6 Weight increase (Δm %) and thickness ($\Delta \delta$ %) after immobilization.	158
Table 7.1 Characteristics of the laboratory Liqui-cel MiniModule® and Extra-flow Module® Contactor, and respective hollow fibers properties, Celgard X-10 and Celgard X-50.	178

List of Figures

- Figure 3.1** Liquid–liquid phase diagram for [C₄mim][SCN] with *n*-hexane³² (◇) (—), benzene³² (▲) (—) and cyclohexane³² (◆) (= =). The symbols and the lines represent respectively the experimental data and the COSMO-RS prediction calculations. 25
- Figure 3.2** Liquid–liquid phase diagram for [C₄mim][SCN] with *n*-hexane³² (◇) (—), *n*-heptane³² (▲) (—), *n*-octane³² (●) (—), *n*-nonane³² (■) (—) and *n*-decane³² (◆) (—). The symbols and the lines represent respectively the experimental data and the COSMO-RS prediction calculations..... 27
- Figure 3.3** Liquid–liquid phase diagram for [C₄mim][CF₃SO₃]⁵⁰ (■) (—), [C₄mpyr][CF₃SO₃]⁵⁰ (▲) (—) and [1,3-C₄mpyr][CF₃SO₃]⁵⁰ (◇) (—) with *n*-hexane. The symbols and the lines represent respectively the experimental data and the COSMO-RS prediction calculations. 28
- Figure 3.4** Liquid–liquid phase diagram for [C₄mim][TOS]³⁶ (■) (—), [1,4-C₄mpyr][TOS]⁴⁹ (◇) (—) and [P_{i(444)1}][TOS]⁴⁷ (▲) (—) with *n*-hexane. The symbols and the lines represent respectively the experimental data and the COSMO-RS prediction calculations. 28
- Figure 3.5** Liquid–liquid phase diagram for [C₄mim][SCN]³² (■) (—) and [C₆mim][SCN]³⁸ (◇) (—) with *n*-hexane. The symbols and the lines represent respectively the experimental data and the COSMO-RS prediction calculations. 30
- Figure 3.6** Liquid–liquid phase diagram for [C₄mim][MeSO₄]³⁵ (●) (—), [C₄mim][PF₆]⁵¹ (◆) (—), [C₄mim][SCN]³² (■) (—), [C₄mim][TOS]³⁶ (×) (—), [C₄mim][CF₃SO₃]⁵⁰ (■) (—) and [C₄mim][MDEGSO₄]³⁹ (▲) (—) with *n*-hexane. The symbols and the lines represent respectively the experimental data and the COSMO-RS prediction calculations. 31
- Figure 3.7** Liquid–liquid phase diagram for [C₄mim][MeSO₄]³⁵ (●) (—) and [C₄mim][OcSO₄]³⁷ (◇) (—) with *n*-hexane. The symbols and the lines represent respectively the experimental data and the COSMO-RS prediction calculations. 32
- Figure 3.8** Liquid–liquid phase diagram for [C₄mim][TOS] with benzene³⁶ (▲) (—), toluene³⁶ (■) (—), ethylbenzene³⁶ (◆) (—) and propylbenzene³⁶ (●) (—). The symbols and the lines represent respectively the experimental data and the COSMO-RS prediction calculations. 34

- Figure 3.9** Liquid–liquid phase diagram for [C₄mim][MeSO₄] with *o*-xylene³⁵ (■) (– · –), *m*-xylene³⁵ (◆) (– – –) and *p*-xylene³⁵ (▲) (—). The symbols and the lines represent respectively the experimental data and the COSMO-RS prediction calculations. 34
- Figure 3.10** Liquid–liquid phase diagram for [C₄mim][CF₃SO₃]⁵⁰ (■) (– · –), [C₄mpyr][CF₃SO₃]⁵⁰ (▲) (—) and [1,3-C₄mpy][CF₃SO₃]⁵⁰ (◆) (—) with benzene. The symbols and the lines represent respectively the experimental data and the COSMO-RS prediction calculations. 36
- Figure 3.11** Liquid–liquid phase diagram for [C₄mim][TOS]³⁶ (■) (– · –), [1,4-C₄mpy][TOS]⁴⁹ (◆) (—) and [P₍₄₄₄₎₁][TOS]⁴⁷ (▲) (—) with toluene. The symbols and the lines represent respectively the experimental data and the COSMO-RS prediction calculations. 36
- Figure 3.12** Liquid–liquid phase diagram for [C₁mim][MeSO₄]³³ (▲) (—) and [C₄mim][MeSO₄]³⁵ (■) (– · –) with benzene. The symbols and the lines represent respectively the experimental data and the COSMO-RS prediction calculations. 37
- Figure 3.13** Liquid–liquid phase diagram for [C₂mim][NTf₂]⁴⁶ (●) (—), [C₄mim][NTf₂]⁴⁶ (■) (– · –), [C₆mim][NTf₂]⁴⁶ (◆) (—), [C₈mim][NTf₂]⁴⁶ (▲) (·····) and [C₁₀mim][NTf₂]⁴⁶ (◆) (— · ·) with benzene. The symbols and the lines represent respectively the experimental data and the COSMO-RS prediction calculations. 38
- Figure 3.14** Liquid–liquid phase diagram for [C₄mim][MeSO₄]³⁵ (●) (– · –), [C₄mim][PF₆]⁵¹ (⊗) (—), [C₄mim][BF₄]⁶³ (●) (—), [C₄mim][NTf₂]⁴⁶ (◆) (– · –), [C₄mim][SCN]³² (■) (– · –), [C₄mim][TOS]³⁶ (×) (—), [C₄mim][CF₃SO₃]⁵⁰ (■) (—) and [C₄mim][MDEGSO₄]³⁹ (▲) (– – –) with benzene. The symbols and the lines represent respectively the experimental data and the COSMO-RS prediction calculations. 39
- Figure 3.15** Liquid–liquid phase diagram for [C₆mim][SCN] with cyclohexane³⁸ (◆) (– –) and cycloheptane³⁸ (▲) (— · –). The symbols and the lines represent respectively the experimental data and the COSMO-RS prediction calculations. 40
- Figure 3.16** Liquid–liquid phase diagram for [C₄mim][CF₃SO₃]⁵⁰ (■) (– · –), [C₄mpyr][CF₃SO₃]⁵⁰ (▲) (—) and [1,3-C₄mpy][CF₃SO₃]⁵⁰ (◆) (—) with cyclohexane. The symbols and the lines represent respectively the experimental data and the COSMO-RS prediction calculations. 41
- Figure 3.17** Liquid–liquid phase diagram for [C₄mim][SCN]³² (■) (– · –) and [C₆mim][SCN]³⁸ (◆) (—) with cyclohexane. The symbols and the lines represent respectively the experimental data and the COSMO-RS prediction calculations. 42

Figure 3.18 Liquid–liquid phase diagram for $[\text{C}_4\text{mim}][\text{PF}_6]$ ⁵¹ (●) (—), $[\text{C}_4\text{mim}][\text{SCN}]$ ³² (■) (- · -), $[\text{C}_4\text{mim}][\text{CF}_3\text{SO}_3]$ ⁵⁰ (□) (= =) and $[\text{C}_4\text{mim}][\text{MDEGSO}_4]$ ³⁹ (△) (- - -) with cyclohexane. The symbols and the lines represent respectively the experimental data and the COSMO-RS prediction calculations. 43

Figure 4.1 a) Experimental and COSMO-RS predicted tie-lines, b) selectivity and c) distribution ratio for the LLE of the ternary systems *n*-hexane + benzene + $[\text{C}_2\text{mim}][\text{EtSO}_4]$ ³² (full diamonds and solid line for experimental data; and empty diamonds and dotted line for COSMO-RS predicted values), and cyclohexane + benzene + $[\text{C}_2\text{mim}][\text{EtSO}_4]$ ⁹ (full triangles and solid line for experimental data; and empty triangles and short dashed line for COSMO-RS predicted values) at 298.15K..... 60

Figure 4.2 a) Experimental and COSMO-RS predicted tie-lines, b) selectivity and c) distribution ratio for the LLE of the ternary systems *n*-hexane + benzene + $[\text{C}_2\text{mim}][\text{EtSO}_4]$ ³² (full diamonds and solid line for experimental data; and empty diamonds and dotted line for COSMO-RS predicted values), *n*-heptane + benzene + $[\text{C}_2\text{mim}][\text{EtSO}_4]$ ³² (full triangles and solid line for experimental data; and empty crossed triangles and dashed line for COSMO-RS predicted values), *n*-octane + benzene + $[\text{C}_2\text{mim}][\text{EtSO}_4]$ ³² (full circles and solid line for experimental data; and empty crossed circles and dot dashed line for COSMO-RS predicted values) and *n*-nonane + benzene + $[\text{C}_2\text{mim}][\text{EtSO}_4]$ ³² (full squares and solid line for experimental data; and empty crossed squares and dot-dot dashed line for COSMO-RS predicted values) at 298.15K..... 63

Figure 4.3 a) Experimental and COSMO-RS predicted tie-lines, b) selectivity and c) distribution ratio for the LLE of the ternary systems *n*-hexane + benzene + $[1,3\text{C}_2\text{mpy}][\text{EtSO}_4]$ ¹⁰ (full triangles and solid line for experimental data; and empty dotted triangles and dashed line for COSMO-RS predicted values), *n*-hexane + toluene + $[1,3\text{C}_2\text{mpy}][\text{EtSO}_4]$ ²⁰ (full squares and solid line for experimental data; and empty dotted squares and dotted line for COSMO-RS predicted values), and *n*-hexane + ethylbenzene + $[1,3\text{C}_2\text{mpy}][\text{EtSO}_4]$ ²⁰ (full diamonds and solid line for experimental data; and empty dotted diamonds and dot dashed line for COSMO-RS predicted values), at 298.15K.... 66

Figure 4.4 a) Experimental and COSMO-RS predicted tie-lines, b) selectivity and c) distribution ratio for the LLE of the ternary systems *n*-hexane + *o*-xylene + $[1,3\text{C}_2\text{mpy}][\text{EtSO}_4]$ ² (full squares and solid line for experimental data; and empty dotted squares and dot-dot dashed line for COSMO-RS predicted values), *n*-hexane + *m*-xylene + $[1,3\text{C}_2\text{mpy}][\text{EtSO}_4]$ ² (full diamonds and solid line for experimental data; and empty dotted diamonds and dotted line for COSMO-RS predicted values), and *n*-hexane + *p*-

xylene + [1,3C₂mpy][EtSO₄]² (full triangles and solid line for experimental data; and empty dotted triangles and dotted line for COSMO-RS predicted values) at 298.15K. .. 67

Figure 4.5 a) Experimental and COSMO-RS predicted tie-lines, b) selectivity and c) distribution ratio for the LLE of the ternary systems *n*-hexane + benzene + [C₂mim][EtSO₄]³² (full square and solid line for experimental data; and empty dotted square and dot dashed line for COSMO-RS predicted values) and *n*-hexane + benzene + [1,3C₂mpy][EtSO₄]¹⁰ (full diamonds and solid line for experimental data; and empty dotted diamonds and long dashed line for COSMO-RS predicted values) at 298.15K... 70

Figure 4.6 a) Experimental and COSMO-RS predicted tie-lines, b) selectivity and c) distribution ratio for the LLE of the ternary systems *n*-hexane + benzene + [C₂mim][NTf₂]³ (full square and solid line for experimental data; and empty dotted square and dot dashed line for COSMO-RS predicted values), *n*-hexane + benzene + [N₂(2OH)_{1,1}][NTf₂]²⁷ (full circles and solid line for experimental data; and empty dotted circles and dotted line for COSMO-RS predicted values), and *n*-hexane + benzene + [P_{666 14}][NTf₂]³ (full triangle and solid line for experimental data) at 298.15K..... 71

Figure 4.7 a) Experimental and COSMO-RS predicted tie-lines, b) selectivity and c) distribution ratio for the LLE of the ternary systems *n*-heptane + toluene + [1,2C₄mpy][BF₄]³³ (full squares and solid line for experimental data; and empty dotted squares and dot-dot dashed line for COSMO-RS predicted values), *n*-heptane + toluene + [1,3C₄mpy][BF₄]³³ (full diamonds and solid line for experimental data; and empty dotted diamonds and dashed line for COSMO-RS predicted values), and *n*-heptane + toluene + [1,4C₄mpy][BF₄]³³ (full triangles and solid line for experimental data; and empty dotted triangles and dotted line for COSMO-RS predicted values) at 313.2K. 72

Figure 4.8 a) Experimental and COSMO-RS predicted tie-lines, b) selectivity and c) distribution ratio for the LLE of the ternary systems *n*-hexane + benzene + [C₂mim][NTf₂]³ (full circles and solid line for experimental data; and empty dotted circles and long dashed line for COSMO-RS predicted values e), *n*-hexane + benzene + [C₄mim][NTf₂]²⁹ (full squares and solid line for experimental data; and empty dotted squares and dot dashed line for COSMO-RS predicted values), *n*-hexane + benzene + [C₈mim][NTf₂]²⁹ (full diamonds and solid line for experimental data; and empty dotted diamonds and short dashed line for COSMO-RS predicted values), *n*-hexane + benzene + [C₁₀mim][NTf₂]²⁹ (full triangles and solid line for experimental data; and empty dotted triangles and dotted line for COSMO-RS predicted values), and *n*-hexane + benzene + [C₁₂mim][NTf₂]²⁹ (full crosses and solid line for experimental data; and empty crosses and dot-dot dashed line for COSMO-RS predicted values) at 298.15K. 75

Figure 4.9 a) Experimental and COSMO-RS predicted tie-lines, b) selectivity and c) distribution ratio for the LLE of the ternary systems *n*-hexane + benzene + [C₂mim][EtSO₄]¹³ (full diamonds and solid line for experimental data; and empty dotted diamonds and dot dashed line for COSMO-RS predicted values), and *n*-hexane + benzene + [C₂mim][NTf₂]³ (full circles and solid line for experimental data; and empty dotted circles and long dashed line for COSMO-RS predicted values), at 298.15K. 78

Figure 4.10 a) Experimental and COSMO-RS predicted tie-lines, b) selectivity and c) distribution ratio for the LLE of the ternary systems *n*-heptane + toluene + [C₄mim][SCN]¹⁷ (full squares and solid line for experimental data; and empty dotted squares and dotted line for COSMO-RS predicted values), *n*-heptane + toluene + [C₄mim][DCA]¹⁷ (full triangles and solid line for experimental data; and empty dotted triangles and long dashed line for COSMO-RS predicted values) at 303.15K and *n*-heptane + toluene + [C₄mim][MeSO₄]⁴⁰ (full circles and solid line for experimental data; and empty dotted circles and dot-dot dashed line) at 313.15K..... 79

Figure 4.11 a) Experimental and COSMO-RS predicted tie-lines, b) selectivity and c) distribution ratio for the LLE of the ternary systems *n*-heptane + toluene + [C₆mim][PF₆]³⁷ (full diamonds and solid line for experimental data; and empty dotted diamonds and dot dashed line for COSMO-RS predicted values) and *n*-heptane + toluene + [C₆mim][BF₄]³⁷ (full squares and solid line for experimental data; and empty dotted squares and dot-dot dashed line for COSMO-RS predicted values) at 298.15K. 80

Figure 4.12 a) Experimental and COSMO-RS predicted tie-lines, b) selectivity and c) distribution ratio for the LLE of the ternary systems *n*-hexane + benzene + [C₂mim][EtSO₄]³² (full circles and solid line for experimental data; and empty crossed circles and long dashed line for COSMO-RS predicted values) and *n*-hexane + benzene + [C₂mim][OcSO₄]¹⁵ (full diamonds and solid line for experimental data; and empty crossed diamonds and short dashed line for COSMO-RS predicted values), at 298.15K. 81

Figure 4.13 a) Experimental and COSMO-RS predicted tie-lines, b) selectivity and c) distribution ratio for the LLE of the ternary systems *n*-hexane + benzene + [1,3C₂mpy][EtSO₄] at the temperatures 283.15K¹⁰ (full triangles and solid line for experimental data; and empty triangles and long dashed line for COSMO-RS predicted values), 293.15K¹⁰ (full circles and solid line for experimental data; and empty circles and short dashed line for COSMO-RS predicted values), 298.15K¹⁰ (full squares and solid line for experimental data; and empty squares and dot dashed line for COSMO-RS

predicted values), and 303.15K ¹⁰ (full diamonds and solid line for experimental data; and empty diamonds and dotted line for COSMO-RS predicted values).	83
Figure 5.1 Experimental and COSMO-RS predicted tie-lines for the LLE of ternary systems composed of [C ₂ mim]-based ionic liquids + 1-hexanethiol + <i>n</i> -dodecane (full symbols and solid lines for experimental data, and empty symbols and dashed lines for COSMO-RS predicted values), at 298.2 K and atmospheric pressure.	106
Figure 5.2 Experimental and COSMO-RS predicted tie-lines for the LLE of ternary systems composed of [C ₂ mpy]-based ionic liquids + 1-hexanethiol + <i>n</i> -dodecane (full symbols and solid lines for experimental data, and empty symbols and dashed lines for COSMO-RS predicted values), at 298.2 K and atmospheric pressure.	107
Figure 5.3 Experimental and COSMO-RS predicted tie-lines for the LLE of ternary systems composed of ionic liquids+ 1-hexanethiol + <i>n</i> -dodecane (full symbols and solid lines for experimental data, and empty symbols and dashed lines for COSMO-RS predicted values), at 313.2 K and atmospheric pressure.....	108
Figure 5.4 Experimental and COSMO-RS predicted tie-lines for the LLE of ternary systems composed of [C ₄ mim]-based ionic liquids + 1-hexanethiol + <i>n</i> -dodecane (full symbols and solid lines for experimental data, and empty symbols and dashed lines for COSMO-RS predicted values), at 298.2 K and atmospheric pressure.	109
Figure 5.5 Experimental and COSMO-RS predicted distribution ratio of 1-hexanethiol in the ternary systems: a) [cation][CH ₃ SO ₃] + 1-hexanethiol + <i>n</i> -dodecane; and b) [cation][NTf ₂]+ 1-hexanethiol + <i>n</i> -dodecane, at 298.2 K and atmospheric pressure.....	112
Figure 5.6 Experimental and COSMO-RS predicted distribution ratio of 1-hexanethiol in the ternary systems: a) [C _{<i>n</i>} mim][MeSO ₄] + 1-hexanethiol + <i>n</i> -dodecane; b) [C _{<i>n</i>} mim][CF ₃ SO ₃]+ 1-hexanethiol + <i>n</i> -dodecane; and c) [C _{<i>n</i>} mim][NTf ₂] + 1-hexanethiol + <i>n</i> -dodecane, at 298.2 K and atmospheric pressure.	113
Figure 5.7 Experimental and COSMO-RS predicted distribution ratio of 1-hexanethiol in the ternary systems: a) [C ₂ mim][anion] + 1-hexanethiol + <i>n</i> -dodecane; b) [C ₄ mim][anion] + 1-hexanethiol + <i>n</i> -dodecane; and c) [C ₂ mpy][anion] + 1-hexanethiol + <i>n</i> -dodecane, at 298.2 K and atmospheric pressure.....	114
Figure 5.8 Experimental and COSMO-RS predicted distribution ratio of 1-hexanethiol in the ternary systems: a) [C ₂ mim][CF ₃ SO ₃] + 1-hexanethiol + <i>n</i> -dodecane, and b) [C ₂ mim][CH ₃ SO ₃] + 1-hexanethiol + <i>n</i> -dodecane, at the temperatures 298.2 K and 313.2 K, and atmospheric pressure.	115

- Figure 5.9** Experimental distribution ratio of 1-hexanethiol in the ternary systems [C₂mim][MeSO₄] + 1-hexanethiol + *n*-dodecane with ionic liquid water content of 130 ppm, and 6840 ppm H₂O; and [C₂mim][CF₃SO₃] + 1-hexanethiol + *n*-dodecane with ionic liquid water content of 305 ppm, and 6583 ppm H₂O, at 298.2 K and atmospheric pressure..... 116
- Figure 6.1** 1-hexanethiol experimental concentration profile in the dodecane and ionic liquid rich-phases (filled and empty symbols, respectively), and data fitting (lines) at 298.2 K and atmospheric pressure, using different extracting ionic liquids: a) [C₂mim][MeSO₄] (diamonds and dot-dashed line), b) [C₂mim][CF₃SO₃] (squares and dotted line), c) [C₂mim][NTf₂] (triangles and dashed line). And d) comparison between the three extraction systems studied (dodecane phase)..... 151
- Figure 6.2** Contact angle of the ionic liquid [C₂mim][CF₃SO₃] with a) the hydrophobic PVDF membrane, and b) the PP membrane. 158
- Figure 6.3** SILM ionic liquid loss along time, for the SILMs composed by PVDF hydrophobic (full symbols) and hydrophilic (dotted symbols), with the ionic liquids [C₂mim][CF₃SO₃] (black symbols and solid line), [C₂mim][NTf₂] (grey symbols and dot-dashed line), and [C₂mim][MeSO₄] (white symbols and dashed line), for positive pressure differences of 0.5 bar (circles), 1.0 bar (squares), 1.4 bar (hexagons), 1.5 bar (diamonds), 1.6 bar (cross), 1.8 bar (inverse triangles), and 2.0 bar (triangles), using a nitrogen gas stream on the AmiconTH 8010 cell. 159
- Figure 6.4** Pressure profile in the permeate side, when applying a negative pressure difference across the hydrophobic PVDF/ionic liquid SILM. Feed compartment: air at atmospheric pressure; Downstream compartment: vacuum at a starting pressure of 0.9 mbar..... 160
- Figure 6.5** Pressure profile in the permeate side, for the *n*-dodecane permeation when applying a negative pressure difference across a) [C₂mim][CF₃SO₃]-based SILMs with different membrane supports; and b) a dense PVDF membrane. A proposed scheme for the *n*-dodecane transport occurring in SILMs is illustrated in c). 162
- Figure 6.6** Mercaptan and *n*-dodecane transport through the membrane under different operating modes with an ionic liquid as the receptor phase, using a) a membrane wetted or b) a membrane not wetted by the ionic liquid. 163
- Figure 6.7** 1-hexanethiol experimental concentration profile in the *n*-dodecane feed phase (filled squares) and ionic liquid receiving phase (empty squares), for the extraction in a Liqui-cel MiniModule[®] Contactor with microporous polypropylene hollow fiber

membranes (Celgard® X-10), at 298.2 K and atmospheric pressure. Shell side: jet-fuel model (1-hexanethiol + *n*-dodecane); Lumen side: ionic liquid ([C₂mim][CF₃SO₃]). 164

Figure 7.1 Experimental set-up. A indicates the ionic liquid direction in the single extraction configuration, and B in the integrated extraction and regeneration configuration. a) extraction hollow fiber membrane contactor, b) regeneration hollow fiber membrane contactor, c) feed stirred vessel, d) ionic liquid stirred vessel, e) recirculating pump, PI = pressure indicator, and FI = flow indicator..... 180

Figure 7.2 1-hexanethiol experimental concentration profile in the *n*-dodecane and ionic liquid rich-phases (filled and empty symbols, respectively), and data fitting (lines), for the single extraction configuration, at 298.2 K and atmospheric pressure. *Extraction module*: shell side – jet-fuel model stream (1-hexanethiol + *n*-dodecane); lumen side – ionic liquid ([C₂mim][CF₃SO₃]). 187

Figure 7.3 1-hexanethiol experimental concentration profile in the *n*-dodecane and ionic liquid phases (filled and empty symbols, respectively), for the extraction/vacuum stripping configuration, at 298.2 K and atmospheric pressure. *Extraction module*: shell side – jet-fuel model stream (1-hexanethiol + *n*-dodecane); lumen side – ionic liquid ([C₂mim][CF₃SO₃]). *Regeneration module*: shell side – vacuum; lumen side – ionic liquid ([C₂mim][CF₃SO₃]). 189

Figure 7.4 1-hexanethiol experimental concentration profile in the *n*-dodecane and ionic liquid phases (filled and empty symbols, respectively) and data fitting (lines), for the extraction/sweep gas stripping configurations, at 298.2 K and atmospheric pressure, with a) sweep gas velocity of 1.23 cm.s⁻¹ (square symbols and dot-dashed lines), b) sweep gas velocity of 7.84 cm.s⁻¹ (triangle symbols and dotted lines) and c) sweep gas velocity of 19.30 cm.s⁻¹ (diamond symbols and dashed lines). 191

Figure 7.5 Simulated 1-hexanethiol concentration profile varying a) the ionic liquid velocity and b) the operating temperature. In c) the simulation is obtained combining both parameters studied in a) and b). 193

Chapter 1

General Introduction

1.1. General Context

Petroleum industries are committed to reducing their sulfur emissions and improve existing or develop new desulfurization technologies, both to comply with regulatory requirements, and optimize the fuel economy achieving a superior treatment capacity.

Sulfur emissions from fossil fuels, coal and chemical burning, as well as by refinery industries have a great impact in human health and in the overall environment. The release of sulfur compounds is responsible for the production of SO_x, which additionally lead to acid rain, ozone depletion, and respiratory insufficiency in humans. Regarding the fuel use, the presence of these sulfurous compounds on fuel acts as a catalyst poison either on the control systems of exhaust emissions by fuel engine's, as in catalyst-aided refinery processes. These compounds deactivate the catalytic converters which further inhibit the pollution control and lead to the release of additional toxic and volatile organic compounds.¹ To minimize these major environmental and health concerns, the authorities implemented more strict policies towards more stringent limits on the fuel sulfur content, envisaging the use of ultra-low sulfur fuels (< 10 ppm S).²⁻³

However, the availability of crudes reserves with superior quality, i.e., with low sulfur content, is decreasing turning refining industries prospect crudes heavier and sourer. The sulfur levels on these crudes can reach values up to 3.5% wt, that are much higher than the found on the light and sweet crudes, commonly treated due to their relative easy and cheap desulfurization.⁴ Obviously, this quality deterioration on the supply side, and the more strict fuel specifications on the demand side, hinder the conventional desulfurization processes capacity and efficiency, demanding an expansion and upgrade of the desulfurization processes.⁵

Along with gasoline and diesel fuel, jet-fuel also follows the growing trend on the worldwide fuel transportation demand, although more steadily.⁵ The current jet-fuel specification allows 3000 ppm of total sulfur, being 30 ppm in the form of mercaptan species (R-SH, R = radical). However, ongoing trends and initiatives expect to reduce these maximum levels of total sulfur down to 350 ppm in 2020, and 50 ppm in 2025.⁵ These facts maintain the interest from industry and research community, reflecting the need of deeper desulfurization for the heavy and inferior crudes to attain the more stringent fuel quality specifications for sulfur content.

The removal of sulfur from fuel streams in the refining industry is currently and primarily carried out by hydrodesulfurization processes, which consist mainly in a catalytic hydrogenation of the organic sulfur compounds, at very high temperatures and hydrogen

partial pressures, 300 – 400 °C and 20 – 100 atm of hydrogen, respectively, producing hydrogen sulfide (H₂S), converted to elemental sulfur in a subsequent recovery sulfur unit (Claus process). The extremely demanding operating conditions make this process very costly, in particular when high molecular weight and more stable sulfur compounds are presented in the fuel, requiring higher residence time and much more severe operating conditions.¹ Concerning the sulfur species, mercaptans (aliphatic sulfur compounds) can also be removed by a sweetening process known as Merox ®, where a liquid-liquid extraction with sodium hydroxide is aided with a catalytic oxidation by air.^{3, 6} For heavier fractions, this process gets more difficult and fixed-bed sweetening alternatives are used.³ Therefore, the refining industry demands a quality upgrading of the existing desulfurization technologies and a continuous development of new alternative approaches. Their goal is to produce ultra-low sulfur fuel at moderate operating conditions, reducing costs with energy and reagents, when compared to the conventional, expensive and difficult desulfurization processes, in the presence of stable or higher molecular weight sulfur compounds.⁴

The challenges presented are being pursued by several research groups, and comprise the development of a more active catalyst for the traditional catalytic hydrodesulfurization, or new alternatives such as oxidative, adsorptive, extractive and biological desulfurization processes, and their combinations.^{2-4, 7-8}

Regarding the desulfurization at mild operating conditions of temperature and pressure, ionic liquids-based processes have shown a high potential.^{7, 9-18 19} Ionic liquids belong to the molten salts group and are generally composed of bulky and asymmetric organic cations and organic or inorganic anions (Appendix A). Most ionic liquids exhibit desirable attributes, namely a negligible vapor pressure, a wide temperature range where they are liquid, high thermal and chemical stabilities, and a good solvating capacity for both organic and inorganic compounds, among others.¹⁹ Therefore, ionic liquids appear as more attractive and competitive solvents compared to the conventional volatile organic solvents, especially due to their negligible vapor pressure and high thermal stability. Additionally, the huge number of possible ionic liquids that can be synthesized by a proper selection of the cation/anion combinations allows for tuning their solvation ability for a variety of solutes. This tailoring feature should make possible to choose an ionic liquid that presents reduced solubility in the feed liquid phase and a high affinity for the target solute to be removed.

Several works have been addressing the use of ionic liquids for the removal of sulfur-compounds from distilled streams, such as gasoline, kerosene and diesel.^{7, 9, 11-17} These studies comprise different forms of desulfurization processes and among them, one may find liquid-liquid extraction,^{17, 20-28} and simultaneous oxidation,^{9, 16, 29-36} oxidative extraction,^{35, 37-38} and the use of ionic liquids in membranes or solid particles.^{15, 39-41} Most studies have focused on aromatic sulfur compounds^{1, 3} (thiophene, benzothiophene, benzothiophene and their derivatives) and only very few studies have been reported in the literature regarding the aliphatic analogues.^{15, 42-43}

Taking into account the scarcity of reported results concerning the removal of mercaptans,^{15, 42-43} this work aims at studying the ionic liquids as potential extracting solvents for organosulfur compounds with the sulfhydryl group and a sided alkyl chain (R-SH), considering kerosene as the fuel fraction to be treated for the production of jet-fuel.

1.2. Scope and objectives

Aiming at replacing the current inefficient and expensive desulfurization processes, ionic liquids have been considered as potential solvents to be used in extraction procedures. In this context, this work provides an evaluation on the feasibility of ionic liquids for the selective extraction of a less studied class of aliphatic sulfur compounds – mercaptans - from “jet-fuel”.

For this desulfurization process, one of the most crucial features is the very low mutual solubility that the selected ionic liquid must exhibit with the hydrocarbons present in the jet-fuel matrix. This is very important in order to avoid contaminations of the fuel stream that can prevent the use of fuel, and losses of hydrocarbons for the extracting solvent. The knowledge of the mutual solubilities between ionic liquids and hydrocarbons is therefore required. The design and selection of the most suitable ionic liquid to be applied through experimental screening is unfeasible due to the huge number of possible combinations between ionic liquids and hydrocarbons. In this context, an evaluation of the performance of COnductor-like Screening MOdel for Real Solvents is provided (COSMO-RS theory described in **Chapter 2**), as a predictive tool to describe the liquid-liquid equilibria of binary and ternary systems, composed by ionic liquids and hydrocarbons.

In **Chapter 3** and **Chapter 4**, reviews of the experimental data of phase behavior concerning ionic liquids and hydrocarbons, available in the literature, are reported. The effect of various structural features of both the ionic liquids and the hydrocarbons through their mutual solubilities behavior is also discussed here. **Chapter 3** reports the study concerning binary systems and **Chapter 4** ternary systems. The gathered information was shown to be essential to the understanding of the molecular interactions and the effect of the various structural features of both the ionic liquids and the hydrocarbons on their phase behavior, allowing the development of guidelines for the choice of the most suitable ionic liquid for target solute separation. It is shown that COSMO-RS provides a correct qualitative trend of the phase behavior dependence regarding the ionic liquids and molecular compounds nature. Therefore, COSMO-RS can be a useful predictive tool with a great potential in the screening of ionic liquids for specific extraction applications.

In **Chapter 5**, the best potential candidates for the extraction of mercaptans from a feed model of kerosene in “jet-fuel” composed a mixture of *n*-dodecane and 1-hexanethiol were assessed. Tie-lines for the ternary systems jet-fuel model and the imidazolium- and pyridinium-based ionic liquids were experimentally measured, at 298.2 K and 313.2 K,

along with the determination of the distribution ratio and selectivity. Using the experimental data determined, the COSMO-RS was also evaluated for the predictions of the liquid-liquid equilibrium of the investigated systems. The extraction behavior with other ionic liquids not experimentally tested was also predicted by COSMO-RS, which allowed an extended screening of the best potential ionic liquids candidates as desulfurization solvents of the target mercaptan. These systems displayed a very high selectivity meaning that the co-extraction of the rest of the fuel compounds can be avoided. However, for the systems at which the co-extraction of the other fuel compounds was prevented, the distribution ratio of the mercaptan towards the ionic liquid was unfavorable. As a result of this limitation, conventional liquid-liquid extraction processes are unfeasible due to the high volume of ionic liquid required. On the other hand, the high selectivity displayed by these systems, still award ionic liquids with a high potential to be applied in separation processes controlled by mass transfer kinetics.

Chapter 6 presents the work developed for a possible application of ionic liquids in an extraction process assisted by membranes. This approach consisted in the use of supported ionic liquid membranes (SILMs) applying vacuum in the downstream side. Here, despite the negligible mutual solubility between *n*-dodecane and the studied ionic liquids, the *n*-dodecane permeated through the membrane support, invalidating the use of SILMs in the specific task of this work. To solve this problem, a second alternative was explored, where the ionic liquid was used as receiving phase in a hollow fibre membrane contactor. Under these conditions, no *n*-dodecane was detected in the receiving ionic liquid phase, which opened a very promising opportunity for integrated extraction/stripping processes of mercaptans from “jet-fuel” streams.

Taking the last results into account, a new methodology for the desulfurization of “jet-fuel” stream is proposed in **Chapter 7**. It consists in a liquid extraction of the mercaptan, using a pre-selected ionic liquid as extracting solvent (1-ethyl-3-methylimidazolium triflate [C₂mim][CF₃SO₃]), followed by its regeneration in an additional step, aiming at maximizing the concentration gradient and an extraction process free of thermodynamic constraints. The performance of two regeneration methods was assessed: stripping applying vacuum and stripping using a sweep gas, both applied in the downstream side of the membrane.

Finally, **Chapter 8** presents the general conclusions and summarizes the achievements of this work and proposes suggestions for further development of this new technology for desulfurization of sulfur compounds from fuels using ionic liquids and hollow fiber membrane contactors.

1.3. References

1. Pawelec, B.; Navarro, R. M.; Campos-Martin, J. M.; Fierro, J. L. G., Towards near zero-sulfur liquid fuels: a perspective review. *Catal Sci Tec* **2011**, 1 (1), 23-42.
2. Song, C., An overview of new approaches to deep desulfurization for ultra-clean gasoline, diesel fuel and jet fuel. *Catal Today* **2003**, 86 (1–4), 211-263.
3. Srivastava, V. C., An evaluation of desulfurization technologies for sulfur removal from liquid fuels. *Rsc Adv* **2012**, 2 (3), 759-783.
4. EIA, U. S. Crude oils have different quality characteristics. http://www.eia.gov/todayinenergy/detail.cfm?id=7110#_(accessed 4/3/2014).
5. OPEC, *World Oil Outlook 2013*. 2013.
6. de Angelis, A., Natural gas removal of hydrogen sulphide and mercaptans. *Appl Catal B* **2012**, 113–114 (0), 37-42.
7. Francisco, M.; Arce, A.; Soto, A., Ionic liquids on desulfurization of fuel oils. *Fluid Phase Equilib* **2010**, 294 (1-2), 39-48.
8. Kulkarni, P. S.; Afonso, C. A. M., Deep desulfurization of diesel fuel using ionic liquids: current status and future challenges. *Green Chem* **2010**, 12 (7), 1139-1149.
9. Liang, W. D.; Zhang, S.; Li, H. F.; Zhang, G. D., Oxidative desulfurization of simulated gasoline catalyzed by acetic acid-based ionic liquids at room temperature. *Fuel Process Technol* **2013**, 109, 27-31.
10. Wang, X. M.; Wan, H.; Han, M. J.; Gao, L.; Guan, G. F., Removal of Thiophene and Its Derivatives from Model Gasoline Using Polymer-Supported Metal Chlorides Ionic Liquid Moieties. *Ind Eng Chem Res* **2012**, 51 (8), 3418-3424.
11. Wang, J. L.; Zhao, D. S.; Li, K. X., Extractive Desulfurization of Gasoline Using Ionic Liquid Based on CuCl. *Pet Sci Technol* **2012**, 30 (23), 2417-2423.
12. Li, F. T.; Liu, Y.; Sun, Z. M.; Chen, L. J.; Zhao, D. S.; Liu, R. H.; Kou, C. G., Deep Extractive Desulfurization of Gasoline with xEt(3)NHCl center dot FeCl3 Ionic Liquids. *Energ Fuel* **2010**, 24, 4285-4289.
13. Alonso, L.; Arce, A.; Francisco, M.; Rodriguez, O.; Soto, A., Gasoline desulfurization using extraction with [C-8 mim][BF4] ionic liquid. *Aiche J* **2007**, 53 (12), 3108-3115.
14. Huang, C. P.; Chen, B. H.; Zhang, J.; Liu, Z. C.; Li, Y. X., Desulfurization of gasoline by extraction with new ionic liquids. *Energ Fuel* **2004**, 18 (6), 1862-1864.

15. Kuhlmann, E.; Haumann, M.; Jess, A.; Seeberger, A.; Wasserscheid, P., Ionic Liquids in Refinery Desulfurization: Comparison between Biphasic and Supported Ionic Liquid Phase Suspension Processes. *Chemsuschem* **2009**, 2 (10), 969-977.
16. Taha, M. F.; Atikah, N.; Chong, F. K.; Shaharun, M. S., Oxidative Desulfurization of Dibenzothiophene From Model Oil Using Ionic Liquids As Extracting Agent. *Aip Conf Proc* **2012**, 1482, 258-262.
17. de Oliveira, L. H.; Alvarez, V. H.; Aznar, M., Liquid-Liquid Equilibrium in N-Methyl-2-hydroxyethylammonium Acetate, Butanoate, or Hexanoate Ionic Liquids plus Dibenzothiophene plus n-Dodecane Systems at 298.2 K and Atmospheric Pressure. *J Chem Eng Data* **2012**, 57 (3), 744-750.
18. Varma, N. R.; Ramalingam, A.; Banerjee, T., Experiments, correlations and COSMO-RS predictions for the extraction of benzothiophene from n-hexane using imidazolium-based ionic liquids. *Chem Eng J* **2011**, 166 (1), 30-39.
19. Werner, S.; Haumann, M.; Wasserscheid, P., Ionic Liquids in Chemical Engineering. *Annu Rev Chem Biomol* **2010**, 1, 203-230.
20. Rodríguez-Cabo, B.; Arce, A.; Soto, A., Desulfurization of fuels by liquid-liquid extraction with 1-ethyl-3-methylimidazolium ionic liquids. *Fluid Phase Equilib* **2013**, 356 (0), 126-135.
21. Krolikowski, M.; Walczak, K.; Domanska, U., Solvent extraction of aromatic sulfur compounds from n-heptane using the 1-ethyl-3-methylimidazolium tricyanomethanide ionic liquid. *J Chem Thermodyn* **2013**, 65, 168-173.
22. Gabric, B.; Sander, A.; Bubalo, M. C.; Macut, D., Extraction of S- and N-Compounds from the Mixture of Hydrocarbons by Ionic Liquids as Selective Solvents. *Sci World J* **2013**.
23. Domańska, U.; Lukoshko, E. V.; Królikowski, M., Separation of thiophene from heptane with ionic liquids. *J Chem Therm* **2013**, 61 (0), 126-131.
24. Dharaskar, S. A.; Wasewar, K. L.; Varma, M. N.; Shende, D. Z.; Yoo, C. K., Deep Removal of Sulfur from Model Liquid Fuels using 1-Butyl-3-Methylimidazolium Chloride. *Procedia Engineering* **2013**, 51 (0), 416-422.
25. Wilfred, C. D.; Kiat, C. F.; Man, Z.; Bustam, M. A.; Mutalib, M. I. M.; Phak, C. Z., Extraction of dibenzothiophene from dodecane using ionic liquids. *Fuel Process Technol* **2012**, 93 (1), 85-89.

26. Kedra-Krolik, K.; Mutelet, F.; Moise, J. C.; Jaubert, J. N., Deep Fuels Desulfurization and Denitrogenation Using 1-Butyl-3-methylimidazolium Trifluoromethanesulfonate. *Energ Fuel* **2011**, *25* (4), 1559-1565.
27. Wang, Y.; Li, H.; Zhu, W.; Jiang, X.; He, L.; Lu, J.; Yan, Y., The Extractive Desulfurization of Fuels Using Ionic Liquids Based on FeCl₃. *Pet Sci Technol* **2010**, *28* (12), 1203-1210.
28. Yu, G. R.; Li, X.; Liu, X. X.; Asumana, C.; Chen, X. C., Deep Desulfurization of Fuel Oils Using Low-Viscosity 1-Ethyl-3-methylimidazolium Dicyanamide Ionic Liquid. *Ind Eng Chem Res* **2011**, *50* (4), 2236-2244.
29. Zhu, W.; Xu, D.; Li, H.; Ding, Y.; Zhang, M.; Liu, H.; Chao, Y., Oxidative Desulfurization of Dibenzothiophene Catalyzed by VO(acac)₂ in Ionic Liquids at Room Temperature. *Pet Sci Technol* **2013**, *31* (14), 1447-1453.
30. Zhu, W.; Wu, P.; Yang, L.; Chang, Y.; Chao, Y.; Li, H.; Jiang, Y.; Jiang, W.; Xun, S., Pyridinium-based temperature-responsive magnetic ionic liquid for oxidative desulfurization of fuels. *Chem Eng J* **2013**, *229* (0), 250-256.
31. Zhang, M.; Zhu, W.; Xun, S.; Li, H.; Gu, Q.; Zhao, Z.; Wang, Q., Deep oxidative desulfurization of dibenzothiophene with POM-based hybrid materials in ionic liquids. *Chem Eng J* **2013**, *220* (0), 328-336.
32. Ma, C. H.; Dai, B.; Xu, C. X.; Liu, P.; Qi, L. L.; Ban, L. L., Deep oxidative desulfurization of model fuel via dielectric barrier discharge plasma oxidation using MnO₂ catalysts and combination of ionic liquid extraction. *Catal Today* **2013**, *211*, 84-89.
33. Zhao, P. P.; Zhang, M. J.; Wu, Y. J.; Wang, J., Heterogeneous Selective Oxidation of Sulfides with H₂O₂ Catalyzed by Ionic Liquid-Based Polyoxometalate Salts. *Ind Eng Chem Res* **2012**, *51* (19), 6641-6647.
34. Li, Z.; Li, C. P.; Chi, Y. S.; Wang, A. L.; Zhang, Z. D.; Li, H. X.; Liu, Q. S.; Welz-Biermann, U., Extraction Process of Dibenzothiophene with New Distillable Amine-Based Protic Ionic Liquids. *Energ Fuel* **2012**, *26* (6), 3723-3727.
35. Zhang, C.; Pan, X. Y.; Wang, F.; Liu, X. Q., Extraction-oxidation desulfurization by pyridinium-based task-specific ionic liquids. *Fuel* **2012**, *102*, 580-584.
36. Rodríguez-Cabo, B.; Rodríguez, H.; Rodil, E.; Arce, A.; Soto, A., Extractive and oxidative-extractive desulfurization of fuels with ionic liquids. *Fuel* **2014**, *117*, Part A (0), 882-889.

37. Nie, Y.; Dong, Y.; Bai, L.; Dong, H.; Zhang, X., Fast oxidative desulfurization of fuel oil using dialkylpyridinium tetrachloroferrates ionic liquids. *Fuel* **2013**, *103* (0), 997-1002.
38. Lu, L.; Cheng, S. F.; Gao, J. B.; Gao, G. H.; He, M. Y., Deep oxidative desulfurization of fuels catalyzed by ionic liquid in the presence of H₂O₂. *Energ Fuel* **2007**, *21* (1), 383-384.
39. Yahaya, G. O.; Hamad, F.; Bahamdan, A.; Tammana, V. V. R.; Hamad, E. Z., Supported ionic liquid membrane and liquid-liquid extraction using membrane for removal of sulfur compounds from diesel/crude oil. *Fuel Process Technol* **2013**, *113*, 123-129.
40. Lin, Y.; Wang, F.; Zhang, Z.; Yang, J.; Wei, Y., Polymer-supported ionic liquids: Synthesis, characterization and application in fuel desulfurization. *Fuel* **2014**, *116* (0), 273-280.
41. Wang, F.; Zhang, Z.; Yang, J.; Wang, L.; Lin, Y.; Wei, Y., Immobilization of room temperature ionic liquid (RTIL) on silica gel for adsorption removal of thiophenic sulfur compounds from fuel. *Fuel* **2013**, *107* (0), 394-399.
42. Martínez-Magadán, J.-M.; Oviedo-Roa, R.; García, P.; Martínez-Palou, R., DFT study of the interaction between ethanethiol and Fe-containing ionic liquids for desulfuration of natural gasoline. *Fuel Process Technol* **2012**, *97* (0), 24-29.
43. Kohler, F.; Roth, D.; Kuhlmann, E.; Wasserscheid, P.; Haumann, M., Continuous gas-phase desulfurisation using supported ionic liquid phase (SILP) materials. *Green Chem* **2010**, *12* (6), 979-984.

Chapter 2

COnductor-like Screening Model for Real Solvents (COSMO-RS)

2.1. Theory

COSMO-RS¹⁻⁴ is a model for the prediction of thermophysical properties and phase behavior of pure fluids and/or mixtures. COSMO-RS combines quantum chemistry, based on the dielectric continuum model known as COSMO (COnductor-like Screening MOdel), with iterative cycles of statistical thermodynamics to reduce the thermodynamics of the mixture to the interaction of a mixture of individual surface segments (chemical potential determination).

COSMO calculations are performed in a perfect/ideal conductor¹⁻⁴, *i.e.*, molecules are assumed to be surrounded by a virtual conductor environment, and the interactions are completely made on the conductor interface taking into account the electrostatic screening and the back-polarization of the solute molecule. As a result, it provides a discrete surface around the solute molecule which is characterized by its geometry and screening charge density (σ) that iteratively corresponds to a minimum energetic state at the conductor. As COSMO-RS treats the surface around the solute molecule as segments it is also necessary the screening charge density of the respective segment, σ' . These data are stored in the so called COSMO files.

In the molecular interaction approach, the electrostatic misfit energy, E_{misfit} , and the hydrogen bonding energy, E_{HB} , are the most relevant and are described as a function of the polarization charges of the two interacting segments - (σ, σ') or $(\sigma_{acceptor}, \sigma_{donor})$. The van der Waals energy (E_{vdW}) is also taken into account, yet it only depends on the atoms involved. These energies are described by the equations 2.1, 2.2 and 2.3, respectively:

$$E_{misfit}(\sigma, \sigma') = a_{eff} \frac{\alpha'}{2} (\sigma + \sigma')^2, \quad (2.1)$$

$$E_{HB} = a_{eff} c_{HB} \min(0; \min(0; \sigma_{donor} + \sigma_{HB})) \times \max(0; \sigma_{acceptor} - \sigma_{HB}), \quad (2.2)$$

$$E_{vdW} = a_{eff} (\tau_{vdW} + \tau'_{vdW}). \quad (2.3)$$

There are five adjustable parameters fitted to the individual atoms properties: a_{eff} is the effective contact area between two surface segments; α' is an interaction parameter;

c_{HB} is the hydrogen bond strength; σ_{HB} is the threshold for hydrogen bonding; and τ_{vdW} and τ'_{vdW} are element specific van der Waals interaction parameters.

COSMO-RS does not explicitly depends on the discrete surface geometry, thus the 3D density distribution on the surface of each solute molecule X_i is converted into a distribution function called σ -profile, $p^X(\sigma)$. This distribution function describes the relative amount of surface segment with polarity σ . The combination of the molecular σ -profiles with the pure or mixture solvents (S) σ -profiles results in the mole fraction weighted sum of σ -profiles of its compounds, $p_S(\sigma)$, that normalized by the total surface area, A_S , gives the normalized σ -profile of the overall system, $p'_S(\sigma)$:

$$p'_S(\sigma) = \frac{p_S(\sigma)}{A_S} = \frac{\sum_i x_i p^{X_i}(\sigma)}{\sum_i x_i A^{X_i}} \quad (2.4)$$

where x_i is the mole fraction of component i , $p^{X_i}(\sigma)$ is the corresponding σ -profile, and A^{X_i} is surface area of the solute molecule X_i .

Since $p'_S(\sigma)$ describes molecular interactions, the chemical potential can be estimated by solving iteratively equation 2.5⁴:

$$\mu_S(\sigma) = -\frac{RT}{a_{eff}} \ln \left[\int p_S(\sigma') \exp \left(\frac{1}{RT} (a_{eff} \mu_S(\sigma') - E_{misfit}(\sigma, \sigma') - E_{HB}(\sigma, \sigma')) \right) d\sigma' \right] \quad (2.5)$$

where $\mu_S(\sigma)$, known as σ -potential, is the chemical potential of a surface segment with screening charge density σ , and it is a measure of the affinity of a solvent S to the surface segment with polarity σ .

Integrating equation 2.6, described below, over the surface of a compound, it is possible to calculate the pseudo-chemical potential of the component X_i in a solvent S¹:

$$\mu_S^{X_i} = \mu_{C,S}^{X_i} + \int p^{X_i}(\sigma) \mu_S(\sigma) d\sigma \quad (2.6)$$

where $\mu_{C,S}^{X_i}$ is a combinatorial contribution of the different size and shape of the molecules in the mixture.

This set of COSMO-RS equations gives the chemical potential of all components in a mixture and allows the estimation of several thermodynamic properties, namely activity coefficients, distribution ratios, phase equilibria, among others.^{1, 3-6}

More complex molecules, such as ionic liquids, present different conformational geometries corresponding to various energy states. Freire et al.⁶ showed that improved results were obtained using the conformers with lower energies (energetically more stable) and then, as in our previous work,⁷ the COSMO-RS calculations were carried out at the lower energy state of the conformers of each IL anion, IL cation and hydrocarbon.

The quantum chemical COSMO calculation was performed in the Turbomole program package⁸⁻⁹ with the BP density functional theory, giving the surface charge density and the Ahlrichs-TZVP (triple- ζ valence polarized large basis set).¹⁰ The binary and ternary liquid-liquid equilibria of ionic liquid and hydrocarbons were estimated employing the COSMOtherm program using the parameter file BP_TZVP_C2.1_0110,¹¹ and the ionic liquid, hydrocarbon and thiol systems, the parameter file BP_TZVP_C3.0_1301.¹²

2.2. References

1. Diedenhofen, M.; Klamt, A., COSMO-RS as a tool for property prediction of IL mixtures--A review. *Fluid Phase Equilib* **2010**, *294* (1-2), 31-38.
2. Klamt, A.; Eckert, F., COSMO-RS: a novel and efficient method for the a priori prediction of thermophysical data of liquids. *Fluid Phase Equilib* **2000**, *172* (1), 43-72.
3. Klamt, A.; Eckert, F.; Arlt, W., COSMO-RS: An alternative to simulation for calculating thermodynamic properties of liquid mixtures. *Annu Rev Chem Biomol* **2010**, *1* (1), 101-122.
4. Klamt, A., *COSMO-RS from quantum chemistry to fluid phase thermodynamics and drug design* Elsevier Amsterdam 2005.
5. Freire, M. G.; Carvalho, P. J.; Santos, L. M. N. B. F.; Gomes, L. R.; Marrucho, I. M.; Coutinho, J. A. P., Solubility of water in fluorocarbons: Experimental and COSMO-RS prediction results. *J Chem Therm* **2010**, *42* (2), 213-219.
6. Freire, M. G.; Santos, L. M. N. B. F.; Marrucho, I. M.; Coutinho, J. A. P., Evaluation of COSMO-RS for the prediction of LLE and VLE of alcohols + ionic liquids. *Fluid Phase Equilib* **2007**, *255* (2), 167-178.

7. Ferreira, A. R.; Freire, M. G.; Ribeiro, J. C.; Lopes, F. M.; Crespo, J. G.; Coutinho, J. A. P., An overview of the liquid-liquid equilibria of (ionic liquid + hydrocarbon) binary systems and their modeling by the Conductor-like Screening Model for Real Solvents. *Ind Eng Chem Res* **2011**, *50* (9), 5279-5294.
8. Ahlrichs, R.; Bär, M.; Häser, M.; Horn, H.; Kölmel, C., Electronic structure calculations on workstation computers: The program system turbomole. *Chem Phys Lett* **1989**, *162*, 165-169.
9. Schäfer, A.; Klamt, A.; Sattel, D.; Lohrenz, J. C. W.; Eckert, F., COSMO implementation in TURBOMOLE: Extension of an efficient quantum chemical code towards liquid systems. *Phys Chem Chem Phys* **2000**, *2* (10), 2187-2193.
10. Schäfer, A.; Huber, C.; Ahlrichs, R., Fully optimized contracted Gaussian Basis Sets of Triple Zeta Valence quality for atoms Li to Kr. *J Chem Phys* **1994**, *100* (8), 5829-5835.
11. Klamt, A.; Eckert, F. *COSMOtherm program (Version C2.1 Release 01.10)*, COSMOlogic GmbH & Co. KG: Leverkusen, Germany, 2010.
12. Klamt, A.; Eckert, F. *COSMOtherm program (Version C3.0 Release 13.01)*, COSMOlogic GmbH & Co. KG: Leverkusen, Germany, 2013.

Chapter 3

An Overview of the Liquid-Liquid Equilibria of (Ionic Liquid + Hydrocarbon) Binary Systems and their Modeling by COSMO-RS

Ferreira, A. R.; Freire, M. G.; Ribeiro, J. C.; Lopes, F. M.; Crespo, J. G.;
Coutinho, J. A. P.

Published at *Industrial and Engineering Chemistry Research*

2011, 50 (9), 5279-5294

DOI: 10.1021/ie102471b

3.1. Introduction

Ionic liquids (ILs) are a new class of solvents that have been object of a growing interest from both academia and industry in the past few years. They are molten salts composed by bulky organic cations, and organic or inorganic anions, which form crystalline structures with low lattice energies, allowing these salts to be in the liquid state at or near room temperature. Ionic liquids exhibit, in general, negligible vapor pressures, often possess high thermal and chemical stabilities, and have good solvating capacity for both organic and inorganic compounds, among others unique properties. Given the huge number of possible ionic liquids, their properties can be fine-tuned by an adequate combination of specific ions and/or functional groups, making of them “designer solvents” that could be tailored to fit the requirements of a specific process.

The interesting properties of ionic liquids are commending their application in numerous chemical and industrial processes aiming at replacing conventional organic solvents, including chemical, catalytic and biological reactions,¹⁻² organic/inorganic synthesis,³⁻⁵ liquid-liquid separation processes,⁶⁻⁸ separation and purification of gases⁹⁻¹⁰ and contaminants removal from aqueous streams.¹¹ There are some industrial processes that already use ionic liquids due to their economical advantages and reaction yields,¹²⁻¹³ such as the BASIL (Biphasic Acid Scavenging utilizing Ionic Liquids) process,¹⁴⁻¹⁶ proposed by BASF technologies, and the Difasol process,¹⁷⁻¹⁸ developed by Institute Français du Pétrole (IFP) that is an improvement of the traditional Dimersol route.

Refining companies belong to an industrial sector that has shown a considerable interest in ionic liquids. Various separation processes relevant for refineries have been studied, namely the desulfurization of fuels,¹⁹⁻²⁴ the selective separation of aromatic/aliphatic hydrocarbon mixtures,^{6-7, 25-27} and extractive distillation^{12, 28}. Besides the ionic liquids enhanced performance on these separations, their low volatility can reduce the energy consumption to separate the solvents from the product streams and to regenerate them^{6, 29}. To evaluate the applicability of ionic liquids in these processes the large body of experimental data of various ionic liquids with a broad range of hydrocarbons that has been reported³⁰⁻⁵⁰ is detailed and reviewed below.

To identify the improved ionic liquids to be used in particular applications it is necessary to know their thermophysical properties and to understand the phase behavior of systems containing such ionic fluids. This cannot be accomplished using only the available experimental data due to the very large number of possible combinations of ionic liquids and hydrocarbons that undergo through liquid-liquid phase equilibria. It is thus necessary to develop a comprehensive understanding of the impact of the

hydrocarbon molecules features (such as aromaticity, chain length and cyclization of aliphatic hydrocarbons), as well as of the ionic liquids structural changes impact (cation and anion nature, alkyl side chain length and additional functional groups), on their phase behavior. The development and testing of predictive models able to describe the phase behavior of systems containing ionic liquids can produce an important tool for this purpose.

A number of models based on the excess Gibbs free energy have been applied on the modeling of the phase behavior of systems involving ionic liquids and hydrocarbons. Some classical local composition models, such as the Non-Random Two Liquid (NRTL)^{31-32, 35-36, 38-43, 45, 50-53} and UNIQUAC,^{35, 40, 51} were applied with success to the description of these systems while their performances were shown to be similar.^{35, 40, 51} The modified Flory-Huggins equation and a lattice model based on polymer-solution models have also been applied,^{30, 54} yielding good quantitative descriptions of the phase diagrams. Although the models employed in these studies provide improved correlations, they present a limited predictive capability since they require parameters fitted to previous experimental data and to the ionic liquid complex groups. A fully predictive alternative relies in the use of the Conductor-like Screening Model for Real Solvents (COSMO-RS) proposed by Klamt and co-workers.⁵⁵⁻⁵⁷ COSMO-RS does not require adjustable parameters, and therefore, it is applicable to virtually all possible ionic liquids and hydrocarbons mixtures. COSMO-RS has already been applied by Domańska et al.³³ in the description of the equilibrium of (ILs + hydrocarbon) systems. Albeit reasonable results were obtained,³³ the limited number of systems studied was insufficient for a detailed evaluation of the COSMO-RS performance and applicability.

In the current work, a review of the experimental data published hitherto, concerning the mutual solubilities of hydrocarbons and ionic liquids, is carried out to garner a broader picture of the structural changes of both hydrocarbons and ionic liquids towards their phase behavior. Aiming at appraising a predictive model for the screening and design of ionic liquids for task specific applications involving hydrocarbons, the performance of COSMO-RS in the description of the (ILs + hydrocarbons) liquid-liquid equilibria (LLE) is further evaluated.

3.2. Ionic liquid + hydrocarbon liquid-liquid equilibria

An extensive search was performed on the liquid-liquid equilibrium experimental data of ionic liquids and hydrocarbons binary systems available in literature. The ionic liquid and hydrocarbon used, measurement technique, temperature and composition ranges, as well as the respective literature reference, are summarized in Tables B1 to B3, in Appendix B. Table B1 reports systems regarding aliphatic hydrocarbons, Table B2 concerns aromatics hydrocarbons, and Table B3 summarizes the available data involving cyclic hydrocarbons.

Owing to the high expectation through the application of ionic liquids in petroleum refineries and fuel production a large number of experimental systems could be found, with ionic liquids ranging from the most common types to task specific compounds. The experimental data available are based on imidazolium, pyridinium, pyrrolidinium, ammonium, and phosphonium cations, and bis(trifluoromethylsulfonyl)imide, alkylsulfate, hexafluorophosphate, tetrafluoroborate, thiocyanate, tosylate, nitrate, dicyanamide, and trifluoromethanesulfonate anions. Their ionic structures are described in Table A1 and Table A2, in Appendix A. LLE measurements were carried out for the *n*-alkanes pentane, hexane, heptane, octane, nonane, decane and hexadecane; for the aromatics benzene, toluene, ethylbenzene, propylbenzene, butylbenzene, *o*-xylene, *m*-xylene and *p*-xylene; and for the cycloalkanes cyclopentane, cyclohexane and cycloheptane.

The large bank of experimental data gathered allows the drawing of the solvents structural features ruling the solvation phenomenon, and to evaluate the performance of COSMO-RS in anticipating their solution behavior.

3.3. Results and Discussion

The systems reported in Tables B1, B2 and B3 at Appendix B were used to study the effect of the various structural characteristics of the hydrocarbons molecules (such as aromaticity, chain length, cyclization and positional isomerism) and of the ionic liquids (cation and anion cores, side alkyl chain length and additional functionalized groups) on their phase behavior. A detailed discussion through the structural features impact in the phase behavior of these systems is reported below. It should be remarked that the solubility data from different researchers/sources show some discrepancies for similar systems.^{30, 33, 35} This fact could derive from the different experimental techniques used, purities of the compounds employed, among others sources of error^{30, 33, 35}. In this work a critical evaluation of the experimental data was carried out by comparing similar

systems and, whenever outsider results were observed, they were not considered in the following discussion.

The COSMO-RS model was applied to the description of selected systems to evaluate its capacity to predict the phase equilibrium data experimentally available. The impact of structural factors of the solvents on the miscibility gap of the LLE diagrams are analyzed and discussed.

3.3.1. Hydrocarbons + ILs binary systems

Fixing a common ionic liquid in several systems allows the investigation of the differences between the mutual solubilities regarding various hydrocarbon families. Data for [C₄mim][SCN] with hexane, cyclohexane and benzene are reported in Figure 3. (for other ionic liquids see Figures B1-B16 in Appendix B). The asymmetric behavior of the ionic-liquid-containing systems is one of the most striking features of these diagrams. As previously observed with alcohols⁵⁸ and water⁵⁹ the solubility of ILs in hydrocarbons is usually orders of magnitude lower (in a mole fraction basis) than the solubility of hydrocarbons in ionic liquids. Particularly, while at the IL-rich phase the solubility of hydrocarbons is quite substantial, at the hydrocarbon-rich phase the solubility of [C₄mim][SCN] is very small. Moreover, the solubility of benzene in aromatic ionic liquids, such as the imidazolium-based ionic liquid presented in Figure 3.1, is significantly higher than that observed for the aliphatic hydrocarbons. Nevertheless, slight differences also exist in the solubilities of both aliphatic hydrocarbons studied and the ionic liquid. Generally, the mutual solubilities between hydrocarbons (with a constant carbon number) and ionic liquids follow the increasing order (*cf.* also Appendix B): aromatics > cyclic aliphatic hydrocarbons > *n*-alkanes. The large solubility of aromatic hydrocarbons in ILs is certainly related with the formation of π - π interactions between the aromatic rings of both ionic liquid ions and aromatic hydrocarbons. On the other hand, the cyclic conformation of aliphatic hydrocarbons can reduce steric hindrance and allows a more effective package of the hydrocarbon at the IL-rich phase.

COSMO-RS predictions for the phase behavior of the studied systems are also depicted in Figure 3.1. COSMO-RS displays an enhanced performance in describing all systems containing the ionic liquid [C₄mim][SCN]. Besides the qualitative trend description, improved quantitative results are also obtained. Nevertheless, COSMO-RS is not able to achieve consistently predictions of this quality for all ionic liquids evaluated (*cf.* Appendix B). However, in general, a semi-quantitative description of the phase diagrams is

achieved, with the model being able to describe the differences between the various types of hydrocarbons. Particularly, the large differences in the mutual solubilities with ionic liquids displayed between the aromatics and aliphatic hydrocarbons are usually well described. As previously observed⁵⁸⁻⁶⁰, the COSMO-RS model performs better for less miscible systems. Since COSMO-RS calculations consider that the interactions are made on the conductor interface surrounding the molecules (thus isolated species), stronger interactions responsible for larger mutual solubilities are not adequately taken into account by COSMO-RS.

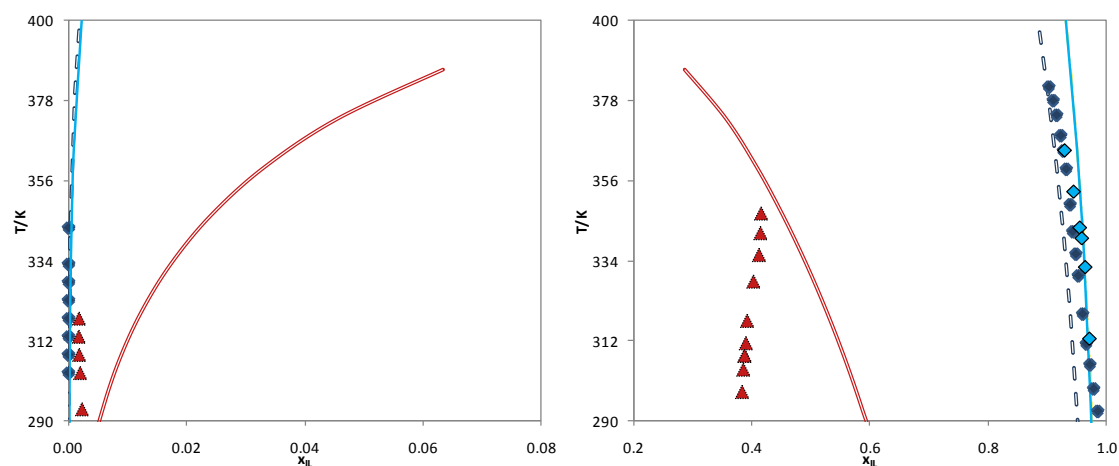


Figure 3.1 Liquid-liquid phase diagram for [C₄mim][SCN] with *n*-hexane³² (◆) (—), benzene³² (▲) (—) and cyclohexane³² (◆) (—). The symbols and the lines represent respectively the experimental data and the COSMO-RS prediction calculations.

3.3.2. N-alkanes + ILs binary systems

As described in Table B1 (at Appendix B) a large number of measured systems of *n*-alkanes + ILs are available. The LLE data taken from the literature are, in general, based on *n*-alkanes from C₅H₁₂ to C₁₀H₂₂ and, in most examples, only data for the solubility of the *n*-alkanes at the ionic-liquid-rich regime are available. The experimental measurements of the solubility of ionic liquids in *n*-alkanes are a challenging task since the equilibrium saturation values of ILs in *n*-alkanes are very small - in the range from 1×10⁻⁵ to 3×10⁻⁵ in mole fraction for the reported systems.^{36, 38, 51} Moreover, the solubility of *n*-alkanes in ionic liquids is extremely low, compared, for instance, with aromatic hydrocarbons, due to the striking strength differences on the type of interactions that take place between the hydrocarbons (dispersion forces) and the ionic liquid ions (mainly hydrogen bonding and electrostatic interactions).

3.3.2.1. Effect of the *n*-alkane chain length upon the phase behavior

Fixing the ionic liquid, the *n*-alkane influence in the liquid-liquid phase diagram of systems IL + *n*-alkane was studied and selected LLE diagrams are shown in Figure 3.2, and in Figures B17 to B36 in Appendix B.

The increase of the *n*-alkane chain length increases the immiscibility of the binary system as shown in Figure 3.2 for [C_{*n*}mim][SCN]. The increasing miscibility gap increases accordingly to the rank: *n*-decane < *n*-nonane < *n*-octane < *n*-heptane < *n*-hexane. This trend is found to be independent on both the ionic liquid cation and anion nature. Although an increase in the dispersive forces is expected between the alkyl chains of the ionic liquids and longer chain hydrocarbons, the decrease in solubility at the IL-rich phase is related with the difficulty that *n*-alkanes with higher chains meet to fit into the free volume between the ionic liquid ions, reducing therefore their packing efficiency³⁴. As can be extrapolated from Figure 3.2, as well as from the Figures B17 to B36 in Appendix B, the alkane chain length increase leads to an increase in the upper critical solution temperature (UCST) of all the binary systems evaluated. Indeed, dealing with aliphatic hydrocarbons, all diagrams converge to an UCST behavior.

The liquid-liquid equilibria of [SCN]-based ionic liquids presented in Figure 3.2 and Figure B24 is quantitatively described by COSMO-RS regarding the alkane chain length effect. For systems with different ionic liquids, with higher miscibility among the binary compounds, a fair qualitative description of the solubilities was obtained as displayed in Appendix B in Figures B17 to B34. For the hydrocarbon-rich phase, no experimental data are available, and thus, COSMO-RS predictions were not attempted.

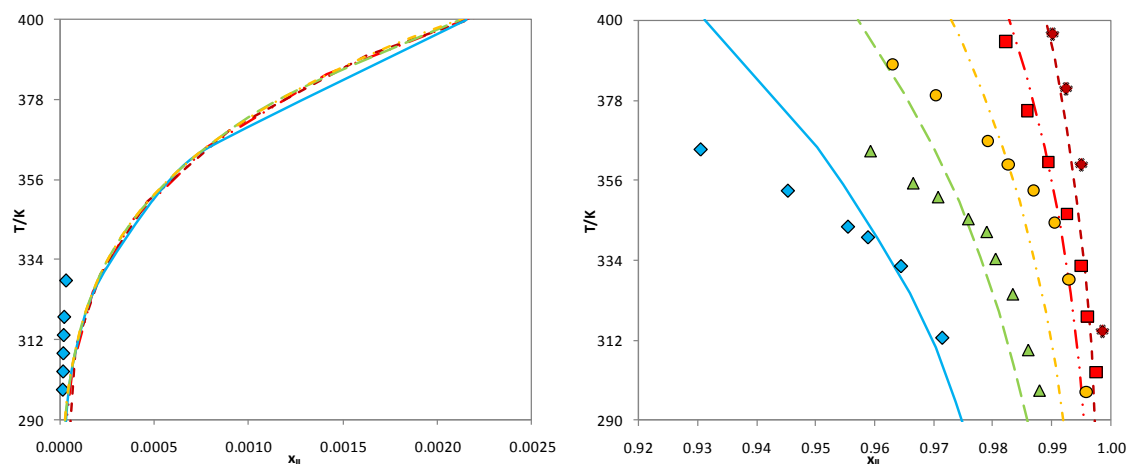


Figure 3.2 Liquid–liquid phase diagram for $[\text{C}_4\text{mim}][\text{SCN}]$ with n -hexane³² (\diamond) (—), n -heptane³² (\triangle) (---), n -octane³² (\circ) (-.-.), n -nonane³² (\square) (-.-.-) and n -decane³² (\star) (----). The symbols and the lines represent respectively the experimental data and the COSMO-RS prediction calculations.

3.3.2.2. Effect of the ionic liquid cation core upon the phase behavior

The effect of the ionic liquid cation core on the solubility of hydrocarbons in ionic liquids is depicted in Figures 3.3 and 3.4 where the solubilities of n -hexane in $[\text{CF}_3\text{SO}_3]^-$ and $[\text{TOS}]^-$ -based ionic liquids are presented. The solubilities seem to be highly anion dependent. Nevertheless, a remarkable effect of the cation family is also observed when comparing, for instance, significantly structural different ionic liquids, such as all, nitrogen-based ILs with the phosphonium-based ionic liquid. Gathering the results displayed in Figures 3.3 and 3.4 the increasing miscibility of n -alkanes in ionic liquids follows the cations trend: $[\text{1,3-C}_4\text{mpy}]^+ < [\text{C}_4\text{mpyr}]^+ < [\text{C}_4\text{mim}]^+ \ll [\text{P}_{i(444)1}]^+$. Among the nitrogen-based ionic liquids the five-sided ring cations (imidazolium- and pyrrolidinium-based) present lower miscibilities with n -alkanes compared to the six-sided ring cation studied (pyridinium-based ionic liquid). Since both pyridinium- and imidazolium-based ionic liquids present an aromatic character while the pyrrolidinium-based cation is aliphatic, it can be anticipated that the size is more relevant than the presence of π molecular orbitals in defining the mutual solubilities. The most significant differences in solubilities, among different ionic liquid cations, were observed with the phosphonium-based ionic liquid, as shown in Figure 3.4, presenting a significantly smaller miscibility envelope. The phosphonium-based structure, based on four alkyl chains, leads to favorable dispersive interactions with n -alkanes than those observed with other families of ionic liquids with a more polar character, and increasing thus the mutual solubilities.

COSMO-RS can satisfactorily predict the solubility dependency with the cation family as can be seen in Figures 3.3 and 3.4 (as well as for other systems presented in Figures B36 to B39 at Appendix B).

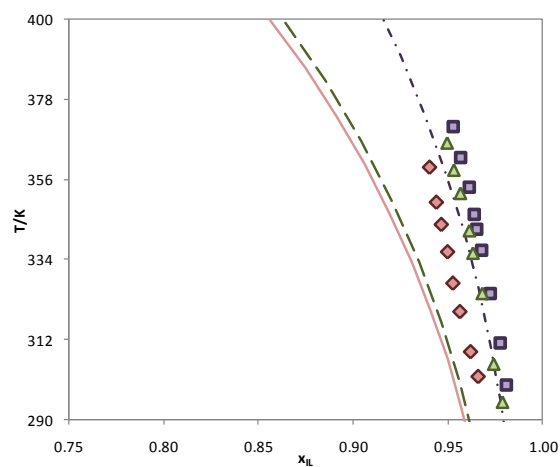


Figure 3.3 Liquid–liquid phase diagram for $[\text{C}_4\text{mim}][\text{CF}_3\text{SO}_3]^{50}$ (\blacksquare) ($-\cdot-$), $[\text{C}_4\text{mpyr}][\text{CF}_3\text{SO}_3]^{50}$ (\blacktriangle) ($- -$) and $[1,3\text{-C}_4\text{mpy}][\text{CF}_3\text{SO}_3]^{50}$ (\blacklozenge) ($—$) with *n*-hexane. The symbols and the lines represent respectively the experimental data and the COSMO-RS prediction calculations.

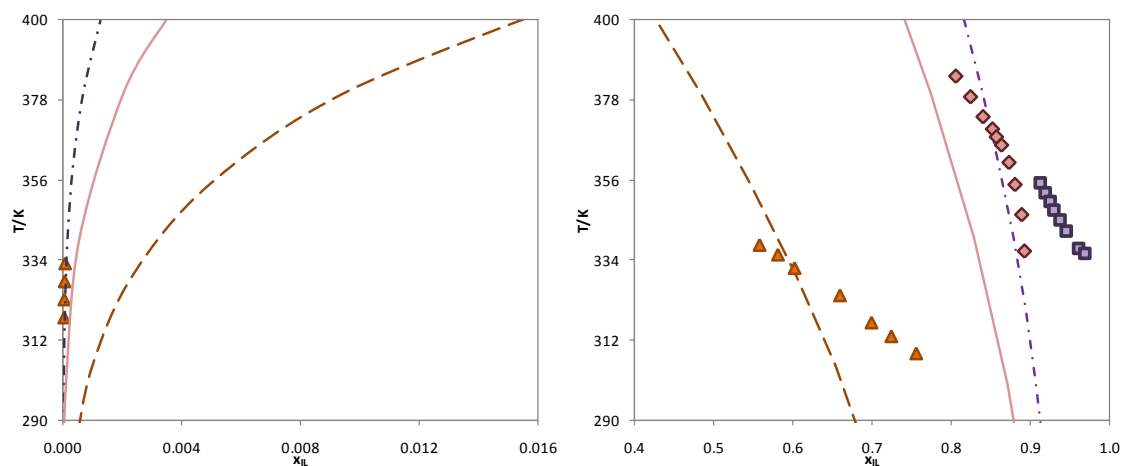


Figure 3.4 Liquid–liquid phase diagram for $[\text{C}_4\text{mim}][\text{TOS}]^{36}$ (\blacksquare) ($-\cdot-$), $[1,4\text{C}_4\text{mpy}][\text{TOS}]^{49}$ (\blacklozenge) ($—$) and $[\text{P}_{i(444)1}][\text{TOS}]^{47}$ (\blacktriangle) ($- -$) with *n*-hexane. The symbols and the lines represent respectively the experimental data and the COSMO-RS prediction calculations.

3.3.2.3. Effect of the ionic liquid cation alkyl chain length upon the phase behavior

The cation alkyl chain length affects the mutual solubilities between ionic liquids and *n*-alkanes. Indeed, the chain length has a significant impact on the phase diagrams as shown in Figure 3.5. Figure 3.5 show that the increase of the ionic liquid cation alkyl chain from [C₄mim]⁺ to [C₆mim]⁺ in the [C_{*n*}mim][SCN] series leads to an increase in the mixture solubility. This enhanced miscibility is the result of a free volume increase in the IL-rich solution and of the prevalence of non polar regions in the ionic liquid that enhance the probability of favorable dispersive interactions with the *n*-alkane chain. Curiously this trend is not observed when changing the ionic liquid anion for the systems containing [C₁mim][MeSO₄] and [C₄mim][MeSO₄] (see Figures B40 and B41 in Appendix B). Nevertheless, it is difficult at present to establish if this is a peculiar behavior related with the [C₁mim]⁺ cation, the [MeSO₄]⁻ anion, or just a problem associated with the limited experimental data available. More data on these systems are required to establish the reasons behind this particular trend.

Moreover, for the alkoxyethyl-based ionic liquids (C_{*n*}H_{2*n*+1}OCH₂) a similar pattern was observed. As shown in Figure B44 in Appendix B, *n*-alkanes are more soluble in [(C₆H₁₃OCH₂)₂im][NTf₂] than in [C₆H₁₃OCH₂mim][NTf₂] at similar temperatures. The substitution of a methyl group by a longer alkoxyethyl chain improves the miscibility with aliphatic hydrocarbons. Most of the imidazolium-based ionic liquids phase diagrams shown presented *n*-alkanes solubilities lower than 0.30 in mole fraction units. For the cations with the hexyloxy-groups, the *n*-alkane solubility increases up to 0.5 in mole fraction. Nevertheless, with the data published hitherto it is not possible to conclude if this is a direct effect of the increased polarity of the chain dominated by the alkoxy group or a simple contribution of the second and longer hexyl chain.

The trend observed with the cation alkyl chain length is similar to that observed for alcohols + ILs binary systems⁵⁸. Also, as the alkyl chain length of the cation increases the UCST of the system decreases. Moreover, the opposite effect verified with the *n*-alkanes chain length increase, leading to higher UCST, is similar to that presented by alcohols and ionic liquids systems⁵⁸.

COSMO-RS provides a correct qualitative description of the experimental data of the systems studied in Figure 3.5 (and Figures B43 and B44 at Appendix B). The effect of the increase in the cation chain length leading to higher mutual miscibilities is well predicted. It should be remarked that this trend is also supported by COSMO-RS for the systems comprising the methylsulfate-based ionic liquids, although experimentally a different pattern was observed.

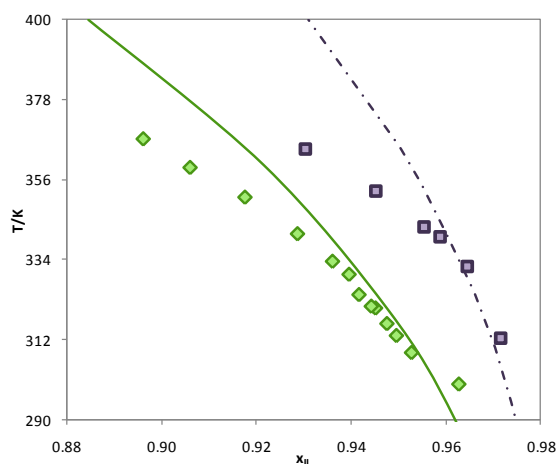


Figure 3.5 Liquid–liquid phase diagram for $[\text{C}_4\text{mim}][\text{SCN}]^{32}$ (\square) (– · –) and $[\text{C}_6\text{mim}][\text{SCN}]^{38}$ (\diamond) (—) with *n*-hexane. The symbols and the lines represent respectively the experimental data and the COSMO-RS prediction calculations.

3.3.2.4. Effect of the ionic liquid anion upon the phase behavior

The experimental data available (Table B1 at Appendix B) allows a comparison of the effect of several ionic liquid anions on the *n*-alkanes solubility in the ionic media. Although more data are available, as described in Table B1, the systems here analyzed are mainly based on the $[\text{C}_4\text{mim}][\text{anion}] + n\text{-hexane}$ and the $[\text{C}_6\text{H}_{13}\text{OCH}_2\text{mim}][\text{anion}] + n\text{-hexane}$ systems, because they allow the direct comparison of the effect of a large number of anions on the mutual solubilities. Results are displayed in Figure 3.6 and Figure B46 (at Appendix B).

The ionic liquid anion nature has a slight influence in the mutual solubilities and similar to that presented before with the ionic liquid cation core. The main deviation was observed with the IL containing the $[\text{PF}_6]^-$ anion. Experimentally, the solubility of *n*-alkanes in $[\text{C}_4\text{mim}]$ -based ionic liquids increases with the following order: $[\text{MeSO}_4]^- < [\text{SCN}]^- < [\text{TOS}]^- < [\text{CF}_3\text{SO}_3]^- < [\text{MDEGSO}_4]^- \ll [\text{PF}_6]^-$, while for $[\text{C}_6\text{H}_{13}\text{OCH}_2\text{mim}]$ -based ionic liquids the increasing solubility follows the rank: $[\text{BF}_4]^- < [\text{NTf}_2]^-$. These patterns closely follow the hydrogen bond basicity (hydrogen-bond accepting strength) of $[\text{C}_4\text{mim}]$ -based ionic liquids regarding their anions. The hydrogen bond basicity, β solvatochromic parameter, accordingly to the ionic liquid anion nature follows the sequence: $[\text{MeSO}_4]^- > [\text{SCN}]^- > [\text{CF}_3\text{SO}_3]^- > [\text{BF}_4]^- > [\text{PF}_6]^- > [\text{NTf}_2]^-$ ⁶¹⁻⁶². Thus, it seems that the solubility of *n*-alkanes in ionic liquids decreases with an increase of the hydrogen-bond basicity of the ionic liquid anion. It should be noted that no liquid-liquid equilibrium data were found regarding the influence of the ionic liquid anion at the hydrocarbon-rich phase.

As previously observed for other systems containing ionic liquids⁵⁸⁻⁵⁹, the solubility dependence with the anions nature is not qualitatively well described by COSMO-RS. Due to the similarity on the solubilities observed for most anions, although COSMO-RS can often provide an acceptable prediction of the phase diagrams, it cannot identify the correct experimental solubility trends as shown in Figure 3.6 for the ionic liquids [C₄mim][MeSO₄], [C₄mim][PF₆] and [C₄mim][TOS]. Nevertheless, in Figure B46 concerning only the [NTf₂]⁻ and [BF₄]⁻ anions, there is a close qualitative agreement with experimental data.

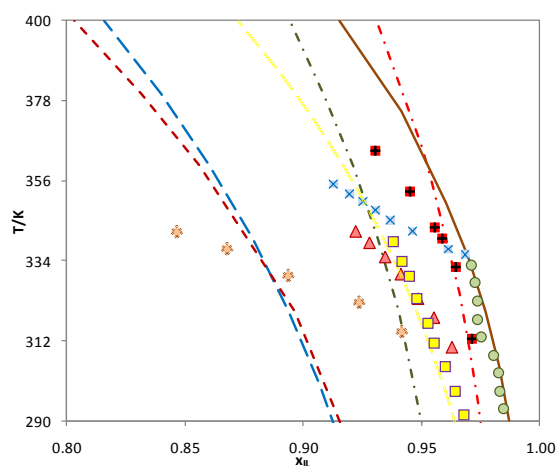


Figure 3.6 Liquid–liquid phase diagram for [C₄mim][MeSO₄]³⁵ (●) (– · –), [C₄mim][PF₆]⁵¹ (★) (—), [C₄mim][SCN]³² (■) (– · –), [C₄mim][TOS]³⁶ (×) (– –), [C₄mim][CF₃SO₃]⁵⁰ (□) (—) and [C₄mim][MDEGSO₄]³⁹ (△) (– –) with *n*-hexane. The symbols and the lines represent respectively the experimental data and the COSMO-RS prediction calculations.

3.3.2.5. Effect of the ionic liquid anion alkyl chain length upon the phase behavior

As discussed before, the increase in the cation alkyl chain length leads to a pronounced increase in the mutual miscibility between ILs and *n*-alkanes. The same trend is observed with the increase of the anion alkyl chain length displayed in Figure 3.7. Ranging from [C₄mim][MeSO₄] to [C₄mim][OcSO₄]-containing systems there is a solubility increase of around 0.5 in mole fraction. Such enhanced solubility results from the decrease in the polarity of the anion and from the increase of the dispersion forces between longer alkyl chain anions and *n*-alkanes. In Figure B47, a similar pattern is observed. [C₄mim][MeSO₄] is less soluble in *n*-hexane than [C₄mim][MDEGSO₄].

Although an oxygenated group is introduced in the former ionic liquid, this ionic liquid possesses a longer alkyl chain that favors liquid-liquid miscibility.

In spite of the limitations of COSMO-RS to describe the ionic liquid anion effect through the binary phase diagrams, as discussed above, the influence of the anion alkyl chain length is correctly described. However, the observed experimental differences in solubilities are more remarkable than those predicted by COSMO-RS.

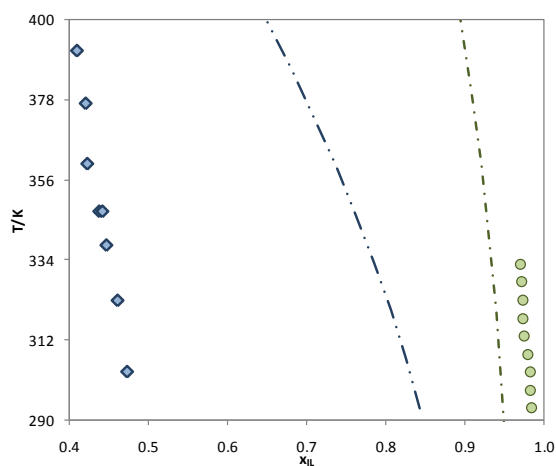


Figure 3.7 Liquid-liquid phase diagram for [C₄mim][MeSO₄]³⁵ (○) (- - -) and [C₄mim][OcSO₄]³⁷ (◇) (— · ·) with *n*-hexane. The symbols and the lines represent respectively the experimental data and the COSMO-RS prediction calculations.

3.3.3. Aromatics + ILs binary systems

The LLE data available in literature for binary systems containing aromatic hydrocarbons and ionic liquids are reported in Table B2 in Appendix B. They are based essentially in benzene, alkyl-substituted benzenes and xylene isomers. The experimental miscibility gap observed for the IL + aromatic hydrocarbons is smaller than with *n*-alkanes, being the aromatics much more soluble in ionic liquids. Nevertheless, the solubility of ionic liquids in the aromatics is still very low, in the order of 10^{-3} in mole fraction^{32, 36, 38, 41, 46, 51, 53, 63}. These important solubility differences observed between aromatics and alkanes in ionic liquids are the basis of the use of ionic liquids for aromatic/aliphatic selective separations^{6-7, 25, 64-65}. The greater solubility of aromatics in ionic liquids can be a consequence of the enhanced interactions between ionic liquids and aromatic hydrocarbons due to π - π interactions (for aromatic ionic liquids) and favorable packing effects (for non-aromatic ionic liquids). The various structural effects of aromatic

hydrocarbons and ionic liquids on the mutual solubilities will be studied and discussed below.

3.3.3.1. Effect of the aromatics structure on the phase behavior

The solubility of the ionic liquid in hydrocarbons increases with their aromaticity. As the alkylation of the benzene ring increases, the solubility of the ionic liquid at such rich phase decreases, as shown in Figure 3.8 (similar results are also shown at Appendix B for other systems in Figure B50 to Figure B91). In general, the miscibility gap increases accordingly to: benzene < toluene < ethylbenzene < propylbenzene.

The solubility of xylene isomers in ionic liquids depends on the second methyl group position as shown in Figure 3.9 for [C₄mim][MeSO₄] and for other systems presented in Figures B50 to B91. The small differences observed among the positional isomers are due to differences in the xylene molecular structure that have an impact in the aromatic induced dipole moment. As a result, and in general, the *ortho* position presents higher solubility at the IL-rich phase.

Moreover, from all the data gathered in Figures 3.8 and 3.9, it can be seen the favorable solvation of ethylbenzene at the IL-rich solution over the xylene similar structures. A single alkyl chain at the ring allows an enhanced solubility in the ionic liquid as a consequence of its larger dipole moment.

For the hydrocarbon aromatic systems, COSMO-RS is able to qualitatively describe the effect of the alkylation of the benzene ring on the miscibility gap between ionic liquids and aromatics, as shown in Figure 3.8. Similar results are reported for other systems at the Appendix B (Figures B50 to B91).

The behavior of the xylene isomers systems predicted by COSMO-RS, although only semi-quantitative, is qualitatively correct, as shown in Figure 3.9. The COSMO-RS can predict the similar experimental solubilities observed for the isomers *meta* and *para*, while providing higher miscibilities at the IL-rich phase for the *ortho*-xylene isomer.

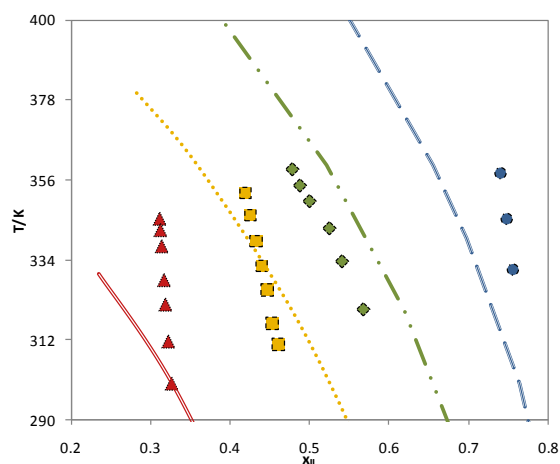


Figure 3.8 Liquid–liquid phase diagram for [C₄mim][TOS] with benzene ³⁶ (▲) (—), toluene ³⁶ (■) (⋯), ethylbenzene ³⁶ (◆) (— ·) and propylbenzene ³⁶ (●) (— —). The symbols and the lines represent respectively the experimental data and the COSMO-RS prediction calculations.

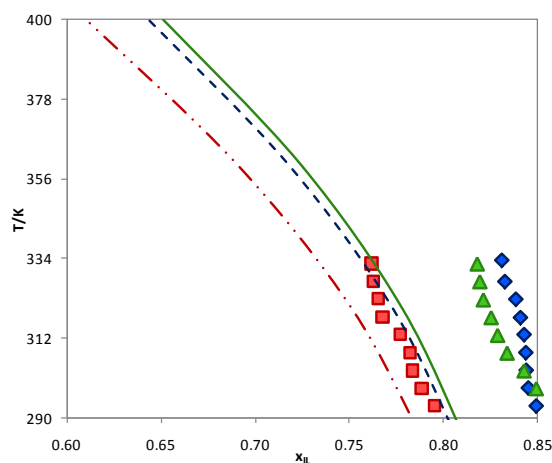


Figure 3.9 Liquid–liquid phase diagram for [C₄mim][MeSO₄] with *o*-xylene ³⁵ (■) (— ·), *m*-xylene ³⁵ (◆) (— —) and *p*-xylene ³⁵ (▲) (—). The symbols and the lines represent respectively the experimental data and the COSMO-RS prediction calculations.

3.3.3.2. Effect of the ionic liquid cation core upon the phase behavior

As discussed for the IL + *n*-alkane systems, the cation family plays a minor role on the mutual miscibilities when the cation is based on nitrogen-containing heterocyclic rings. Imidazolium-, pyridinium- and pyrrolidinium-based ionic liquids exhibit similar solubilities as shown in Figure 3.10. However, pyridinium-based ionic liquids are slightly more soluble in aromatic hydrocarbons, and as observed before with *n*-alkanes. Other types of

cation may however present a different behavior, as suggested by the data for the $[P_{i(444)1}][TOS]$ displayed in Figure 3.11, that presents a large solubility for aromatic hydrocarbons.

In all systems evaluated, COSMO-RS can satisfactorily predict the trend of the influence of the cation family on the mutual solubilities, as shown in Figures 3.10 and 3.11. Nevertheless, significant quantitative differences were observed between the experimental and predicted data. Contrary to what was observed for *n*-alkanes, COSMO-RS predicts more significant differences in solubilities between the imidazolium, the pyridinium, and the pyrrolidinium cations, than those experimentally observed. Again, and as observed before with *n*-alkanes, COSMO-RS predicts an inversion in the solubility trends between the pyridinium- and pyrrolidinium-based ionic liquids at the hydrocarbon phase. Moreover, the experimental data suggest that a number of IL + aromatic systems may have a phase diagram of the lower critical solution temperature (LCST) type (for instance, $[C_4mim][CF_3SO_3]$ ⁵⁰, $[1,3C_4mpy][CF_3SO_3]$ ⁵⁰ and $[C_4mpyr][CF_3SO_3]$ ⁵⁰ presented in Figure 3.10, as well as other systems provided at Appendix B, such as $[C_2mim][NTf_2]$ ⁴⁶, $[C_4mim][SCN]$ ³² and $[C_6mim][SCN]$ ³⁸ in Figures B60, B5 and B78, respectively). In all systems COSMO-RS seems to be unable to describe correctly this particular behavior, predicting UCST diagrams instead. LCST is caused by the conjugation of attractive interactions and free volume effects which result in negative enthalpies of mixing, and these are not well described by COSMO-RS predictions.

The COSMO-RS predictions usually deteriorate with the increasing miscibility between the compounds⁵⁸⁻⁵⁹. For the systems here studied, the COSMO-RS model does not seem to describe correctly the π - π interactions between aromatic rings. The COSMO-RS calculations consider that the interactions are made at the interface of the virtual conductor environment surrounding the molecules, and stronger interactions responsible for larger mutual solubilities are thus not adequately taken into account. This makes the model less able to describe the aromatic containing systems as compared to the *n*-alkanes systems presented previously. Nevertheless, the model always provides a qualitative description of the ionic liquid cation influence on the mutual solubilities and can be an *a priori* screening tool for particular systems.

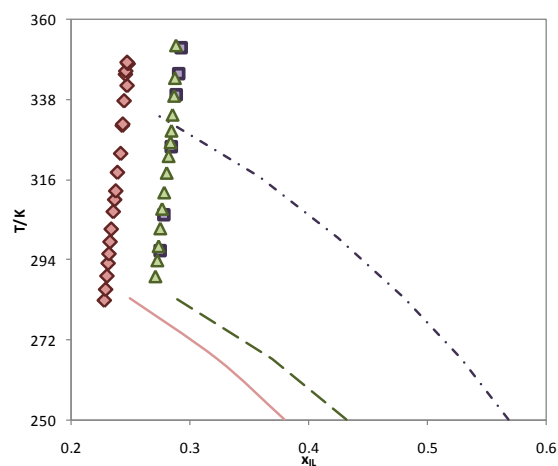


Figure 3.10 Liquid-liquid phase diagram for $[\text{C}_4\text{mim}][\text{CF}_3\text{SO}_3]^{50}$ (\blacksquare) ($-\cdot-$), $[\text{C}_4\text{mpyr}][\text{CF}_3\text{SO}_3]^{50}$ (\blacktriangle) ($- -$) and $[1,3\text{-C}_4\text{mpy}][\text{CF}_3\text{SO}_3]^{50}$ (\blacklozenge) ($- -$) with benzene. The symbols and the lines represent respectively the experimental data and the COSMO-RS prediction calculations.

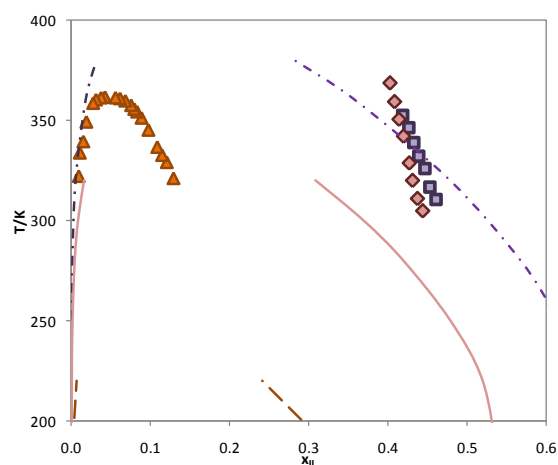


Figure 3.11 Liquid-liquid phase diagram for $[\text{C}_4\text{mim}][\text{TOS}]^{36}$ (\blacksquare) ($-\cdot-$), $[1,4\text{C}_4\text{mpy}][\text{TOS}]^{49}$ (\blacklozenge) ($- -$) and $[\text{P}_{(444)1}][\text{TOS}]^{47}$ (\blacktriangle) ($- -$) with toluene. The symbols and the lines represent respectively the experimental data and the COSMO-RS prediction calculations.

3.3.3.3. Effect of the ionic liquid cation alkyl chain length upon the phase behavior

The cation alkyl chain length has an important impact on the solubility of aromatic hydrocarbons in ionic liquids as shown in Figures 3.12 and 3.13. The increase of the alkyl chain length decreases the polarity of the ionic liquid cation enhancing favorable

interactions with the hydrocarbon. Moreover the alkyl chain length also increases the entropic effects that contribute to an enhanced solubility, such as the asymmetry and the free volume of the ionic liquid. Figure B104 (Appendix B) shows the effect of the addition of a hexyloxy-group to the imidazolium cation and its impact in the liquid-liquid equilibrium with benzene. The presence of a more polar and electronegative element, such as oxygen, increases the miscibility between the aromatic and the ionic liquid.

Although the COSMO-RS predictions presented in Figures 3.12 and 3.13 are quite different from experimental data they can, even so, correctly predict the miscibility trends with the cation alkyl chain length. The only limitation observed in this section was the inability of COSMO-RS to predict the alkoxymethyl group effect on the systems solubility shown in Figure B104.

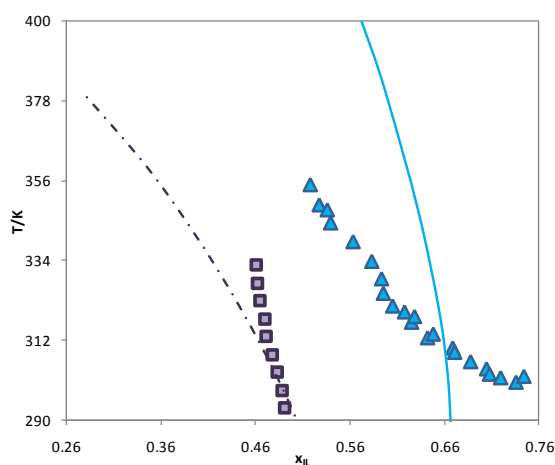


Figure 3.12 Liquid-liquid phase diagram for [C₁mim][MeSO₄]³³ (▲) (—) and [C₄mim][MeSO₄]³⁵ (■) (- · -) with benzene. The symbols and the lines represent respectively the experimental data and the COSMO-RS prediction calculations.

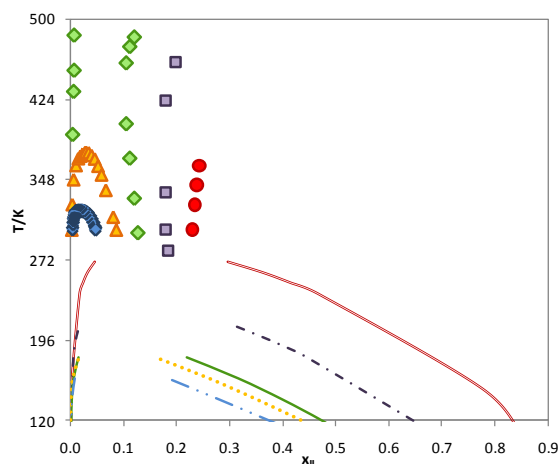


Figure 3.13 Liquid–liquid phase diagram for $[\text{C}_2\text{mim}][\text{NTf}_2]$ 46 (●) (—), $[\text{C}_4\text{mim}][\text{NTf}_2]$ 46 (■) (---), $[\text{C}_6\text{mim}][\text{NTf}_2]$ 46 (◇) (—), $[\text{C}_8\text{mim}][\text{NTf}_2]$ 46 (▲) (····) and $[\text{C}_{10}\text{mim}][\text{NTf}_2]$ 46 (◆) (—·) with benzene. The symbols and the lines represent respectively the experimental data and the COSMO-RS prediction calculations.

3.3.3.4. Effect of the ionic liquid anion upon the phase behavior

The anion effect on the mutual solubilities between aromatic hydrocarbons and ionic liquids is a well-studied field with a large body of data available as described in Table B2. As shown in Figure 3.14 the ionic liquid anion has a more important influence on the mutual solubilities with aromatic hydrocarbons than that observed before with *n*-alkanes.

The solubility of benzene in the $[\text{C}_4\text{mim}]$ - and $[\text{C}_2\text{mim}]$ -based ionic liquids, shown in Figure 3.14, and Figures B105 and B109, range from 0.4 to 0.8 in mole fraction. The solubility increases with the ionic liquids anions sequences: $[\text{MeSO}_4]^- < [\text{SCN}]^- < [\text{MDEGSO}_4]^- < [\text{PF}_6]^- < [\text{TOS}]^- < [\text{CF}_3\text{SO}_3]^- < [\text{NTf}_2]^-$ for the $[\text{C}_4\text{mim}]$ -based ionic liquid and $[\text{EtSO}_4]^- < [\text{PF}_6]^- < [\text{NTf}_2]^-$ for the $[\text{C}_2\text{mim}]$ -based ionic liquid. In Figure B109 the solubility with an IL containing a 2-(2-methoxyethoxy)ethyl group at the cation increases as follows: $[\text{BF}_4]^- < [\text{NTf}_2]^-$. These patterns follow, with few exceptions, the general trend for the dipolarity/polarisability measurements of ionic liquids (π^*): $[\text{MeSO}_4]^- \approx [\text{SCN}]^- > [\text{BF}_4]^- > [\text{PF}_6]^- > [\text{CF}_3\text{SO}_3]^- > [\text{NTf}_2]^-$ ⁶². Thus, the mutual solubilities of aromatic hydrocarbons and ionic liquids increase with the decrease of the polarity of the ionic liquid anion.

The COSMO-RS predictions are quantitatively acceptable for a number of ionic liquids but, as observed before for the *n*-alkanes, the correct qualitative trend predictions present some limitations with the ionic liquid anion nature.

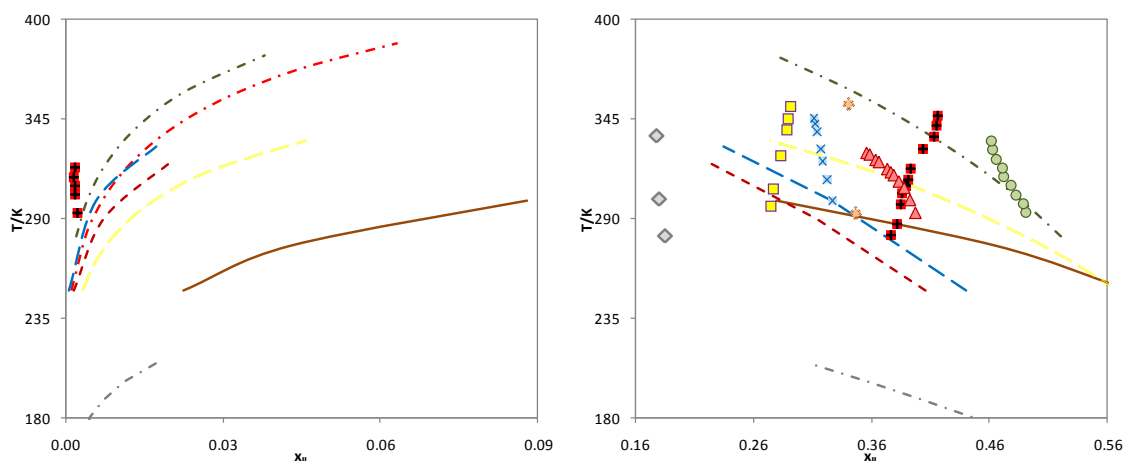


Figure 3.14 Liquid–liquid phase diagram for $[\text{C}_4\text{mim}][\text{MeSO}_4]$ ³⁵ (●) (---), $[\text{C}_4\text{mim}][\text{PF}_6]$ ⁵¹ (◊) (—), $[\text{C}_4\text{mim}][\text{BF}_4]$ ⁶³ (○) (—), $[\text{C}_4\text{mim}][\text{NTf}_2]$ ⁴⁶ (◇) (---), $[\text{C}_4\text{mim}][\text{SCN}]$ ³² (■) (— · —), $[\text{C}_4\text{mim}][\text{TOS}]$ ³⁶ (×) (— —), $[\text{C}_4\text{mim}][\text{CF}_3\text{SO}_3]$ ⁵⁰ (□) (— —) and $[\text{C}_4\text{mim}][\text{MDEGSO}_4]$ ³⁹ (△) (— — —) with benzene. The symbols and the lines represent respectively the experimental data and the COSMO-RS prediction calculations.

3.3.4. Cycloalkanes + ILs binary systems

The LLE of binary mixtures of IL + cycloalkanes available in literature are based in C_5 , C_6 and C_7 cycloalkanes and are summarized in Table B3. In general the solubilities of these compounds in ionic liquids are slightly larger than those observed for n -alkanes due to their lower molecular volume and cyclic structure responsible by a more effective packing effect. As discussed before, for the solubility of the ionic liquids in other hydrocarbons, the solubility in cycloalkanes is also very small, being of the order of 3×10^{-5} (in mole fraction)^{36, 38, 51} for systems for which data are available.

The predictions provided by COSMO-RS for the description of the LLE experimental data for IL + cycloalkanes systems are discussed below.

3.3.4.1. Effect of the cycloalkanes structure upon the phase behavior

The cycloalkanes size has an important effect on the solubilities of these compounds in ionic liquids. The immiscibility region increases with the cycloalkanes size (or carbon number increase) as shown in Figure 3.15. A number of other systems with distinct ionic liquids, yet a similar behavior, are reported in Appendix B (Figures B11 to B114).

The COSMO-RS predictions can describe correctly the decreased miscibility with the increase of the cycloalkane size. In the most part of the studied examples a fine quantitative description of the data was also achieved.

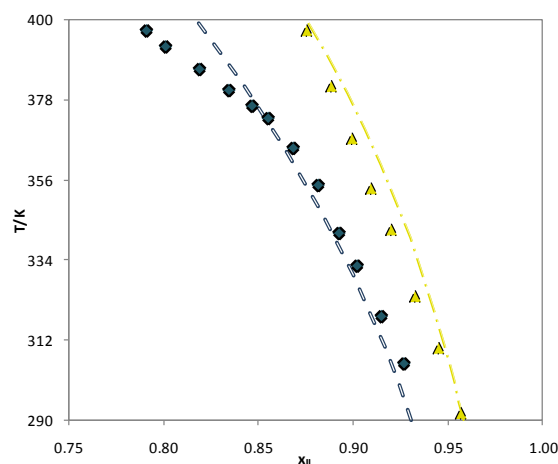


Figure 3.15 Liquid–liquid phase diagram for $[C_6mim][SCN]$ with cyclohexane³⁸ (\blacklozenge) ($- -$) and cycloheptane³⁸ (\blacktriangle) ($- \cdot -$). The symbols and the lines represent respectively the experimental data and the COSMO-RS prediction calculations.

3.3.4.2. Effect of the ionic liquid cation core upon the phase behavior

As previously observed for different hydrocarbons, the cycloalkane containing systems do not vary appreciably with the cations based on nitrogen-containing heterocycles, such as the imidazolium-, pyrrolidinium- and pyridinium-based ionic liquids, and presented in Figure 3.16. Again slightly higher solubilities were observed with the pyridinium-based ionic liquid. Therefore, the increasing solubility of hydrocarbons in ionic liquids follows the general rank that is independent on the hydrocarbon nature: pyridinium- > pyrrolidinium- \approx imidazolium- based ionic liquids. Other types of cations (such as phosphonium- and ammonium-based ionic liquids) may however present quite different behaviors. Yet, the experimental data available are too scarce to draw any conclusions concerning this matter.

COSMO-RS can correctly predict the solubility trends experimentally observed in Figure 3.16 and, as observed for the aromatic hydrocarbons, it predicts a larger difference in solubility between the imidazolium, the pyridinium, and pyrrolidinium cations than that observed experimentally.

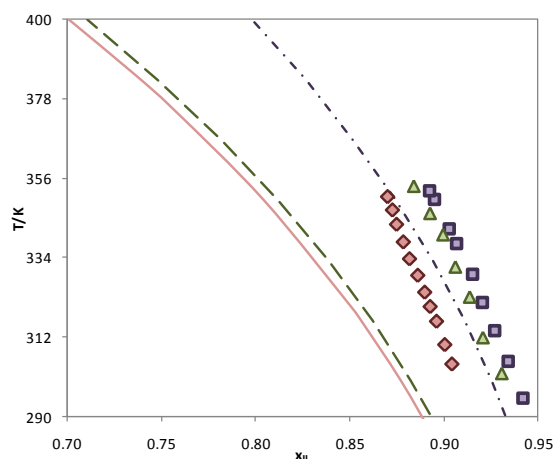


Figure 3.16 Liquid–liquid phase diagram for $[\text{C}_4\text{mim}][\text{CF}_3\text{SO}_3]^{50}$ (\square) (---), $[\text{C}_4\text{mpyr}][\text{CF}_3\text{SO}_3]^{50}$ (\triangle) (---) and $[\text{1,3C}_4\text{mpy}][\text{CF}_3\text{SO}_3]^{50}$ (\diamond) (—) with cyclohexane. The symbols and the lines represent respectively the experimental data and the COSMO-RS prediction calculations.

3.3.4.3. Effect of the ionic liquid cation alkyl chain length upon the phase behavior

From Figure 3.17, the increase of the cation alkyl chain length allows dispersive type interactions between the hydrocarbon and the ionic liquid, which that along with a higher free volume and the favorable packing effect, contribute to an increase in the miscibility between both solvents. Moreover, at Figure B118, the replacement of a methyl group by a longer alkoxymethyl group at the ionic liquid cation also leads to a higher solubility of the cyclohexane in the ionic liquid. In fact, this general trend was observed for the three types of hydrocarbons studied.

Although the experimental data is scarce for a full evaluation of the model, COSMO-RS can provide an excellent quantitative and qualitative description of the systems behavior presented in Figure 3.17 and Figure B118 (at Appendix B).

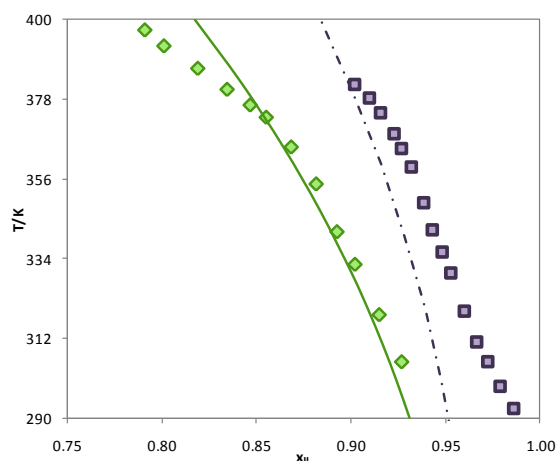


Figure 3.17 Liquid–liquid phase diagram for $[\text{C}_4\text{mim}][\text{SCN}]$ ³² (\blacksquare) (– · –) and $[\text{C}_6\text{mim}][\text{SCN}]$ ³⁸ (\blacklozenge) (—) with cyclohexane. The symbols and the lines represent respectively the experimental data and the COSMO-RS prediction calculations.

3.3.4.4. Effect of the ionic liquid anion upon the phase behavior

The experimental data available, reported in Table B3, allow the comparison of the effect of several anions towards the liquid-liquid equilibria with cycloalkanes. Two main examples are displayed in Figure 3.18 and Figure B120 for ($[\text{C}_4\text{mim}]^-$ and $[\text{C}_6\text{H}_{13}\text{OCH}_2\text{mim}]^-$ -based ionic liquids + cyclohexane) binary systems.

The influence of the anion is more relevant in the cycloalkanes solubility in ionic liquids than the cation family effect discussed above. In the $[\text{C}_4\text{mim}]^-$ -based ionic liquids the miscibility with cyclohexane increases in the order: $[\text{SCN}]^- < [\text{CF}_3\text{SO}_3]^- < [\text{MDEGSO}_4]^- < [\text{PF}_6]^-$. For the $[\text{C}_6\text{H}_{13}\text{OCH}_2\text{mim}]^-$ -based ionic liquid the solubility with cyclohexane increases from $[\text{BF}_4]^-$ to $[\text{NTf}_2]^-$ composing anions. As observed before with *n*-alkanes, these sequences closely follow the solvatochromic β parameter trend (hydrogen bond basicity of the ionic liquid):⁶¹⁻⁶² $[\text{SCN}]^- > [\text{CF}_3\text{SO}_3]^- > [\text{MDEGSO}_4]^- > [\text{PF}_6]^-$.

The COSMO-RS predictions are not complete reliable to describe the ionic liquids anions influence in their mutual solubilities with cycloalkanes, and as previously observed for *n*-alkanes and for aromatic hydrocarbons. The results reported in Figure 3.18 show that some anions are correctly described, e.g. $[\text{SCN}]^-$, $[\text{CF}_3\text{SO}_3]^-$ and $[\text{MDEGSO}_4]^-$, while for others, such as $[\text{PF}_6]^-$, the model fails in describing their correct trend. COSMO-RS seems to fail with high charge density anions. These anions have stronger coulombic interactions with the combined cation that are underestimated by the COSMO-RS calculations. In spite of these anions, for which the COSMO-RS qualitative description

fails, the solubility predictions are correct at least from a semi-quantitative point of view and for, some anions, even a close quantitative description is achieved.

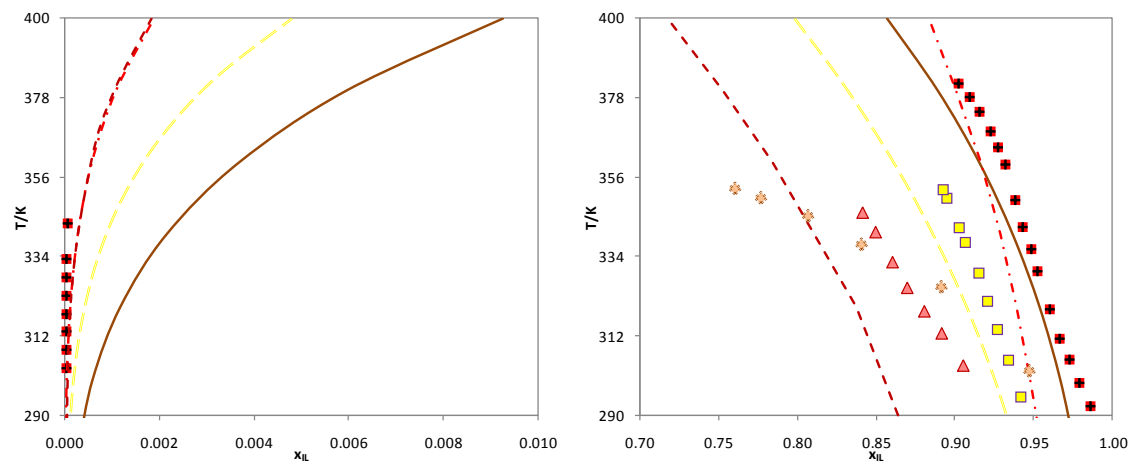


Figure 3.18 Liquid–liquid phase diagram for $[\text{C}_4\text{mim}][\text{PF}_6]$ ⁵¹ (—) (—), $[\text{C}_4\text{mim}][\text{SCN}]$ ³² (— · —) (— · —), $[\text{C}_4\text{mim}][\text{CF}_3\text{SO}_3]$ ⁵⁰ (— — —) (— — —) and $[\text{C}_4\text{mim}][\text{MDEGSO}_4]$ ³⁹ (— — —) (— — —) with cyclohexane. The symbols and the lines represent respectively the experimental data and the COSMO-RS prediction calculations.

3.3.5. Summary of the various effects studied upon the phase behavior

The influence of various factors studied on this work through the mutual solubilities of hydrocarbons and ionic liquids is summarized in Table 3.1, along with the performance of the COSMO-RS model towards the description of the experimentally observed trends. With the exception of the ionic liquid anion nature influence in the solubility behavior, which was not fully captured by the COSMO-RS iterative calculations, the model seems to be able to produce a semi-quantitative description of the experimental data. Often, for the most immiscible systems, even an acceptable quantitative prediction of the phase diagrams, although far from the critical point, is achieved. It seems thus that COSMO-RS could be a useful tool for the screening of ionic liquids to be used in processes dealing with hydrocarbons.

Although binary systems can be of use to identify the ionic liquids for which the solubilities of hydrocarbons are quite different, and therefore are potentially interesting for extraction purposes, they provide limited information. To study the application of ionic liquids to perform extractions in more complex real systems, ternary systems studies are required. For that purpose a companion article to this work, dealing with ternary systems of ionic liquids and hydrocarbon mixtures, is under preparation.

Table 3.1 Summary of the factors that influence the solubility and the performance of COSMO-RS.

Factor	Influence on the solubility	COSMO-RS performance
Hydrocarbon type	Aromatics >> cycloalkanes > <i>n</i> -alkanes	✓
<i>n</i>-alkanes + ILs systems		
<i>n</i> -alkane chain length	↑ C_n → ↓ Solubility	✓
IL cation core	≈	✓
IL cation alkyl chain length	↑ C_n → ↑ Solubility	✓
IL anion family	[MeSO ₄] ⁻ > [SCN] ⁻ > [TOS] ⁻ > [CF ₃ SO ₃] ⁻ > [MDEGSO ₄] ⁻ > [PF ₆] ⁻ [BF ₄] ⁻ > [NTf ₂] ⁻	×
IL anion alkyl chain length	↑ C_n → ↑ Solubility	✓
Aromatics + ILs systems		
Aromatic alkyl chain substituted length	↑ C_n → ↓ Solubility	✓
IL cation core	≈	✓
IL cation alkyl chain length	↑ C_n → ↑ Solubility	✓
IL anion family	[BF ₄] ⁻ > [MeSO ₄] ⁻ > [SCN] ⁻ > [EtSO ₄] ⁻ > [MDEGSO ₄] ⁻ > [TOS] ⁻ > [PF ₆] ⁻ > [CF ₃ SO ₃] ⁻ > [NTf ₂] ⁻	×
IL anion alkyl chain length	↑ C_n → ↑ Solubility	✓
Cycloalkanes + ILs systems		
Cycloalkane size	↑ C_n → ↓ Solubility	✓
IL cation core	≈	✓
IL cation alkyl chain length	↑ C_n → ↑ Solubility	✓
IL anion family	[SCN] ⁻ > [CF ₃ SO ₃] ⁻ > [MDEGSO ₄] ⁻ > [PF ₆] ⁻	×
IL anion alkyl chain length	↑ C_n → ↑ Solubility	✓

Legend: ≈ negligible influence; ✓ COSMO-RS describes the experimental trend correctly; × COSMO-RS does not correctly describes the experimental trend.

3.4. Conclusions

The use of ionic liquids in refineries and petrochemical industries requires the knowledge and the complete understanding of the several structural factors that influence the liquid phase behavior of systems containing such fluids. Therefore, an overview of the mutual solubilities of hydrocarbons and ionic liquids was carried out in this work to evaluate both the structural features of the hydrocarbons (chain length and molecular size, aromaticity, positional isomerism and cyclization) and of the ionic liquids (cation family, cation alkyl chain and anion nature) upon the phase behavior. The ability of COSMO-RS, a predictive model based on the quantum chemical model combined with statistical thermodynamics, was also evaluated in describing the phase behavior of these binary systems.

The influence of various structural factors studied in the mutual solubilities of hydrocarbons and ionic liquids is summarized in Table 3.1. Concerning the COSMO-RS predictions it was shown to be possible to achieve a good qualitative and a semi-quantitative description of the structural effects of different hydrocarbons and ionic liquids in the mutual solubilities of the studied systems. The only exception appears in the ionic liquid anion influence for which COSMO-RS is not able to fully capture the different ionic liquids inducing behavior. Another limitation of COSMO-RS is the solubility prediction of systems presenting large mutual miscibilities (far from the infinite dilution regime). For less miscible systems (near complete immiscibility), the predicted values are in good quantitative agreement with experimental data. Despite these limitations, the capability of COSMO-RS to predict the LLE of IL + hydrocarbon binary systems suggests that it can be used as an *a priori* tool for the screening of ionic liquids suitable for applications involving hydrocarbons.

3.5. References

1. Lu, J.; Yan, F.; Texter, J., Advanced applications of ionic liquids in polymer science. *Prog Polym Sci* **2009**, *34* (5), 431-448.
2. Zhao, D.; Wu, M.; Kou, Y.; Min, E., Ionic liquids: applications in catalysis. *Catal Today* **2002**, *74* (1-2), 157-189.
3. Tian, G.-c.; Li, J.; Hua, Y.-x., Application of ionic liquids in hydrometallurgy of nonferrous metals. *Trans Nonferr Metal Soc* **2010**, *20* (3), 513-520.
4. Li, Z.; Jia, Z.; Luan, Y.; Mu, T., Ionic liquids for synthesis of inorganic nanomaterials. *Curr Opin Solid State Mater Sci* **2008**, *12* (1), 1-8.
5. Vioux, A.; Viau, L.; Volland, S.; Le Bideau, J., Use of ionic liquids in sol-gel; ionogels and applications. *Comptes Rendus de l' Academie des Sciences Serie IIc:Chemie* **2010**, *13* (1-2), 242-255.
6. Meindersma, G. W.; de Haan, A. B., Separation of Aromatic and Aliphatic Hydrocarbons with Ionic Liquids. In *Ionic Liquids: From Knowledge to Application*, American Chemical Society: Washington DC, 2009; pp 255-272.
7. Arce, A.; Earle, M. J.; Katdare, S. P.; Rodriguez, H.; Seddon, K. R., Application of mutually immiscible ionic liquids to the separation of aromatic and aliphatic hydrocarbons by liquid extraction: a preliminary approach. *Phys Chem Chem Phys* **2008**, *10* (18), 2538-2542.
8. Bélafi-Bakó, K.; Dörmö, N.; Ulbert, O.; Gubicza, L., Application of pervaporation for removal of water produced during enzymatic esterification in ionic liquids. *Desalination* **2002**, *149* (1-3), 267-268.
9. Shiflett, M. B.; Yokozeki, A., Separation of Carbon Dioxide and Sulfur Dioxide Using Room-Temperature Ionic Liquid [bmim][MeSO₄]. *Energ Fuel* **2009**, *24* (2), 1001-1008.
10. Yokozeki, A.; Shiflett, M. B., Hydrogen purification using room-temperature ionic liquids. *Appl Energ* **2007**, *84* (3), 351-361.
11. Kubisa, P., Ionic liquids as solvents for polymerization processes--Progress and challenges. *Prog Polym Sci* **2009**, *34* (12), 1333-1347.
12. Werner, S.; Haumann, M.; Wasserscheid, P., Ionic Liquids in Chemical Engineering. *Annu Rev Chem Biomol Eng* **2010**, *1* (1), 203-230.
13. Olivier-Bourbigou, H.; Magna, L.; Morvan, D., Ionic liquids and catalysis: Recent progress from knowledge to applications. *Appl Catal A-Gen* **2010**, *373* (1-2), 1-56.

14. Rogers, R. D.; Seddon, K. R., Ionic Liquids--Solvents of the Future? *Science* **2003**, *302* (5646), 792-793.
15. Seddon, K. R., Ionic liquids: A taste of the future. *Nat Mater* **2003**, *2* (6), 363-365.
16. BASF The BASIL process: Acid scavenging <http://www.basionics.com/en/ionic-liquids/processes/acid.htm> (accessed 29/11/2010).
17. Favre, F.; Forestiere, A.; Hugues, F.; Olivier-Bourbigou, H.; Chodorge, J. A., From monophasic Dimersol (TM) to biphasic Difasol (TM). *Oil Gas-Eur Mag* **2005**, *31* (2), 83-87.
18. Chauvin, Y.; Olivier, H.; Wyrvalski, C. N.; Simon, L. C.; de Souza, R. F., Oligomerization of n-Butenes Catalyzed by Nickel Complexes Dissolved in Organochloroaluminate Ionic Liquids. *J Catal* **1997**, *165* (2), 275-278.
19. Li, H. M.; Jiang, X.; Zhu, W. H.; Lu, J. D.; Shu, H. M.; Yan, Y. S., Deep Oxidative Desulfurization of Fuel Oils Catalyzed by Decatungstates in the Ionic Liquid of Bmim PF6. *Ind Eng Chem Res* **2009**, *48* (19), 9034-9039.
20. Arce, A.; Francisco, M.; Soto, A., Evaluation of the polysubstituted pyridinium ionic liquid [hmmpy][Ntf2] as a suitable solvent for desulfurization: Phase equilibria. *J Chem Therm* **2010**, *42* (6), 712-718.
21. Gao, H. S.; Guo, C.; Xing, J. M.; Zhao, J. M.; Liu, H. Z., Extraction and oxidative desulfurization of diesel fuel catalyzed by a Bronsted acidic ionic liquid at room temperature. *Green Chem* **2010**, *12* (7), 1220-1224.
22. Kuhlmann, E.; Haumann, M.; Jess, A.; Seeberger, A.; Wasserscheid, P., Ionic Liquids in Refinery Desulfurization: Comparison between Biphasic and Supported Ionic Liquid Phase Suspension Processes. *Chemsuschem* **2009**, *2* (10), 969-977.
23. Francisco, M.; Arce, A.; Soto, A., Ionic liquids on desulfurization of fuel oils. *Fluid Phase Equilib* **2010**, *294* (1-2), 39-48.
24. Wu, Z. L.; Ondruschka, B., Ultrasound-assisted oxidative desulfurization of liquid fuels and its industrial application. *Ultrasonics Sonochemistry* **2010**, *17* (6), 1027-1032.
25. Pereiro, A. B.; Rodriguez, A., Application of the ionic liquid Ammoeng 102 for aromatic/aliphatic hydrocarbon separation. *J Chem Therm* **2009**, *41* (8), 951-956.
26. Arce, A.; Earle, M. J.; Rodriguez, H.; Seddon, K. R.; Soto, A., Bis((trifluoromethyl)sulfonyl)amide ionic liquids as solvents for the extraction of aromatic hydrocarbons from their mixtures with alkanes: effect of the nature of the cation. *Green Chem* **2009**, *11* (3), 365-372.

27. Poole, C. F.; Poole, S. K., Extraction of organic compounds with room temperature ionic liquids. *J Chromatogr A* **2010**, 1217 (16), 2268-2286.
28. Lei, Z.; Li, C.; Chen, B., Extractive Distillation: A Review. *Sep Purif Rev* **2003**, 32 (2), 121 - 213.
29. Wytze Meindersma, G.; Podt, A.; de Haan, A. B., Selection of ionic liquids for the extraction of aromatic hydrocarbons from aromatic/aliphatic mixtures. *Fuel Process Technol* **2005**, 87 (1), 59-70.
30. Bendová, M.; Wagner, Z., Thermodynamic description of liquid-liquid equilibria in systems 1-ethyl-3-methylimidazolium ethylsulfate+C7-hydrocarbons by polymer-solution models. *Fluid Phase Equilib* **2009**, 284 (2), 80-85.
31. Domańska, U.; Laskowska, M.; Marciniak, A., Phase equilibria of (1-ethyl-3-methylimidazolium ethylsulfate plus hydrocarbon, plus ketone, and plus ether) binary systems. *J Chem Eng Data* **2008**, 53 (2), 498-502.
32. Domańska, U.; Laskowska, M.; Pobudkowska, A., Phase Equilibria Study of the Binary Systems (1-Butyl-3-methylimidazolium Thiocyanate Ionic Liquid plus Organic Solvent or Water). *J Phys Chem B* **2009**, 113 (18), 6397-6404.
33. Domańska, U.; Pobudkowska, A.; Eckert, F., Liquid-liquid equilibria in the binary systems (1,3-dimethylimidazolium, or 1-butyl-3-methylimidazolium methylsulfate plus hydrocarbons). *Green Chem* **2006**, 8 (3), 268-276.
34. Domańska, U.; Zolek-Tryznowska, Z.; Krolkowski, M., Thermodynamic phase behavior of ionic liquids. *J Chem Eng Data* **2007**, 52, 1872-1880.
35. García, J.; Torrecilla, J. S.; Fernández, A.; Oliet, M.; Rodríguez, F., (Liquid + liquid) equilibria in the binary systems (aliphatic, or aromatic hydrocarbons + 1-ethyl-3-methylimidazolium ethylsulfate, or 1-butyl-3-methylimidazolium methylsulfate ionic liquids). *J Chem Therm* **2010**, 42 (1), 144-150.
36. Domańska, U.; Królikowski, M., Phase equilibria study of the binary systems (1-butyl-3-methylimidazolium tosylate ionic liquid + water, or organic solvent). *J Chem Therm* **2010**, 42 (3), 355-362.
37. Domańska, U.; Pobudkowska, A.; Wisniewska, A., Solubility and excess molar properties of 1,3-dimethylimidazolium methylsulfate, or 1-butyl-3-methylimidazolium methylsulfate, or 1-butyl-3-methylimidazolium octylsulfate ionic liquids with n-alkanes and alcohols: Analysis in terms of the PFP and FBT models. *J Solution Chem* **2006**, 35 (3), 311-334.

38. Domańska, U.; Krlukowska, M.; Arasimowicz, M., Phase Equilibria of (1-Hexyl-3-methylimidazolium Thiocyanate + Water, Alcohol, or Hydrocarbon) Binary Systems. *J Chem Eng Data* **2010**, *55* (2), 773-777
39. Domańska, U.; Marciniak, A., Liquid phase behaviour of 1-butyl-3-methylimidazolium 2-(2-methoxyethoxy)-ethylsulfate with organic solvents and water. *Green Chem* **2007**, *9* (3), 262-266.
40. Pereiro, A. B.; Rodriguez, A., Binary mixtures containing OMIM PF6: density, speed of sound, refractive index and LLE with hexane, heptane and 2-propanol at several temperatures. *Phys Chem Liq* **2008**, *46* (2), 172-184.
41. Domańska, U.; Marciniak, A., Liquid phase behaviour of 1-hexyloxymethyl-3-methyl-imidazolium-based ionic liquids with hydrocarbons: The influence of anion. *J Chem Thermodyn* **2005**, *37* (6), 577-585.
42. Domańska, U.; Marciniak, A., Phase behaviour of 1-hexyloxymethyl-3-methyl-imidazolium and 1,3-dihexyloxymethyl-imidazolium based ionic liquids with alcohols, water, ketones and hydrocarbons: The effect of cation and anion on solubility. *Fluid Phase Equilib* **2007**, *260* (1), 9-18.
43. Domańska, U.; Bakala, I.; Pernak, J., Phase equilibria of an ammonium ionic liquid with organic solvents and water. *J Chem Eng Data* **2007**, *52* (1), 309-314.
44. Domańska, U.; Lugowska, K.; Pernak, J., Phase equilibria of didecyldimethylammonium nitrate ionic liquid with water and organic solvents. *J Chem Thermodyn* **2007**, *39* (5), 729-736.
45. Domańska, U.; Marciniak, A.; Krolkowski, M., Phase equilibria and modeling of ammonium ionic liquid, C₂N₂F₂, solutions. *J Phys Chem B* **2008**, *112* (4), 1218-1225.
46. Lachwa, J.; Szydłowski, J.; Makowska, A.; Seddon, K. R.; Esperanca, J.; Guedes, H. J. R.; Rebelo, L. P. N., Changing from an unusual high-temperature demixing to a UCST-type in mixtures of 1-alkyl-3-methylimidazolium bis{(trifluoromethyl)sulfonyl}amide and arenes. *Green Chem* **2006**, *8* (3), 262-267.
47. Domańska, U.; Paduszynski, K., (Solid + liquid) and (liquid + liquid) phase equilibria measurements and correlation of the binary systems {tri-iso-butyl(methyl)phosphonium tosylate + alcohol, or +hydrocarbon}. *Fluid Phase Equilib* **2009**, *278* (1-2), 90-96.

48. Domańska, U.; Mazurowska, L., Solubility of 1,3-dialkylimidazolium chloride or hexafluorophosphate or methylsulfonate in organic solvents: effect of the anions on solubility. *Fluid Phase Equilib* **2004**, *221* (1-2), 73-82.
49. Domańska, U.; Królikowski, M.; Pobudkowska, A.; Letcher, T. M., Phase Equilibria Study of the Binary Systems (N-Butyl-4-methylpyridinium Tosylate Ionic Liquid + Organic Solvent, or Water)†‡. *J Chem Eng Data* **2009**, *54* (5), 1435-1441.
50. Marciniak, A.; Karczemna, E., Influence of Cation Structure on Binary Liquid-Liquid Equilibria for Systems Containing Ionic Liquids Based on Trifluoromethanesulfonate Anion with Hydrocarbons. *J Physl Chem B* **2010**, *114* (16), 5470–5474.
51. Domańska, U.; Marciniak, A., Solubility of 1-alkyl-3-methylimidazolium hexafluorophosphate in hydrocarbons. *J Chem Eng Data* **2003**, *48* (3), 451-456.
52. Domańska, U.; Królikowski, M.; Paduszynski, K., Phase equilibria study of the binary systems (N-butyl-3-methylpyridinium tosylate ionic liquid + an alcohol). *J Chem Therm* **2009**, *41* (8), 932-938.
53. Chen, C.-C.; Simoni, L. D.; Brennecke, J. F.; Stadtherr, M. A., Correlation and prediction of phase behavior of organic compounds in ionic liquids using the Nonrandom Two-Liquid Segment Activity Coefficient model. *Ind. Eng. Chem. Res.* **2008**, *47* (18), 7081-7093.
54. Domańska, U.; Królikowski, M.; Ramjugernath, D.; Letcher, T. M.; Tumba, K., Phase Equilibria and Modeling of Pyridinium-Based Ionic Liquid Solutions. *J Physl Chem B* **2010**, *114* (46), 15011–15017.
55. Klamt, A.; Eckert, F., COSMO-RS: a novel and efficient method for the a priori prediction of thermophysical data of liquids. *Fluid Phase Equilib* **2000**, *172* (1), 43-72.
56. Klamt, A., Summary, limitations, and perspectives. In *COSMO-RS*, Elsevier: Amsterdam, 2005; 205-207.
57. Diedenhofen, M.; Klamt, A., COSMO-RS as a tool for property prediction of IL mixtures--A review. *Fluid Phase Equilib* **2010**, *294* (1-2), 31-38.
58. Freire, M. G.; Santos, L. M. N. B. F.; Marrucho, I. M.; Coutinho, J. A. P., Evaluation of COSMO-RS for the prediction of LLE and VLE of alcohols + ionic liquids. *Fluid Phase Equilib* **2007**, *255* (2), 167-178.

59. Freire, M. G.; Ventura, S. P. M.; Santos, L. M. N. B. F.; Marrucho, I. M.; Coutinho, J. A. P., Evaluation of COSMO-RS for the prediction of LLE and VLE of water and ionic liquids binary systems. *Fluid Phase Equilib* **2008**, *268* (1-2), 74-84.
60. Freire, M. G.; Carvalho, P. J.; Santos, L. M. N. B. F.; Gomes, L. R.; Marrucho, I. M.; Coutinho, J. A. P., Solubility of water in fluorocarbons: Experimental and COSMO-RS prediction results. *J Chem Therm* **2010**, *42* (2), 213-219.
61. Lungwitz, R.; Spange, S., A hydrogen bond accepting (HBA) scale for anions, including room temperature ionic liquids. *New J Chem* **2008**, *32* (3), 392-394.
62. Lungwitz, R.; Strehmel, V.; Spange, S., The dipolarity/polarisability of 1-alkyl-3-methylimidazolium ionic liquids as function of anion structure and the alkyl chain length. *New J Chem* **2010**, *34* (6), 1135-1140.
63. Shang, H. T.; Wu, J. S.; Zhou, Q.; Wang, L. S., Solubilities of benzene, toluene, and xylene isomers in 1-butyl-3-methylimidazolium tetrafluoroborate. *J Chem Eng Data* **2006**, *51* (4), 1286-1288.
64. Arce, A.; Earle, M. J.; Rodriguez, H.; Seddon, K. R.; Soto, A., 1-Ethyl-3-methylimidazolium bis{(trifluoromethyl)sulfonyl}amide as solvent for the separation of aromatic and aliphatic hydrocarbons by liquid extraction - extension to C7- and C8-fractions. *Green Chem* **2008**, *10* (12), 1294-1300.
65. Domańska, U.; Pobudkowska, A.; Królikowski, M., Separation of aromatic hydrocarbons from alkanes using ammonium ionic liquid C₂N₂Tf₂ at T = 298.15 K. *Fluid Phase Equilib* **2007**, *259* (2), 173-179.
66. Blesic, M.; Lopes, J. N. C.; Gomes, M. F. C.; Rebelo, L. s. P. N., Solubility of alkanes, alkanols and their fluorinated counterparts in tetraalkylphosphonium ionic liquids. *Phys Chem Chem Phys* **2010**, *12* (33), 9685-9692.
67. Shiflett, M. B.; Niehaus, A. M. S., Liquid-Liquid Equilibria in Binary Mixtures Containing Substituted Benzenes with Ionic Liquid 1-Ethyl-3-methylimidazolium Bis(trifluoromethylsulfonyl)imide. *J Chem Eng Data* **2009**, *55* (1), 346-353.
68. Dreiseitlová, J.; Řehák, K.; Vreekamp, R., Mutual Solubility of Pyridinium-Based Tetrafluoroborates and Toluene. *J Chem Eng Data* **2010**, *55* (9), 3051-3054.

Chapter 4

An Overview of the Liquid-Liquid Equilibria of Ternary Systems composed of Ionic Liquid, Aromatic and Aliphatic Hydrocarbons, and its Modeling by COSMO-RS

Ferreira, A. R.; Freire, M. G.; Ribeiro, J. C.; Lopes, F. M.; Crespo, J. G.;
Coutinho, J. A. P.

Published at *Industrial and Engineering Chemistry Research*

2012, 51 (8), 3483-3507

DOI: 10.1021/ie2025322

4.1. Introduction

Concerning the aliphatic/aromatic separation of hydrocarbons by ionic liquids, the number of experimentally studied systems increased considerably in the past few years,¹⁻⁵³ as shown in Tables C1 and C2 at Appendix C. These tables report the experimental data available on the liquid-liquid equilibrium of ternary systems of the type ionic liquid + aromatic hydrocarbon + aliphatic hydrocarbon (*n*-alkanes in Table C1 and cycloalkanes in Table C2). The huge number of potential ionic liquids that can be synthesized makes impossible the selection of the optimal ionic liquid for a specific task, or any extraction/separation process, only through experimental measurements. For an adequate selection of an ionic liquid it is necessary the development of heuristics, or predictive models and correlations that, based on some few selected experimental measurements, will be able to predict the phase behavior of these systems.

A number of models have been applied to the description of the phase behavior of systems constituted by one ionic liquid and two hydrocarbons as described in Tables C1 and C2. Two classical local composition models, the Non-Random Two Liquid (NRTL)^{1-2, 4, 8-10, 16-22, 24, 27, 31-35, 37-39, 44, 49, 53-54} and the UNIQUAC^{9, 32, 54-55} models, have been often applied, both showing a good correlation ability yet with no predictive capacity. The only predictive model that has been studied so far for the description of these systems is the ASOG model,⁵⁶⁻⁵⁷ but it has been only applied to a limited number of systems.

An alternative approach, the Conductor-like Screening Model for Real Solvents (COSMO-RS), proposed by Klamt and co-workers,⁵⁸⁻⁶⁰ is a predictive model that can be used for an initial screening of ionic liquids for various applications.⁶⁰⁻⁷³ The COSMO-RS does not require adjustable parameters from experimental data and only uses the information on the molecular structure of the compounds. Hence, it can be applied to a large number of ionic liquids and hydrocarbons combinations. Following our previous work⁷³, where COSMO-RS has been studied for the description of the liquid-liquid equilibrium of IL + hydrocarbon binary systems, in this work, the COSMO-RS is evaluated in the prediction of the phase behavior of IL + hydrocarbons ternary systems. It should be pointed out that this model has already been applied previously to the description of a limited number of systems.^{62-63, 65-67, 69-70}

This study aims at evaluating the effect of the structural characteristics of the hydrocarbons molecules and ionic liquids on their phase behavior from the analysis of the compiled experimental data published hitherto, aspiring at a better understanding on the main molecular interactions that control the liquid-liquid equilibrium. In addition, the

experimental data were used to evaluate the COSMO-RS ability in describing the phase behavior of these systems.

4.2. Ionic Liquid + Hydrocarbons Liquid–Liquid Equilibria

Tables C1 and C2, at Appendix C, summarize the experimental data of liquid-liquid equilibrium of ternary systems composed of ionic liquids, aromatic hydrocarbons and aliphatic hydrocarbons (*n*-alkanes in Table C1 and cycloalkanes in Table C2) available on the literature and published hitherto.¹⁻⁵³ Circa 188 systems were collected and comprise several ionic liquids and hydrocarbons. These systems were experimentally addressed in the past decade regarding the applicability of ionic liquids through petrochemical and refinery processes. In particular, these systems deal with the separation of aromatics from aliphatic hydrocarbons. The *n*-alkanes studied were *n*-hexane, *n*-heptane, *n*-octane, *n*-nonane, *n*-decane, *n*-undecane, *n*-dodecane and *n*-hexadecane; the aromatic hydrocarbons were benzene, toluene, ethylbenzene, propylbenzene, butylbenzene, *o*-xylene, *m*-xylene and *p*-xylene; and the cycloalkanes were cyclohexane, methylcyclohexane and cyclooctane. In what concerns ionic liquids, 22 different cations belonging to the imidazolium, pyridinium, ammonium and phosphonium families, combined with 20 anions, such as bis(trifluoromethylsulfonyl)imide, alkylsulfates, hexafluorophosphate, tetrafluoroborate, thiocyanate, dicyanamide, tetracyanoborate, chloride, triiodide and dialkylphosphates, were studied. The data used were measured at atmospheric pressure and at several temperatures - reported in Tables C1 and C2. The abbreviations and ionic structures of the ions composing the ionic liquids are depicted in Tables A1 and A2, in Appendix A.

The large number of systems available allows a comprehensive study on the effect of the structural characteristics of the hydrocarbons molecules and ionic liquids through their phase behavior, selectivities and distribution ratio among the co-existing phases.

4.3. Results and Discussion

The experimental data reported in Tables C1 and C2, at Appendix C, were the basis for the study of the effect of the structural characteristics of the hydrocarbons and ionic liquids into their phase behavior. The structural factors, such as aromaticity, chain length, cyclization and positional isomerism of the hydrocarbons, and the cation core and anion

nature, and length of the side alkyl chain of ionic liquids are analyzed and discussed below regarding the impact that they have on the liquid-liquid phase behavior.

Phase diagrams describing the liquid-liquid equilibria (LLE) for selected ternary systems composed of ionic liquid + aromatic hydrocarbon + aliphatic hydrocarbon are displayed in Figures 4.1 to 4.13. Further results are presented in Figures C1 to C35 at Appendix C. These diagrams allow a global overview of the phase behavior of the ternary systems under study. Most ternary phase diagrams reported in literature are of type 2⁷⁴ presenting a partial miscibility in two pairs of compounds: the ionic liquid + aliphatic hydrocarbon and the ionic liquid + aromatic hydrocarbon. The binodal curves at the aliphatic hydrocarbon-rich phase lie close to the edge of the phase diagram due to the low solubilities displayed by the ionic liquid on the aliphatic hydrocarbon. Moreover, the addition of aromatic hydrocarbons to the ionic liquid + aliphatic hydrocarbon mixtures does not lead to a significant increase of the aliphatic miscibility in the ionic liquid-rich phase. Although the aromatic hydrocarbons present a significant miscibility with both compounds they do not extensively act as co-solvents. The ternary diagrams presented are also characterized by tie-lines with negative slopes and often solutropy, *i.e.*, there is a change in the slope of the tie-lines as the aromatic content increases. The absolute slope of the tie-lines increases with the amount of aromatic hydrocarbon since the mutual solubilities between the two co-existing phases also increases. Thus, at this stage, an increase of at least one of phase-forming components is needed for phase separation. The features observed on the ternary phase diagrams, such as large immiscibility regions, and favorable distribution ratios and selectivities, are encouraging issues towards the use of these systems in aromatic-aliphatic separations by liquid-liquid extraction. Moreover, the very low solubility of the ionic liquid in aliphatic hydrocarbons minimizes the loss of the ionic liquid and the contamination of the refined stream.

Besides the binodal curves and the tie-lines assessment to discuss and interpret the phase diagrams, we further evaluated the solvent selectivity (*S*) and distribution ratio (*D*). These parameters, defined by equations 4.1 and 4.2, respectively, provide a quantitative description of the partitioning of the aromatic hydrocarbons between the co-existing phases:

$$S = \frac{\frac{x_{aro}^{II}}{x_{aliph}^{II}}}{\frac{x_{aro}^I}{x_{aliph}^I}} \quad (4.1)$$

$$D = \frac{x_{aro}^{II}}{x_{aro}^I} \quad (4.2)$$

where x is the mole fraction, the subscripts *aliph* and *aro* are related with the aliphatic and aromatic hydrocarbons, respectively, and the superscript *I* refers to the aliphatic hydrocarbon-rich-phase, while *II* refers to the ionic liquid-rich phase.

In order to evaluate the performance of COSMO-RS to predict the LLE of the ternary systems experimentally available, the root mean square deviation (RMSD) between the experimental and predicted data was additionally determined and is defined according to the following equation:

$$RMSD = \left[\frac{\sum_i \sum_n \left(x_{i,n}^{\text{exp.}I} - x_{i,n}^{\text{pred.}I} \right)^2 + \left(x_{i,n}^{\text{exp.}II} - x_{i,n}^{\text{pred.}II} \right)^2}{(2 \times N \times R)} \right]^{1/2} \times 100 \quad (4.3)$$

where x is the mole fraction of compound i , R is the total number of compounds ($R=3$), n is the tie-line number, and N is the total number of experiments. The root mean square deviations for the studied systems are shown in Table C3 at the Appendix C.

The selectivity and the distribution ratio for the aromatic hydrocarbons among the several systems evaluated were also predicted. Both COSMO-RS predicted LLE phase diagrams, and selectivity and distribution ratios, are compared with the experimental data in Figures 4.1 to 4.13, and are discussed below.

4.3.1. Effect of the structural characteristics of the aliphatic hydrocarbons upon the phase behavior

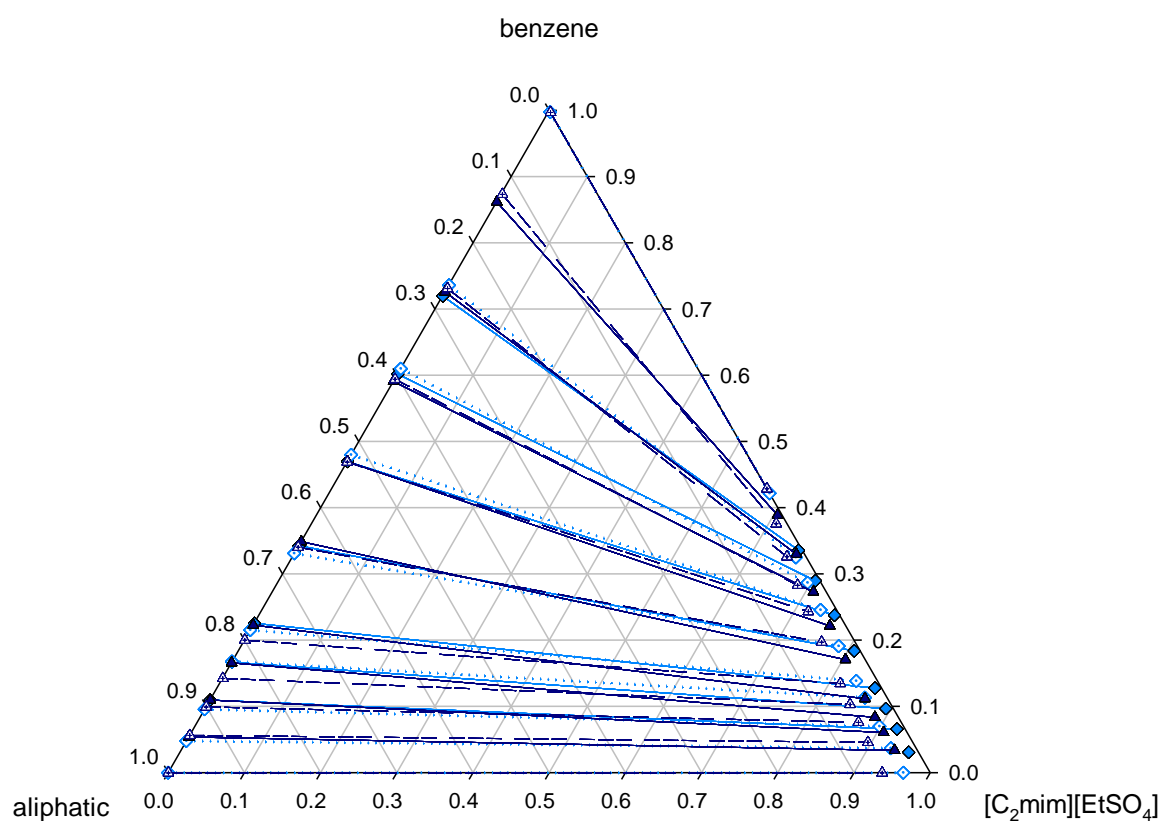
4.3.1.1. Effect of cyclization

A common ionic liquid and an aromatic hydrocarbon were fixed to study the influence of the structural features of cyclization on the phase behavior. This allows the observation of the effects of the cyclic or linear nature of the alkane upon the phase diagrams. The ternary systems investigated were those constituted by *n*-hexane/cyclohexane + benzene + [C₂mim][EtSO₄], and the corresponding diagrams are shown in Figure 4.1, and the *n*-octane/cyclooctane + benzene + [1,3C₂mpy][EtSO₄] (Figure C1 at Appendix C). A slight difference is observed between the two systems containing the cycloalkanes where a higher mutual solubility is observed when compared with the *n*-alkane systems. This trend is related to the reduction of the steric hindrance between the cyclic hydrocarbons and the ionic liquid allowing a slightly increase on the effectiveness on the packing of the fluids. The selectivity and the distribution ratio are plotted in Figure 4.1 at panels b) and c), respectively, as a function of the mole fraction of the aromatics in the aliphatic phase. The selectivity values of the studied systems are superior to unit confirming thus the potential of the ionic liquids as solvents for extraction processes when applied to aromatic/aliphatic hydrocarbon matrixes. The distribution ratio is low and inferior to 1, due to the negative slope of the tie-lines, meaning that large volumes of ionic liquid are required for liquid-liquid extraction processes. This behavior results from the predominant interactions in the ionic liquid-rich phase and is dependent on the global composition. When the global composition has a low content in hydrocarbons, the interaction forces in the ionic liquid-rich phase are dominated by interactions between the ionic fluid and the hydrocarbons leading to high selectivity and distribution ratio values. At higher hydrocarbon contents, the influence of the interactions between the ionic liquid and the hydrocarbons decreases being replaced by interactions between the aromatic and the aliphatic hydrocarbon that do not favor the separation.

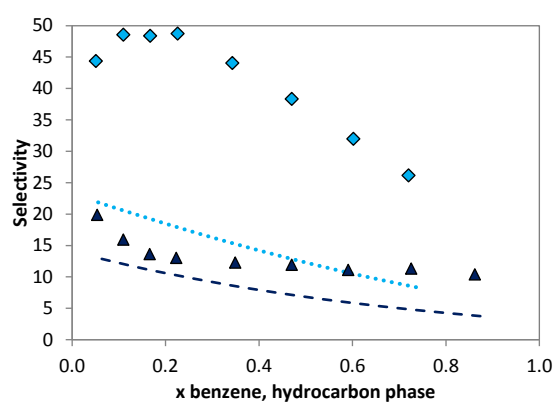
The results of COSMO-RS for the studied systems are depicted in Figure 4.1 and in Appendix C (Figure C1). COSMO-RS provides a good prediction of the shape and size of the miscibility gap and of the binodal curves and tie-lines for the systems composed of aliphatic hydrocarbons + benzene + [C₂mim][EtSO₄]. The differences between the predicted values and the experimental data are more significant for the systems with cycloalkanes (*RSMD* = 1.9%) as the immiscibility region decreases when compared with

the systems containing *n*-alkanes ($RSMD = 1.4\%$). The model provides a very good description of the very low solubilities of ionic liquids on the hydrocarbon-rich phase.

a)



b)



c)

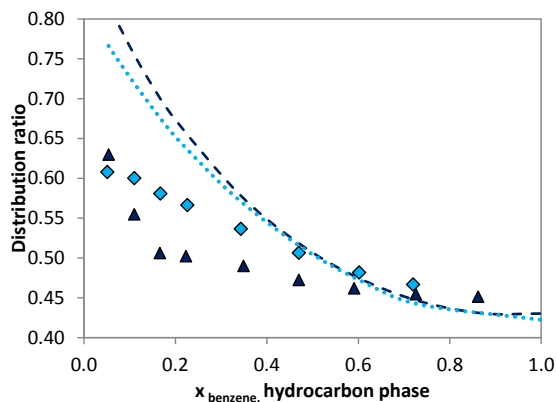


Figure 4.1 a) Experimental and COSMO-RS predicted tie-lines, b) selectivity and c) distribution ratio for the LLE of the ternary systems *n*-hexane + benzene + $[C_2mim][EtSO_4]^{32}$ (full diamonds and solid line for experimental data; and empty diamonds and dotted line for COSMO-RS predicted values), and cyclohexane + benzene + $[C_2mim][EtSO_4]^9$ (full triangles and solid line for experimental data; and empty triangles and short dashed line for COSMO-RS predicted values) at 298.15K.

4.3.1.2. *Effect of the alkane chain length*

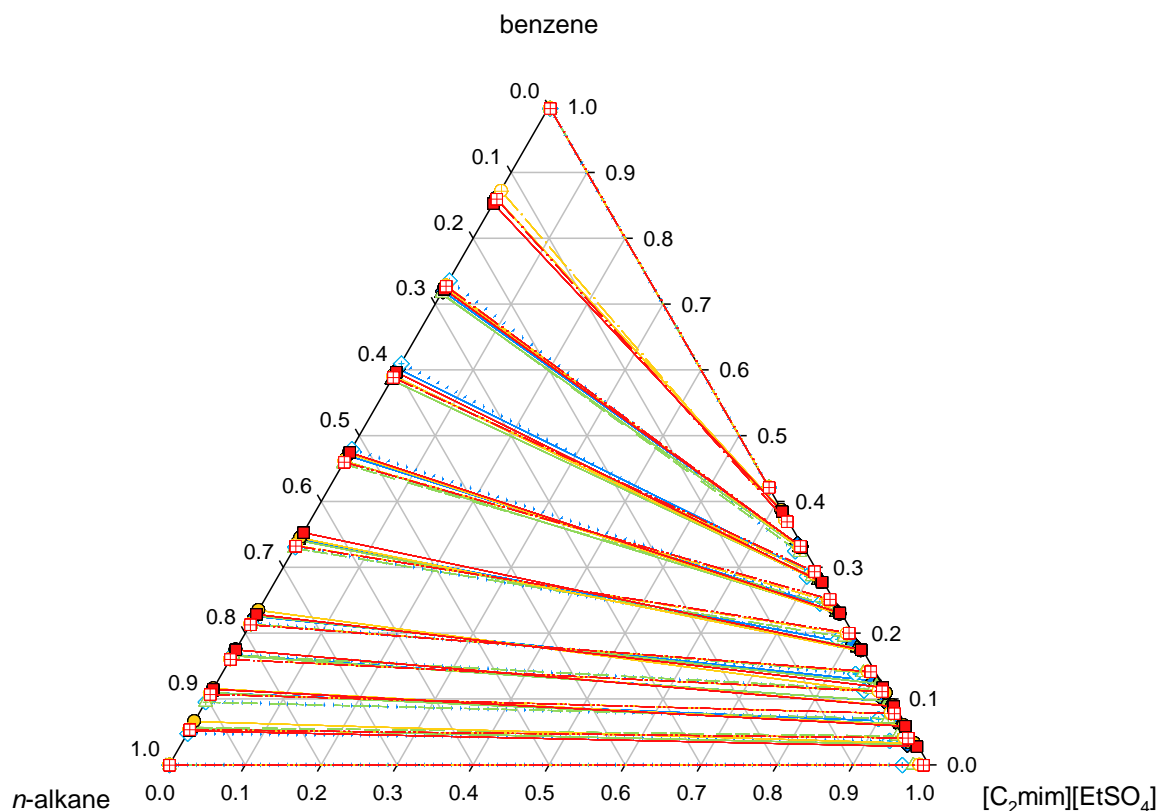
It was possible to study the *n*-alkane and the cycloalkane size on the phase behavior for systems with a common ionic liquid and an aromatic hydrocarbon compound. The ternary phase diagrams of the systems studied with linear alkanes are depicted in Figure 4.2, and in Figures C2 – C9 at Appendix C, and for cyclic alkanes in Figures C10 and C12 at Appendix C. The increase on the alkyl chain length is responsible for an increase in the immiscibility gap on the phase diagrams. This effect is more pronounced for the *n*-alkanes than for the cycloalkanes, since the shape of *n*-alkanes leads to more variable and complex molecular conformations. An increase on the alkyl chain increases the entropy of the system which makes difficult the packing between the hydrocarbon molecules and the ionic liquid ions. The selectivity and the distribution ratio, as a function of the mole fraction of the aromatic hydrocarbons at the hydrocarbon-rich phase, are shown in Figure 4.2, panels b) and c), respectively, and at the Appendix C (Figures C2 – C12). The increase in the hydrocarbon molecular weight leads to an increase in the selectivity, as expected from the observed increase in the miscibility gap. The selectivity is influenced by the aromatic concentration in the hydrocarbon-rich phase whereas a decrease of selectivity with the increase of aromatic concentration is observed. A decrease in the distribution ratio is also observed with the increase of the alkane chain length, yet less significant than that observed with the selectivity. The distribution ratio also decreases with the concentration of the aromatic hydrocarbon at the hydrocarbon-rich phase being its variation more pronounced for aliphatics with longer chain lengths. A similar behavior is observed for the systems containing the cycloalkanes, and as shown in Figures C11 – C12.

The COSMO-RS model is able to describe the effect of the alkane size on the mutual solubilities of the ternary systems, as depicted in Figure 4.2 and in Appendix C (Figures C2 – C12). The binodal curves are predicted with good accuracy. The RMSD values are displayed in Table C3 at Appendix C. Their description is nevertheless better at the hydrocarbon-rich phase where the ionic liquid concentration is very low and is not influenced by the alkane size. At the ionic-liquid-rich phase, the binodal curve shows lower deviations for the systems with longer alkane chain lengths, which present, therefore, higher immiscibility.

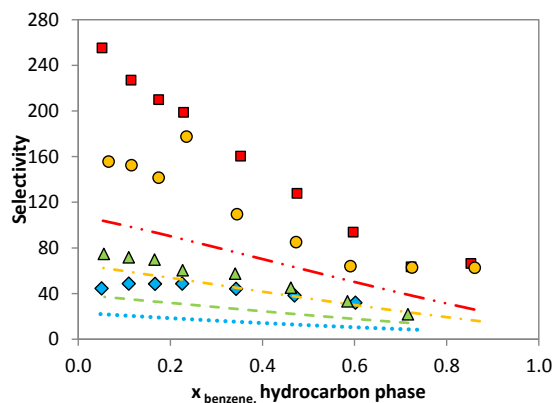
The change on the selectivity and distribution ratio with the alkane size was also estimated with COSMO-RS. For both, the quality of the COSMO-RS predictions seems to decrease with increasing the alkane size. This may be related with the large sensitivity of the selectivity and distribution ratio on the very low concentrations of the alkane at the ionic-liquid-rich phase. In what concerns the distribution ratios, COSMO-RS provides a

good representation of the small dependency on the alkane size through the phase diagrams, although an opposite trend to what is observed from the experimental values is predicted.

a)



b)



c)

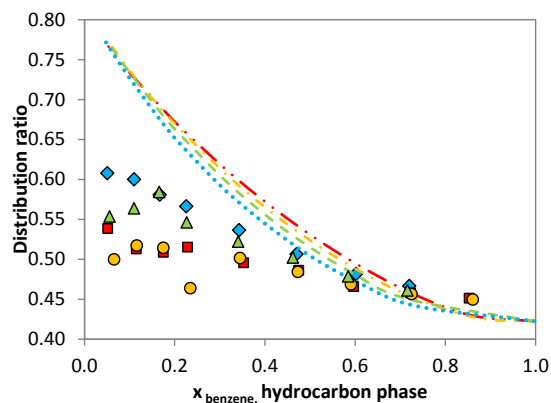


Figure 4.2 a) Experimental and COSMO-RS predicted tie-lines, b) selectivity and c) distribution ratio for the LLE of the ternary systems n -hexane + benzene + $[\text{C}_2\text{mim}][\text{EtSO}_4]$ ³² (full diamonds and solid line for experimental data; and empty diamonds and dotted line for COSMO-RS predicted values), n -heptane + benzene + $[\text{C}_2\text{mim}][\text{EtSO}_4]$ ³² (full triangles and solid line for experimental data; and empty crossed triangles and dashed line for COSMO-RS predicted values), n -octane + benzene + $[\text{C}_2\text{mim}][\text{EtSO}_4]$ ³² (full circles and solid line for experimental data; and empty crossed circles and dot dashed line for COSMO-RS predicted values) and n -nonane + benzene +

[C₂mim][EtSO₄]³² (full squares and solid line for experimental data; and empty crossed squares and dot-dot dashed line for COSMO-RS predicted values) at 298.15K.

4.3.1.3. *Effect of the aromatic structural characteristics upon the phase behavior*

The influence of the aromatic structure and the aromatic isomers upon the phase behavior of the studied ternary systems was also investigated. The resulting ternary diagrams are depicted in Figures 4.3 and 4.4 and at Appendix C, Figures C13 – C20. As previously mentioned, the presence of aromatic compounds does not significantly affect the miscibility of the ternary systems of the type aliphatic + aromatic + ionic liquid. Nevertheless, the solubility of the mixture is increased for simpler aromatic compounds. The increase of the alkyl side chain length on the aromatic structure leads to a decrease on the mixture miscibility, as depicted in Figure 4.3. The systems solubility follows the order: benzene > toluene > ethylbenzene. The tie-lines slopes seem to be more influenced by the alkylation of the aromatics than the binodal curve itself. Moreover, there is an increase of the absolute slope of the tie-lines as the aromatic content and the alkyl side chain length increase.

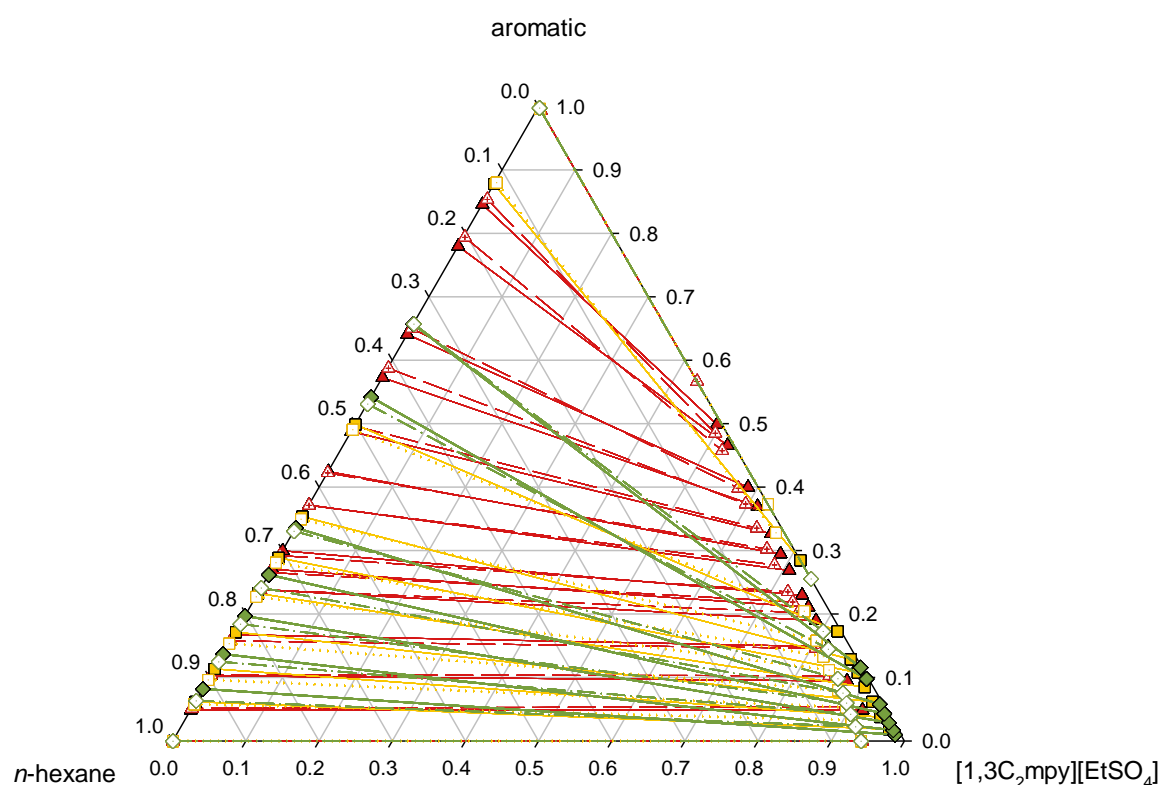
Concerning the xylene isomers, the solubility of the systems constituted by ionic liquid + xylene + aliphatic hydrocarbon is only slightly affected by the position of the second methyl group, as shown in Figure 4.4. The tie-lines slopes for these systems are also similar at the extremes of the ternary diagram and show some variation in the transient slope zone. For the *o*-xylene system, the slope variation is less pronounced being the change more abrupt in the region with a higher aromatic content. For the systems with *m*-xylene and *p*-xylene, the progression of the tie-line slope does not display a significant variation.

The selectivity for the various aromatic systems studied presents large values and decreases with the increase on the aromatic alkyl side chain, fluctuating nevertheless in a range of identical magnitude. An interesting feature is observed for the systems based on the [1,3C₂mpy][EtSO₄] ionic liquid (Figure 4.3 and Figure C19 at Appendix C). For these systems, the selectivity shows a divergent behavior if the aromatic has or not a substituent alkyl chain. The system with benzene shows a decreasing selectivity with the increase of benzene content at the aliphatic rich-phase, whereas, the presence of an alkyl chain on the aromatics leads to its increase. Though, the observed trend for other systems consists in the decrease of the selectivity with the increase of the aromatic mole fraction at the aliphatic-rich phase, as can be seen for the systems composed of ionic

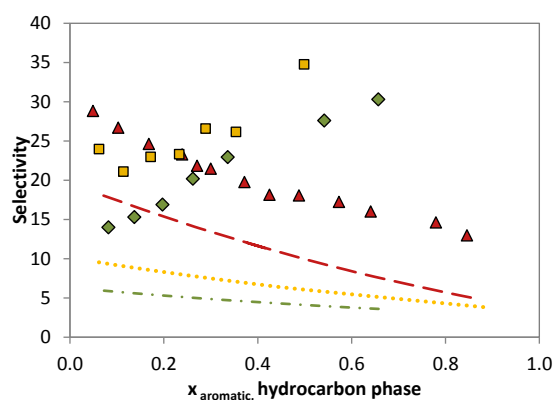
liquid + toluene/ethylbenzene + aliphatic hydrocarbon, and displayed in Figures C20, C22, C23, C24, C26, C27 and C28 in the Appendix C. This suggests that these systems present an anomalous behavior that must be confirmed by further experimental data. The distribution ratio is also much dependent on the alkyl chain while being reduced by the increase of the alkyl chain length, and where the benzene system presents the higher distribution ratio. It is also shown that the alkylation of the aromatics leads to a small variation on the distribution ratio as a function of the aromatic content in the aliphatic-rich phase.

The impact of the aromatic structure on the systems behavior is well captured by the COSMO-RS model. Only a small discrepancy is observed between the experimental data and the predicted binodal curves. The description of the tie-lines slope is in good agreement with the experimental data for the benzene systems ($RMSD = 1.8\%$) and shows a slight difference with the increase on the aromatic alkyl side chain ($RMSD > 2.8\%$ as shown at Table C3 at Appendix C) that decreases with the increase of the aromatic content. As for the selectivity and the distribution ratio, COSMO-RS is able to adequately predict the trends observed experimentally. Given the very low concentrations of ionic liquid in the alkane phase, the experimental uncertainties in the selectivities and distribution ratios may be responsible for part of the observed differences. In view of the differences observed between the predicted and measured selectivities for the system with [1,3C₂mpy][EtSO₄], and the remaining systems, COSMO-RS model can be used as an indicative of an irregular behavior that can be present.

a)



b)



c)

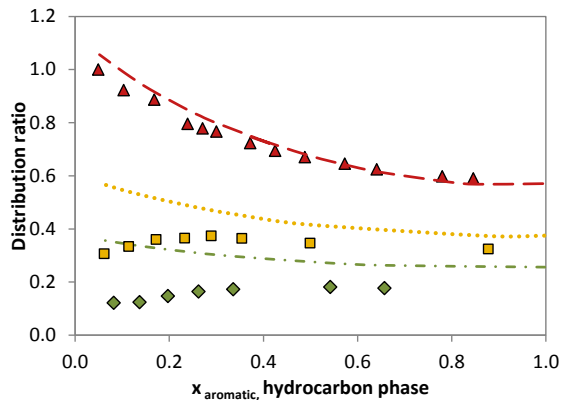
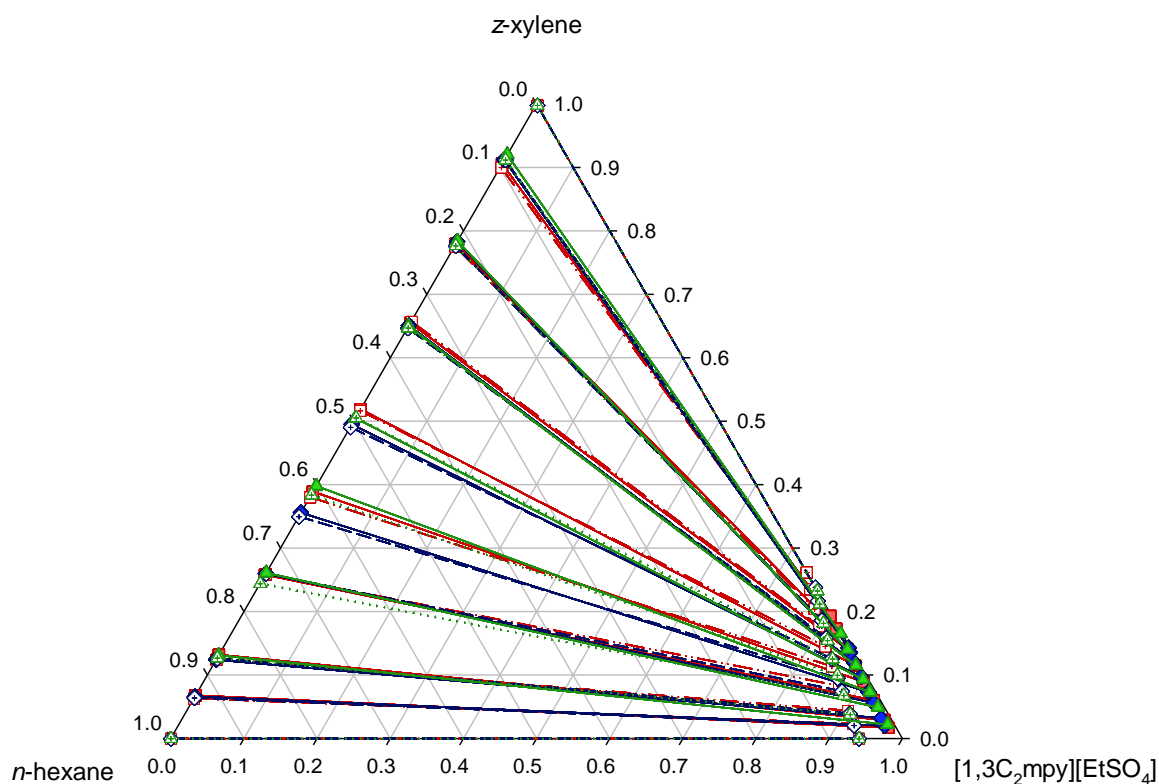
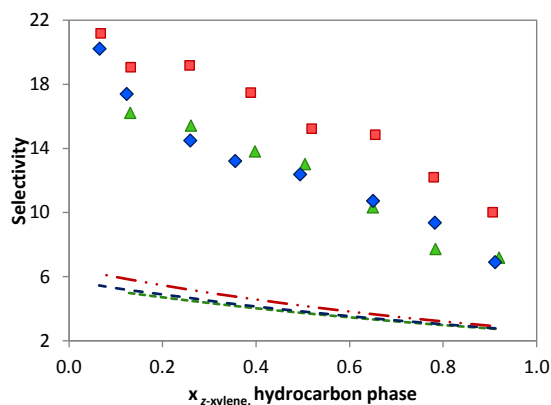


Figure 4.3 a) Experimental and COSMO-RS predicted tie-lines, b) selectivity and c) distribution ratio for the LLE of the ternary systems *n*-hexane + benzene + [1,3C₂mpy][EtSO₄]¹⁰ (full triangles and solid line for experimental data; and empty dotted triangles and dashed line for COSMO-RS predicted values), *n*-hexane + toluene + [1,3C₂mpy][EtSO₄]²⁰ (full squares and solid line for experimental data; and empty dotted squares and dotted line for COSMO-RS predicted values), and *n*-hexane + ethylbenzene + [1,3C₂mpy][EtSO₄]²⁰ (full diamonds and solid line for experimental data; and empty dotted diamonds and dot dashed line for COSMO-RS predicted values), at 298.15K.

a)



b)



c)

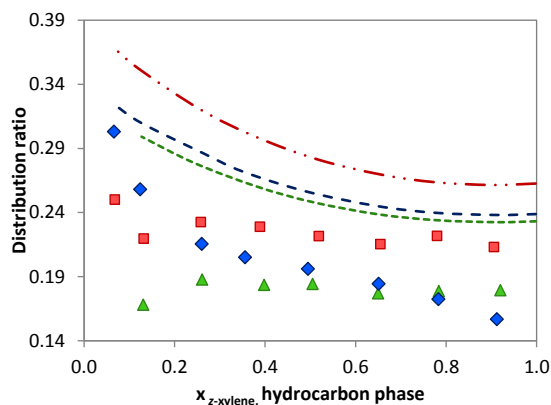


Figure 4.4 a) Experimental and COSMO-RS predicted tie-lines, b) selectivity and c) distribution ratio for the LLE of the ternary systems *n*-hexane + *o*-xylene + [1,3C₂mpy][EtSO₄]² (full squares and solid line for experimental data; and empty dotted squares and dot-dot dashed line for COSMO-RS predicted values), *n*-hexane + *m*-xylene + [1,3C₂mpy][EtSO₄]² (full diamonds and solid line for experimental data; and empty dotted diamonds and dotted line for COSMO-RS predicted values), and *n*-hexane + *p*-xylene + [1,3C₂mpy][EtSO₄]² (full triangles and solid line for experimental data; and empty dotted triangles and dotted line for COSMO-RS predicted values) at 298.15K.

4.3.2. Effect of the ionic liquid cation family upon the phase behavior

The effect of the ionic liquid cation family upon the phase behavior is described in Figures 4.5 and 4.6 and Figure C21 (*cf.* Appendix C). The systems with the ionic liquid containing the common [EtSO₄]⁻ anion, *n*-hexane and benzene allow to study the effect upon the phase diagrams of different ionic liquid cations, such as imidazolium and pyridinium (Figure 4.5), and the systems based on the [NTf₂]⁻ anion with *n*-hexane and benzene allow the study of the influence of the cation cores imidazolium, ammonium and phosphonium (Figure 4.6). The phosphonium-based IL show a large miscibility domain when compared with the nitrogen-based cations, being therefore not suitable for selective extractions from hydrocarbons' matrixes. The large miscibility presented by the ionic liquid with the phosphonium cation is due to its low polarity that results from the large alkyl chains. These large aliphatic chains lead to an increase of the dispersion forces with the alkanes enhancing thus the miscibility between the ionic liquid and the hydrocarbon.

For different nitrogen-based cations, it is shown that the imidazolium- and the pyridinium-based cations display similar binodal curves and therefore similar solubilities. These ternary diagrams show higher solubilities between the aromatic hydrocarbons and the ionic liquid due to π - π interactions that can occur. The ammonium-based cation (Figure 4.6) leads to lower solubilities than the other nitrogen-based cations.

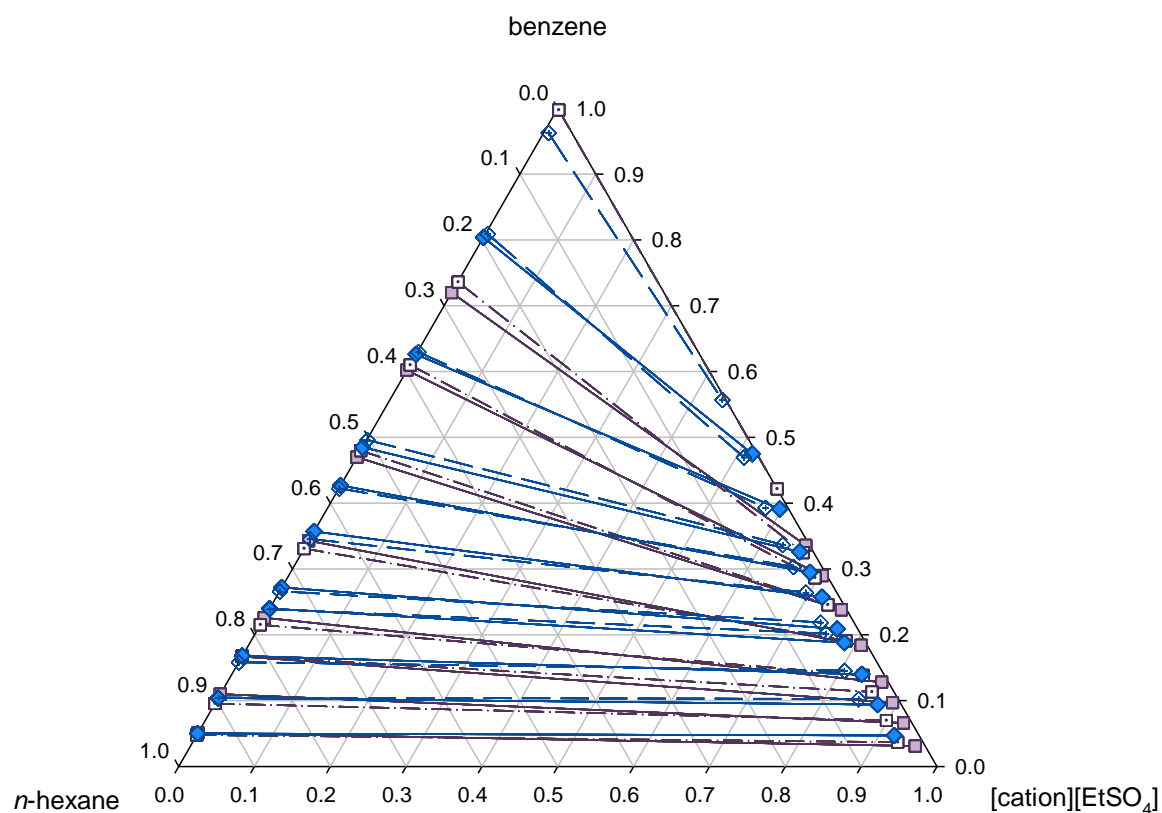
The tie-lines of the nitrogen-based cations, imidazolium and pyridinium, show similar slopes (except in the aromatic-rich region), and those for ammonium are steeper. The selectivity for these systems is high and presents comparable decreasing behavior with the increase of the aromatic content in the alkane-rich phase. On the other hand, the diagram with the ammonium cation shows an increase from low to middle aromatic concentrations. The distribution ratios and selectivities of the studied systems show a decrease with the increase of the aromatic content. The imidazolium and pyridinium containing systems show similar distribution ratios while those for the ammonium system are lower. These ratios are expectable since the cation structure is distinct from the aromatic structures of the imidazolium and pyridinium cations, presenting therefore different interactions with the hydrocarbons.

Regarding the ionic liquid cation isomers, presented at Figure 4.7, and Figure C22 at Appendix C, it is shown that this feature has a low impact in the solubility of the aromatic in the ionic liquid. It is possible to see a minor reduction of the immiscibility region for the *meta* and *para* positions of the methyl group, being this more significant for the isomer in the *ortho* position. The same trend is observed for the selectivity. It is higher for the *ortho*

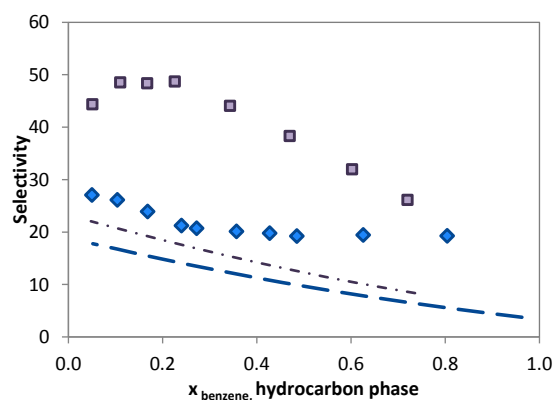
substitution, and similar and smaller for the *meta* and *para* substitutions. For the tie-lines, a similar behavior is also observed for the *meta* and *para* isomers that translates into similar distribution ratios with values that are somewhat higher than for the *ortho* isomer. These trends result from an improved distribution of charge at the IL cation and to a more efficient packing provided by the lower sterical hindrance for the *meta* and *para* substitutions.⁷⁵

The study of the COSMO-RS performance on the description of the different cation families is shown in Figures 4.5 to 4.7. Regarding the cation families, COSMO-RS is capable of describing the binodal curves for the studied systems, with less accuracy at the region with higher aromatic content as observed previously for other systems, presenting *RMSD* values around 5 to 6 %. An exception is verified with the phosphonium cation and for which the COSMO-RS model predicts a complete miscibility. The model can describe correctly the behavior of the pyridinium isomers with *RMSD* = 2.4 % for the *ortho* substitution, which present a slightly higher immiscibility than the *meta* and *para* isomers which present 4.6 % and 6.4 % of *RMSD*, respectively. The predicted selectivities and distribution ratios for the various cations are described satisfactorily if the uncertainty on the hydrocarbon-rich phase concentrations is taken into account.

a)



b)



c)

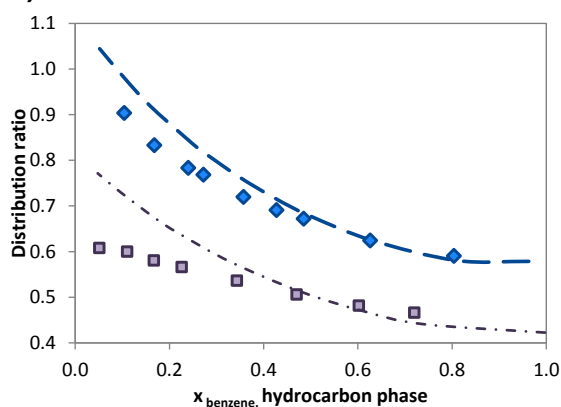


Figure 4.5 a) Experimental and COSMO-RS predicted tie-lines, b) selectivity and c) distribution ratio for the LLE of the ternary systems n -hexane + benzene + $[\text{C}_2\text{mim}][\text{EtSO}_4]^{32}$ (full square and solid line for experimental data; and empty dotted square and dot dashed line for COSMO-RS predicted values) and n -hexane + benzene + $[1,3\text{C}_2\text{mpy}][\text{EtSO}_4]^{10}$ (full diamonds and solid line for experimental data; and empty dotted diamonds and long dashed line for COSMO-RS predicted values) at 298.15K.

a)

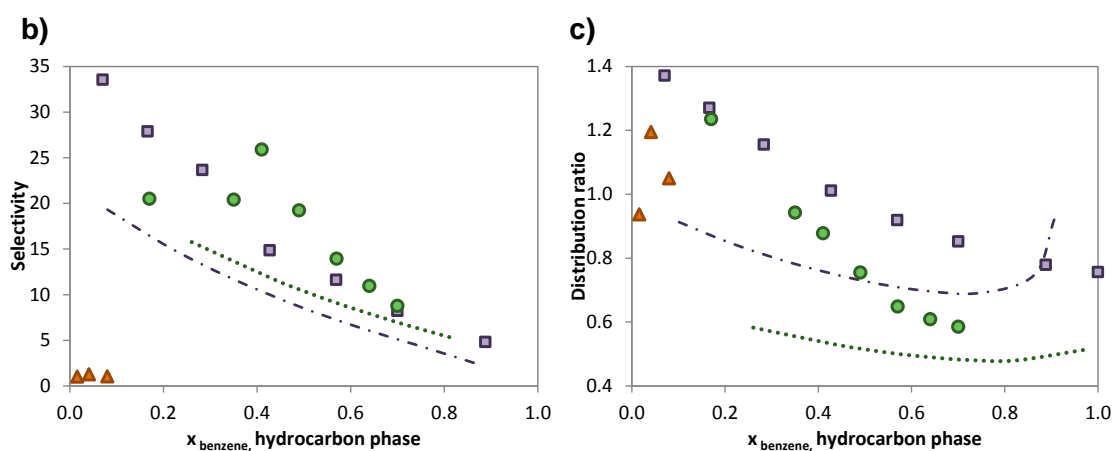
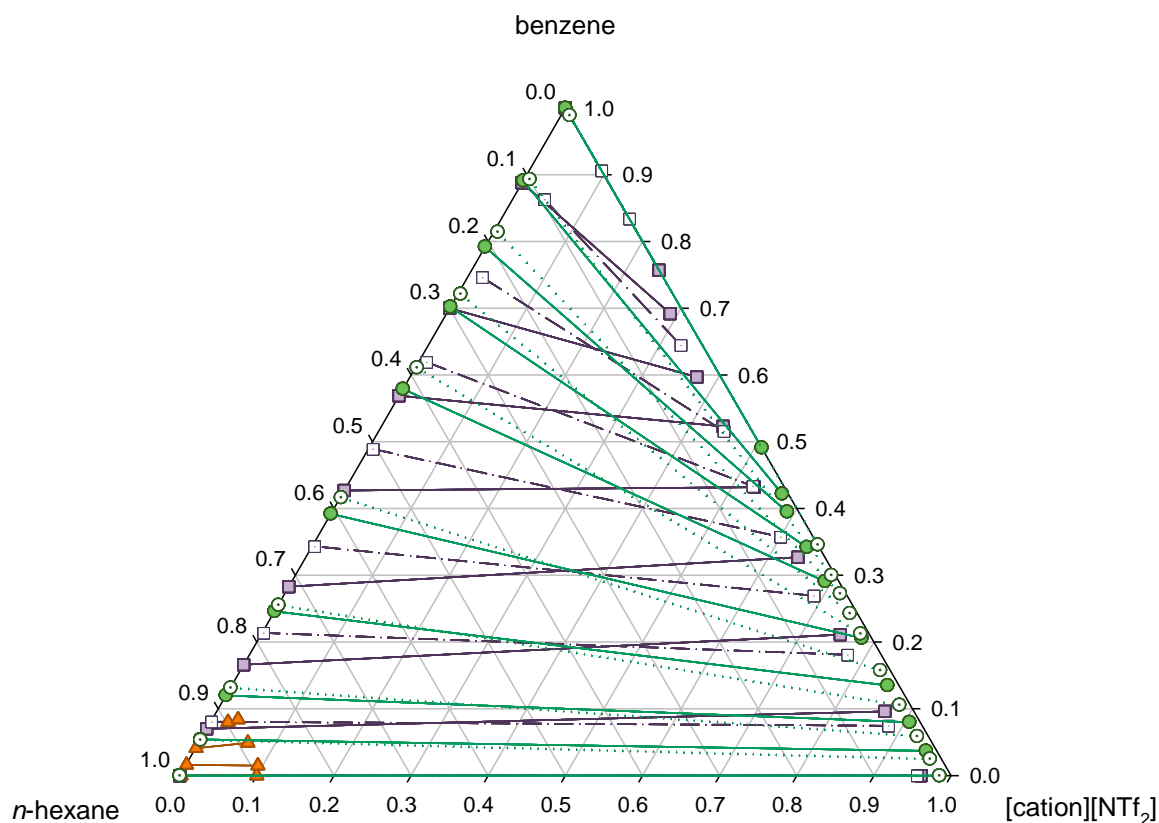
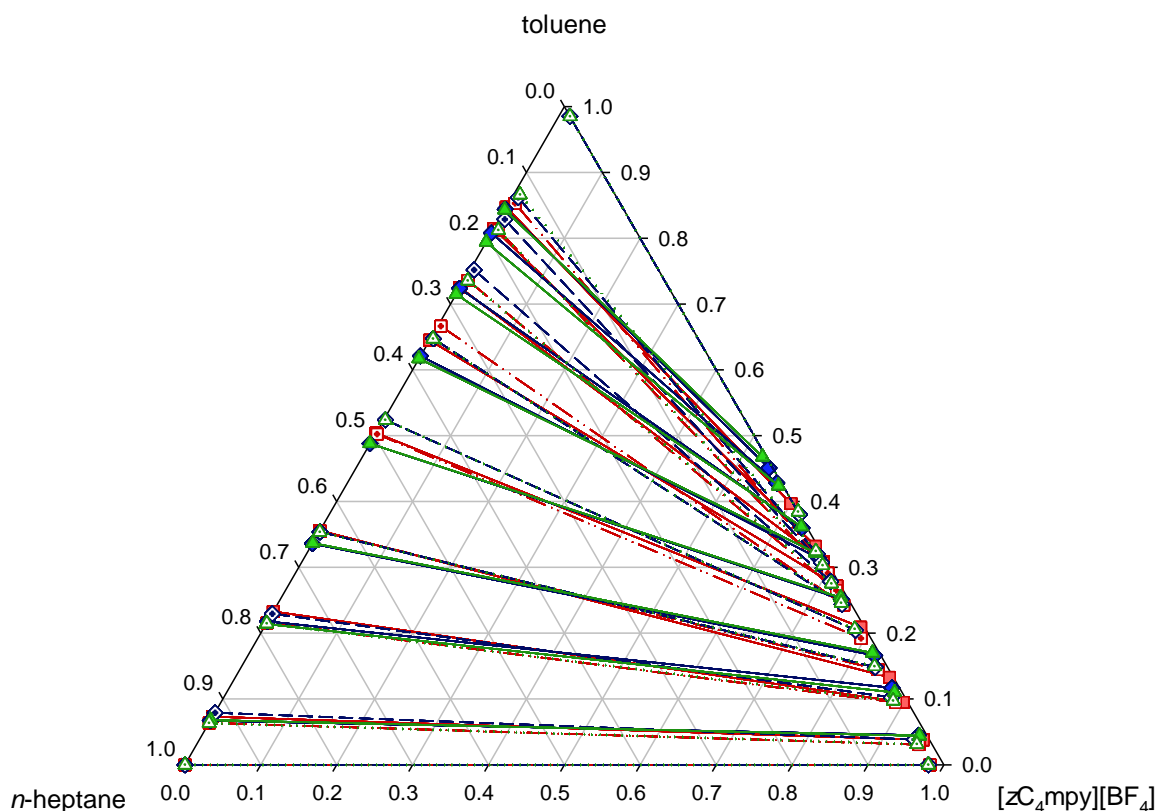
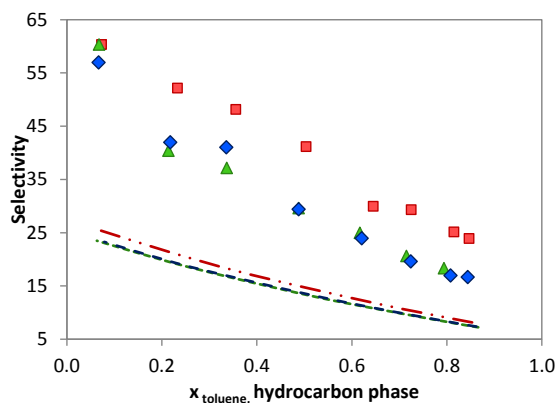


Figure 4.6 a) Experimental and COSMO-RS predicted tie-lines, b) selectivity and c) distribution ratio for the LLE of the ternary systems n -hexane + benzene + $[\text{C}_2\text{mim}][\text{NTf}_2]^3$ (full square and solid line for experimental data; and empty dotted square and dot dashed line for COSMO-RS predicted values), n -hexane + benzene + $[\text{N}_{2(2\text{OH})_{11}}][\text{NTf}_2]^{27}$ (full circles and solid line for experimental data; and empty dotted circles and dotted line for COSMO-RS predicted values), and n -hexane + benzene + $[\text{P}_{66614}][\text{NTf}_2]^3$ (full triangle and solid line for experimental data) at 298.15K.

a)



b)



c)

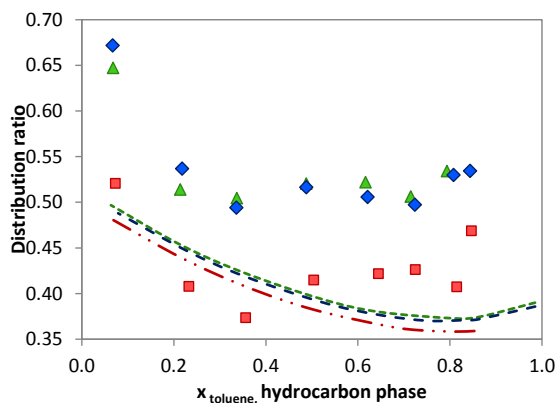


Figure 4.7 a) Experimental and COSMO-RS predicted tie-lines, b) selectivity and c) distribution ratio for the LLE of the ternary systems *n*-heptane + toluene + [1,2C₄mpy][BF₄]³³ (full squares and solid line for experimental data; and empty dotted squares and dot-dot dashed line for COSMO-RS predicted values), *n*-heptane + toluene + [1,3C₄mpy][BF₄]³³ (full diamonds and solid line for experimental data; and empty dotted diamonds and dashed line for COSMO-RS predicted values), and *n*-heptane + toluene + [1,4C₄mpy][BF₄]³³ (full triangles and solid line for experimental data; and empty dotted triangles and dotted line for COSMO-RS predicted values) at 313.2K.

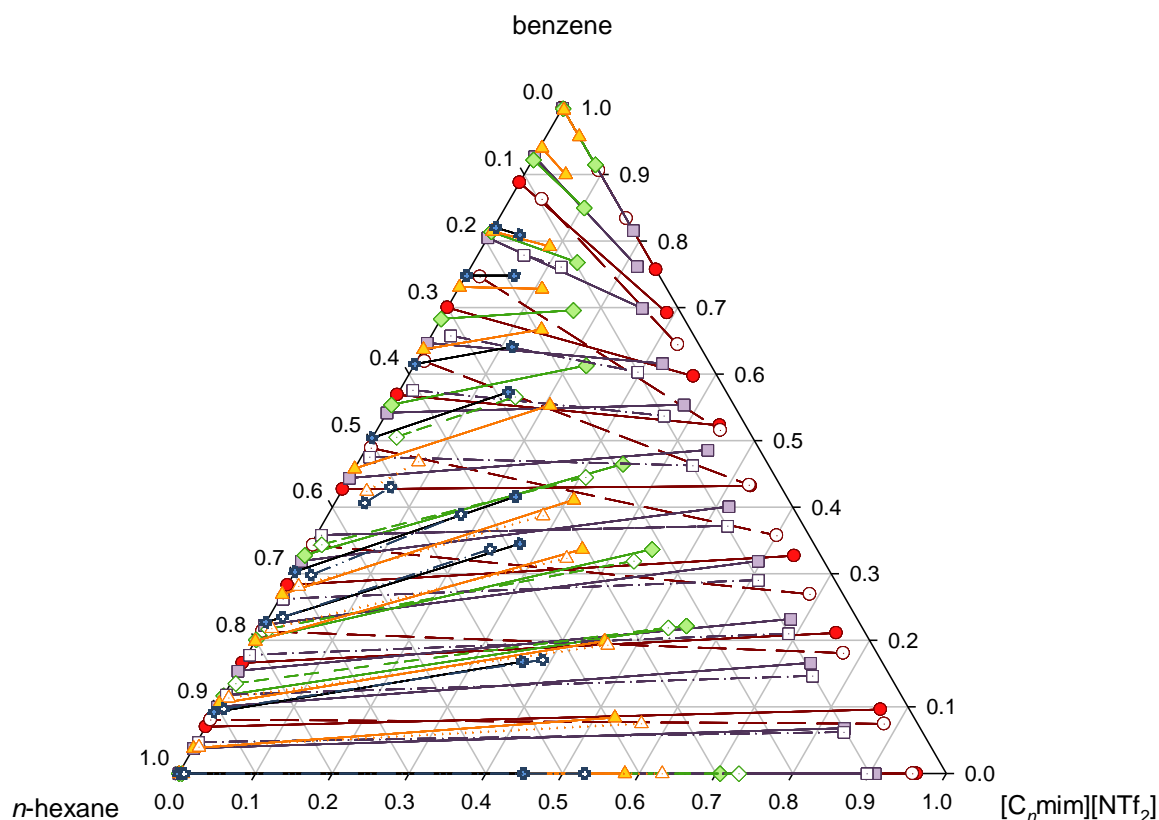
4.3.3. Effect of the ionic liquid cation alkyl chain length upon the phase behavior

The binodal curves and the tie-lines of the systems *n*-hexane + benzene + [C_{*n*}mim][NTf₂], with the number of carbons at the cation side alkyl chain (*n*) ranging from 2 to 12, are plotted in Figure 4.8. At Appendix C, similar systems are shown in Figures C23 – C25. These systems allow the study of the influence of the substituted alkyl chain length at the ionic liquid cation through the phase diagrams behavior. It is shown that the size of the alkyl chain length is the factor that has the higher influence on the mutual solubilities of the systems under analysis. This is patent in the significant decrease of the immiscibility region with the increase on the cation side alkyl chain length. The increase of the alkyl chain length leads to enhanced dispersive interactions with *n*-alkanes. At these nonpolar regions, the aromatic hydrocarbons can also be solvated, being therefore also responsible for the increased mutual solubility with the ionic liquid. Moreover, the effect of the cation side alkyl chain length is not only evident in the binodal curve deviation, but also the phase diagrams change from the type 2 to a type 1 ternary diagram for [C₁₂mim][NTf₂]. For the evaluated IL with the longest alkyl chain complete miscibility with benzene is observed. The tie-lines also show some dependence on the alkyl chain length. Comparing the experimental tie-line slopes, at a region with the same aromatic concentration, it is visible that they become more steep, from *n* = 2 to *n* = 12. In Figure 4.8, b) and c), the selectivity and the distribution ratio are plotted. The visible trends are consistent with the binodal curve and tie-lines analysis, where the alkyl chain length has a great impact. The selectivity increases as the cation alkyl chain length decreases. It is also dependent on the aromatic content and this dependence decreases with the alkyl chain length increase. Moreover, in the range of 0.5 – 1.0 of aromatic mole fraction content in the alkane-rich phase, the selectivity for *n* = 8, 10 and 12 becomes similar. Contrarily to what is observed for selectivity, the distribution ratio increases with the alkyl chain length until *n* = 8. Above that value the distribution ratio is similar for *n* = 8 and *n* = 10, and lower for *n* = 12. As discussed before, this results from the significant aliphatic and aromatic hydrocarbon solubility in the ionic liquid [C₁₂mim][NTf₂].

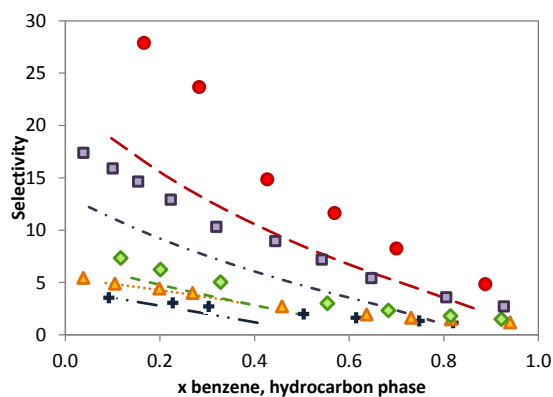
For the systems studied, COSMO-RS can describe the trends observed for the mutual solubility, binodal curves and tie-line slopes, and selectivity and distribution ratio. As expected, an increase in the mutual solubilities among these systems is observed with the alkyl chain length increase. Nevertheless, the quality of the binodal curves prediction decreases for systems with longer alkyl chains, reflected by the increase of the RMSD values from 4 % for *n* = 2, to > 27 % for *n* > 8 (Table C3 in Appendix C). In addition, a ternary diagram of type 1 for the system with the longer alkyl chain length is predicted,

and for which a diagram of type 2 is experimentally observed. The predicted selectivities and distribution ratios are satisfactory.

a)



b)



c)

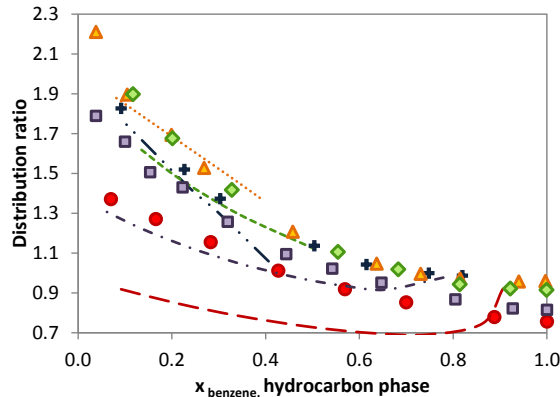


Figure 4.8 a) Experimental and COSMO-RS predicted tie-lines, b) selectivity and c) distribution ratio for the LLE of the ternary systems n -hexane + benzene + $[C_2\text{mim}][\text{NTf}_2]$ ³ (full circles and solid line for experimental data; and empty dotted circles and long dashed line for COSMO-RS predicted values e), n -hexane + benzene + $[C_4\text{mim}][\text{NTf}_2]$ ²⁹ (full squares and solid line for experimental data; and empty dotted squares and dot dashed line for COSMO-RS predicted values), n -hexane + benzene + $[C_8\text{mim}][\text{NTf}_2]$ ²⁹ (full diamonds and solid line for experimental data; and empty dotted diamonds and short dashed line for COSMO-RS predicted values), n -hexane + benzene + $[C_{10}\text{mim}][\text{NTf}_2]$ ²⁹ (full triangles and solid line for experimental data; and empty dotted triangles and dotted

line for COSMO-RS predicted values), and *n*-hexane +benzene + [C₁₂mim][NTf₂]²⁹ (full crosses and solid line for experimental data; and empty crosses and dot-dot dashed line for COSMO-RS predicted values) at 298.15K.

4.3.4. Effect of the ionic liquid anion upon the phase behavior

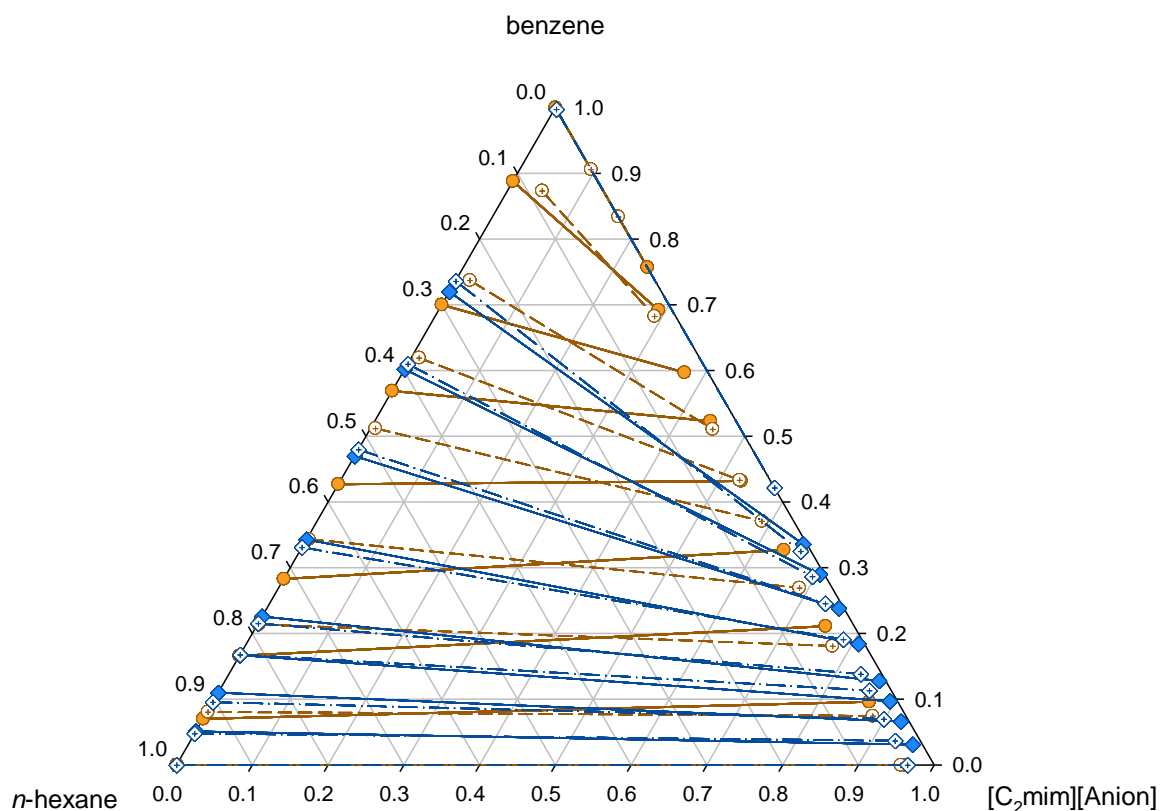
The influence of the anion nature on the systems composed of ionic liquid + aromatic + aliphatic hydrocarbon is displayed in Figures 4.9 to 4.11. The experimental data collected, and described in the Tables C1 and C2, allowed to study the anions [EtSO₄]⁻ and [NTf₂]⁻ with the fixed [C₂mim]⁺ cation, *n*-hexane and benzene systems (Figure 4.9). It was also possible to study the [SCN]⁻, [DCA]⁻, and [MeSO₄]⁻ with [C₄mim]⁺, *n*-heptane and toluene (Figure 4.10) and, given the low dependence of the solubility with the temperature, the [MeSO₄]⁻ was also used in the comparison. Finally the systems with [C₆mim]⁺, *n*-heptane and toluene allowed to study the influence of the anions [BF₄]⁻ and [PF₆]⁻ (Figure 4.11). Other systems are reported at Appendix C (Figure C28). As shown in Figures 4.9 – 4.11, the ionic liquid anion does not have, in general, a significantly impact on the mutual solubilities among the ternary systems. The only exception to this behavior seems to be the [NTf₂]-based ionic liquids. They show a narrower immiscibility region when compared to the other anions, as seen in Figure 4.9 and Figure C28 (at Appendix C). This feature occurs due to the lower polarity, large volume, and dispersive charge of the anion [NTf₂]⁻, which improve the aliphatic hydrocarbons solubility in the ionic-liquid-rich phase. In addition, for the ternary systems with this fluorinated anion, the aromatics solubility in the ionic liquid is not only favored by the anion large volume, the π - π stacking between the aromatic hydrocarbon and the imidazolium cation, but also by inclusion-type interactions. These interactions occur for ionic liquids with weak interactions between the cation and the anion, as it happens for the [NTf₂]⁻ anion. Weaker cation-anion interactions favor CH $\cdots\pi$ bonds between the C2-H at the imidazolium ring and the aromatic hydrocarbon. Thus, the aromatic hydrocarbons have more facility in disrupting the supramolecular clusters formed by the cations and the anions of the ionic liquid, promoting thus their easy incorporation in the ionic-liquid-rich phase. Furthermore, there also further interactions between the hydrogen atoms of the aromatic compound and the oxygen atoms of the sulfonyl group that enhance the mutual solubilities.⁷⁶⁻⁷⁸

Regarding the anions impact at the systems selectivity and distribution ratio, it is noticed that for the [C₂mim]-based ionic liquids, the selectivity of the anion [EtSO₄]⁻ is higher than for the [NTf₂]⁻ anion, and an inverse trend is verified for the distribution ratio. With respect

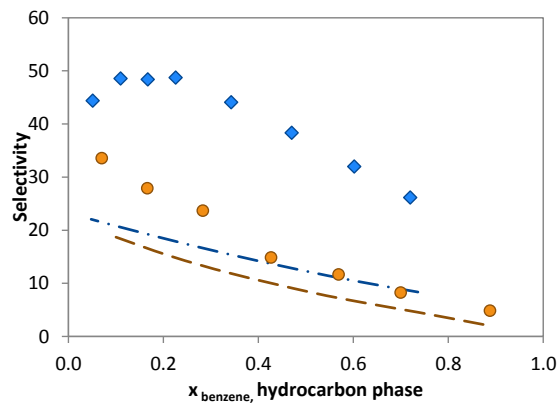
to the [C₄mim]-based ionic liquid, the selectivity and the distribution ratio follow the same trend: [DCA]⁻ > [SCN]⁻ > [MeSO₄]⁻. The same happens for the [C₆mim]-based ionic liquid where the order is [PF₆]⁻ > [BF₄]⁻. The trends observed for the selectivity and for the distribution ratio for the different anions, apparently follows the β solvatochromic parameter, which reflects the hydrogen-bond basicity (hydrogen-bonding accepting ability). The β solvatochromic parameter, regarding the anion nature, follows the trend [EtSO₄]⁻ > [MeSO₄]⁻ > [SCN]⁻ > [DCA]⁻ > [BF₄]⁻ > [PF₆]⁻ > [NTf₂]⁻.⁷⁹⁻⁸⁰ Thus, it seems that the selectivity and the distribution ratio decrease with the hydrogen-bond basicity increase. However, an exception appears for the [C₂mim]-based ionic liquids, where the [EtSO₄]⁻ is higher than the [NTf₂]⁻. Nevertheless, further experimental confirmation is required. For the anions with alkyl side chains it was possible to study the influence of the alkyl chain length on the miscibility gap of the respective systems. As shown in Figure 4.12, the increase of the sulfate alkyl side chain leads to a contraction of the immiscibility domain whereas the tie-line slopes became less negative. As expected, the selectivity decreases and the distribution ratio increases with the increase on the anion alkyl chain length. The same results were already noticed for the increase in the cation alkyl chain, although with stronger impact than what is observed with the anions.

According to the results obtained with COSMO-RS, the change of the ionic liquid anion and its alkyl chain length, and their impact on the binodal curve and tie-line slopes, and at the selectivity and distribution ratio criteria, are qualitatively and satisfactorily captured for most of the anions studied. However, the model shows a worst performance on describing the systems containing the anions [MeSO₄]⁻, [EtSO₄]⁻, [PF₆]⁻ and [BF₄]⁻. The predicted binodal curves for these systems present slightly larger deviations what seems to indicate that COSMO-RS is less reliable in the description of the effect of the anions on the phase behavior of mixtures, in particular of anions that present strong interactions with the cations.

a)



b)



c)

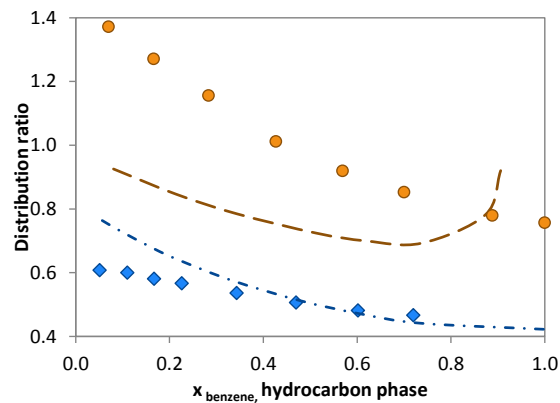
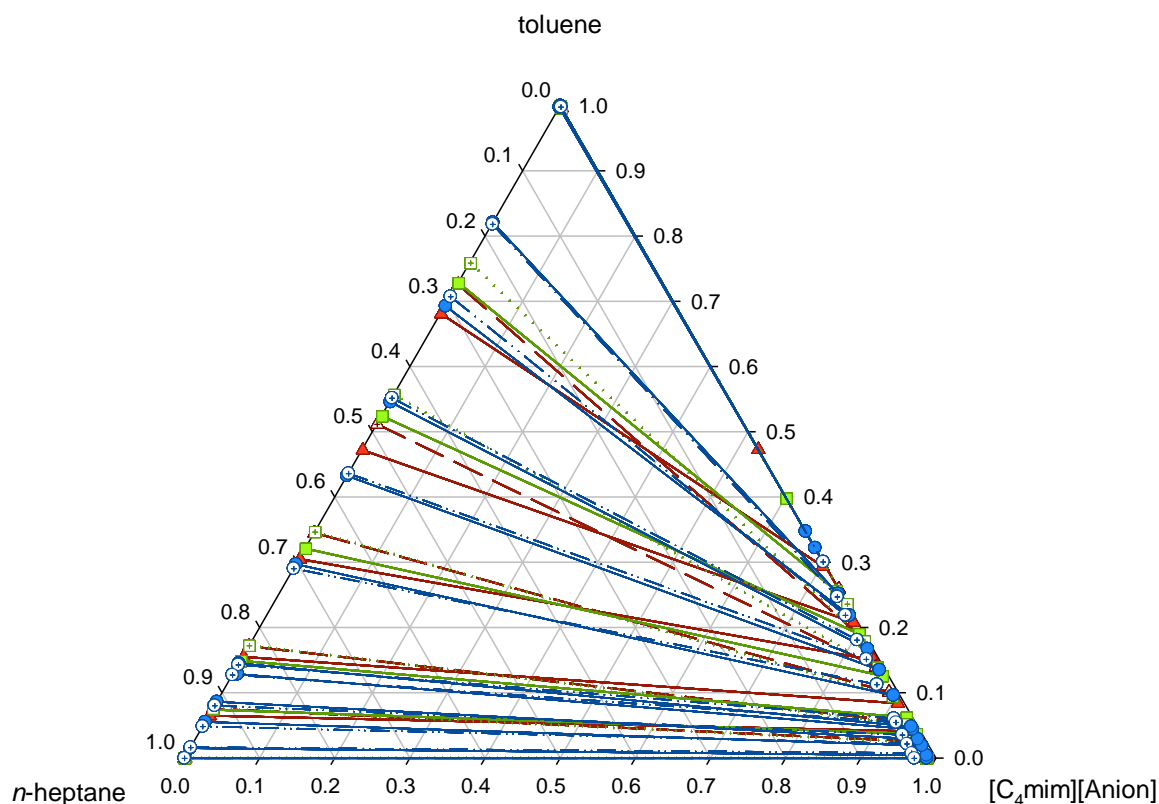
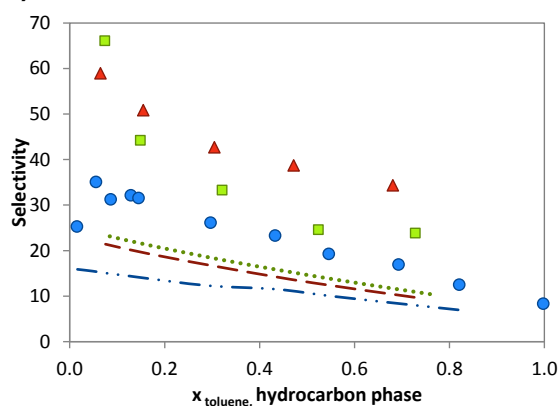


Figure 4.9 a) Experimental and COSMO-RS predicted tie-lines, b) selectivity and c) distribution ratio for the LLE of the ternary systems *n*-hexane + benzene + $[\text{C}_2\text{mim}][\text{EtSO}_4]^{13}$ (full diamonds and solid line for experimental data; and empty dotted diamonds and dot dashed line for COSMO-RS predicted values), and *n*-hexane + benzene + $[\text{C}_2\text{mim}][\text{NTf}_2]^3$ (full circles and solid line for experimental data; and empty dotted circles and long dashed line for COSMO-RS predicted values), at 298.15K.

a)



b)



c)

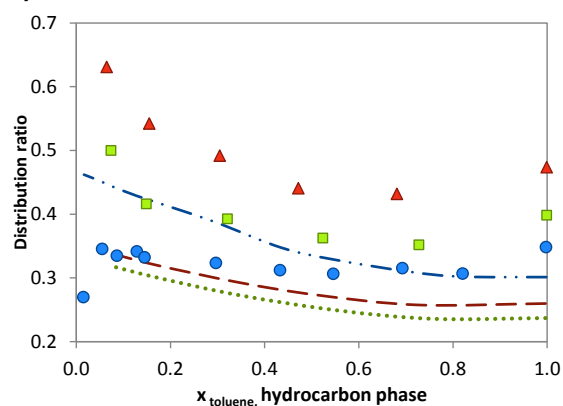
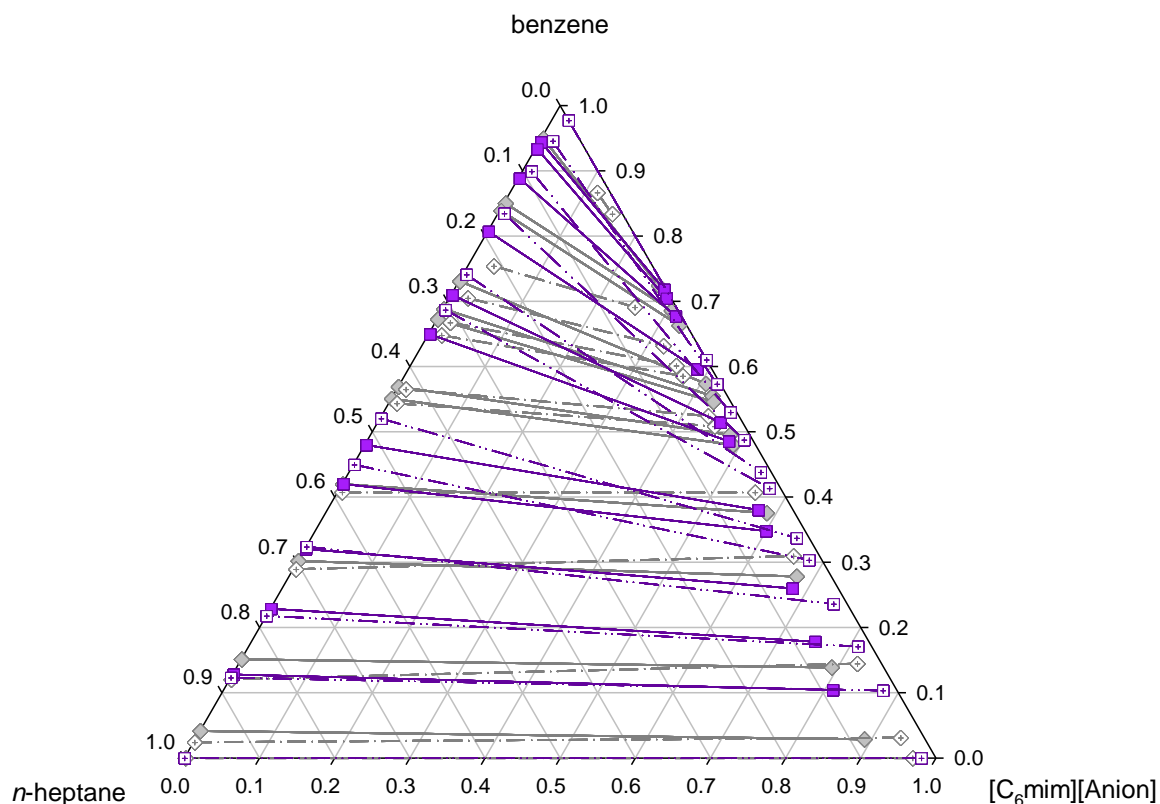
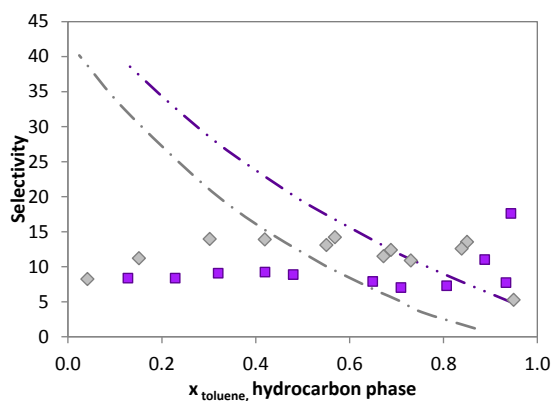


Figure 4.10 a) Experimental and COSMO-RS predicted tie-lines, b) selectivity and c) distribution ratio for the LLE of the ternary systems *n*-heptane + toluene + [C₄mim][SCN]¹⁷ (full squares and solid line for experimental data; and empty dotted squares and dotted line for COSMO-RS predicted values), *n*-heptane + toluene + [C₄mim][DCA]¹⁷ (full triangles and solid line for experimental data; and empty dotted triangles and long dashed line for COSMO-RS predicted values) at 303.15K and *n*-heptane + toluene + [C₄mim][MeSO₄]⁴⁰ (full circles and solid line for experimental data; and empty dotted circles and dot-dot dashed line) at 313.15K.

a)



b)



c)

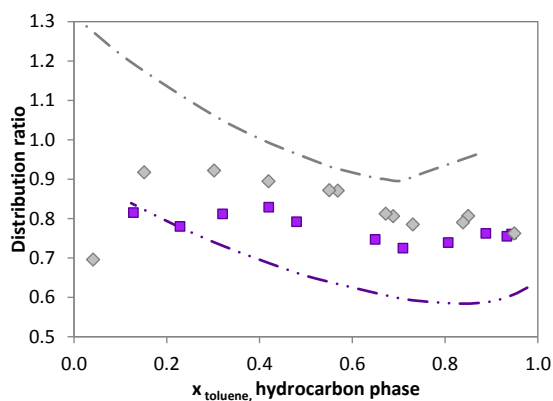
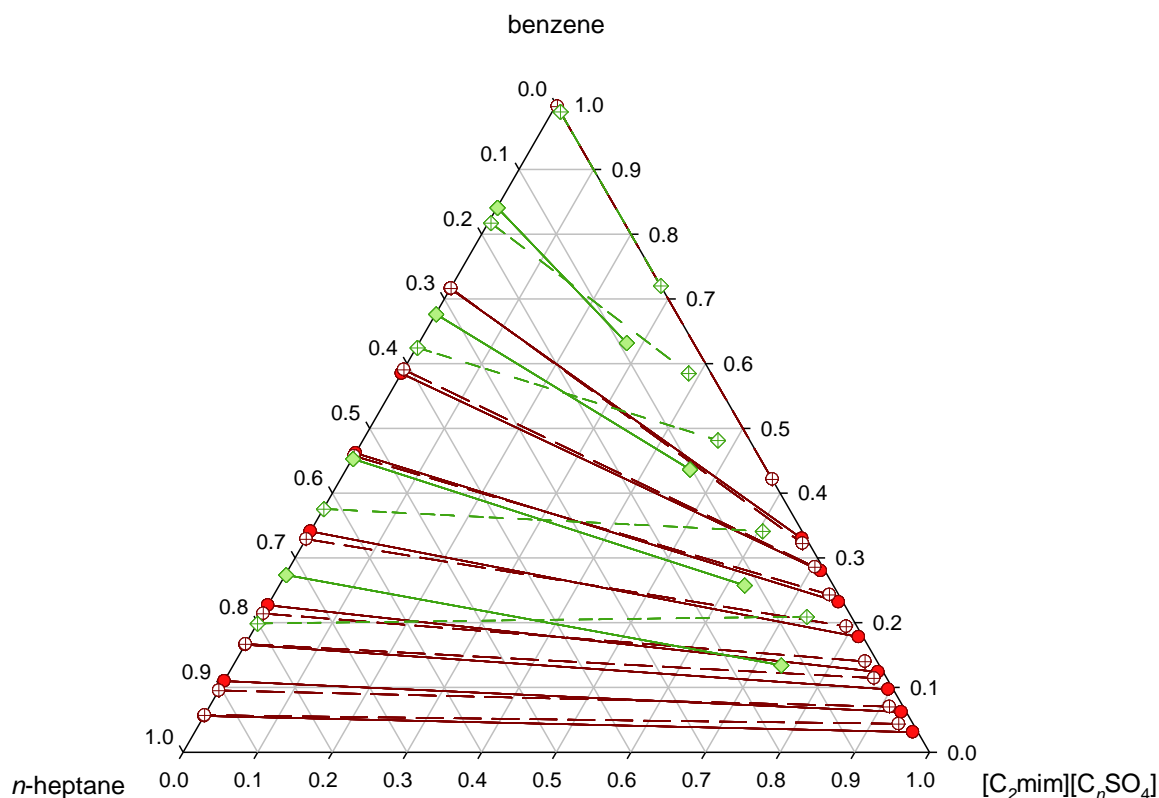
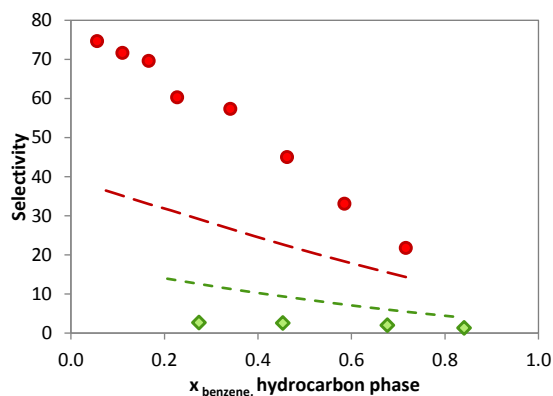


Figure 4.11 a) Experimental and COSMO-RS predicted tie-lines, b) selectivity and c) distribution ratio for the LLE of the ternary systems n -heptane + toluene + $[\text{C}_6\text{mim}][\text{PF}_6]$ ³⁷ (full diamonds and solid line for experimental data; and empty dotted diamonds and dot dashed line for COSMO-RS predicted values) and n -heptane + toluene + $[\text{C}_6\text{mim}][\text{BF}_4]$ ³⁷ (full squares and solid line for experimental data; and empty dotted squares and dot-dot dashed line for COSMO-RS predicted values) at 298.15K.

a)



b)



c)

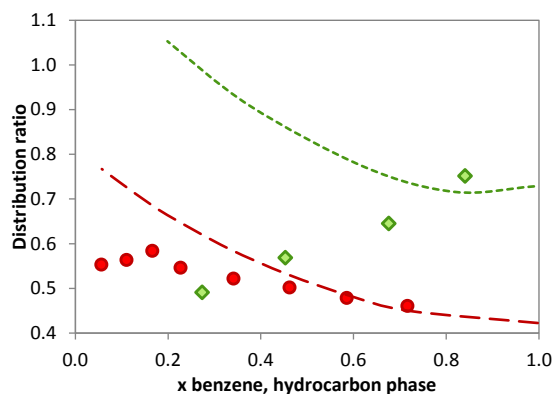


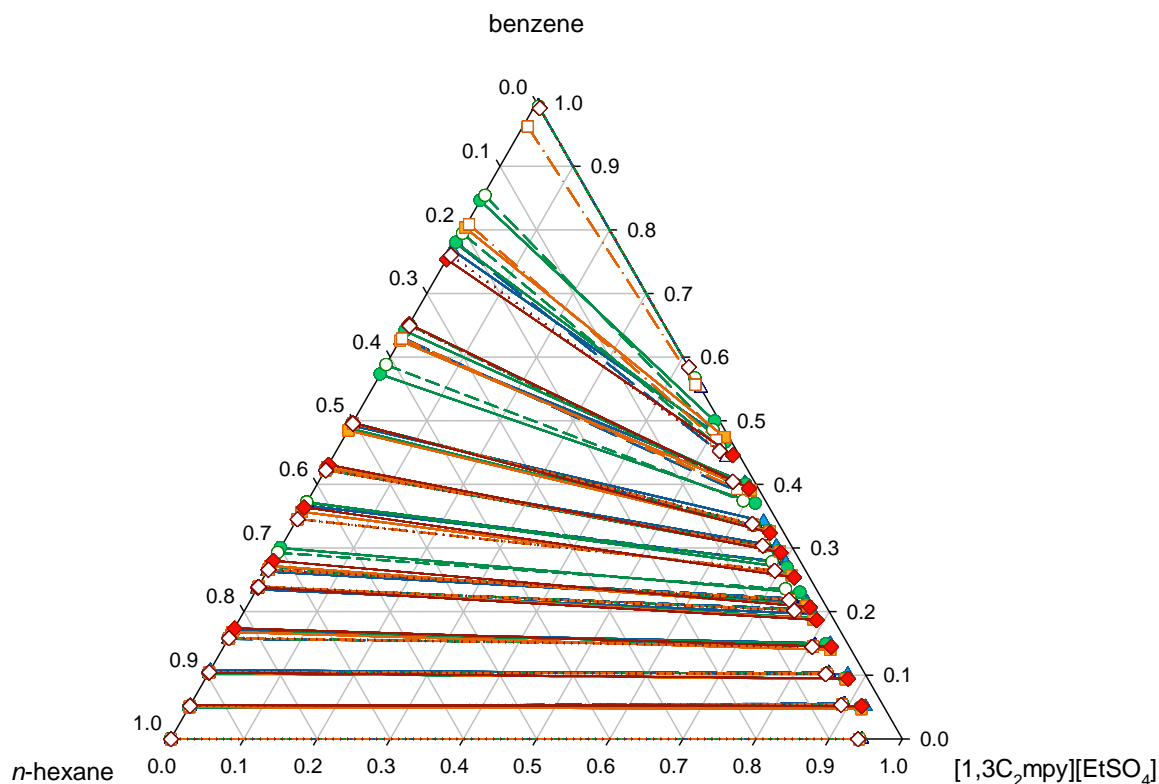
Figure 4.12 a) Experimental and COSMO-RS predicted tie-lines, b) selectivity and c) distribution ratio for the LLE of the ternary systems n -hexane + benzene + $[C_2mim][EtSO_4]$ ³² (full circles and solid line for experimental data; and empty crossed circles and long dashed line for COSMO-RS predicted values) and n -hexane + benzene + $[C_2mim][OcSO_4]$ ¹⁵ (full diamonds and solid line for experimental data; and empty crossed diamonds and short dashed line for COSMO-RS predicted values), at 298.15K.

4.3.5. Effect of the temperature upon the phase behavior

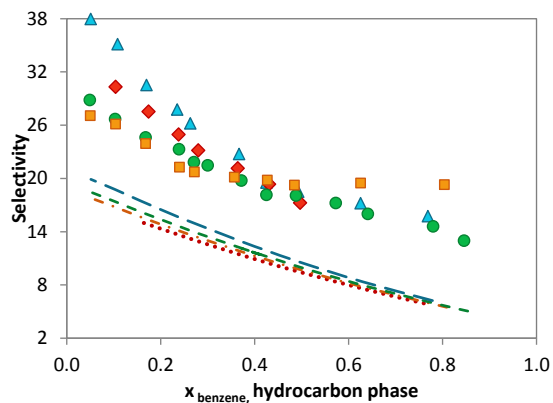
The influence of temperature upon the equilibrium behavior, selectivity and distribution ratio for the systems of the type aliphatic + aromatic + ionic liquid was also evaluated. The results of this study are reported in Figure 4.13 for the *n*-hexane + benzene + [1,3C₂mpy][EtSO₄] system for temperatures ranging between 283.15 K and 303.15 K, and at Appendix C, Figures C29 – C35, for temperatures in the range of 283.15 K to 328.15 K. For the rank of temperatures evaluated, a small variation of the experimental LLE binodal curve is noticed with temperature. A temperature increase leads to an increased miscibility with a contraction of the immiscibility region, and mostly visible at the ionic liquid-rich phase. The tie-line slopes become more negative as the temperature rises. The selectivity and the distribution ratio are mildly influenced by the temperature while they decrease with the increasing on temperature. This trend indicates that the aromatic extraction process is more efficient at low temperatures.

The COSMO-RS predictions for these systems are presented at Figure 4.13 and in Appendix C, Figures C29 – C35, and the respective RMSD to the experimental values at Table C3 in Appendix C. The results show that COSMO-RS can reproduce the temperature effect on the ternary LLE phase diagrams, with small differences between the experimental and the predicted binodal curve at the ionic liquid-rich phase. The temperature effect on the tie-line slopes is also well described, showing a good quantitative agreement, especially at the lower temperatures, with RMSD ranging between 1.3 % and 1.8 % for the *n*-hexane + benzene + [1,3C₂mpy][EtSO₄] system for the temperatures 283.15 K and 303.15 K, respectively. Concerning the selectivity and the distribution ratios, the model presents some discrepancies compared to the experimental values, being however the trend satisfactorily described. For instance, for the distribution ratio, its small variation with temperature is well captured by the COSMO-RS model. Nevertheless, the results suggest that COSMO-RS performance degrades with an increase on temperature; yet, more experimental data are necessary to confirm this behavior.

a)



b)



c)

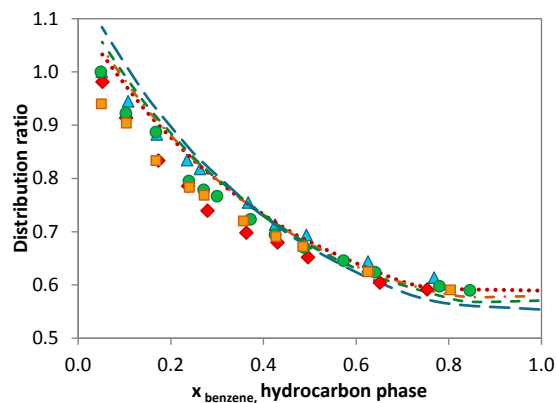


Figure 4.13 a) Experimental and COSMO-RS predicted tie-lines, b) selectivity and c) distribution ratio for the LLE of the ternary systems *n*-hexane + benzene + [1,3C₂mpy][EtSO₄] at the temperatures 283.15K¹⁰ (full triangles and solid line for experimental data; and empty triangles and long dashed line for COSMO-RS predicted values), 293.15K¹⁰ (full circles and solid line for experimental data; and empty circles and short dashed line for COSMO-RS predicted values), 298.15K¹⁰ (full squares and solid line for experimental data; and empty squares and dot dashed line for COSMO-RS predicted values), and 303.15K¹⁰ (full diamonds and solid line for experimental data; and empty diamonds and dotted line for COSMO-RS predicted values).

4.3.6. Summary

The systems studied allowed the drawing of a global picture of the influence of the structural features of ionic liquids and hydrocarbons on their mutual solubilities. A summary of the results here compiled is reported in Table 4.1. From the gathered information, it is possible to conclude that ILs containing cations with shorter alkyl chains favor the aromatic extraction process. However, it is necessary to achieve some balance between the selectivity and the distribution ratio values since the latter increases with the increase on the alkyl chain length. Concerning the ions families, the aromatic nitrogen-based cations, and anions with low hydrogen-bond basicity, such as [EtSO₄]⁻, [MeSO₄]⁻, [SCN]⁻, and [DCA]⁻, are preferred. Regarding the operation temperatures, the phase diagrams behavior suggest that lower temperatures favor the aromatic-aliphatic separation, which is encouraging since the energy consumption is reduced.

The COSMO-RS model presents a good performance on the description of these systems, presenting root mean square deviations below 6 % for most of the systems studied, where higher RMSD (> 10 %) were only obtained for the ionic liquids with longer alkyl side chains. The COSMO-RS prediction ability, resulting from the various features that were evaluated, is summarized in Table 4.1. The predictions obtained by the COSMO-RS show that this predictive model, based only on the individual atoms properties, is able to qualitatively describe the phase equilibria of the ternary systems composed of ionic liquid + aromatic hydrocarbon + aliphatic hydrocarbon, and provide reliable quantitative predictions for the most immiscible systems. This results from the fact that COSMO-RS calculations consider that the interactions are completely performed at the interface of the virtual conductor environment surrounding the molecules (isolated species) and thus performs better for poorly miscible systems.

Making use of the COSMO-RS prediction potential, the selectivity and the distribution ratio for ternary mixtures of *n*-hexane + benzene + ionic liquid at 298.15K, with an aromatic content around 0.1 in mole fraction, were predicted and compiled in Table 4.2. The most studied cations, like 1-ethyl-3-methylimidazolium, 1-ethyl-3-methylpyridinium, 1-ethyl-3-methylpyrrolidinium, 1-butyl-3-methylpyrrolidinium, methyl(2-hydroxyethyl)dimethylammonium (choline), and other not so used, such as guanidinium, hexamethylguanidinium, *N*-butyl-isoquinolinium, *O*-ethyl-*N,N,N,N*-tetramethylisouronium, *O*-methyl-*N,N,N,N*-tetramethylisouronium, *S*-ethyl-*N,N,N,N*-tetramethylisothiouronium, and the anions methylsulfate, ethylsulfate, bis(trifluoromethylsulfonyl)imide, dicyanamide, tricyanomethane, and tetracyanoborate, were covered and compared. The results displayed in Table 4.2 were compared with the selectivity and distribution ratio of one the most conventional solvents used at aromatic extraction units – sulfolane (S = 25 and D =

0.74 for the same operation conditions and similar molar composition)⁸¹. As can be seen the families imidazolium, pyridinium and pyrrolidinium cations families combined with the methylsulfate and ethylsulfate anions show similar performance with sulfolane. Regarding the ammonium cation, the several ionic liquids based in this cation, higher selectivities and lower distribution ratios than sulfolane are shown. The guanidinium cation with all the anions show a very high selectivity and a very low distribution ratio, whereas the hexamethylguanidinium cation show high distribution ratio, and combined with the methylsulfate, ethylsulfate, tricyanomethane, and tetracyanoborate being therefore a good candidate to the aromatic/aliphatic separation. The not so known *N*-butyl-isoquinolinium, O-ethyl-N,N,N,N-tetramethylisouronium, O-methyl-N,N,N,N-tetramethylisouronium, S-ethyl-N,N,N,N-tetramethylisothiouronium cations present distribution ratios superior to one and the best selectivity predicted with the dicyanamide, tricyanomethane, and tetracyanoborate anions.

In brief, some of the ionic liquids evaluated present similar or higher values of selectivity than the conventional molecular solvent sulfolane, being therefore strong candidates for its substitution. In addition, besides the so exhausted imidazolium-based and sulfate-based ionic liquids studied, other ions, such as the isoquinolinium and isouronium cations or the cyano-based anion can offer an improved performance for the specific task of the selective extraction of aromatics from aliphatic streams.

Table 4.1 Summary of the different factors that influence the solubility, selectivity and distribution ratio, and the performance of COSMO-RS in describing these factors.

factor	influence on the solubility	Selectivity	distribution ratio	COSMO-RS performance
hydrocarbon type	cycloalkanes > <i>n</i> -alkanes	<i>n</i> -alkanes > cycloalkanes	<i>n</i> -alkanes ≈ cycloalkanes	Good
<i>n</i> -alkane chain length	↑ C_n → ↓ Solubility	↑ C_n → ↑ <i>S</i>	Variable	Good
aromatic alkyl chain substituted length	↑ C_n → ↓ Solubility	↑ C_n → ↓ <i>S</i>	↑ C_n → ↓ <i>D</i>	Good
temperature	≈ for 298.15 K - 303.15 K ≈ for 283.15 K - 328.15 K	↑ <i>T</i> → ↓ <i>S</i>	↑ <i>T</i> → ↓ <i>D</i>	Good
ionic liquid cation core	ammonium < imidazolium < pyridinium < phosphonium	ammonium > imidazolium > pyridinium > phosphonium	Pyridinium > imidazolium > ammonium > phosphonium	Good
ionic liquid cation alkyl chain length	↑ C_n → ↑↑ Solubility	↑ C_n → ↓ <i>S</i>	↑ C_n → ↑ <i>D</i>	Good
ionic liquid anion	[DCA] ⁻ ≈ [SCN] ⁻ ≈ [MeSO ₄] ⁻ [PF ₆] ⁻ ≈ [BF ₄] ⁻ [NTf ₂] ⁻ > [BF ₄] ⁻ [NTf ₂] ⁻ > [EtSO ₄] ⁻	[DCA] ⁻ > [SCN] ⁻ > [MeSO ₄] ⁻ [PF ₆] ⁻ > [BF ₄] ⁻ [BF ₄] ⁻ > [NTf ₂] ⁻ [EtSO ₄] ⁻ > [NTf ₂] ⁻	[DCA] ⁻ > [SCN] ⁻ > [MeSO ₄] ⁻ [PF ₆] ⁻ > [BF ₄] ⁻ [NTf ₂] ⁻ > [BF ₄] ⁻ [EtSO ₄] ⁻ > [NTf ₂] ⁻	Trends do not always follow the experimental
ionic liquid anion alkyl chain length	↑ C_n → ↑ Solubility	↑ C_n → ↓ <i>S</i>	↑ C_n → ↑ <i>D</i>	Good

Table 4.2 COSMO-RS predicted selectivity and distribution ratio for several *n*-hexane + benzene + ionic liquid systems at 298.15K.

ionic liquid cation	<i>S</i>	<i>D</i>	<i>S</i>	<i>D</i>
	[MeSO ₄] ⁻		[EtSO ₄] ⁻	
1-ethyl-3-methylimidazolium	23	0.68	20	0.73
1-ethyl-3-methylpyridinium	19	0.93	17	0.98
1-ethyl-3-methylpyrrolidinium	14	1.13	14	1.11
methyl(2-hydroxyethyl)dimethylammonium	24	0.38	24	0.37
guanidinium	641	0.003	202	0.01
hexamethylguanidinium	9	2.26	9	2.42
N-butyl-isoquinolinium	15	1.13	13	1.23
O-ethyl-N,N,N,N-tetramethylisouronium	12	1.97	11	1.98
O-methyl-N,N,N,N-tetramethylisouronium	13	1.85	13	1.76
S-ethyl-N,N,N,N-tetramethylisothiouronium	12	2.06	11	2.09
	[NTf ₂] ⁻		[DCA] ⁻	
1-ethyl-3-methylimidazolium	18	0.91	37	0.43
1-ethyl-3-methylpyridinium	14	1.20	26	0.66
1-ethyl-3-methylpyrrolidinium	14	1.02	21	0.89
methyl(2-hydroxyethyl)dimethylammonium	27	0.45	51	0.20
guanidinium	41	0.13	1475	0.01
hexamethylguanidinium	0.16	1.79	0.09	2.36
N-butyl-isoquinolinium	8	1.68	17	1.01
O-ethyl-N,N,N,N-tetramethylisouronium	9	1.60	15	1.60
O-methyl-N,N,N,N-tetramethylisouronium	11	1.38	18	1.47
S-ethyl-N,N,N,N-tetramethylisothiouronium	8	1.66	15	1.74
	[B(CN) ₄] ⁻		[C(CN) ₃] ⁻	
1-ethyl-3-methylimidazolium	58	0.65	55	0.47
1-ethyl-3-methylpyridinium	39	0.93	36	0.73
1-ethyl-3-methylpyrrolidinium	35	1.09	32	0.86
methyl(2-hydroxyethyl)dimethylammonium	94	0.35	94	0.21
guanidinium	315	0.24	420	0.07
hexamethylguanidinium	13	2.14	12	2.05
N-butyl-isoquinolinium	19	1.56	19	1.29
O-ethyl-N,N,N,N-tetramethylisouronium	19	1.71	19	1.61
O-methyl-N,N,N,N-tetramethylisouronium	27	1.37	24	1.25
S-ethyl-N,N,N,N-tetramethylisothiouronium	18	1.93	18	1.80

4.4. Conclusions

The selective separation of compounds from hydrocarbons streams are of a great importance to the refining and petrochemical industries. Taking into account the large selectivities presented by the systems composed of alkanes + aromatic hydrocarbons + ionic liquids there seems to be a huge potential for the use of ionic liquids as solvents in separation processes involving hydrocarbons matrixes. The experimental data, taken from the literature (and reported in Tables C1 and C2 at Appendix C), allowed the understanding of the impact of the diverse structural features of the hydrocarbons and of the ILs in the ternary phase diagrams behavior.

As the number of ionic liquids is incredibly vast and the scanning of IL systems by simple trial and error is almost impossible, it was here accomplished an extensive evaluation on the use of COSMO-RS in the description of ternary systems composed of alkanes + aromatic hydrocarbons + ionic liquids. The results presented show that the quality of the predictions is enhanced with a decrease in the miscibility among all the components. The results here reported show that the COSMO-RS model can be successfully applied to the *a priori* screening of ILs to be used in separations of aliphatic-aromatic hydrocarbons mixtures.

4.5. References

1. Arce, A.; Earle, M. J.; Rodriguez, H.; Seddon, K. R.; Soto, A., 1-Ethyl-3-methylimidazolium bis{(trifluoromethyl)sulfonyl}amide as solvent for the separation of aromatic and aliphatic hydrocarbons by liquid extraction - extension to C7- and C8-fractions. *Green Chem* **2008**, *10* (12), 1294-1300.
2. González, E. J.; González, B.; Calvar, N.; Domínguez, Á., Application of [EMpy][ESO4] ionic liquid as solvent for the liquid extraction of xylenes from hexane. *Fluid Phase Equilib* **2010**, *295* (2), 249-254.
3. Arce, A.; Earle, M. J.; Katdare, S. P.; Rodriguez, H.; Seddon, K. R., Application of mutually immiscible ionic liquids to the separation of aromatic and aliphatic hydrocarbons by liquid extraction: a preliminary approach. *Phys Chem Chem Phys* **2008**, *10* (18), 2538-2542.
4. Arce, A.; Earle, M. J.; Rodriguez, H.; Seddon, K. R.; Soto, A., Bis{(trifluoromethyl)sulfonyl}amide ionic liquids as solvents for the extraction of aromatic hydrocarbons from their mixtures with alkanes: effect of the nature of the cation. *Green Chem* **2009**, *11* (3), 365-372.
5. Domańska, U.; Pobudkowska, A.; Żolek-Tryznowska, Z., Effect of an ionic liquid (IL) cation on the ternary system (IL + p-xylene + hexane) at T = 298.15 K. *J Chem Eng Data* **2007**, *52* (6), 2345-2349.
6. Al-Tuwaim, M. S.; Alkhaldi, K. H. A. E.; Fandary, M. S.; Al-Jimaz, A. S., Extraction of propylbenzene or butylbenzene from dodecane using 4-methyl-N-butylpyridinium tetrafluoroborate, [mebupy][BF4], as an ionic liquid at different temperatures. *J Chem Therm* **2011**, *43* (12), 1804-1809.
7. González, E. J.; Calvar, N.; Domínguez, I.; Domínguez, Á., Extraction of toluene from aliphatic compounds using an ionic liquid as solvent: Influence of the alkane on the liquid-liquid equilibrium. *J Chem Therm* **2011**, *43* (4), 562-568.
8. Arce, A.; Earle, M. J.; Rodríguez, H.; Seddon, K. R.; Soto, A., Isomer effect in the separation of octane and xylenes using the ionic liquid 1-ethyl-3-methylimidazolium bis{(trifluoromethyl)sulfonyl}amide. *Fluid Phase Equilib* **2010**, *294* (1-2), 180-186.
9. González, E. J.; Calvar, N.; González, B. a.; Domínguez, A. n., Liquid extraction of benzene from its mixtures using 1-ethyl-3-methylimidazolium ethylsulfate as a solvent. *J Chem Eng Data* **2010**, *55* (11), 4931-4936.

10. González, E. J.; Calvar, N.; González, B.; Domínguez, Á., (Liquid + liquid) equilibria for ternary mixtures of (alkane + benzene + [EMpy] [ESO4]) at several temperatures and atmospheric pressure. *J Chem Therm* **2009**, *41* (11), 1215-1221.
11. González, E. J.; Calvar, N.; Dominguez, I.; Domínguez, Á., (Liquid + liquid) equilibrium data for the ternary systems (cycloalkane + ethylbenzene + 1-ethyl-3-methylimidazolium ethylsulfate) at T = 298.15 K and atmospheric pressure. *J Chem Therm* **2011**, *43* (5), 725-730.
12. García, S.; Larriba, M.; García, J.; Torrecilla, J. S.; Rodríguez, F., (Liquid + liquid) equilibrium for the ternary systems {heptane + toluene + 1-allyl-3-methylimidazolium bis(trifluoromethylsulfonyl)imide} and {heptane + toluene + 1-methyl-3-propylimidazolium bis(trifluoromethylsulfonyl)imide} ionic liquids. *J Chem Therm* **2011**, *43* (11), 1641-1645.
13. García, J.; Fernández, A.; Torrecilla, J. S.; Oliet, M.; Rodríguez, F., Liquid-liquid equilibria for {hexane + benzene + 1-ethyl-3-methylimidazolium ethylsulfate} at (298.2, 313.2 and 328.2) K. *Fluid Phase Equilib* **2009**, *282* (2), 117-120.
14. Wang, R.; Wang, J.; Meng, H.; Li, C.; Wang, Z., Liquid-liquid equilibria for benzene + cyclohexane + 1-methyl-3-methylimidazolium dimethylphosphate or + 1-ethyl-3-methylimidazolium diethylphosphate. *J Chem Eng Data* **2008**, *53* (5), 1159-1162.
15. Deenadayalu, N.; Ngcongco, K. C.; Letcher, T. M.; Ramjugernath, D., Liquid-liquid equilibria for ternary mixtures (an ionic liquid + benzene + heptane or hexadecane) at T = 298.2 K and atmospheric pressure. *J Chem Eng Data* **2006**, *51* (3), 988-991.
16. García, J.; García, S.; Torrecilla, J. S.; Oliet, M.; Rodríguez, F., Liquid-liquid equilibria for the ternary systems {heptane + toluene + N-butylpyridinium tetrafluoroborate or N-hexylpyridinium tetrafluoroborate} at T = 313.2 K. *J Chem Eng Data* **2010**, *55* (8), 2862-2865.
17. Hansmeier, A. R.; Ruiz, M. M.; Meindersma, G. W.; de Haan, A. B., Liquid-liquid equilibria for the three ternary systems (3-methyl-N-butylpyridinium dicyanamide + toluene + heptane), (1-butyl-3-methylimidazolium dicyanamide + toluene + heptane) and (1-butyl-3-methylimidazolium thiocyanate + toluene + heptane) at T = (313.15 and 348.15) K and p = 0.1 MPa. *J Chem Eng Data* **2009**, *55* (2), 708-713.
18. Selvan, M. S.; McKinley, M. D.; Dubois, R. H.; Atwood, J. L., Liquid-liquid equilibria for toluene + heptane + 1-ethyl-3-methylimidazolium triiodide and toluene + heptane + 1-butyl-3-methylimidazolium triiodide. *J Chem Eng Data* **2000**, *45* (5), 841-845.

19. Gómez, E.; Domínguez, I.; González, B. a.; Domínguez, A. n., Liquid-liquid equilibria of the ternary systems of alkane + aromatic + 1-ethylpyridinium ethylsulfate ionic liquid at T = (283.15 and 298.15) K. *J Chem Eng Data* **2010**, *55* (11), 5169-5175.
20. González, E. J.; Calvar, N.; González, B. a.; Domínguez, A. n., Liquid-liquid equilibrium for ternary mixtures of hexane + aromatic compounds + [EMpy][ESO4] at T = 298.15 K. *J Chem Eng Data* **2009**, *55* (2), 633-638.
21. Maduro, R. M.; Aznar, M., Liquid-liquid equilibrium of ternary systems 1-butyl-3-methylimidazolium hexafluorophosphate + aromatic + aliphatic. *Fluid Phase Equilib* **2008**, *265* (1-2), 129-138.
22. Maduro, R. M.; Aznar, M., Liquid-liquid equilibrium of ternary systems 1-octyl-3-methylimidazolium hexafluorophosphate + aromatic + aliphatic hydrocarbons. *Fluid Phase Equilib* **2010**, *296* (2), 88-94.
23. García, S.; Larriba, M.; García, J.; Torrecilla, J. S.; Rodríguez, F., Liquid-liquid extraction of toluene from heptane using 1-alkyl-3-methylimidazolium bis(trifluoromethylsulfonyl)imide ionic liquids. *J Chem Eng Data* **2011**, *56* (1), 113-118.
24. Hansmeier, A. R.; Jongmans, M.; Wytze Meindersma, G.; de Haan, A. B., LLE data for the ionic liquid 3-methyl-N-butyl pyridinium dicyanamide with several aromatic and aliphatic hydrocarbons. *J Chem Therm* **2010**, *42* (4), 484-490.
25. García, J.; García, S.; Torrecilla, J. S.; Rodríguez, F., N-butylpyridinium bis-(trifluoromethylsulfonyl)imide ionic liquids as solvents for the liquid-liquid extraction of aromatics from their mixtures with alkanes: Isomeric effect of the cation. *Fluid Phase Equilib* **2011**, *301* (1), 62-66.
26. Meindersma, G. W.; Simons, B. T. J.; de Haan, A. B., Physical properties of 3-methyl-N-butylpyridinium tetracyanoborate and 1-butyl-1-methylpyrrolidinium tetracyanoborate and ternary LLE data of [3-mebupy]B(CN)₄ with an aromatic and an aliphatic hydrocarbon at T = 303.2 K and 328.2 K and p = 0.1 MPa. *J Chem Therm* **2011**, *43* (11), 1628-1640.
27. Domańska, U.; Pobudkowska, A.; Królikowski, M., Separation of aromatic hydrocarbons from alkanes using ammonium ionic liquid C₂N₂Tf₂ at T = 298.15 K. *Fluid Phase Equilib* **2007**, *259* (2), 173-179.
28. Arce, A.; Earle, M. J.; Rodriguez, H.; Seddon, K. R., Separation of aromatic hydrocarbons from alkanes using the ionic liquid 1-ethyl-3-methylimidazolium bis{(trifluoromethyl) sulfonyl} amide. *Green Chem* **2007**, *9* (1), 70-74.

29. Arce, A.; Earle, M. J.; Rodriguez, H.; Seddon, K. R., Separation of benzene and hexane by solvent extraction with 1-alkyl-3-methylimidazolium bis{(trifluoromethyl)sulfonyl}amide ionic liquids: Effect of the alkyl-substituent length. *J Phys Chem B* **2007**, *111* (18), 4732-4736.
30. Gómez, E.; Domínguez, I.; Calvar, N.; Domínguez, Á., Separation of benzene from alkanes by solvent extraction with 1-ethylpyridinium ethylsulfate ionic liquid. *J Chem Therm* **2010**, *42* (10), 1234-1239.
31. González, E. J.; Calvar, N.; Gómez, E.; Domínguez, Á., Separation of benzene from alkanes using 1-ethyl-3-methylpyridinium ethylsulfate ionic liquid at several temperatures and atmospheric pressure: Effect of the size of the aliphatic hydrocarbons. *J Chem Therm* **2010**, *42* (1), 104-109.
32. González, E. J.; Calvar, N.; Gómez, E.; Domínguez, A. n., Separation of benzene from linear alkanes (C₆-C₉) using 1-ethyl-3-methylimidazolium ethylsulfate at T = 298.15 K. *J Chem Eng Data* **2010**, *55* (9), 3422-3427.
33. García, J.; García, S.; Torrecilla, J. S.; Oliet, M.; Rodríguez, F., Separation of toluene and heptane by liquid-liquid extraction using z-methyl-N-butylpyridinium tetrafluoroborate isomers (z = 2, 3, or 4) at T = 313.2 K. *J Chem Therm* **2010**, *42* (8), 1004-1008.
34. González, E. J.; Calvar, N.; González, B.; Domínguez, Á., Separation of toluene from alkanes using 1-ethyl-3-methylpyridinium ethylsulfate ionic liquid at T = 298.15 K and atmospheric pressure. *J Chem Therm* **2010**, *42* (6), 752-757.
35. García, J.; García, S.; Torrecilla, J. S.; Rodríguez, F., Solvent extraction of toluene from heptane with the ionic liquids N-ethylpyridinium bis(trifluoromethylsulfonyl)imide and z-methyl-N-ethylpyridinium bis(trifluoromethylsulfonyl)imide (z = 2, 3, or 4) at T = 313.2 K. *J Chem Eng Data* **2010**, *55* (11), 4937-4942.
36. González, E. J.; González, B.; Calvar, N.; Domínguez, Á., Study of [EMim][ESO₄] ionic liquid as solvent in the liquid-liquid extraction of xylenes from their mixtures with hexane. *Fluid Phase Equilib* **2011**, *305* (2), 227-232.
37. Letcher, T. M.; Reddy, P., Ternary (liquid + liquid) equilibria for mixtures of 1-hexyl-3-methylimidazolium (tetrafluoroborate or hexafluorophosphate) + benzene + an alkane at T=298.2 K and p=0.1 MPa. *J Chem Thermodyn* **2005**, *37* (5), 415-421.
38. Fletcher, K. A.; Baker, S. N.; Baker, G. A.; Pandey, S., Probing solute and solvent interactions within binary ionic liquid mixtures. *New J Chem* **2003**, *27* (12), 1706-1712.

39. Meindersma, G. W.; Podt, A.; de Haan, A. B., Ternary liquid-liquid equilibria for mixtures of an aromatic + an aliphatic Hydrocarbon + 4-methyl-N-butylpyridinium tetrafluoroborate. *J Chem Eng Data* **2006**, *51* (5), 1814-1819.
40. Meindersma, G. W.; Podt, A. J. G.; de Haan, A. B., Ternary liquid-liquid equilibria for mixtures of toluene + n-heptane + an ionic liquid. *Fluid Phase Equilib* **2006**, *247* (1-2), 158-168.
41. Wang, R.; Li, C.; Meng, H.; Wang, J.; Wang, Z., Ternary liquid-liquid equilibria measurement for benzene + cyclohexane + N-methylimidazole, or N-ethylimidazole, or N-methylimidazolium dibutylphosphate at 298.2 K and atmospheric pressure. *J Chem Eng Data* **2008**, *53* (9), 2170-2174.
42. García, J.; Fernández, A.; Torrecilla, J. S.; Oliet, M.; Rodríguez, F., Ternary liquid-liquid equilibria measurement for hexane and benzene with the ionic liquid 1-butyl-3-methylimidazolium methylsulfate at T = (298.2, 313.2, and 328.2) K. *J Chem Eng Data* **2009**, *55* (1), 258-261.
43. Gutierrez, J. P.; Meindersma, W.; de Haan, A. B., Binary and ternary (liquid + liquid) equilibrium for {methylcyclohexane (1) + toluene (2) + 1-hexyl-3-methylimidazolium tetracyanoborate (3)/1-butyl-3-methylimidazolium tetracyanoborate (3)}. *J Chem Therm* **2011**, *43* (11), 1672-1677.
44. González, E. J.; Calvar, N.; Canosa, J.; Domínguez, A. n., Effect of the Chain Length on the Aromatic Ring in the Separation of Aromatic Compounds from Methylcyclohexane Using the Ionic Liquid 1-Ethyl-3-methylpyridinium Ethylsulfate. *J. Chem. Eng. Data* **2010**, *55* (6), 2289-2293.
45. Poole, C. F.; Poole, S. K., Extraction of organic compounds with room temperature ionic liquids. *J Chromatogr A* **2010**, *1217* (16), 2268-2286.
46. Mirkhani, S. A.; Vossoughi, M.; Pazuki, G. R.; Safekordi, A. A.; Heydari, A.; Akbari, J.; Yavari, M., (Liquid + liquid) equilibrium for ternary mixtures of {heptane + aromatic compounds + [EMpy][ESO4]} at T = 298.15 K. *J Chem Therm* **2011**, *43* (10), 1530-1534.
47. González, E. J.; Domínguez, I.; González, B.; Canosa, J., Liquid-liquid equilibria for ternary systems of {cyclohexane + aromatic compounds + 1-ethyl-3-methylpyridinium ethylsulfate}. *Fluid Phase Equilib* **2010**, *296* (2), 213-218.
48. Abu-Eishah, S. I.; Dowaidar, A. M., Liquid-liquid equilibrium of ternary systems of cyclohexane + (benzene, + toluene, + ethylbenzene, or + o-xylene) + 4-methyl-N-butyl

pyridinium tetrafluoroborate ionic liquid at 303.15 K. *J Chem Eng Data* **2008**, *53* (8), 1708-1712.

49. González, E. J.; Calvar, N.; González, B.; Domínguez, Á., Measurement and correlation of liquid-liquid equilibria for ternary systems {cyclooctane + aromatic hydrocarbon + 1-ethyl-3-methylpyridinium ethylsulfate} at T = 298.15 K and atmospheric pressure. *Fluid Phase Equilib* **2010**, *291* (1), 59-65.

50. Domínguez, I.; Calvar, N.; Gómez, E.; Domínguez, Á., Separation of toluene from cyclic hydrocarbons using 1-butyl-3-methylimidazolium methylsulfate ionic liquid at T = 298.15 K and atmospheric pressure. *J Chem Therm* **2011**, *43* (5), 705-710.

51. García, S.; García, J. n.; Larriba, M.; Torrecilla, J. S.; Rodríguez, F., Sulfonate-Based Ionic Liquids in the Liquid-Liquid Extraction of Aromatic Hydrocarbons. *J Chem Eng Data* **2011**, *56* (7), 3188-3193.

52. Revelli, A.-L.; Mutelet, F.; Jaubert, J.-N. I., Extraction of Benzene or Thiophene from n-Heptane Using Ionic Liquids. NMR and Thermodynamic Study. *J Phys Chem B* **2010**, *114* (13), 4600-4608.

53. García, S.; Larriba, M.; García, J. n.; Torrecilla, J. S.; Rodríguez, F., 1-Alkyl-2,3-dimethylimidazolium Bis(trifluoromethylsulfonyl)imide Ionic Liquids for the Liquid-Liquid Extraction of Toluene from Heptane. *J Chem Eng Data* **2011**, *56* (8), 3468-3474.

54. Simoni, L. D.; Lin, Y.; Brennecke, J. F.; Stadtherr, M. A., Modeling liquid-liquid equilibrium of ionic liquid systems with NRTL, Electrolyte-NRTL, and UNIQUAC. *Ind Eng Chem Res* **2007**, *47* (1), 256-272.

55. Santiago, R. S.; Santos, G. R.; Aznar, M., UNIQUAC correlation of liquid-liquid equilibrium in systems involving ionic liquids: The DFT-PCM approach. *Fluid Phase Equilib* **2009**, *278* (1-2), 54-61.

56. Robles, P. A.; Graber, T. A.; Aznar, M., Prediction by the ASOG method of liquid-liquid equilibrium for binary and ternary systems containing 1-alkyl-3-methylimidazolium hexafluorophosphate. *Fluid Phase Equilib* **2009**, *287* (1), 43-49.

57. Robles, P. A.; Graber, T. A.; Aznar, M., Prediction of liquid-liquid equilibrium for ternary systems containing ionic liquids with the tetrafluoroborate anion using ASOG. *Fluid Phase Equilib* **2010**, *296* (2), 154-158.

58. Klamt, A.; Eckert, F., COSMO-RS: a novel and efficient method for the a priori prediction of thermophysical data of liquids. *Fluid Phase Equilib* **2000**, *172* (1), 43-72.

59. Klamt, A., Summary, limitations, and perspectives. In *COSMO-RS*, Elsevier: Amsterdam, 2005; 205-207.
60. Diedenhofen, M.; Klamt, A., COSMO-RS as a tool for property prediction of IL mixtures--A review. *Fluid Phase Equilib* **2010**, *294* (1-2), 31-38.
61. Anantharaj, R.; Banerjee, T., COSMO-RS-based screening of ionic liquids as green solvents in denitrification studies. *Ind Eng Chem Res* **2010**, *49* (18), 8705-8725.
62. Banerjee, T.; Sahoo, R. K.; Rath, S. S.; Kumar, R.; Khanna, A., Multicomponent liquid-liquid equilibria prediction for aromatic extraction systems using COSMO-RS. *Ind Eng Chem Res* **2007**, *46* (4), 1292-1304.
63. Banerjee, T.; Singh, M. K.; Khanna, A., Prediction of binary VLE for imidazolium based ionic liquid systems using COSMO-RS. *Ind Eng Chem Res* **2006**, *45* (9), 3207-3219.
64. Domańska, U.; Pobudkowska, A.; Eckert, F., Liquid-liquid equilibria in the binary systems (1,3-dimethylimidazolium, or 1-butyl-3-methylimidazolium methylsulfate plus hydrocarbons). *Green Chem* **2006**, *8* (3), 268-276.
65. Freire, M. G.; Carvalho, P. J.; Santos, L. M. N. B. F.; Gomes, L. R.; Marrucho, I. M.; Coutinho, J. A. P., Solubility of water in fluorocarbons: Experimental and COSMO-RS prediction results. *J Chem Therm* **2010**, *42* (2), 213-219.
66. Freire, M. G.; Santos, L. M. N. B. F.; Marrucho, I. M.; Coutinho, J. A. P., Evaluation of COSMO-RS for the prediction of LLE and VLE of alcohols + ionic liquids. *Fluid Phase Equilib* **2007**, *255* (2), 167-178.
67. Freire, M. G.; Ventura, S. P. M.; Santos, L. M. N. B. F.; Marrucho, I. M.; Coutinho, J. A. P., Evaluation of COSMO-RS for the prediction of LLE and VLE of water and ionic liquids binary systems. *Fluid Phase Equilib* **2008**, *268* (1-2), 74-84.
68. Klamt, A.; Eckert, F.; Arlt, W., COSMO-RS: An alternative to simulation for calculating thermodynamic properties of liquid mixtures. *Annu Rev Chem Biomol* **2010**, *1* (1), 101-122.
69. Kumar, A. A. P.; Banerjee, T., Thiophene separation with ionic liquids for desulphurization: A quantum chemical approach. *Fluid Phase Equilib* **2009**, *278* (1-2), 1-8.
70. Palomar, J.; Torrecilla, J. S.; Ferro, V. R.; Rodríguez, F., Development of an a priori ionic liquid design tool. 2. ionic liquid selection through the prediction of COSMO-

RS molecular descriptor by inverse neural network. *Ind Eng Chem Res* **2009**, *48* (4), 2257-2265.

71. Shimoyama, Y.; Iwai, Y.; Yoda, S.; Furuya, T., Prediction of partition coefficients of benzothiophene and benzothiophene 1,1-dioxide in octane/acetonitrile system using COSMO theory. *Ind Eng Chem Res* **2008**, *47* (9), 3247-3252.

72. Varma, N. R.; Ramalingam, A.; Banerjee, T., Experiments, correlations and COSMO-RS predictions for the extraction of benzothiophene from n-hexane using imidazolium-based ionic liquids. *Chem Eng J* **2011**, *166* (1), 30-39.

73. Ferreira, A. R.; Freire, M. G.; Ribeiro, J. C.; Lopes, F. M.; Crespo, J. G.; Coutinho, J. A. P., An overview of the liquid-liquid equilibria of (ionic liquid + hydrocarbon) binary systems and their modeling by the Conductor-like Screening Model for Real Solvents. *Ind Eng Chem Res* **2011**, *50* (9), 5279-5294.

74. Sørensen, J. M.; Arlt, W., *Liquid-liquid equilibrium data collection. Ternary systems*. DECHEMA: Frankfurt, 1980; Vol. V, part 2.

75. Freire, M. G.; Neves, C. M. S. S.; Shimizu, K.; Bernardes, C. E. S.; Marrucho, I. M.; Coutinho, J. A. P.; Lopes, J. N. C.; Rebelo, L. P. N., Mutual solubility of water and structural/positional isomers of N-alkylpyridinium-based ionic liquids. *J Phys Chem B* **2010**, *114* (48), 15925-15934.

76. Cassol, C.; Umpierre, A.; Ebeling, G.; Ferrera, B.; Chiaro, S.; Dupont, J., On the Extraction of Aromatic Compounds from Hydrocarbons by Imidazolium Ionic Liquids. *Int J Mol Sci* **2007**, *8* (7), 593-605.

77. Lachwa, J.; Bento, I.; Duarte, M. T.; Lopes, J. N. C.; Rebelo, L. P. N., Condensed phase behaviour of ionic liquid-benzene mixtures: congruent melting of a [emim][NTf₂]-C₆H₆ inclusion crystal. *Chem Commun* **2006**, (23), 2445-2447.

78. Fernandes, A. M.; Rocha, M. A. A.; Freire, M. G.; Marrucho, I. M.; Coutinho, J. o. A. P.; Santos, L. s. M. N. B. F., Evaluation of Cation-Anion Interaction Strength in Ionic Liquids. *J Phys Chem B* **2011**, *115* (14), 4033-4041.

79. Lungwitz, R.; Strehmel, V.; Spange, S., The dipolarity/polarisability of 1-alkyl-3-methylimidazolium ionic liquids as function of anion structure and the alkyl chain length. *New J Chem* **2010**, *34* (6), 1135-1140.

80. Lungwitz, R.; Spange, S., A hydrogen bond accepting (HBA) scale for anions, including room temperature ionic liquids. *New J Chem* **2008**, *32* (3), 392-394.

81. Chen, J.; Duan, L.-P.; Mi, J.-G.; Fei, W.-Y.; Li, Z.-C., Liquid-liquid equilibria of multi-component systems including n-hexane, n-octane, benzene, toluene, xylene and sulfolane at 298.15 K and atmospheric pressure. *Fluid Phase Equilib* **2000**, 173 (1), 109-119.
82. Chen, C.-C.; Simoni, L. D.; Brennecke, J. F.; Stadtherr, M. A., Correlation and prediction of phase behavior of organic compounds in ionic liquids using the Nonrandom Two-Liquid Segment Activity Coefficient model. *Ind Eng Chem Res* **2008**, 47 (18), 7081-7093.

Chapter 5

Ionic Liquids for Mercaptans Desulfurization: Experimental Liquid-Liquid Equilibrium and COSMO-RS Description

Ferreira, A. R.; Freire, M. G.; Ribeiro, J. C.; Lopes, F. M.; Crespo, J. G.;
Coutinho, J. A. P.

Published at *Fuel*

2014, 128 (0), 314-329

DOI: 10.1016/j.fuel.2014.03.020

5.1. Introduction

Desulfurization is today one of the most important processes on a refinery. Commonly, the reduction of the sulfur content is attained through the conventional hydrodesulfurization process (HDS). This treatment consists in the hydrogenation of the sulfur compound (aliphatics and aromatics) into hydrogen sulfides and hydrocarbons at elevated temperatures and high hydrogen pressure.¹⁻² Despite the hydrocarbon recovery, there is also an octane number decrease by the saturation of olefins. However, this type of treatment represents high economic investments and operation costs. In addition, for the distilled branches with higher molecular weight sulfur-compounds, which present lower reactivity, more severe conditions are even required since these compounds are more difficult to hydrogenate, increasing therefore the operation costs.¹⁻² The sulfur removal by the HDS process needs a quality upgrading of the existing technologies and a continuous development of new alternative desulfurization approaches. Various options were already considered, such as selective and/or oxidative extractions, reactive adsorption, bio-desulfurization, membrane separation, among others.¹⁻⁷

Regarding the aliphatic sulfur compounds in a hydrocarbon matrix, the study of ionic liquids as extracting solvents were already addressed. Wasserscheid et al.^{14, 41} studied the removal of *n*-butyl mercaptan from *n*-heptane and *n*-decane using imidazolium-phosphate-, chloride- and bis[(trifluoromethyl)sulfonyl]imide-based ionic liquids, either in simple liquid extractions or in absorptive processes using the ionic liquid immobilized in a ceramic support. The ethanethiol extraction from gasoline was proposed by Martínez-Palou et al.⁴² and its interactions with both anhydrous Fe(III) chloride anions and 1-butyl-3-methylimidazolium-based ionic liquids were investigated.

Though this hydrocarbon mixture is very complex, the “jet-fuel” model assumed here is a *n*-alkane, *n*-dodecane, and the mercaptan 1-hexanethiol. The liquid-liquid equilibrium for the ternary mixture composed of 1-hexanethiol, *n*-dodecane and several ionic liquids, based either on imidazolium or pyridinium cations, combined with the anions methylsulfate, methanesulfonate, triflate, bis(trifluoromethylsulfonyl)imide and tetrafluoroborate, was determined at 298.2 K and 313.2 K, and at atmospheric pressure. The large number of ionic liquids studied further allowed the understanding of the ionic liquid features that enhance the extraction of high molecular weight mercaptans.

Keeping in mind that the screening of the huge number of possible ionic liquids and hydrocarbons mixtures is experimentally unfeasible, the use of predictive models and/or computational methods is a viable option for the design of the best solvent. Thus, the

COnductor-like Screening MOdel for Real Solvents (COSMO-RS)⁴¹⁻⁴³ was also employed to describe the liquid-liquid equilibria experimentally addressed aiming at evaluating its prediction performance. Albeit COSMO-RS was already applied in the description of equilibrium behavior of sulfur compounds, mainly aromatic sulfur compounds, with ionic liquid and hydrocarbon,⁴⁴⁻⁵⁵ the ability of COSMO-RS to describe the ternary systems comprising aliphatic sulfur compounds, is here assessed. Due to its fundamental nature, COSMO-RS only requires the information on the molecular structure of the compounds and has gained a spot place in the *a priori* prediction of phase behavior, activity coefficients and other thermophysical data.^{47-48, 50, 52, 56-61}

Supported on the good agreement obtained between the experimental data and COSMO-RS results, the model was further used in the identification of other potential ionic liquids for the mercaptan extraction.

5.2. Materials and methods

5.2.1. Liquid-liquid equilibrium

The selection of the ionic liquids to be tested was carried out taking into account the mutual solubility between aliphatic/aromatic hydrocarbons and ionic liquids. Low mutual solubilities are required in order to minimize the solvent loss or the contamination of the hydrocarbon-rich sample. Besides these conditions it is also necessary to choose ionic liquids with a high selectivity and distribution ratio values for mercaptans. As demonstrated in our previous work⁶², the cation side alkyl chain length of ionic liquids is the feature with the major impact within these system's miscibility. Longer alkyl side chains or the predominance of non-polar regions increases the dispersive interactions between the ionic liquid and the hydrocarbons which can lead to a significant loss of the feed. Therefore, the longest alkyl side chains of the ionic liquid cations studied here are ethyl and butyl to reduce the mutual solubility between the ionic liquid and the hydrocarbons. Both imidazolium- and pyridinium-based ionic liquids were evaluated. Others cations, such as alkylphosphoniums or alkylammoniums, were not tested due to their high miscibility with *n*-alkanes and aromatics hydrocarbons.⁶²

Materials

The *n*-dodecane and 1-hexanethiol were acquired from Sigma-Aldrich, 99% and 95% pure, respectively, and were used as received. The imidazolium-based ionic liquids

investigated were: 1-ethyl-3-methylimidazolium methylsulfate ([C₂mim][MeSO₄]), 1-ethyl-3-methylimidazolium methanesulfonate ([C₂mim][CH₃SO₃]), 1-ethyl-3-methylimidazolium triflate ([C₂mim][CF₃SO₃]), 1-ethyl-3-methylimidazolium bis(trifluoromethylsulfonyl)imide ([C₂mim][NTf₂]), 1-ethyl-3-methylimidazolium tetrafluoroborate ([C₂mim][BF₄]), 1-butyl-3-methylimidazolium methylsulfate ([C₄mim][MeSO₄]), 1-butyl-3-methylimidazolium triflate ([C₄mim][CF₃SO₃]), and 1-butyl-3-methylimidazolium bis(trifluoromethylsulfonyl)imide ([C₄mim][NTf₂]). The pyridinium-based ionic liquids studied were: 1-ethyl-3-methylpyridinium methanesulfonate ([C₂mpy][CH₃SO₃]), 1-ethyl-3-methylpyridinium triflate ([C₂mpy][CF₃SO₃]), and 1-ethyl-3-methylpyridinium bis(trifluoromethylsulfonyl)imide ([C₂mpy][NTf₂]). The chemical structures of the studied ionic liquids, divided by cations and anions, are depicted in Tables A1 and A2, in Appendix A. All the ionic liquids were acquired from IoLiTec, Ionic Liquid Technology, Germany, with a purity level > 99 wt%. Before use, the ionic liquids were dried and purified by heating (313.2 K) under moderate vacuum, and with constant stirring for a minimum of 24h. The ionic liquid water content was determined by Karl-Fischer titration, using a Metrohm 831 Karl Fischer coulometer. The water content values are presented in the Appendix D, Table D1.

Experimental procedure

The ionic liquids were selected present a very low solubility in the hydrocarbon under study (*n*-dodecane). All the ternary systems investigated present two distinct liquid phases, an upper phase rich in *n*-dodecane and a lower IL-rich phase. The 1-hexanethiol is partitioned between the two phases. As the real sulfur content in crude oils is very low, the measured equilibrium tie-lines correspond to the lowest region of the ternary phase diagram with the mole fraction of 1-hexanethiol ranging between 0.015 and 0.025 in the overall mixture composition.

The ternary mixtures were prepared in glass vials (10 mL) with screw caps to prevent the evaporation of volatile compounds as well as to avoid the adsorption of moisture from atmosphere. Known quantities of each component were weighed within 10⁻⁴ g (Precisa, model XT220A, Sweden), and added directly to the glass vials.

The ternary mixtures were stirred and left at rest for at least 24 h at the desired temperature (± 0.5 K). When the equilibrium was attained two clear liquid phases were observed. After the equilibration, individual samples were carefully taken from the upper and bottom phases using syringes for further quantification.

The mercaptan, in each phase, was quantified by potentiometric titration, using a TitraLab® 865 titration workstation, with an alcoholic solution of AgNO_3 at 0.01 M, according to the ASTM D3227 standard.⁶³ The ionic liquid content in the hydrocarbon-rich phase was determined by UV spectroscopy, using a Helios α UV-Vis spectrophotometer from Thermo Scientific. However, it should be highlighted that no peaks corresponding to each ionic liquid were found in all the tested samples meaning that their concentration is below the lower detection limit of the equipment. Therefore, in all situations, the content of ionic liquid in the hydrocarbon-rich phase was considered as insignificant or null. The *n*-dodecane in the ionic-liquid-rich phase was determined gravimetrically ($\pm 10^{-4}$ g) after a drying process under vacuum in which the *n*-alkane and the mercaptan are removed. At this step, samples of circa 0.5 g were used. However, and as happened with the ionic liquids in the hydrocarbon-rich phase, the amount of *n*-dodecane in the ionic-liquid-rich phase was found to be negligible in all situations. In summary, the quantification of each component in each layer allowed the determination of the corresponding tie-lines.

5.3. Results and Discussion

The phase equilibrium studies carried out in this work intent to support the selection of the most suitable ionic liquids for the extraction of sulfur compounds from hydrocarbon's streams by understanding of the effect of the ionic liquids nature and/or chemical structure on the ternary systems behavior.

Besides the determination of the corresponding tie-lines, the feasibility of the liquid-liquid extraction of 1-hexanethiol from the dodecane-rich layer using ionic liquids was further evaluated by the solvent selectivity (*S*) and distribution ratio (*D*) values. These parameters provide a quantitative description of the partitioning behavior of the thiol between the coexisting phases and can be determined according to the following equations:

$$S = \frac{\frac{x_{RSH}^{II}}{x_{HC}^{II}}}{\frac{x_{RSH}^I}{x_{HC}^I}} \quad (5.1)$$

$$D = \frac{x_{RSH}^{II}}{x_{RSH}^I} \quad (5.2)$$

where x is the mole fraction and the subscripts *RSH* and *HC* correspond to 1-hexanethiol and to the aliphatic hydrocarbon *n*-dodecane, respectively. The superscript I refers to the dodecane-rich-phase (upper phase) while II refers to the ionic-liquid-rich phase (bottom phase).

5.3.1. Ternary liquid-liquid equilibrium (tie-lines data)

The experimental liquid-liquid equilibrium (LLE) results are presented in Table D 1, in the Appendix D, and are plotted in Figures 5.1 to 5.4. The tie-line data are plotted in an orthogonal ternary phase diagram, in which the *n*-dodecane was omitted, for a better visualization of the low experimental mole fraction values. In all the phase diagrams, the feed overall composition and the two equilibrium phase compositions are represented.

The ternary LLE obtained here are of type 2⁶⁴, and which consist of two pairs of partially miscible components, namely 1-hexanethiol + *n*-dodecane and 1-hexanethiol + ionic liquid pairs. The binodal curves appear adjacent to the diagram axes; this trend is indicative of large immiscible regions mainly resulting from the very low mutual solubility between the ionic liquid and *n*-dodecane. Moreover, and as experimentally observed in the studied concentration ranges, no ionic liquid or *n*-dodecane were detected in the respective *n*-dodecane- and ionic-liquid-rich phases.

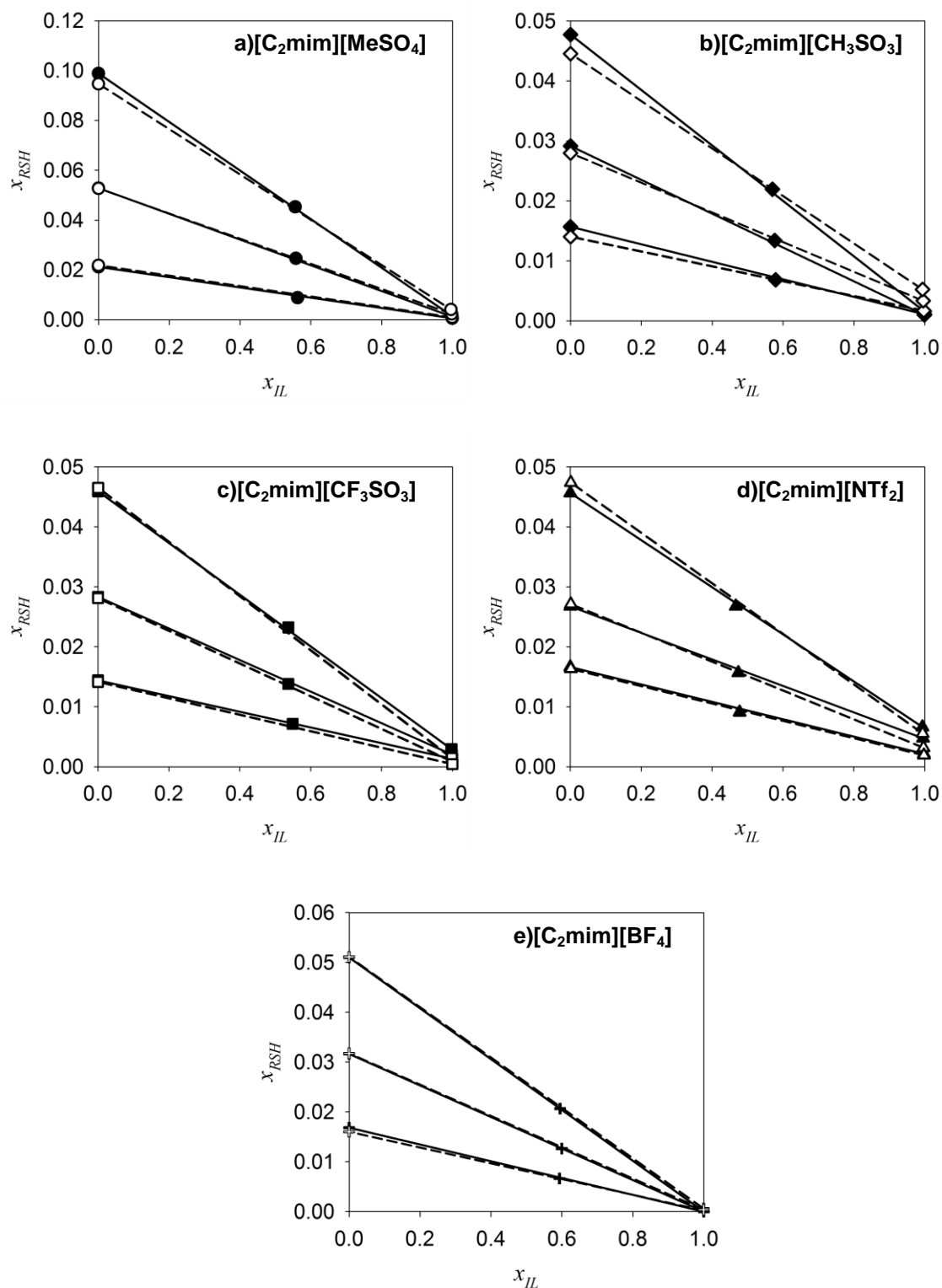


Figure 5.1 Experimental and COSMO-RS predicted tie-lines for the LLE of ternary systems composed of [C₂mim]-based ionic liquids + 1-hexanethiol + n -dodecane (full symbols and solid lines for experimental data, and empty symbols and dashed lines for COSMO-RS predicted values), at 298.2 K and atmospheric pressure.

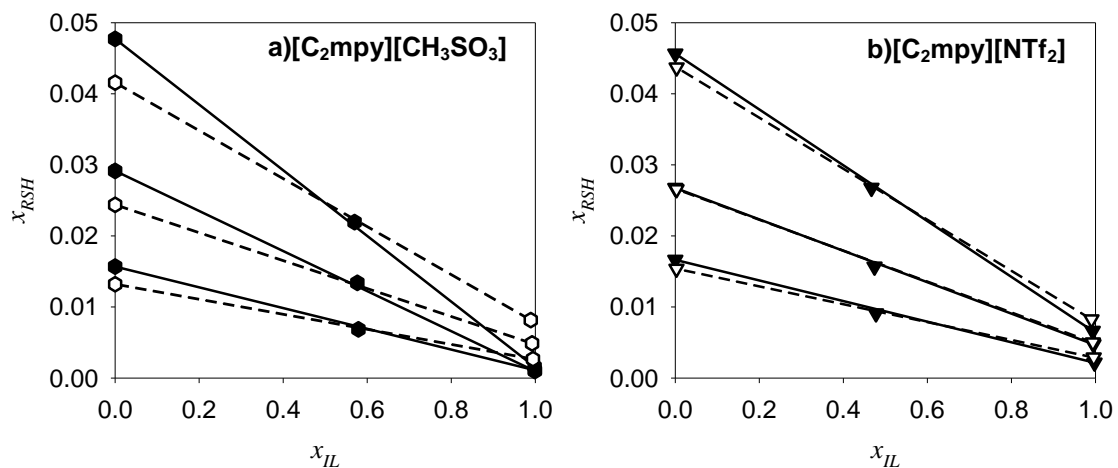


Figure 5.2 Experimental and COSMO-RS predicted tie-lines for the LLE of ternary systems composed of $[C_2mpy]$ -based ionic liquids + 1-hexanethiol + n -dodecane (full symbols and solid lines for experimental data, and empty symbols and dashed lines for COSMO-RS predicted values), at 298.2 K and atmospheric pressure.

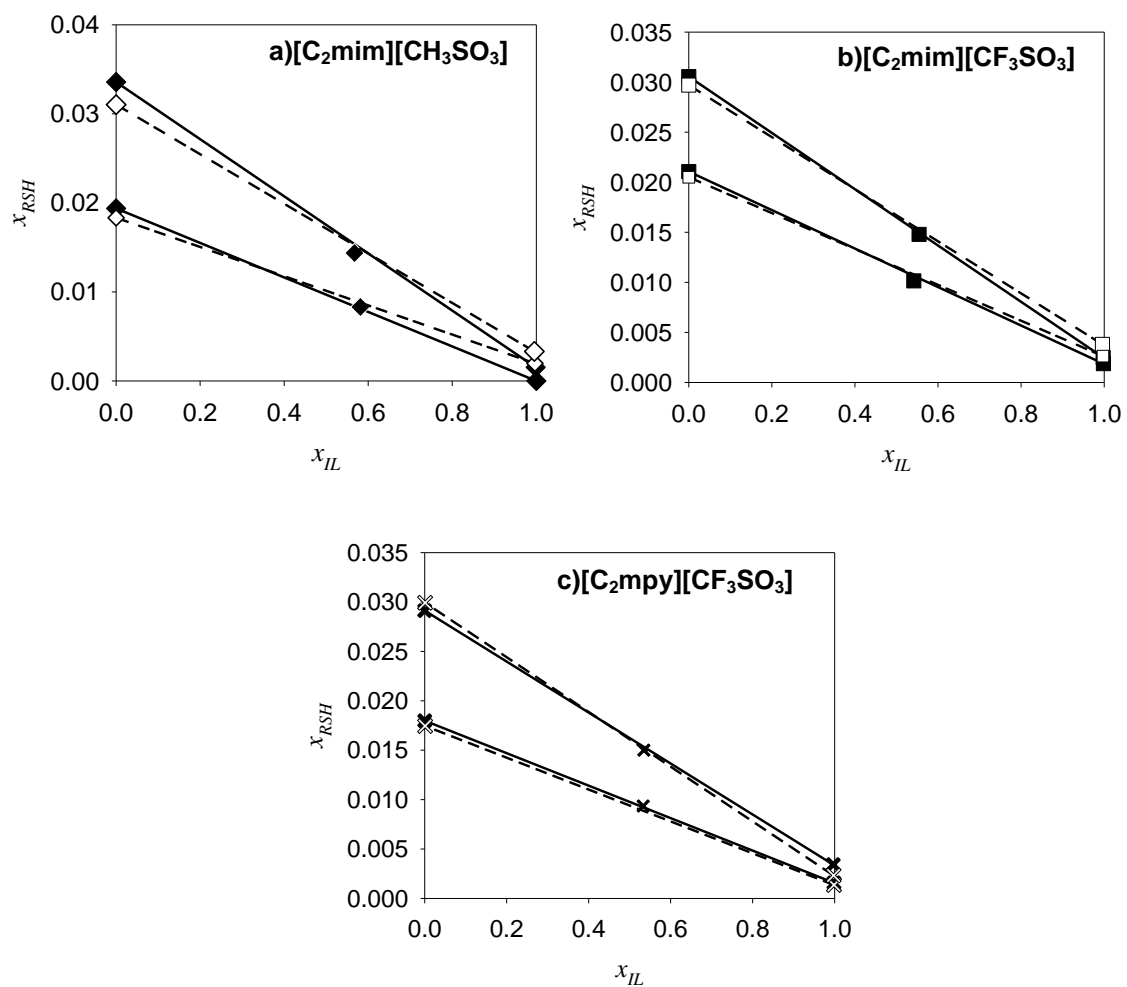


Figure 5.3 Experimental and COSMO-RS predicted tie-lines for the LLE of ternary systems composed of ionic liquids+ 1-hexanethiol + *n*-dodecane (full symbols and solid lines for experimental data, and empty symbols and dashed lines for COSMO-RS predicted values), at 313.2 K and atmospheric pressure.

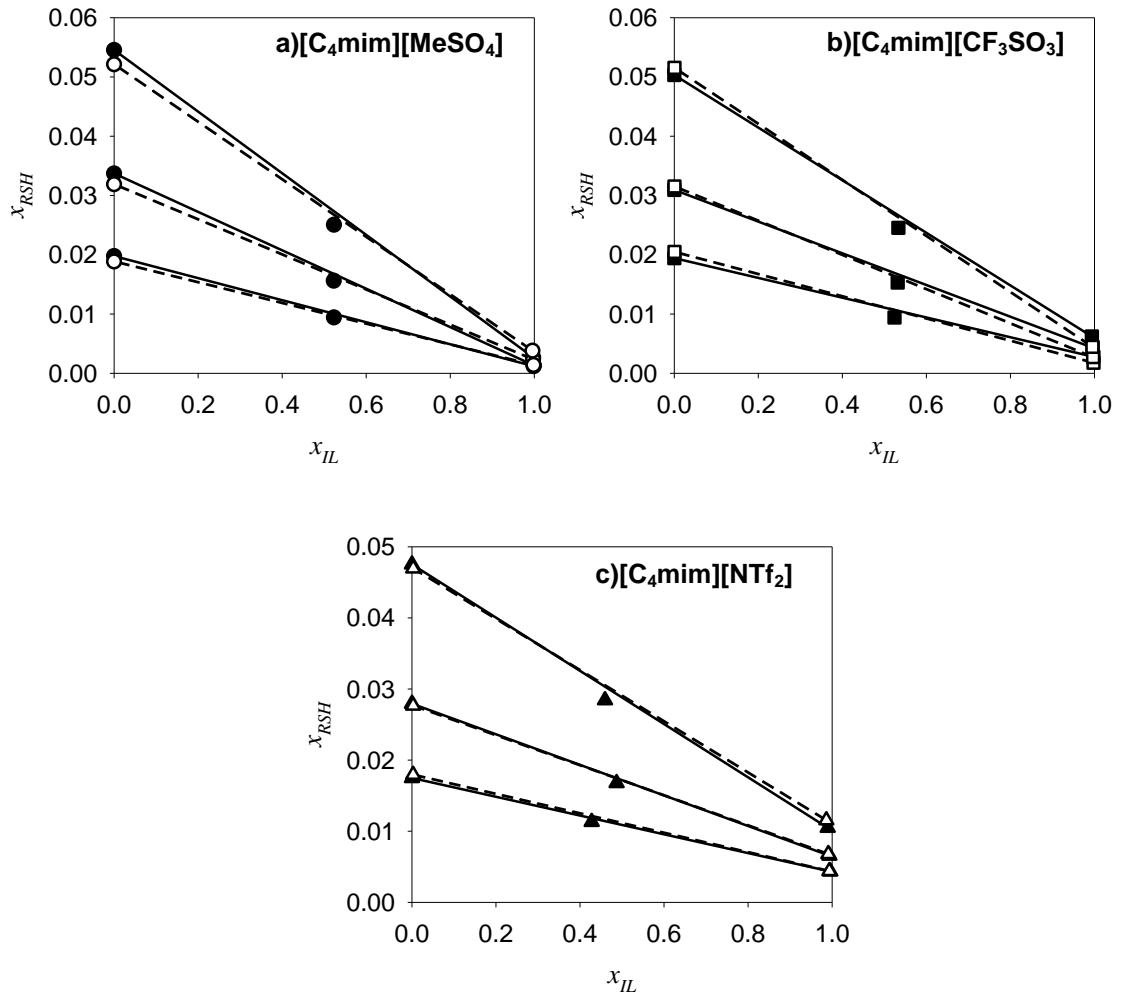


Figure 5.4 Experimental and COSMO-RS predicted tie-lines for the LLE of ternary systems composed of [C₄mim]-based ionic liquids + 1-hexanethiol + *n*-dodecane (full symbols and solid lines for experimental data, and empty symbols and dashed lines for COSMO-RS predicted values), at 298.2 K and atmospheric pressure.

5.3.2. Selectivity and distribution ratio

For a better understanding of the influence of the ionic liquid structural characteristics through the selectivity and distribution ratio values for 1-hexanethiol, the following discussion is presented in different sections. The comparison between the different systems is expressed in distribution ratio, instead of using the LLE data, due to its overlapping values and undistinguishable differences in the ternary phase diagrams. Accordingly, using the experiments here carried out, the distribution ratio values are depicted in Figures 5.5 to 5.9, divided by the effect of the cation core (Figure 5.5), cation alkyl chain length (Figure 5.6), anion nature (Figure 5.7), temperature (Figure 5.8) and water content (Figure 5.9), as a function of the 1-hexanethiol concentration (mole fraction) in the *n*-dodecane-rich phase.

In face of the negligible mutual solubilities between the studied ionic liquids and *n*-dodecane (Figures 5.1 to 5.4), the selectivity of the ionic liquids for the mercaptan is almost complete while minimizing the loss of the ionic liquid and the contamination of the hydrocarbon stream. This trend represents a clear evidence of the ionic liquids potential for the extraction of mercaptans from hydrocarbon streams. On the other hand, the low distribution ratio values are related with the low affinity of the mercaptan for the ionic liquid and reflected by the negative tie-line slopes in the ternary phase diagrams. Regarding the selectivity and distribution ratio criteria, all the studied ternary systems display a similar behavior: high selectivity ($S \gg 1$) and distribution ratio lower than unit ($D \ll 1$). The weak interaction between 1-hexanethiol and imidazolium- or pyridinium-based ionic liquids can be explained by the different types of intermolecular forces that occur in the mixture. While mercaptans' interactions essentially comprise dispersion forces and less prominent dipole-dipole interactions between the individual –SH groups, the ionic liquids mainly present electrostatic and hydrogen-bonding type interactions. Thus, the intermolecular interactions which could exist between both types of compounds are mainly van der Waals and dipole-dipole interactions. Since the tested ionic liquids have a short alkyl chain length the dispersive forces between the two compounds are small. The dipole-dipole attractions are also weak since the electronegativity difference between sulfur and hydrogen is low, making the S–H bond less polar than –OH, –NH or –FH bonds, where the hydrogen is bounded to highly electronegative atoms. Therefore, it is expectable that ion-mercaptan interactions are weaker than ion-ion or mercaptan-alkane interactions.

5.3.2.1. Effect of the ionic liquid cation core

Fixing the ionic liquid anion, it is possible to study the influence of the ionic liquid cation core on the distribution ratio of 1-hexanethiol towards the ionic-liquid-rich layer. Figures 5.5 a) and b) cover the common anions $[\text{CH}_3\text{SO}_3]^-$ and $[\text{NTf}_2]^-$, respectively, and allow the study of the effect of the imidazolium and the pyridinium cations. In both examples, the distribution ratio for the pyridinium-based systems is higher than for the imidazolium-based and which corresponds to a higher affinity of mercaptan for the first type of systems. For the fixed anion $[\text{CH}_3\text{SO}_3]^-$, the imidazolium-based system shows a distribution ratio of circa 0.05 whereas for the pyridinium cation it is 0.07. For the $[\text{NTf}_2]^-$ anion, the distribution ratio ranges from 0.06, for the imidazolium-based compound, to 0.21 for the pyridinium-based ionic liquid. Both cations are aromatic meaning that the higher affinity of 1-hexanethiol for the pyridinium-based ionic liquids should be related with its larger ring size. The pyridinium cation is a six-sided ring (Table A1, Appendix A), which being larger than the imidazolium five-sided ring, suffers a higher ring deformation by the charge density delocalization.⁶⁵ This delocalization of charge contributes to an increase in the van der Waals interactions between the mercaptan and the ionic liquid cation.

A significant aspect also observed when comparing the distribution ratio data is that they are more pronounced in the $[\text{NTf}_2]^-$ -based ionic liquids than for the $[\text{CH}_3\text{SO}_3]^-$ analogues. This reveals the importance of the anion, that has a high impact on the systems behavior, not only due to its nature, but that is reflected in the cation-anion interaction strength.⁶⁵⁻⁶⁶ Coulombic attractions and hydrogen-bonding can be so strong that they attenuate the cation-mercaptan interactions. These type of interactions are dependent on the radius and polarity of the anion and on the electronegativity of the atom with which the hydrogen bond is formed. In this way, a decrease in the anion charge density reflects a weaker interaction between the ionic liquid ions. $[\text{NTf}_2]^-$ is a non-polar anion whereas $[\text{CH}_3\text{SO}_3]^-$ is polar. Therefore, the cation-anion interactions are stronger for $[\text{CH}_3\text{SO}_3]^-$.⁶⁵⁻
⁶⁶ In this case the ionic liquid cation is less available to interact with the mercaptan compound, leading to smaller variations in the distribution ratio when the cation is replaced.

It is also noteworthy to highlight that the influence of the cation family can be significantly distinct of the one presented in this work and that other structural cations should be considered for a more complete analysis.

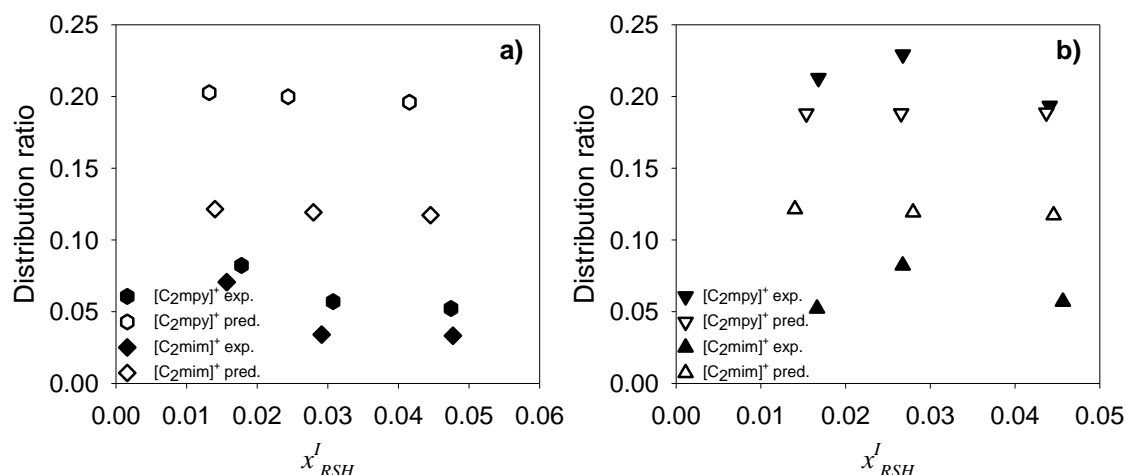


Figure 5.5 Experimental and COSMO-RS predicted distribution ratio of 1-hexanethiol in the ternary systems: **a)** [cation][CH₃SO₃]⁺ + 1-hexanethiol + *n*-dodecane; and **b)** [cation][NTf₂]⁺ + 1-hexanethiol + *n*-dodecane, at 298.2 K and atmospheric pressure.

5.3.2.2. Effect of cation alkyl side chain length

The length of the aliphatic moiety in the ionic liquid cation is a very important characteristic regarding the mutual solubilities between ionic liquids and hydrocarbons.⁶² The impact of the alkyl side chain length in imidazolium-based ionic liquids is illustrated in Figures 5.6 a) to c) for the [MeSO₄]⁻, [CF₃SO₃]⁻ and [NTf₂]⁻ anions. It is shown that an increase in the alkyl chain length from [C₂mim]⁺ to [C₄mim]⁺ results in an increase of the distribution ratio due to more favorable interactions between 1-hexanethiol and the ionic liquids. Longer aliphatic moieties increment the non-polar region of the cation, resulting in a more diffusive charge density, which slightly improves the dispersive interactions that take place between the mercaptan and the ionic liquids. For longer alkyl chains, an additional effect can also be expected by the increase of the free volume that allows a more efficient packing of the mercaptan on the cation-anion network. In addition, and as observed before with the cation core analysis, the effect of the alkyl side chain length is also influenced by the diverse ionic liquid anions. The most significant variation on the distribution ratios occurs for the weaker cation-anion interactions in [NTf₂]-based ionic liquids.⁶⁵⁻⁶⁶

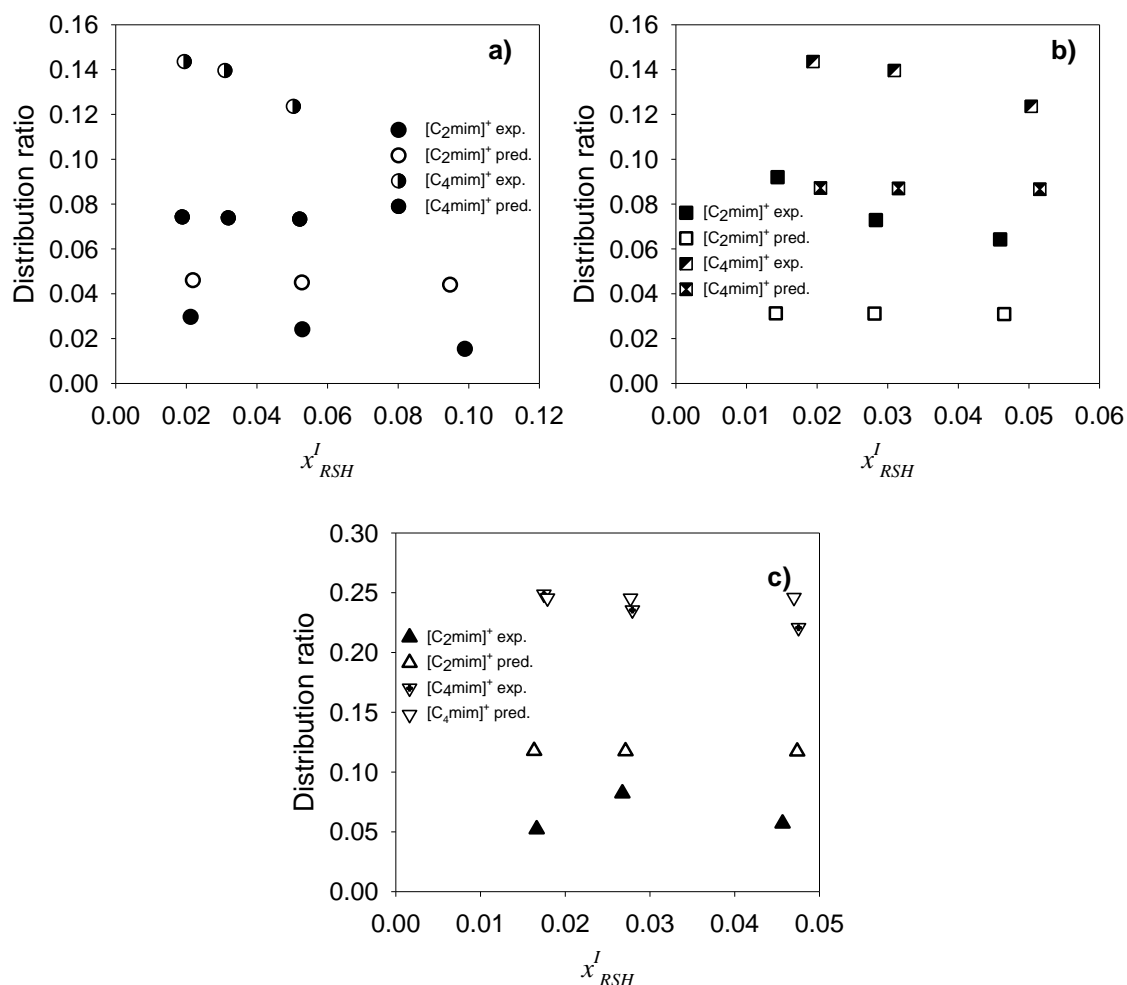


Figure 5.6 Experimental and COSMO-RS predicted distribution ratio of 1-hexanethiol in the ternary systems: **a)** $[C_n\text{mim}][\text{MeSO}_4]$ + 1-hexanethiol + *n*-dodecane; **b)** $[C_n\text{mim}][\text{CF}_3\text{SO}_3]$ + 1-hexanethiol + *n*-dodecane; and **c)** $[C_n\text{mim}][\text{NTf}_2]$ + 1-hexanethiol + *n*-dodecane, at 298.2 K and atmospheric pressure.

5.3.2.3. Effect of the ionic liquid anion nature

To further evaluate the effect associated with the anion nature, the distribution ratio of is presented in Figures 5.7 a) to c). Figure 5.7 a), for the $[C_2\text{mim}]$ -based ionic liquids, reveals an increase on the distribution ratio following the order: $[\text{BF}_4]^- < [\text{MeSO}_4]^- < [\text{CH}_3\text{SO}_3]^- < [\text{CF}_3\text{SO}_3]^- \sim [\text{NTf}_2]^-$, and ranging from 0 to 0.11. For the $[C_4\text{mim}]^+$ cation (Figure 5.7 b)), the trend follows the rank: $[\text{MeSO}_4]^- < [\text{CF}_3\text{SO}_3]^- < [\text{NTf}_2]^-$. In the previous example, the distribution ratio varies from 0.04 to 0.25 since the alkyl chain is slightly longer and additional interactions can occur. The results for the $[C_2\text{mpy}]$ -based ionic liquids combined with the $[\text{CH}_3\text{SO}_3]^-$ and $[\text{NTf}_2]^-$ anions are compared in Figure 5.7 c). The variation in the distribution ratio values obtained is also large ranging from 0.05 to

0.23. The higher distribution ratio values occur in the [NTf₂]-based ionic liquids. Mercaptan-anion interactions are mainly due to weak dispersive forces and the dependency behavior with the anions nature strongly ensues from their polarity. In this way, with the exception of the [BF₄]⁻ anion, the experimental trend on the distribution ratio values closely follows the dipolarity/polarisability solvatochromic parameter (π^*) in [C₄mim]-based ionic liquids: [MeSO₄]⁻ > [CH₃SO₃]⁻ > [BF₄]⁻ > [CF₃SO₃]⁻ > [NTf₂]⁻.⁶⁷

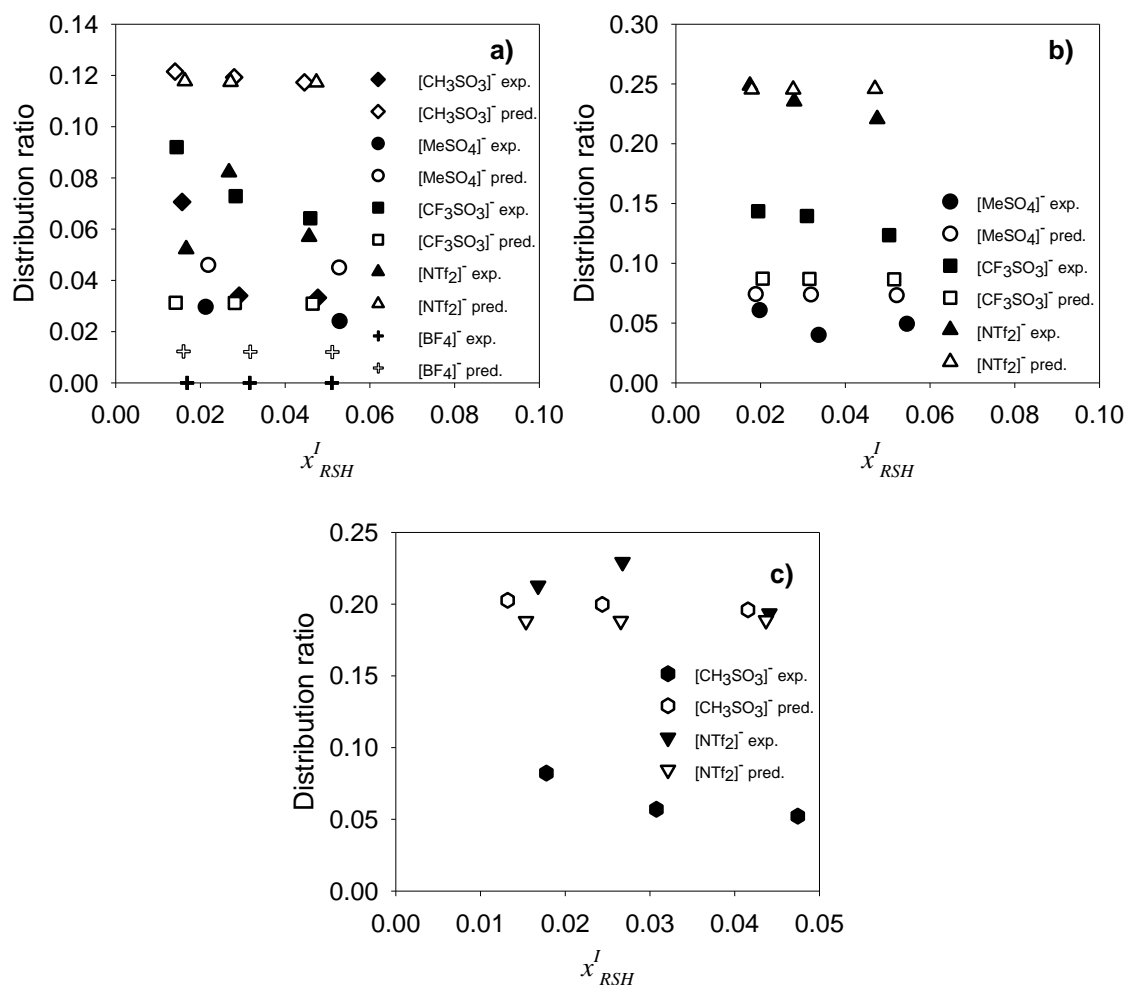


Figure 5.7 Experimental and COSMO-RS predicted distribution ratio of 1-hexanethiol in the ternary systems: **a)** [C₂mim][anion]+ 1-hexanethiol + *n*-dodecane; **b)** [C₄mim][anion] + 1-hexanethiol + *n*-dodecane; and **c)** [C₂mpy][anion]+ 1-hexanethiol + *n*-dodecane, at 298.2 K and atmospheric pressure.

5.3.2.4. Effect of the temperature

Aiming at the improvement of the distribution ratio of the systems composed of ionic liquid + 1-hexanethiol + *n*-dodecane, the effect of temperature in the LLE was also evaluated for the ionic liquids [C₂mim][CH₃SO₃] and [C₂mim][CF₃SO₃]. The distribution ratio values for both ionic liquids at 298.2 K and 313.2 K are plotted in Figures 5.8 a) and b). The increase of temperature from 298.2 K to 313.2 K does not lead to enhanced distribution ratios. This behavior denotes that ionic liquids, for the extraction of mercaptans, can be used at temperatures close to room temperature without losing their performance. A separation process using ionic liquids at mild operational conditions and with lower energy costs is thus conceivable when compared to the traditional hydrodesulfurization process.

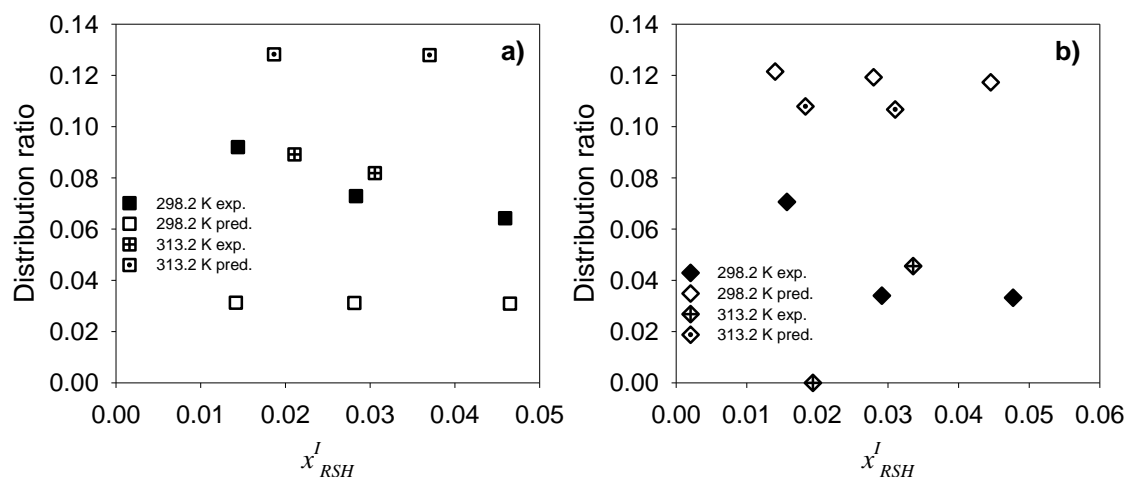


Figure 5.8 Experimental and COSMO-RS predicted distribution ratio of 1-hexanethiol in the ternary systems: **a)** [C₂mim][CF₃SO₃]+ 1-hexanethiol + *n*-dodecane, and **b)** [C₂mim][CH₃SO₃]+ 1-hexanethiol + *n*-dodecane, at the temperatures 298.2 K and 313.2 K, and atmospheric pressure.

5.3.2.5. Effect of the ionic liquid water content

Since ionic liquids are highly hygroscopic, the water content has an important role in their thermophysical properties and phase behavior.⁶⁸⁻⁷⁰ Therefore, the ionic liquids [C₂mim][MeSO₄] and [C₂mim][CF₃SO₃] with different water contents were also tested and the distribution ratio values were compared. The results obtained are shown in Figure 5.9. An increase in the water content from 130.1 ppm and 305.4 ppm to 6840.2 ppm and 6583.1 ppm, for the [C₂mim][MeSO₄] and [C₂mim][CF₃SO₃] ionic liquids, respectively,

was studied. From the results depicted in Figure 5.9, the increase in the water content leads to an increase in the distribution ratio of 1-hexanethiol. Thus, the ionic liquid moisture adsorption can be seen as advantageous in the process separation at industrial scale.

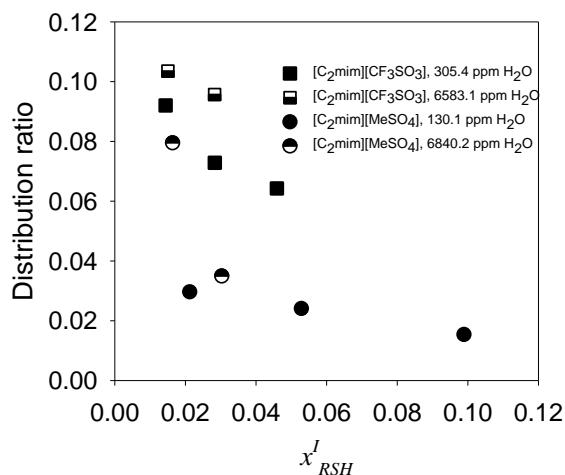


Figure 5.9 Experimental distribution ratio of 1-hexanethiol in the ternary systems [C₂mim][MeSO₄]+ 1-hexanethiol + *n*-dodecane with ionic liquid water content of 130 ppm, and 6840 ppm H₂O; and [C₂mim][CF₃SO₃] + 1-hexanethiol + *n*-dodecane with ionic liquid water content of 305 ppm, and 6583 ppm H₂O, at 298.2 K and atmospheric pressure.

5.3.3. Evaluation of the COSMO-RS prediction capability

The ionic liquids and conditions experimentally investigated allowed the understanding of the influence of the ionic liquid ions nature and temperature upon the phase behavior. Therefore, these data can be used to evaluate the predictive ability of COSMO-RS.

Along with the LLE experimental data (Figures 5.1 to 5.4) and the distribution ratio results (Figures 5.5 to 5.8), the COSMO-RS predicted values are also represented.

The COSMO-RS aptitude to describe the LLE results was also evaluated by the root mean square deviation (RMSD) to the experimental data. The RMSD is defined by equation 5.3:

$$RMSD = \left[\frac{\sum_i \sum_n (x_{i,n}^{pred.I} - x_{i,n}^{exp.I})^2 + (x_{i,n}^{pred.II} - x_{i,n}^{exp.II})^2}{(2 \times N \times R)} \right]^{1/2} \times 100 \quad (5.3)$$

where x is the mole fraction of compound i , R is the total number of compounds ($R = 3$), n is the tie-line number, and N is the total number of experiments. The RMSD values are listed in Table 5.1.

The results obtained with COSMO-RS for the tie-lines description (Figures 5.1 – 5.4) are in good agreement with the experimental data. The low relative deviations presented in Table 5.1 between the predicted and experimental values also support this statement. The relative deviations vary from 0.04 to 0.8%, for the systems containing 1-hexanethiol in the mole fraction between 0.015 and 0.025, and in the overall mixture composition with n -dodecane. It is also visible that the RMSD values depend on the anion, and the ability of COSMO-RS to describe the liquid-liquid phase behavior of systems decreases with the anion polarity. Nonetheless, the low RMSD values achieved confirm the good performance of the COSMO-RS model on describing, quantitatively and qualitatively, systems containing ionic liquids and hydrocarbon mixtures. These results allow the use of COSMO-RS for a quick and easy screening of the vast number of ionic liquid and hydrocarbon combinations.

The COSMO-RS predictive ability was also analyzed individually regarding the several aspects that can influence the behavior of systems constituted by ionic liquid + 1-hexanethiol + n -dodecane. The differences in the phase behavior by the change of the imidazolium cation for the pyridinium cation (Figure 5.5), and also by the increase of the alkyl side chain length in the imidazolium cation (Figure 5.6), in systems with the $[\text{MeSO}_4]$, $[\text{CH}_3\text{SO}_3]$, $[\text{CF}_3\text{SO}_3]$, and $[\text{NTf}_2]$ anions, are well described by COSMO-RS. However, and as previously observed for the binary phase behavior of ionic liquid + water systems⁵⁷, better predictions are obtained for the systems with the ionic liquids containing the less polar anions.

Taking into account the lower ability of COSMO-RS to predict the phase behavior of systems composed of ionic liquids with more polar anions, it is thus expectable a poorer performance of COSMO-RS to predict the influence of the anion nature on the liquid-liquid equilibrium (Figure 5.7). Even though, the COSMO-RS results correctly correlate with the anion influence in the distribution ratio values, as depicted in Figure 5.7 b), better results are achieved for the $[\text{C}_4\text{mim}]$ -based ionic liquids due to a decrease on the cation-anion interactions by the increase of the cation alkyl side chain from ethyl to butyl.

The minor increase on the distribution ratio with the increase on temperature from 298.2 K to 313.2 K is well predicted for the system containing [C₂mim][CF₃SO₃]. However, some disagreement is observed in the ternary system with [C₂mim][CH₃SO₃] (Figures 5.8 a) and b)). Once again, a better description is obtained by COSMO-RS when dealing with more hydrophobic anions such as triflate.

Table 5.1 Root mean square deviation (RMSD) between the compositions predicted by the COSMO-RS model and the experimental data for the ternary phase diagrams studied.

Ternary system: ionic liquid + 1-hexanethiol + <i>n</i> -dodecane	RMSD %
[C ₂ mim][MeSO ₄] at 298.2 K	0.2
[C ₂ mim][CH ₃ SO ₃] at 298.2 K	0.2
[C ₂ mim][CF ₃ SO ₃] at 298.2 K	0.07
[C ₂ mim][NTf ₂] at 298.2 K	0.1
[C ₂ mim][BF ₄] at 298.2 K	0.04
[C ₄ mim][MeSO ₄] at 298.2 K	0.1
[C ₄ mim][CF ₃ SO ₃] at 298.2 K	0.1
[C ₄ mim][NTf ₂] at 298.2 K	0.2
[C ₂ mim][CH ₃ SO ₃] at 313.2 K	0.8
[C ₂ mim][CF ₃ SO ₃] at 313.2 K	0.08
[C ₂ mpy][CH ₃ SO ₃] at 298.2 K	0.5
[C ₂ mpy][NTf ₂] at 298.2 K	0.2
[C ₂ mpy][CF ₃ SO ₃] at 313.2 K	0.07

5.4. Ionic liquid screening

COSMO-RS has been widely used in the modelling and prediction of many properties of systems comprising ionic liquids and petroleum constituents, such as aromatic and aliphatic hydrocarbons⁶⁰⁻⁶², as well as nitrogen and sulfur-based compounds.^{47, 71} Taking into account the evaluation carried out in this work on the COSMO-RS capability to predict the phase behavior of systems containing ionic liquids, mercaptans and alkanes, this model was used in the screening of a vaster number of ionic liquids with the goal of identifying the best candidates for the extraction of mercaptans.

5.4.1. Tested ionic liquids

The ternary systems evaluated are composed of an ionic liquid, a mercaptan (1-hexanethiol) and a *n*-alkane (*n*-dodecane). Around 280 ionic liquids were tested by the combination of 16 cations and 19 anions available on the COSMO-RS database. The cations investigated belong to very distinctive families and are: 1-ethyl-3-methylimidazolium, 1-butyl-3-methylimidazolium, 1-hexyl-3-methylimidazolium, 1-methyl-3-octylimidazolium, 1,3-diethylimidazolium, 1,3-dibutylimidazolium, 1-ethyl-3-methylpyridinium, 1-ethyl-3-methylpyrrolidinium, N-butyl-isoquinolinium, 3-butyl-4-methylthiazolium, cholinium (ethyl(2-hydroxyethyl)dimethylammonium), guanidinium, hexamethylguanidinium, trihexyl(tetradecyl)phosphonium, O-ethyl-N,N,N,N-tetramethylisothiuronium and S-ethyl-N,N,N,N-tetramethylisothiuronium. Furthermore, the anions tested are methylsulfate, ethylsulfate, butylsulfate, octylsulfate, methylsulfonate, trifluoromethanesulfonate (triflate), perfluorobutanesulfonate, acetate, bis[(trifluoromethyl)sulfonyl]imide, hexafluorophosphate, tetrafluoroborate, dicyanamide, tricyanomethanide, tetracyanoborate, tosylate, diethylphosphate, dibutylphosphate, nitrate and tetrachloroferrate. The anions/cations chemical structures and respective abbreviations are presented in Tables A1 and A2 in Appendix A.

5.4.2. Selectivity, distribution ratio and σ -profiles

The ionic liquids screening was performed based on the predicted selectivity and distribution ratio with circa 2 mol/mol% of mercaptan present at the alkane-rich phase. Additionally, the estimated COSMO-RS energies and σ -profiles for each aliphatic compound and ionic liquid ion were also used to achieve a better understanding of the ternary systems behavior. The selectivity and the distribution ratio values were

calculated by equations 5.1 and 5.2. These values, for the different cation and anion combinations, are presented in Tables D2 and D3 and depicted in Figures D1 a) – p), D2 a) – k), D3 a) – d) and D4 a) – d) in the Appendix D. While Figure D1 shows the impact of the cation family and Figure D2 the anion nature effect, Figure D3 shows the cation alkyl chain length and the cation symmetry influence and Figure D4 the anion alkyl chain length impact, estimated by COSMO-RS on the mentioned parameters. Their simultaneous analysis with the σ -profiles of each compound and the COSMO-RS mixture energies, allows a better understanding of the interactions taking place and the most appropriate ionic liquid characteristics required for the mercaptans extraction process.

The COSMO-RS σ -profiles are represented in Figures D5 to D16 in the Appendix D. The σ -profiles represent the charge density distribution, $\rho(\sigma)$, based on the virtual σ -surface, and provide information on the molecular surface polarity. The σ axis represents the surface polarity charge and has negative values for molecule positive charges and vice-versa; when $\sigma < -0.0082 \text{ e}/\text{Å}^2$ or $> 0.0082 \text{ e}/\text{Å}^2$ there is evidence on the hydrogen-bonding ability, representing, respectively, donor and acceptor molecule regions.⁷²

The COSMO-RS σ -profiles for the kerosene model compounds, 1-hexanethiol and *n*-dodecane, are depicted in Figure D5 in the Appendix D. Both compounds show a thin and high peak, centered in the overall plot ($-0.008 < \sigma \text{ (e}/\text{Å}^2) < 0.006$ and $-0.006 < \sigma \text{ (e}/\text{Å}^2) < 0.006$, respectively), as a result of the non-polar and homogeneity of the charge density along the molecules chains. At this region, the dominant interactions are van der Waals forces. Being the 1-hexanethiol a more polar compound, it is also possible to observe two small peaks, at $\sigma = 0.007 \text{ e}/\text{Å}^2$ and $\sigma = 0.012 \text{ e}/\text{Å}^2$, due to the two electron concentration regions caused by the electronegative sulfur atom, and a third peak, at $\sigma = -0.009 \text{ e}/\text{Å}^2$, by the electron delocalization of the sulfur atom leaving the hydrogen atom partially and positively charged. Although small, these peaks indicate a slight ability to hydrogen-bond.

Based on these considerations, it is thus expectable to be able to tailor the flexible affinity of ionic liquids for mercaptans by changing their chemical structures. In fact, the cation and anion σ -profiles show more distinct type of interactions than the fuel model compounds. The σ -profiles of the ionic liquids cations and anions are presented in Figures D5 – D16 in the Appendix D. In the σ -profiles plot, the positive peaks correspond, in general, to the ionic liquid anions, and the negative to the ionic liquid cation. It is also noteworthy to mention that these strength peaks can also provide information on the cation-anion cohesion forces.

Considering the σ -profile diagram of 1-hexanethiol, the most suitable ionic liquid should present a cation with a peak close to $\sigma = -0.012 \text{ e}/\text{Å}^2$ and an anion with a peak around $\sigma = 0.009 \text{ e}/\text{Å}^2$ aiming at promoting a strong interaction with the mercaptan. However, these mercaptan peaks are small and the expected hydrogen-bonding is weak. On the other hand, the van der Waals interactions between the non-polar regions of the compounds, due to the centered high peak, and misfit electrostatic interactions caused by the ionic liquid charges, will be dominant. Nevertheless, these interactions also improve the affinity of the ionic liquids to the alkane, and consequently a decrease on the systems selectivity is further observed. Therefore, the most suitable ionic liquids should not present high peaks in the region $-0.006 < \sigma (\text{e}/\text{Å}^2) < 0.006$.

COSMO-RS split the interaction energy into three specific energies, the misfit electrostatic energy, the hydrogen-bonding energy and the van der Waals energy, being the first two energies dependent on the σ -profiles of each compound. The third energy is only dependent on the individual atoms properties. The estimated energies can be assessed in Tables D4 and D5 in the Appendix D, for the model feed 1-hexanethiol + *n*-dodecane and for the ternary systems ionic liquid + 1-hexanethiol + *n*-dodecane, respectively. Higher van der Waals energies are found in the model feed confirming that the interactions between these compounds are mainly due to dispersive forces, as expected. Comparing the COSMO-RS energies of 1-hexanethiol in the model mixture (Table D4) with its energies when ionic liquids are added (Table D5), it is possible to notice that strong van der Waals energies are also determined for the ionic liquid ions, which promote the main interactions between both compounds. A significant increase in the 1-hexanethiol misfit and hydrogen-bonding energies is also observed with all the ionic liquids studied, which demonstrates that these type of interactions also take place in the 1-hexanethiol and ionic liquid mixtures.

5.4.2.1. Predicted effect of the ionic liquid cation core

The selectivity and distribution ratio for the mercaptan are dependent on the ionic liquid cation structural differences as shown in Figures D1 a) – p), as well as in the σ -profiles plots in Figures D5 – D15, in the Appendix D.

COSMO-RS predicts the complete miscibility with the fuel model compounds, high distribution ratios and small selectivities for quaternary phosphonium-based ionic liquids ($[\text{P}_{666(14)}]^+$). Their long alkyl chains largely increase the van der Waals energies of the cation (Table D5 k)) and promote dispersive interactions with non-polar compounds. This is consistent with the $[\text{P}_{666(14)}]$ cation σ -profile (Figure D5), which shows a very high

pronounced peak in the region $-0.008 < \sigma \text{ (e/A}^2\text{)} < 0.006$, covering and overlapping both 1-hexanethiol and *n*-dodecane peaks.

For the acyclic guanidinium and isouronium cations, namely $[(\text{C}_1)_6\text{Gu}]^+$, $[\text{OC}_2(\text{C}_1)4\text{iU}]^+$ and $[\text{SC}_2(\text{C}_1)4\text{iU}]^+$, a high distribution ratio is observed. This is a result of these cations higher affinity for mercaptan. Indeed, COSMO-RS forecasts the stronger van der Waals and mild misfit energies (Tables D5 i), k) and l)) in these species. This can also be confirmed by their σ -profiles (Figure D6), which show a peak very close to the higher 1-hexanethiol peak related with its non-polar region, and also a part of the area of 1-hexanethiol is covered by those cations. The more negative peaks (cationic charges), at $\sigma = -0.006\text{e/A}^2$ for the $[(\text{C}_1)_6\text{Gu}]^+$ cation, and $\sigma = -0.007 \text{ e/A}^2$ for the $[\text{OC}_2(\text{C}_1)4\text{iU}]^+$ and $[\text{SC}_2(\text{C}_1)4\text{iU}]^+$ cations, lead to a charge delocalization allowing therefore the increase of the 1-hexanethiol partial negative charge interaction with the positive charge of the cations. The lower selectivity of these cations compared to others is also dependent on these factors that, on the other hand, improve the interaction of the ionic liquids with the linear alkane *n*-dodecane.

Comparing the guanidinium cation ($[\text{Gu}]^+$), with no alkyl groups, with the alkylated one, $[(\text{C}_1)_6\text{Gu}]^+$, the selectivity vs. distribution ratio values occur at the opposite plot region. The van der Waals energies in $[\text{Gu}]^+$ (Table D5 i)) are smaller when compared to $[(\text{C}_1)_6\text{Gu}]^+$ (Table D5 j)). In addition, the cation $[\text{Gu}]^+$ displays a much higher hydrogen bonding capacity (higher hydrogen-bonding energies and $\sigma_{\text{HB}} \ll -0.0082 \text{ e/A}^2$, Figure D7), which fortify the cohesion between the cation and the anion and reduces the interaction with mercaptan compounds while making these mixtures less miscible.

For the cholinium cation ($[\text{Ch}]^+$), although with non-insignificant van der Waals and electrostatic interactions energies, the hydrogen-bonding is a very significant interaction (Table D5 h)). The small peak at $\sigma_{\text{HB}} = -0.017 \text{ e/A}^2$ and the more pronounced peak at $\sigma_{\text{HB}} = -0.009 \text{ e/A}^2$, (Figure D7) reinforce the cation-anion forces and hinder the mercaptan interactions.

For other ringed nitrogen-based cations, the predicted values of selectivity decreases and the distribution ratio increases according to the following order: imidazolium, pyridinium, thiazolium, pyrrolidinium and quinolinium. Analyzing the COSMO-RS energies (Tables D5 a) – f)), it is observed that for these cation-based mixtures, the dominant energies are van der Waals, followed by mild misfit and hydrogen-bonding. All of these cations show similar σ -profiles (Figure D8) even for the non-aromatic pyrrolidinium cation and for the quinolinium cation with two aromatic groups. Comparing the σ -profiles for the various cations, it is possible to notice an increase of the peak area

from the imidazolium to the pyridinium, leading to a slight increase of the van der Waals interactions and to a respective increase on the distribution ratio. Indeed, this increment in the van der Waals forces in the pyridinium-based ionic liquids fully agree with the experimental data presented before regarding the ionic liquid cation influence. The increase of the distribution ratio observed on the thiazolium cation is related with the increase of the intensity of the peak corresponding to the van der Waals interactions, resulting thus in an improved interaction with the mercaptan. The higher pyrrolidinium distribution ratio, when compared with these two cations, is related with the negligible hydrogen-bonding since the van der Waals and the misfit energies show lower values. This pattern also reflects lower cation-anion interactions, liberating the cation for interacting with the mercaptan. Regarding the quinolinium cation, it shows a large peak area that covers practically the area peak of 1-hexanethiol and thus results in its higher affinity and distribution ratios. Concluding, for these cations, both tendencies, namely the increase on the distribution ratio and the decrease on selectivity, are a result of the improvement of the interactions between both the mercaptan and *n*-dodecane with the ionic liquid cations, mainly due to the improvement of the van der Waals forces.

5.4.2.2. Predicted effect of the ionic liquid anion

The anions impact on the mercaptans partition predicted by COSMO-RS, namely the selectivity vs. distribution ratio for the different ionic liquid anions is depicted in Figures D2 a) – k) in the Appendix D. The COSMO-RS energies were also determined and are presented in Tables D5 a) – l) in the Appendix D.

The anions $[\text{PF}_6]^-$ and $[\text{BF}_4]^-$ show the highest selectivity amongst the studied anions. In addition, for both anions, a very small distribution ratio is predicted. Analyzing the COSMO-RS mixture energy values, these fluorinated anions present relative small van der Waals and hydrogen-bonding energies. Therefore, there is a very low affinity of both anions for the mercaptan.

For the sulfur-based anions, the COSMO-RS predicted distribution ratios and selectivities follow the order: $[\text{CF}_3\text{SO}_3]^-$, $[\text{MeSO}_4]^-$ and $[\text{CH}_3\text{SO}_3]^-$. The van der Waals and the electrostatic energies are similar in these sulfurous-based systems. In addition, all the anions display relatively low hydrogen-bonding energies. However, the highest hydrogen-bonding energy was observed for the anion $[\text{CH}_3\text{SO}_3]^-$, leading to a COSMO-RS prediction of a high distribution ratio and low selectivity with this anion. The σ -profiles of the sulfurous-based anions are shown in Figure D10 in the Appendix D. The $[\text{MeSO}_4]^-$ and the $[\text{CH}_3\text{SO}_3]^-$ anions present small peaks in the negative region and inside the 1-

hexanethiol peak area, which further indicate weak van der Waals interactions. The $[\text{CH}_3\text{SO}_3]^-$ also presents a peak at $-0.007 \text{ e}/\text{Å}^2$, that suits the 1-hexanethiol peak at $0.007 \text{ e}/\text{Å}^2$, and may be responsible for the high affinity between this anion and 1-hexanethiol. The $[\text{CF}_3\text{SO}_3]^-$ shows a first peak at $0.003 \text{ e}/\text{Å}^2$ that covers part of the 1-hexanethiol peak, and a second peak very close to the one of the $[\text{CH}_3\text{SO}_3]^-$, at $0.014 \text{ e}/\text{Å}^2$, due to their structural similarity. For $[(\text{PFBu})\text{SO}_3]^-$, the same peak at $0.014 \text{ e}/\text{Å}^2$ is found due to the $-\text{SO}_3$ group, and a higher peak is also observed at $0.001 \text{ e}/\text{Å}^2$ covering a great part of the 1-hexanethiol peak and explaining their predicted higher distribution ratios and selectivity.

The $[\text{CH}_3\text{CO}_2]^-$ anion leads to a high distribution ratio and to a low selectivity for the mercaptan. This anion displays a slightly higher misfit energy when compared to van der Waals forces. In addition, significant hydrogen-bonding energies are found that are correlated with its positive peak at $0.020 \text{ e}/\text{Å}^2$ (Figure D11 in the Appendix D).

Regarding the systems based on cyano-based anions ($[\text{N}(\text{CN})_2]^-$, $[\text{C}(\text{CN})_3]^-$ and $[\text{B}(\text{CN})_4]^-$), their predicted distribution ratio and selectivity are not satisfactory for all the ionic liquid cations tested. Figure D12, in Appendix D, presents their σ -profiles where it is shown that these anions have peaks inside the 1-hexanethiol and the *n*-dodecane, at $0.004 \text{ e}/\text{Å}^2$, $0.002 \text{ e}/\text{Å}^2$, and $0.001 \text{ e}/\text{Å}^2$, respectively.

For the systems studied, the anions that show a higher distribution ratio and a lower selectivity for 1-hexanethiol are: $[\text{NTf}_2]^-$, $[\text{TOS}]^-$, $[\text{DEP}]^-$, $[\text{DBP}]^-$ and $[\text{FeCl}_4]^-$. Regarding the COSMO-RS results, these anions present higher van der Waals and misfit energies when compared to smaller hydrogen-bonding energies. All these factors provide the required dispersive forces to interact with both the alkane and the mercaptan. From their σ -profiles (in Figure D13 in the Appendix D), it can be seen that most of these anions contain peaks inside the range $-0.006 < \sigma \text{ (e}/\text{Å}^2) < 0.006$, and with a large area covering part of the 1-hexanethiol and *n*-dodecane peaks. Nevertheless, additional care must be taken when combining such anions with different cations. Exceptions on their performance appear for the anions $[\text{TOS}]^-$, $[\text{DEP}]^-$ and $[\text{DBP}]^-$ if combined with the more polar cations, such as $[\text{Gu}]^+$ and $[\text{Ch}]^+$.

5.4.2.3. Predicted effect of the alkyl side chain length and symmetry

The influence of the alkyl chain length on the systems selectivity and distribution ratio can be observed in Figures D3 a) – d) and D4 a) – d) in the Appendix D for the imidazolium cation ($[\text{C}_n\text{mim}]^+$, with $n = 2, 4, 6$ and 8), and for the anions of the type $[\text{RSO}_4]^+$, with R = methyl (Me), ethyl (Et), butyl (Bu) and octyl (Oc), respectively. In both

situations an increase in the alkyl chain length leads to an increase on the distribution ratio and to a decrease on the selectivity values. This pattern is a result of the enlargement of their non-polar region, increasing, therefore, their van der Waals interactions with the mercaptan.

The cation symmetry impact was evaluated for the dialkylimidazolium cation, $[C_nC_n\text{im}]^+$, with $n = 2$ and 4, and is also shown in Figure D3. The COSMO-RS predicts a slight increase in the distribution ratio and a decrease in the selectivity, compared to the asymmetric $[C_2\text{mim}]^+$ and $[C_4\text{mim}]^+$, respectively. Moreover, the symmetry effect is positively influenced by the cation alkyl chain size. The existence of two alkyl side chains duplicates the non-polar surface available for van der Waals interactions.

The σ -profiles presented in Figures D14 to D16 in the Appendix D also corroborate the trends observed.

5.4.3. Potential ionic liquids candidates

From the screening approach used here, the ionic liquids that could provide the best performance, based on their liquid-liquid equilibrium, comprise ions that are able to interact either by van der Waals interactions or with the $-\text{SH}$ group. Nevertheless, some of the ionic liquid features that allow improved mercaptan-ionic-liquid interactions also lead to a higher affinity for the remaining feed compounds. Therefore, a balance between the distribution ratio and selectivity must exist. Considering the σ -profiles, an important aspect is that the ionic liquid ions should present some enveloping of the mercaptan peak indicative of their favorable interaction; yet, this should not be in excess to avoid the interactions with n -dodecane. The cation should present a peak close to $\sigma = -0.012 \text{ e}/\text{Å}^2$ and the anion close to $\sigma = 0.009 \text{ e}/\text{Å}^2$. Having these features in mind, the best ionic liquid candidates are those composed of imidazolium, pyridinium and pyrrolidinium cations, with short alkyl side chains, combined with the anions $[\text{TOS}]^-$, $[\text{DEP}]^-$, $[\text{EtSO}_4]^-$ and $[\text{CF}_3\text{SO}_3]^-$. Some of them are already studied on this work.

Comparison between the selection of ionic liquids for aliphatic or for aromatic sulfur compounds removal from fuels

In the last years, many research works have been reported addressing the fuels desulfurization assisted by ionic liquids, aiming at finding the best ionic liquid able to perform an efficient extraction of the sulfur contaminants. These works mainly addressed the study of aromatic compounds such as thiophene, benzothiophene and dibenzothiophene.^{4, 73} Their interactions with the ionic liquids are quite distinct from the van der Waals forces observed with the aliphatic sulfur compounds, and consist of hydrogen bonds, CH- π bonds, and π - π interactions.^{48, 74} These favorable interactions promote a greater affinity and solubility on the ionic liquids than the observed for the aliphatic sulfur compounds.

Although many ionic liquids achieve an excellent extraction capacity and distribution ratios, either for aliphatic or aromatic sulfur compounds, these ionic liquids are also capable of co-extracting the fuel constituents, corresponding to lower selectivities. Therefore, as presented before and stated elsewhere,^{48, 62, 75-78} some structural features, that provide favorable interactions with the fuel hydrocarbons of the ionic liquid, should be avoided, such as the long cation alkyl side chains or anions with low polarity. By this fact, many authors, recognized the importance of the selectivity and the need of a balance between the selectivity and distribution ratio for this type of systems, in order to avoid the cross contamination of the fuel.^{17, 25, 48, 52, 75, 79-82} They chose to apply ionic liquids based on cations with small alkyl side chains, in order to promote higher selectivities, mainly from the imidazolium and pyridinium cation families. Regarding the anions, a greater diversity was tested and no defined pattern was identified. Various anions were mentioned as more suitable: $[\text{N}(\text{CN})_2]^-$,^{25, 51} $[\text{C}(\text{CN})_3]^-$,²⁰ $[\text{B}(\text{CN})_4]^-$,⁴⁸ $[\text{BF}_4]^-$,⁴⁸ $[\text{PF}_6]^-$,⁴⁷⁻⁴⁸ $[\text{CF}_3\text{SO}_3]^-$,⁴⁷⁻⁴⁸ $[\text{NTf}_2]^-$,^{17, 47} $[\text{CH}_3\text{CO}_2]^-$,⁴⁷ $[\text{SCN}]^-$ (thiocyanate),^{47, 82} $[\text{EtSO}_4]^-$,⁵² $[\text{DEP}]^-$,⁸³ among others.

Taking into account the ionic liquids' cations and anions here selected, along with the findings in this work, similarities are observed between the chosen ionic liquid features. Moreover, the feasibility of the ionic liquid based desulfurization processes for the integrated aliphatic and aromatics sulfur compounds extraction is further supported by the negligible mutual solubility between the ionic liquid and the fuel main constituents. Even so, the distribution ratios determined for both aliphatic and organic sulfur species^{14, 39, 82-83} are, in many cases, low and unfavorable, which implies large volumes of ionic liquid for an efficient liquid-liquid extraction process. Nonetheless, since ionic liquids have negligible volatility and are chemically stable, their regeneration can be easily performed in an additional step through different techniques, as distillation, adsorption or

back-extraction processes.⁴ This allows its reuse in the extraction process leading to a more economic and sustainable separation process for the sulfur species removal.⁴

5.5. Conclusions

This work aimed at studying ionic liquids as potential extracting solvents for the removal of mercaptans from kerosene streams to fulfil the urgent need on lowering the sulfur content in industrial units. As a first approach, the experimental liquid-liquid equilibrium for the ternary systems composed of 1-hexanethiol + *n*-dodecane + ionic liquids was determined at 298.2 K and 313.2 K. Both imidazolium and pyridinium-based ionic liquids were investigated. Albeit the values of the distribution ratio for the tested systems are always lower than unit, these systems display a negligible mutual solubility between the ionic liquids and *n*-dodecane avoiding the solvent losses and the contamination of the hydrocarbon-rich phase.

Due to the innumerable possibilities of cation/anion combinations in ionic liquids, the COSMO-RS was evaluated in the predictive description of the experimental data. The root mean square deviations between the predicted and the experimental data are lower than 1% and prove the COSMO-RS ability to describe the phase behavior of systems involving ionic liquids, sulfur compounds and hydrocarbons. Based on this good performance, a large number of ionic liquid cations and anions was further investigated with COSMO-RS. For the separation of 1-hexanethiol from hydrocarbon mixtures, the recommended ionic liquids comprise short-alkyl chain imidazolium, pyridinium and pyrrolidinium cations, combined with the [TOS]⁻, [DEP]⁻, [EtSO₄]⁻ and [CF₃SO₃]⁻ anions.

5.6. References

1. Song, C., An overview of new approaches to deep desulfurization for ultra-clean gasoline, diesel fuel and jet fuel. *Catal Today* **2003**, *86* (1–4), 211-263.
2. Srivastava, V. C., An evaluation of desulfurization technologies for sulfur removal from liquid fuels. *Rsc Adv* **2012**, *2* (3), 759-783.
3. Francisco, M.; Arce, A.; Soto, A., Ionic liquids on desulfurization of fuel oils. *Fluid Phase Equilib* **2010**, *294* (1-2), 39-48.
4. Kulkarni, P. S.; Afonso, C. A. M., Deep desulfurization of diesel fuel using ionic liquids: current status and future challenges. *Green Chem* **2010**, *12* (7), 1139-1149.
5. Wang, W.; Wang, S.; Liu, H.; Wang, Z., Desulfurization of gasoline by a new method of electrochemical catalytic oxidation. *Fuel* **2007**, *86* (17–18), 2747-2753.
6. Seredych, M.; Wu, C. T.; Brender, P.; Ania, C. O.; Vix-Guterl, C.; Bandosz, T. J., Role of phosphorus in carbon matrix in desulfurization of diesel fuel using adsorption process. *Fuel* **2012**, *92* (1), 318-326.
7. Mochizuki, Y.; Sugawara, K., Selective adsorption of organic sulfur in coal extract by using metal-loaded carbon. *Fuel* **2011**, *90* (10), 2974-2980.
8. Werner, S.; Haumann, M.; Wasserscheid, P., Ionic Liquids in Chemical Engineering. *Annu Rev Chem Biomol* **2010**, *1*, 203-230.
9. Liang, W. D.; Zhang, S.; Li, H. F.; Zhang, G. D., Oxidative desulfurization of simulated gasoline catalyzed by acetic acid-based ionic liquids at room temperature. *Fuel Process Technol* **2013**, *109*, 27-31.
10. Wang, J. L.; Zhao, D. S.; Li, K. X., Extractive Desulfurization of Gasoline Using Ionic Liquid Based on CuCl. *Pet Sci Technol* **2012**, *30* (23), 2417-2423.
11. Li, F. T.; Liu, Y.; Sun, Z. M.; Chen, L. J.; Zhao, D. S.; Liu, R. H.; Kou, C. G., Deep Extractive Desulfurization of Gasoline with xEt(3)NHCl center dot FeCl3 Ionic Liquids. *Energ Fuel* **2010**, *24*, 4285-4289.
12. Alonso, L.; Arce, A.; Francisco, M.; Rodriguez, O.; Soto, A., Gasoline desulfurization using extraction with [C-8 mim][BF4] ionic liquid. *Aiche J* **2007**, *53* (12), 3108-3115.
13. Huang, C. P.; Chen, B. H.; Zhang, J.; Liu, Z. C.; Li, Y. X., Desulfurization of gasoline by extraction with new ionic liquids. *Energ Fuel* **2004**, *18* (6), 1862-1864.

14. Kuhlmann, E.; Haumann, M.; Jess, A.; Seeberger, A.; Wasserscheid, P., Ionic Liquids in Refinery Desulfurization: Comparison between Biphasic and Supported Ionic Liquid Phase Suspension Processes. *Chemsuschem* **2009**, 2 (10), 969-977.
15. Taha, M. F.; Atikah, N.; Chong, F. K.; Shaharun, M. S., Oxidative Desulfurization of Dibenzothiophene From Model Oil Using Ionic Liquids As Extracting Agent. *Aip Conf Proc* **2012**, 1482, 258-262.
16. de Oliveira, L. H.; Alvarez, V. H.; Aznar, M., Liquid-Liquid Equilibrium in N-Methyl-2-hydroxyethylammonium Acetate, Butanoate, or Hexanoate Ionic Liquids plus Dibenzothiophene plus n-Dodecane Systems at 298.2 K and Atmospheric Pressure. *J Chem Eng Data* **2012**, 57 (3), 744-750.
17. Rodríguez-Cabo, B.; Arce, A.; Soto, A., Desulfurization of fuels by liquid-liquid extraction with 1-ethyl-3-methylimidazolium ionic liquids. *Fluid Phase Equilib* **2013**, 356 (0), 126-135.
18. Krolikowski, M.; Walczak, K.; Domanska, U., Solvent extraction of aromatic sulfur compounds from n-heptane using the 1-ethyl-3-methylimidazolium tricyanomethanide ionic liquid. *J Chem Thermodyn* **2013**, 65, 168-173.
19. Gabric, B.; Sander, A.; Bubalo, M. C.; Macut, D., Extraction of S- and N-Compounds from the Mixture of Hydrocarbons by Ionic Liquids as Selective Solvents. *Sci World J* **2013**.
20. Domańska, U.; Lukoshko, E. V.; Królikowski, M., Separation of thiophene from heptane with ionic liquids. *J Chem Therm* **2013**, 61 (0), 126-131.
21. Dharaskar, S. A.; Wasewar, K. L.; Varma, M. N.; Shende, D. Z.; Yoo, C. K., Deep Removal of Sulfur from Model Liquid Fuels using 1-Butyl-3-Methylimidazolium Chloride. *Procedia Engineering* **2013**, 51 (0), 416-422.
22. Wilfred, C. D.; Kiat, C. F.; Man, Z.; Bustam, M. A.; Mutalib, M. I. M.; Phak, C. Z., Extraction of dibenzothiophene from dodecane using ionic liquids. *Fuel Process Technol* **2012**, 93 (1), 85-89.
23. Kedra-Krolik, K.; Mutelet, F.; Moise, J. C.; Jaubert, J. N., Deep Fuels Desulfurization and Denitrogenation Using 1-Butyl-3-methylimidazolium Trifluoromethanesulfonate. *Energ Fuel* **2011**, 25 (4), 1559-1565.
24. Wang, Y.; Li, H.; Zhu, W.; Jiang, X.; He, L.; Lu, J.; Yan, Y., The Extractive Desulfurization of Fuels Using Ionic Liquids Based on FeCl₃. *Pet Sci Technol* **2010**, 28 (12), 1203-1210.

25. Yu, G. R.; Li, X.; Liu, X. X.; Asumana, C.; Chen, X. C., Deep Desulfurization of Fuel Oils Using Low-Viscosity 1-Ethyl-3-methylimidazolium Dicyanamide Ionic Liquid. *Ind Eng Chem Res* **2011**, *50* (4), 2236-2244.
26. Zhu, W.; Xu, D.; Li, H.; Ding, Y.; Zhang, M.; Liu, H.; Chao, Y., Oxidative Desulfurization of Dibenzothiophene Catalyzed by VO(acac)₂ in Ionic Liquids at Room Temperature. *Pet Sci Technol* **2013**, *31* (14), 1447-1453.
27. Zhu, W.; Wu, P.; Yang, L.; Chang, Y.; Chao, Y.; Li, H.; Jiang, Y.; Jiang, W.; Xun, S., Pyridinium-based temperature-responsive magnetic ionic liquid for oxidative desulfurization of fuels. *Chem Eng J* **2013**, *229* (0), 250-256.
28. Zhang, M.; Zhu, W.; Xun, S.; Li, H.; Gu, Q.; Zhao, Z.; Wang, Q., Deep oxidative desulfurization of dibenzothiophene with POM-based hybrid materials in ionic liquids. *Chem Eng J* **2013**, *220* (0), 328-336.
29. Ma, C. H.; Dai, B.; Xu, C. X.; Liu, P.; Qi, L. L.; Ban, L. L., Deep oxidative desulfurization of model fuel via dielectric barrier discharge plasma oxidation using MnO₂ catalysts and combination of ionic liquid extraction. *Catal Today* **2013**, *211*, 84-89.
30. Zhao, P. P.; Zhang, M. J.; Wu, Y. J.; Wang, J., Heterogeneous Selective Oxidation of Sulfides with H₂O₂ Catalyzed by Ionic Liquid-Based Polyoxometalate Salts. *Ind Eng Chem Res* **2012**, *51* (19), 6641-6647.
31. Li, Z.; Li, C. P.; Chi, Y. S.; Wang, A. L.; Zhang, Z. D.; Li, H. X.; Liu, Q. S.; Welz-Biermann, U., Extraction Process of Dibenzothiophene with New Distillable Amine-Based Protic Ionic Liquids. *Energ Fuel* **2012**, *26* (6), 3723-3727.
32. Zhang, C.; Pan, X. Y.; Wang, F.; Liu, X. Q., Extraction-oxidation desulfurization by pyridinium-based task-specific ionic liquids. *Fuel* **2012**, *102*, 580-584.
33. Rodríguez-Cabo, B.; Rodríguez, H.; Rodil, E.; Arce, A.; Soto, A., Extractive and oxidative-extractive desulfurization of fuels with ionic liquids. *Fuel* **2014**, *117*, Part A (0), 882-889.
34. Nie, Y.; Dong, Y.; Bai, L.; Dong, H.; Zhang, X., Fast oxidative desulfurization of fuel oil using dialkylpyridinium tetrachloroferrates ionic liquids. *Fuel* **2013**, *103* (0), 997-1002.
35. Lu, L.; Cheng, S. F.; Gao, J. B.; Gao, G. H.; He, M. Y., Deep oxidative desulfurization of fuels catalyzed by ionic liquid in the presence of H₂O₂. *Energ Fuel* **2007**, *21* (1), 383-384.

36. Yahaya, G. O.; Hamad, F.; Bahamdan, A.; Tammana, V. V. R.; Hamad, E. Z., Supported ionic liquid membrane and liquid-liquid extraction using membrane for removal of sulfur compounds from diesel/crude oil. *Fuel Process Technol* **2013**, *113*, 123-129.
37. Lin, Y.; Wang, F.; Zhang, Z.; Yang, J.; Wei, Y., Polymer-supported ionic liquids: Synthesis, characterization and application in fuel desulfurization. *Fuel* **2014**, *116* (0), 273-280.
38. Wang, F.; Zhang, Z.; Yang, J.; Wang, L.; Lin, Y.; Wei, Y., Immobilization of room temperature ionic liquid (RTIL) on silica gel for adsorption removal of thiophenic sulfur compounds from fuel. *Fuel* **2013**, *107* (0), 394-399.
39. Kohler, F.; Roth, D.; Kuhlmann, E.; Wasserscheid, P.; Haumann, M., Continuous gas-phase desulfurisation using supported ionic liquid phase (SILP) materials. *Green Chem* **2010**, *12* (6), 979-984.
40. Martínez-Magadán, J.-M.; Oviedo-Roa, R.; García, P.; Martínez-Palou, R., DFT study of the interaction between ethanethiol and Fe-containing ionic liquids for desulfuration of natural gasoline. *Fuel Process Technol* **2012**, *97* (0), 24-29.
41. Klamt, A.; Eckert, F., COSMO-RS: a novel and efficient method for the a priori prediction of thermophysical data of liquids. *Fluid Phase Equilib* **2000**, *172* (1), 43-72.
42. Klamt, A., Summary, limitations, and perspectives. In *COSMO-RS*, Elsevier: Amsterdam, 2005; pp 205-207.
43. Diedenhofen, M.; Klamt, A., COSMO-RS as a tool for property prediction of IL mixtures--A review. *Fluid Phase Equilib* **2010**, *294* (1-2), 31-38.
44. Vega, E.; Lemus, J.; Anfruns, A.; Gonzalez-Olmos, R.; Palomar, J.; Martin, M. J., Adsorption of volatile sulphur compounds onto modified activated carbons: Effect of oxygen functional groups. *J Hazard Mater* **2013**, *258*, 77-83.
45. Shah, M. R.; Anantharaj, R.; Banerjee, T.; Yadav, G. D., Quaternary (liquid plus liquid) equilibria for systems of imidazolium based ionic liquid plus thiophene plus pyridine plus cyclohexane at 298.15 K: Experiments and quantum chemical predictions. *J Chem Thermodyn* **2013**, *62*, 142-150.
46. Anantharaj, R.; Banerjee, T., Fast Solvent Screening for the Simultaneous Hydrodesulfurization and Hydrodenitrification of Diesel Oil Using Ionic Liquids. *J Chem Eng Data* **2011**, *56* (6), 2770-2785.

47. Anantharaj, R.; Banerjee, T., COSMO-RS based predictions for the desulphurization of diesel oil using ionic liquids: Effect of cation and anion combination. *Fuel Process Technol* **2011**, *92* (1), 39-52.
48. Kumar, A. A. P.; Banerjee, T., Thiophene separation with ionic liquids for desulphurization: A quantum chemical approach. *Fluid Phase Equilib*. **2009**, *278* (1-2), 1-8.
49. Anantharaj, R.; Banerjee, T., Liquid-liquid equilibria for quaternary systems of imidazolium based ionic liquid plus thiophene plus pyridine plus iso-octane at 298.15K: Experiments and quantum chemical predictions. *Fluid Phase Equilib* **2011**, *312*, 20-30.
50. Anantharaj, R.; Banerjee, T., Evaluation and comparison of global scalar properties for the simultaneous interaction of ionic liquids with thiophene and pyridine. *Fluid Phase Equilib* **2010**, *293* (1), 22-31.
51. Wilfred, C. D.; Man, Z.; Chan, Z. P., Predicting methods for sulfur removal from model oils using COSMO-RS and partition coefficient. *Chem Eng Sci* **2013**, *102*, 373-377.
52. Varma, N. R.; Ramalingam, A.; Banerjee, T., Experiments, correlations and COSMO-RS predictions for the extraction of benzothiophene from n-hexane using imidazolium-based ionic liquids. *Chem Eng J* **2011**, *166* (1), 30-39.
53. Anantharaj, R.; Banerjee, T., Thermodynamic properties of 1-ethyl-3-methylimidazolium methanesulphonate with aromatic sulphur, nitrogen compounds at T = 298.15-323.15 K and P = 1 bar. *Can J Chem Eng* **2013**, *91* (2), 245-256.
54. Anantharaj, R.; Banerjee, T., Aromatic Sulfur-Nitrogen Extraction using Ionic Liquids: Experiments and Predictions using an a priori Model. *Aiche J* **2013**, *59* (12), 4806-4815.
55. Anantharaj, R.; Banerjee, T., Quantum Chemical Studies on the Simultaneous Interaction of Thiophene and Pyridine with Ionic Liquid. *Aiche J* **2011**, *57* (3), 749-764.
56. Palomar, J.; Torrecilla, J. S.; Ferro, V. R.; Rodríguez, F., Development of an a priori ionic liquid design tool. 2. ionic liquid selection through the prediction of COSMO-RS molecular descriptor by inverse neural network. *Ind Eng Chem Res* **2009**, *48* (4), 2257-2265.
57. Freire, M. G.; Ventura, S. P. M.; Santos, L. M. N. B. F.; Marrucho, I. M.; Coutinho, J. A. P., Evaluation of COSMO-RS for the prediction of LLE and VLE of water and ionic liquids binary systems. *Fluid Phase Equilib* **2008**, *268* (1-2), 74-84.

58. Freire, M. G.; Santos, L. M. N. B. F.; Marrucho, I. M.; Coutinho, J. A. P., Evaluation of COSMO-RS for the prediction of LLE and VLE of alcohols + ionic liquids. *Fluid Phase Equilib* **2007**, *255* (2), 167-178.
59. Freire, M. G.; Carvalho, P. J.; Santos, L. M. N. B. F.; Gomes, L. R.; Marrucho, I. M.; Coutinho, J. A. P., Solubility of water in fluorocarbons: Experimental and COSMO-RS prediction results. *J Chem Therm* **2010**, *42* (2), 213-219.
60. Banerjee, T.; Singh, M. K.; Khanna, A., Prediction of binary VLE for imidazolium based ionic liquid systems using COSMO-RS. *Ind Eng Chem Res* **2006**, *45* (9), 3207-3219.
61. Banerjee, T.; Sahoo, R. K.; Rath, S. S.; Kumar, R.; Khanna, A., Multicomponent liquid-liquid equilibria prediction for aromatic extraction systems using COSMO-RS. *Ind Eng Chem Res* **2007**, *46* (4), 1292-1304.
62. Ferreira, A. R.; Freire, M. G.; Ribeiro, J. C.; Lopes, F. M.; Crespo, J. G.; Coutinho, J. A. P., Overview of the Liquid-Liquid Equilibria of Ternary Systems Composed of Ionic Liquid and Aromatic and Aliphatic Hydrocarbons, and Their Modeling by COSMO-RS. *Ind Eng Chem Res* **2012**, *51* (8), 3483-3507.
63. ASTM D3227 - Standard Test Method for (Thiol Mercaptan) Sulfur in Gasoline, Kerosine, Aviation Turbine, and Distillate Fuels (Potentiometric Method). ASTM International: 2013; Vol. ASTM D3227.
64. Sørensen, J. M.; Arlt, W., *Liquid-liquid equilibrium data collection. Ternary systems*. DECHEMA: Frankfurt, 1980; Vol. V, part 2.
65. Fernandes, A. M.; Rocha, M. A. A.; Freire, M. G.; Marrucho, I. M.; Coutinho, J. A. P.; Santos, L. s. M. N. B. F., Evaluation of Cation-Anion Interaction Strength in Ionic Liquids. *J Phys Chem B* **2011**, *115* (14), 4033-4041.
66. Bini, R.; Bortolini, O.; Chiappe, C.; Pieraccini, D.; Siciliano, T., Development of Cation/Anion "Interaction" Scales for Ionic Liquids through ESI-MS Measurements. *J Phys Chem B* **2006**, *111* (3), 598-604.
67. Lungwitz, R.; Strehmel, V.; Spange, S., The dipolarity/polarisability of 1-alkyl-3-methylimidazolium ionic liquids as function of anion structure and the alkyl chain length. *New J Chem* **2010**, *34* (6), 1135-1140.
68. Freire, M. G.; Carvalho, P. J.; Fernandes, A. M.; Marrucho, I. M.; Queimada, A. J.; Coutinho, J. A. P., Surface tensions of imidazolium based ionic liquids: Anion, cation, temperature and water effect. *J Colloid Interf Sci* **2007**, *314* (2), 621-630.

69. Bhattacharjee, A.; Varanda, C.; Freire, M. G.; Matted, S.; Santos, L. M. N. B. F.; Marrucho, I. M.; Coutinho, J. A. P., Density and Viscosity Data for Binary Mixtures of 1-Alkyl-3-methylimidazolium Alkylsulfates + Water. *J Chem Eng Data* **2012**, *57* (12), 3473-3482.
70. Carvalho, P. J.; Regueira, T.; Santos, L. M. N. B. F.; Fernandez, J.; Coutinho, J. o. A. P., Effect of Water on the Viscosities and Densities of 1-Butyl-3-methylimidazolium Dicyanamide and 1-Butyl-3-methylimidazolium Tricyanomethane at Atmospheric Pressure†. *J Chem Eng Data* **2009**, *55* (2), 645-652.
71. Anantharaj, R.; Banerjee, T., COSMO-RS-based screening of ionic liquids as green solvents in denitrification studies. *Ind Eng Chem Res* **2010**, *49* (18), 8705-8725.
72. Klamt, A., *COSMO-RS from quantum chemistry to fluid phase thermodynamics and drug design* Elsevier Amsterdam 2005.
73. Hansmeier, A. R.; Meindersma, G. W.; de Haan, A. B., Desulfurization and denitrogenation of gasoline and diesel fuels by means of ionic liquids. *Green Chem* **2011**, *13* (7), 1907-1913.
74. Lu, R. Q.; Lin, J.; Qu, Z. Q., Theoretical study on interactions between ionic liquids and organosulfur compounds. *Comput Theor Chem* **2012**, *1002*, 49-58.
75. Rodriguez, H.; Francisco, M.; Soto, A.; Arce, A., Liquid-liquid equilibrium and interfacial tension of the ternary system heptane plus thiophene+1-ethyl-3-methylimidazolium bis(trifluoromethanesulfonyl)imide. *Fluid Phase Equilib* **2010**, *298* (2), 240-245.
76. Alonso, L.; Arce, A.; Francisco, M.; Soto, A., Phase behaviour of 1-methyl-3-octylimidazolium bis[trifluoromethylsulfonyl]imide with thiophene and aliphatic hydrocarbons: The influence of n-alkane chain length. *Fluid Phase Equilib* **2008**, *263* (2), 176-181.
77. Alonso, L.; Arce, A.; Francisco, M.; Soto, A., Liquid-liquid equilibria for [C(8)mim][NTf(2)]+thiophene+2,2,4-trimethylpentane or plus toluene. *J Chem Eng Data* **2008**, *53* (8), 1750-1755.
78. Alonso, L.; Arce, A.; Francisco, M.; Soto, A., Solvent extraction of thiophene from n-alkanes (C7, C12, and C16) using the ionic liquid [C8mim][BF4]. *J Chem Therm* **2008**, *40* (6), 966-972.

79. Alonso, L.; Arce, A.; Francisco, M.; Soto, A., Thiophene separation from aliphatic hydrocarbons using the 1-ethyl-3-methylimidazolium ethylsulfate ionic liquid. *Fluid Phase Equilib* **2008**, *270* (1-2), 97-102.
80. de Oliveira, L. H.; Aznar, M., Phase Equilibria in Ionic Liquids plus Dibenzothiophene plus n-Dodecane Systems. *Ind Eng Chem Res* **2011**, *50* (4), 2289-2295.
81. Cheruku, S. K.; Banerjee, T., Liquid-Liquid Equilibrium Data for 1-Ethyl-3-methylimidazolium Acetate-Thiophene-Diesel Compound: Experiments and Correlations. *J Solution Chem* **2012**, *41* (5), 898-913.
82. Holbrey, J. D.; Lopez-Martin, I.; Rothenberg, G.; Seddon, K. R.; Silvero, G.; Zheng, X., Desulfurisation of oils using ionic liquids: selection of cationic and anionic components to enhance extraction efficiency. *Green Chem* **2008**, *10* (1), 87-92.
83. Jiang, X. C.; Nie, Y.; Li, C. X.; Wang, Z., Imidazolium-based alkylphosphate ionic liquids - A potential solvent for extractive desulfurization of fuel. *Fuel* **2008**, *87* (1), 79-84.

Chapter 6

Removal of Mercaptans from “Jet-Fuel” Streams assisted by Ionic Liquid Membrane Extraction

Ferreira, A. R.; Neves, L. A.; Ribeiro, J. C.; Lopes, F. M.; Coutinho, J. A. P.;
Coelhoso, I. M.; Crespo, J. G.

Published at *Chemical Engineering Journal*

DOI: 10.1016/j.cej.2014.06.107

6.1. Introduction

Among the several proposals^{1,2, 4-13} from other research groups for the upgrading of the desulfurization technology, liquid-liquid extraction appears to be an attractive alternative related with the moderate operating conditions (low temperature and pressure) and low energy cost.¹⁻¹¹ Regarding the extracting solvents, ionic liquids have shown a great potential on substituting the conventional volatile organic solvents used^{1,2, 12-21} due to their negligible volatility, liquid state at a wide temperature, including room temperature, high thermal and chemical stabilities, among others.²² Moreover, being composed by bulky and asymmetric organic cations and organic or inorganic anions, their endless possible combinations rise as another key characteristic, the ability of tailoring their physical, chemical and solvation properties, towards a specific application.

Taking the latest into account, our previous work²³ presented an intensive ionic liquid screening aiming to understand and select the most suitable ionic liquid as extracting solvent for the removal of mercaptans from kerosene, by experimental and COSMO-RS predictions of liquid-liquid equilibrium, selectivity and distribution ratio. Based in the ternary system model considered of ionic liquid, 1-hexanethiol and *n*-dodecane, it was found that these systems present a very high selectivity towards the target mercaptan compound, due to the almost negligible mutual solubility of the ionic liquid and the *n*-alkane studied. This is a remarkable feature since mutual contamination and losses of fuel and ionic liquid can be avoided in the separation process. Nevertheless, the mercaptan distribution ratios observed towards the ionic liquids tested were lower than unit, imposing extremely large volumes of ionic liquid in the liquid-liquid extraction process in order to attain the desired separation.

Yet, it is important to reiterate that, in spite of the unfavorable aspect referred, the difference between the mercaptan and alkane solubilities in the ionic liquid still qualifies the use of ionic liquids as a solvent in separation processes regulated by mass transfer kinetics, or by combining it with an efficient regeneration process.

For this purpose, membrane assisted extraction using supported ionic liquid membranes (SILMs) is considered a potential separation process, as suggested by several works that used an immobilized ionic liquid phase either for gas separation,²⁴⁻²⁶ or liquid-liquid extraction²⁷⁻³⁰. SILMs result from the immobilization of a selected ionic liquid, which acts as the selective medium, on a polymeric or ceramic porous support, responsible for the mechanical resistance of the membrane. By using an ionic liquid supported in a porous membrane, it is possible to provide a short diffusion path for the transport of the target mercaptan solute from the jet-fuel feed phase to a receiving compartment. Other

advantages are the solvent volume required, much lower than in a conventional liquid-liquid extraction and, additionally, the low mass transfer resistance when compared with solid membranes.³¹⁻³⁹

In this work, making use of the non-volatility of ionic liquids, the mercaptan transport is driven by a chemical potential gradient across the SILM, by reducing the target solute concentration in the receiving compartment, where a reduced vacuum pressure is applied. The mercaptan permeates selectively across the liquid membrane from the liquid feed phase to the vapor phase in the permeate side. This approach assures a simultaneous extraction and stripping in one single stage, avoiding the equilibrium restrictions previously identified in these systems.

The stability and lifetime performance of the SILMs have an important impact on their industrial potential use.⁴⁰ Due to their negligible volatility and very low affinity for the feed phase mixture, the use of ionic liquids reduces drastically the deterioration of SILMs in comparison with conventional supported liquid membranes where the evaporation or dissolution of solvent into the contiguous phases may occur. Still, the integrity of the prepared SILMs should be tested under pressure differences identical to the ones employed during the extraction/stripping process, in order to assure that the ionic liquid is not displaced from the porous support.

Taking into account all previous considerations, the work here developed started with the study of the diffusion and mass transfer of the target mercaptan compound from the *n*-dodecane jet-fuel model feed to the ionic liquid phase, by performing liquid-liquid extraction experiments. As referred before, mercaptan species show low solubility in the ionic liquids, limiting the extraction capacity of the ionic liquid, which turns more relevant the selection of the most promising ionic liquids based on their transport characteristics. Nonetheless, the concern with a possible co-extraction of valuable fuel constituents requires the use of ionic liquids based on imidazolium cations, with small alkyl side chains, to guarantee the lowest mutual solubility with the aliphatic hydrocarbon.⁴¹

Since the application of SILMs depends from the membrane stability and selectivity behaviors, the previous ionic liquids were also tested with different support materials in order to find the SILM that fulfills the necessary requisites.

6.2. Mass transfer model

The liquid-liquid extraction experiments were performed using an adapted Lewis cell which allows the two phases contacting with a well-defined interface. These experiments consist in registering the solute concentration along time, which provides information about the 1-hexanethiol transport from the feed phase (rich in *n*-dodecane) to the ionic liquid phase.

During these experiments, it was assumed that at the interface, an equilibrium state is established. Therefore, a mass balance over the feed phase leads to the mass transfer of the 1-hexanethiol compound between the *n*-dodecane feed phase and the ionic liquid phase, described by the equation 6.1:

$$-V_f \frac{d(C_f)}{dt} = K_f A_i (C_f - C_f^*) \quad (6.1)$$

In this equation, V_f (m^3) is the feed phase volume, C_f and the C_f^* ($\text{mol} \cdot \text{m}^{-3}$) are the 1-hexanethiol concentration in the phase under consideration and in equilibrium with the 1-hexanethiol concentration in the ionic liquid phase, respectively. The K_f represents the overall mass transfer coefficient ($\text{m} \cdot \text{s}^{-1}$), being the interfacial area of the cell, A_i (m^2), and the extraction time, t (s).

C_f^* is related with the 1-hexanethiol concentration in the ionic liquid rich phase (C_{IL}) through the distribution ratio (D), calculated using the experimental concentration of the feed and the ionic liquid phases at the equilibrium:

$$C_f^* = \frac{C_{IL}}{D} \quad (6.2)$$

A simple mass balance to the solute at the initial conditions is applied to obtain an expression for the concentration C_{IL} :

$$C_{IL} = \frac{V_f}{V_{IL}} (C_f^0 - C_f) \quad t = 0, C_f = C_f^0, C_{IL} = C_{IL}^0 = 0 \quad (6.3)$$

where the C_f^0 and C_{IL}^0 are the concentration of 1-hexanethiol in the feed and ionic liquid phases, at the initial time, and V_{IL} is the ionic liquid phase volume.

Substituting equations 6.2 and 6.3 in 6.1, and integrating using the initial conditions, the overall mass transfer coefficient, K_f , can be determined by fitting the experimental concentrations of the mercaptan as a function of time.

The resistances-in-series model was used to estimate the overall mass transfer coefficient, based on the combination of the two individual mass transfer coefficients of both feed and ionic liquid boundary films, k_f and k_{IL} , respectively:

$$\frac{1}{K_f} = \frac{1}{k_f} + \frac{1}{Dk_{IL}} \quad (6.4)$$

Taking into account that the mass transfer in each phase depends on the hydrodynamic conditions, mass transfer correlations using the Sherwood (Sh), Reynolds (Re) and Schmidt (Sc) numbers were used to estimate the solute individual mass transfer coefficients.

The following correlation, described in equation 6.5, was selected to describe the individual mass transfer coefficients, k , in the laminar layers occurring at each side of the interface of the two individual mechanically stirred phases.⁴²⁻⁴⁴

$$Sh = 0.664Re^{1/2}Sc^{1/3} \quad (6.5)$$

The dimensional numbers of Sherwood, Reynolds and Schmidt are defined as $Sh = \frac{k d_i}{\mathcal{D}}$,

$Re = \frac{N d_i^2 \rho}{\mu}$ (impeller Reynolds number), $Sc = \frac{\mu}{\rho \mathcal{D}}$, respectively.

\mathcal{D} is the diffusion coefficient of 1-hexanethiol in the feed (*n*-dodecane) or in the ionic liquid ($\text{m}^2 \cdot \text{s}^{-1}$), d_i and N are the impeller diameter (m) and speed ($\text{rad} \cdot \text{s}^{-1}$), and ρ and μ the density ($\text{kg} \cdot \text{m}^{-3}$) and the dynamic viscosity (Pa.s) for each phase, respectively.

Information about the diffusion coefficient of liquids in ionic liquids is very scarce, and consequently, there are no specific correlations for the transport and molecular

properties for this type of systems. Therefore, the Wilke-Chang correlation (equation 6.6) was chosen to estimate the 1-hexanethiol diffusion coefficient in the ionic liquids tested, due to its vast and general application and good agreement with experimental values determined for organic solute diffusion in ionic liquids.⁴⁵

For the 1-hexanethiol diffusion coefficient in the *n*-dodecane solvent, the most suitable correlation for organic mixtures is the Scheibel correlation (equation 6.7).⁴⁶

$$\mathfrak{D}_{Wilke-Chang} = \frac{7.4 \times 10^{-8} (\emptyset M_{solv.})^{1/2} T}{\mu_{solv.} V_{RSH}^{0.6}} \quad (6.6)$$

$$\mathfrak{D}_{Scheibel} = 8.2 \times 10^{-8} \left(1 + \left(\frac{3V_{solv.}}{V_{RSH}} \right)^{0.66} \right) \frac{T}{\mu_{solv.} V_{RSH}^{0.33}} \quad (6.7)$$

In these expressions, $\mathfrak{D}_{Wilke-Chang}$ and $\mathfrak{D}_{Scheibel}$ are the mutual diffusion coefficient of solute 1-hexanethiol at very low concentrations in solvent ionic liquid or *n*-dodecane ($\text{cm}^2 \cdot \text{s}^{-1}$), by the Wilke-Chang correlation or the Scheibel correlation, respectively, at a *T* temperature (K). The $M_{solv.}$ is the molecular weight of solvent ionic liquid or *n*-dodecane ($\text{g} \cdot \text{mol}^{-1}$), \emptyset is the association factor of solvent, dimensionless, being 1 considering in this case the ionic liquid as non-associating compound, $\mu_{solv.}$ is the viscosity of solvent (mPa.s), and V_{RSH} , $V_{solv.}$ are the molar volume ($\text{cm}^3 \cdot \text{mol}^{-1}$) of the solute 1-hexanethiol and the solvent ionic liquid or *n*-dodecane, respectively, at their normal boiling temperature (K).

Being the studied ionic liquids composed by organic ions, the Scheibel method was also applied to the mercaptan diffusion in the ionic liquids, for comparison of the estimated values.

The molar volume for the 1-hexanethiol, ionic liquid and *n*-dodecane, at their normal boiling temperature, are also values that needed to be estimated and were calculated by the Schroeder method.⁴⁶

6.3. Materials and methods

6.3.1. Materials

The model “jet-fuel” constituents selected were the hydrocarbon *n*-dodecane and the mercaptan 1-hexanethiol, 99% and 95% pure, respectively, from Sigma-Aldrich, Germany.

Three ionic liquids with different density and viscosity properties were tested: 1-ethyl-3-methylimidazolium methylsulfate, 1-ethyl-3-methylimidazolium triflate, and 1-ethyl-3-methylimidazolium bis (trifluoromethylsulfonyl)imide. All the ionic liquids were acquired at IoLiTec, Ionic Liquid Technology, Germany, with a purity superior to 99%. Before using, the ionic liquids were dried and purified by heating (313.15 K), under constant stirring and at moderate vacuum (1 mPa) for a minimum of 24h.

Each ionic liquid content in water, after the drying procedure, and the respective physical properties are reported in Table 6.1.

Table 6.1 Solvents (*n*-dodecane and ionic liquids) physical properties, at 298.2 K.

Solvent	$M_{solv.}$ (mol.g ⁻¹)	w_{H_2O} (ppm)	$\rho_{solv.}$ (kg.m ⁻³)	$\mu_{solv.}$ (mPa.s)
<i>n</i> -dodecane	170.33	28.2	745.7 ⁴⁷	1.36 ⁴⁸
[C ₂ mim][MeSO ₄]	222.3	130.1	1278.3 ⁴⁹	84.19 ⁴⁹
[C ₂ mim][CF ₃ SO ₃]	260.2	305.2	1379.1 ⁵⁰	40.58 ⁵⁰
[C ₂ mim][NTf ₂]	391.3	283.3	1519.3 ⁵¹	32.46 ⁵²

6.3.2. Liquid-liquid extraction kinetic experiments

The extraction cell used for these studies consists of a modified Lewis cell⁵³⁻⁵⁴ with a total volume of 22.8 ml. A double paddle vertical stirrer, 15 mm of diameter, promotes the individual phase mixing by a regulated motor with a tachometer (Model 461895, Exttech Instruments). To maintain a constant temperature fixed at 298.2 K (± 0.1 K), the cell is thermostated by circulating water through a tube enfolding the cell. The water was thermo-regulated with a temperature stability of ± 0.1 K by means of a thermostat bath circulator (Julabo MC).

The ionic liquid and the feed mixture (*n*-dodecane + 1-hexanethiol) were added to the extraction cell (11.4 ml each phase), remaining the ionic liquid as the lower phase, and the feed as the upper phase, due to their different densities (Table 6.1). Samples of each

phase (0.3 ml) were collected simultaneously and analyzed at suitable intervals until the equilibrium was reached.

Analytical methods

The mercaptan concentration, in each phase, was analyzed by potentiometric titration ($\pm 2.6\%$ for the *n*-dodecane rich phase and $\pm 7.9\%$ for the ionic liquid rich phase), using a TitraLab® 865 titration workstation, with an alcoholic solution of AgNO₃ at 0.01 M, according to the ASTM D3227 standard.⁵⁵ This method has a detection threshold of 1 mol/m³ for the mercaptan concentration for the sample volumes analyzed.

Supporting our previous work results,⁴¹ no peaks corresponding to the tested ionic liquid in the hydrocarbon-rich phase were found by UV spectroscopy. For the ionic-liquid-rich phase, also no dodecane was found by gravimetric analysis ($\pm 10^{-4}$ g). Therefore, the content of ionic liquid and *n*-dodecane in the dodecane and ionic liquid-rich phases, respectively, were considered negligible. Nevertheless, traces of these compounds might be present at each phase in concentrations below the detection threshold.

The water content of the solvents tested was determined by Karl-Fischer titration, using a Metrohm 831 Karl Fischer coulometer.

Calculation methods

The software package Matlab™, from Math Works Inc. (USA), was applied to perform the fitting of the mercaptan concentration variation with time, for the kinetic experiments, using the *nlinfit* routine. The overall mass transfer coefficients were determined performing a nonlinear regression, using the iterative least squares algorithm, and simultaneously solving the differential equations system specified in mass transfer modelling. The parameters' errors were calculated within a 95% confidence interval.

6.3.3. Supported ionic liquid membranes (SILMs) experiments

In order to assess the feasibility of the application of supported ionic liquid membranes for mercaptan desulfurization by a reduced pressure driven process, different ionic liquids and support membrane materials were investigated.

The ionic liquids studied comprised the previous ionic liquids of the liquid-liquid extraction experiments (1-ethyl-3-methylimidazolium methylsulfate, 1-ethyl-3-

methylimidazolium triflate, and 1-ethyl-3-methylimidazolium bis (trifluoromethylsulfonyl)imide), in order to understand the impact of their properties on the stability and permeation behavior of the resulting supported liquid membranes.⁴⁰

In terms of membrane materials, both PVDF supports were already tested hitherto for gas separation processes⁵⁶⁻⁵⁷ and a higher stability behavior was obtained for the hydrophobic PVDF. Hydrophilic PVDF and hydrophilic PES with imidazolium ionic liquids were applied and compared in gas separation experiments⁵⁸ and long term stabilities were achieved for both materials. Nevertheless, in order to determine which support would be more appropriate to produce stable SILMs for this specific desulfurization task, stability experiments were carried out for these and other materials with different composition and properties, identified in Table 6.2, with the respective specifications and supplier.

Table 6.2 Membrane support specifications and properties.

Membrane support properties	Hydrophobic polyvinylidene fluoride (hb-PVDF)	Hydrophilic polyvinylidene fluoride (hl-PVDF)	Teflon (PTFE)	Polyethersulfone (PES)	Cellulose acetate (CA)	Polypropylene (PP)
	Millipore Corporation	Pall Corporation	Sartorius Stedim Biotech GmbH	Pall Corporation	GVS Group	Celgard®
Thickness (µm)	125	129	50.5	145	80	130
Pore diameter (µm)	0.22	0.20	0.2	0.2	0.22	0.05
Porosity (%)	70	80	30	80	70	30
Wettability to the ionic liquids	high	high	low	high	membrane is dissolved	low

6.3.3.1. *SILMs preparation*

The ionic liquid was immobilized on the support membranes by first removing the air from the pores of the membrane applying vacuum for 1h on a stainless steel vacuum chamber, which facilitates the incorporation of the ionic liquids into the porous structure. After spreading ionic liquid drops on the membrane surface, still under vacuum and, after stabilization for at least 1h, the SILM excess of ionic liquid was removed using a tissue. The amount of ionic liquid incorporated was determined gravimetrically, and the membrane thickness change due to swelling was also measured using a micrometer Metric z169048, Sigma-Aldrich, Spain ($\pm 5 \mu\text{m}$).

6.3.3.2. *SILMs characterization*

Regarding the supported ionic liquid membranes characterization, the weight and thickness of the membrane, before and after the immobilization procedure, were measured using an analytical balance Sartorius A.G. Göttingen CP225D, Germany ($\pm 10^{-4}$ g), and a micrometer Metric z169048, Sigma-Aldrich, Spain ($\pm 5 \mu\text{m}$), respectively.

The contact angle of 1-ethyl-3-methylimidazolium triflate in the hydrophobic polyvinylidene fluoride and polypropylene supports were also measured using a sessile drop method measured by a KSV's CAM 101 goniometer, which captures and automatically analyses video images for the contact angles measured.

6.3.3.3. *SILMs stability*

The SILMs stability was investigated by two different techniques, which allowed to evaluate the ionic liquid displacement from the membrane support by the permeation of air, as a result of a pressure gradient applied to the membrane system.

The first set of experiments consisted in measuring the SILM ionic liquid loss when submitted to a pressure higher than atmospheric pressure. For this, the SILMs were placed in a dead-end filtration cell (10 mL AmiconTH ultrafiltration unit), and a nitrogen stream was used to apply pressure up to 2 bar in the feed circuit. At regular periods of time, the SILMs were weighed, using a Sartorius balance (A.G. Göttingen CP225D, Germany), to determine the reduction of the SILM weight caused by ionic liquid losses.

The second type of experiments was carried out in a stainless steel flat circular unit composed by two compartments, separated by the SILM. A lower pressure was applied to the downstream compartment, while the upper compartment was exposed to air. After

stabilization of the pressure in the downstream compartment, vacuum was cut and the pressure evolution, due to the permeation through the membrane, was registered over time. The SILMs were weighed before and after this experimental procedure, also to measure the ionic liquid loss.

6.3.3.4. Permeation through the SILMs

The permeation behavior of the components of the jet-fuel model through the SILMs is an important aspect to be considered, since these SILMs must present a high selectivity to be viable for a membrane assisted desulfurization process.

The *n*-dodecane permeation tests were performed in a stainless steel flat circular module. This unit is composed by two compartments that were separated by the SILM. To evaluate the SILM stability using organic solvents, after applying vacuum at the downstream compartment and stabilization of the pressure, the upper compartment was filled with *n*-dodecane. Then, the vacuum was cut and the pressure evolution over time was registered. The SILM was also weighed before and after this experimental procedure.

6.4. Results and discussion

In consequence of the extremely low mutual solubility between the alkanes and the ionic liquids, and despite the low mercaptan partition for these extracting solvents, shown in our previous work ⁴¹, that makes the conventional liquid-liquid extraction process unviable, the liquid extraction process was here evaluated using a supported ionic liquid membrane.

Due to the importance of the extraction kinetics on this process, this section presents the study of the diffusion and mass transfer of 1-hexanethiol to the selected imidazolium based ionic liquids. In order to evaluate the application of SILMs in the membrane extraction process, their stability and selectivity are also analyzed testing the aforementioned ionic liquids and different support materials.

6.4.1. Liquid-liquid extraction kinetics

To further understand the mercaptan mass transfer between the hydrocarbon phase and the selected ionic liquids, extraction experiments were carried out with different ionic liquids, in a modified Lewis cell, previously described.

The experimental 1-hexanethiol concentrations (C_{RSH} , mol.m⁻³) in the dodecane and ionic liquid phases during the extraction process, for the ionic liquids [C₂mim][MeSO₄], [C₂mim][CF₃SO₃], and [C₂mim][NTf₂], are depicted in Figure 6.1. The different experiments were carried out at a fixed stirrer speed of 200 rpm, to not disturb the interface, and at a constant temperature of 298.2K. The mercaptan concentration was measured for the dodecane and ionic liquid rich phase, except for the samples with concentration of mercaptan below the detection threshold.

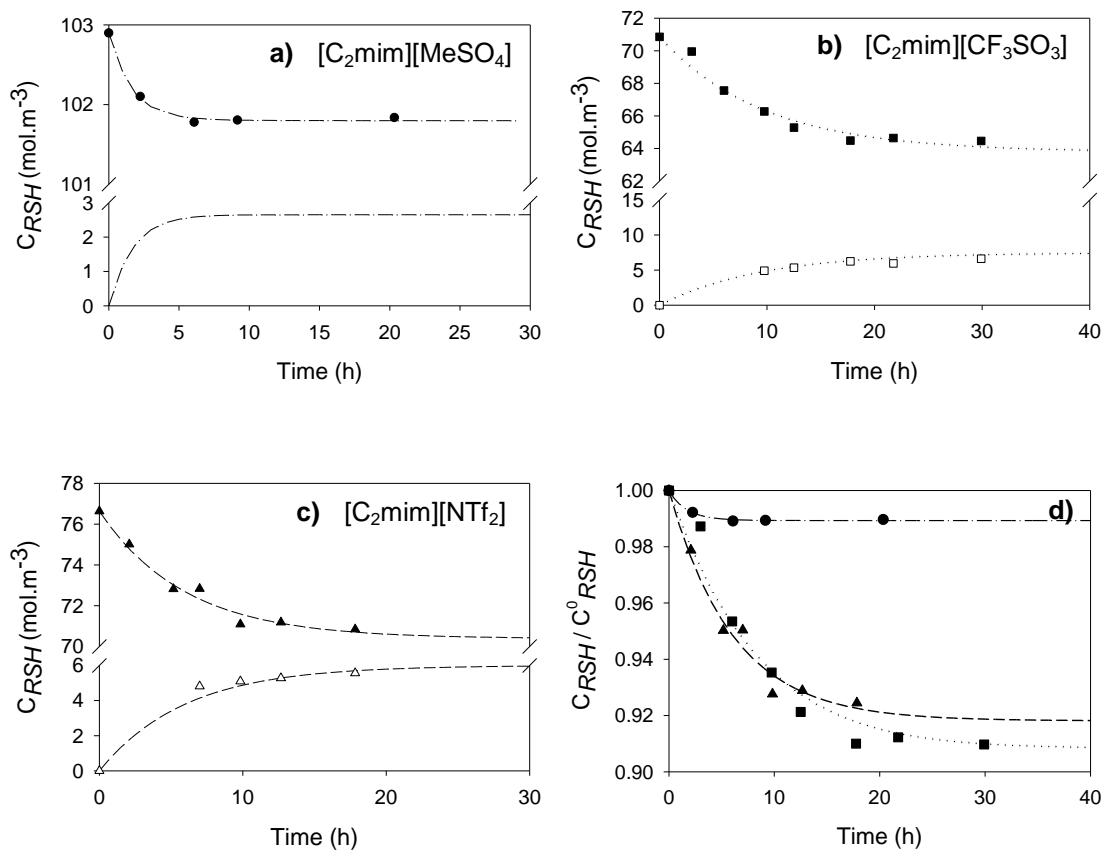


Figure 6.1 1-hexanethiol experimental concentration profile in the dodecane and ionic liquid rich-phases (filled and empty symbols, respectively), and data fitting (lines) at 298.2 K and atmospheric pressure, using different extracting ionic liquids: **a)** $[C_2mim][MeSO_4]$ (diamonds and dot-dashed line), **b)** $[C_2mim][CF_3SO_3]$ (squares and dotted line), **c)** $[C_2mim][NTf_2]$ (triangles and dashed line). And **d)** comparison between the three extraction systems studied (dodecane phase).

6.4.1.1. Mass transfer kinetics

By fitting the experimental concentrations of the feed phase with the set of differential equations (equations 6.1 – 6.3), the overall mass transfer coefficient was determined for each system studied. The respective distribution ratio values were calculated by using the experimental concentration at the equilibrium for the feed and the ionic liquid phases (Figure 6.1). The values obtained for each parameter are gathered in Table 6.3.

Table 6.3 Overall mass transfer and coefficient distribution ratio for the systems ionic liquid + 1-hexanethiol + *n*-dodecane, at 298.2 K and atmospheric pressure.

Ionic liquid	$\mu_{solv.}$ (mPa.s)	$K_{f,exp.} \times 10^7$ (m.s ⁻¹)	D
[C ₂ mim][MeSO ₄]	84.19 ⁴⁹	0.67 ± 0.32	0.010 ± 0.008
[C ₂ mim][CF ₃ SO ₃]	40.58 ⁵⁰	1.72 ± 0.80	0.095 ± 0.026
[C ₂ mim][NTf ₂]	32.46 ⁵²	2.01 ± 0.48	0.079 ± 0.017

Regarding the mass transfer kinetics, the values obtained for the fitted overall mass transfer coefficients were $0.67 \pm 0.32 \times 10^{-7} \text{ m.s}^{-1}$, $1.72 \pm 0.80 \times 10^{-7} \text{ m.s}^{-1}$, and $2.01 \pm 0.48 \times 10^{-7} \text{ m.s}^{-1}$, for the systems with the ionic liquids [C₂mim][MeSO₄], [C₂mim][CF₃SO₃], and [C₂mim][NTf₂], respectively (Table 6.3). From these fitted coefficients, and analyzing the 1-hexanethiol concentration profile plots (Figure 6.1), the extraction rates observed can be considered as low, taking between 5 to 20 hours to achieve the concentration plateau for the various systems tested.

Given that the operating conditions are similar for the individual experiments, the differences observed are directly related with the ionic liquid tested, and consequently, with their physical properties. The behavior observed is determined by the ionic liquids viscosity, which has a significant impact on the mass transfer coefficients. In fact, high ionic liquid viscosities are responsible for increasing the boundary layer immediately adjacent to the interface, hindering the molecular transport in this region.⁵⁹ Consequently, the decrease of the ionic liquid viscosity contributes for the mass transfer coefficients increase from [C₂mim][MeSO₄], [C₂mim][CF₃SO₃], to [C₂mim][NTf₂]. Additionally and as supported by the resistances-in-series model (equation 6.4), the distribution coefficient within also attains a large contribution in the overall mass transfer coefficients. For the systems studies, this impact is be estimated to be between 10 – 100.

Regarding the distribution ratio, the values obtained were low due to the low solubility of the 1-hexanethiol in the tested ionic liquids (Table 6.3). The [C₂mim][MeSO₄] ionic liquid shows the lowest distribution ratio, with a value of 0.010 ± 0.008 , whereas the [C₂mim][CF₃SO₃] and the [C₂mim][NTf₂] exhibit higher values, 0.095 ± 0.026 and 0.079 ± 0.017 , respectively. Comparing these results with the distribution ratios obtained by ternary liquid-liquid equilibrium experiments in our recent work⁴¹, the values found are in

accordance (0.010 ± 0.007 , 0.113 ± 0.009 and 0.115 ± 0.011 , values converted from molar fraction ratio to concentration ratio, as defined in equation 6.2).

The low distribution ratios observed are a result of the weak interactions between the 1-hexanethiol and the ionic liquids in study. The *n*-dodecane and the 1-hexanethiol are essentially non- and very low polar molecules, respectively, where the main intermolecular interactions are van der Waals forces, albeit the mercaptan can also involve less significant dipole-dipole interactions, due to the individual –SH group. On the other hand, much different electrostatic and hydrogen-bonding type interactions occur in the ionic liquids. Combining these compounds, the interaction forces between them contemplate essentially weak dispersive forces and dipole-dipole attractions. Since the cation $[C_2mim]^+$ is common in the ionic liquids tested, the differences observed are related with anions mostly due to their different polarity. Here anions with lower polarity tend to interact through dispersive van der Waal forces, which promote a better affinity between the mercaptan and the ionic liquid. A more extensive explanation on the mercaptan/alkane/ ionic liquid interaction can be found in our prior work.⁴¹ Nonetheless, it is necessary to have in mind that fuels are a very complex mixture, and improving the affinity of ionic liquids to the target compounds for extraction, can also lead to increasing the undesirable ability to extract alike fuel compounds.

6.4.1.2. Mass transfer correlations

The individual mass transfer coefficients were estimated using the Sherwood correlation for the laminar layers at the system interface (equation 6.5). To apply this correlation, the 1-hexathiol diffusion coefficients in the feed and ionic liquid phases were evaluated using the Scheibel and the Wilke-Chang correlation, respectively. The calculated values are shown in Table 6.4. The results estimated are in the order of 10^{-9} m.s⁻¹ in the feed phase and two orders lower (10^{-11} m.s⁻¹) in the different ionic liquids studied. This is a consequence of the significative differences on the solvents viscosity, being superior two orders of magnitude for the ionic liquids. For the systems tested, the *n*-dodecane viscosity is slightly higher than 1 mPa.s, whereas for the ionic liquids, it is superior to 30 mPa.s.

In the case of the feed *n*-dodecane, the diffusion coefficient is consistent with others reported in the literature for diffusion of solvents in organic solvents⁴⁶. For the ionic liquids, the data on liquid diffusion coefficients in ionic liquids are still very scarce and, in spite of the diffusivity coefficient deviations encountered, the values here estimated are in the same range of other values reported in the literature for solute diffusivity in ionic

liquids.^{34, 60} It is also noticeable that, the diffusion of the mercaptan in the ionic liquids depends from the ionic liquids viscosity. Regarding the comparison between the use of the Wilke-Chang or the Scheibel correlations, the estimated diffusion coefficients are very similar.

Table 6.4 Estimated diffusion of 1-hexanethiol in the n-dodecane and several ionic liquids, by the Scheibel ($\mathcal{D}_{Scheibel}$) and the Wilke-Chang ($\mathcal{D}_{Wilke-Chang}$) correlations, with the molar volume at the boiling point temperature calculated by the Schroeder correlation.

Solvent	$\mu_{solv.}$ (mPa.s)	$\mathcal{D}_{Scheibel}$ ($m^2 \cdot s^{-1}$)	$\mathcal{D}_{Wilke-Chang}$ ($m^2 \cdot s^{-1}$)
<i>n</i> -dodecane	1.36 ⁴⁸	1.20×10^{-9}	-----
[C ₂ mim][MeSO ₄]	84.19 ⁴⁹	1.86×10^{-11}	1.86×10^{-11}
[C ₂ mim][CF ₃ SO ₃]	40.58 ⁵⁰	3.83×10^{-11}	4.12×10^{-11}
[C ₂ mim][NTf ₂]	32.46 ⁵²	5.60×10^{-11}	6.38×10^{-11}

Having estimated the diffusion coefficients, the individual mass transfer coefficients were predicted by the Sherwood correlation described in equation 6.5. The mass transfer coefficients were obtained by summing the individual mass transfer coefficients (equation 6.4). All values determined are shown in Table 6.5 a) and b), with the respective Reynolds, Schmidt and Sherwood numbers.

For the systems studied, the values determined for the individual mass transfer coefficients in the laminar layer in the feed phase side, are identical and have a magnitude in the order of $10^{-5} m \cdot s^{-1}$. With concern to the ionic liquid phase film, the values obtained are one order lower than the feed phase, standing on $10^{-6} m \cdot s^{-1}$.

Since the inverse of these estimated individual mass transfer coefficients, weighted by the respective distribution coefficients (equation 6.4), reflects the resistance of the 1-hexanethiol transport through the phase films, it is possible to state that the solute finds higher resistances for mass transfer in the ionic liquid phase. Also, in light of the selected Sherwood correlation, combined with the equation of the resistances-in-series model, it is also possible to infer about the controlling step. Therefore, independent variation of the phases' hydrodynamics shows that the rate of 1-hexanethiol extraction is controlled by the ionic liquid phase.

Analyzing specifically the ionic liquid phase, the low mass transfer coefficients are determined by the viscosity, as can be seen by the viscosity contribution to the decrease

of the diffusion coefficients (Table 6.4), and the reduced agitation degree (low Reynolds numbers), which are responsible for a slow mercaptan transport in a thick boundary layer. For the tested ionic liquids, the individual mass transfer coefficients increase following the order $[\text{C}_2\text{mim}][\text{MeSO}_4]$, $[\text{C}_2\text{mim}][\text{CF}_3\text{SO}_3]$, and $[\text{C}_2\text{mim}][\text{NTf}_2]$, obeying to the decrease of the viscosity and the respective increase of the diffusivity.

With relation to the overall mass transfer coefficients, a good agreement between the experimental and the estimated values by the selected Sherwood correlation was achieved.

From the previous experiments, it was possible to conclude that, due to the very slow extraction rates of the mercaptan compound from the feed to the ionic liquid along with the low partition of the 1-hexanethiol towards the ionic liquid, the use of conventional liquid-liquid extraction equipment is discouraged in real conditions as a viable separation process, since it would require high operation time and very high volume of ionic liquid to achieve the mandatory mercaptan limits in the fuel.

On the other hand, the negligible mutual solubility between the majority aliphatic compounds of jet-fuel compounds, as is the *n*-dodecane, and the large variety of ionic liquids, still makes very attractive the application of these non-volatile solvents for the removal of mercaptans. Thus, the addition of a regeneration step of the ionic liquid to the liquid-liquid extraction process might overcome the problems perceived, since the ionic liquid might be continuously cleaned, promoting a higher concentration gradient and a separation process kinetically controlled.

In view of these considerations, the next section presents the extraction of mercaptans using supported ionic liquid membranes as an alternative approach to the desulfurization process.

Table 6.5 a) Estimated individual mass transfer coefficients for the several tested ionic liquids, with the respective Reynolds, Schmidt and Sherwood numbers determined.

Note: the subscripts *Sche* and *WC* indicate if the value estimated was calculated using the Scheibel or the Wilke-Chang diffusion coefficient, respectively.

Ionic liquid	Feed phase				Ionic liquid phase						
	Re	Sc_{Sche}	Sh_{Sche}	$k_f \times 10^5$ ($m.s^{-1}$)	Re	$Sc_{Sche} \times 10^5$	$Sc_{WC} \times 10^5$	Sh_{Sche}	Sh_{WC}	$k_{ILSche} \times 10^6$ ($m.s^{-1}$)	$k_{ILWC} \times 10^6$ ($m.s^{-1}$)
[C ₂ mim][MeSO ₄]	2871	1518	406	3.25	80	35.11	35.05	898	898	1.11	1.11
[C ₂ mim][CF ₃ SO ₃]	2806	1518	401	3.21	172	7.77	7.22	795	777	2.03	1.98
[C ₂ mim][NTf ₂]	2754	1518	398	3.19	235	3.82	3.35	734	703	2.74	2.62

Table 6.5 b) Estimated and experimental overall mass transfer coefficients for the several tested ionic liquids.

Note: the subscripts *Sche* and *WC* indicate if the value estimated was calculated using the Scheibel or the Wilke-Chang diffusion coefficient, respectively.

Ionic liquid	Overall mass transfer		
	Estimated		Experimental
	$K_{f_{Sche}} \times 10^7$ ($m.s^{-1}$)	$K_{f_{WC}} \times 10^7$ ($m.s^{-1}$)	$K_{f_{exp.}} \times 10^7$ ($m.s^{-1}$)
[C ₂ mim][MeSO ₄]	0.11	0.11	0.67 ± 0.32
[C ₂ mim][CF ₃ SO ₃]	1.92	1.87	1.72 ± 0.80
[C ₂ mim][NTf ₂]	2.15	2.06	2.01 ± 0.48

6.4.2. Supported ionic liquid membrane experiments

The extraction of 1-hexanethiol from the fuel stream by the selected ionic liquids can be performed using supported ionic liquid membranes (SILMs). The ionic liquid confined inside the pores of the membrane works as a liquid membrane and, by applying vacuum on the permeated side, the 1-hexanethiol selectively solubilizes and diffuses across the ionic liquid and is continuously stripped.

With regard to the SILMs requisites, such as chemical and mechanical resistance, and high selectivity to the target solute, SILMs are expected to benefit from the almost negligible mutual solubility between the aliphatic hydrocarbons and ionic liquids. In this way, the ionic liquid will work as a carrier to the target compounds and, due to the differences between the mercaptan and the dodecane partition, their separation should occur in a very selective mode, with a minimal volume of ionic liquid, filling the porous supporting membrane.⁶¹⁻⁶²

Nevertheless, as stated before, the instability of supported liquid membranes is usually a critical issue for industrial application. For the separation in question, the SILMs should exhibit long term integrity with no liquid losses nor swelling and degradation of the supporting membrane material, and favorable transport towards the target solute.

6.4.2.1. Membrane support

Both hydrophobic and hydrophilic polyvinylidene fluoride (PVDF) and the polyethersulfone (PES) supports are easily wettable by the tested ionic liquids. Figure 6.2 a) shows the low contact angle of the $[C_2mim][CF_3SO_3]$ ionic liquid on the hydrophobic membrane of PVDF. For the ionic liquid incorporation in polypropylene (PP) and Teflon (PTFE) membrane supports, the method and/or period of immobilization used in this work were not effective. This can be explained by the smaller pores of the PP support and higher hydrophobicity of the PTFE support, that promote lower wettability (high contact angle) of the supports by the ionic liquids (Figure 6.2 b for the PP support)). As for the cellulose acetate (CA) support, it was visually observed a physical degradation of the support material.

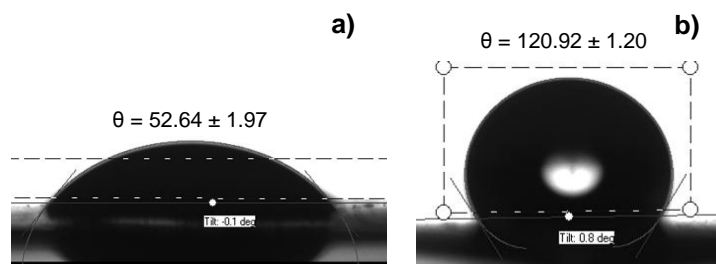


Figure 6.2 Contact angle of the ionic liquid $[C_2mim][CF_3SO_3]$ with **a)** the hydrophobic PVDF membrane, and **b)** the PP membrane.

The incorporation of ionic liquid into the hydrophobic PVDF, hydrophilic PVDF and PES supports resulted in an increase of the weight and thickness of the membranes, as can be seen in Table 6.6. The weight variation corresponds to the necessary amount of ionic liquid to fill the pores, and the thickness expansion is related to the swelling effect of the ionic liquid in the support material, being more pronounced when the hydrophilic PVDF support was used.

Table 6.6 Weight increase (Δm %) and thickness ($\Delta \delta$ %) after immobilization.

		$[C_2mim][MeSO_4]$ (2745.3 ppm H_2O , $\mu = 84.17$ mPa.s)	$[C_2mim][CF_3SO_3]$ (1020.8 ppm H_2O , $\mu = 39.38$ mPa.s)	$[C_2mim][NTf_2]$ (202.9 ppm H_2O , $\mu = 32.46$ mPa.s)
Hydrophobic PVDF SILM	Δm %	141.9	154.7	179.1
	$\Delta \delta$ %	5.4	9.0	17.3
Hydrophilic PVDF SILM	Δm %	252.3	273.7	310.7
	$\Delta \delta$ %	11.3	13.5	22.4
PES SILM	Δm %	-----	386.8	-----
	$\Delta \delta$ %	-----	9.6	-----

6.4.2.2. Ionic liquid losses

In order to evaluate the integrity of the SILMs when operated under pressure differences due to ionic liquid displacement from the membrane support pores, two different approaches were used. In the first set of experiments, a positive pressure difference is applied using a nitrogen gas stream in the feed compartment; in the second case, the SILM was submitted to a negative pressure difference (vacuum in the

downstream compartment). In both cases, the SILM weight was measured before and after the experiment.

From the positive pressure difference experiments, Figure 6.3 shows that the SILMs prepared with hydrophobic PVDF support are more stable than the ones prepared with hydrophilic PVDF. As can be seen, the ionic liquid loss from the hydrophobic support is lower than 4% for all the ionic liquids tested up to 2 bar, with exception of the $[\text{C}_2\text{mim}][\text{MeSO}_4]/\text{hb-PVDF}$ SILM, that start showing a more pronounced ionic liquid displacement after 1.5 bar of pressure difference. When comparing the ionic liquids tested, it can be concluded that the $[\text{C}_2\text{mim}][\text{CF}_3\text{SO}_3]/\text{hb-PVDF}$ SILM is the most stable membrane, presenting losses lower than 2% up to 1.4 bar, followed by the $[\text{C}_2\text{mim}][\text{NTf}_2]$ up to 1 bar. These losses are extremely low and they may be due to a removal of excess of ionic liquid from the membrane surface and not to a displacement of ionic liquid from the membrane pores.

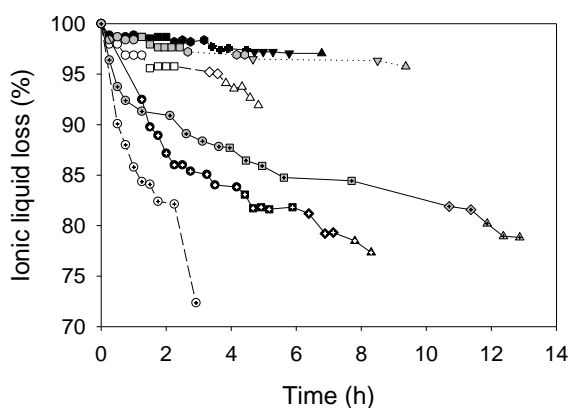


Figure 6.3 SILM ionic liquid loss along time, for the SILMs composed by PVDF hydrophobic (full symbols) and hydrophilic (dotted symbols), with the ionic liquids $[\text{C}_2\text{mim}][\text{CF}_3\text{SO}_3]$ (black symbols and solid line), $[\text{C}_2\text{mim}][\text{NTf}_2]$ (grey symbols and dot-dashed line), and $[\text{C}_2\text{mim}][\text{MeSO}_4]$ (white symbols and dashed line), for positive pressure differences of 0.5 bar (circles), 1.0 bar (squares), 1.4 bar (hexagons), 1.5 bar (diamonds), 1.6 bar (cross), 1.8 bar (inverse triangles), and 2.0 bar (triangles), using a nitrogen gas stream on the AmiconTH 8010 cell.

When filling the feed compartment of the permeation cell with air at atmospheric pressure and applying vacuum in the downstream side (negative pressure difference), an increase of the permeate pressure side is observed due to air permeation through the SILM (Figure 6.4), as a result of air solubility in the ionic liquid. A linear pressure profile confirms that the membrane pores are totally filled with the ionic liquid since no

abrupt gas leak is observed. Moreover, it indicates that no pronounced removal of the ionic liquid from pores of the membrane occurs. The losses observed are lower than 0.7%, 2.2% and 4.7%, for the $[\text{C}_2\text{mim}][\text{MeSO}_4]$, $[\text{C}_2\text{mim}][\text{CF}_3\text{SO}_3]$, and $[\text{C}_2\text{mim}][\text{NTf}_2]$ -SILMs, respectively.

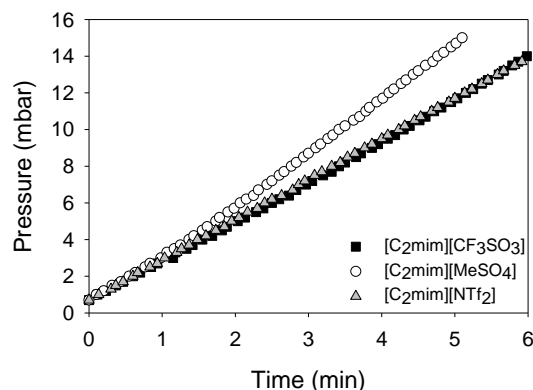


Figure 6.4 Pressure profile in the permeate side, when applying a negative pressure difference across the hydrophobic PVDF/ionic liquid SILM. Feed compartment: air at atmospheric pressure; Downstream compartment: vacuum at a starting pressure of 0.9 mbar.

6.4.2.3. Permeation through SILMs

The mercaptan removal from fuel requires the highest SILM selectivity possible, i.e., a high permeability for the target mercaptans and very low, rather negligible, permeation of the hydrocarbons. Based on the jet-fuel model assumed in this work, the pure *n*-dodecane permeation across the studied SILMs was evaluated in first place.

Taking into account the results of the good and stable ionic liquid incorporation in the membrane support, the hydrophobic PVDF membrane support was tested with the ionic liquid $[\text{C}_2\text{mim}][\text{CF}_3\text{SO}_3]$, due to its low mutual solubility with aliphatic hydrocarbons, aiming to assure no permeation these compounds. The experimental results obtained for the hydrophobic PVDF/ $[\text{C}_2\text{mim}][\text{CF}_3\text{SO}_3]$ are plotted in Figure 6.5 a), represented by the full square symbols. They show the pressure increase in the permeate side during operation time, which results from the *n*-dodecane permeation across the SILM. This result was unexpected given the high stability of the SILM prepared with this specific membrane support and ionic liquid. The observed permeation of *n*-dodecane cannot be explained by a displacement of ionic liquid from the membrane pores.

In order to understand the undesirable transport of *n*-dodecane through the hydrophobic PVDF-based SILMs, other support materials were evaluated, namely hydrophilic PVDF (aiming at increasing the polarity of the SILM), and PES. Still, the results were unsatisfactory in both cases, as depicted in Figure 6.5 a). For these SILMs, a faster *n*-dodecane permeation through the [C₂mim][CF₃SO₃] hydrophilic SILM was even observed, and the ionic liquid loss with the hydrophilic PVDF and PES supports was higher (7.4%wt. and 8.7%wt., respectively).

As the permeation of *n*-dodecane could not be attributed to transport through empty pores, due to ionic liquids displacement, neither transport through the ionic liquid itself (as result of the extremely low affinity of *n*-dodecane to the ionic liquids), it was decided to investigate the transport of *n*-dodecane through the polymeric materials that constitute the supporting porous membrane.

To understand if the *n*-dodecane SILM permeation was due to the support, a dense PVDF membrane was used in the reduced pressure unit. It was found that the PVDF polymer is extremely permeable to *n*-dodecane, as can be seen by the very fast pressure increase in the permeate side (Figure 6.5 b)). Comparing Figure 6.5a) and b), it can be concluded that the ionic liquid in the pores of the membrane acts as a barrier to the *n*-dodecane transport, as can be inferred from the different operation time to achieve the same pressure increase of 16 mbar. While for the tested SILMs it requires between 5 to 16 minutes, for the dense PVDF, it is almost instantaneous. Therefore, it may be concluded that although the membrane pores are well impregnated with ionic liquid, *n*-dodecane permeation occurs through the membrane support material.

Figure 6.5 c) explains how the transport of *n*-dodecane take place in SILMs.

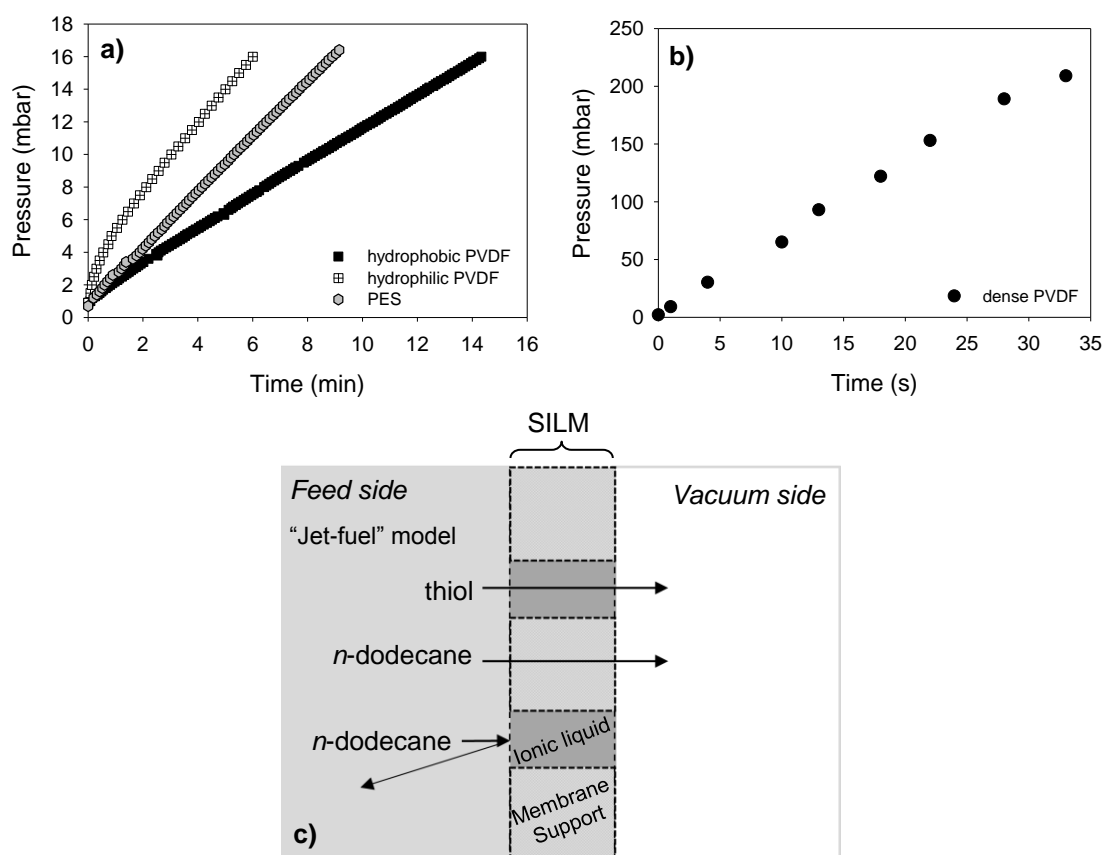


Figure 6.5 Pressure profile in the permeate side, for the *n*-dodecane permeation when applying a negative pressure difference across **a)** [C₂mim][CF₃SO₃]-based SILMs with different membrane supports; and **b)** a dense PVDF membrane. A proposed scheme for the *n*-dodecane transport occurring in SILMs is illustrated in **c)**.

To overcome the undesirable permeation of the alkane through the polymer, an alternative could be the use of ionic liquid as an additional barrier after the SILM, in order to block the *n*-dodecane crossing over to the permeate side. This approach is shown in a schematic illustration in Figure 6.6. In this approach a membrane wettable or non-wettable by the ionic liquid can be used, however, the overall resistance to the mercaptans transport must be evaluated. Considering the study carried out in this work concerning the mass transfer of the 1-hexanethiol from the feed phase to the ionic liquid, from which it was concluded that the dominant resistance to the mercaptan transport occurs in the ionic liquid, it would be more adequate the use of a non-wettable membrane by the ionic liquid, in order to reduce the resistance in the membrane, as shown in Fig. 6 b). In both cases, the alkanes presented in the “jet-fuel” are expected to not permeate to the receiving ionic liquid phase.

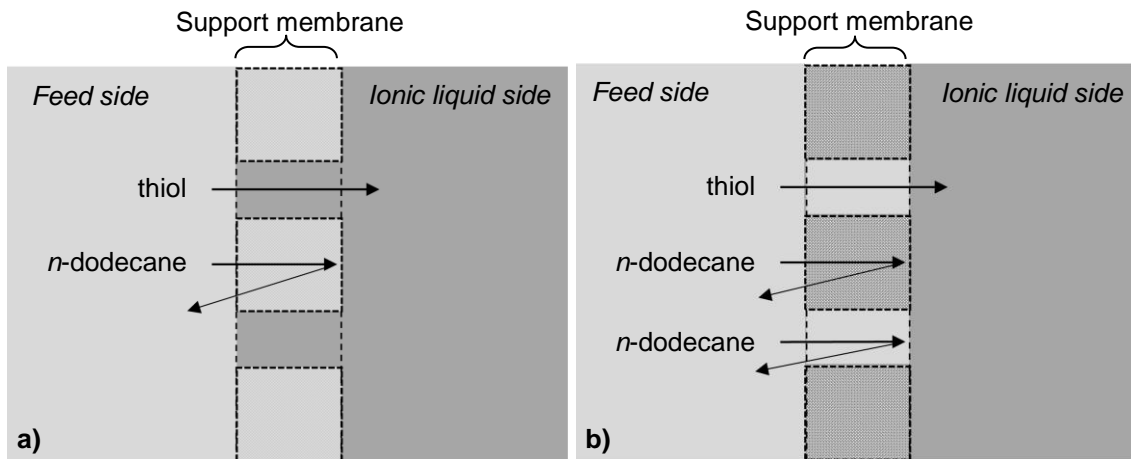


Figure 6.6 Mercaptan and *n*-dodecane transport through the membrane under different operating modes with an ionic liquid as the receptor phase, using **a)** a membrane wetted or **b)** a membrane not wetted by the ionic liquid.

Taking into account the previous discussion, a membrane not wetted by the selected ionic liquid ($[\text{C}_2\text{mim}][\text{CF}_3\text{SO}_3]$) was evaluated. The experiments were carried out in a Liqui-cel MiniModule[®] Contactor with microporous polypropylene hollow fiber membranes (Celgard[®] X-10), circulating the feed phase in the shell side and the ionic liquid inside of the fibres.

With this configuration, no *n*-dodecane was detected in the ionic liquid phase, eliminating the problem of *n*-dodecane transport. Additionally, the use of this equipment favors the extraction step of the process since it promotes a very high interfacial area of transport ($3225 \text{ m}^2/\text{m}^3$), reducing the extraction time from 20h to 2h. Figure 6.7 shows the transport of the target solute 1-hexanethiol from the *n*-dodecane feed phase to the ionic liquid phase, when operating this equipment.

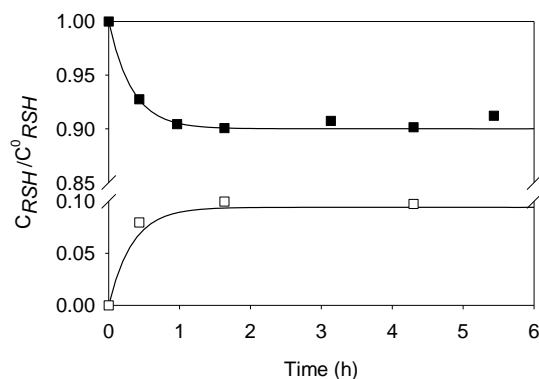


Figure 6.7 1-hexanethiol experimental concentration profile in the *n*-dodecane feed phase (filled squares) and ionic liquid receiving phase (empty squares), for the extraction in a Liqui-cel MiniModule[®] Contactor with microporous polypropylene hollow fiber membranes (Celgard[®] X-10), at 298.2 K and atmospheric pressure. Shell side: jet-fuel model (1-hexanethiol + *n*-dodecane); Lumen side: ionic liquid ([C₂mim][CF₃SO₃]).

Having in mind the mass transfer steps taking place in the extraction process with SILMs, the mass transfer mechanism can be decoupled into simultaneous actions in two membrane contactors. This methodology consists in the use of a first membrane contactor in which occurs the selective extraction of the target solute from the feed phase, without losses of other fuel constituents (as shown). Then, the ionic liquid with the extracted mercaptan can be regenerated in a second membrane contactor, by applying vacuum or using a sweep gas in the downstream compartment. This step should allow for a complete cleaning of the ionic liquid allowing its reuse in the extraction step. Integrating both steps, the ionic liquid circulates in a closed loop between both membrane contactors, requiring therefore much lower volumes of ionic liquid than in conventional equipment. Additionally, this configuration allows for maximizing of the concentration driving force, making possible a continuous desulfurization of the fuel feed.

6.5. Conclusions

This work addressed the study of ionic liquids for the removal of mercaptans from jet-fuel streams. As the affinity of the mercaptans compounds towards the ionic liquids is relatively low, high volumes of extracting ionic liquid would be required in conventional liquid-liquid extraction. This requirement turns the conventional process unviable.

This work proposes an alternative method. It was investigated the incorporation of ionic liquid in the pores of a membrane support (supported ionic liquid membrane – SILM) to be applied in the extraction of mercaptans from a jet-fuel model stream, composed by a mixture of 1-hexanethiol and *n*-dodecane. Making use of the ionic liquids' negligible volatility and their very low mutual solubility with the aliphatic compounds, SILMs can be applied in a separation process in which vacuum is applied in the downstream side to remove the mercaptan selectively extracted by the SILM.

To understand the transport behavior of the mercaptan from the *n*-dodecane-rich phase to the ionic liquid, extraction experiments were carried out testing an ionic liquid from the family of the 1-ethyl-3-methylimidazolium cation. The systems tested presented low mass transfer rates, controlled by the mercaptan transport in the ionic liquid phase, which can be overcome due to the permanent removal of the ionic liquid in the SILM to the receiving phase.

The stability behavior of SILMs was also evaluated. The tested SILMs demonstrated an efficient immobilization of the ionic liquid and a good stability when using an organic feed and applying vacuum. However, the permeation of *n*-dodecane observed through the SILM polymeric support was noteworthy, even though the negligible mutual solubility between the *n*-dodecane and the studied ionic liquids.

This problem was surpassed by using ionic liquid as a receiving phase in the downstream side of a hollow fibre membrane contactor, in counter-flow with the feed stream. The ionic liquid tested was [C₂mim][CF₃SO₃], which has a very low mutual solubility with *n*-dodecane and, as a result, no dodecane was detected in the ionic liquid phase. This work opens the possibility for an integrated extraction/stripping of mercaptans from “jet-fuel” streams by using two membrane contactors in series, where extraction to a selected ionic liquid takes place in the first contactor, and stripping from the ionic liquid occurs in a second contactor. Using this configuration, the ionic liquids used can be continuously regenerated and recycled between both contactors.

6.6. References

1. Ho, W. S. W.; Sirkar, K. K., *Membrane Handbook*. Kluwer Academic Publishers: Boston 1992.
2. Yang, X.; Cao, Y.-M.; Wang, R.; Yuan, Q., Study on highly hydrophilic cellulose hollow fiber membrane contactors for thiol sulfur removal. *J Membrane Sci* **2007**, *305* (1–2), 247-256.
3. Gong, Y. W.; Liu, H. X.; Cheng, X. N., Experiments of mercaptans removal from FCC gasoline by NaOH aqueous in membrane contactor. *Pet Sci Technol* **2010**, *28* (9), 903-910.
4. Wang, W.; Wang, S.; Liu, H.; Wang, Z., Desulfurization of gasoline by a new method of electrochemical catalytic oxidation. *Fuel* **2007**, *86* (17–18), 2747-2753.
5. Seredych, M.; Wu, C. T.; Brender, P.; Ania, C. O.; Vix-Guterl, C.; Bandosz, T. J., Role of phosphorus in carbon matrix in desulfurization of diesel fuel using adsorption process. *Fuel* **2012**, *92* (1), 318-326.
6. Mochizuki, Y.; Sugawara, K., Selective adsorption of organic sulfur in coal extract by using metal-loaded carbon. *Fuel* **2011**, *90* (10), 2974-2980.
7. Liang, W. D.; Zhang, S.; Li, H. F.; Zhang, G. D., Oxidative desulfurization of simulated gasoline catalyzed by acetic acid-based ionic liquids at room temperature. *Fuel Process Technol* **2013**, *109*, 27-31.
8. Wang, J. L.; Zhao, D. S.; Li, K. X., Extractive Desulfurization of Gasoline Using Ionic Liquid Based on CuCl. *Pet Sci Technol* **2012**, *30* (23), 2417-2423.
9. Li, F. T.; Liu, Y.; Sun, Z. M.; Chen, L. J.; Zhao, D. S.; Liu, R. H.; Kou, C. G., Deep Extractive Desulfurization of Gasoline with xEt(3)NHCl center dot FeCl₃ Ionic Liquids. *Energ Fuel* **2010**, *24*, 4285-4289.
10. Alonso, L.; Arce, A.; Francisco, M.; Rodriguez, O.; Soto, A., Gasoline desulfurization using extraction with [C-8 mim][BF₄] ionic liquid. *Aiche J* **2007**, *53* (12), 3108-3115.
11. Huang, C. P.; Chen, B. H.; Zhang, J.; Liu, Z. C.; Li, Y. X., Desulfurization of gasoline by extraction with new ionic liquids. *Energ Fuel* **2004**, *18* (6), 1862-1864.
12. Taha, M. F.; Atikah, N.; Chong, F. K.; Shaharun, M. S., Oxidative Desulfurization of Dibenzothiophene From Model Oil Using Ionic Liquids As Extracting Agent. *Aip Conf Proc* **2012**, *1482*, 258-262.

13. Jin, Z. W.; Wang, S.; Wang, J. Q.; Zhao, M. X., Effects of plasticization conditions on the structures and properties of cellulose packaging films from ionic liquid [BMIM]Cl. *J Appl Polym Sci* **2012**, *125* (1), 704-709.
14. Rodríguez-Cabo, B.; Arce, A.; Soto, A., Desulfurization of fuels by liquid–liquid extraction with 1-ethyl-3-methylimidazolium ionic liquids. *Fluid Phase Equilib* **2013**, *356* (0), 126-135.
15. Krolikowski, M.; Walczak, K.; Domanska, U., Solvent extraction of aromatic sulfur compounds from n-heptane using the 1-ethyl-3-methylimidazolium tricyanomethanide ionic liquid. *J Chem Thermodyn* **2013**, *65*, 168-173.
16. Gabric, B.; Sander, A.; Bubalo, M. C.; Macut, D., Extraction of S- and N-Compounds from the Mixture of Hydrocarbons by Ionic Liquids as Selective Solvents. *Sci World J* **2013**.
17. Domańska, U.; Lukoshko, E. V.; Królikowski, M., Separation of thiophene from heptane with ionic liquids. *J Chem Therm* **2013**, *61* (0), 126-131.
18. Dharaskar, S. A.; Wasewar, K. L.; Varma, M. N.; Shende, D. Z.; Yoo, C. K., Deep Removal of Sulfur from Model Liquid Fuels using 1-Butyl-3-Methylimidazolium Chloride. *Procedia Engineering* **2013**, *51* (0), 416-422.
19. Wilfred, C. D.; Kiat, C. F.; Man, Z.; Bustam, M. A.; Mutalib, M. I. M.; Phak, C. Z., Extraction of dibenzothiophene from dodecane using ionic liquids. *Fuel Process Technol* **2012**, *93* (1), 85-89.
20. Kedra-Krolik, K.; Mutelet, F.; Moise, J. C.; Jaubert, J. N., Deep Fuels Desulfurization and Denitrogenation Using 1-Butyl-3-methylimidazolium Trifluoromethanesulfonate. *Energ Fuel* **2011**, *25* (4), 1559-1565.
21. Wang, Y.; Li, H.; Zhu, W.; Jiang, X.; He, L.; Lu, J.; Yan, Y., The Extractive Desulfurization of Fuels Using Ionic Liquids Based on FeCl₃. *Pet Sci Technol* **2010**, *28* (12), 1203-1210.
22. Yu, G. R.; Li, X.; Liu, X. X.; Asumana, C.; Chen, X. C., Deep Desulfurization of Fuel Oils Using Low-Viscosity 1-Ethyl-3-methylimidazolium Dicyanamide Ionic Liquid. *Ind Eng Chem Res* **2011**, *50* (4), 2236-2244.
23. Ferreira, A. R.; Freire, M. G.; Ribeiro, J. C.; Lopes, F. M.; Crespo, J. G.; Coutinho, J. A. P., Ionic liquids for thiols desulfurization: Experimental liquid–liquid equilibrium and COSMO-RS description. *Fuel* **2014**, *128* (0), 314-329.

24. Neves, L. A.; Nemestóthy, N.; Alves, V. D.; Cserjési, P.; Bélafi-Bakó, K.; Coelho, I. M., Separation of biohydrogen by supported ionic liquid membranes. *Desalination* **2009**, *240* (1-3), 311-315.
25. Scovazzo, P.; Kieft, J.; Finan, D. A.; Koval, C.; DuBois, D.; Noble, R., Gas separations using non-hexafluorophosphate [PF₆]⁽⁻⁾ anion supported ionic liquid membranes. *J Membrane Sci* **2004**, *238* (1-2), 57-63.
26. Seeberger, A.; Kern, C.; Jess, A., Gas Desulfurization by Supported Ionic Liquid Membranes (SILMs). *Oil Gas-Eur Mag* **2009**, *35* (2), 94-100.
27. de los Rios, A. P.; Hernandez-Fernandez, F. J.; Lozano, L. J.; Sanchez-Segado, S.; Ginesta-Anzola, A.; Godinez, C.; Tomas-Alonso, F.; Quesada-Medina, J., On the selective separation of metal ions from hydrochloride aqueous solution by pertraction through supported ionic liquid membranes. *J Membrane Sci* **2013**, *444*, 469-481.
28. Kilulya, K. F.; Msagati, T. A. M.; Mamba, B. B.; Ngila, J. C.; Bush, T., Ionic Liquid-Liquid Extraction and Supported Liquid Membrane Analysis of Lipophilic Wood Extractives from Dissolving-Grade Pulp. *Chromatographia* **2012**, *75* (9-10), 513-520.
29. Yahaya, G. O.; Hamad, F.; Bahamdan, A.; Tammana, V. V. R.; Hamad, E. Z., Supported ionic liquid membrane and liquid-liquid extraction using membrane for removal of sulfur compounds from diesel/crude oil. *Fuel Process Technol* **2013**, *113* (0), 123-129.
30. Fortunato, R.; Gonzalez-Munoz, M. J.; Kubasiewicz, M.; Luque, S.; Alvarez, J. R.; Afonso, C. A. M.; Coelho, I. M.; Crespo, J. G., Liquid membranes using ionic liquids: the influence of water on solute transport. *J Membrane Sci* **2005**, *249* (1-2), 153-162.
31. Lozano, L. J.; Godínez, C.; de los Ríos, A. P.; Hernández-Fernández, F. J.; Sánchez-Segado, S.; Alguacil, F. J., Recent advances in supported ionic liquid membrane technology. *J Membrane Sci* **2011**, *376* (1-2), 1-14.
32. Luis, P.; Neves, L. A.; Afonso, C. A. M.; Coelho, I. M.; Crespo, J. G.; Garea, A.; Irabien, A., Facilitated transport of CO₂ and SO₂ through Supported Ionic Liquid Membranes (SILMs). *Desalination* **2009**, *245* (1-3), 485-493.
33. Malik, M. A.; Hashim, M. A.; Nabi, F., Ionic liquids in supported liquid membrane technology. *Chem Eng J* **2011**, *171* (1), 242-254.

34. Rodríguez-Cabo, B.; Rodríguez, H.; Rodil, E.; Arce, A.; Soto, A., Extractive and oxidative-extractive desulfurization of fuels with ionic liquids. *Fuel* **2014**, *117*, Part A (0), 882-889.
35. Fortunato, R.; Afonso, C. A. M.; Reis, M. A. M.; Crespo, J. G., Supported liquid membranes using ionic liquids: study of stability and transport mechanisms. *J Membrane Sci* **2004**, *242* (1-2), 197-209.
36. Lu, L.; Cheng, S. F.; Gao, J. B.; Gao, G. H.; He, M. Y., Deep oxidative desulfurization of fuels catalyzed by ionic liquid in the presence of H₂O₂. *Energ Fuel* **2007**, *21* (1), 383-384.
37. Zhu, W.; Wu, P.; Yang, L.; Chang, Y.; Chao, Y.; Li, H.; Jiang, Y.; Jiang, W.; Xun, S., Pyridinium-based temperature-responsive magnetic ionic liquid for oxidative desulfurization of fuels. *Chem Eng J* **2013**, *229* (0), 250-256.
38. Yahaya, G. O.; Hamad, F.; Bahamdan, A.; Tammana, V. V. R.; Hamad, E. Z., Supported ionic liquid membrane and liquid-liquid extraction using membrane for removal of sulfur compounds from diesel/crude oil. *Fuel Process Technol* **2013**, *113*, 123-129.
39. Kulkarni, P. S.; Neves, L. A.; Coelho, I. M.; Afonso, C. A. M.; Crespo, J. G., Supported Ionic Liquid Membranes for Removal of Dioxins from High-Temperature Vapor Streams. *Environ Sci Technol* **2012**, *46* (1), 462-468.
40. Wang, F.; Zhang, Z.; Yang, J.; Wang, L.; Lin, Y.; Wei, Y., Immobilization of room temperature ionic liquid (RTIL) on silica gel for adsorption removal of thiophenic sulfur compounds from fuel. *Fuel* **2013**, *107* (0), 394-399.
41. Zhu, W.; Xu, D.; Li, H.; Ding, Y.; Zhang, M.; Liu, H.; Chao, Y., Oxidative Desulfurization of Dibenzothiophene Catalyzed by VO(acac)₂ in Ionic Liquids at Room Temperature. *Pet Sci Technol* **2013**, *31* (14), 1447-1453.
42. Lye, G. J.; Stuckey, D. C., Extraction of erythromycin-A using colloidal liquid aphrons: Part II. Mass transfer kinetics. *Chem Eng Sci* **2001**, *56* (1), 97-108.
43. Welty, J. R.; Wicks, C. E.; Wilson, R. E.; Rorrer, G. L., *Fundamentals of Momentum, Heat, and Mass Transfer*. John Wiley & Sons, Inc.: Hoboken, 2008.
44. Treybal, R. E., *Mass-transfer operations*. McGraw-Hill: Michigan, 1955.
45. Bedia, J.; Ruiz, E.; de Riva, J.; Ferro, V. R.; Palomar, J.; Jose Rodriguez, J., Optimized Ionic Liquids for Toluene Absorption. *Aiche J* **2013**, *59* (5), 1648-1656.

46. Reid, R. C.; Prausnitz, J. M.; Poling, B. E., *The properties of gases and liquids*. 4th ed.; McGraw-Hill: New York, 1987.
47. E.W. Lemmon, M. O. M. a. D. G. F., Thermophysical Properties of Fluid Systems. In *NIST Chemistry WebBook, NIST Standard Reference Database Number 69*, Eds. P.J. Linstrom and W.G. Mallard, National Institute of Standards and Technology: Gaithersburg.
48. Shah, M. R.; Anantharaj, R.; Banerjee, T.; Yadav, G. D., Quaternary (liquid plus liquid) equilibria for systems of imidazolium based ionic liquid plus thiophene plus pyridine plus cyclohexane at 298.15 K: Experiments and quantum chemical predictions. *J Chem Thermodyn* **2013**, *62*, 142-150.
49. Anantharaj, R.; Banerjee, T., Fast Solvent Screening for the Simultaneous Hydrodesulfurization and Hydrodenitrification of Diesel Oil Using Ionic Liquids. *J Chem Eng Data* **2011**, *56* (6), 2770-2785.
50. Anantharaj, R.; Banerjee, T., COSMO-RS based predictions for the desulphurization of diesel oil using ionic liquids: Effect of cation and anion combination. *Fuel Process Technol* **2011**, *92* (1), 39-52.
51. Schreiner, C.; Zugmann, S.; Hartl, R.; Gores, H. J., Fractional Walden Rule for Ionic Liquids: Examples from Recent Measurements and a Critique of the So-Called Ideal KCl Line for the Walden Plot†. *J Chem Eng Data* **2009**, *55* (5), 1784-1788.
52. Kumar, A. A. P.; Banerjee, T., Thiophene separation with ionic liquids for desulphurization: A quantum chemical approach. *Fluid Phase Equilib* **2009**, *278* (1-2), 1-8.
53. Lewis, J. B., The mechanism of mass transfer of solutes across liquid-liquid interfaces: Part I: the determination of individual transfer coefficients for binary systems. *Chem Eng Sci* **1954**, *3* (6), 248-259.
54. Taylor, R.; Krishna, R., *Multicomponent Mass Transfer*. John Wiley & Sons, Inc.: New York, 1993.
55. Wilfred, C. D.; Man, Z.; Chan, Z. P., Predicting methods for sulfur removal from model oils using COSMO-RS and partition coefficient. *Chem Eng Sci* **2013**, *102*, 373-377.
56. Neves, L. A.; Crespo, J. G.; Coelho, I. M., Gas permeation studies in supported ionic liquid membranes. *J Membrane Sci* **2010**, *357* (1-2), 160-170.

57. Albo, J.; Santos, E.; Neves, L. A.; Simeonov, S. P.; Afonso, C. A. M.; Crespo, J. G.; Irabien, A., Separation performance of CO₂ through Supported Magnetic Ionic Liquid Membranes (SMILMs). *Sep Purif Technol* **2012**, *97*, 26-33.
58. Scovazzo, P.; Havard, D.; McShea, M.; Mixon, S.; Morgan, D., Long-term, continuous mixed-gas dry fed CO₂/CH₄ and CO₂/N₂ separation performance and selectivities for room temperature ionic liquid membranes. *J Membrane Sci* **2009**, *327* (1–2), 41-48.
59. Klamt, A.; Eckert, F., COSMO-RS: a novel and efficient method for the a priori prediction of thermophysical data of liquids. *Fluid Phase Equilib* **2000**, *172* (1), 43-72.
60. Cascon, H. R.; Choudhari, S. K., 1-Butanol pervaporation performance and intrinsic stability of phosphonium and ammonium ionic liquid-based supported liquid membranes. *J Membrane Sci* **2013**, *429* (0), 214-224.
61. Lin, Y.; Wang, F.; Zhang, Z.; Yang, J.; Wei, Y., Polymer-supported ionic liquids: Synthesis, characterization and application in fuel desulfurization. *Fuel* **2014**, *116* (0), 273-280.
62. Noble, R. D.; Gin, D. L., Perspective on ionic liquids and ionic liquid membranes. *J Membrane Sci* **2011**, *369* (1-2), 1-4.

Chapter 7

Mercaptans Extraction from “Jet-Fuel” assisted by Ionic Liquids in Hollow Fiber Membrane Contactors

Ferreira, A. R.; Neves, L. A.; Ribeiro, J. C.; Lopes, F. M.; Coutinho, J. A. P.;
Coelhoso, I. M.; Crespo, J. G.

Submitted at Journal of Membrane Science

7.1. Introduction

Regarding the extraction of mercaptans (aliphatic sulfur species) from “jet-fuel” streams, our previous work¹ showed the high potential of ionic liquids as extracting solvents, despite the low mercaptan affinity towards the ionic liquids. This feature makes the conventional liquid-liquid extraction not viable due to the high volumes of extracting ionic liquid that would be required. However, the ionic liquids studied and *n*-dodecane, used as the “jet-fuel” model, presented almost negligible mutual solubility, which avoids mutual contamination and losses of fuel and ionic liquid in the separation process. For this reason, the use of ionic liquids as solvents is potentially interesting, as discussed in our previous work,¹ where supported ionic liquid membranes (SILMs) were studied. SILMs were evaluated for the selective extraction of a mercaptan target solute applying vacuum in the downstream side, in order to benefit from the very low mutual solubility between the aliphatic compounds and the ionic liquids. Though, it was observed a significant permeation of *n*-dodecane through the SILM polymeric support. This problem was overcome using the ionic liquid as a receiving phase and no dodecane was detected, opening opportunities for new approaches. This extraction process experiment was carried out in a hollow fiber membrane contactor, in a counter-current flow mode.

Hollow fiber membrane contactors have proven to be very advantageous in separation processes, as shown by the large variety of systems tested in both liquid and gas separations,²⁻⁹ including mercaptans removal from a simulated naphtha stream under a reactive extraction with an aqueous NaOH solution.¹⁰⁻¹¹ Membrane contactors provide large interfacial area between the two contacting phases, through the pores of the membrane, not requiring density differences and dispersion between the two phases. Consequently, back-mixing and formation of stable emulsions are prevented. Additionally, each fluid phase can be independently operated within a wide range of flow rates.^{6, 9}

The present work addresses the study of an integrated process using hydrophobic hollow fiber membrane contactors of polypropylene, where the selective mercaptan extraction occurs in a first membrane contactor and, simultaneously, regeneration takes place in a second contactor aiming at a complete removal of the mercaptan from the ionic liquid. This configuration offers several advantages, such as the reuse of the ionic liquid in the extraction process, by recirculation in a closed loop between the two membrane contactors. Therefore, the volume of ionic liquid required is much lower than in conventional equipment. Moreover, the driving force for solute transport is maximized, which is particularly important when the partitioning of the target solute is not

thermodynamically favored. The ionic liquid regeneration can be performed by different techniques, such as direct distillation,¹²⁻¹⁵ evaporation,¹⁶⁻¹⁸ re-extraction by an organic or aqueous solvent¹⁹⁻²¹ or by using supercritical carbon dioxide²²⁻²⁴, membrane separation,²⁵⁻²⁷ stripping with a sweep gas or vacuum, with or without thermal treatment,²⁸⁻³² or by a combination of methods. In this work, stripping applying vacuum and by using a sweep gas in the downstream of the membrane compartment were studied for the regeneration of the ionic liquid.

7.2. Experimental Section

The membrane contactors experiments were carried out using three different configurations in order to study the most promising set-up for the mercaptans removal from a jet-fuel model mixture. The configurations tested were: single extraction, simultaneous extraction and stripping with vacuum, and simultaneous extraction and stripping by using a sweep gas.

The most suitable ionic liquid to be used in the extraction of mercaptans from a jet-fuel supply should present high affinity to the target compound and low mutual solubility with other feed compounds, avoiding their co-extraction,³³ and should present high mass transfer kinetics coefficients. Based on our previous work¹ on liquid-liquid equilibrium and mass transfer kinetics in a classical liquid-liquid extraction process, the ionic liquid that was identified to fulfill these separation requirements was the 1-ethyl-3-methylimidazolium triflate, $[C_2mim][CF_3SO_3]$.³³

To perform these experiments, two hollow fiber membrane contactors with porous polypropylene membranes were selected based on their wetting properties. These hydrophobic membranes are not easily wetted by the selected ionic liquid. Therefore, in the first extraction contactor, the membranes pores are wetted and filled with the n-dodecane phase, while in the stripping contactor, the pores are filled by air (both in the case of the vacuum stripping and the sweep gas stripping). This selection of an hydrophobic material allows, therefore, to minimize the mass transfer resistance for solute transport through the membrane area. Additionally, given the positive mercaptan partition towards the hydrocarbon feed, it is also favorable to have the feed wetting the membrane pores, instead of the ionic liquid.

7.3. Materials

The jet-fuel feed solution is composed by the hydrocarbon *n*-dodecane and circa 1% of the mercaptan 1-hexanethiol, which were acquired from Sigma-Aldrich, with 99% and 95% purity, respectively.

The [C₂mim][CF₃SO₃] ionic liquid was acquired from IoLiTec, Ionic Liquid Technology, Germany, with purity superior to 99% and, before use, it was vacuum dried (1 mPa) at 313.2 K, under constant stirring for a minimum of 24h.

The sweep gas selected to perform the re-extraction of the mercaptan from the ionic liquid was compressed air, since it is the most economic option.

The membrane contactors used were supplied by Membrana GmbH, Germany. The single extraction and the extraction stage in the integrated configurations were carried out in a Liqui-cel MiniModule[®] Contactor, while for the ionic liquid regeneration stage, either by vacuum or sweep gas, it was used a Liqui-cel ExtraFlow[®] Contactor. Both modules comprise microporous polypropylene hollow fiber membranes by Celgard[®], Hoechst Celanese, Germany. In the case of the MiniModule[®] the membranes are Celgard[®] X-10, while for the ExtraFlow[®], it was used the Celgard[®] X-50 type fibers. Additional information about the membrane contactors and fibers can be accessed in Table 7.1.

Table 7.1 Characteristics of the laboratory Liqui-cel MiniModule® and Extra-flow Module®Contactor, and respective hollow fibers properties, Celgard X-10 and Celgard X-50.

<i>Module</i>	Mini-module	<i>Extra-flow</i>
Shell inner diameter (cm)	2.5	6.6
Length (cm)	20	28
Effective area (m ²)	0.23	1.4
Specific area (cm ² /cm ³)	40	40
Number of fibers	2100	10200
<i>Membrane fiber</i>	<i>Celgard X-10</i>	<i>Celgard X-50</i>
Internal diameter (μm)	240	220
External diameter (μm)	300	300
Porosity (%)	30	40
Effective pore size (μm)	0.05	0.04
Pore dimensions (μm)	0.05 x 0.15	Not available
Effective fiber length (cm)	16	16

7.3.1. Experimental procedure

The membrane contactor experimental set-up, for the single extraction of 1-hexanethiol from the model feed stream, is depicted in Figure 7.1. A second membrane contactor was coupled to the extraction module to perform the ionic liquid regeneration, either by applying vacuum or a sweep gas, as can also be seen in Figure 7.1.

Closed vessels (500 mL) with small headspaces were used in order to minimize the loss of the feed compounds to the atmosphere and variations of phase volume and concentration.

In the extraction module the feed was pumped into the shell side, while the ionic liquid extracting phase was circulated in counter-current inside the hollow fibers (lumen side). This operating mode was selected due to the different viscosities of the fluids, being thirty times higher for the ionic liquid [C₂mim][CF₃SO₃] compared with the hydrocarbon feed. Therefore, circulating the ionic liquid in the lumen side allowed for a better fluid hydrodynamics and avoided death volumes that could easily occur in the shell side. For

this reason, the ionic liquid was also circulated in the lumen side of the regeneration module.

In order to assure appropriate starting conditions, all independent experiments started by circulating the ionic liquid in the lumen side and, only after completion of this procedure, the feed stream was then circulated in the shell side. This procedure assured that no feed stream was able to permeate through the pores to the lumen side (remember that the membrane used is hydrophobic and, therefore, wetted by the *n*-dodecane feed).

The higher viscosity of the ionic liquid promoted a slight overpressure on the lumen side, which also helped to obtain a more stable interface between the feed and the ionic liquid in the extraction module. For the integrated process, the same procedure was adopted, circulating the ionic liquid in each contactor before introducing the feed in the extraction contactor in order to reduce the delay related with the regeneration of the ionic liquid.

During all experiments, representative samples of the feed and ionic liquid phases (0.3 – 0.5 ml) were collected and analyzed along time.

During the experiments, the flow-rate of each fluid was controlled by magnetic drive gear pumps (Ismatec, Switzerland), and measured using variable area flowmeters at the exit of the contactor. These pumps allowed for eliminating flow-rate oscillations and pulsating effects. During the experiments, the pressures at the inlet and outlet of the shell and lumen were also measured with analogical manometers. To achieve a better control of the operation temperature, the feed and ionic liquid reservoirs and the membrane contactor were jacketed by circulating thermo-regulated water using a thermostat bath (Julabo MC), with a temperature stability of ± 0.01 K. The temperature in the vessels was measured using a thermometer (± 0.1 K).

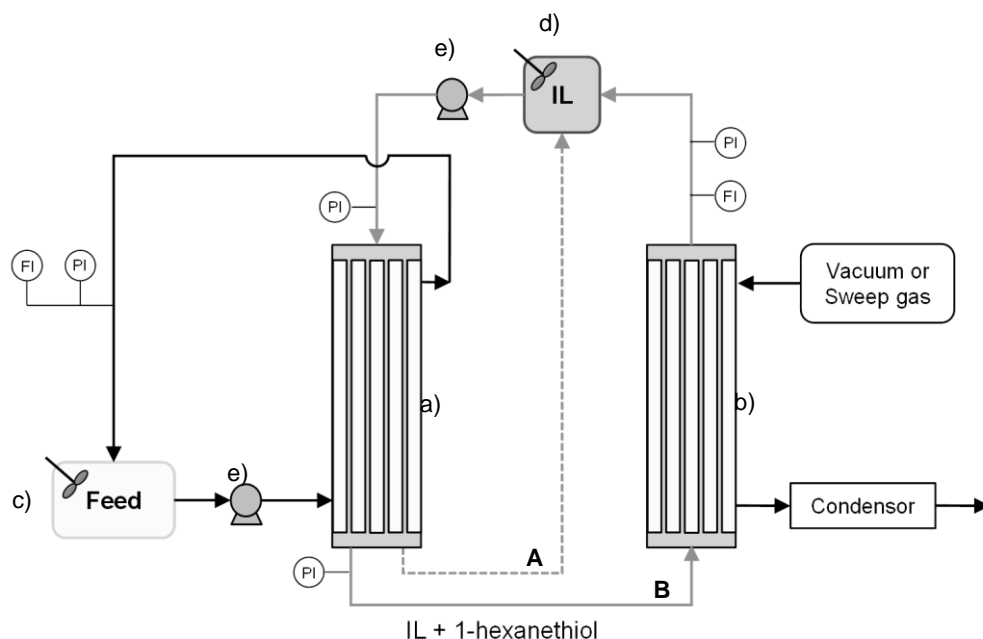


Figure 7.1 Experimental set-up. **A** indicates the ionic liquid direction in the single extraction configuration, and **B** in the integrated extraction and regeneration configuration. a) extraction hollow fiber membrane contactor, b) regeneration hollow fiber membrane contactor, c) feed stirred vessel, d) ionic liquid stirred vessel, e) recirculating pump, PI = pressure indicator, and FI = flow indicator.

7.3.2. Operating conditions

All experiments for the study of the removal of mercaptans were carried out under controlled operating conditions. It was decided to operate at a temperature of 298.15 ± 0.2 K. However, as discussed later in this work, higher operating temperatures were also considered and their potential impact was simulated, supported on the knowledge about their effect on viscosity and diffusion coefficient of the target solute.

For all configurations studied, the modules were operated in a counter-current mode in order to guarantee the highest possible mass transfer.

In terms of selection of the stream flow rates, some precautions were considered: it was assured that the pressure drop inside the membrane fibers does not overcome the pores' breakthrough pressure (minimum pressure required to force the ionic liquid into the membrane pores), in order to maintain a stable interface between the ionic liquid phase and the feed phase.

The breakthrough pressure (ΔP_{cr}) was determined using the Young-Laplace equation, $\Delta P_{cr} = \frac{2\gamma \cos \theta}{r_{pore}} \times 10^{-5}$ bar.⁸ For the interfacial tension (γ) determination, it was assumed, that the low concentration of the mercaptan in the feed phase does not have a significant impact on the interfacial tension. Thus, the interfacial tension measured between the *n*-dodecane and the [C₂mim][CF₃SO₃], at 298.15 K, by the du Nouy ring method using a Attension Sigma 702ET, was of 15.2 mN.m⁻¹. The contact angle between the ionic liquid and the polypropylene membrane θ has the value of 121° (2.11 rad). The r_{pore} is the pore radius (m), assuming parallel cylindrical pores.

Taking into account the ellipsoidal shape of the pores of the membrane Celgard X-10, an average breakthrough pressure of 3.85 bar was obtained. Therefore pressures differences up to 3.85 bar can be applied without interface disturbance and ionic liquid penetration inside the membrane pores. Experimentally, the flow rate of the ionic liquid in the lumen side of both contactors, was set at 0.96 cm³/s for all experiments. Under these conditions, the inlet pressure for the ionic liquid side was observed to be at 0.65 bar during the single extraction experiments, and between 0.70 bar to 0.75 bar for the integrated configuration, to assure a stable interface. The outlet pressures were kept at atmospheric pressure and 0.2 bar, respectively, for the single extraction and the integration operation. This last value of outlet pressure corresponded to the inlet pressure in the regeneration contactor.

For the feed flow, circulating in the shell side of the extraction contactor, it was set at a flow-rate of 6.5 cm³/s. The operating pressures for the feed phase, in the extraction module, were lower than 0.05 bar at the inlet, and in its exit was atmospheric pressure.

From these pressures values, the membrane pressure differences varied from 0.7 to 0.0 bar, due to the pressure drop observed along the lumen side, quite below the estimated breakthrough pressure.

The fluid velocity for the feed phase, considering the hydraulic diameter, is 1.90 cm.s⁻¹, and for the ionic liquid phase, the velocities varied between 1.01 cm.s⁻¹ and 1.04 cm.s⁻¹ in the extraction module and between 0.248 cm.s⁻¹ and 0.255 cm.s⁻¹ in the regeneration module.

In the integrated set-up, vacuum or sweep gas were applied at the module shell side. The experiments started by testing vacuum at a pressure of 1 mbar. For the experiments carried out using the sweep gas, compressed air flow rates of 1.23 cm.s⁻¹, 7.84 cm.s⁻¹ and 19.30 cm.s⁻¹ were tested to study its impact in the mass transfer.

The membrane contactors were cleaned after each experiment in order to maintain the same initial conditions. The washing procedure consisted in removing the highest amount of the solvents without using any external agents. Then, water was added to the lumen side for removing the ionic liquid and, in the feed side, isopropanol helped to eliminate the hydrocarbon compounds. This procedure was repeated two to three times and then compressed air was passed through the system until it was completely dried and free of solvents.

7.3.3. Analytical methods

The concentration of the model mercaptan compound was measured in each stream by a potentiometric titration, using a TitrLab® 865 titration workstation, with an alcoholic solution of AgNO₃ at 0.01 M, according to the ASTM D3227 standard³⁴. The ionic liquid content in the feed phase was analyzed by UV spectroscopy, using a Helios α UV-Vis spectrophotometer from Thermo Scientific, though no peaks corresponding to the ionic liquid were found, assuring that no contamination of the feed stream by the ionic liquid took place (at least, not above the detection limit). The *n*-dodecane content in the ionic liquid stream was determined gravimetrically ($\pm 10^{-4}$ g) using a vacuum drying process and was found negligible. Nevertheless, even considering that the contents of ionic liquid in *n*-dodecane and of *n*-dodecane in ionic liquid-rich streams are insignificant, it must be kept in mind that traces of these compounds can occur at concentrations below the detection threshold.

7.4. Mass transfer model

In order to model the extraction of 1-hexanethiol from the feed stream into the ionic liquid phase in the all the configurations tested, single extraction and integrated extraction/stripping, a material balance was performed to the membrane contactor and vessel.

Considering the extraction module and assuming equilibrium at the feed/ionic liquid interface, the differential mass balance is described as:

$$-Q_f \frac{dC_f}{dA_M} = K_f (C_f - C_f^*) \quad (7.1)$$

where Q_f ($\text{m}^3 \cdot \text{s}^{-1}$) is the feed flow rate, C_f and the C_f^* ($\text{mol} \cdot \text{m}^{-3}$) are the 1-hexanethiol concentration in the phase under consideration and in equilibrium with the 1-hexanethiol concentration in the other phase. K_f represents the overall mass transfer coefficient ($\text{m} \cdot \text{s}^{-1}$), and $A_M = \pi d_{fi} L_f N_f$ (m^2) the module membrane area, where d_{fi} is the internal fiber diameter (m), L_f is the fiber length (m) and N_f the number of fibers in the membrane contactor.

The differential mass balance to the feed fluid vessel can be written as:

$$-V_f \frac{dC_f}{dt} = Q_f (C_f^{out} - C_f^{in}) \quad (7.2)$$

where V_f (m^3) is the feed phase volume, C_f^{in} and C_f^{out} ($\text{mol} \cdot \text{m}^{-3}$) are the inlet and outlet 1-hexanethiol concentrations in the membrane contactor. The operating time is defined by t (s).

Since the feed stream is operated with recirculation and assuming that the driving force variation in a single passage over the membrane contactor can be assumed negligible for the small interfacial area, A_E (0.23 m^2), and the fluid vessels have a high degree of mixture, which turns the mercaptan concentration in the feed vessel equal to the inlet concentration of the module, equations 7.1 and 7.2 can be combined in the following equation:

$$-V_f \frac{dC_f}{dt} = K_f A_E (C_f - C_f^*) \quad (7.3)$$

The C_f^* is related with the 1-hexanethiol concentration in the ionic liquid rich phase (C_{IL}) applying the distribution ratio (D) definition:

$$C_f^* = \frac{C_{IL}}{D} \quad (7.4)$$

The distribution ratio was determined in a previous work ¹ and a value of 0.095 ± 0.026 for the system $[C_2mim][CF_3SO_3] + 1\text{-hexanethiol} + n\text{-dodecane}$ was obtained.

For the single extraction process, the concentration C_{IL} is obtained from a simple mass balance to the solute, at the initial conditions, in the feed phase and ionic liquid phase, C_f^0 and C_{IL}^0 , respectively:

$$C_{IL} = \frac{V_f}{V_{IL}}(C_f^0 - C_f) \quad t = 0, C_f = C_f^0, C_{IL} = C_{IL}^0 = 0 \quad (7.5)$$

The overall mass transfer coefficient, K_f , is determined by fitting the experimental mercaptan concentration in function of time with the integration of equations 7.3, 7.4 and 7.5, considering the initial conditions.

In the case of the integrated process, when applying regeneration by sweep gas, a differential material balance to the ionic liquid must also be done, to a more accurate description of the solute mass transport in this stream:

$$V_{IL} \frac{dC_{IL}}{dt} = K_E A_E (C_f - C_f^*) - K_R A_R (C_{IL} - C_{IL}^*) \quad (7.6)$$

In this equation, K_E and K_R are the overall mass transfer coefficients associated with each module of the integrated process, extraction and regeneration, with the respective membrane areas A_E and A_R . Here, C_{IL}^* is the concentration of mercaptan in the ionic liquid in equilibrium with its concentration in the gaseous phase (C_g) inside the pore of the membrane ($C_{IL}^* = \frac{C_g}{H}$, H = Henry's constant). The value of H was estimated ³⁵ by the product of the vapor pressure of 1-hexanethiol at the operating temperature (298.15 K) and the activity coefficient at infinite dilution. The H value was calculated to be 0.0022 ($\text{mol.m}^{-3}/\text{mol.m}^{-3}$).

By a material mass balance to the system, the mercaptan concentration in the gas phase can be described as:

$$C_g = \frac{V_f(C_f^0 - C_f) - C_{IL}V_{IL}}{tQ_g} \quad t = 0, C_f = C_f^0, C_{IL} = C_{IL}^0 = 0, C_g = C_g^0 = 0 \quad (7.7)$$

Considering an efficient regeneration process where the mercaptan is completely removed from the ionic liquid ($C_{IL} \approx 0 \text{ mol.m}^{-3}$), and assuming the extraction process as the limiting stage of the integrated process, the overall mass transfer can be determined by fitting the experimental mercaptan concentration of the feed phase with equation 7.3 for $C_{IL}^* = 0$.

The resistances-in-series model, based on the combination of the individual mass transfer resistances, is helpful understanding the mercaptan extraction/stripping process.

Equations 7.8 and 7.9 describe the resistances in the extraction and regeneration modules, respectively:

$$\frac{1}{K_E} = \frac{d_{fi,E}}{d_{fo,E}k_f} + \frac{d_{fi,E}}{d_{flm,E}k_{M_f}} + \frac{1}{Dk_{IL,E}} \quad (7.8)$$

$$\frac{1}{K_R} = \frac{d_{fi,R}}{d_{fo,R}k_gH} + \frac{d_{fi,R}}{d_{flm,R}k_{M_g}H} + \frac{1}{k_{IL,R}} \quad (7.9)$$

K_E and the K_R (m.s^{-1}) represent the overall mass transfer coefficient for the extraction and the regeneration process, respectively. In terms of the individual mass transfer coefficients, they are described by k_f , $k_{IL,E}$, $k_{IL,R}$ and k_g (m.s^{-1}) for the boundary films associated with the feed, the ionic liquid and the gaseous phase, respectively. The d_{fi} , d_{fo} and d_{flm} (m) are the inner, outer and logarithmic mean fiber diameters in the extraction and regeneration modules.

The mass transfer coefficients associated with transport through the membrane in each module are the k_{M_f} and k_{M_g} (m.s^{-1}) and are determined accordingly with the phase wetting the membrane:

$$k_{M_f} = \frac{\mathfrak{D}_{M_f} \varepsilon_{M,E}}{\delta_{M,E} \tau_{M,E}} \quad \text{and} \quad k_{M_g} = \frac{\mathfrak{D}_{M_g} \varepsilon_{M,R}}{\delta_{M,R} \tau_{M,R}} \quad (7.10)$$

where \mathfrak{D} is the diffusion coefficient ($\text{m}^2.\text{s}^{-1}$) at a T temperature (K), ε , δ and τ are the porosity, thickness (m) and tortuosity of the membrane, in the extraction (E) and regeneration (R) modules.

As shown in our previous work,¹ due to the high ionic liquid viscosity and low mercaptan diffusion in the ionic liquid, the ionic liquid phase presents the highest mass transfer resistance to the transport of mercaptan. Moreover, since the membranes in the extraction and regeneration modules are wetted by the feed and gas phases (not-controlling phases), respectively, the resistance in series equations can be simplified to the resistance in the ionic liquid boundary film.

Calculation methods

The fitting of the mercaptan concentration variation with time, for the various experiments were performed using the *nlinfit* routine, from the software package MatlabTM, from Math Works Inc. (USA). The overall mass transfer coefficients for the single extraction process and for the integrated process were determined by performing a nonlinear regression, using the iterative least squares algorithm, and simultaneously solving the differential equations system previously specified for each configuration. The parameters' errors were calculated within a 95% confidence interval.

7.5. Results and discussion

The work here developed aims at demonstrating the potential use of membrane contactors and ionic liquids in an efficient desulfurization process. The liquid extraction process using membrane contactors is explored using a mixture of 1-hexanethiol and *n*-dodecane, as jet-fuel model feed, and the ionic liquid [C₂mim][CF₃SO₃]. This ionic liquid, was selected in order to avoid the co-extraction of the *n*-dodecane and other fuel compounds.

The methodology followed in this work involved a pre-evaluation of the membrane contactor applicability in the extraction process, followed by regeneration of the extractant in a coupled contactor. The regeneration step aims at re-extract the target solute from the ionic liquid, and reuse this extractant in the extraction module, in a closed loop, allowing for reducing the amount required and costs associated with the extractant.

This integrated process, proposed for the removal of mercaptans from the jet-fuels, is not only dependent from the behavior of the extraction step, but it is also determined by the stripping process and its regeneration efficiency.

7.5.1. Single extraction in a membrane contactor

The 1-hexanethiol extraction was firstly studied in a single membrane contactor and the experimental data is plotted in Figure 7.2. The 1-hexanethiol concentration profile obtained is very regular and smooth, reaching equilibrium at circa 1.5h of operation time. Comparing this profile with the profile obtained in mass transfer studies in an extraction cell, previously reported,¹ it was found that these extraction profiles present the same behavior, except for the time needed to reach equilibrium, due to the different interfacial areas available for mass transfer. As expected, the mass transfer rate was faster using the membrane contactor, due to a higher interfacial area of 0.23 m² (3225 m²/m³) assured by the membrane contactor, against the 0.0002 m² (20 m²/m³) available in the stirred extraction cell.

Regarding the overall mass transfer coefficient for this single extraction, the experimental concentration data were fitted considering equations 7.3, 7.4 and 7.5 and the value obtained was $7.88 \pm 0.35 \times 10^{-8} \text{ m}\cdot\text{s}^{-1}$, which can be considered relatively low when comparing with other extraction systems using this type of equipment.

Though the low mass transfer rate, the mercaptan extraction using the selected ionic liquid shows a high potential since, as a result of the very low mutual solubility between the ionic liquid and the *n*-dodecane, no *n*-dodecane was detected in the ionic liquid phase. The ionic liquid worked as a liquid barrier to the transport of the *n*-dodecane and the undesirable co-extraction of the fuel compounds was prevented.

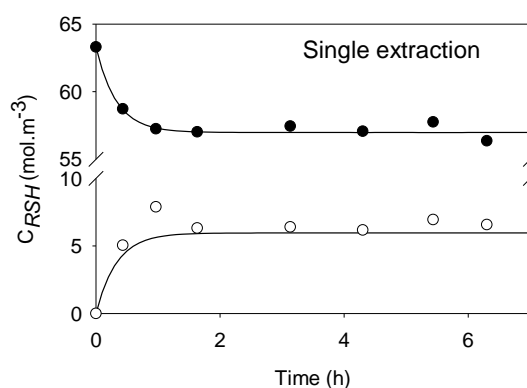


Figure 7.2 1-hexanethiol experimental concentration profile in the *n*-dodecane and ionic liquid rich-phases (filled and empty symbols, respectively), and data fitting (lines), for the single extraction configuration, at 298.2 K and atmospheric pressure. *Extraction module*: shell side – jet-fuel model stream (1-hexanethiol + *n*-dodecane); lumen side – ionic liquid ([C₂mim][CF₃SO₃]).

7.5.2. Simultaneous extraction and regeneration in membrane contactors

The thermodynamic equilibrium observed and the consequent low extraction capacity is a limitation for the extraction process, even in a membrane contactor with the high interfacial area that favors high mass transfer rates. However, this constrain can be solved by adding a regeneration step of the ionic liquid, which impacts favorably on the extraction step by the continuous cleaning of the ionic liquid and increasing of the driving force for solute extraction.

The following experiments aim at evaluating the regeneration technique more suitable to be integrated with the extraction unit. The extraction and regeneration processes were run in two membrane contactors (Figure 7.1). The first experiment consisted in testing the use of vacuum in the shell side of the second contactor to strip the mercaptan from the ionic liquid stream. The second approach used a sweep gas stream also circulated in the shell side. In these experiments, the ionic liquid stream was operated in a closed cycle, between the extraction and the regeneration contactors, and the effect of the regeneration process was monitored by analyzing the mercaptan concentration variation in the jet-fuel feed phase.

7.5.2.1. Vacuum-based regeneration

The regeneration with vacuum was performed at 1 mbar and room temperature to allow the evaporation of 1-hexanethiol at 298.2 K under vacuum, which has a vapor pressure around 6 mbar at this temperature. The experimental concentrations of mercaptan in the feed and the ionic liquid phase are plotted in Figure 7.3.

As can be observed from the mercaptan extraction results, its extraction from the feed stream stops after 2h and tends to a constant value. The use of vacuum does not have a positive impact on the extraction of the target solute and, therefore, cannot be considered as a potential process for the re-extraction of mercaptans from the ionic liquid extractant. This unfavorable behavior results from the partial penetration of the ionic liquid inside the pores of the polypropylene membrane. Under these circumstances, the ionic liquid wets the pores of fibers creating an additional significant mass transfer resistance to the process of solute transfer. This additional resistance cannot be neglected since the ionic liquid has a high viscosity (41 mPa.s). Consequently, the transport of mercaptan by diffusion from the ionic liquid phase to the vacuum phase becomes extremely slow. This negative effect on the overall mass transfer of solute does not allow for an effective regeneration of the extractant in a short operating time. This problem was difficult to anticipate, since the ionic liquid has a negligible vapor pressure

and, from our previous work ¹, the polypropylene membrane tested is not easily wetted by the $[\text{C}_2\text{mim}][\text{CF}_3\text{SO}_3]$ ionic liquid. The continuous application of vacuum in the downstream circuit might force its partial penetration into the pores of the polypropylene membrane, reducing the mass transfer rate.

Taking this result into consideration, it was decided to evaluate the removal of the mercaptan compound from the ionic liquid phase by applying a sweep gas stream, avoiding the displacement of the ionic liquid to the pores of the membrane.

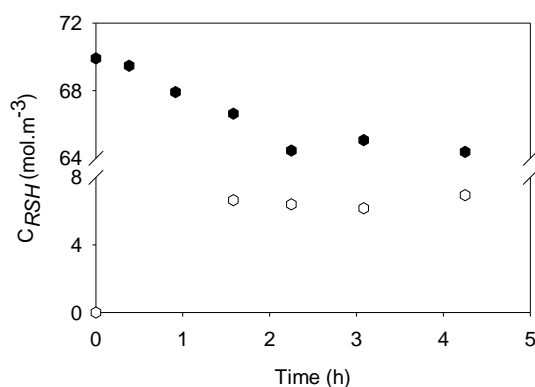


Figure 7.3 1-hexanethiol experimental concentration profile in the *n*-dodecane and ionic liquid phases (filled and empty symbols, respectively), for the extraction/vacuum stripping configuration, at 298.2 K and atmospheric pressure. *Extraction module*: shell side – jet-fuel model stream (1-hexanethiol + *n*-dodecane); lumen side – ionic liquid ($[\text{C}_2\text{mim}][\text{CF}_3\text{SO}_3]$). *Regeneration module*: shell side – vacuum; lumen side – ionic liquid ($[\text{C}_2\text{mim}][\text{CF}_3\text{SO}_3]$).

7.5.2.2. Sweep-gas based regeneration

As an alternative to vacuum regeneration, a sweep gas stream of compressed air was used in the downstream circuit of the second membrane contactor, aiming an efficient cleaning of the ionic liquid. This unit worked under gentle conditions of temperature and pressure, avoiding the permeation of the ionic liquid through the membrane.

Three sweep gas flow-rates were tested with linear velocities from 1.23 cm.s⁻¹ to 19.30 cm.s⁻¹ and their impact on the mercaptan extraction is shown in Figure 7.4. Comparing the results obtained, it is possible to observe that the use of sweep gas allows overcoming the unfavorable low thermodynamic equilibrium observed in the single extraction (Figure 7.2), since it was possible to reduce the mercaptan concentration in the feed stream to values very close to zero, i.e. lower than 2 ppm, as targeted by the

legislation. This result proves the high potential of this integrated process as an alternative method to the deep-desulfurization process. This process not only allows the production of ultra-low sulfur fuels, but also allows reducing the operating costs due to the mild conditions of temperature and pressures applied.

In what concerns the mass transfer occurring in these processes, a significant variation of the mercaptan concentration in the ionic liquid phase is observed for different experiments. It is shown that the increase of the sweep gas flow rate leads to a more efficient removal of mercaptan from the ionic liquid and to a consequent improvement of the extraction of the mercaptan from the feed stream. This increase of the gas velocity in the shell side of the module reduces the residence time of the gas inside the membrane contactor, which increases the driving force for mass transfer by lowering the concentration of this solute in the gaseous phase.

The effect of increasing the velocity of the sweep gas on the extraction process is important up to a point where a complete re-extraction of the mercaptan from the ionic liquid is achieved. For higher sweep gas flow-rates (lower residence time), at which the regeneration is complete, the integrated process becomes controlled by the extraction of the mercaptan from the feed phase.

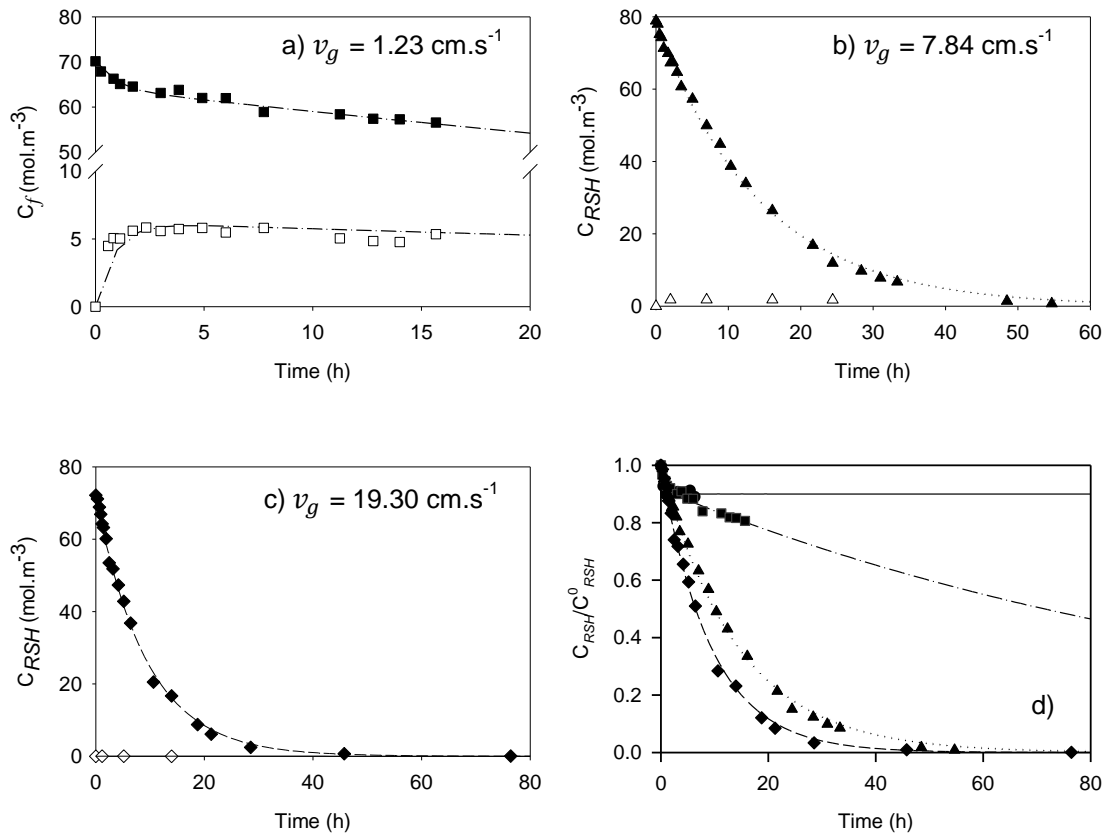


Figure 7.4 1-hexanethiol experimental concentration profile in the *n*-dodecane and ionic liquid phases (filled and empty symbols, respectively) and data fitting (lines), for the extraction/sweep gas stripping configurations, at 298.2 K and atmospheric pressure, with **a)** sweep gas velocity of 1.23 cm.s⁻¹ (square symbols and dot-dashed lines), **b)** sweep gas velocity of 7.84 cm.s⁻¹ (triangle symbols and dotted lines) and **c)** sweep gas velocity of 19.30 cm.s⁻¹ (diamond symbols and dashed lines). And **d)** comparison between the single extraction (solid line) and the three extraction/sweep gas stripping systems studied (dodecane phase). *Extraction module*: shell side – jet-fuel model (1-hexanethiol + *n*-dodecane); lumen side – ionic liquid ([C₂mim][CF₃SO₃]). *Regeneration module*: shell side – sweep gas; lumen side – ionic liquid ([C₂mim][CF₃SO₃]).

Mass transfer kinetics

For the case of the lower sweep gas flow rate ($v_g = 1.23$ cm.s⁻¹), where the mercaptan concentration in the ionic liquid stream remains considerable along time, the overall mass transfer coefficient was calculated by fitting the experimental mercaptan concentration profile with equations 7.3, 7.4, 7.6 and 7.7.

The extraction and regeneration mass transfer coefficients determined were $4.90 \pm 1.49 \times 10^{-8} \text{ m.s}^{-1}$ and $1.06 \pm 0.20 \times 10^{-8} \text{ m.s}^{-1}$, respectively. Knowing that the dominant resistance in each module is the transport of the mercaptan in the ionic liquid phase, these values should be equal if the fluid dynamics of the ionic liquid phase in both modules were identical. The difference observed results from the different ionic liquid stream velocity rates: 1.01 cm.s^{-1} in the extraction module and 0.248 cm.s^{-1} in the regeneration module.

For the experiments with $v_g = 7.84 \text{ cm.s}^{-1}$ and $v_g = 19.30 \text{ cm.s}^{-1}$, the mercaptan concentration remaining in the ionic liquid phase was extremely low, practically zero (0.04 mol.m^{-3} and below the detection threshold, respectively), due to a very efficient stripping of the ionic liquid. For these experiments, the differential mass balance described in equation 7.5, with $C_f^* = 0$, can be used to determine the extraction overall mass transfer. The values obtained for the overall mass transfer coefficient were $3.59 \pm 0.11 \times 10^{-8} \text{ m.s}^{-1}$ and $5.24 \pm 0.21 \times 10^{-8} \text{ m.s}^{-1}$, respectively. Although slightly different, these values of the same magnitude as the overall mass transfer coefficient determined for the single extraction process ($7.88 \pm 0.35 \times 10^{-8} \text{ m.s}^{-1}$). Having in mind that the transport of the mercaptan in the ionic liquid phase is the limiting step in each module, the overall mass transfer coefficient for the regeneration module can be assumed as equal to the value determined for the regeneration mass transfer coefficient for the case with lower sweep gas velocity.

Simulation of mercaptan transport

As aforementioned, considering a complete regeneration of the ionic liquid, the mass transfer performance in the integrated process is controlled by the 1-hexanethiol transport in the ionic liquid phase, in the extraction module. Therefore, the overall mass transfer coefficient is directly affected by the operating conditions of the ionic liquid stream in the extraction membrane contactor. Aiming at understanding the effect of the ionic liquid fluid dynamics on the extraction process, the impact of increasing the ionic liquid linear velocities in the extraction contactor was evaluated by simulation, using the mass transfer model previously discussed. Additionally, the impact of operating at higher extraction temperature was also evaluated.

The ionic liquid velocities tested, 5 cm.s^{-1} and 10 cm.s^{-1} , at a temperature of 298.2 K , were chosen having in mind the limiting pressure drop allowed inside the module,

considering the critical breakthrough pressure (3.85 bar at 298.2 K). For each velocity, the pressure drop between the inlet and the outlet of the module was estimated, by using the Hagen-Poiseuille equation ⁸, $\Delta P = \frac{32\mu_{IL}v_{IL}L_f}{d_{fi}^2} \times 10^{-5}$ bar, where the μ_{IL} is the ionic liquid viscosity (Pa.s) at the operating temperature, the L_f is the fiber length (m) and the d_{fi} is the fiber internal diameter (m).

The pressure drop estimated for each tested velocity was of 1.8 bar and 3.6 bar, respectively, which do not exceed the critical breakthrough pressure.

Using the mass transfer relation $\frac{K_{simulated}}{K_E} = \left(\frac{v_{IL,simulated}}{v_{IL,E}}\right)^{1.01}$, ³⁶ the ionic liquid mass transfer coefficients increased significantly from 4.90×10^{-8} m.s⁻¹ at 1 cm.s⁻¹, to 2.46×10^{-7} m.s⁻¹ at 5 cm.s⁻¹, and 4.96×10^{-7} m.s⁻¹ at 10 cm.s⁻¹. This effect is shown in Figure 7.5 a). The increase of the ionic liquid velocity allows for enhancing the extraction performance due to its direct impact on the mass transfer coefficient increase, with a decreasing resistance to the mercaptan transport in the ionic liquid boundary layer.

A temperature increase leads to an improvement of the mass transfer (Figure 7.5 b)) by reducing the viscosity and density of the ionic liquid (reducing the ionic liquid boundary layer thickness) and increasing of the diffusion coefficient. The effect of temperature was simulated taking into consideration its various impacts on these properties, and also respecting the temperature restrictions of the hollow fiber membrane contactor of Liqui-Cel[®], indicated by the manufacturer. Simulations for temperatures of 313.2 K and 333.2 K led to a the viscosity reduction of [C₂mim][CF₃SO₃] from 41 mPa.s at 298.2 K to 26.8 mPa.s ³⁷ and 14.7 mPa.s ³⁷, and the density from 1379.1 kg.m⁻³ to 1371.5 kg.m⁻³ and 1354.9 kg.m⁻³, respectively. The diffusion coefficient, estimated by the Wilke-Chang correlation ³⁸, increases from 4.12×10^{-11} m².s⁻¹ to 6.79×10^{-11} m².s⁻¹ and 1.28×10^{-10} m².s⁻¹, respectively.

Estimating the mass transfer coefficient using the relation

$$\frac{K_{simulated}}{K_{E,298.2 K}} = \frac{\left[\left(\frac{\rho}{\mu}\right)^{1.01} \left(\frac{\mu}{\rho D}\right)^{0.33}\right]_{T_{simulated}}}{\left[\left(\frac{\rho}{\mu}\right)^{1.01} \left(\frac{\mu}{\rho D}\right)^{0.33}\right]_{298.2 K}},$$

³⁶ the benefit in the mass transfer coefficient can be

observed in Figure 7.5 c). The corresponding overall mass transfer coefficients are 5.51×10^{-8} m.s⁻¹ and 6.54×10^{-8} m.s⁻¹.

As observed, the extraction process can be remarkably improved if optimal operating conditions are employed. By the combination of the ionic liquid fluid dynamics and the operating temperature, the mercaptan extraction performance is significantly improved. When increasing the temperature, the pressure drop associated with the ionic liquid flow inside the fibers is also reduced. Therefore, higher ionic liquid velocities can be applied without exceeding the critical breakthrough pressure at the operating temperature. Due to the lack of data for estimation of the critical breakthrough pressure at the operating temperature of 333.2 K, the ionic liquid velocity selected for simulation, at 333.2 K, was chosen to cause a pressure drop lower than 2 bar. A pressure drop of 1.96 bar is estimated for an ionic liquid velocity of 15 cm.s⁻¹. Figure 7.5 c) shows the overall improvement when increasing the ionic liquid velocity and temperature. The estimated extraction mass transfer coefficient for these conditions is 1.0 × 10⁻⁶ m.s⁻¹, which allows reducing drastically the mercaptan extraction time from 50h to only 3.5h. These results were not validated due to experimental restrictions.

Still, the results presented attest the remarkable potential for an effective mercaptan removal from a jet-fuel feed phase using an ionic liquid as a solvent in an integrated extraction/stripping process carried out in hollow fiber membrane contactors.

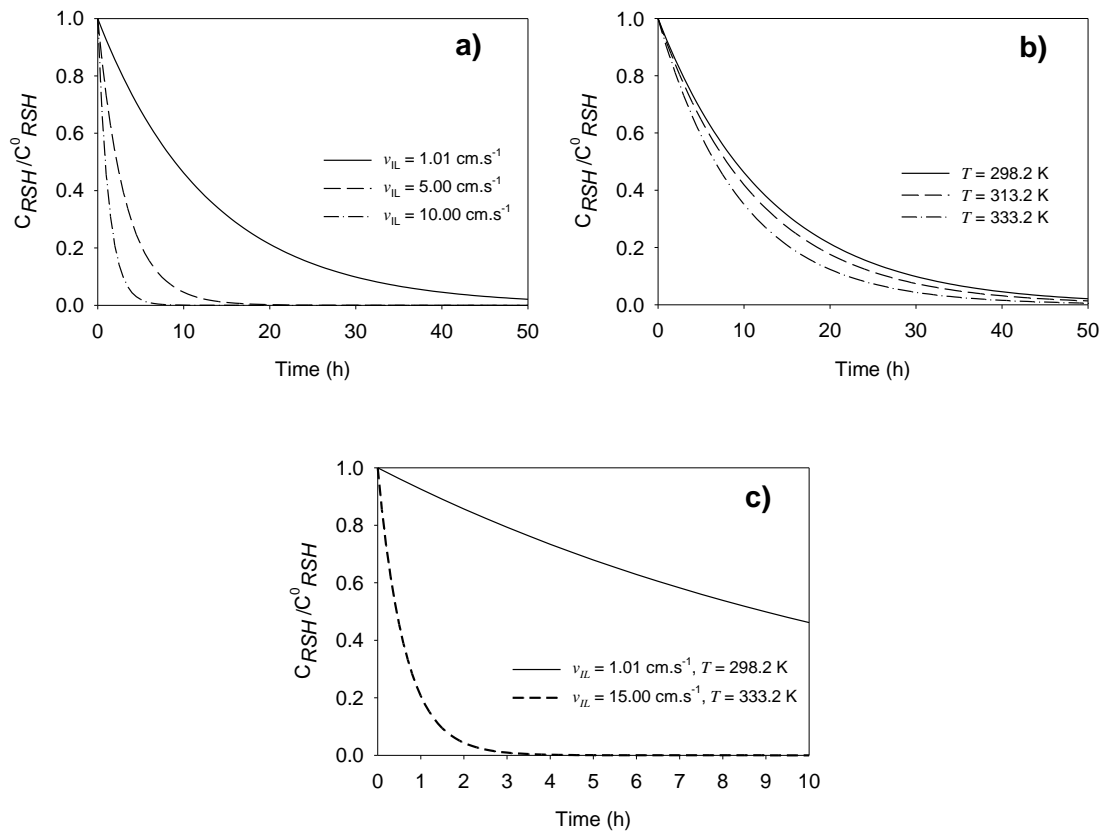


Figure 7.5 Simulated 1-hexanethiol concentration profile varying a) the ionic liquid velocity and b) the operating temperature. In c) the simulation is obtained combining both parameters studied in a) and b).

7.6. Conclusions

A new methodology for the desulfurization of “jet-fuel” streams, using a mixture of 1-hexanethiol and *n*-dodecane as a model system, was proposed in this work. It consisted in a liquid extraction of the mercaptan using as an ionic liquid as the extracting solvent (1-ethyl-3-methylimidazolium triflate [C₂mim][CF₃SO₃]), followed by its integrated regeneration. The separation process was carried out in hollow fiber membrane contactor in counter-current mode, which allowed for reducing the extraction time due to its high interfacial area (3335 m²/m³). This equipment also requires a low volume of ionic liquid than that required in conventional processes, which is particularly important considering the relatively low distribution ratio towards the target solute.

Simultaneously to the extraction, the ionic liquid was regenerated in an integrated system. Two regeneration methods were tested: vacuum stripping and a sweep gas stream in the downstream side of the membrane. In the vacuum stripping process, the ionic liquid partially filled the fiber pores which add a second significant resistance to the mercaptan transport. This method was considered unfeasible for the re-extraction of mercaptans. Using a sweep gas stripping, a complete regeneration of the ionic liquid was possible, allowing for an improvement of the extraction performance as a result of the maximization of the concentration gradient, reducing the constraints related with the low distribution ratio of the system under study. A complete extraction of the mercaptan from the “jet-fuel” model stream was achieved, producing an ultra-low sulfur jet-fuel with sulfur content lower than 2 ppm, as envisaged by legislation for the use of ultra-low sulfur jet-fuel (< 10 ppm S).

In an efficient integrated regeneration of the ionic liquid, the controlling step becomes the extraction of mercaptan from the feed phase to the ionic liquid phase. Simulations showed that the increase of the ionic liquid velocity and operating temperature can lead to a high decrease of the extraction time, i.e. from 50h to 3.5h.

These results prove the potential of the integrated extraction/sweep gas stripping process using ionic liquid as solvent in hollow fiber membrane contactors for the removal of mercaptans from “jet-fuel” streams, where the ionic liquid used can be continuously regenerated and reused.

After this successful proof of principle, the development of a full-scale unit to fulfill the need of ultra-low sulfur fuels from real fuel streams requires a continued research effort aiming at assessing the feasibility of this process, followed by pilot-plant test with real fuel streams.

7.7. References

1. Ferreira, A. R.; Neves, L. A.; Ribeiro, J. C.; Lopes, F. M.; Coutinho, J. A. P.; Coelho, I. M.; Crespo, J. G., Removal of Thiols from “Jet-Fuel” Streams assisted by Ionic Liquid Membrane Extraction. Submitted at *Chem Eng J* **2014**.
2. Williams, N. S.; Ray, M. B.; Gomaa, H. G., Removal of ibuprofen and 4-isobutylacetophenone by non-dispersive solvent extraction using a hollow fibre membrane contactor. *Sep Purif Technol* **2012**, *88*, 61-69.
3. Viegas, R. M. C.; Afonso, C. A. M.; Crespo, J. G.; Coelho, I. M., Racemic resolution of propranolol in membrane contactors: Modelling and process optimisation. *J Membrane Sci* **2007**, *305* (1-2), 203-214.
4. Viegas, R. M. C.; Afonso, C. A. M.; Crespo, J. G.; Coelho, I. M., Modelling of the enantio-selective extraction of propranolol in a biphasic system. *Sep Purif Technol* **2007**, *53* (3), 224-234.
5. Viegas, R. M. C.; Crespo, J. G.; Coelho, I. M., Hybrid modelling of the racemic resolution of propranolol in membrane contactors. *Desalination* **2006**, *200* (1-3), 595-597.
6. João G. Crespo; Isabel M. Coelho; Viegas, R. C., Membrane Contactors. In *Encyclopedia of Separation Processes*, Academic Press: London, 2000; p 3303.
7. Pabby, A. K.; Sastre, A. M., State-of-the-art review on hollow fibre contactor technology and membrane-based extraction processes. *J Membrane Sci* **2013**, *430*, 263-303.
8. Ho, W. S. W.; Sirkar, K. K., *Membrane Handbook*. Kluwer Academic Publishers: Boston 1992.
9. Coelho, I. M.; Cardoso, M. M.; Viegas, R. M. C.; Crespo, J. P. S. G., Transport mechanisms and modelling in liquid membrane contactors. *Sep Purif Technol* **2000**, *19* (3), 183-197.
10. Gong, Y. W.; Liu, H. X.; Cheng, X. N., Experiments of mercaptans removal from FCC gasoline by NaOH aqueous in membrane contactor. *Pet Sci Technol* **2010**, *28* (9), 903-910.
11. Yang, X.; Cao, Y.-M.; Wang, R.; Yuan, Q., Study on highly hydrophilic cellulose hollow fiber membrane contactors for thiol sulfur removal. *J Membrane Sci* **2007**, *305* (1-2), 247-256.

12. Gordon, C. M.; Muldoon, M. J., Synthesis and purification. *Ionic Liquids in Synthesis* **2008**, 7-55.
13. Welton, T.; Endres, F.; Abedin, S. Z. E.; Antonietti, M.; Smarsly, B.; Zhou, Y., *Inorganic Synthesis*. 2008; Vol. 1, 569-617.
14. Maase, M., Ionic liquids in industrial processes: Re-invention of the wheel or true innovation? *Ionic Liquids in Synthesis* **2008**, 663-687.
15. Dennewald, D.; Pitner, W.-R.; Weuster-Botz, D., Recycling of the ionic liquid phase in process integrated biphasic whole-cell biocatalysis. *Process Biochem* **2011**, *46* (5), 1132-1137.
16. Meindersma, W. G. W.; Onink, F. S. A. F.; Hansmeier, A. R.; de Haan, A. B., Long Term Pilot Plant Experience on Aromatics Extraction with Ionic Liquids. *Sep Sci Technol* **2012**, *47* (2), 337-345.
17. Gan, Q.; Xue, M. L.; Rooney, D., A study of fluid properties and microfiltration characteristics of room temperature ionic liquids [C-10-min][NTf₂] and N-8881[NTf₂] and their polar solvent mixtures. *Sep Purif Technol* **2006**, *51* (2), 185-192.
18. Jongmans, M. T. G.; Trampe, J.; Schuur, B.; de Haan, A. B., Solute recovery from ionic liquids: A conceptual design study for recovery of styrene monomer from 4-mebupy BF₄. *Chem Eng Process* **2013**, *70*, 148-161.
19. Andanson, J.-M.; Jutz, F.; Baiker, A., Purification of ionic liquids by supercritical CO₂ monitored by infrared spectroscopy. *J Supercrit Fluids* **2010**, *55* (1), 395-400.
20. Kuhlmann, E.; Haumann, M.; Jess, A.; Seeberger, A.; Wasserscheid, P., Ionic Liquids in Refinery Desulfurization: Comparison between Biphasic and Supported Ionic Liquid Phase Suspension Processes. *Chemsuschem* **2009**, *2* (10), 969-977.
21. Claudio, A. F. M.; Marques, C. F. C.; Boal-Palheiros, I.; Freire, M. G.; Coutinho, J. A. P., Development of back-extraction and recyclability routes for ionic-liquid-based aqueous two-phase systems. *Green Chem* **2014**, *16* (1), 259-268.
22. Wellens, S.; Goovaerts, R.; Moller, C.; Luyten, J.; Thijs, B.; Binnemans, K., A continuous ionic liquid extraction process for the separation of cobalt from nickel. *Green Chem* **2013**, *15* (11), 3160-3164.
23. Wellens, S.; Vander Hoogerstraete, T.; Möller, C.; Thijs, B.; Luyten, J.; Binnemans, K., Dissolution of metal oxides in an acid-saturated ionic liquid solution and investigation of the back-extraction behaviour to the aqueous phase. *Hydrometallurgy* **2014**, *144-145* (0), 27-33.

24. Kroon, M. C.; van Spronsen, J.; Peters, C. J.; Sheldon, R. A.; Witkamp, G.-J., Recovery of pure products from ionic liquids using supercritical carbon dioxide as a co-solvent in extractions or as an anti-solvent in precipitations. *Green Chem* **2006**, *8* (3), 246-249.
25. Haerens, K.; Van Deuren, S.; Matthijs, E.; Van der Bruggen, B., Challenges for recycling ionic liquids by using pressure driven membrane processes. *Green Chem* **2010**, *12* (12), 2182-2188.
26. Abels, C.; Redepenning, C.; Moll, A.; Melin, T.; Wessling, M., Simple purification of ionic liquid solvents by nanofiltration in biorefining of lignocellulosic substrates. *J Membrane Sci* **2012**, *405–406* (0), 1-10.
27. García, V.; Valkama, H.; Sliz, R.; King, A. W. T.; Myllylä, R.; Kilpeläinen, I.; Keiski, R. L., Pervaporation recovery of [AMIM]Cl during wood dissolution; effect of [AMIM]Cl properties on the membrane performance. *J Membrane Sci* **2013**, *444* (0), 9-15.
28. Shiflett, M. B.; Shiflett, A. D.; Yokozeki, A., Separation of tetrafluoroethylene and carbon dioxide using ionic liquids. *Sep Purif Technol* **2011**, *79* (3), 357-364.
29. Lu, J. G.; Lu, C. T.; Chen, Y.; Gao, L.; Zhao, X.; Zhang, H.; Xu, Z. W., CO₂ capture by membrane absorption coupling process: Application of ionic liquids. *Appl Energ* **2014**, *115*, 573-581.
30. Guo, H. X.; Zhou, Z. M.; Jing, G. H., Kinetics of carbon dioxide absorption into aqueous [Hmim][Gly] solution. *Int J Greenh Gas Con* **2013**, *16*, 197-205.
31. Mortaheb, H. R.; Mafi, M.; Mokhtarani, B.; Sharifi, A.; Mirzaei, M.; Khodapanah, N.; Ghaemmaghami, F., Experimental kinetic analysis of ethylene absorption in ionic liquid [Bmim]NO₃ with dissolved AgNO₃ by a semi-continuous process. *Chem Eng J* **2010**, *158* (3), 384-392.
32. Ren, S.; Hou, Y.; Wu, W.; Liu, W., Purification of Ionic Liquids: Sweeping Solvents by Nitrogen. *J Chem Eng Data* **2010**, *55* (11), 5074-5077.
33. Ferreira, A. R.; Freire, M. G.; Ribeiro, J. C.; Lopes, F. M.; Crespo, J. G.; Coutinho, J. A. P., Ionic liquids for thiols desulfurization: Experimental liquid–liquid equilibrium and COSMO-RS description. *Fuel* **2014**, *128* (0), 314-329.
34. ASTM D3227 - Standard Test Method for (Thiol Mercaptan) Sulfur in Gasoline, Kerosine, Aviation Turbine, and Distillate Fuels (Potentiometric Method). ASTM International: 2013; Vol. ASTM D3227.

35. Green, D. W.; Perry, R. H., *Perry's Chemical Engineers' Handbook*. The McGraw-Hill Companies, Inc.: United States of America, 1934.
36. Viegas, R. M. C.; Rodríguez, M.; Luque, S.; Alvarez, J. R.; Coelho, I. M.; Crespo, J. P. S. G., Mass transfer correlations in membrane extraction: Analysis of Wilson-plot methodology. *J Membrane Sci* **1998**, *145* (1), 129-142.
37. Rodríguez, H.; Brennecke, J. F., Temperature and Composition Dependence of the Density and Viscosity of Binary Mixtures of Water + Ionic Liquid. *J Chem Eng Data* **2006**, *51* (6), 2145-2155.
38. Reid, R. C.; Prausnitz, J. M.; Poling, B. E., *The properties of gases and liquids*. 4th ed.; McGraw-Hill: New York, 1987.

Chapter 8

General Conclusions and Future Work

8.1. General conclusions

The present work aimed at developing an alternative desulfurization process for the removal of aliphatic sulfur compounds, known as mercaptans, from jet-fuel streams. Envisaging the fulfillment of environmental concerns and legislation requisites, jet-fuel streams with sulfur content lower than 10 ppm in elemental sulfur should be produced.

To achieve this goal, a model feed of 1-hexanethiol and *n*-dodecane, representing the mercaptan solute target and aliphatic compounds of the jet-fuel, respectively, was selected to carry out all the studies and experimental work required.

The work developed can be divided into two different parts. The first stage attempted the selection of the most suitable ionic liquid to be used as a mercaptan extractant, and the second part explored the more appropriate separation process to carry out the desulfurization process.

For the selection of the ionic liquid two requirements needed to be satisfied:

1. The aliphatic and the aromatic compounds of the jet-fuel should not dissolve into the ionic liquid selected, neither the ionic liquid into the jet-fuel compounds. These demands intend to avoid the contamination of the jet-fuel and the loss of fuel compounds to the extracting solvent.
2. The ionic liquid selected should have a high affinity with the mercaptan species, being able to extract them selectively from the jet-fuel feed stream.

The solubility behavior of the ionic liquid and the jet-fuel hydrocarbons was studied using the extensive literature available and predicted results, using the completely predictive thermodynamic model COSMO-RS, on binary and ternary systems along with other estimated behaviors for non-tested systems. This allowed an understanding of the interactions and molecular structural impacts occurring between the ionic liquid and the hydrocarbons. It was also possible to conclude that for the desulfurization of jet-fuel, the ionic liquid with cations with shorter alkyl chains from the imidazolium, pyridine and pyrrolidinium families promoted higher selectivities.

Considering the systems with mercaptans, no phase diagrams with ionic liquids were found in literature, at the time of this work. Therefore, based on the pre-screening performed, various ionic liquids were experimentally investigated. It was found that these systems show very high selectivities due to the very low mutual solubility between the ionic liquids and the *n*-dodecane (practically immiscible systems). The distribution ratio values determined were, however, not very favorable ($\ll 1$) for the extraction of mercaptans using ionic liquids, as a result of the low intermolecular interactions

occurring between the ionic liquid and the mercaptan. Given the good ability of COSMO-RS in the description of these systems, other ionic liquid cations and anions were studied. It was found that, when the distribution ratio is enhanced, the selectivity of the system is reduced, jeopardizing the extraction process due to a possible co-extraction of other jet-fuel constituents. Taking into account the necessary balance between the selectivity and distribution ratio of the mercaptan towards the ionic liquid, the ionic liquid selection must be done prudently and, therefore, the shorter alkyl chain imidazolium-based ionic liquids were considered an acceptable choice, as mentioned before, additionally to their commercial availability and cost, comparing with other ionic liquids.

Having studied and selected the ionic liquids with the expected best potential and performance, the separation process technology was assessed.

Considering that the distribution ratios of the mercaptan towards the selected ionic liquids were low, the conventional liquid-liquid extraction processing was discarded since the volume of ionic liquids required to perform the extraction would be extremely large. Therefore, separation techniques controlled by the solute transport kinetics were studied. Moreover, this concept deals with the ionic liquid regeneration after mercaptan “contamination” due to the extraction process. The first studies considered the use of supported ionic liquid membranes (SILMs), applying vacuum in the downstream side of the system, allowing for a simultaneous and *in-situ* extraction of the mercaptan from the feed phase to the ionic liquid and stripping of the ionic liquid immobilized on the pores of the membrane support. This process was shown to be unfeasible for the system studied due to the permeation of the *n*-dodecane through the material of the supporting membrane of the SILM .

Based on the negligible solubility of the *n*-dodecane in the ionic liquid, the ionic liquid was then used as a receiving phase in a hollow fibre membrane contactor and no dodecane was detected in the ionic liquid phase, solving the problem related with the fuel losses. The extraction process was here carried out in a hollow fibre membrane contactor since it provides an extremely high interfacial area and requires a lower ionic liquid volume than conventional equipment.

In order to reduce the limitations imposed by thermodynamic equilibrium and low distribution ratio, a regeneration process for the mercaptan re-extraction from the ionic liquid was integrated into the extraction process. Among the several processes available, two methods were tested: vacuum stripping and a sweep gas stripping using a air stream in the downstream side of the membrane. It was found that stripping with a sweep gas

allows for a complete regeneration of the ionic liquid which permits a maximization of the concentration gradient and an improvement of the extraction process.

The mercaptan extraction achieved with this new methodology was complete and a jet-fuel model with sulfur content lower than 2 ppm of S was produced.

Additionally, the effect of increasing the fluid velocity and operating temperature of the ionic liquid stream in this separation process was estimated and the simulations show that it is possible to improve the separation performance with a significant reduction of the extraction time.

These results are extremely promising, proving that the integrated extraction/regeneration in hollow fibre membrane contactors using ionic liquid as extractant has a high potential for development of ultra-deep desulfurization process application.

8.2. Future work

Aiming an improvement of the desulfurization process developed in this work and in view of a potential industrial application further work, complementary to the presented here, must be developed.

Regarding the operating conditions for the system tested in this work, there is an opportunity for significant improvements. Therefore, experimental investigation of the estimated effects of ionic liquid stream velocity and temperature should be performed. These studies will help understanding the real limitation of the operating conditions and extend the process to optimal conditions of operation.

The next step should consider the use of a more complex jet-fuel feed, taking into account the aromatic compounds, which are in a lower concentration, around 10 – 20%wt, compared with the aliphatic compounds, in order to understand their impact on the extraction process viability. Moreover, aromatic sulfur species can be also added to the system and their removal, using the proposed extraction/stripping process, should be evaluated. In terms of feed composition, validation experiments should address the use of real jet-fuel stream and the desulfurization yield and efficiency in real situation should be evaluated.

Given that a successful separation process was achieved after various attempts and that the extraction process becomes controlling in the presence of an effective regeneration process, the affinity of ionic liquid, used as extractant, for the target mercaptan could be

improved in order to increase the mass transfer from the feed phase to the ionic liquid phase. The ionic liquids suggested in Chapter 5, as promising candidates for the extraction process, could be tested in the integrated extraction/stripping process. Along with this study, other ionic liquids with higher distribution ratio to the mercaptan species can also be tested and the co-extraction of jet-fuel compounds must be analyzed and evaluated. The physical properties of the ionic liquids tested should be taken into account in order to adapt the operating conditions accordingly.

Analogous to several research works developed for the aromatic sulfur compounds extraction with ionic liquids¹⁻², oxidative extraction of mercaptan compounds could be tested. The oxidant agent could be solubilized in the ionic liquid, and the oxidized sulfur species in the extraction/oxidation contactor would be easily separated from the ionic liquid/oxidant agent in the regeneration contactor. Various oxidation processes for mercaptans desulfurization have been reported in literature.³⁻⁷

More recently, the reactive extraction of mercaptans using functionalized ionic liquids was suggested.⁸ This approach uses ionic liquids that react with mercaptans through reversible sulfur-bound, in a 'mole per mole' reaction. These ionic liquids would increase the interaction with the mercaptan compounds in the jet-fuel feed, compared to the ionic liquids studied, only capable of physisorption. This type of reactive ionic liquids applied in the integrated extraction/regeneration process would drastically increase the partition of the mercaptans in the extraction contactor and the regeneration of the ionic liquid would also be possible, allowing for its recycle and reuse.

For an industrial practice, an assessment of the practical viability and feasibility of this process is essential for its acceptance by the industrial community, along with pilot-scale experiments using real jet-fuel streams and validation studies.

8.3. References

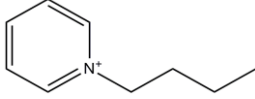
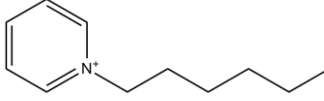
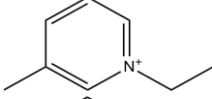
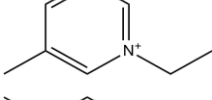
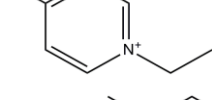
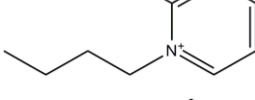
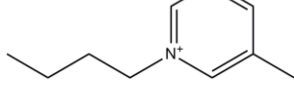
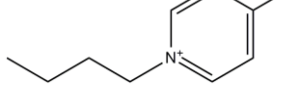
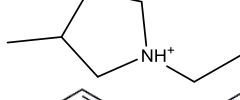
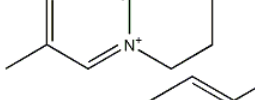
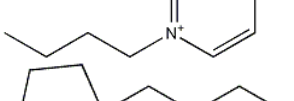
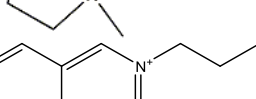
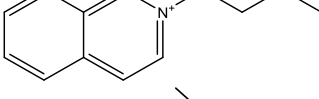
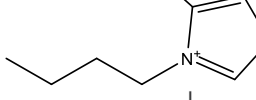

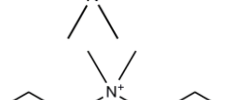

1. Rodríguez-Cabo, B.; Rodríguez, H.; Rodil, E.; Arce, A.; Soto, A., Extractive and oxidative-extractive desulfurization of fuels with ionic liquids. *Fuel* **2014**, *117*, Part A (0), 882-889.
2. Pawelec, B.; Navarro, R. M.; Campos-Martin, J. M.; Fierro, J. L. G., Towards near zero-sulfur liquid fuels: a perspective review. *Catal Sci Technol* **2011**, *1* (1), 23-42.
3. Das, G.; Sain, B.; Kumar, S., Synthesis, characterization and catalytic activity of cobalt phthalocyanine dichloride in sweetening of heavier petroleum fractions. *Catal Today* **2012**, *198* (1), 228-232.
4. Bricker, J. C.; Laricchia, L., Advances in Merox (TM) Process and Catalysis for Thiol Oxidation. *Top Catal* **2012**, *55* (19-20), 1315-1323.
5. Yang, X.; Cao, Y.-M.; Wang, R.; Yuan, Q., Study on highly hydrophilic cellulose hollow fiber membrane contactors for thiol sulfur removal. *J Membrane Sci* **2007**, *305* (1-2), 247-256.
6. Song, C., An overview of new approaches to deep desulfurization for ultra-clean gasoline, diesel fuel and jet fuel. *Catal Today* **2003**, *86* (1-4), 211-263.
7. Srivastava, V. C., An evaluation of desulfurization technologies for sulfur removal from liquid fuels. *Rsc Adv* **2012**, *2* (3), 759-783.
8. Gunaratne, H. Q. N.; Nockemann, P.; Seddon, K. R., Ionic liquids for efficient hydrogen sulfide and thiol scavenging. *Green Chem* **2014**, *16* (5), 2411-2417.

Appendix A

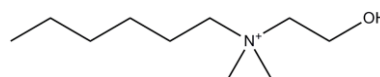
Ionic Liquid Cations and Anions

Table A1 Abbreviations and chemical structures of the ionic liquids cations.

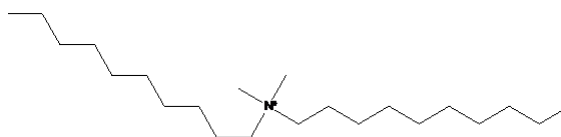
abbreviation	description	chemical structure
[C ₁ im] ⁺	1-methylimidazolium	
[C ₁ mim] ⁺	1,3-dimethylimidazolium	
[C ₂ mim] ⁺	1-ethyl-3-methylimidazolium	
[C ₄ mim] ⁺	1-butyl-3-methylimidazolium	
[C ₆ mim] ⁺	1-hexyl-3-methylimidazolium	
[C ₈ mim] ⁺	1-methyl-3-octylimidazolium	
[C ₂ C ₂ im] ⁺	1,3-diethylimidazolium	
[C ₄ C ₄ im] ⁺	1,3-dibutylimidazolium	
[C ₂ C ₁ mim] ⁺	1-ethyl-2,3-dimethylimidazolium	
[C ₃ C ₁ mim] ⁺	1-propyl-2,3-dimethylimidazolium	
[C ₄ C ₁ mim] ⁺	1-butyl-2,3-dimethylimidazolium	
[amim] ⁺	1-allyl-3-methylimidazolium	
[C ₆ H ₁₃ OCH ₂ mim] ⁺	1-hexyloxymethyl-3-methylimidazolium	
[(C ₆ H ₁₃ OCH ₂) ₂ im] ⁺	1,3-dihexyloxymethyl-imidazolium	
[C ₂ py] ⁺	1-ethylpyridinium	

$[\text{C}_4\text{py}]^+$	1-butylpyridinium	
$[\text{C}_6\text{py}]^+$	1-hexylpyridinium	
$[\text{C}_2\text{mpy}]^+$ $[\text{1,2C}_2\text{mpy}]^+$	1-ethyl-3-methylpyridinium	
$[\text{1,3C}_2\text{mpy}]^+$	1-ethyl-3-methylpyridinium	
$[\text{1,4C}_2\text{mpy}]^+$	1-ethyl-4-methylpyridinium	
$[\text{1,2C}_4\text{mpy}]^+$	1-butyl-2-methylpyridinium	
$[\text{1,3C}_4\text{mpy}]^+$	1-butyl-3-methylpyridinium	
$[\text{1,4C}_4\text{mpy}]^+$	1-butyl-4-methylpyridinium	
$[\text{C}_2\text{mpyr}]^+$	1-ethyl-3-methylpyrrolidinium	
$[\text{1,3C}_4\text{mpy}]^+$	1-butyl-3-methylpyridinium	
$[\text{1,4C}_4\text{mpy}]^+$	1-butyl-4-methylpyridinium	
$[\text{C}_4\text{mpyr}]^+$	1-butyl-1-methylpyrrolidinium	
$[\text{C}_4\text{iQuin}]^+$	N-butyl-isoquinolinium	
$[\text{C}_4\text{TZO}]^+$	3-butyl-4-methylthiazolium	
$[\text{N}_{1(2\text{OH})11}]^+$	methyl(2-hydroxyethyl)dimethylammonium	
$[\text{Ch}]^+$ $[\text{N}_{22(2\text{OH})11}]^+$	ethyl(2-hydroxyethyl)dimethylammonium (cholinium)	
$[\text{N}_{4(2\text{OH})11}]^+$	butyl(2-hydroxyethyl)dimethylammonium	

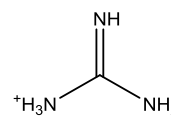
$[\text{N}_{6(2\text{OH})11}]^+$ hexyl(2-hydroxyethyl)dimethylammonium



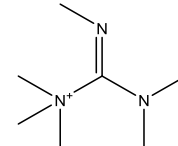
$[\text{N}_{101011}]^+$ didecyldimethylammonium



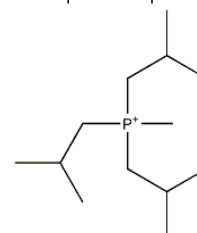
$[\text{Gu}]^+$ guanidinium



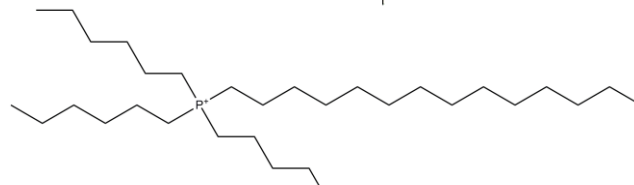
$[(\text{C}_1)_6\text{Gu}]^+$ hexamethylguanidinium



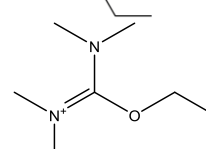
$[\text{P}_{i(444)1}]^+$ tri-iso-butyl(methyl)phosphonium



$[\text{P}_{666(14)}]^+$ trihexyl(tetradecyl)phosphonium



$[\text{OC}_2(\text{C}_1)_4\text{iU}]^+$ O-ethyl-N,N,N,N-tetramethylisothiuronium



$[\text{SC}_2(\text{C}_1)_4\text{iU}]^+$ S-ethyl-N,N,N,N-tetramethylisothiuronium

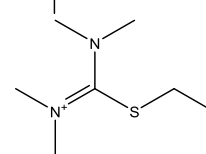
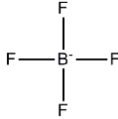

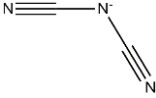
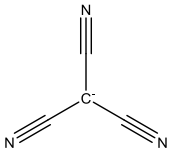
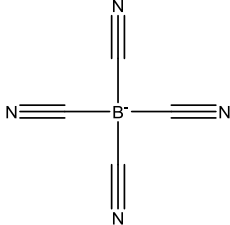
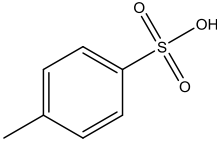
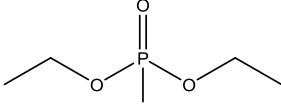
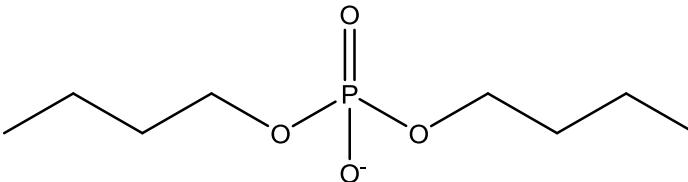
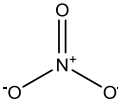
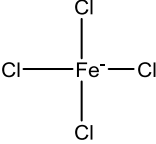
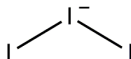
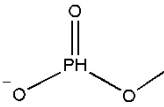
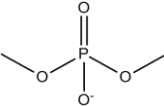
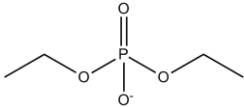
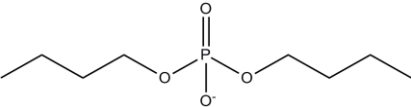


Table A2 Abbreviations and chemical structures of the ionic liquids anions.

abbreviation	description	chemical structure
[MeSO ₄] ⁻	methylsulfate	
[EtSO ₄] ⁻	ethylsulfate	
[BuSO ₄] ⁻	butylsulfate	
[OcSO ₄] ⁻	octylsulfate	
[MDEGSO ₄] ⁻	2-(2-methoxyethoxy)ethylsulfate	
[CH ₃ SO ₃] ⁻	methylsulfonate	
[CF ₃ SO ₃] ⁻	trifluoromethanesulfonate	
[(PFBu)SO ₃] ⁻	perfluorobutanesulfonate	
[CHF ₂ CF ₂ SO ₃] ⁻	1,1,2,2-tetrafluoroethanesulfonate	
[CH ₃ CO ₂] ⁻	acetate	
[NTf ₂] ⁻	bis[(trifluoromethyl)sulfonyl]imide	
[PF ₆] ⁻	hexafluorophosphate	

$[\text{BF}_4]^-$	tetrafluoroborate	
$[\text{SCN}]^-$	thiocyanate	
$[\text{N}(\text{CN})_2]^-$ [DCA] ⁻	dicyanamide	
$[\text{C}(\text{CN})_3]^-$	tricyanomethane	
$[\text{B}(\text{CN})_4]^-$	tetracyanoborate	
[TOS] ⁻	tosylate	
[DEP] ⁻	diethylphosphate	
[DBP] ⁻	dibutylphosphate	
$[\text{NO}_3]^-$	nitrate	
$[\text{FeCl}_4]^-$	tetrachloroferrate	
Cl^-	chloride	Cl^-
I_3^-	triiodide	

[P ₁] ⁻	methylphosphonate	
[P ₁₁] ⁻	dimethylphosphate	
[P ₂₂] ⁻	diethylphosphate	
[P ₄₄] ⁻	dibutylphosphate	

Appendix B

**An Overview of the
Liquid-Liquid Equilibria of
(Ionic Liquid + Hydrocarbon)
Binary Systems
and their Modeling by COSMO-RS**

Table B1 Published LLE experimental data, measurement technique used, and composition and temperature range, of ILs + *n*-alkanes binary systems.

	Ionic liquid	<i>n</i> -alkane	Experimental measurement technique	Composition range (x_{IL})	Temperature range (K)	References
1	[C ₁ mim][MeSO ₄]	Pentane ³³	Visual cloud point detection ³³	0.8619-0.7814 ³³	288.21 - 306.32 ³³	33
2		Hexane ³³	Visual cloud point detection ³³	0.9731-0.6977 ³³	295.87 – 341.49 ³³	33
3		Heptane ³³	Visual cloud point detection ³³	0.9666-0.7020 ³³	313.07-367.52 ³³	33
4		Octane ³³	Visual cloud point detection ³³	0.9595-0.5462 ³³	319.32-396.20 ³³	33
5		Decane ³³	Visual cloud point detection ³³	1.0000-0.5381 ³³	308.30-442.81 ³³	33
6	[C ₂ mim][EtSO ₄]	Hexane ^{31, 34-35}	Visual cloud point detection ^{31, 34} Volumetric method ³⁵	0.8552-0.6772 ³⁴	301.2-339.2 ³⁴	31, 34-35
				0.8552 -0.6772 ³¹	301.21-339.18 ³¹	
				0.9913-0.9901 ³⁵	293.2 - 333.1 ³⁵	
7	[C ₂ mim][EtSO ₄]	Heptane ^{30, 35}	Volumetric method ³⁰ Volumetric method ³⁵	0.0038-0.0095/0.9968-0.9942 ³⁰	239.15-333.15 ³⁰	30, 35
				0.9956-0.9927 ³⁵	293.3- 333.1 ³⁵	
8	[C ₂ mim][EtSO ₄]	Octane ³¹	Volumetric method ³¹	0.9871-0.8184 ³¹	317.15-368.97 ³¹	31
9	[C ₄ mim][MeSO ₄]	Pentane ³³	Visual cloud point detection ³³	0.9522-0.8640 ³³	288.48-325.00 ³³	33
10		Hexane ^{33, 35}	Visual cloud point detection ³³ Volumetric method ³⁵	0.9770-0.8048 ³³	302.52-346.77 ³³	33, 35
				0.9849-0.9710 ³⁵	293.3-332.8 ³⁵	
11	[C ₄ mim][MeSO ₄]	Heptane ^{33, 35}	Visual cloud point detection ³³ Volumetric method ³⁵	0.9883-0.4433 ³³ 0.9927-0.9866 ³⁵	299.85-442.73 ³³ 293.2-333.0 ³⁵	33, 35

12		Octane ³³	Visual cloud point detection ³³	0.9655-0.6109 ³³	319.49-401.69 ³³	33
13		Decane ³³	Visual cloud point detection ³³	0.9912-0.5612 ³³	320.76-445.70 ³³	33
14	[C ₄ mim][OcSO ₄]	Hexane ³⁷	Visual cloud point detection ³⁷	0.394-0.472 ³⁷	421.4-303.2 ³⁷	37
15		Heptane ³⁷	Visual cloud point detection ³⁷	0.462-0.487 ³⁷	483.0-300.0 ³⁷	37
16		Octane ³⁷	Visual cloud point detection ³⁷	0.516-0.649 ³⁷	473.1-292.3 ³⁷	37
17		Decane ³⁷	Visual cloud point detection ³⁷	0.776-0.807 ³⁷	454.2-304.8 ³⁷	37
18	[C ₄ mim][PF ₆]	Pentane ⁵¹	Visual cloud point detection ⁵¹	0.8595-0.9477 ⁵¹	308.7-293.5 ⁵¹	51
19		Hexane ⁵¹	Visual cloud point detection ⁵¹	0.8467-0.9416 ⁵¹	342.0-314.4 ⁵¹	51
20		Heptane ⁵¹	Visual cloud point detection ⁵¹	0.8714-0.9551 ⁵¹	371.1-341.0 ⁵¹	51
21		Octane ⁵¹	Visual cloud point detection ⁵¹	0.8818-0.9740 ⁵¹	394.2-347.5 ⁵¹	51
22	[C ₄ mim][TOS]	Hexane ³⁶	Visual cloud point detection ³⁶	0.9128-0.9684 ³⁶	329.48-335.76 ³⁶	36
23	[C ₄ mim][SCN]	Hexane ³²	Visual cloud point detection ³²	0.000017-0.000035 ³² 0.9305-0.9840 ³²	298.15-328.15 ³² 364.38-253.15 ³²	32
24		Heptane ³²	Visual cloud point detection ³²	0.9594-0.9939 ³²	364.18-248.09 ³²	32
25		Octane ³²	Visual cloud point detection ³²	0.9631-0.9958 ³²	387.84-297.70 ³²	32
26		Nonane ³²	Visual cloud point detection ³²	0.9713-0.9987 ³²	422.97-288.15 ³²	32
27		Decane ³²	Visual cloud point detection ³²	0.9831-0.9986 ³²	432.49-314.41 ³²	32
28	[C ₄ mim][CF ₃ SO ₃]	Hexane ⁵⁰	Visual cloud point detection ⁵⁰	0.9678-0.9382 ⁵⁰	291.5-339.4 ⁵⁰	50
29		Heptane ⁵⁰	Visual cloud point detection ⁵⁰	0.9811-0.9528 ⁵⁰	299.5-370.6 ⁵⁰	50

30	[C ₄ mim][MDEGSO ₄]	Hexane ³⁹	Visual cloud point detection ³⁹	0.9220-0.9631 ³⁹	341.95-310.25 ³⁹	39
31	[C ₆ mim][SCN]	Hexane ³⁸	Visual cloud point detection ³⁸	0.9755-0.8962 ³⁸	286.6-367.3 ³⁸	38
32		Heptane ³⁸	Visual cloud point detection ³⁸	0.9839-0.9012 ³⁸	282.6-408.8 ³⁸	38
33		Octane ³⁸	Visual cloud point detection ³⁸	0.9906-0.9402 ³⁸	284.7-402.3 ³⁸	38
34		Nonane ³⁸	Visual cloud point detection ³⁸	0.9901-0.9613 ³⁸	312.15-416.8 ³⁸	38
35		Decane ³⁸	Visual cloud point detection ³⁸	0.9941-0.9740 ³⁸	310.4-410.6 ³⁸	38
36	[C ₈ mim][PF ₆]	Hexane ⁴⁰	Density + correlation ⁴⁰	0.0001-0.0002/0.8852-0.8615 ⁴⁰	278.15-328.15 ⁴⁰	40
37		Heptane ⁴⁰	Density + correlation ⁴⁰	0.0001-0.0002/0.9124-0.8915 ⁴⁰	278.15-343.15 ⁴⁰	40
38	[C ₆ H ₁₃ OCH ₂ mim][NTf ₂]	Hexane ⁴¹	Visual cloud point detection ⁴¹	0.6823-0.7819 ⁴¹	341.45-299.95 ⁴¹	41
39		Heptane ⁴¹	Visual cloud point detection ⁴¹	0.7368-0.8274 ⁴¹	368.95-303.25 ⁴¹	41
40	[C ₆ H ₁₃ OCH ₂ mim][BF ₄]	Pentane ⁴¹	Visual cloud point detection ⁴¹	0.7427-0.8153 ⁴¹	309.05-299.05 ⁴¹	41
41		Hexane ⁴¹	Visual cloud point detection ⁴¹	0.7862-0.8443 ⁴¹	341.32-307.65 ⁴¹	41
42		Heptane ⁴¹	Visual cloud point detection ⁴¹	0.8387-0.8945 ⁴¹	366.55-306.75 ⁴¹	41
43		Octane ⁴¹	Visual cloud point detection ⁴¹	0.8508-0.9319 ⁴¹	396.95-308.95 ⁴¹	41
44	[(C ₆ H ₁₃ OCH ₂) ₂ im][NTf ₂]	Hexane ⁴²	Visual cloud point detection ⁴²	0.5012-0.4430 ⁴²	300.05-341.25 ⁴²	42
45	[1,3C ₄ mpy][CF ₃ SO ₃]	Hexane ⁵⁰	Visual cloud point detection ⁵⁰	0.9549-0.9327 ⁵⁰	303.0-339.9 ⁵⁰	50
46		Heptane ⁵⁰	Visual cloud point detection ⁵⁰	0.9660-0.9404 ⁵⁰	301.8-359.2 ⁵⁰	50
47	[1,4C ₄ mpy][NTf ₂]	Hexane ⁵⁴	Visual cloud point detection ⁵⁴	0.8812- 0.8266 ⁵⁴	294.2-347.0 ⁵⁴	54

48		Heptane ⁵⁴	Visual cloud point detection ⁵⁴	0.9300-0.8666 ⁵⁴	292.3-346.0 ⁵⁴	54
49		Octane ⁵⁴	Visual cloud point detection ⁵⁴	0.9413-0.9151 ⁵⁴	302.7-347.6 ⁵⁴	54
50	[1,4C ₄ mpy][TOS]	Hexane ⁴⁹	Visual cloud point detection ⁴⁹	0.000017-0.000051 ⁴⁹ 0.8054-0.8930 ⁴⁹	318.15-333.15 ⁴⁹ 384.68-336.44 ⁴⁹	49
51		Heptane ⁴⁹	Visual cloud point detection ⁴⁹	0.8631-0.9481 ⁴⁹	386.98-329.06 ⁴⁹	49
52		Octane ⁴⁹	Visual cloud point detection ⁴⁹	0.9335-0.9751 ⁴⁹	387.07-328.40 ⁴⁹	49
53	[C ₄ mpyr][CF ₃ SO ₃]	Hexane ⁵⁰	Visual cloud point detection ⁵⁰	0.9641-0.9357 ⁵⁰	292.7-340.2 ⁵⁰	50
54		Heptane ⁵⁰	Visual cloud point detection ⁵⁰	0.9791-0.9495 ⁵⁰	294.7-366.2 ⁵⁰	50
55	[P _{i(444)1}][TOS]	Hexane ⁴⁷	Visual cloud point detection ⁴⁷	0.7556-0.5578 ⁴⁷	308.40-338.12 ⁴⁷	47
56		Heptane ⁴⁷	Visual cloud point detection ⁴⁷	0.8195-0.5536 ⁴⁷	315.86-353.78 ⁴⁷	47
57		Octane ⁴⁷	Visual cloud point detection ⁴⁷	0.8840-0.5801 ⁴⁷	317.79-360.10 ⁴⁷	47
58		Nonane ⁴⁷	Visual cloud point detection ⁴⁷	0.9605-0.6836 ⁴⁷	320.04-361.51 ⁴⁷	47
59		Decane ⁴⁷	Visual cloud point detection ⁴⁷	0.8641-0.8108 ⁴⁷	347.02-356.40 ⁴⁷	47
60	[P _{666 14}][Ac]	Hexane ⁶⁶	Visual cloud point detection ⁶⁶	0.005-0.121 ⁶⁶	283.5-247.8 ⁶⁶	66
61		Decane ⁶⁶	Visual cloud point detection ⁶⁶	0.002-0.146 ⁶⁶	277.9-287.0 ⁶⁶	66
62		Tetradecane ⁶⁶	Visual cloud point detection ⁶⁶	0.008-0.173 ⁶⁶	320.7-319.0 ⁶⁶	66
63	[P _{666 14}][CF ₃ SO ₃]	Hexane ⁶⁶	Visual cloud point detection ⁶⁶	0.002-0.141 ⁶⁶	287.4-303.4 ⁶⁶	66
64	[P _{666 14}][DCA]	Hexane ⁶⁶	Visual cloud point detection ⁶⁶	0.273-0.224 ⁶⁶	289.2-350.8 ⁶⁶	66

65	[P _{666 14}][NTf ₂]	Hexane ⁶⁶	Visual cloud point detection ⁶⁶	0.002-0.13 ⁶⁶	296.6- 261.1 ⁶⁶	66
66		Octane ⁶⁶	Visual cloud point detection ⁶⁶	0.008-0.223 ⁶⁶	350.6-250.6 ⁶⁶	66
67	[N _{22(OH)11}][NTf ₂]	Hexane ⁴⁵	Visual cloud point detection ⁴⁵	0.9717-0.2806 ⁴⁵	283.36-441.31 ⁴⁵	45
68		Octane ⁴⁵	Visual cloud point detection ⁴⁵	0.9846-0.5850 ⁴⁵	303.50-428.91 ⁴⁵	45
69	[N _{62(OH)11}][BF ₄]	Hexane ³⁴	Visual cloud point detection ³⁴	0.3265-0.9780 ³⁴	427.0-352.0 ³⁴	34
70	[N ₁₀₁₀₁₁][NO ₃]	Hexane ⁴⁴	Visual cloud point detection ⁴⁴	0.3445-0.4868	323.3-303.7 ⁴⁴	44
71		Hexadecane ₄₄	Visual cloud point detection ⁴⁴	0.0006-0.6807 ⁴⁴ 0.7705-0.9918 ⁴⁴	>433.1 ⁴⁴ 424.3-393.7 ⁴⁴	44

Table B2 Published LLE experimental data, measurement technique used, and composition and temperature range, of ILs + aromatics binary systems.

	Ionic liquid	Aromatic	Experimental measurement technique	Composition range (x_{IL})	Temperature range (K)	References
1	[C ₁ mim][MeSO ₄]	Benzene ³³	Visual cloud point detection ³³	0.7437-0.5186 ³³	301.92-354.99 ³³	33
2		Toluene ³³	Visual cloud point detection ³³	1.0000-0.6319 ³³	305.65-383.03 ³³	33
3		Ethylbenzene ³³	Visual cloud point detection ³³	0.9207-0.8222 ³³	301.88-408.78 ³³	33
4		Propylbenzene ³³	Visual cloud point detection ³³	0.9261-0.8570 ³³	312.17-428.26 ³³	33
5		<i>o</i> -xylene ³³	Visual cloud point detection ³³	0.9527-0.6231 ³³	311.42-410.68 ³³	33
6		<i>m</i> -xylene ³³	Visual cloud point detection ³³	0.9436-0.6238 ³³	306.34-415.97 ³³	33
7		<i>p</i> -xylene ³³	Visual cloud point detection ³³	0.9602-0.6397 ³³	309.56-411.50 ³³	33
8	[C ₂ mim][EtSO ₄]	Benzene ^{31, 34-35}	Visual cloud point detection ^{31, 34} Volumetric method ³⁵	0.4883-0.2445 ³¹ 0.4881-0.2451 ³⁴ 0.5683-0.5517 ³⁵	288.00-346.31 ³¹ 288.0- 346.3 ³⁴ 293.1- 333.1 ³⁵	31, 34-35
9		Toluene ^{30-31, 35}	Volumetric method ³⁰ Visual volumetric detection ³¹ Volumetric method ³⁵	0.0061-0.0046/0.7588- 0.7594 ³⁰ 0.7246-0.6351 ³¹ 0.7583-0.6757 ³⁵	293.15-323.15 ³⁰ 311.75-359.15 ³¹ 293.3-332.8 ³⁵	30-31, 35
10		Ethylbenzene ³¹	Volumetric method ³¹	0.8890-0.7500 ³¹	297.12-375.15 ³¹	31
11		<i>o</i> -xylene ³⁵	Volumetric method ³⁵	0.8528-0.8413 ³⁵	293.4-332.7 ³⁵	35
12		<i>m</i> -xylene ³⁵	Volumetric method ³⁵	0.9014-0.8835 ³⁵	293.3-332.7 ³⁵	35

13		<i>p</i> -xylene ³⁵	Volumetric method ³⁵	0.8971-0.8653 ³⁵	293.5-332.7 ³⁵	35
14	[C ₂ mim][PF ₆]	Benzene ⁵¹	Visual cloud point detection ⁵¹	0.4307-0.4500 ⁵¹	348.1-327.0 ⁵¹	51
15		Toluene ⁵¹	Visual cloud point detection ⁵¹	0.5990-0.6880 ⁵¹	378.1-327.0 ⁵¹	51
16		Ethylbenzene ⁵¹	Visual cloud point detection ⁵¹	0.7043-0.8423 ⁵¹	405.6-332.6 ⁵¹	51
17		<i>o</i> -xylene ⁵¹	Visual cloud point detection ⁵¹	0.6975-0.8473 ⁵¹	413.6-327.4 ⁵¹	51
18		<i>m</i> -xylene ⁵¹	Visual cloud point detection ⁵¹	0.7571-0.8277 ⁵¹	394.7-346.1 ⁵¹	51
19		<i>p</i> -xylene ⁵¹	Visual cloud point detection ⁵¹	0.7270-0.8367 ⁵¹	398.3-330.6 ⁵¹	51
20	[C ₂ mim][NTf ₂]	Benzene ⁴⁶	Visual cloud point detection ⁴⁶	0.22927-0.24222 ⁴⁶	300.58-360.91 ⁴⁶	46
21		Toluene ^{46, 67}	Visual cloud point detection ⁴⁶ Mass–volume technique ⁶⁷	0.3376-0.3513 ⁴⁶ 0.344-0.369 ⁶⁷	302.25-323.65 ⁴⁶ 297.7-372.9 ⁶⁷	46, 67
22		Ethylbenzene ⁶⁷	Mass–volume technique ⁶⁷	0.485-0.502 ⁶⁷	293.4-373.0 ⁶⁷	67
23		Propylbenzene ⁶⁷	Mass–volume technique ⁶⁷	0.639-0.632 ⁶⁷	293.1-373.0 ⁶⁷	67
24		<i>o</i> -xylene ⁶⁷	Mass–volume technique ⁶⁷	0.444-0.461 ⁶⁷	297.7-372.9 ⁶⁷	67
25		<i>m</i> -xylene ⁶⁷	Mass–volume technique ⁶⁷	0.498-0.519 ⁶⁷	297.7-372.9 ⁶⁷	67
26		<i>p</i> -xylene ⁶⁷	Mass–volume technique ⁶⁷	0.509-0.525 ⁶⁷	297.7-372.9 ⁶⁷	67
27	[C ₄ mim][MeSO ₄]	Benzene ^{33, 35}	Visual cloud point detection ³³ Volumetric method ³⁵	0.4533-0.2767 ³³ 0.4910-0.4615 ³⁵	303.12-348.37 ³³ 293.2-332.7 ³⁵	33, 35
28		Toluene ^{33, 35}	Visual cloud point detection ³³ Volumetric method ³⁵	0.6740-0.4153 ³³ 0.6749-0.5831 ³⁵	295.76-381.40 ³³ 293.2-332.7 ³⁵	33, 35
29		Ethylbenzene ³³	Visual cloud point detection ³³	0.6664-0.5038 ³³	317.19-408.81 ³³	33

30		Propylbenzene ³³	Visual cloud point detection ³³	0.9278-0.6457 ³³	275.50-430.20 ³³	33
31		<i>o</i> -xylene ^{33, 35}	Visual cloud point detection ³³ Volumetric method ³⁵	0.8094-0.5870 ³³ 0.7953-0.7617 ³⁵	307.93-412.47 ³³ 293.3-332.6 ³⁵	33, 35
32		<i>m</i> -xylene ^{33, 35}	Visual cloud point detection ³³ Volumetric method ³⁵	0.8322-0.6075 ³³ 0.8490-0.8311 ³⁵	305.77-410.08 ³³ 293.2-333.6 ³⁵	33, 35
33		<i>p</i> -xylene ^{33, 35}	Visual cloud point detection ³³ Volumetric method ³⁵	0.8218-0.5750 ³³ 0.8524-0.8180 ³⁵	302.37-411.18 ³³ 293.4-332.6 ³⁵	33, 35
34	[C ₄ mim][PF ₆]	Benzene ⁵¹	Visual cloud point detection ⁵¹	0.3411-0.3471 ⁵¹	353.2-293.1 ⁵¹	51
35		Toluene ⁵¹	Visual cloud point detection ⁵¹	0.5639-0.5680 ⁵¹	383.7-293.1 ⁵¹	51
36		Ethylbenzene ⁵¹	Visual cloud point detection ⁵¹	0.6548-0.7459 ⁵¹	401.1-294.1 ⁵¹	51
37		<i>o</i> -xylene ⁵¹	Visual cloud point detection ⁵¹	0.6441-0.7400 ⁵¹	401.1-293.1 ⁵¹	51
38		<i>m</i> -xylene ⁵¹	Visual cloud point detection ⁵¹	0.6937-0.7325 ⁵¹	391.1-294.1 ⁵¹	51
39		<i>p</i> -xylene ⁵¹	Visual cloud point detection ⁵¹	0.6905-0.7386 ⁵¹	393.1-297.1 ⁵¹	51
40	[C ₄ mim][BF ₄]	Benzene ⁶³	Visual cloud point detection ⁶³	0.00016-0.00095 ⁶³ 0.9993-0.9946 ⁶³	298.47-343.96 ⁶³ 298.21-343.53 ⁶³	63
41		Toluene ⁶³	Visual cloud point detection ⁶³	0.0003-0.0015 ⁶³ 0.9989-0.9946 ⁶³	301.47-353.41 ⁶³ 298.55-353.15 ⁶³	63
42		<i>o</i> -xylene ⁶³	Visual cloud point detection ⁶³	0.9995-0.9909 ⁶³	298.63-353.35 ⁶³	63
43		<i>m</i> -xylene ⁶³	Visual cloud point detection ⁶³	0.9992-0.9934 ⁶³	298.65-352.49 ⁶³	63
44		<i>p</i> -xylene ⁶³	Visual cloud point detection ⁶³	0.9994-0.9930 ⁶³	298.28-353.65 ⁶³	63
45	[C ₄ mim][NTf ₂]	Benzene ⁴⁶	Visual cloud point detection ⁴⁶	0.17802-0.19727 ⁴⁶	335.55-459.42 ⁴⁶	46

46		Toluene ⁴⁶	Visual cloud point detection ⁴⁶	0.2591 ⁴⁶	298.5 ⁴⁶	46
47	[C ₄ mim][TOS]	Benzene ³⁶	Visual cloud point detection ³⁶	0.3114-0.3270 ³⁶	345.48-300.01 ³⁶	36
48		Toluene ³⁶	Visual cloud point detection ³⁶	0.4195-0.4608 ³⁶	352.36-310.73 ³⁶	36
49		Ethylbenzene ³⁶	Visual cloud point detection ³⁶	0.4781-0.5675 ³⁶	358.87-320.46 ³⁶	36
50		Propylbenzene ³⁶	Visual cloud point detection ³⁶	0.7409-0.7559 ³⁶	357.96-331.33 ³⁶	36
51	[C ₄ mim][SCN]	Benzene ³²	Visual cloud point detection ³²	0.00167-0.00223 ³² 0.3765-0.4166 ³²	313.15-293.15 ³² 281.07-346.99 ³²	32
52		Toluene ³²	Visual cloud point detection ³²	0.6175-0.6290 ³²	281.28-345.18 ³²	32
53		Ethylbenzene ³²	Visual cloud point detection ³²	0.7500-0.7604 ³²	280.06-335.46 ³²	32
54	[C ₄ mim][CF ₃ SO ₃]	Benzene ⁵⁰	Visual cloud point detection ⁵⁰	0.2745-0.2921 ⁵⁰	296.7-352.2 ⁵⁰	50
55		Toluene ⁵⁰	Visual cloud point detection ⁵⁰	0.4403-0.4630 ⁵⁰	301.4-370.9 ⁵⁰	50
56	[C ₄ mim][MDEGSO ₄]	Benzene ³⁹	Visual cloud point detection ³⁹	0.3555-0.3969 ³⁹	326.55-293.25 ³⁹	39
57	[C ₆ mim][NTf ₂]	Benzene ⁴⁶	Visual cloud point detection ⁴⁶	0.00356-0.00631 ⁴⁶ 0.10540-0.12080 ⁴⁶	390.55-484.38 ⁴⁶ 297.71-482.63 ⁴⁶	46
58		Toluene ⁴⁶	Visual cloud point detection ⁴⁶	0.1798 ⁴⁶	298.52 ⁴⁶	46
59	[C ₆ mim][SCN]	Benzene ³⁸	Visual cloud point detection ³⁸	0.2824-0.2598 ³⁸	346.3-279.2 ³⁸	38
60		Toluene ³⁸	Visual cloud point detection ³⁸	0.4356-0.3509 ³⁸	355.7-221.8 ³⁸	38
61		Ethylbenzene ³⁸	Visual cloud point detection ³⁸	0.5835-0.4305 ³⁸	359.0-211.7 ³⁸	38
62	[C ₈ mim][NTf ₂]	Benzene ⁴⁶	Visual cloud point detection ⁴⁶	0.00171-0.02833 ⁴⁶ 0.03379-0.08667 ⁴⁶	300.32-374.31 ⁴⁶ 373.93-300.32 ⁴⁶	46

63		Toluene ⁴⁶	Visual cloud point detection ⁴⁶	0.1127-0.1217 ⁴⁶	317.75-286.65 ⁴⁶	46
64	[C ₁₀ mim][NTf ₂]	Benzene ⁴⁶	Visual cloud point detection ⁴⁶	0.00337-0.01790 ⁴⁶ 0.01874-0.04729 ⁴⁶	300.84-318.58 ⁴⁶ 318.27-300.60 ⁴⁶	46
65		Toluene ⁴⁶	Visual cloud point detection ⁴⁶	0.00192-0.01667 ⁴⁶ 0.01713-0.08282 ⁴⁶	282.75-340.25 ⁴⁶ 339.35-276.65 ⁴⁶	46
66	[C ₆ H ₁₃ OCH ₂ mim][BF ₄]	Benzene ⁴¹	Visual cloud point detection ⁴¹	0.0023-0.0010/0.1870-0.1991 ₄₁	351.25-292.65 ⁴¹	41
67		Toluene ⁴¹	Visual cloud point detection ⁴¹	0.3137-0.3530 ⁴¹	382.95-288.15 ⁴¹	41
68		Ethylbenzene ⁴¹	Visual cloud point detection ⁴¹	0.4348-0.4937 ⁴¹	408.35-306.85 ⁴¹	41
69		<i>o</i> -xylene ⁴¹	Visual cloud point detection ⁴¹	0.3785-0.4895 ⁴¹	416.05-294.75 ⁴¹	41
70		<i>m</i> -xylene ⁴¹	Visual cloud point detection ⁴¹	0.4496-0.5148 ⁴¹	408.35-310.85 ⁴¹	41
71		<i>p</i> -xylene ⁴¹	Visual cloud point detection ⁴¹	0.4335-0.5084 ⁴¹	410.95-298.55 ⁴¹	41
72	[C ₆ H ₁₃ OCH ₂ mim][NTf ₂]	Benzene ⁴¹	Visual cloud point detection ⁴¹	0.0201-0.0800/0.0189-0.0019 ₄₁	351.70-298.45 ⁴¹	41
73		Toluene ⁴¹	Visual cloud point detection ⁴¹	0.0116-0.1374/0.0835-0.0016 ₄₁	383.42-298.13 ⁴¹	41
74		Ethylbenzene	Visual cloud point detection ⁴¹	0.1136-0.1950/0.0095-0.0013 ₄₁	407.35-299.95 ⁴¹	41
75		<i>o</i> -xylene ⁴¹	Visual cloud point detection ⁴¹	0.1435-0.2018/0.0099-0.0018 ₄₁	416.89-295.58 ⁴¹	41
76		<i>m</i> -xylene ⁴¹	Visual cloud point detection ⁴¹	0.1500-0.2007/0.0094-0.0021 ₄₁	411.15-301.95 ⁴¹	41
77		<i>p</i> -xylene ⁴¹	Visual cloud point detection ⁴¹	0.1613-0.2023/0.0071-0.0014	411.55-295.25 ⁴¹	41

				41		
78	[C ₄ py][BF ₄]	Toluene ⁶⁸	Direct analytical method ⁶⁸	1.0×10^{-5} - 1.5×10^{-5} ⁶⁸ 0.680-0.676 ⁶⁸	298.15-338.15 ⁶⁸	68
79	[C ₆ py][BF ₄]	Toluene ⁶⁸	Direct analytical method ⁶⁸	2.8×10^{-5} - 1.3×10^{-5} ⁶⁸ 0.421-0.453 ⁶⁸	298.15-338.15 ⁶⁸	68
80	[1,2C ₄ mpy][BF ₄]	Toluene ⁶⁸	Direct analytical method ⁶⁸	1.6×10^{-5} - 3.5×10^{-5} ⁶⁸ 0.628-0.661 ⁶⁸	298.15-338.15 ⁶⁸	68
81	[1,3C ₄ mpy][CF ₃ SO ₃]	Benzene ⁵⁰	Visual cloud point detection ⁵⁰	0.2276-0.2467 ⁵⁰	282.9-348.4 ⁵⁰	50
82		Toluene ⁵⁰	Visual cloud point detection ⁵⁰	0.3601-0.3781 ⁵⁰	285.9-360.2 ⁵⁰	50
83	[1,4C ₄ mpy][BF ₄]	Toluene ⁶⁸	Direct analytical method ⁶⁸	4.1×10^{-5} - 5.2×10^{-5} ⁶⁸ 0.525-0.554 ⁶⁸	298.15-338.15 ⁶⁸	68
84	[1,4C ₄ mpy][NTf ₂]	Benzene ⁵⁴	Visual cloud point detection ⁵⁴	0.1578-0.1467 ⁵⁴	285.4-344.9 ⁵⁴	54
85		Toluene ⁵⁴	Visual cloud point detection ⁵⁴	0.1983-0.1941 ⁵⁴	299.8-253.5 ⁵⁴	54
86		Ethylbenzene ⁵⁴	Visual cloud point detection ⁵⁴	0.2860-0.2638 ⁵⁴	317.6-257.4 ⁵⁴	54
87		Propylbenzene ⁵⁴	Visual cloud point detection ⁵⁴	0.3623-0.3376 ⁵⁴	303.2-265.1 ⁵⁴	54
88	[1,4C ₄ mpy][TOS]	Benzene ⁴⁹	Visual cloud point detection ⁴⁹	0.2334-0.2539 ⁴⁹	336.72-280.94 ⁴⁹	49
89		Toluene ⁴⁹	Visual cloud point detection ⁴⁹	0.4031-0.4448 ⁴⁹	368.82-304.93 ⁴⁹	49
90		Ethylbenzene ⁴⁹	Visual cloud point detection ⁴⁹	0.5276-0.5826 ⁴⁹	378.51-316.22 ⁴⁹	49
91		Propylbenzene ⁴⁹	Visual cloud point detection ⁴⁹	0.6526-0.6937 ⁴⁹	390.40-329.49 ⁴⁹	49
92	[C ₄ mpyr][CF ₃ SO ₃]	Benzene ⁵⁰	Visual cloud point detection ⁵⁰	0.2703-0.2876 ⁵⁰	289.4-353.0 ⁵⁰	50

93		Toluene ⁵⁰	Visual cloud point detection ⁵⁰	0.4179-0.4421 ⁵⁰	286.0-365.3 ⁵⁰	50
94	[P _{i(444)}] ₁][TOS]	Toluene ⁴⁷	Visual cloud point detection ⁴⁷	0.1287-0.0111 ⁴⁷	320.93-333.68 ⁴⁷	47
95		Ethylbenzene ⁴⁷	Visual cloud point detection ⁴⁷	0.0064-0.2146 ⁴⁷	320.38-359.39 ⁴⁷	47
96		Propylbenzene ⁴⁷	Visual cloud point detection ⁴⁷	0.40.89-0.0056 ⁴⁷	304.23-362.43 ⁴⁷	47
97		Butylbenzene ⁴⁷	Visual cloud point detection ⁴⁷	0.5277-0.0016 ⁴⁷	303.89-340.52 ⁴⁷	47
98	[N _{22(OH)11}][NTf ₂]	Benzene ⁴⁵	Visual cloud point detection ⁴⁵	0.3668-0.1822 ⁴⁵	283.33-423.81 ⁴⁵	45
99		Toluene ⁴⁵	Visual cloud point detection ⁴⁵	0.5793-0.4056 ⁴⁵	300.56-431.30 ⁴⁵	45
100	[N _{62(OH)11}][Br]	Benzene ³⁴	Visual cloud point detection ³⁴	0.6893-0.3378 ³⁴	364.5- 398.0 ³⁴	34

Table B3 Published LLE experimental data, measurement technique used and composition and temperature range of ILs + cycloalkanes binary systems.

	Ionic liquid	Cycloalkane	Experimental measurement technique	Composition range (x_{IL})	Temperature range (K)	References
1	[C ₁ mim][MeSO ₄]	Cyclohexane ³³	Visual cloud point detection ³³	0.9531-0.7404 ³³	316.90-348.12 ³³	33
2		Cycloheptane ³³	Visual cloud point detection ³³	0.9571-0.6145 ³³	313.98-362.50 ³³	33
3	[C ₂ mim][EtSO ₄]	Methylcyclohexane ₃₀	Volumetric method ³⁰	0.0145-0.0063/0.9792-0.9600 ³⁰	293.15-333.15 ³⁰	30
4	[C ₂ mim][TOS]	Cycloheptane ³⁴	Visual cloud point detection ³⁴	0.5854-0.8981 ³⁴	363.6-342.6 ³⁴	34
5	[C ₄ mim][MeSO ₄]	Cyclohexane ³³	Visual cloud point detection ³³	0.9136-0.6627 ³³	296.25-353.35 ³³	33
6		Cycloheptane ³³	Visual cloud point detection ³³	0.9416-0.7342 ³³	318.11-406.33 ³³	33
7	[C ₄ mim][PF ₆]	Cyclopentane ⁵¹	Visual cloud point detection ⁵¹	0.7974-0.9633 ⁵¹	322.8-293.1 ⁵¹	51
8		Cyclohexane ⁵¹	Visual cloud point detection ⁵¹	0.7605-0.9471 ⁵¹	352.7-302.1 ⁵¹	51
9	[C ₄ mim][SCN]	Cyclohexane ³²	Visual cloud point detection ³²	0.0000212-0.0000435 ³² 0.9023-0.9860 ³²	303.15-343.15 ³² 381.99-292.61 ³²	32
10		Cycloheptane ³²	Visual cloud point detection ³²	0.9277-0.9890 ³²	416.32-290.91 ³²	32
11	[C ₄ mim][CF ₃ SO ₃]	Cyclohexane ⁵⁰	Visual cloud point detection ⁵⁰	0.9423-0.8925 ⁵⁰	295.1-352.6 ⁵⁰	50
12	[C ₄ mim][MDEGSO ₄]	Cyclohexane ³⁹	Visual cloud point detection ³⁹	0.8418-0.9054 ³⁹	346.05-303.75 ³⁹	39
13	[C ₆ mim][SCN]	Cyclohexane ³⁸	Visual cloud point detection ³⁸	0.9727-0.7613 ³⁸	289.1-407.8 ³⁸	38
14		Cycloheptane ³⁸	Visual cloud point detection ³⁸	0.9698-0.8640 ³⁸	279.6-411.1 ³⁸	38

15	[C ₆ H ₁₃ OCH ₂ mim][BF ₄]	Cyclohexane ⁴¹	Visual cloud point detection ⁴¹	0.6609-0.7187 ⁴¹	353.20-300.38 ⁴¹	41
16	[C ₆ H ₁₃ OCH ₂ mim][NTf ₂]	Cyclohexane ⁴¹	Visual cloud point detection ⁴¹	0.5105-0.6279 ⁴¹	352.65-305.75 ⁴¹	41
17	[(C ₆ H ₁₃ OCH ₂) ₂ im][NTf ₂]	Cyclohexane ⁴²	Visual cloud point detection ⁴²	0.3704-0.2605 ⁴²	300.65-352.75 ⁴²	42
18	[1,3C ₄ mpy][CF ₃ SO ₃]	Cyclohexane ⁵⁰	Visual cloud point detection ⁵⁰	0.9044-0.8701 ⁵⁰	304.4-351.0 ⁵⁰	50
19	[1,4C ₄ mpy][NTf ₂]	Cyclohexane ⁵⁴	Visual cloud point detection ⁵⁴	0.8163-0.6938 ⁵⁴	300.5-353.0 ⁵⁴	54
20	[C ₄ mpyr][CF ₃ SO ₃]	Cyclohexane ⁵⁰	Visual cloud point detection ⁵⁰	0.9307-0.8841 ⁵⁰	302.0-353.7 ⁵⁰	50

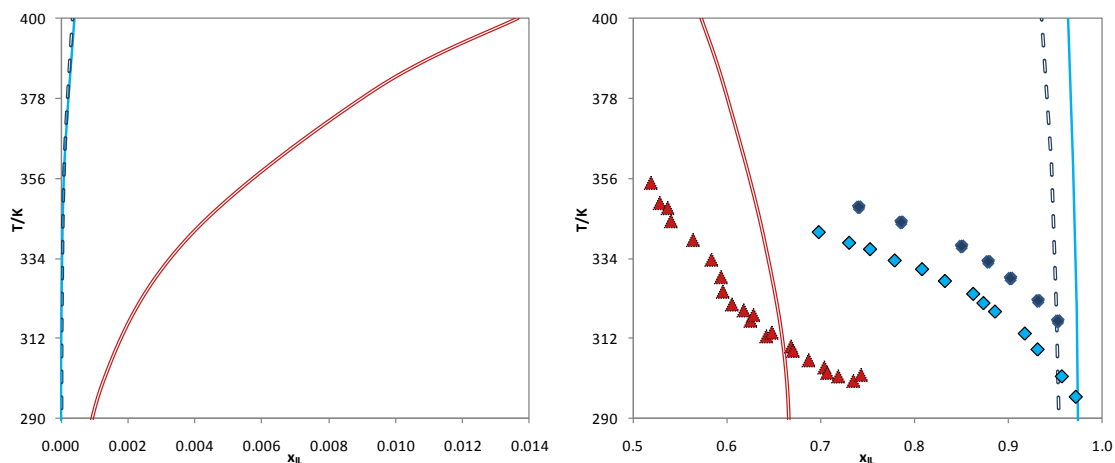


Figure B1 Liquid–liquid phase diagram for $[C_1mim][MeSO_4]$ with n -hexane³³ (\diamond) (—), benzene³³ (\blacktriangle) (—) and cyclohexane³³ (\blacklozenge) (—). The symbols and the lines represent respectively the experimental data and the COSMO-RS prediction calculations.

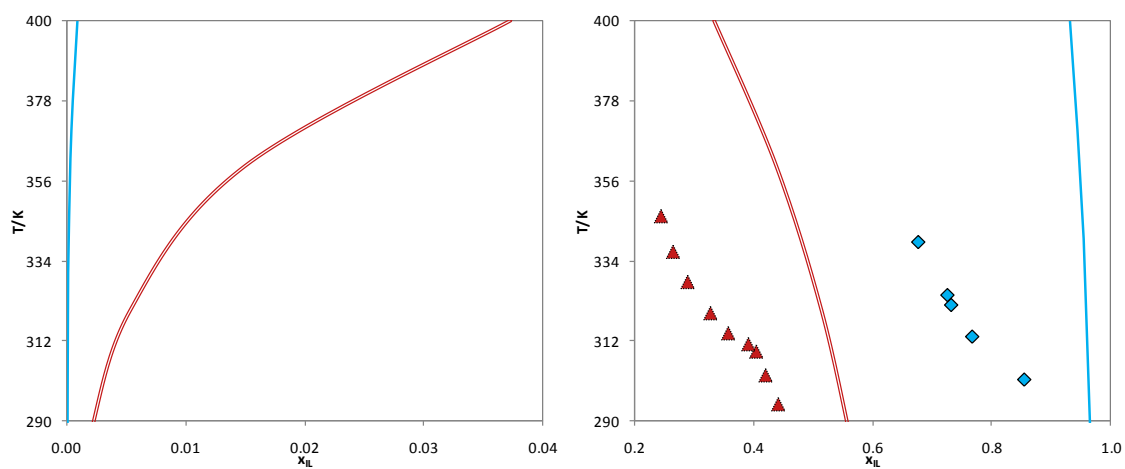


Figure B2 Liquid–liquid phase diagram for $[C_2mim][EtSO_4]$ with n -hexane³¹ (\diamond) (—) and benzene³¹ (\blacktriangle) (—). The symbols and the lines represent respectively the experimental data and the COSMO-RS prediction calculations.

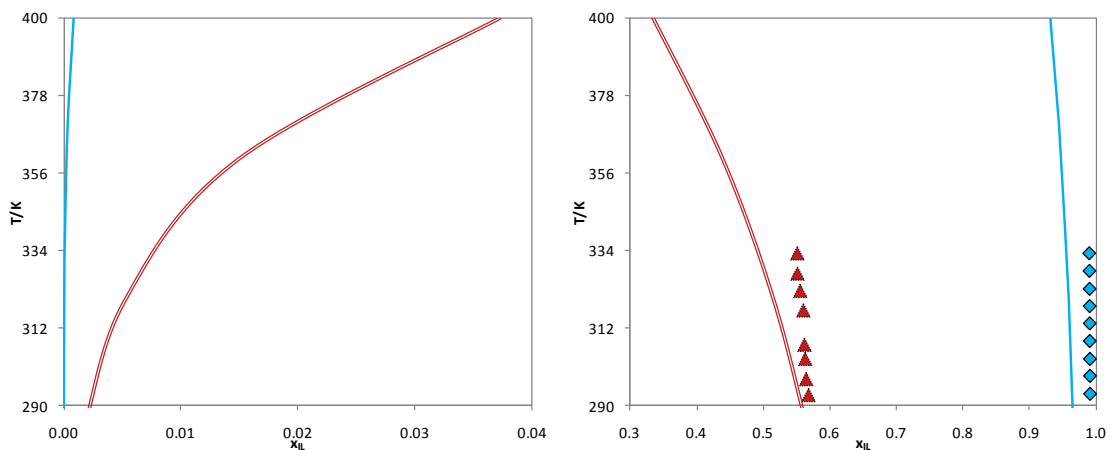


Figure B3 Liquid–liquid phase diagram for $[C_2mim][EtSO_4]$ with n -hexane³⁵ (\diamond) (—) and benzene³⁵ (\blacktriangle) (—). The symbols and the lines represent respectively the experimental data and the COSMO-RS prediction calculations.

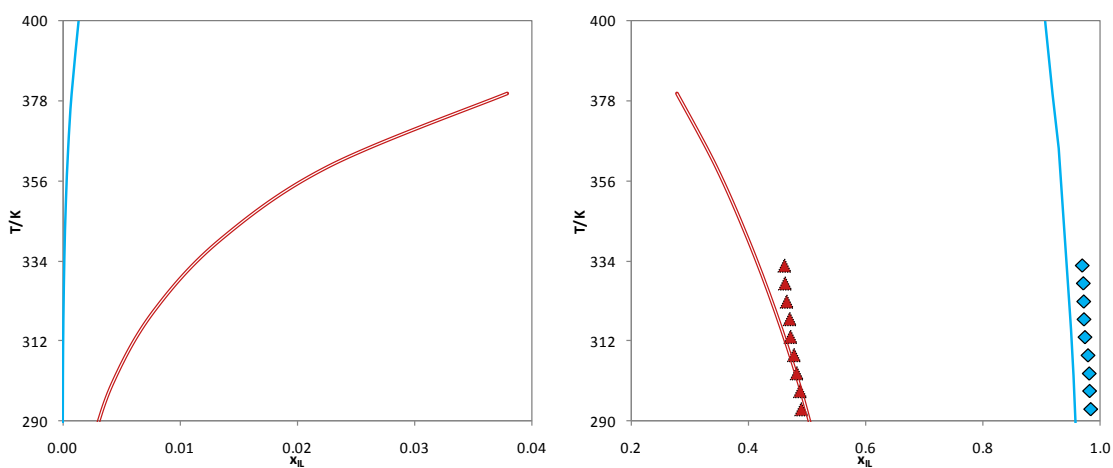


Figure B4 Liquid–liquid phase diagram for $[C_4mim][MeSO_4]$ with n -hexane³⁵ (\diamond) (—) and benzene³⁵ (\blacktriangle) (—). The symbols and the lines represent respectively the experimental data and the COSMO-RS prediction calculations.

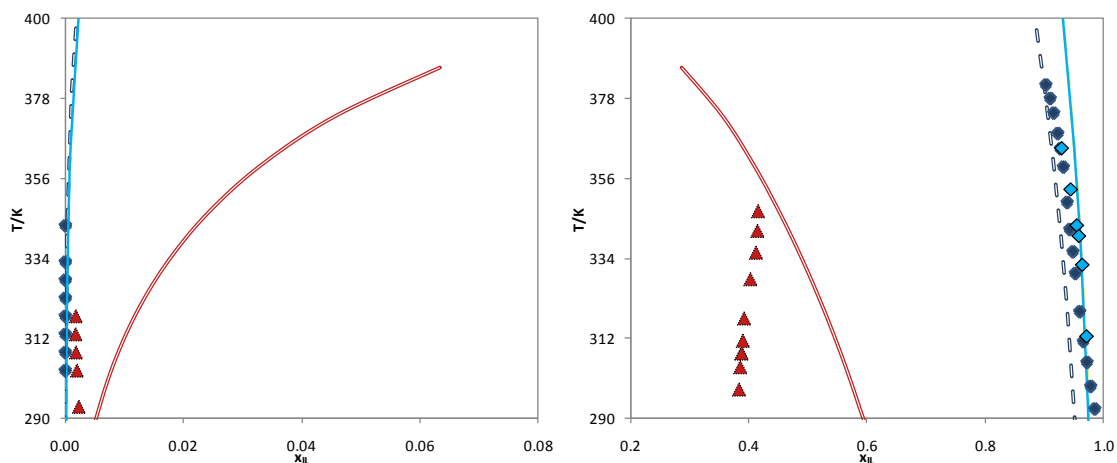


Figure B5 Liquid–liquid phase diagram for $[\text{C}_4\text{mim}][\text{SCN}]$ with *n*-hexane³² (\blacklozenge) (—), benzene³² (\blacktriangle) (—) and cyclohexane³² (\blacklozenge) (—). The symbols and the lines represent respectively the experimental data and the COSMO-RS prediction calculations.

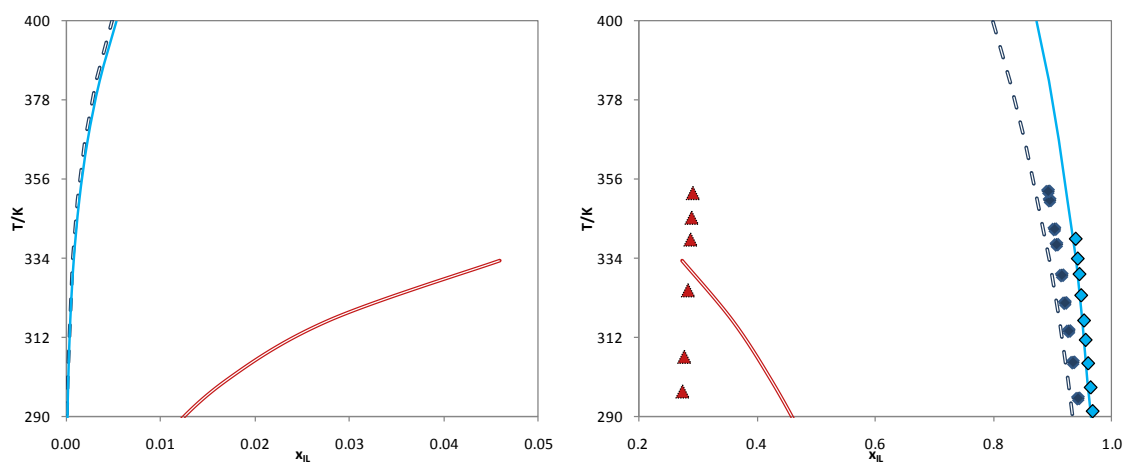


Figure B6 Liquid–liquid phase diagram for $[\text{C}_4\text{mim}][\text{CF}_3\text{SO}_3]$ with *n*-hexane⁵⁰ (\blacklozenge) (—), benzene⁵⁰ (\blacktriangle) (—) and cyclohexane⁵⁰ (\blacklozenge) (—). The symbols and the lines represent respectively the experimental data and the COSMO-RS prediction calculations.

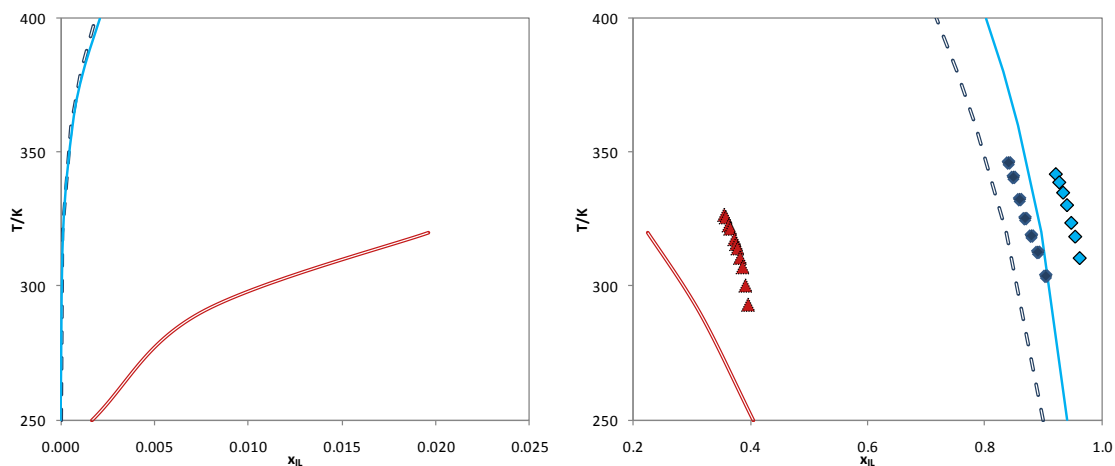


Figure B7 Liquid–liquid phase diagram for $[\text{C}_4\text{mim}][\text{MDEGSO}_4]$ with n -hexane³⁹ (\blacklozenge) (—), benzene³⁹ (\blacktriangle) (—) and cyclohexane³⁹ (\blacklozenge) (—). The symbols and the lines represent respectively the experimental data and the COSMO-RS prediction calculations.

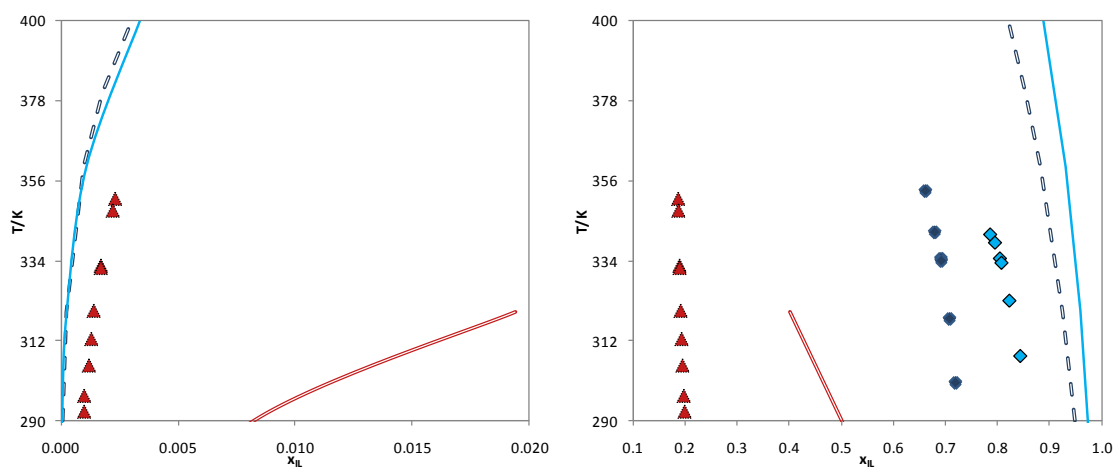


Figure B8 Liquid–liquid phase diagram for $[\text{C}_6\text{H}_{13}\text{OCH}_2\text{mim}][\text{BF}_4]$ with n -hexane⁴¹ (\blacklozenge) (—), benzene⁴¹ (\blacktriangle) (—) and cyclohexane⁴¹ (\blacklozenge) (—). The symbols and the lines represent respectively the experimental data and the COSMO-RS prediction calculations.

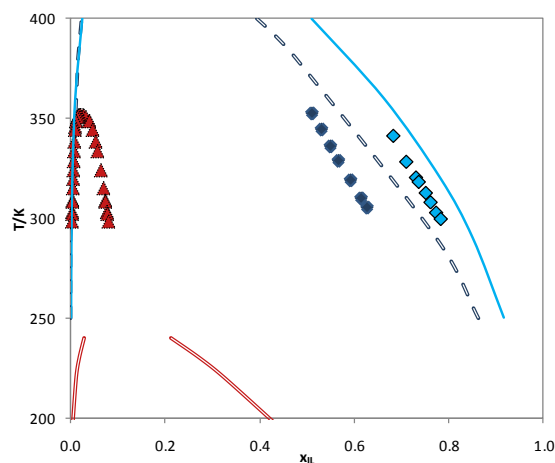


Figure B9 Liquid–liquid phase diagram for $[\text{C}_6\text{H}_{13}\text{OCH}_2\text{mim}][\text{NTf}_2]$ with *n*-hexane ⁴¹ (◆) (—), benzene ⁴¹ (▲) (—) and cyclohexane ⁴¹ (◆) (—). The symbols and the lines represent respectively the experimental data and the COSMO-RS prediction calculations.

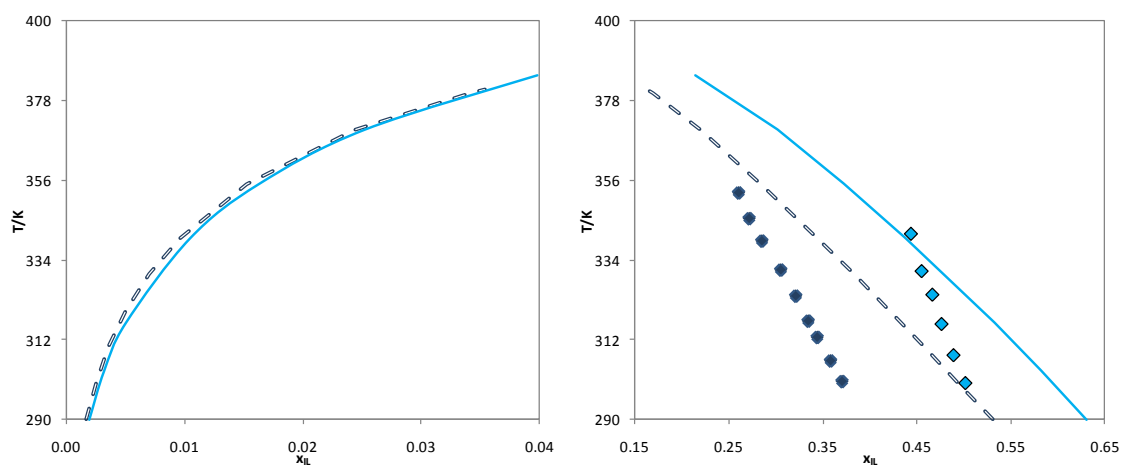


Figure B10 Liquid–liquid phase diagram for $[(\text{C}_6\text{H}_{13}\text{OCH}_2)_2\text{im}][\text{NTf}_2]$ with *n*-hexane (◆) (—) and cyclohexane (◆) (—). The symbols and the lines represent respectively the experimental data and the COSMO-RS prediction calculations.

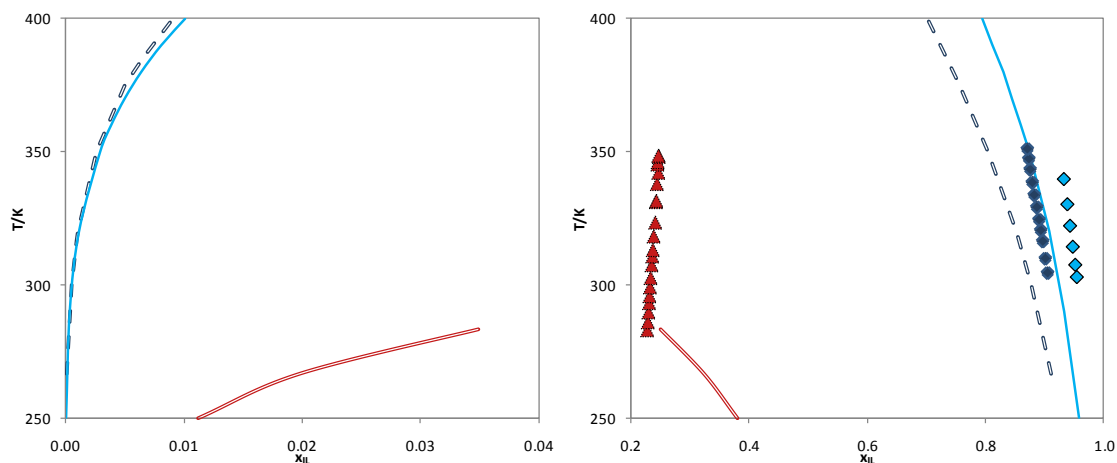


Figure B11 Liquid–liquid phase diagram for [1,3C₄mpy][CF₃SO₃] with *n*-hexane⁵⁰ (◆) (—), benzene⁵⁰ (▲) (—) and cyclohexane⁵⁰ (◆) (—). The symbols and the lines represent respectively the experimental data and the COSMO-RS prediction calculations.

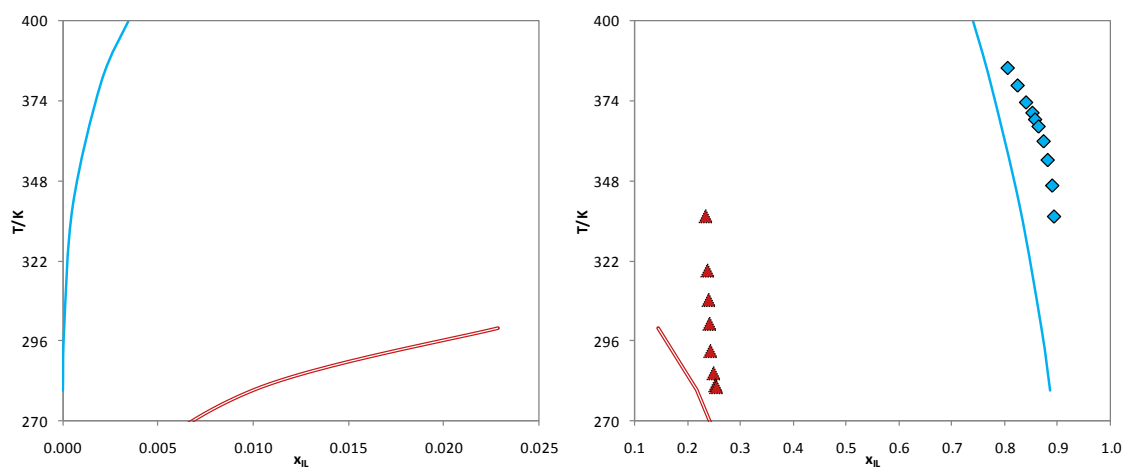


Figure B12 Liquid–liquid phase diagram for [1,4C₄mpy][TOS] with *n*-hexane⁴⁹ (◆) (—) and benzene⁴⁹ (▲) (—). The symbols and the lines represent respectively the experimental data and the COSMO-RS prediction calculations.

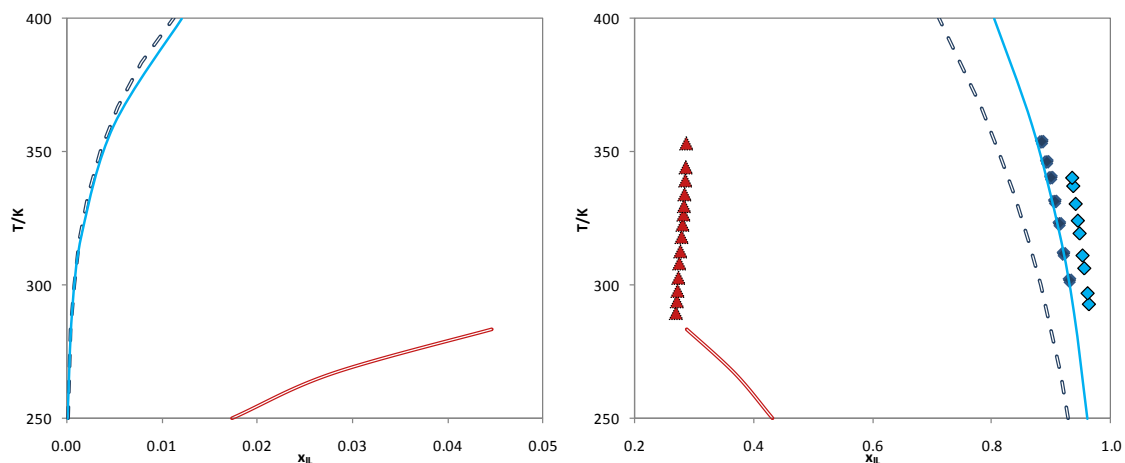


Figure B13 Liquid–liquid phase diagram for $[\text{C}_4\text{mpyr}][\text{CF}_3\text{SO}_3]$ with *n*-hexane⁵⁰ (\blacklozenge) (—), benzene⁵⁰ (\blacktriangle) (—) and cyclohexane⁵⁰ (\blacklozenge) (—). The symbols and the lines represent respectively the experimental data and the COSMO-RS prediction calculations.

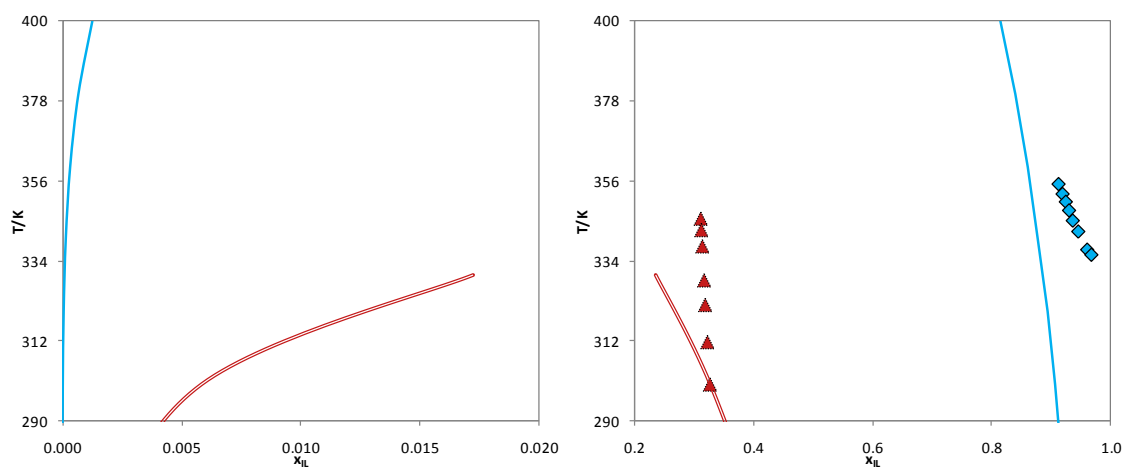


Figure B14 Liquid–liquid phase diagram for $[\text{C}_4\text{mim}][\text{TOS}]$ with *n*-hexane³⁶ (\blacklozenge) (—) and benzene³⁶ (\blacktriangle) (—). The symbols and the lines represent respectively the experimental data and the COSMO-RS prediction calculations.

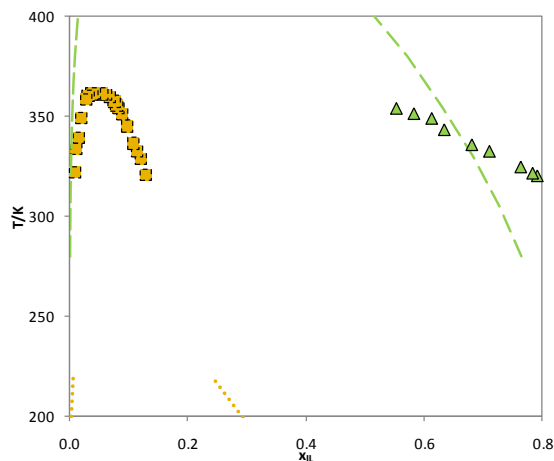


Figure B15 Liquid–liquid phase diagram for $[P_{(444)1}][TOS]$ with n -heptane⁴⁷ (Δ) (—) and toluene⁴⁷ (\square) (⋯). The symbols and the lines represent respectively the experimental data and the COSMO-RS prediction calculations.

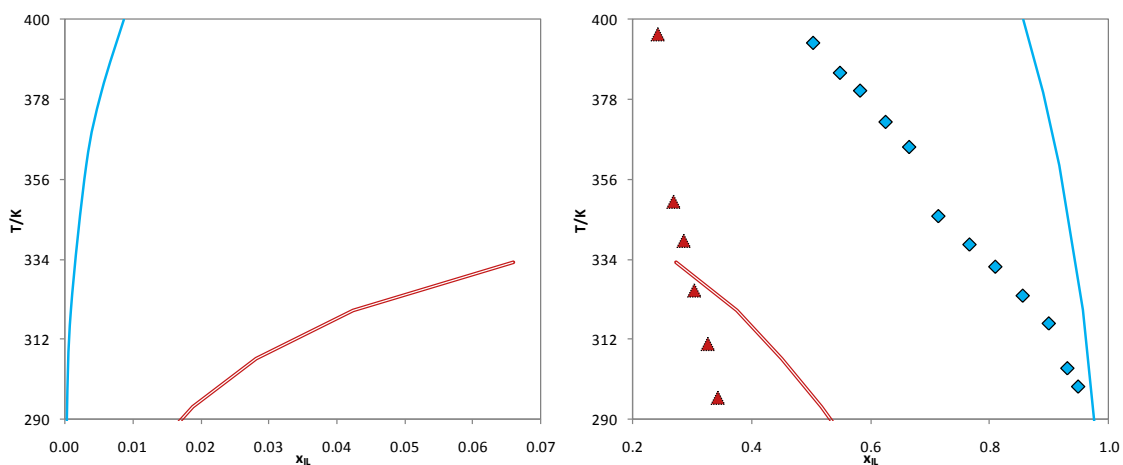


Figure B16 Liquid–liquid phase diagram for $[N_{20H211}][NTf_2]$ with n -hexane⁴⁵ (\diamond) (—) and benzene^{31, 35, 45} (\blacktriangle) (—). The symbols and the lines represent respectively the experimental data and the COSMO-RS prediction calculations.

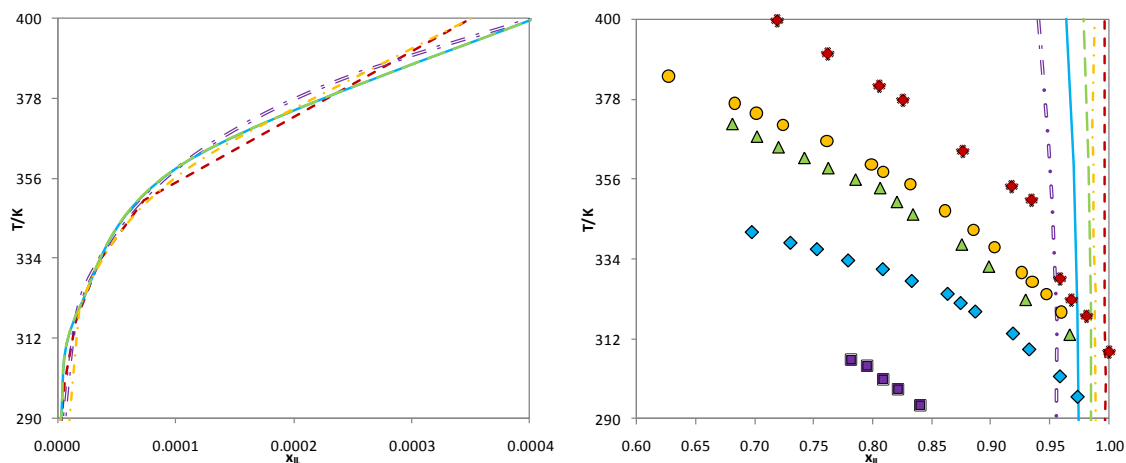


Figure B17 Liquid–liquid phase diagram for $[\text{C}_1\text{mim}][\text{MeSO}_4]$ with n -pentane³³ (\blacksquare) (---), n -hexane³³ (\blacklozenge) (---), n -heptane³³ (\blacktriangle) (---), n -octane³³ (\bullet) (---) and n -decane³³ (\blacklozenge) (---). The symbols and the lines represent respectively the experimental data and the COSMO-RS prediction calculations.

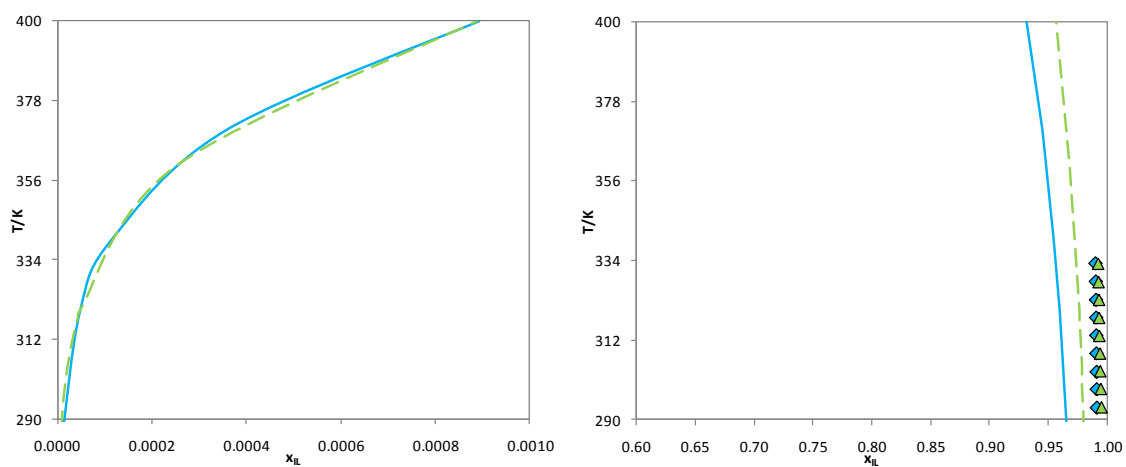


Figure B18 Liquid–liquid phase diagram for $[\text{C}_2\text{mim}][\text{EtSO}_4]$ with n -hexane³⁵ (\blacklozenge) (---) and n -heptane³⁵ (\blacktriangle) (---). The symbols and the lines represent respectively the experimental data and the COSMO-RS prediction calculations.

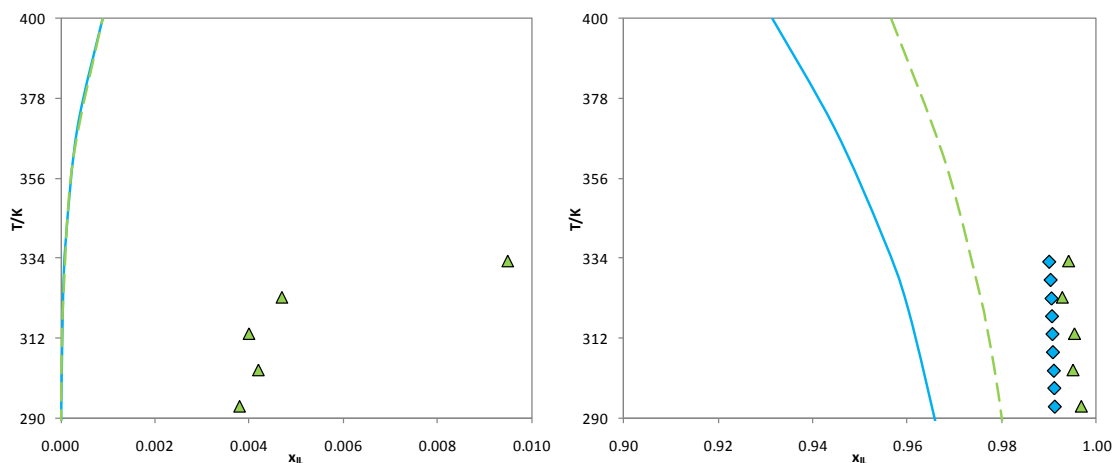


Figure B19 Liquid–liquid phase diagram for [C₂mim][EtSO₄] with *n*-hexane³⁵ (◆) (—) and *n*-heptane³⁰ (▲) (---). The symbols and the lines represent respectively the experimental data and the COSMO-RS prediction calculations.

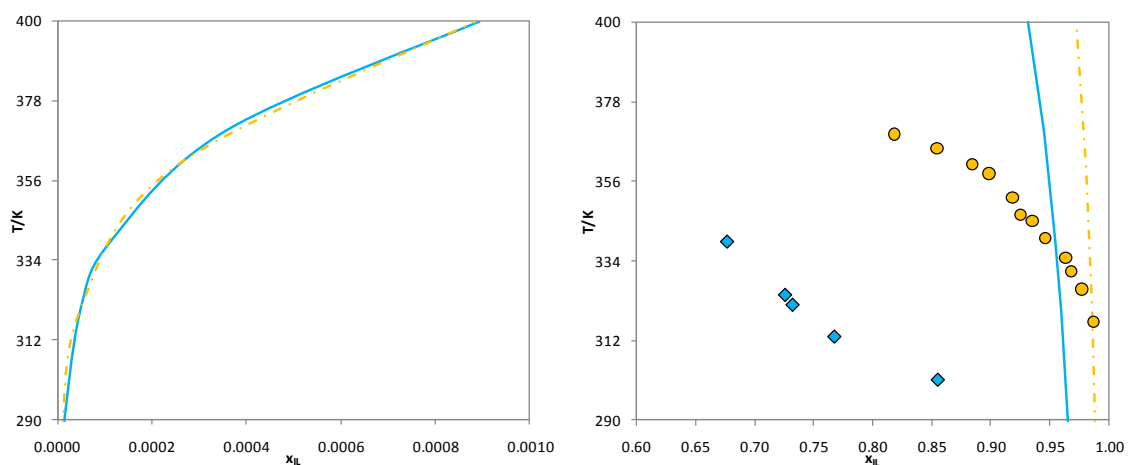


Figure B20 Liquid–liquid phase diagram for [C₂mim][EtSO₄] with *n*-hexane³¹ (◆) (—) and *n*-octane³¹ (●) (---). The symbols and the lines represent respectively the experimental data and the COSMO-RS prediction calculations.

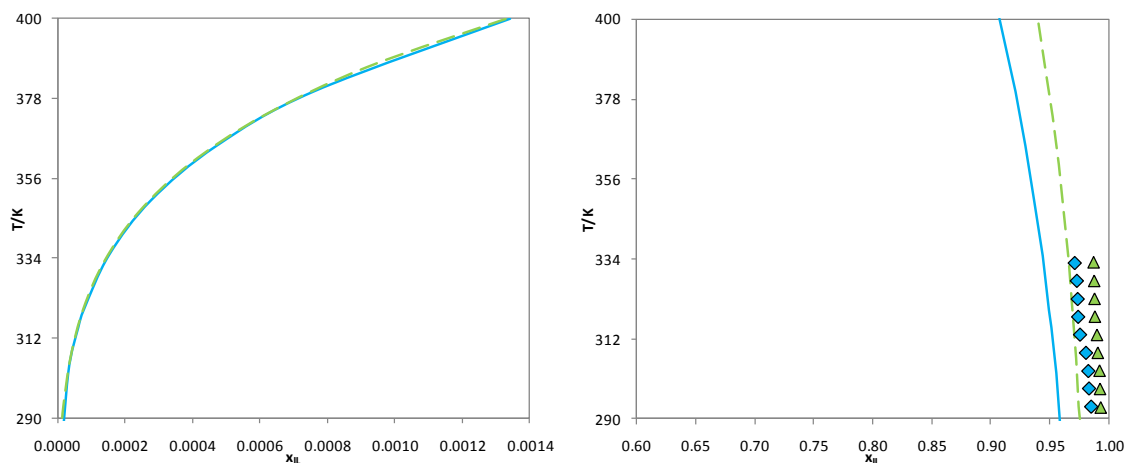


Figure B21 Liquid–liquid phase diagram for $[\text{C}_4\text{mim}][\text{MeSO}_4]$ with n -hexane³⁵ (\diamond) (—) and n -heptane³⁵ (\triangle) (— —). The symbols and the lines represent respectively the experimental data and the COSMO-RS prediction calculations.

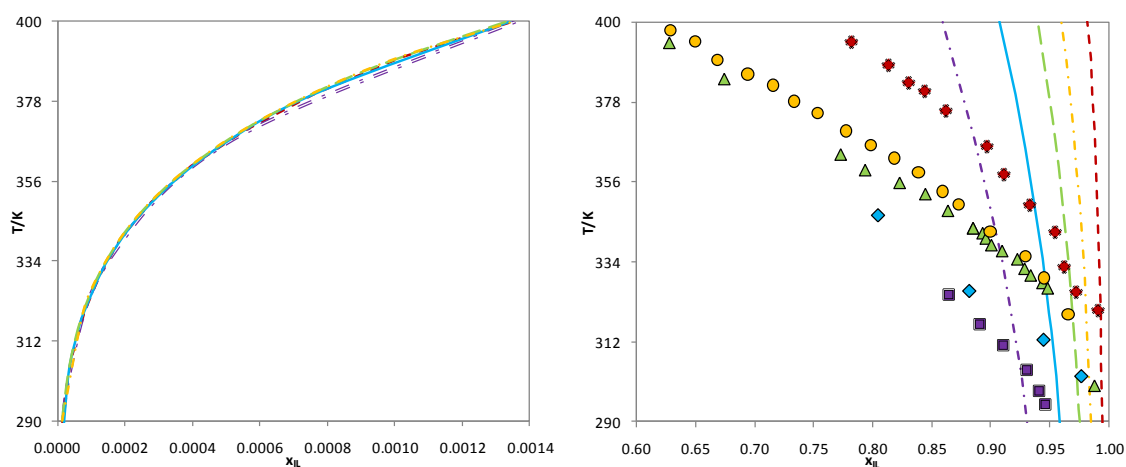


Figure B22 Liquid–liquid phase diagram for $[\text{C}_4\text{mim}][\text{MeSO}_4]$ with n -pentane³³ (\blacksquare) (— · —), n -hexane³³ (\diamond) (—), n -heptane³³ (\triangle) (— —), n -octane³³ (\circ) (— · —) and n -decane³³ (\blacklozenge) (— · —). The symbols and the lines represent respectively the experimental data and the COSMO-RS prediction calculations.

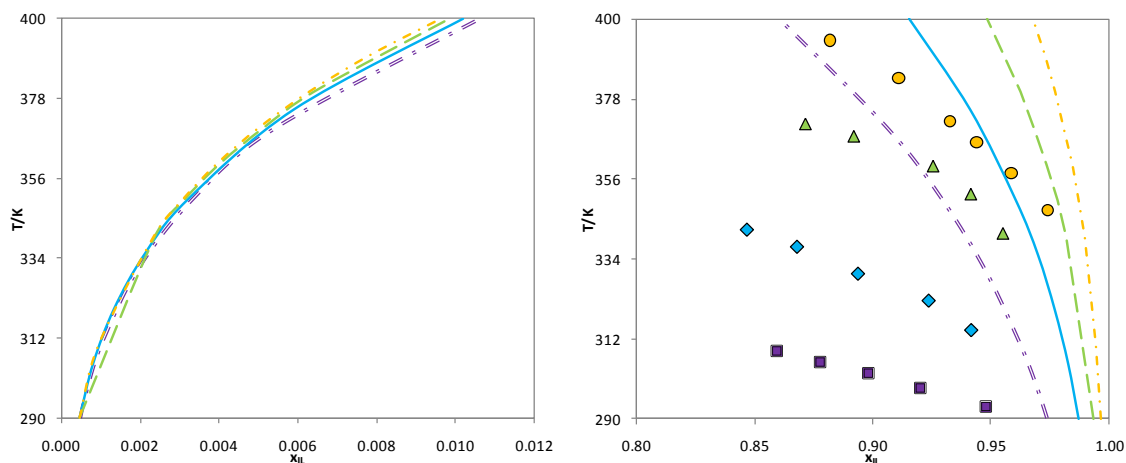


Figure B23 Liquid–liquid phase diagram for [C₄mim][PF₆] with *n*-pentane⁵¹ (■) (— · —), *n*-hexane⁵¹ (◆) (—), *n*-heptane⁵¹ (▲) (— —) and *n*-octane⁵¹ (●) (— · —). The symbols and the lines represent respectively the experimental data and the COSMO-RS prediction calculations.

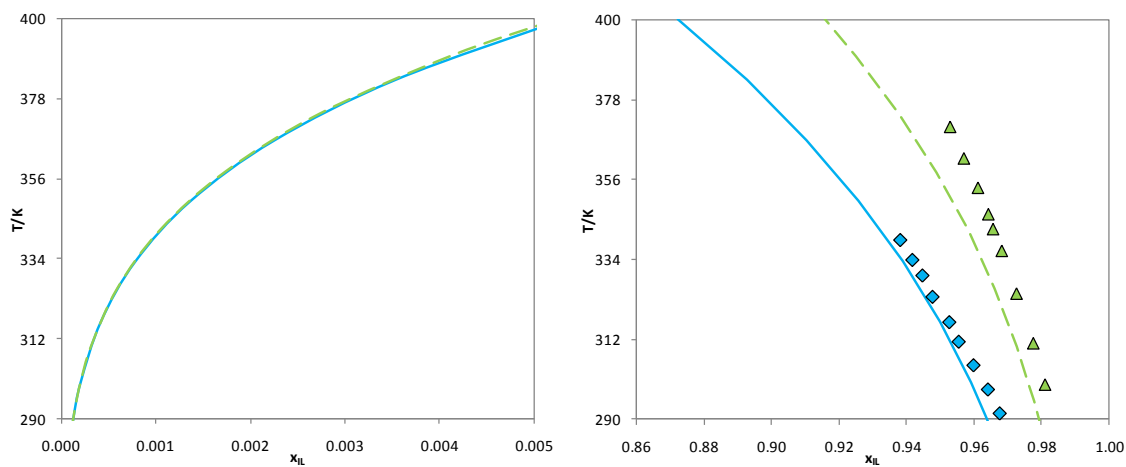


Figure B24 Liquid–liquid phase diagram for [C₄mim][CF₃SO₃] with *n*-hexane⁵⁰ (◆) (—) and *n*-heptane⁵⁰ (▲) (— —). The symbols and the lines represent respectively the experimental data and the COSMO-RS prediction calculations.

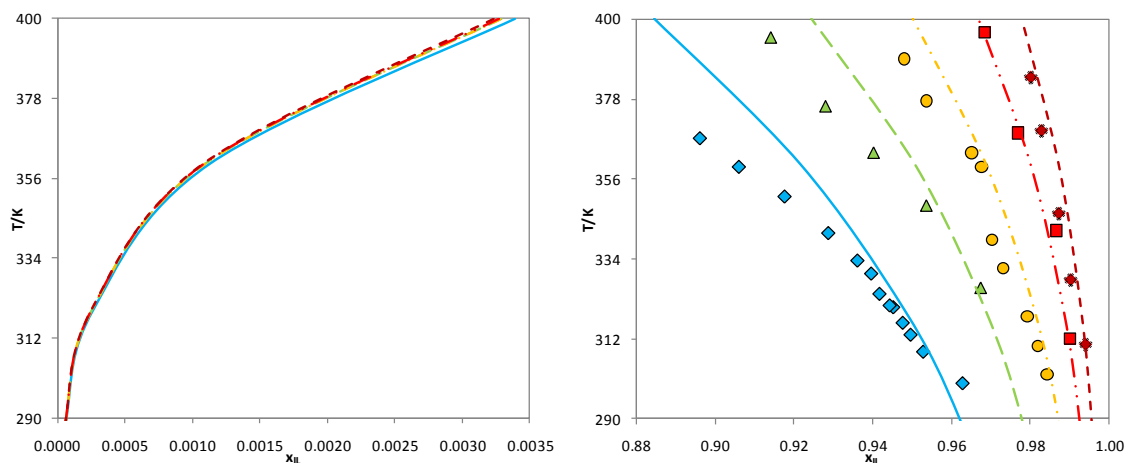


Figure B25 Liquid–liquid phase diagram for $[\text{C}_6\text{mim}][\text{SCN}]$ with n -hexane³⁸ (\diamond) (—), n -heptane³⁸ (\triangle) (— —), n -octane³⁸ (\circ) (- · - ·), n -nonane³⁸ (\square) (- · · -) and n -decane³⁸ (\star) (- - -). The symbols and the lines represent respectively the experimental data and the COSMO-RS prediction calculations.

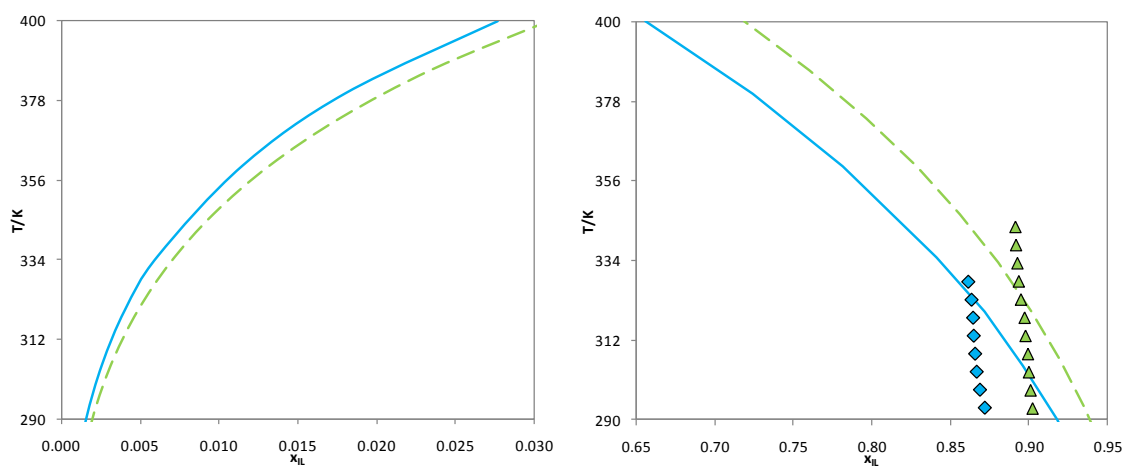


Figure B26 Liquid–liquid phase diagram for $[\text{C}_8\text{mim}][\text{PF}_6]$ with n -hexane⁴⁰ (\diamond) (—) and n -heptane⁴⁰ (\triangle) (— —). The symbols and the lines represent respectively the experimental data and the COSMO-RS prediction calculations.

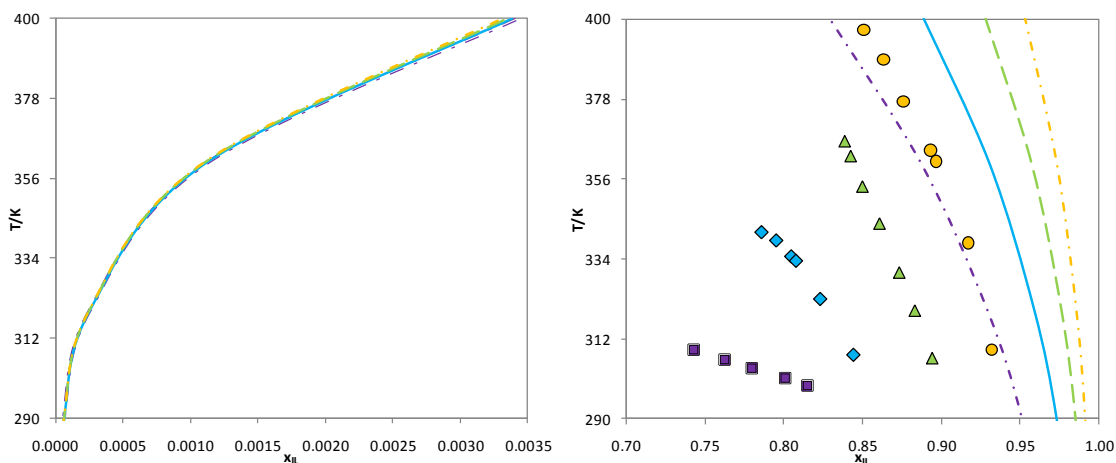


Figure B27 Liquid–liquid phase diagram for $[\text{C}_6\text{H}_{13}\text{OCH}_2\text{mim}][\text{BF}_4]$ with *n*-pentane⁴¹ (■) (— · —), *n*-hexane⁴¹ (◆) (—), *n*-heptane⁴¹ (▲) (— —), and *n*-octane⁴¹ (●) (— · —). The symbols and the lines represent respectively the experimental data and the COSMO-RS prediction calculations.

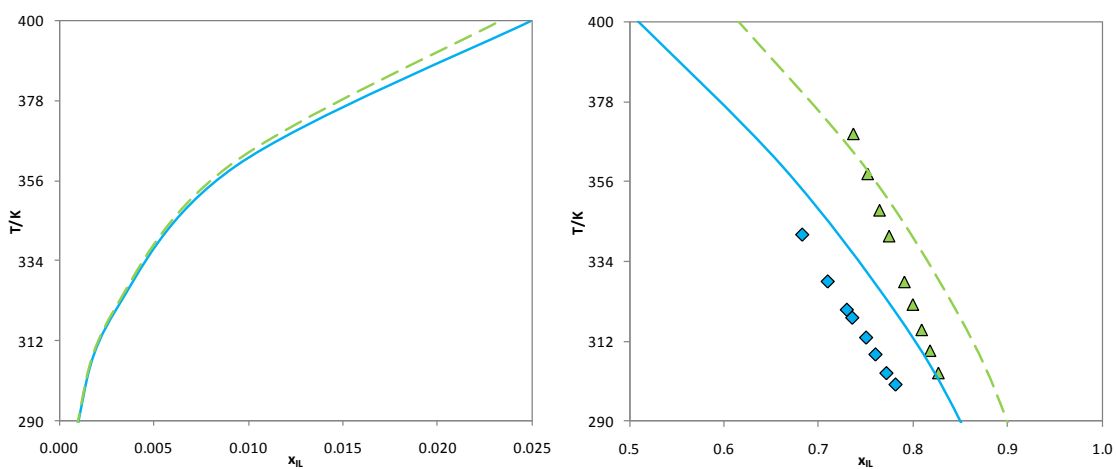


Figure B28 Liquid–liquid phase diagram for $[\text{C}_6\text{H}_{13}\text{OCH}_2\text{mim}][\text{NTf}_2]$ with *n*-hexane⁴¹ (◆) (—) and *n*-heptane⁴¹ (▲) (— —). The symbols and the lines represent respectively the experimental data and the COSMO-RS prediction calculations.

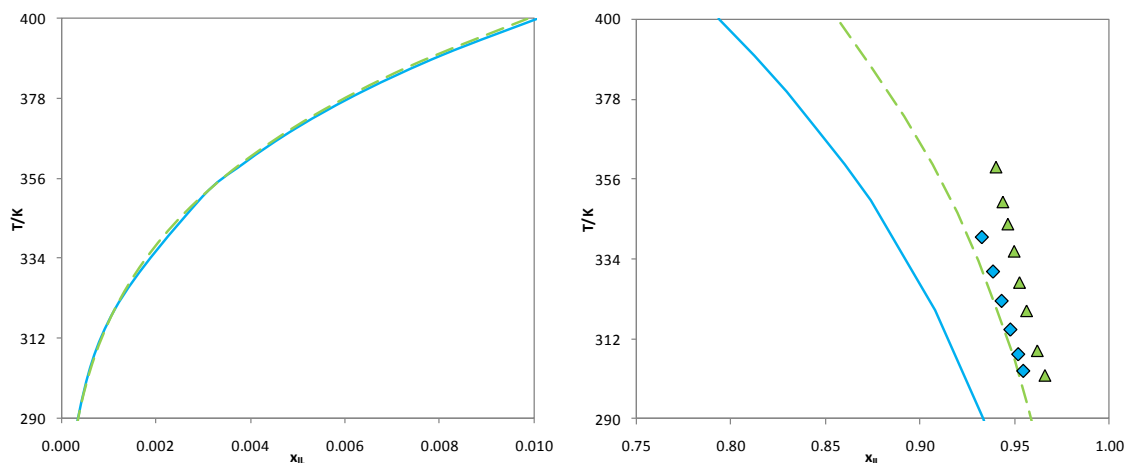


Figure B29 Liquid–liquid phase diagram for [1,3C₄mpy][CF₃SO₃] with *n*-hexane⁵⁰ (◆) (—) and *n*-heptane⁵⁰ (▲) (---). The symbols and the lines represent respectively the experimental data and the COSMO-RS prediction calculations.

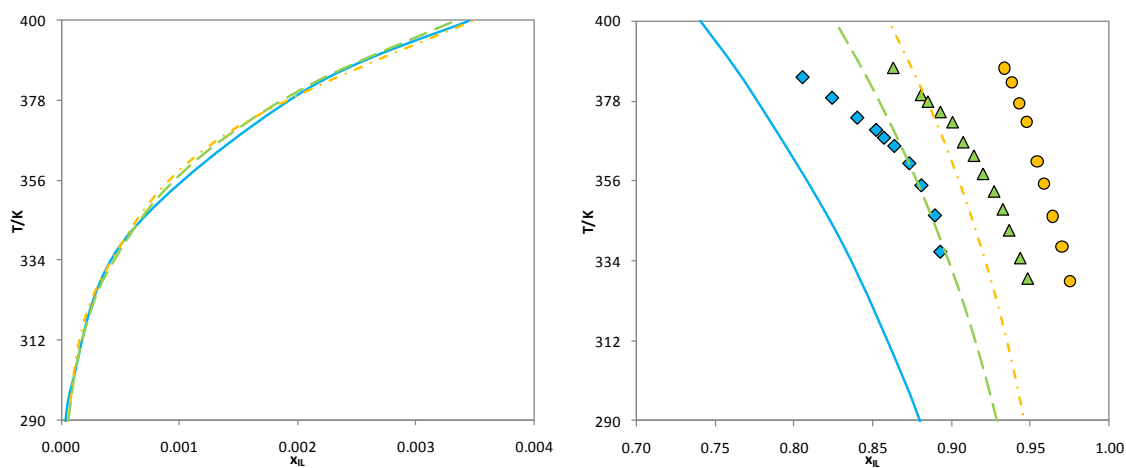


Figure B30 Liquid–liquid phase diagram for [1,4C₄mpy][TOS] with *n*-hexane⁴⁹ (◆) (—), *n*-heptane⁴⁹ (▲) (---) and *n*-octane⁴⁹ (●) (-.-). The symbols and the lines represent respectively the experimental data and the COSMO-RS prediction calculations.

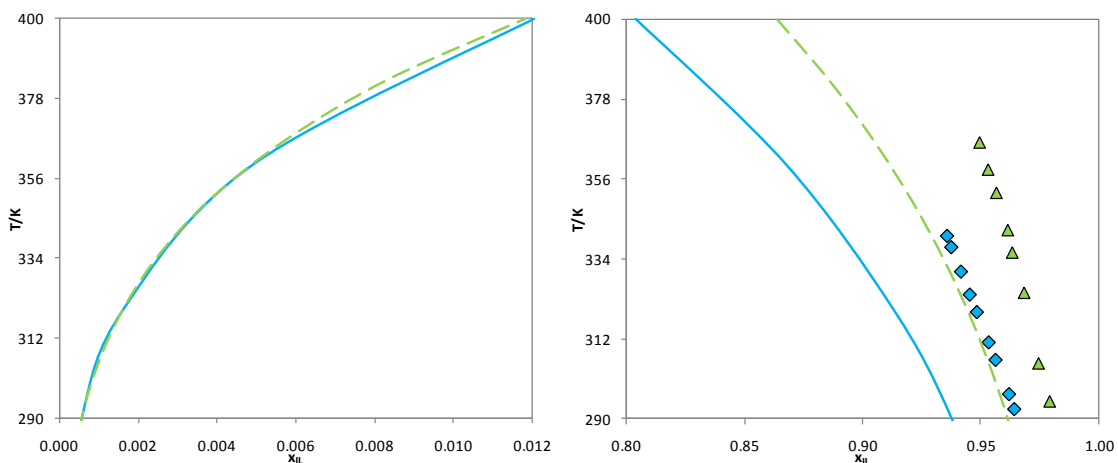


Figure B31 Liquid–liquid phase diagram for $[C_4\text{mpyr}][CF_3SO_3]$ with *n*-hexane⁵⁰ (\diamond) (—) and *n*-heptane⁵⁰ (\triangle) (---). The symbols and the lines represent respectively the experimental data and the COSMO-RS prediction calculations.

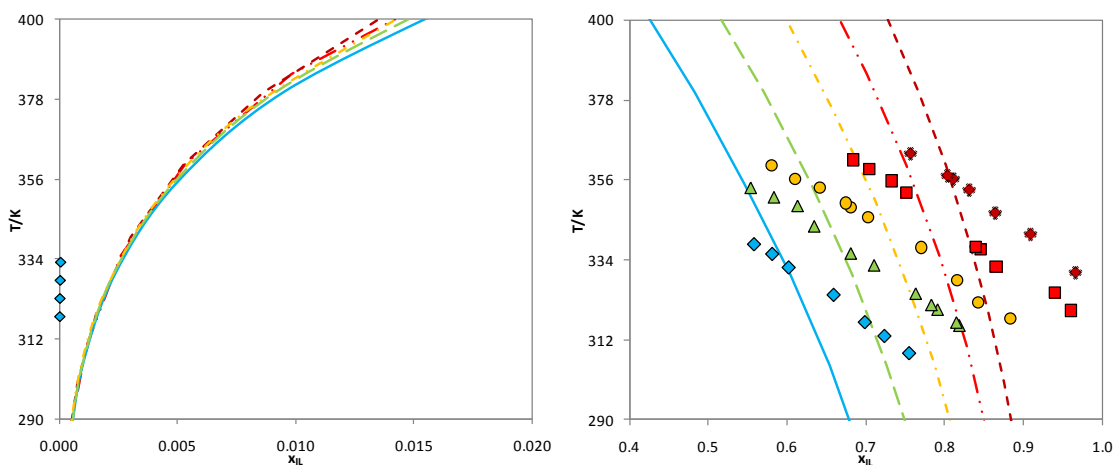


Figure B32 Liquid–liquid phase diagram for $[P_{(444)}_1][TOS]$ with *n*-hexane⁴⁷ (\diamond) (—), *n*-heptane⁴⁷ (\triangle) (---), *n*-octane⁴⁷ (\circ) (-.-), *n*-nonane⁴⁷ (\square) (-.-), and *n*-decane⁴⁷ (\ast) (---). The symbols and the lines represent respectively the experimental data and the COSMO-RS prediction calculations.

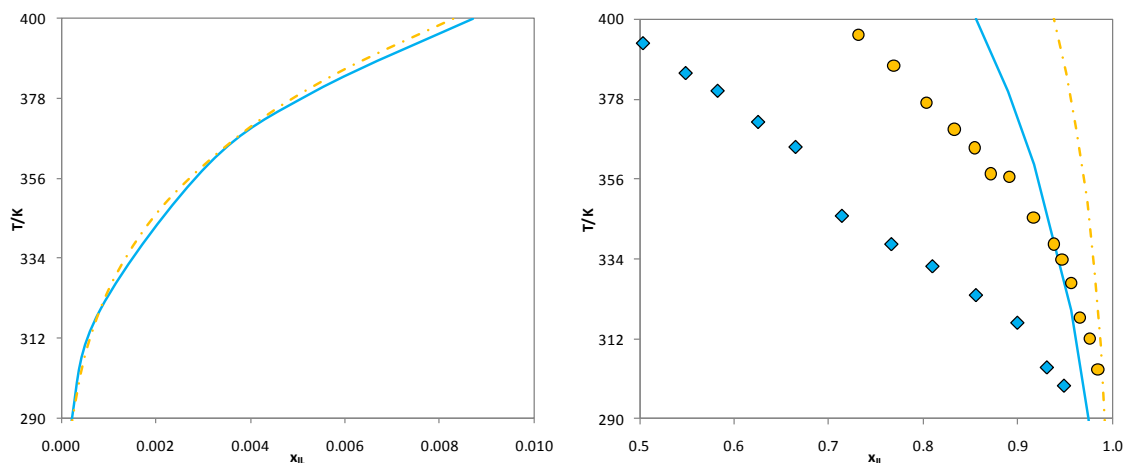


Figure B33 Liquid–liquid phase diagram for $[\text{N}_{2\text{OH}211}][\text{NTf}_2]$ with *n*-hexane⁴⁵ (\blacklozenge) (—) and *n*-octane⁴⁵ (\bullet) (---). The symbols and the lines represent respectively the experimental data and the COSMO-RS prediction calculations.

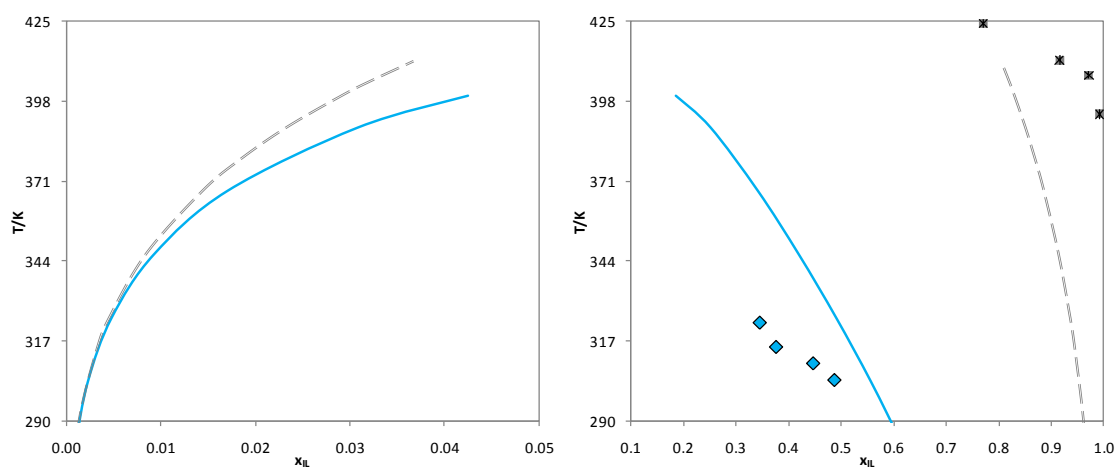


Figure B34 Liquid–liquid phase diagram for $[\text{N}_{101011}][\text{NO}_3]$ with *n*-hexane⁴⁴ (\blacklozenge) (—) and *n*-hexadecane⁴⁴ (\ast) (---). The symbols and the lines represent respectively the experimental data and the COSMO-RS prediction calculations.

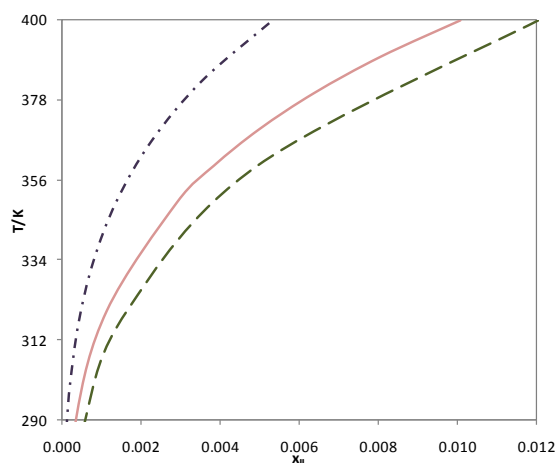


Figure B35 Liquid–liquid phase diagram for $[\text{C}_4\text{mim}][\text{CF}_3\text{SO}_3]^{50}$ (\square) (— · —), $[\text{C}_4\text{mpyr}][\text{CF}_3\text{SO}_3]^{50}$ (\triangle) (— —) and $[\text{1,3-C}_4\text{mpy}][\text{CF}_3\text{SO}_3]^{50}$ (\diamond) (—) with *n*-hexane. The symbols and the lines represent respectively the experimental data and the COSMO-RS prediction calculations.

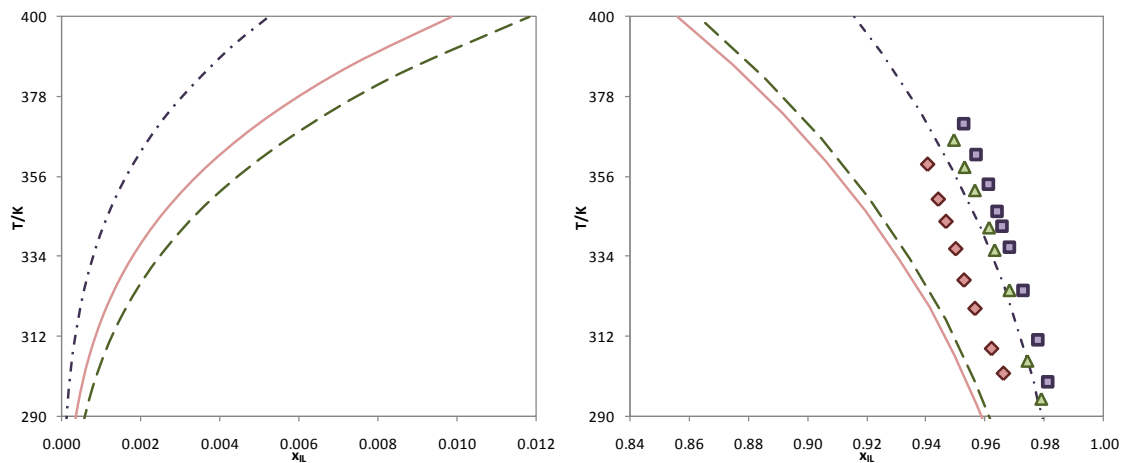


Figure B36 Liquid–liquid phase diagram for $[\text{C}_4\text{mim}][\text{CF}_3\text{SO}_3]^{50}$ (\square) (— · —), $[\text{C}_4\text{mpyr}][\text{CF}_3\text{SO}_3]^{50}$ (\triangle) (— —) and $[\text{1,3-C}_4\text{mpy}][\text{CF}_3\text{SO}_3]^{50}$ (\diamond) (—) with *n*-heptane. The symbols and the lines represent respectively the experimental data and the COSMO-RS prediction calculations.

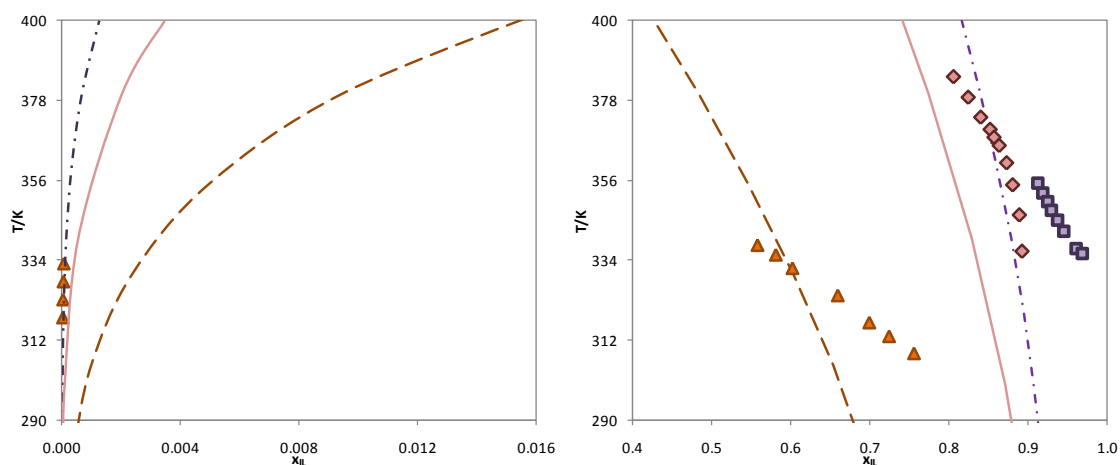


Figure B37 Liquid-liquid phase diagram for $[\text{C}_4\text{mim}][\text{TOS}]$ ³⁶ (\square) (— · —), $[1,4\text{C}_4\text{mpy}][\text{TOS}]$ ⁴⁹ (\diamond) (—) and $[\text{P}_{(444)1}][\text{TOS}]$ ⁴⁷ (\blacktriangle) (— · —) with *n*-hexane. The symbols and the lines represent respectively the experimental data and the COSMO-RS prediction calculations.

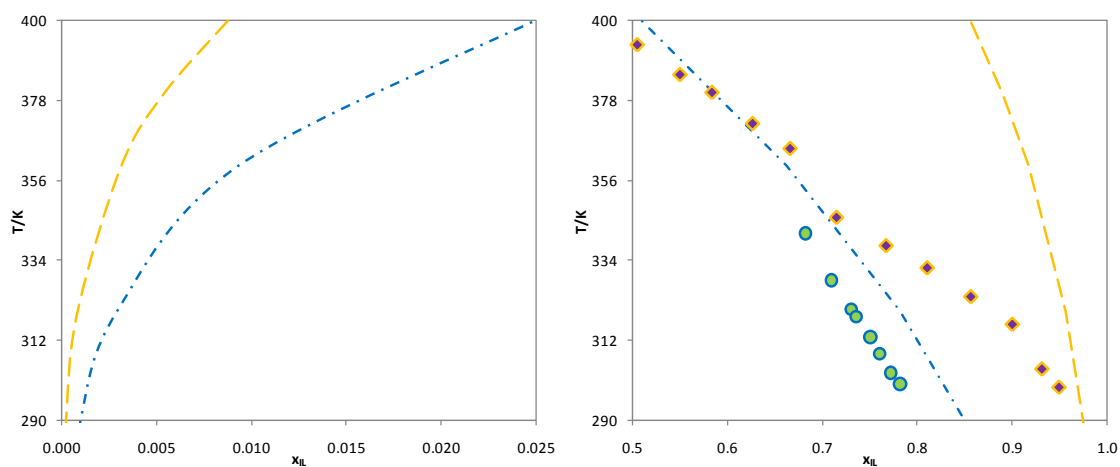


Figure B38 Liquid-liquid phase diagram for $[\text{N}_{2\text{OH}21,1}][\text{NTf}_2]$ ⁴⁵ (\diamond) (— —) and $[\text{C}_6\text{H}_{13}\text{OCH}_2\text{mim}][\text{NTf}_2]$ ⁴¹ (\bullet) (— · —) with *n*-hexane. The symbols and the lines represent respectively the experimental data and the COSMO-RS prediction calculations.

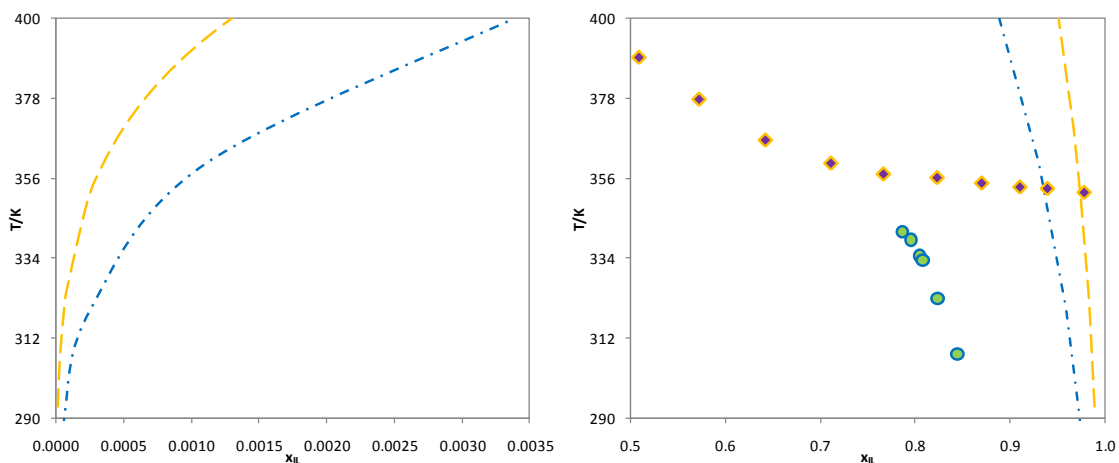


Figure B39 Liquid–liquid phase diagram for $[\text{N}_{6\text{OH}211}][\text{BF}_4]^{34}$ (\diamond) (— —) and $[\text{C}_6\text{H}_{13}\text{OCH}_2\text{mim}][\text{BF}_4]^{41}$ (\bullet) (- · -) with *n*-hexane. The symbols and the lines represent respectively the experimental data and the COSMO-RS prediction calculations.

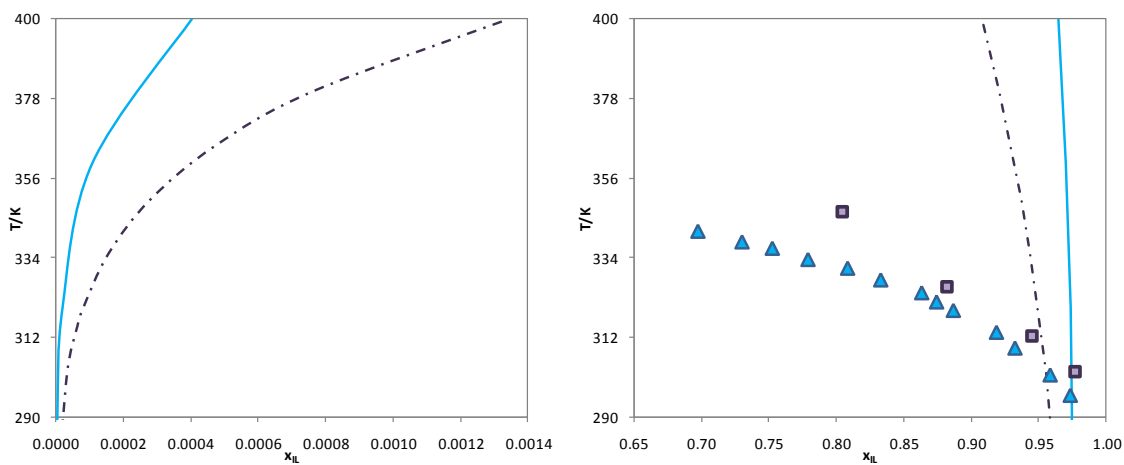


Figure B40 Liquid–liquid phase diagram for $[\text{C}_1\text{mim}][\text{MeSO}_4]^{33}$ (\blacktriangle) (—) and $[\text{C}_4\text{mim}][\text{MeSO}_4]^{33}$ (\blacksquare) (- - -) with *n*-hexane. The symbols and the lines represent respectively the experimental data and the COSMO-RS prediction calculations.

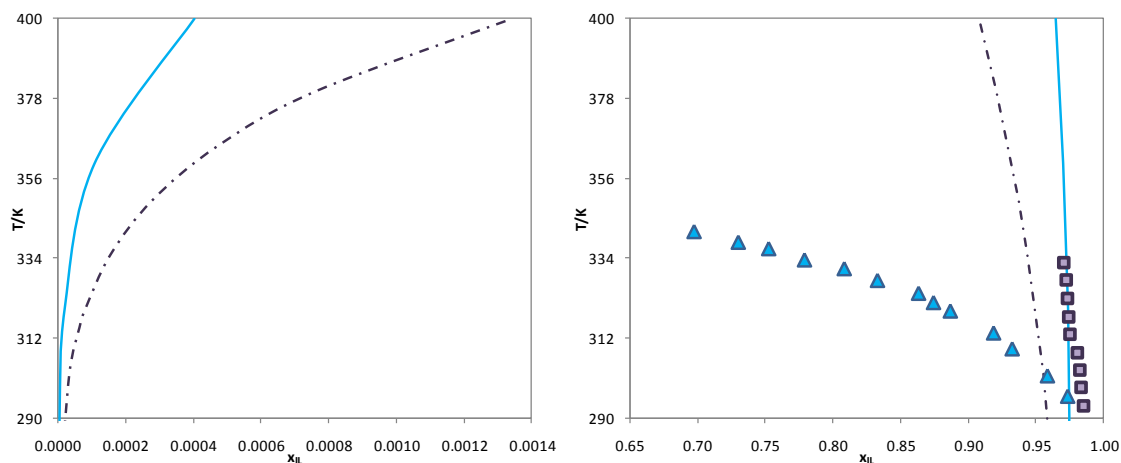


Figure B41 Liquid–liquid phase diagram for $[\text{C}_1\text{mim}][\text{MeSO}_4]$ ³³ (\blacktriangle) (—) and $[\text{C}_4\text{mim}][\text{MeSO}_4]$ ³⁵ (\blacksquare) (- - -) with *n*-hexane. The symbols and the lines represent respectively the experimental data and the COSMO-RS prediction calculations.

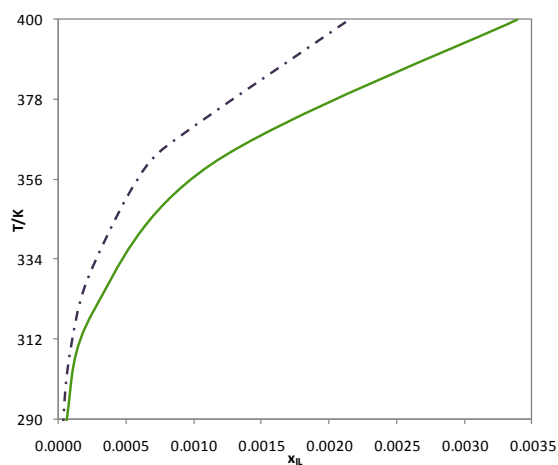


Figure B42 Liquid–liquid phase diagram for $[\text{C}_4\text{mim}][\text{SCN}]$ ³² (\blacksquare) (- - -) and $[\text{C}_6\text{mim}][\text{SCN}]$ ³⁸ (\blacklozenge) (—) with *n*-hexane. The symbols and the lines represent respectively the experimental data and the COSMO-RS prediction calculations.

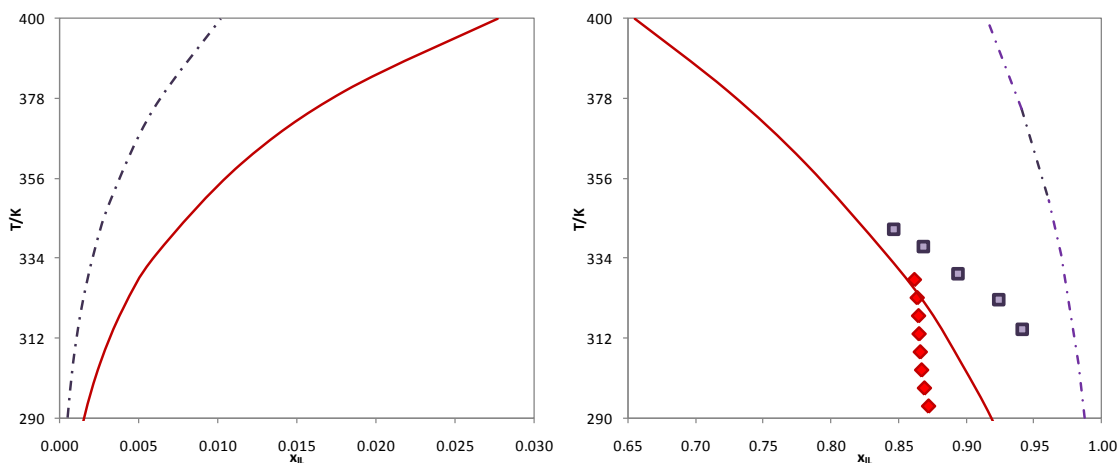


Figure B43 Liquid–liquid phase diagram for $[\text{C}_4\text{mim}][\text{PF}_6]^{51}$ (\square) (---) and $[\text{C}_8\text{mim}][\text{PF}_6]^{40}$ (\blacklozenge) (—) with *n*-hexane. The symbols and the lines represent respectively the experimental data and the COSMO-RS prediction calculations.

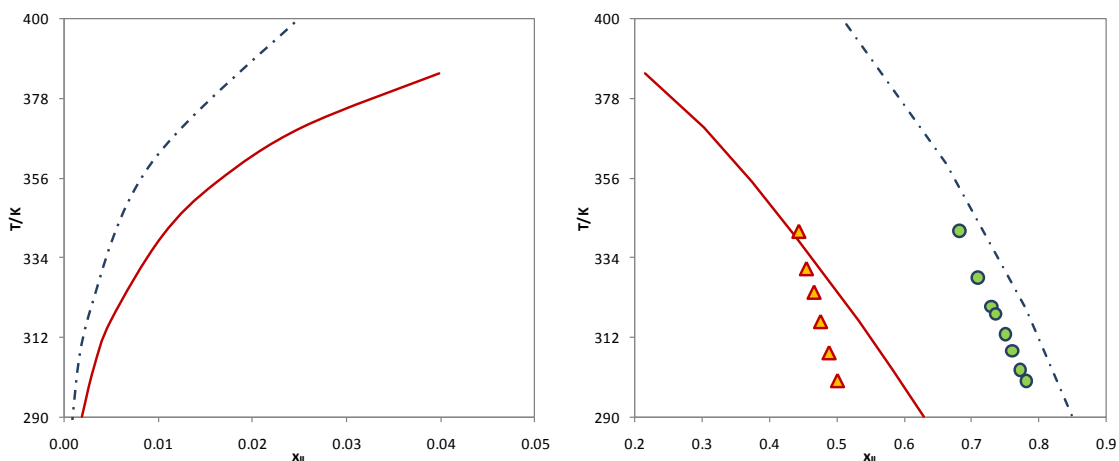


Figure B44 Liquid–liquid phase diagram for $[\text{C}_6\text{H}_{13}\text{OCH}_2\text{mim}][\text{NTf}_2]^{41}$ (\bullet) (---) and $[(\text{C}_6\text{H}_{13}\text{OCH}_2)_2\text{im}][\text{NTf}_2]^{42}$ (\blacktriangle) (—) with *n*-hexane. The symbols and the lines represent respectively the experimental data and the COSMO-RS prediction calculations.

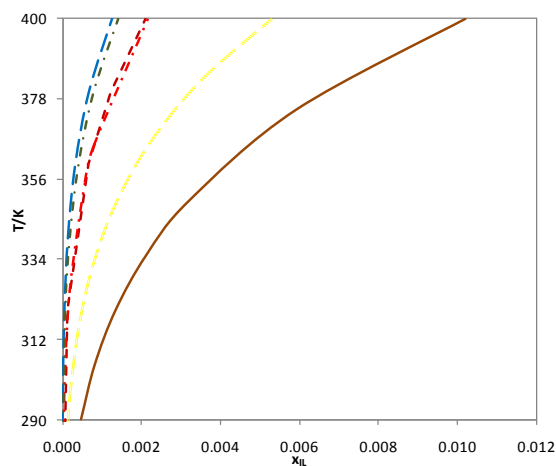


Figure B45 Liquid–liquid phase diagram for $[\text{C}_4\text{mim}][\text{MeSO}_4]$ ³⁵ (\circ) (— · —), $[\text{C}_4\text{mim}][\text{PF}_6]$ ⁵¹ (\diamond) (—), $[\text{C}_4\text{mim}][\text{SCN}]$ ³² (\blacksquare) (— · —), $[\text{C}_4\text{mim}][\text{TOS}]$ ³⁶ (\times) (— —), $[\text{C}_4\text{mim}][\text{CF}_3\text{SO}_3]$ ⁵⁰ (\square) (— —) and $[\text{C}_4\text{mim}][\text{MDEGSO}_4]$ ³⁹ (\triangle) (— —) with *n*-hexane. The symbols and the lines represent respectively the experimental data and the COSMO-RS prediction calculations.

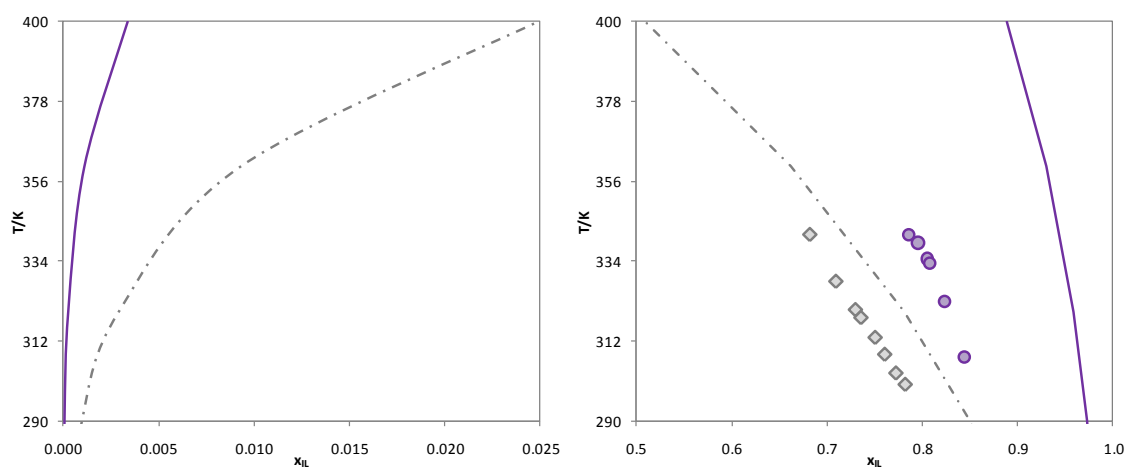


Figure B46 Liquid–liquid phase diagram for $[\text{C}_6\text{H}_{13}\text{OCH}_2\text{mim}][\text{BF}_4]$ ⁴¹ (\circ) (—) and $[\text{C}_6\text{H}_{13}\text{OCH}_2\text{mim}][\text{NTf}_2]$ ⁴¹ (\diamond) (— · —) with *n*-hexane. The symbols and the lines represent respectively the experimental data and the COSMO-RS prediction calculations.

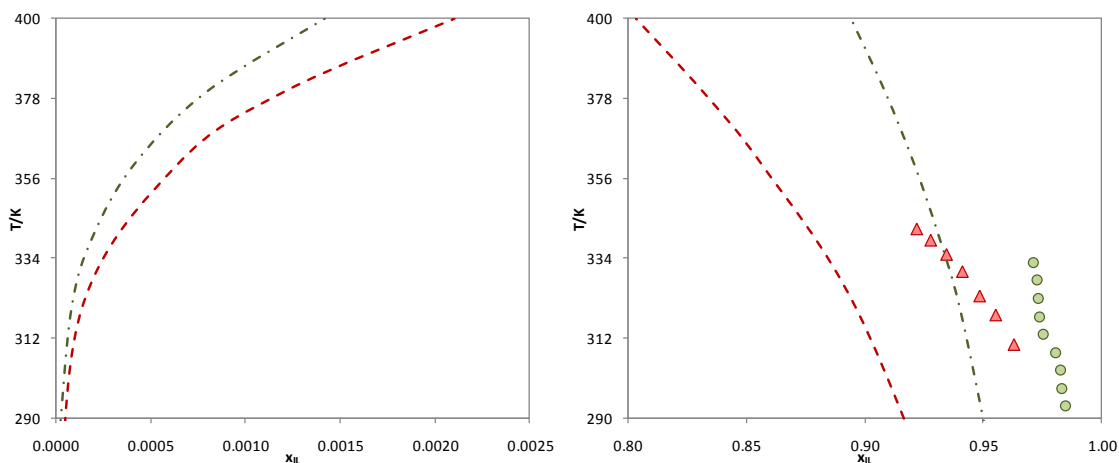


Figure B47 Liquid-liquid phase diagram for [C₄mim][MeSO₄]³⁵ (●) (-.-) and [C₄mim][MDEGSO₄]³⁹ (▲) (- - -) with *n*-hexane. The symbols and the lines represent respectively the experimental data and the COSMO-RS prediction calculations.

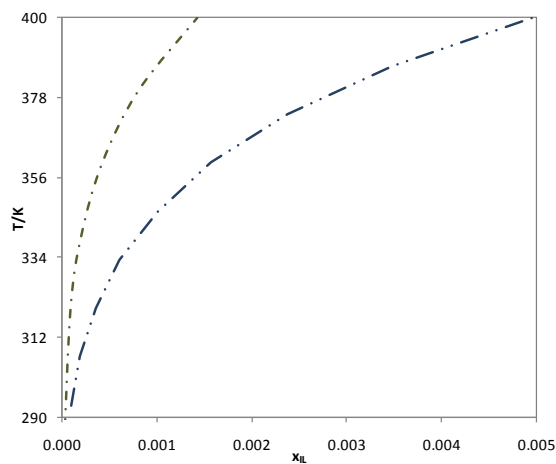


Figure B48 Liquid-liquid phase diagram for [C₄mim][MeSO₄]³⁵ (●) (-.-) and [C₄mim][OcSO₄]³⁷ (◆) (-.-) with *n*-hexane. The symbols and the lines represent respectively the experimental data and the COSMO-RS prediction calculations.

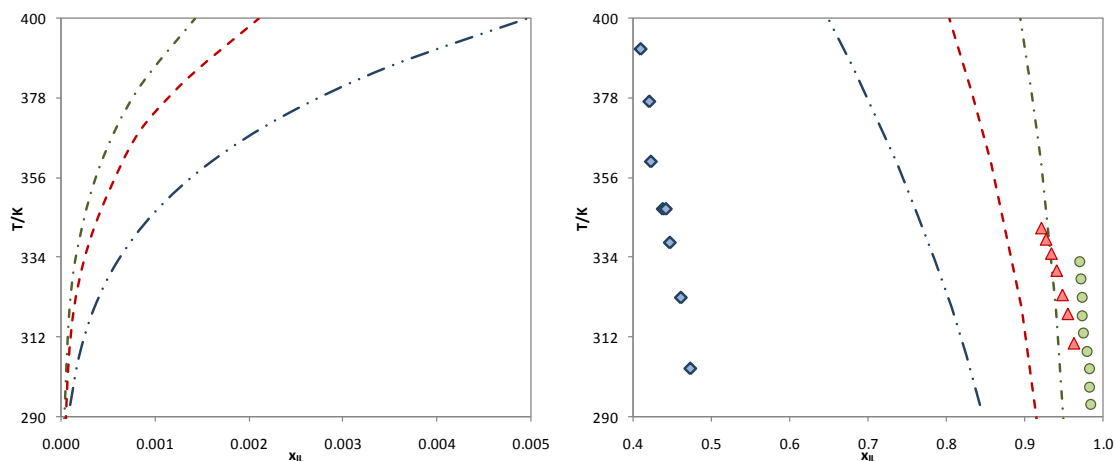


Figure B49 Liquid–liquid phase diagram for $[\text{C}_4\text{mim}][\text{MeSO}_4]$ ³⁵ (\circ) (---), $[\text{C}_4\text{mim}][\text{OcSO}_4]$ ³⁷ (\diamond) (— · ·) and $[\text{C}_4\text{mim}][\text{MDEGSO}_4]$ ³⁹ (\triangle) (— — —) with *n*-hexane. The symbols and the lines represent respectively the experimental data and the COSMO-RS prediction calculations.

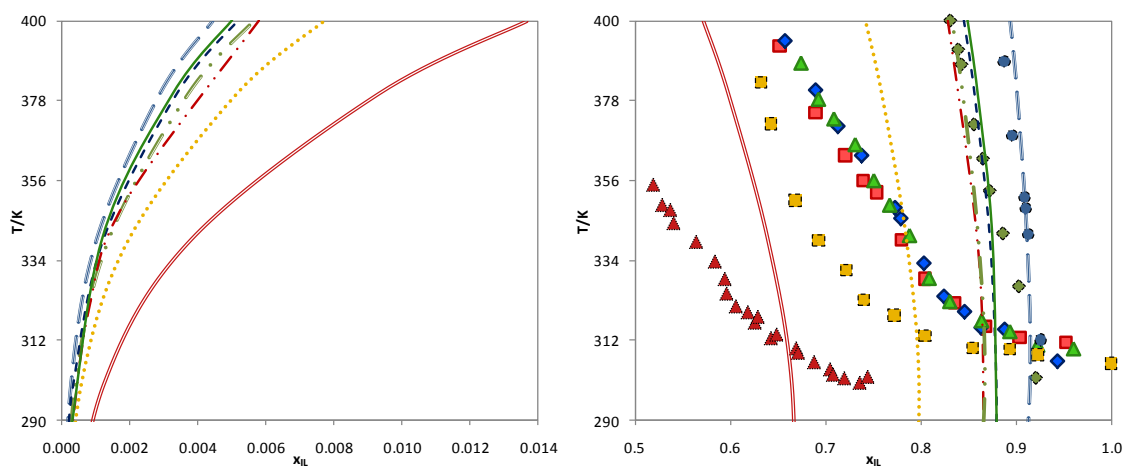


Figure B50 Liquid–liquid phase diagram for $[\text{C}_1\text{mim}][\text{MeSO}_4]$ with benzene³³ (\blacktriangle) (— · ·), toluene³³ (\blacksquare) (· · · · ·), ethylbenzene³³ (\blacklozenge) (— · ·), propylbenzene³³ (\blacklozenge) (— · ·), *o*-xylene³³ (\blacklozenge) (— · ·), *m*-xylene³³ (\blacklozenge) (— · ·) and *p*-xylene³³ (\blacklozenge) (— · ·). The symbols and the lines represent respectively the experimental data and the COSMO-RS prediction calculations.

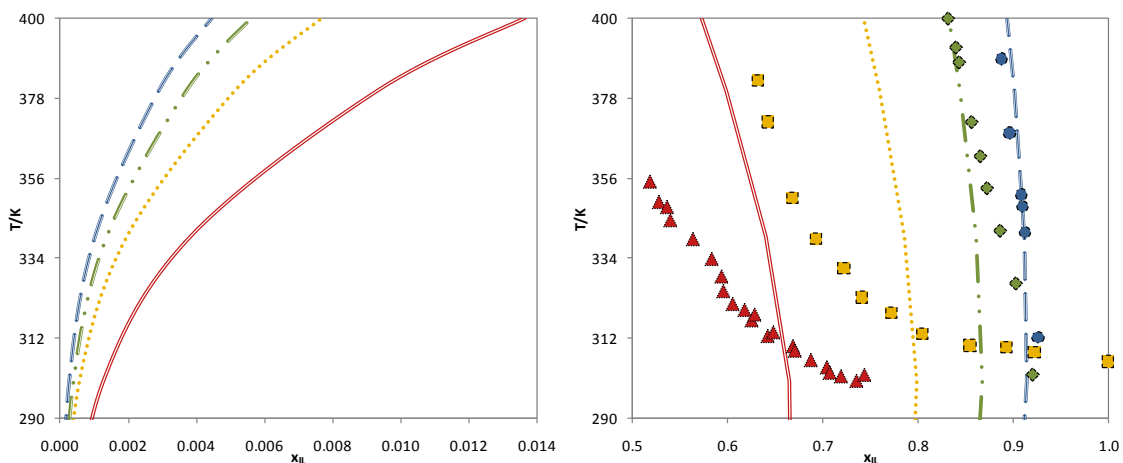


Figure B51 Liquid–liquid phase diagram for $[C_1mim][MeSO_4]$ with benzene ³³ (\blacktriangle) (—), toluene ³³ (\blacksquare) (⋯), ethylbenzene ³³ (\blacklozenge) (— ·) and propylbenzene ³³ (\bullet) (—). The symbols and the lines represent respectively the experimental data and the COSMO-RS prediction calculations.

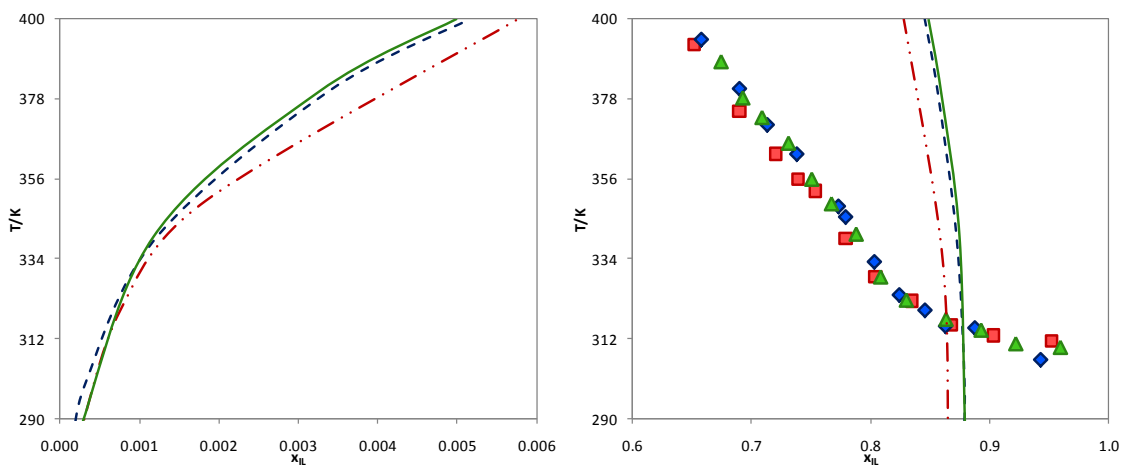


Figure B52 Liquid–liquid phase diagram for $[C_1mim][MeSO_4]$ with *o*-xylene ³³ (\blacksquare) (— ·), *m*-xylene ³³ (\blacklozenge) (---) and *p*-xylene ³³ (\blacktriangle) (—). The symbols and the lines represent respectively the experimental data and the COSMO-RS prediction calculations.

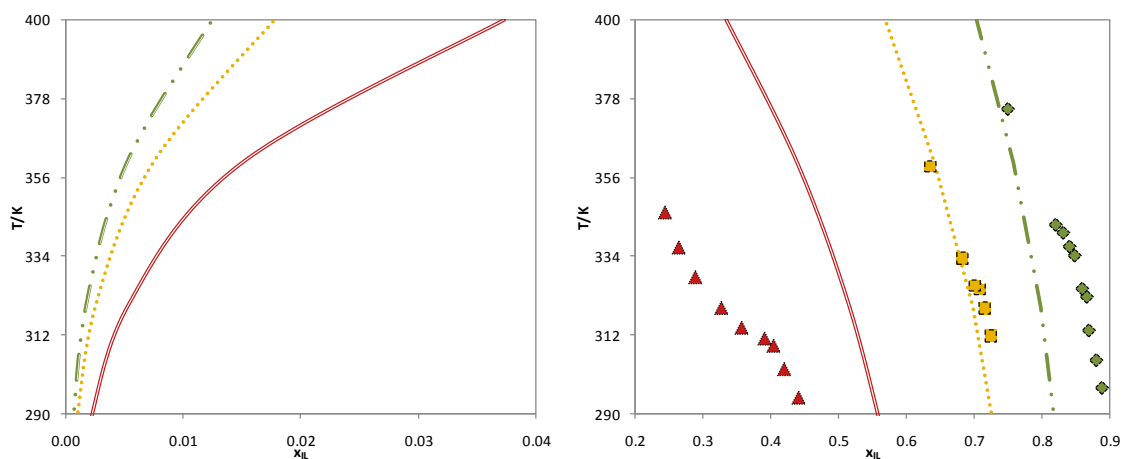


Figure B53 Liquid–liquid phase diagram for $[\text{C}_2\text{mim}][\text{EtSO}_4]$ with benzene³¹ (\blacktriangle) (—), toluene³¹ (\blacksquare) (\cdots) and ethylbenzene³¹ (\blacklozenge) ($- \cdot -$). The symbols and the lines represent respectively the experimental data and the COSMO-RS prediction calculations.

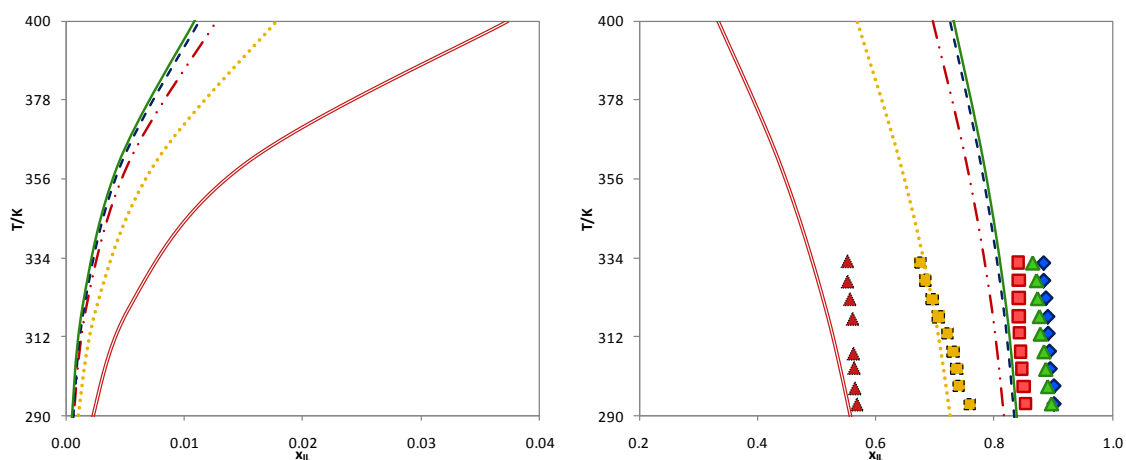


Figure B54 Liquid–liquid phase diagram for $[\text{C}_2\text{mim}][\text{EtSO}_4]$ with benzene³⁵ (\blacktriangle) (—), toluene³⁵ (\blacksquare) (\cdots), *o*-xylene³⁵ (\blacksquare) ($- \cdot -$), *m*-xylene³⁵ (\blacklozenge) ($- - -$) and *p*-xylene³⁵ (\blacktriangle) (—). The symbols and the lines represent respectively the experimental data and the COSMO-RS prediction calculations.

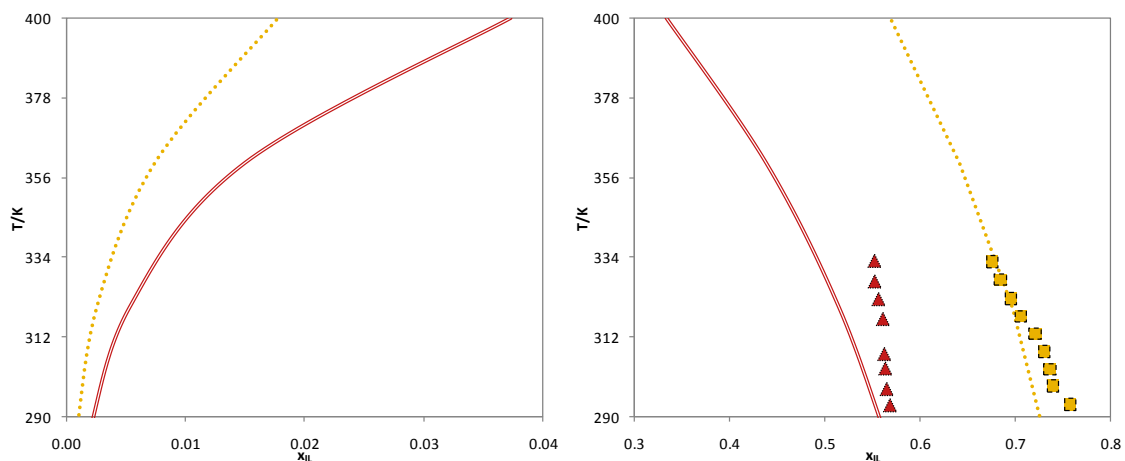


Figure B55 Liquid–liquid phase diagram for [C₂mim][EtSO₄] with benzene^{31, 35} (▲) (—) and toluene³⁵ (■) (⋯). The symbols and the lines represent respectively the experimental data and the COSMO-RS prediction calculations.

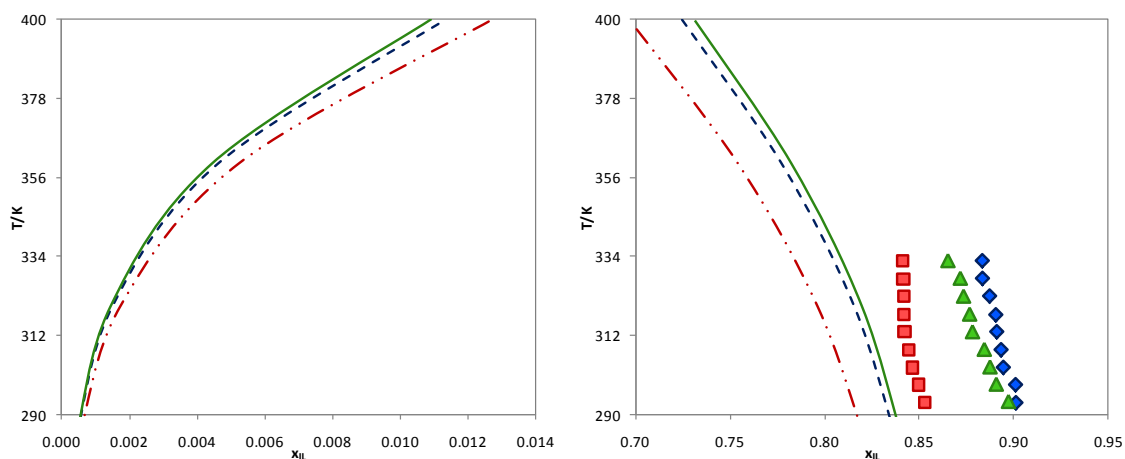


Figure B56 Liquid–liquid phase diagram for [C₂mim][EtSO₄] with *o*-xylene³⁵ (■) (— · —), *m*-xylene³⁵ (◆) (---) and *p*-xylene³⁵ (▲) (—). The symbols and the lines represent respectively the experimental data and the COSMO-RS prediction calculations.

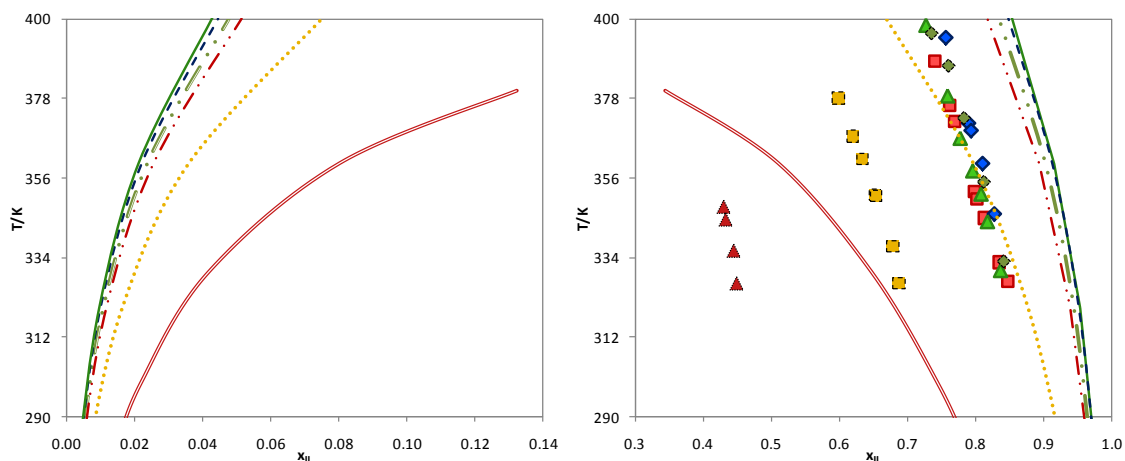


Figure B57 Liquid–liquid phase diagram for $[\text{C}_2\text{mim}][\text{PF}_6]$ with benzene⁵¹ (\blacktriangle) (—), toluene⁵¹ (\blacksquare) (\cdots), ethylbenzene⁵¹ (\blacklozenge) ($-\cdot-$), *o*-xylene⁵¹ (\blacksquare) ($-\cdot-$), *m*-xylene⁵¹ (\blacklozenge) ($-\cdot-$) and *p*-xylene⁵¹ (\blacktriangle) (—). The symbols and the lines represent respectively the experimental data and the COSMO-RS prediction calculations.

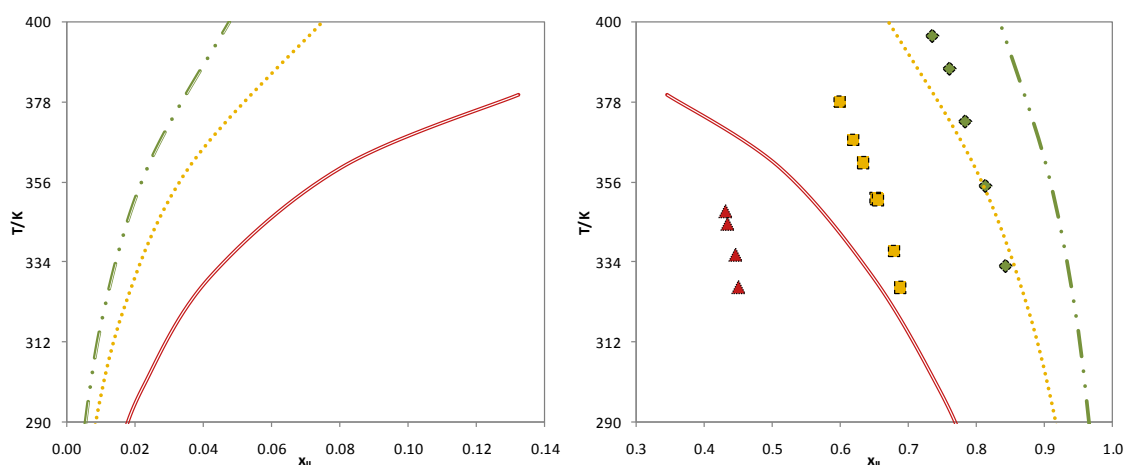


Figure B58 Liquid–liquid phase diagram for $[\text{C}_2\text{mim}][\text{PF}_6]$ with benzene⁵¹ (\blacktriangle) (—), toluene⁵¹ (\blacksquare) (\cdots) and ethylbenzene⁵¹ (\blacklozenge) ($-\cdot-$). The symbols and the lines represent respectively the experimental data and the COSMO-RS prediction calculations.

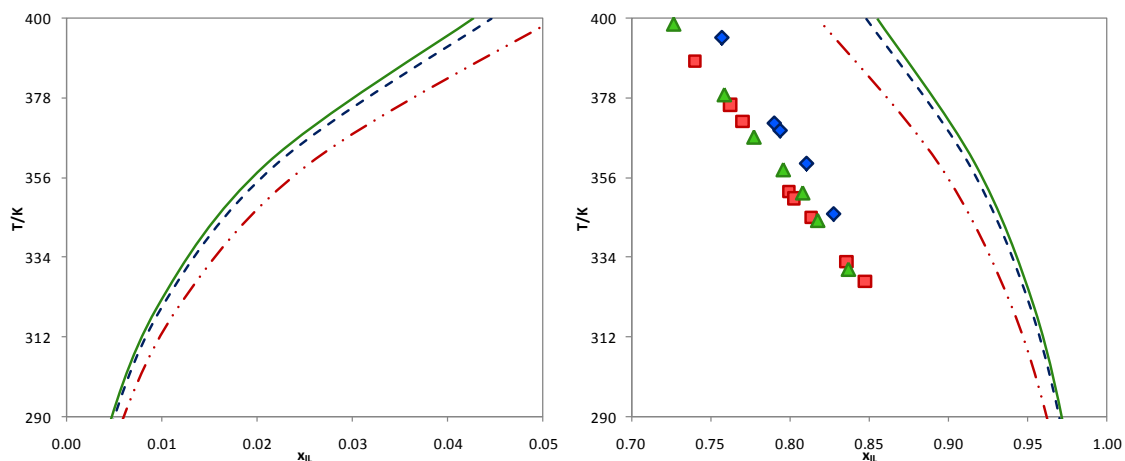


Figure B59 Liquid–liquid phase diagram for $[\text{C}_2\text{mim}][\text{PF}_6]$ with *o*-xylene⁵¹ (\blacksquare) (— · —), *m*-xylene⁵¹ (\blacklozenge) (---) and *p*-xylene⁵¹ (\blacktriangle) (—). The symbols and the lines represent respectively the experimental data and the COSMO-RS prediction calculations.

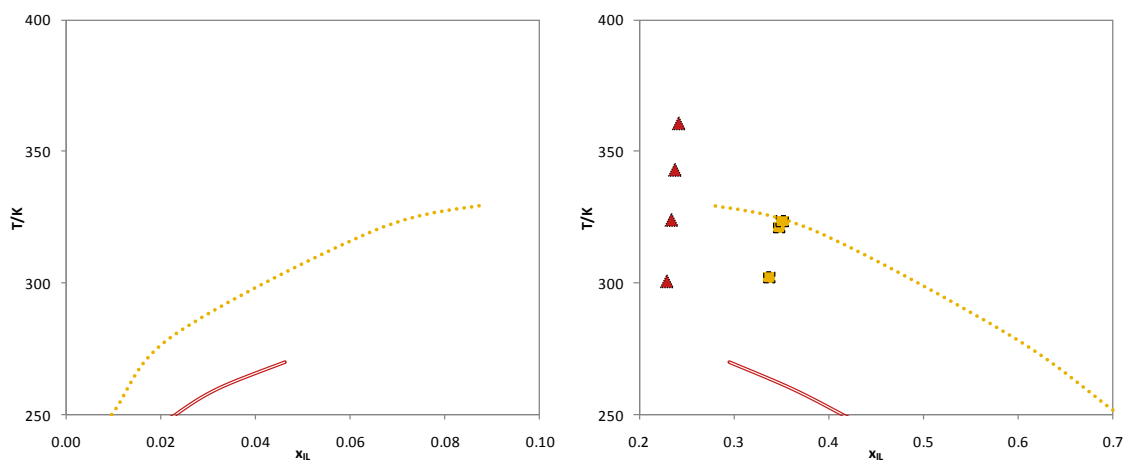


Figure B60 Liquid–liquid phase diagram for $[\text{C}_2\text{mim}][\text{NTf}_2]$ with benzene⁴⁶ (\blacktriangle) (—) and toluene⁴⁶ (\blacksquare) (····). The symbols and the lines represent respectively the experimental data and the COSMO-RS prediction calculations.

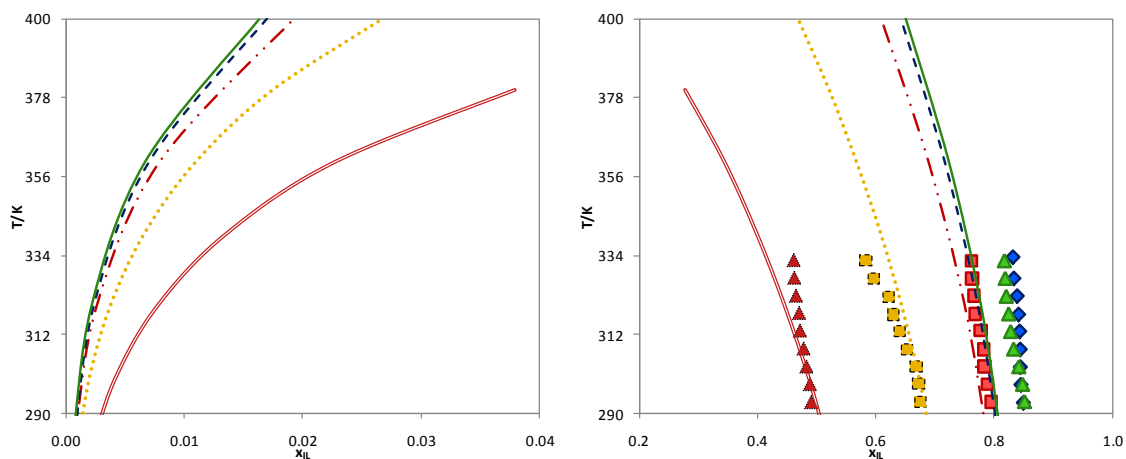


Figure B61 Liquid–liquid phase diagram for $[\text{C}_4\text{mim}][\text{MeSO}_4]$ with benzene³⁵ (\blacktriangle) (—), toluene³⁵ (\blacksquare) (\cdots), *o*-xylene³⁵ (\blacksquare) ($-\cdot-$), *m*-xylene³⁵ (\blacklozenge) ($---$) and *p*-xylene³⁵ (\blacktriangle) (—). The symbols and the lines represent respectively the experimental data and the COSMO-RS prediction calculations.

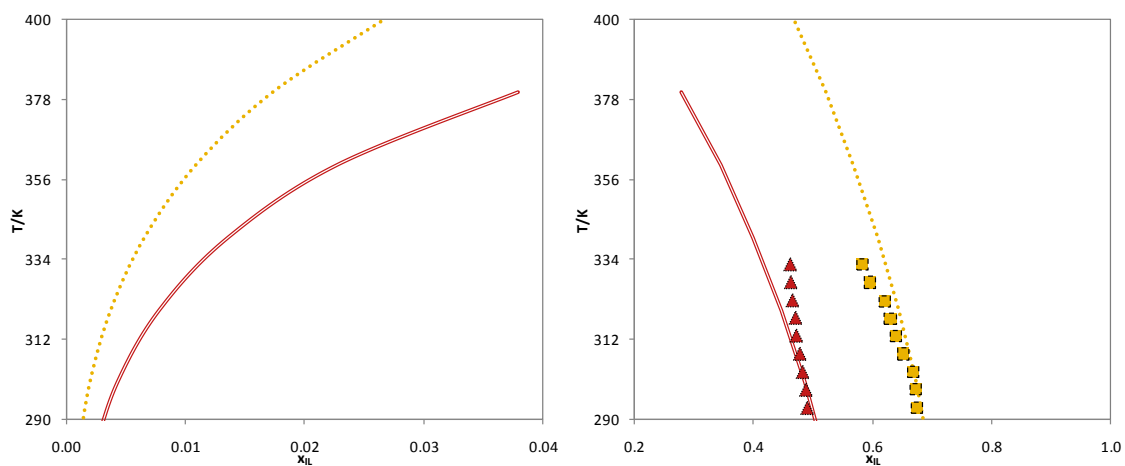


Figure B62 Liquid–liquid phase diagram for $[\text{C}_4\text{mim}][\text{MeSO}_4]$ with benzene³⁵ (\blacktriangle) (—) and toluene³⁵ (\blacksquare) (\cdots). The symbols and the lines represent respectively the experimental data and the COSMO-RS prediction calculations.

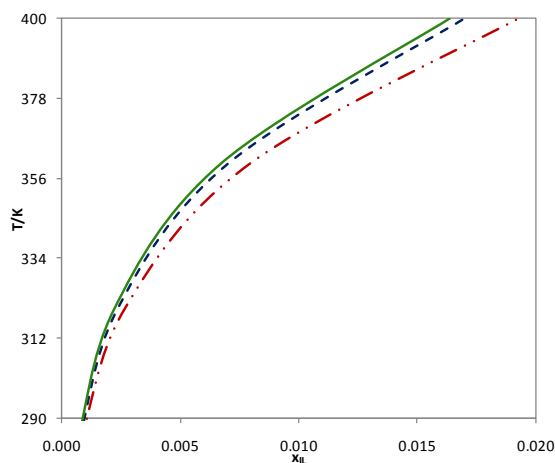


Figure B63 Liquid–liquid phase diagram for $[C_4mim][MeSO_4]$ with *o*-xylene³⁵ (■) (— · —), *m*-xylene³⁵ (◆) (---) and *p*-xylene³⁵ (▲) (—). The symbols and the lines represent respectively the experimental data and the COSMO-RS prediction calculations.

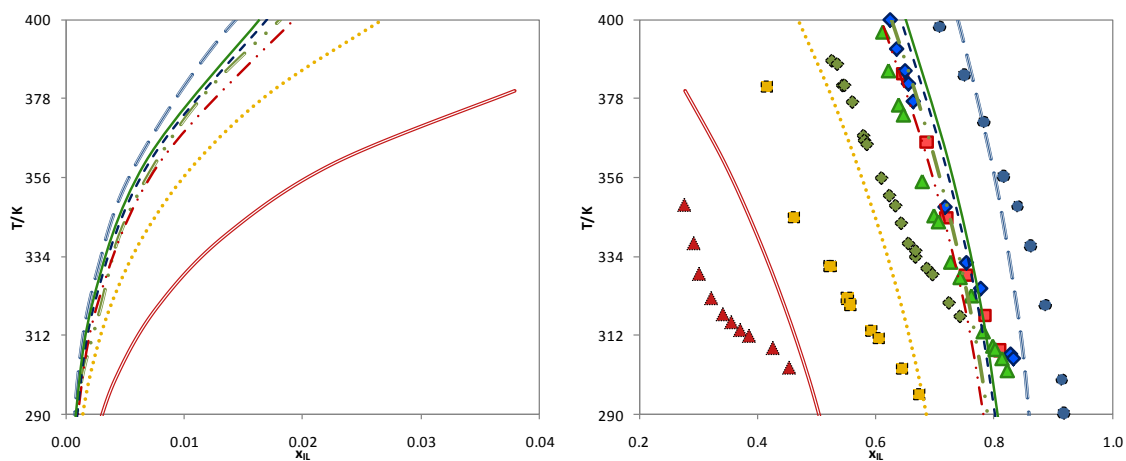


Figure B64 Liquid–liquid phase diagram for $[C_4mim][MeSO_4]$ with benzene³³ (▲) (—), toluene³³ (■) (.....), ethylbenzene³³ (◆) (— · —), propylbenzene³³ (●) (—), *o*-xylene³³ (■) (— · —), *m*-xylene³³ (◆) (---) and *p*-xylene³³ (▲) (—). The symbols and the lines represent respectively the experimental data and the COSMO-RS prediction calculations.

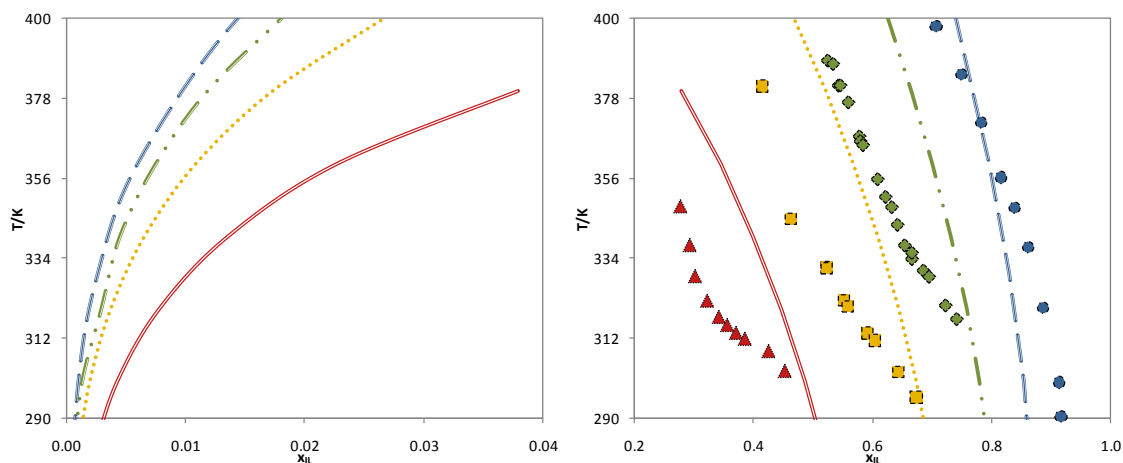


Figure B65 Liquid–liquid phase diagram for $[\text{C}_4\text{mim}][\text{MeSO}_4]$ with benzene³³ (\blacktriangle) (—), toluene³³ (\blacksquare) (⋯), ethylbenzene³³ (\blacklozenge) (— ·) and propylbenzene³³ (\bullet) (—). The symbols and the lines represent respectively the experimental data and the COSMO-RS prediction calculations.

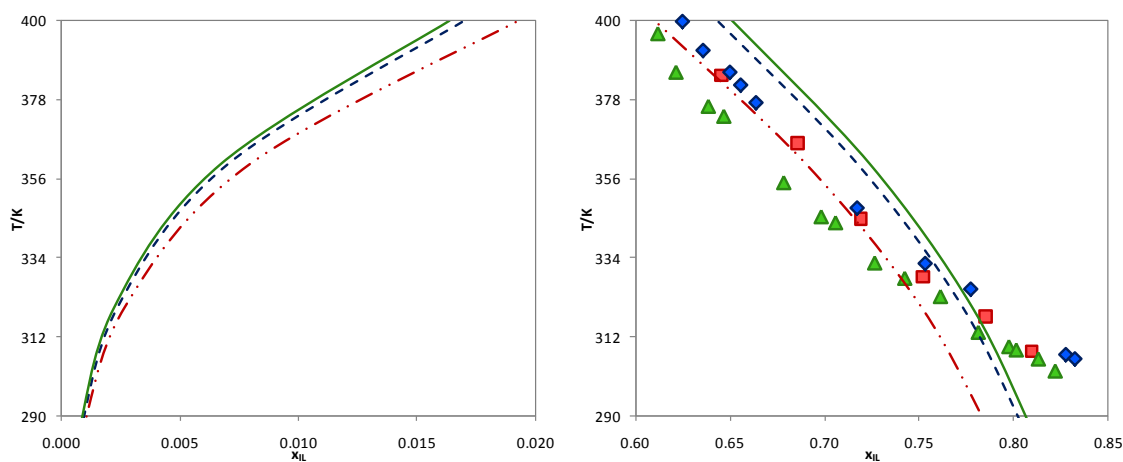


Figure B66 Liquid–liquid phase diagram for $[\text{C}_4\text{mim}][\text{MeSO}_4]$ with *o*-xylene³³ (\blacksquare) (— ·), *m*-xylene³³ (\blacklozenge) (---) and *p*-xylene³³ (\blacktriangle) (—). The symbols and the lines represent respectively the experimental data and the COSMO-RS prediction calculations.

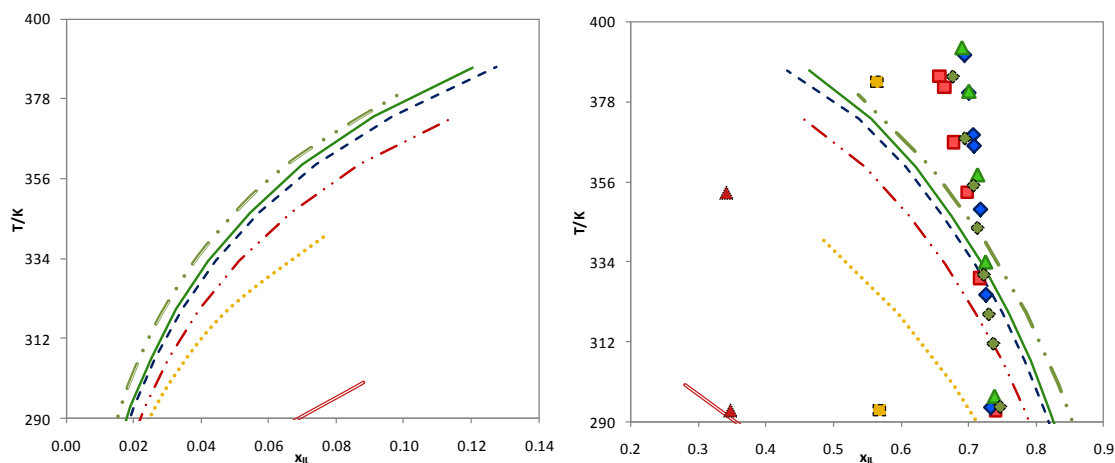


Figure B67 Liquid–liquid phase diagram for $[\text{C}_4\text{mim}][\text{PF}_6]$ with benzene⁵¹ (\blacktriangle) (—), toluene³³ (\blacksquare) (⋯), ethylbenzene⁵¹ (\blacklozenge) (— ·), *o*-xylene⁵¹ (\blacksquare) (— · ·), *m*-xylene³³ (\blacklozenge) (— · ·) and *p*-xylene⁵¹ (\blacktriangle) (—). The symbols and the lines represent respectively the experimental data and the COSMO-RS prediction calculations.

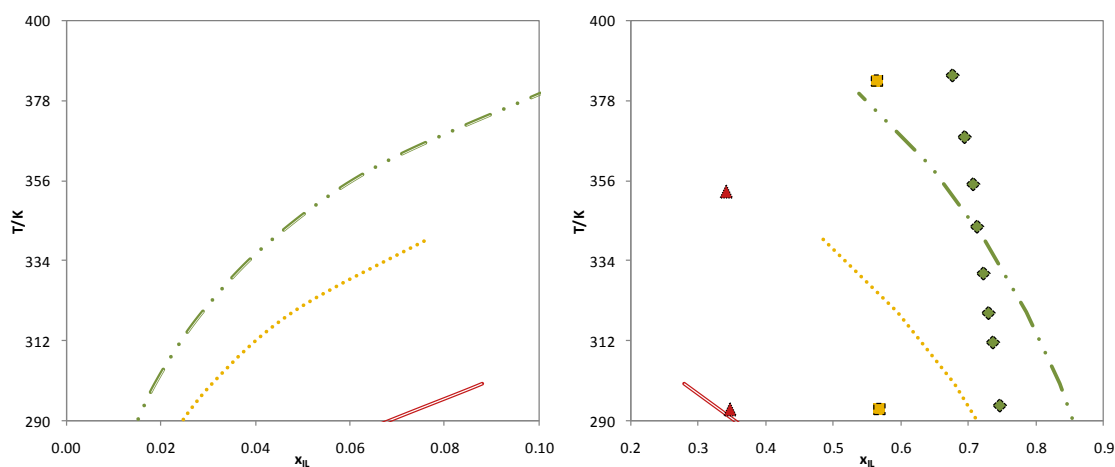


Figure B68 Liquid–liquid phase diagram for $[\text{C}_4\text{mim}][\text{PF}_6]$ with benzene⁵¹ (\blacktriangle) (—), toluene³³ (\blacksquare) (⋯) and ethylbenzene⁵¹ (\blacklozenge) (— ·). The symbols and the lines represent respectively the experimental data and the COSMO-RS prediction calculations.

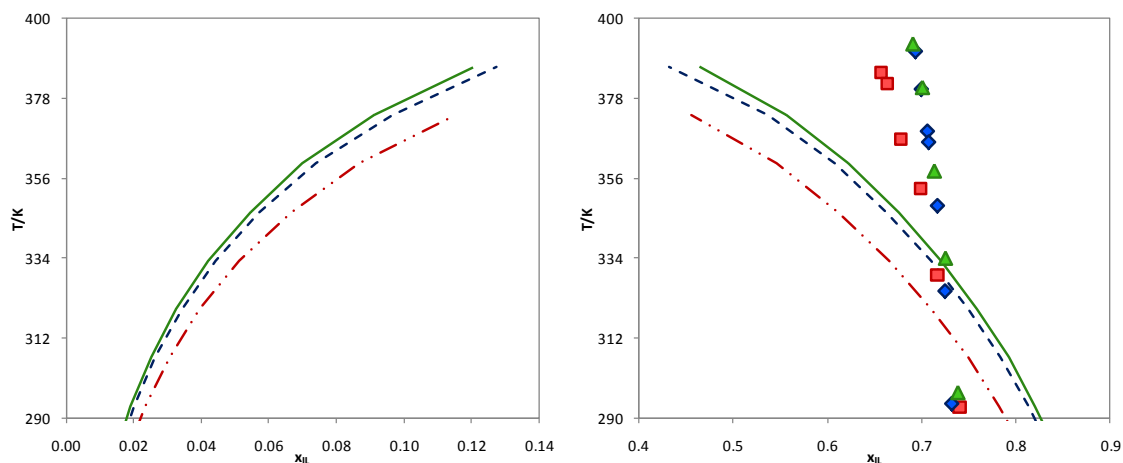


Figure B69 Liquid–liquid phase diagram for $[\text{C}_4\text{mim}][\text{PF}_6]$ with *o*-xylene⁵¹ (\blacksquare) (— · —), *m*-xylene⁵¹ (\blacklozenge) (— — —) and *p*-xylene⁵¹ (\blacktriangle) (—). The symbols and the lines represent respectively the experimental data and the COSMO-RS prediction calculations.

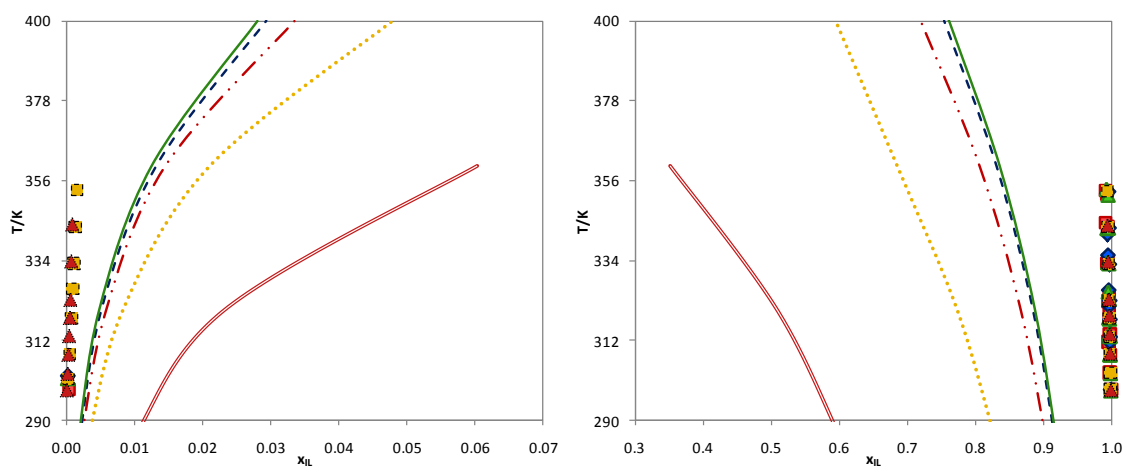


Figure B70 Liquid–liquid phase diagram for $[\text{C}_4\text{mim}][\text{BF}_4]$ with benzene⁶³ (\blacktriangle) (—), toluene⁶³ (\blacksquare) (· · · · ·), *o*-xylene⁶³ (\blacksquare) (— · —), *m*-xylene⁶³ (\blacklozenge) (— — —) and *p*-xylene⁶³ (\blacktriangle) (—). The symbols and the lines represent respectively the experimental data and the COSMO-RS prediction calculations.

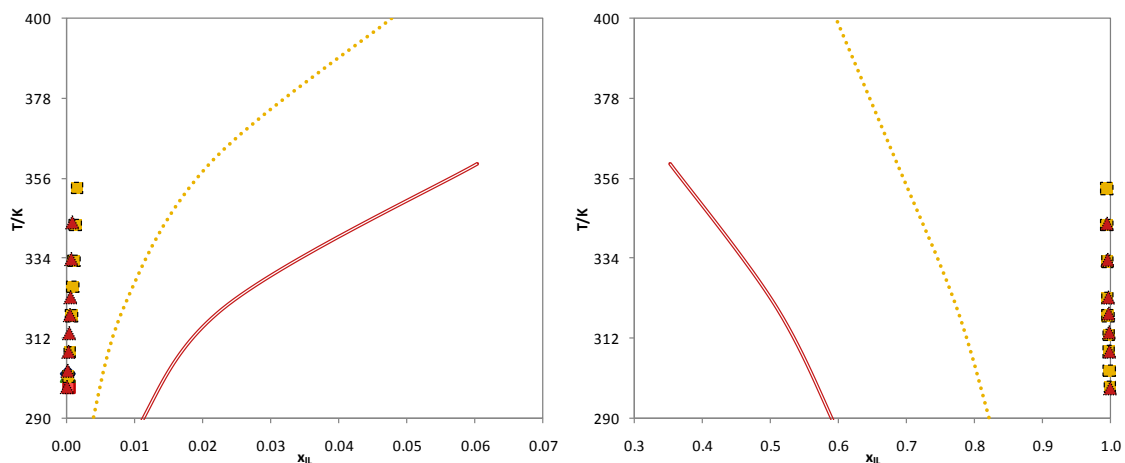


Figure B71 Liquid–liquid phase diagram for $[\text{C}_4\text{mim}][\text{BF}_4]$ with benzene⁶³ (\blacktriangle) (—) and toluene⁶³ (\blacksquare) (⋯). The symbols and the lines represent respectively the experimental data and the COSMO-RS prediction calculations.

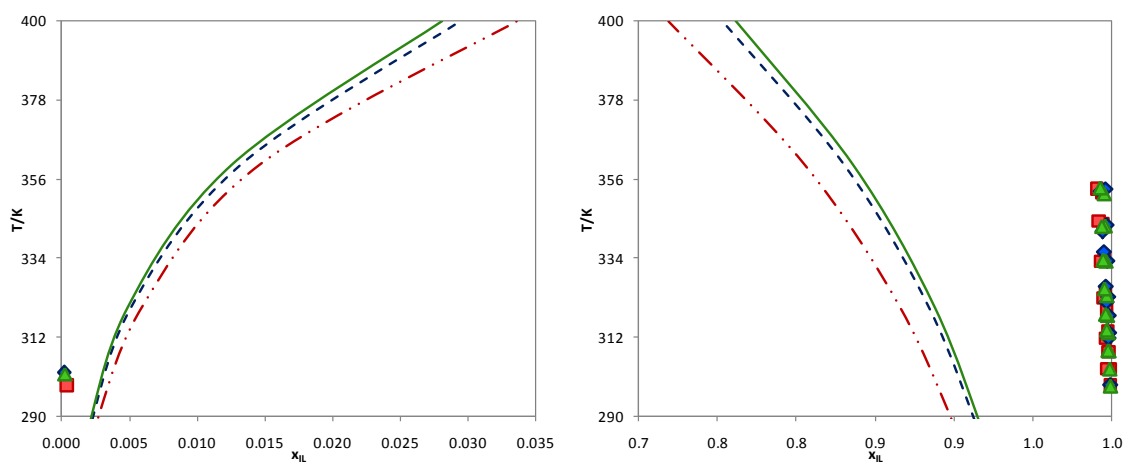


Figure B72 Liquid–liquid phase diagram for $[\text{C}_4\text{mim}][\text{BF}_4]$ with *o*-xylene⁶³ (\blacksquare) (— · —), *m*-xylene⁶³ (\blacklozenge) (---) and *p*-xylene⁶³ (\blacktriangle) (—). The symbols and the lines represent respectively the experimental data and the COSMO-RS prediction calculations.

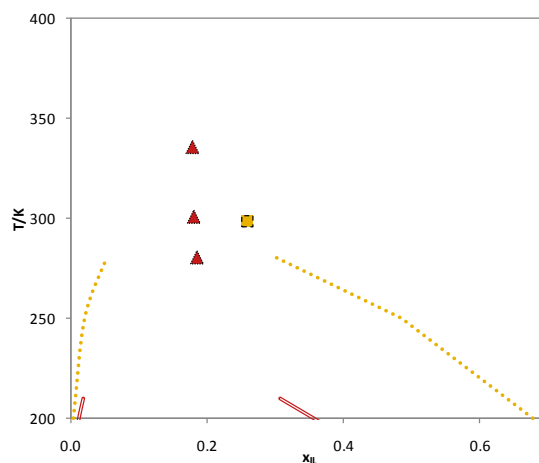


Figure B73 Liquid–liquid phase diagram for $[\text{C}_4\text{mim}][\text{NTf}_2]$ with benzene ⁴⁶ (\blacktriangle) (—) and toluene ⁴⁶ (\blacksquare) (\cdots). The symbols and the lines represent respectively the experimental data and the COSMO-RS prediction calculations.

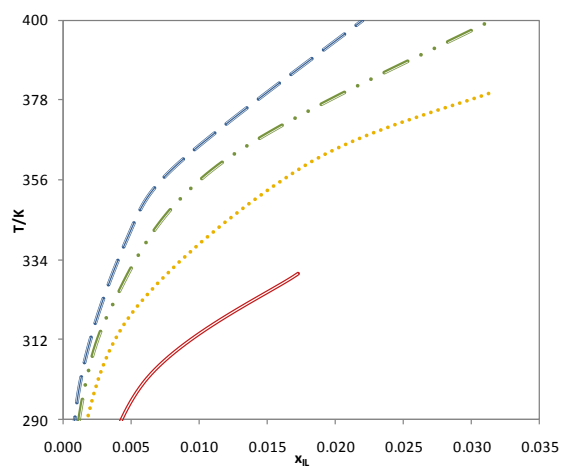


Figure B74 Liquid–liquid phase diagram for $[\text{C}_4\text{mim}][\text{TOS}]$ with benzene ³⁶ (\blacktriangle) (—), toluene ³⁶ (\blacksquare) (\cdots), ethylbenzene ³⁶ (\blacklozenge) ($-\cdot-$) and propylbenzene ³⁶ (\blacklozenge) ($-\cdot-$). The symbols and the lines represent respectively the experimental data and the COSMO-RS prediction calculations.

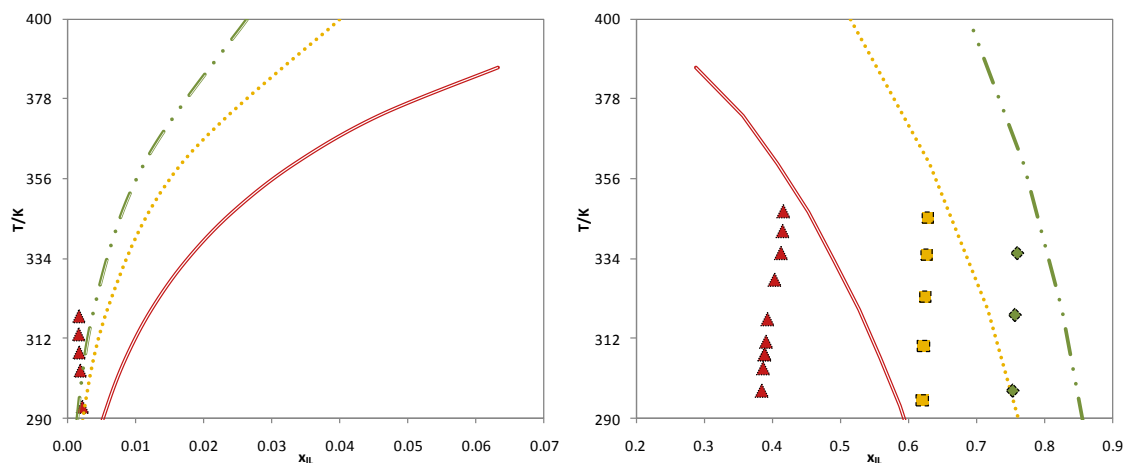


Figure B75 Liquid–liquid phase diagram for $[\text{C}_4\text{mim}][\text{SCN}]$ with benzene³² (\blacktriangle) (—), toluene³² (\blacksquare) (\cdots) and ethylbenzene³² (\blacklozenge) ($-\cdot-$). The symbols and the lines represent respectively the experimental data and the COSMO-RS prediction calculations.

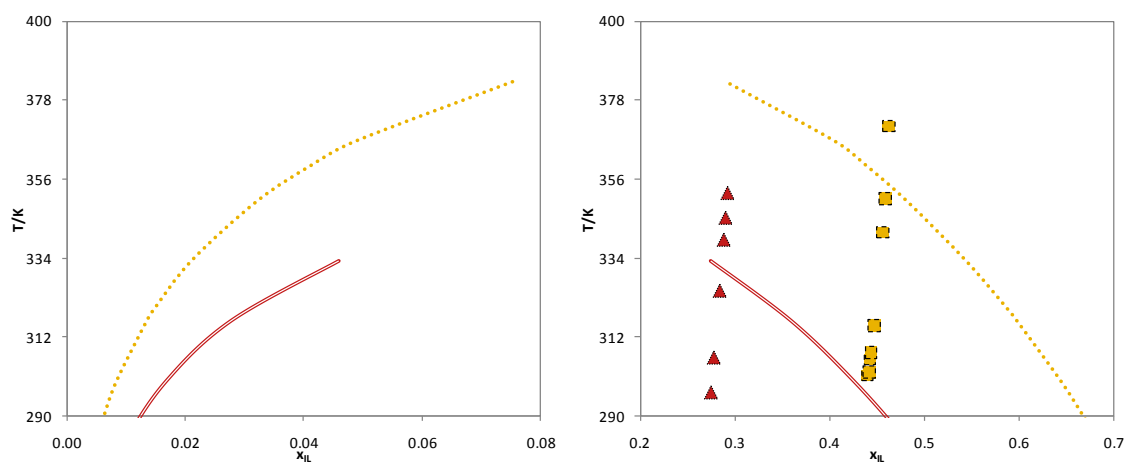


Figure B76 Liquid–liquid phase diagram for $[\text{C}_4\text{mim}][\text{CF}_3\text{SO}_3]$ with benzene⁵⁰ (\blacktriangle) (—) and toluene⁵⁰ (\blacksquare) (\cdots). The symbols and the lines represent respectively the experimental data and the COSMO-RS prediction calculations.

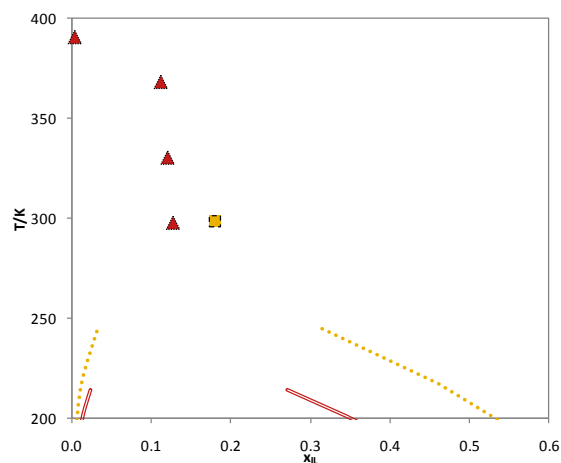


Figure B77 Liquid–liquid phase diagram for $[\text{C}_6\text{mim}][\text{NTf}_2]$ with benzene ⁴⁶ (\blacktriangle) (—) and toluene ⁴⁶ (\blacksquare) (⋯). The symbols and the lines represent respectively the experimental data and the COSMO-RS prediction calculations.

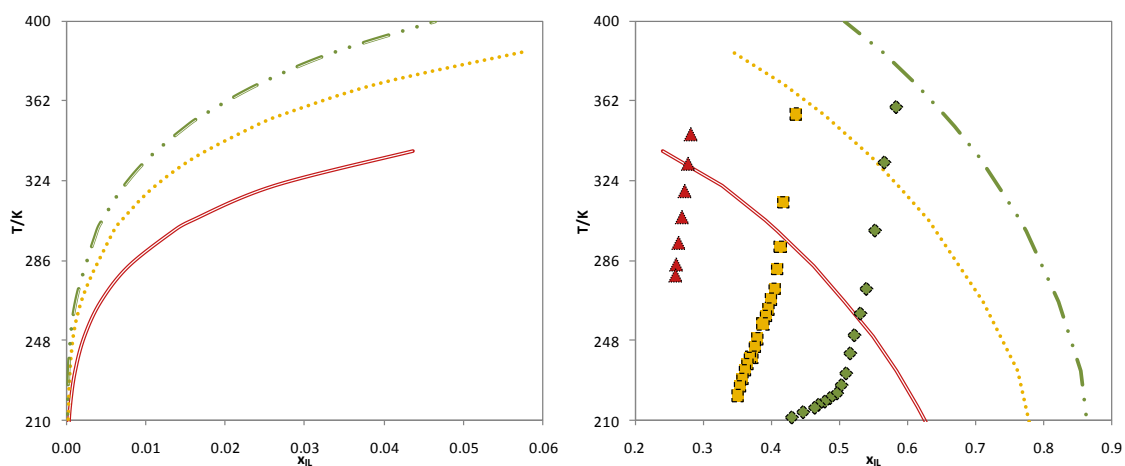


Figure B78 Liquid–liquid phase diagram for $[\text{C}_6\text{mim}][\text{SCN}]$ with benzene ³⁸ (\blacktriangle) (—), toluene ³⁸ (\blacksquare) (⋯) and ethylbenzene ³⁸ (\blacklozenge) (— ·). The symbols and the lines represent respectively the experimental data and the COSMO-RS prediction calculations.

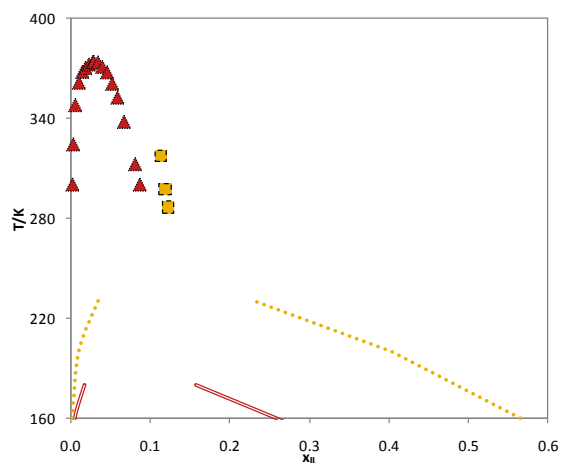


Figure B79 Liquid–liquid phase diagram for [C₈mim][NTf₂] with benzene ⁴⁶ (▲) (—) and toluene ⁴⁶ (■) (⋯). The symbols and the lines represent respectively the experimental data and the COSMO-RS prediction calculations.

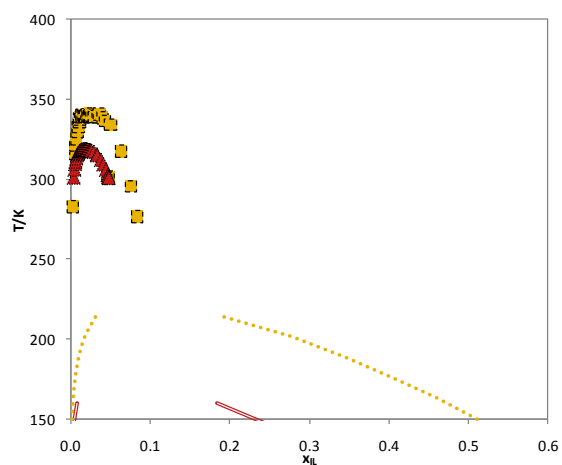


Figure B80 Liquid–liquid phase diagram for [C₁₀mim][NTf₂] with benzene ⁴⁶ (▲) (—) and toluene ⁴⁶ (■) (⋯). The symbols and the lines represent respectively the experimental data and the COSMO-RS prediction calculations.

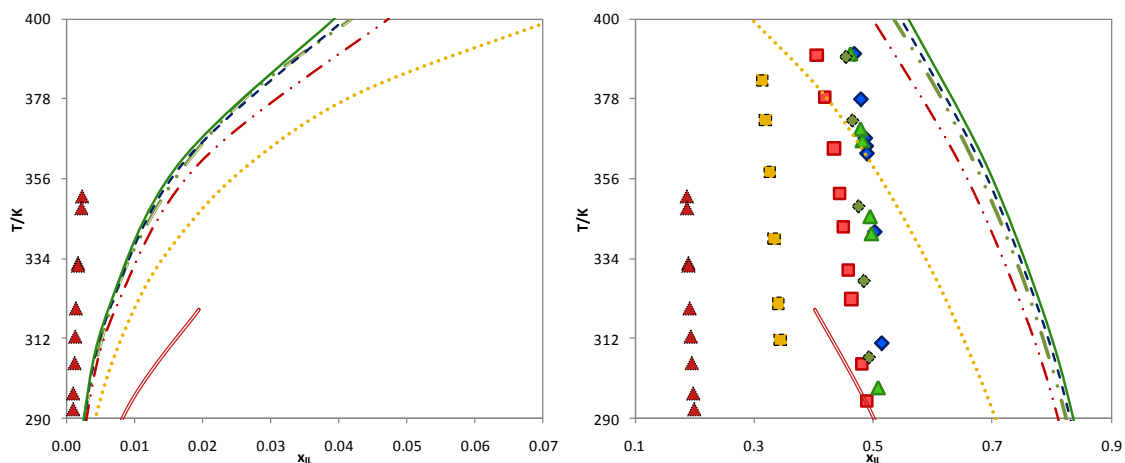


Figure B81 Liquid–liquid phase diagram for $[\text{C}_6\text{H}_{13}\text{OCH}_2\text{mim}][\text{BF}_4]$ with benzene ⁴¹ (\blacktriangle) (—), toluene ⁴¹ (\blacksquare) (\cdots), ethylbenzene ⁴¹ (\blacklozenge) (\dashv), *o*-xylene ⁴¹ (\blacksquare) (\dashv), *m*-xylene ⁴¹ (\blacklozenge) (\dashv) and *p*-xylene ⁴¹ (\blacktriangle) (—). The symbols and the lines represent respectively the experimental data and the COSMO-RS prediction calculations.

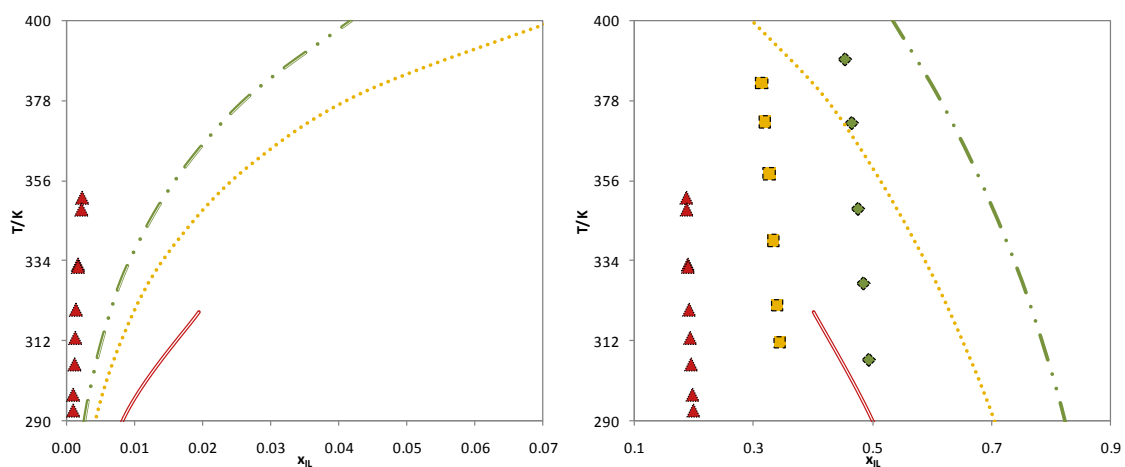


Figure B82 Liquid–liquid phase diagram for $[\text{C}_6\text{H}_{13}\text{OCH}_2\text{mim}][\text{BF}_4]$ with benzene ⁴¹ (\blacktriangle) (—), toluene ⁴¹ (\blacksquare) (\cdots) and ethylbenzene ⁴¹ (\blacklozenge) (\dashv). The symbols and the lines represent respectively the experimental data and the COSMO-RS prediction calculations.

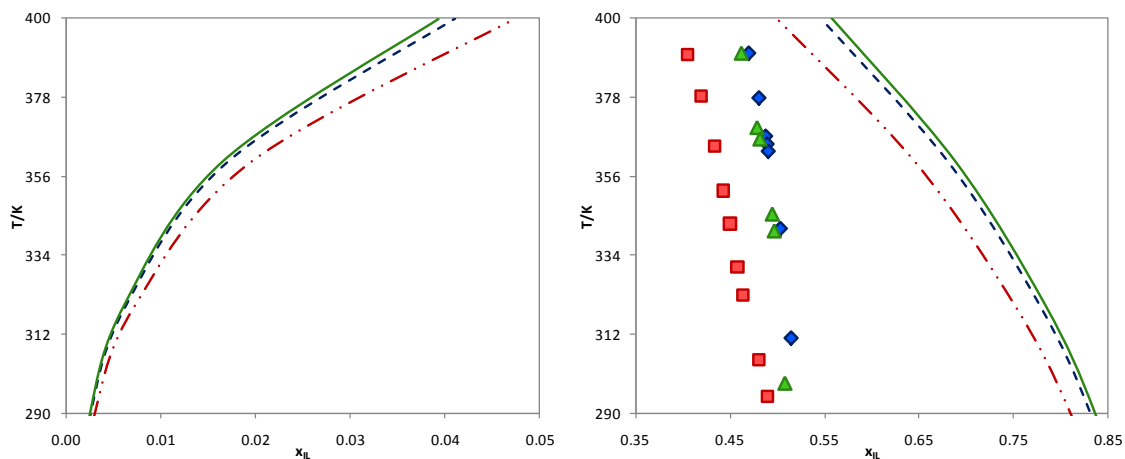


Figure B83 Liquid–liquid phase diagram for $[\text{C}_6\text{H}_{13}\text{OCH}_2\text{mim}][\text{BF}_4]$ with *o*-xylene⁴¹ (■) (— · —), *m*-xylene⁴¹ (◆) (---) and *p*-xylene⁴¹ (▲) (—). The symbols and the lines represent respectively the experimental data and the COSMO-RS prediction calculations.

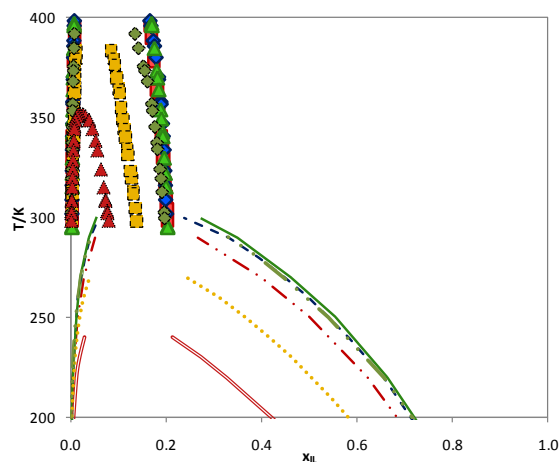


Figure B84 Liquid–liquid phase diagram for $[\text{C}_6\text{H}_{13}\text{OCH}_2\text{mim}][\text{NTf}_2]$ with benzene⁴¹ (▲) (—), toluene⁴¹ (■) (···), ethylbenzene⁴¹ (◆) (— ·), *o*-xylene⁴¹ (■) (— ·), *m*-xylene⁴¹ (◆) (---) and *p*-xylene⁴¹ (▲) (—). The symbols and the lines represent respectively the experimental data and the COSMO-RS prediction calculations.

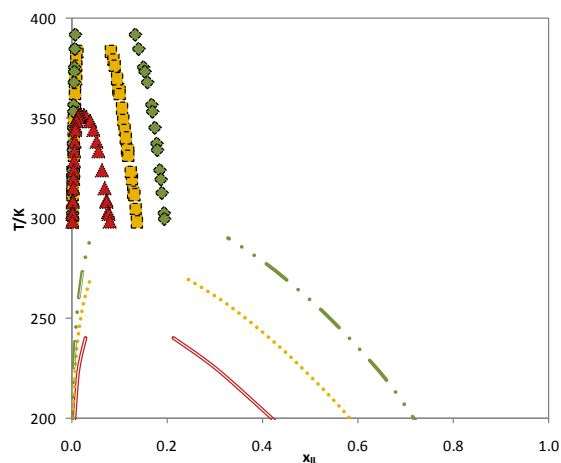


Figure B85 Liquid–liquid phase diagram for $[\text{C}_6\text{H}_{13}\text{OCH}_2\text{mim}][\text{NTf}_2]$ with benzene⁴¹ (\blacktriangle) (---), toluene⁴¹ (\blacksquare) (---) and ethylbenzene⁴¹ (\blacklozenge) (---). The symbols and the lines represent respectively the experimental data and the COSMO-RS prediction calculations.

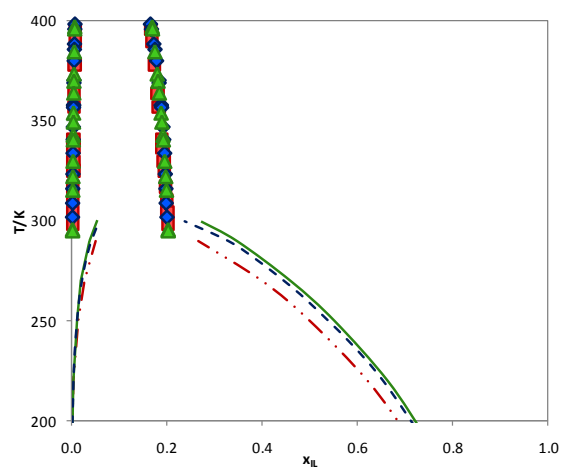


Figure B86 Liquid–liquid phase diagram for $[\text{C}_6\text{H}_{13}\text{OCH}_2\text{mim}][\text{NTf}_2]$ with *o*-xylene⁴¹ (\blacksquare) (---), *m*-xylene⁴¹ (\blacklozenge) (---) and *p*-xylene⁴¹ (\blacktriangle) (---). The symbols and the lines represent respectively the experimental data and the COSMO-RS prediction calculations.

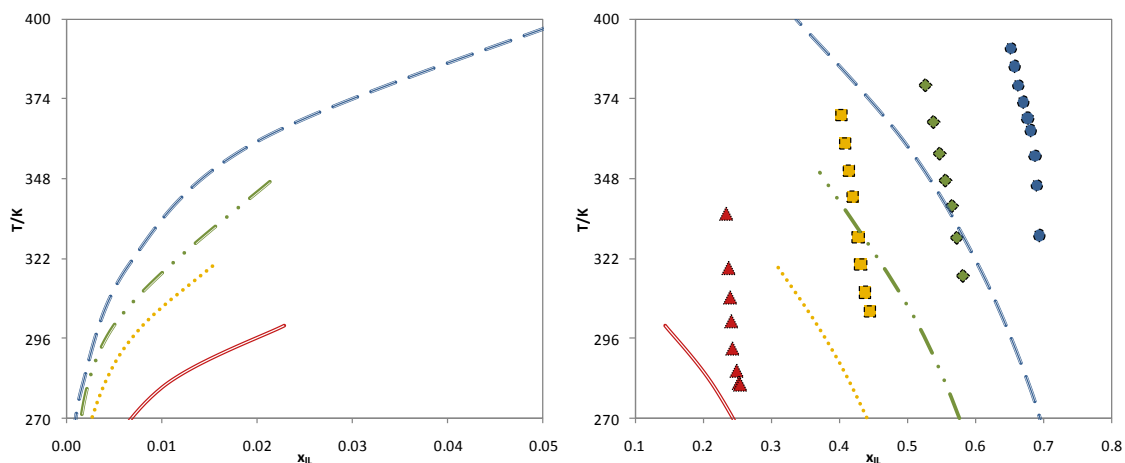


Figure B87 Liquid–liquid phase diagram for [1,4C₄mpy][TOS] with benzene⁴⁹ (\blacktriangle) (—), toluene⁴⁹ (\blacksquare) (⋯), ethylbenzene⁴⁹ (\blacklozenge) (— ·) and propylbenzene⁴⁹ (\bullet) (—). The symbols and the lines represent respectively the experimental data and the COSMO-RS prediction calculations.

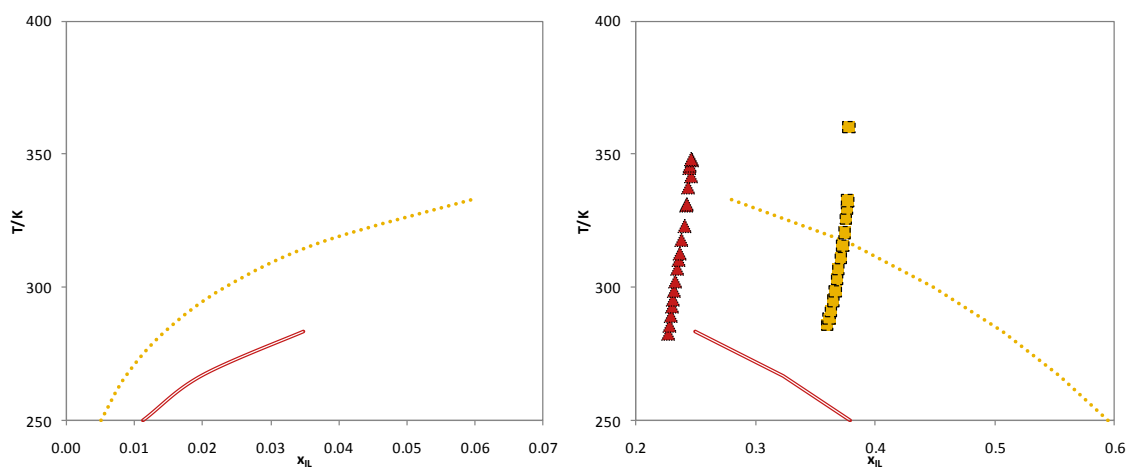


Figure B88 Liquid–liquid phase diagram for [1,3C₄mpy][CF₃SO₃] with benzene⁵⁰ (\blacktriangle) (—) and toluene⁵⁰ (\blacksquare) (⋯). The symbols and the lines represent respectively the experimental data and the COSMO-RS prediction calculations.

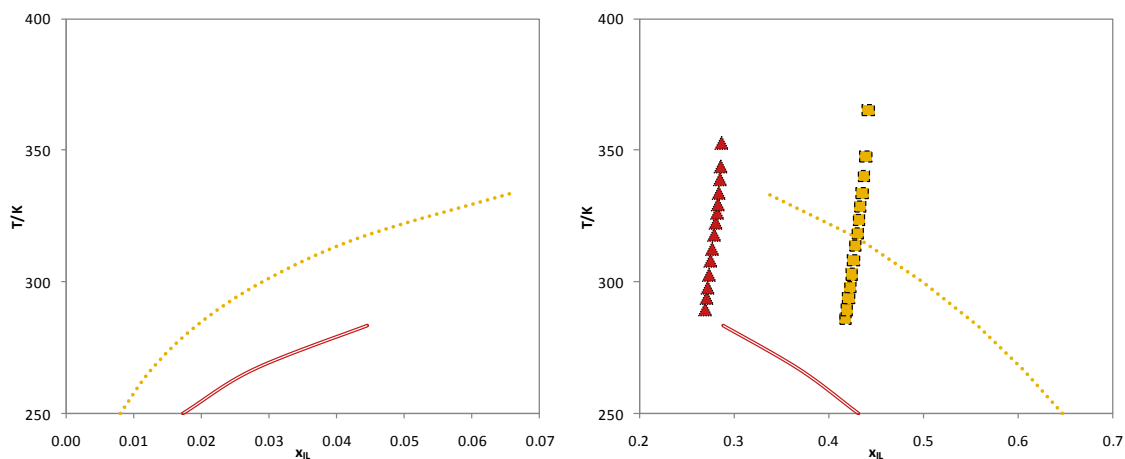


Figure B89 Liquid–liquid phase diagram for $[\text{C}_4\text{mpyr}][\text{CF}_3\text{SO}_3]$ with benzene⁵⁰ (\blacktriangle) (—) and toluene⁵⁰ (\blacksquare) (\cdots). The symbols and the lines represent respectively the experimental data and the COSMO-RS prediction calculations.

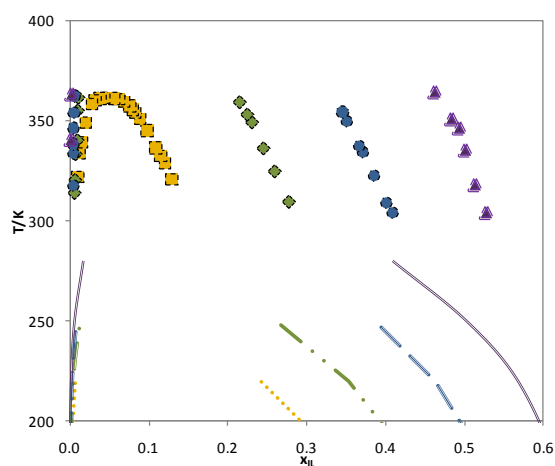


Figure B90 Liquid–liquid phase diagram for $[(i\text{-}b)_3\text{mP}][\text{TOS}]$ with toluene⁴⁷ (\blacksquare) (\cdots), ethylbenzene⁴⁷ (\blacklozenge) ($\text{—}\cdot$), propylbenzene⁴⁷ (\bullet) (--) and butylbenzene⁴⁷. The symbols and the lines represent respectively the experimental data and the COSMO-RS prediction calculations.

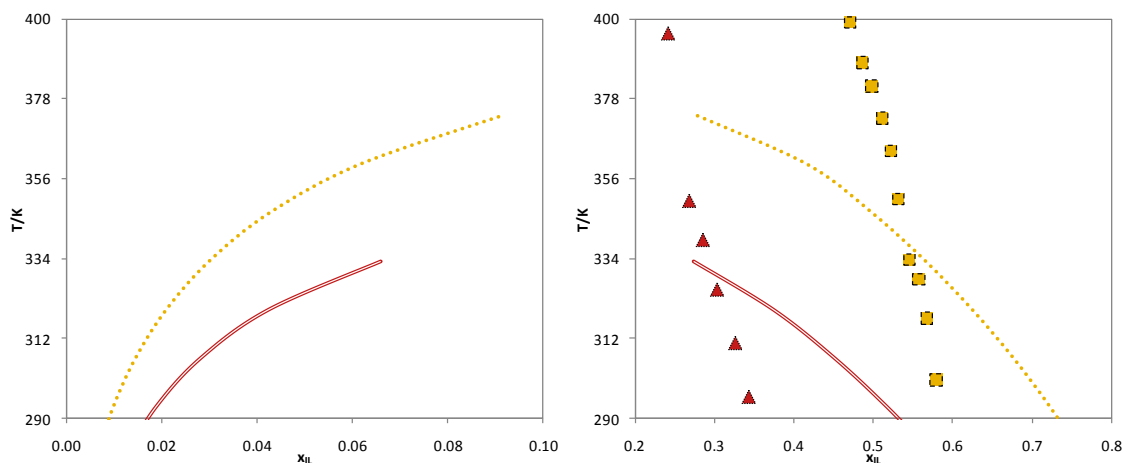


Figure B91 Liquid–liquid phase diagram for $[N_{20}H_{211}][NTf_2]$ with benzene ⁴⁵ (\blacktriangle) (—) and toluene ⁴⁵ (\blacksquare) (\cdots). The symbols and the lines represent respectively the experimental data and the COSMO-RS prediction calculations.

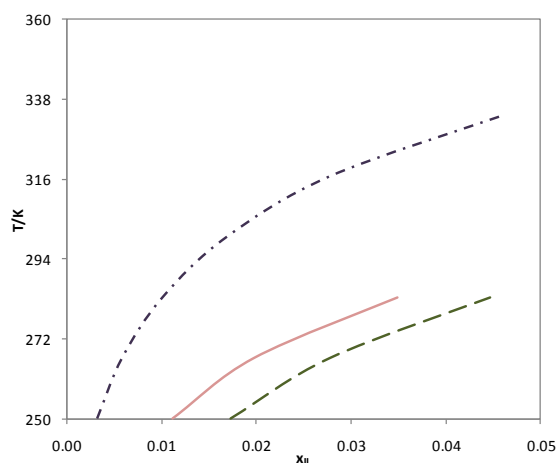


Figure B92 Liquid–liquid phase diagram for $[C_4mim][CF_3SO_3]$ ⁵⁰ (\blacksquare) ($-\cdot-\cdot-$), $[C_4mpyr][CF_3SO_3]$ ⁵⁰ (\blacktriangle) ($-\cdot-\cdot-$) and $[1,3-C_4mpyr][CF_3SO_3]$ ⁵⁰ (\blacklozenge) (—) with benzene. The symbols and the lines represent respectively the experimental data and the COSMO-RS prediction calculations.

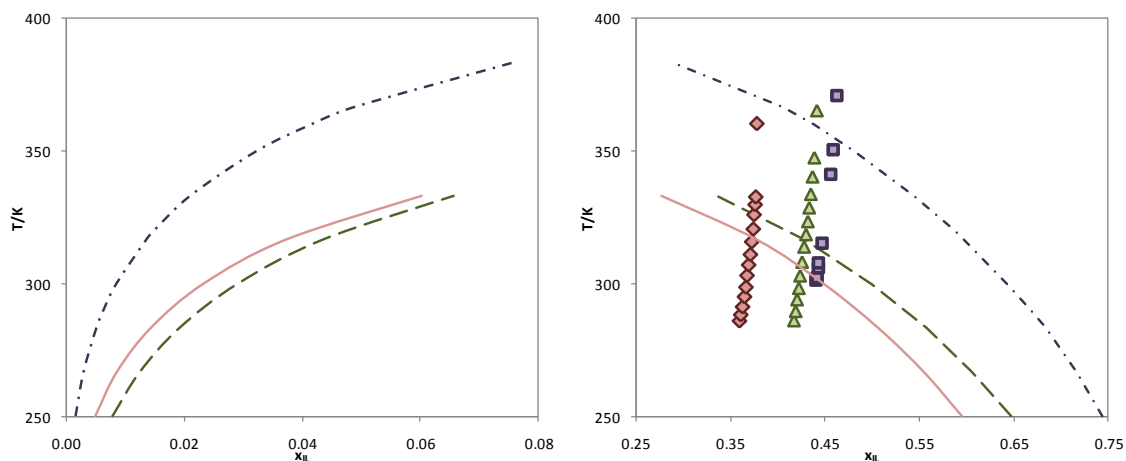


Figure B93 Liquid–liquid phase diagram for $[\text{C}_4\text{mim}][\text{CF}_3\text{SO}_3]^{50}$ (\blacksquare) ($-\cdot-\cdot-$), $[\text{C}_4\text{mpyr}][\text{CF}_3\text{SO}_3]^{50}$ (\blacktriangle) ($- -$) and $[1,3\text{-C}_4\text{mpy}][\text{CF}_3\text{SO}_3]^{50}$ (\blacklozenge) ($—$) with toluene. The symbols and the lines represent respectively the experimental data and the COSMO-RS prediction calculations.

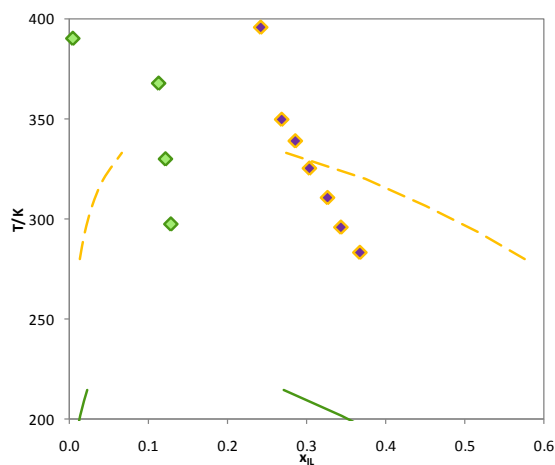


Figure B94 Liquid–liquid phase diagram for $[\text{C}_6\text{mim}][\text{NTf}_2]^{46}$ (\blacklozenge) ($—$) and $[\text{N}_{20}\text{H}_{211}][\text{NTf}_2]^{45}$ (\blacklozenge) ($- -$) with benzene. The symbols and the lines represent respectively the experimental data and the COSMO-RS prediction calculations.

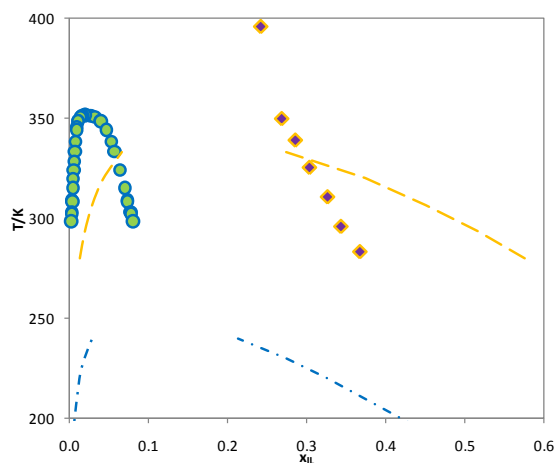


Figure B95 Liquid–liquid phase diagram for [N₂OH₂11][NTf₂]⁴⁵ (♦) (— —) and [C₆H₁₃OCH₂mim][NTf₂]⁴¹ (●) (- · -) with benzene. The symbols and the lines represent respectively the experimental data and the COSMO-RS prediction calculations.

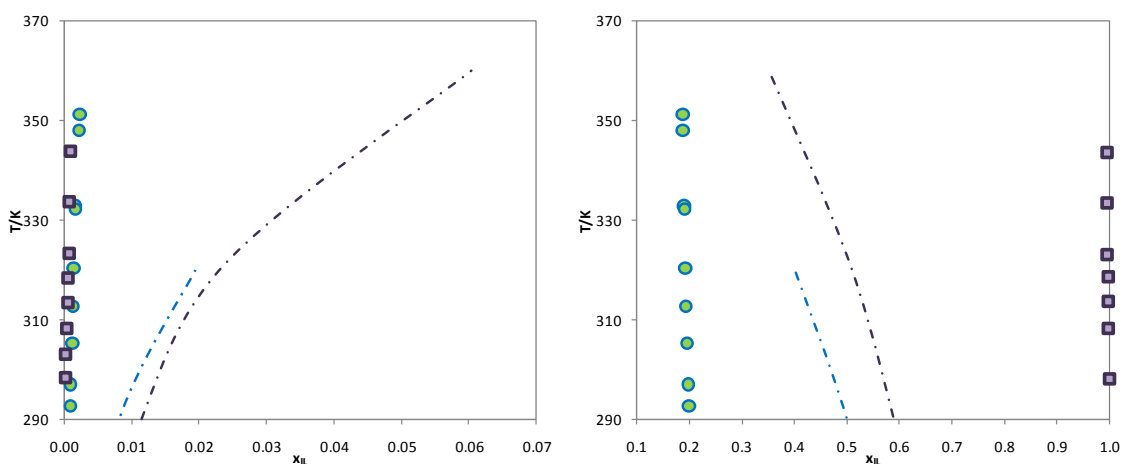


Figure B96 Liquid–liquid phase diagram for [C₄mim][BF₄]⁶³ (■) (- · -) and [C₆H₁₃OCH₂mim][BF₄]⁴¹ (●) (- · -) with benzene. The symbols and the lines represent respectively the experimental data and the COSMO-RS prediction calculations.

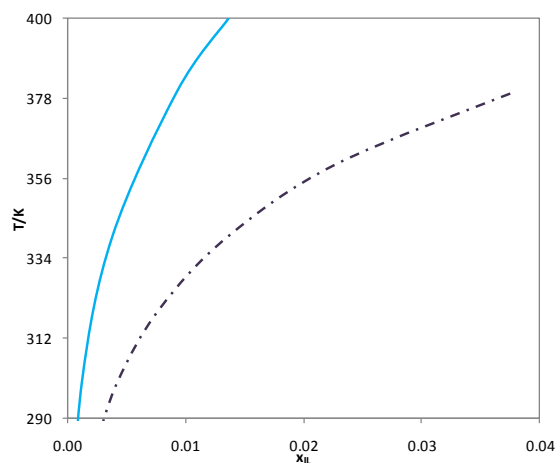


Figure B97 Liquid–liquid phase diagram for $[\text{C}_1\text{mim}][\text{MeSO}_4]$ ³³ (\blacktriangle) (—) and $[\text{C}_4\text{mim}][\text{MeSO}_4]$ ³⁵ (\blacksquare) (- · -) with benzene. The symbols and the lines represent respectively the experimental data and the COSMO-RS prediction calculations.

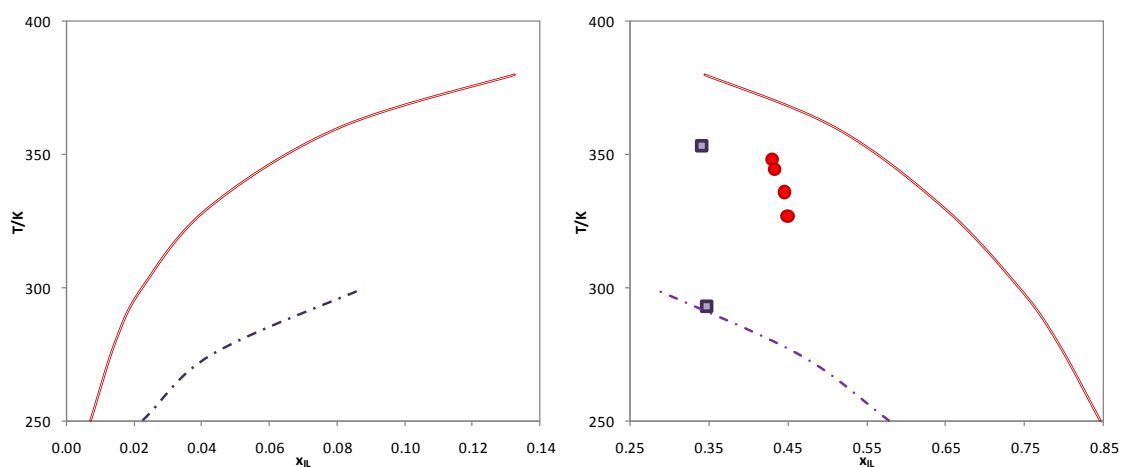


Figure B98 Liquid–liquid phase diagram for $[\text{C}_2\text{mim}][\text{PF}_6]$ ⁵¹ (\bullet) (—) and $[\text{C}_4\text{mim}][\text{PF}_6]$ ⁵¹ (\blacksquare) (- · -) with benzene. The symbols and the lines represent respectively the experimental data and the COSMO-RS prediction calculations.

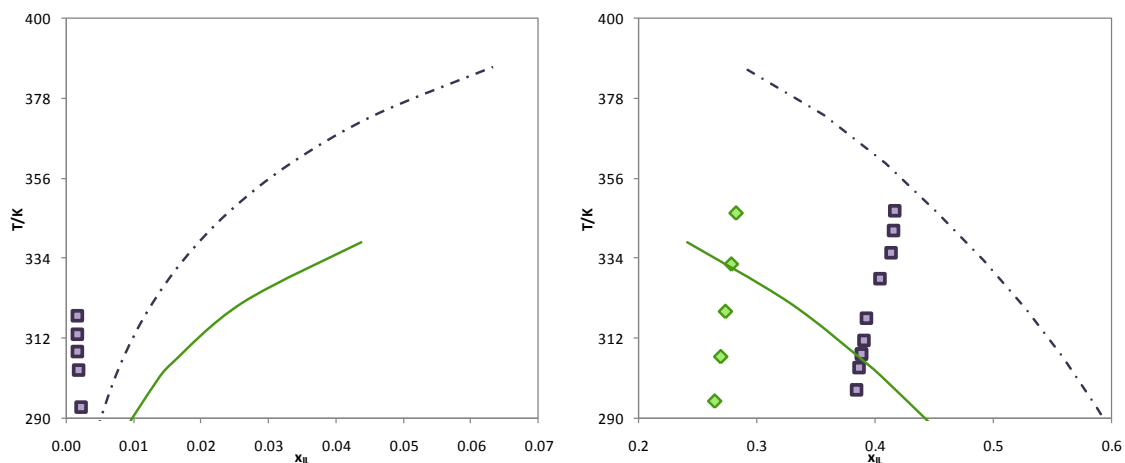


Figure B99 Liquid–liquid phase diagram for $[\text{C}_4\text{mim}][\text{SCN}]^{32}$ (\blacksquare) (---) and $[\text{C}_6\text{mim}][\text{SCN}]^{38}$ (\blacklozenge) (—) with benzene. The symbols and the lines represent respectively the experimental data and the COSMO-RS prediction calculations.

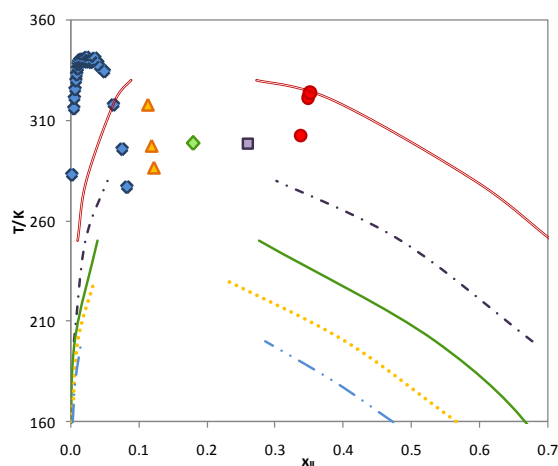


Figure B100 Liquid–liquid phase diagram for $[\text{C}_2\text{mim}][\text{NTf}_2]^{46}$ (\bullet) (—), $[\text{C}_4\text{mim}][\text{NTf}_2]^{46}$ (\blacksquare) (---), $[\text{C}_6\text{mim}][\text{NTf}_2]^{46}$ (\blacklozenge) (—), $[\text{C}_8\text{mim}][\text{NTf}_2]^{46}$ (\blacktriangle) (.....) and $[\text{C}_{10}\text{mim}][\text{NTf}_2]^{46}$ (\blacklozenge) (— · —) with toluene. The symbols and the lines represent respectively the experimental data and the COSMO-RS prediction calculations.

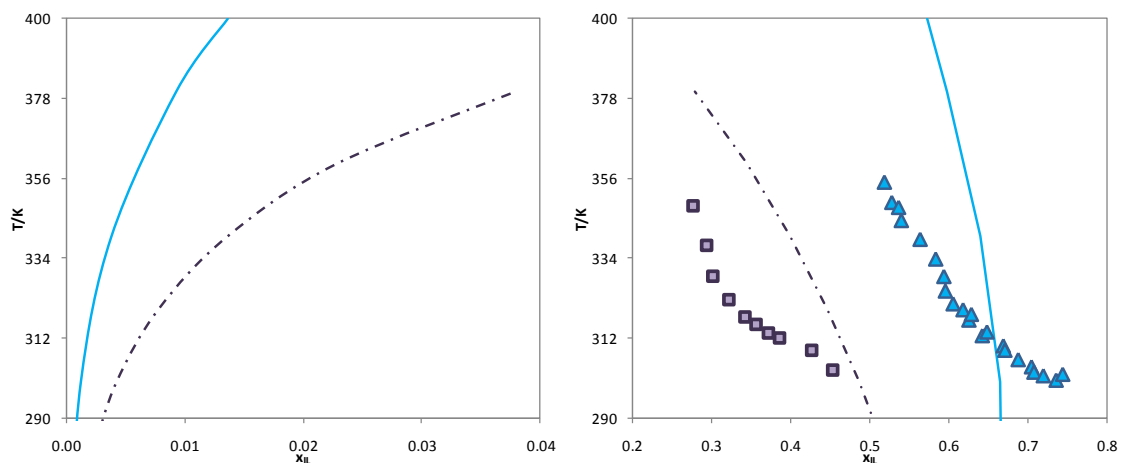


Figure B101 Liquid–liquid phase diagram for [C₁mim][MeSO₄]³³ (▲) (—) and [C₄mim][MeSO₄]³³ (■) (- - -) with benzene. The symbols and the lines represent respectively the experimental data and the COSMO-RS prediction calculations.

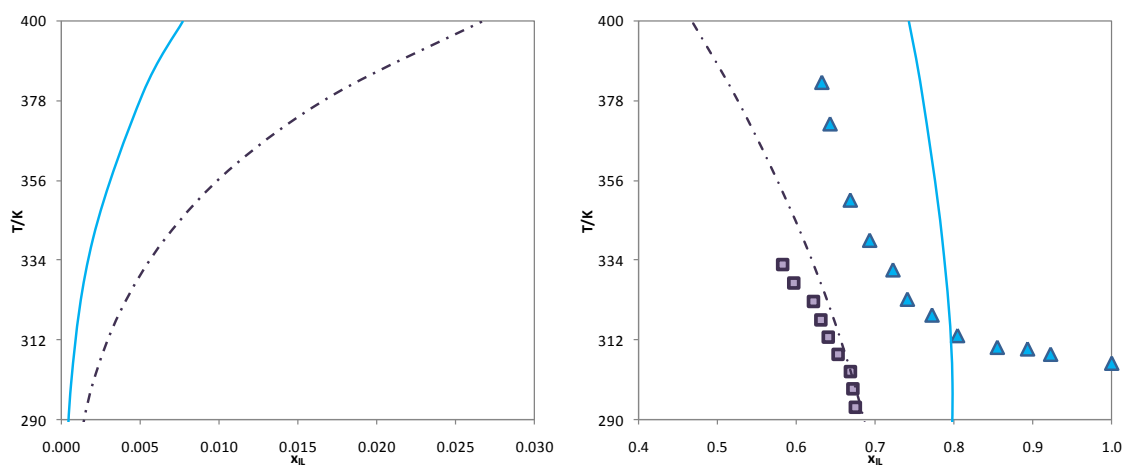


Figure B102 Liquid–liquid phase diagram for [C₁mim][MeSO₄]³³ (▲) (—) and [C₄mim][MeSO₄]³⁵ (■) (- - -) with toluene. The symbols and the lines represent respectively the experimental data and the COSMO-RS prediction calculations.

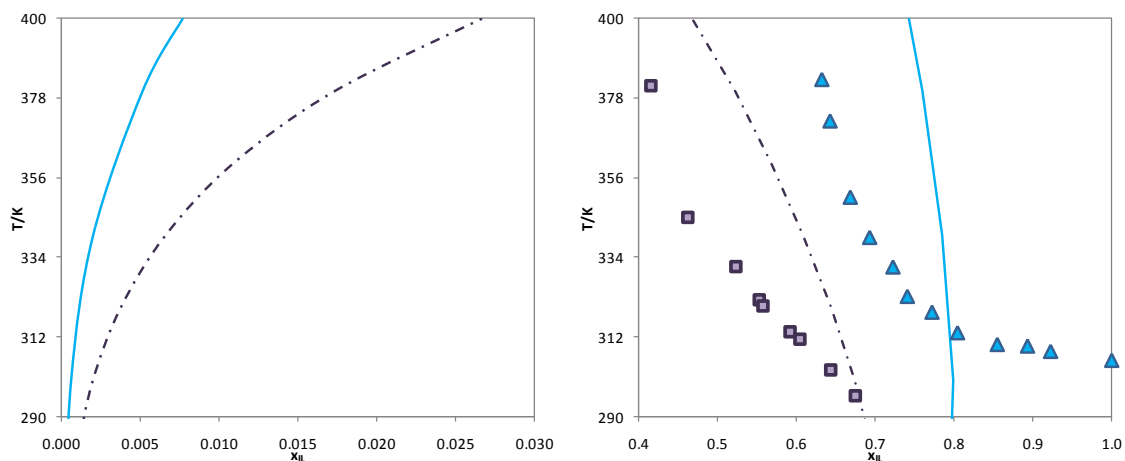


Figure B103 Liquid–liquid phase diagram for $[\text{C}_1\text{mim}][\text{MeSO}_4]$ ³³ (\blacktriangle) (—) and $[\text{C}_4\text{mim}][\text{MeSO}_4]$ ³³ (\blacksquare) (---) with toluene. The symbols and the lines represent respectively the experimental data and the COSMO-RS prediction calculations.

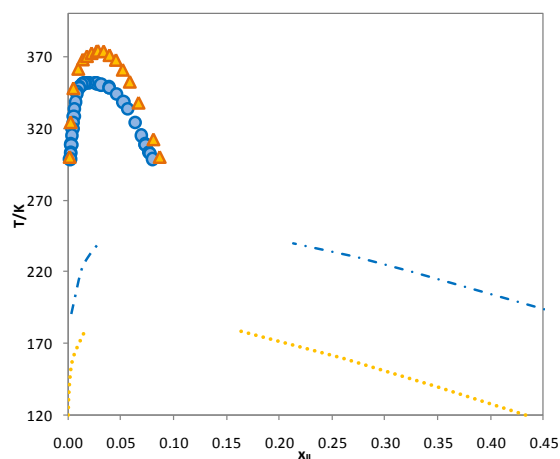


Figure B104 Liquid–liquid phase diagram for $[\text{C}_8\text{mim}][\text{NTf}_2]$ ⁴⁶ (\blacktriangle) (\cdots) and $[\text{C}_6\text{H}_{13}\text{OCH}_2\text{mim}][\text{NTf}_2]$ ⁴¹ (\bullet) (---) with benzene. The symbols and the lines represent respectively the experimental data and the COSMO-RS prediction calculations.

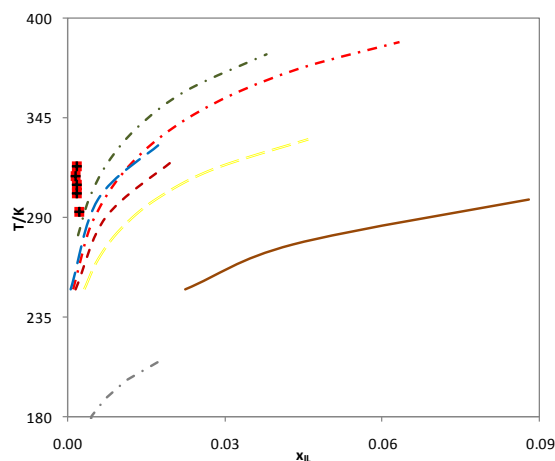


Figure B105 Liquid–liquid phase diagram for $[\text{C}_4\text{mim}][\text{MeSO}_4]^{35}$ (\circ) (— · —), $[\text{C}_4\text{mim}][\text{PF}_6]^{51}$ (\otimes) (—), $[\text{C}_4\text{mim}][\text{BF}_4]^{63}$ (\bullet) (—), $[\text{C}_4\text{mim}][\text{NTf}_2]^{46}$ (\diamond) (— · —), $[\text{C}_4\text{mim}][\text{SCN}]^{32}$ (\blacksquare) (— · —), $[\text{C}_4\text{mim}][\text{TOS}]^{36}$ (\times) (— —), $[\text{C}_4\text{mim}][\text{CF}_3\text{SO}_3]^{50}$ (\square) (— —) and $[\text{C}_4\text{mim}][\text{MDEGSO}_4]^{39}$ (\triangle) (— —) with benzene. The symbols and the lines represent respectively the experimental data and the COSMO-RS prediction calculations.

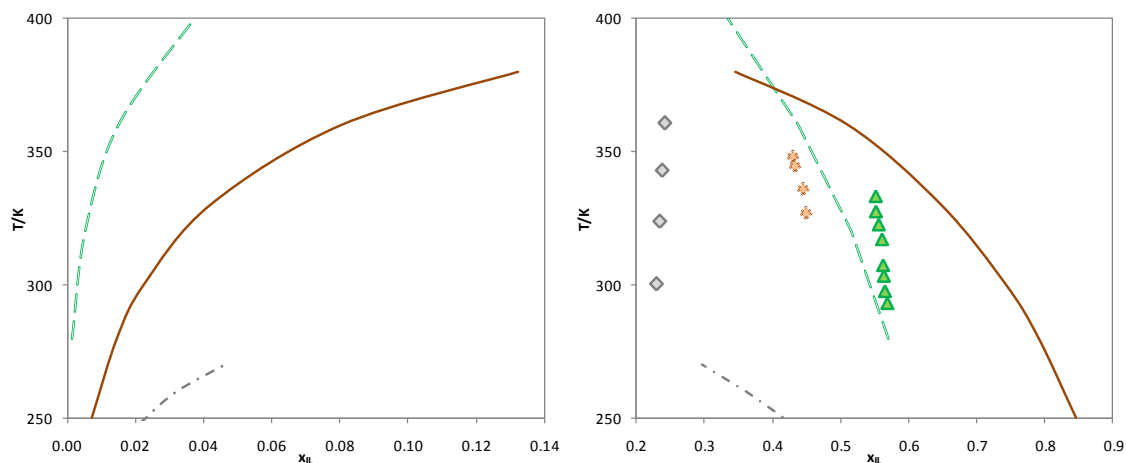


Figure B106 Liquid–liquid phase diagram for $[\text{C}_2\text{mim}][\text{EtSO}_4]^{35}$ (\triangle) (— —), $[\text{C}_2\text{mim}][\text{PF}_6]^{51}$ (\otimes) (—), and $[\text{C}_2\text{mim}][\text{NTf}_2]^{46}$ (\diamond) (— · —) with benzene. The symbols and the lines represent respectively the experimental data and the COSMO-RS prediction calculations.

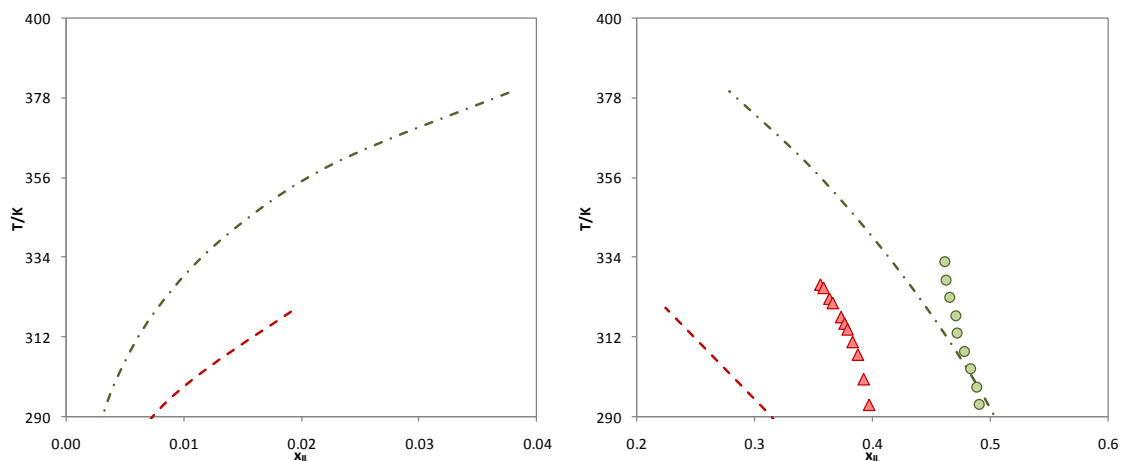


Figure B107 Liquid–liquid phase diagram for $[\text{C}_4\text{mim}][\text{MeSO}_4]$ ³⁵ (●) (– · –) and $[\text{C}_4\text{mim}][\text{MDEGSO}_4]$ ³⁹ (▲) (– – –) with benzene. The symbols and the lines represent respectively the experimental data and the COSMO-RS prediction calculations.

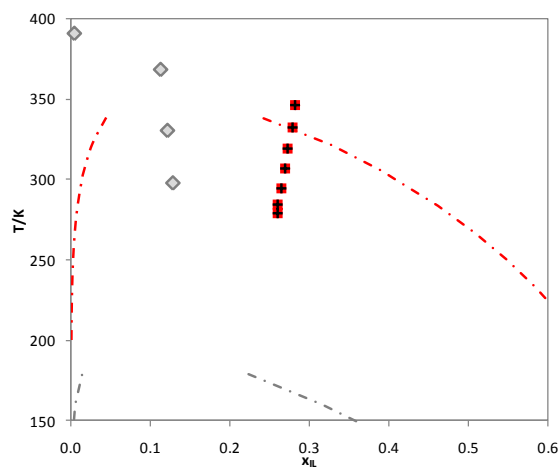


Figure B108 Liquid–liquid phase diagram for $[\text{C}_4\text{mim}][\text{NTf}_2]$ ⁴⁶ (◆) (– · –) and $[\text{C}_4\text{mim}][\text{SCN}]$ ³² (■) (– · –) with benzene. The symbols and the lines represent respectively the experimental data and the COSMO-RS prediction calculations.

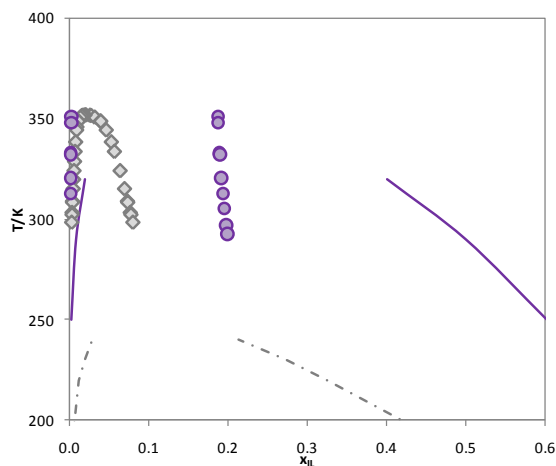


Figure B109 Liquid–liquid phase diagram for [C₆H₁₃OCH₂mim][BF₄]⁴¹ (●) (—) and [C₆H₁₃OCH₂mim][NTf₂]⁴¹ (◆) (-.-) with benzene. The symbols and the lines represent respectively the experimental data and the COSMO-RS prediction calculations.

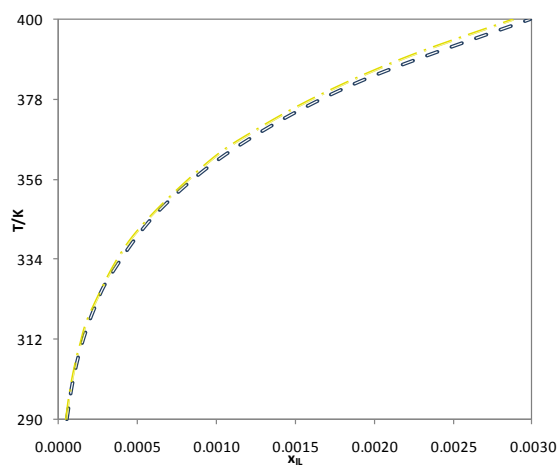


Figure B110 Liquid–liquid phase diagram for [C₆mim][SCN] with cyclohexane³⁸ (◆) (- -) and cycloheptane³⁸ (▲) (-.-). The symbols and the lines represent respectively the experimental data and the COSMO-RS prediction calculations.

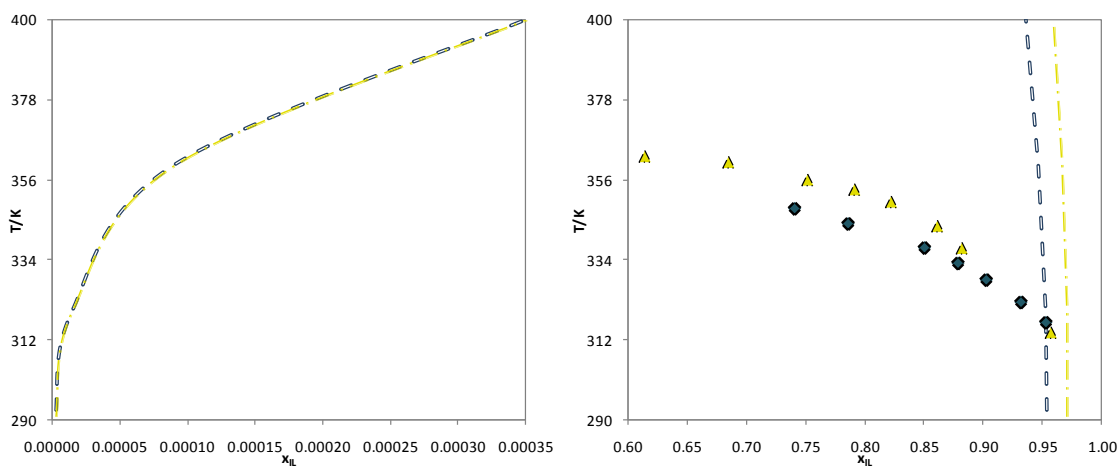


Figure B111 Liquid–liquid phase diagram for [C₁mim][MeSO₄] with cyclohexane³³ (◆) (—) and cycloheptane³³ (▲) (— · —). The symbols and the lines represent respectively the experimental data and the COSMO-RS prediction calculations.

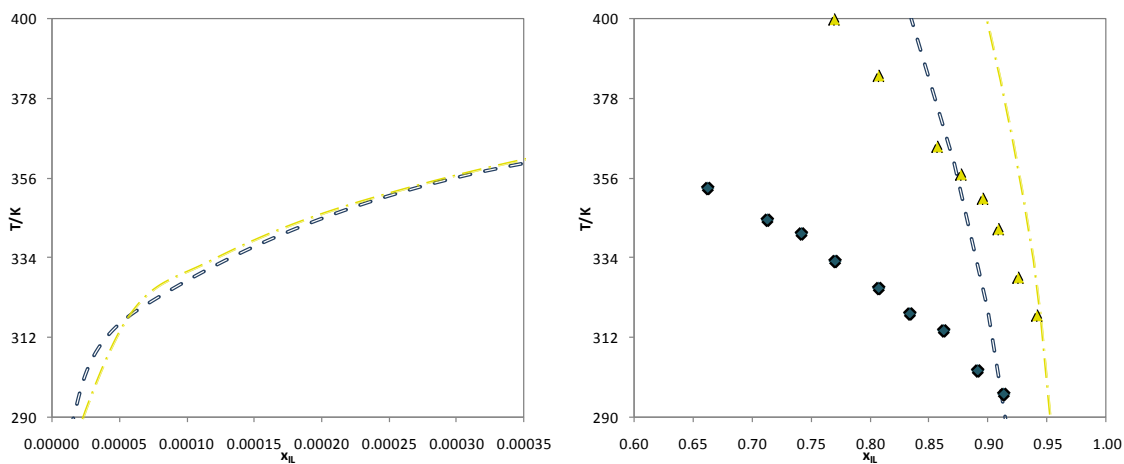


Figure B112 Liquid–liquid phase diagram for [C₄mim][MeSO₄] with cyclohexane³³ (◆) (—) and cycloheptane³³ (▲) (— · —). The symbols and the lines represent respectively the experimental data and the COSMO-RS prediction calculations.

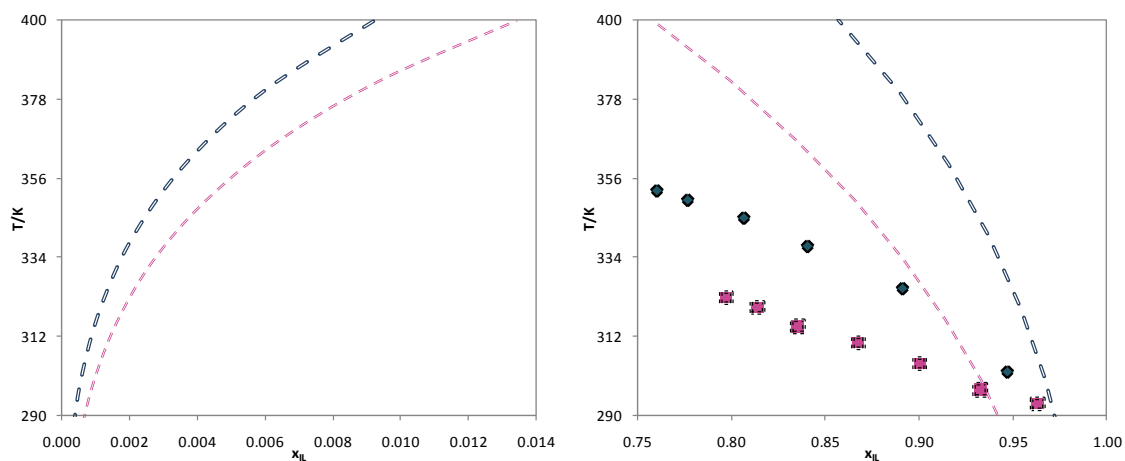


Figure B113 Liquid–liquid phase diagram for $[\text{C}_4\text{mim}][\text{PF}_6]$ with cyclopentane⁵¹ (\blacksquare) (—) and cyclohexane⁵¹ (\blacklozenge) (—). The symbols and the lines represent respectively the experimental data and the COSMO-RS prediction calculations.

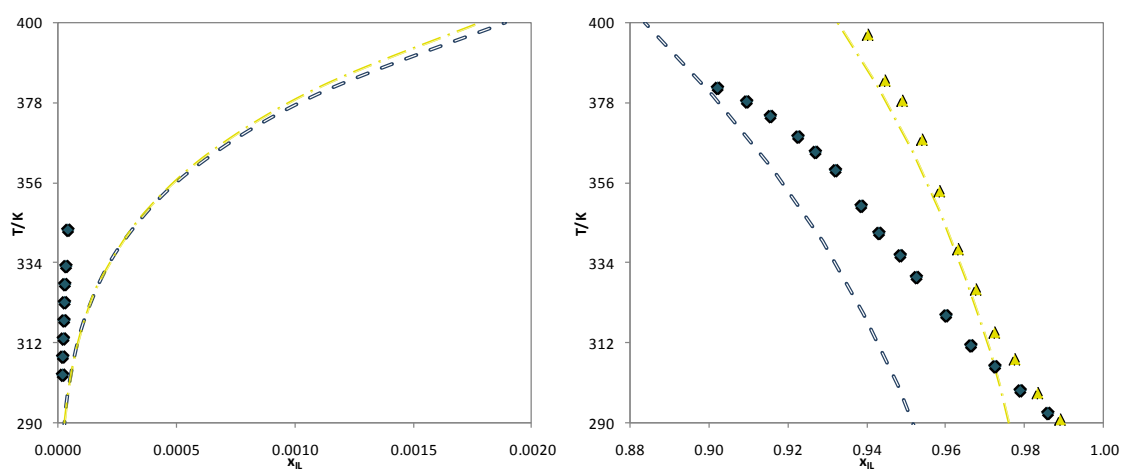


Figure B114 Liquid–liquid phase diagram for $[\text{C}_4\text{mim}][\text{SCN}]$ with cyclohexane³² (\blacklozenge) (—) and cycloheptane³² (\blacktriangle) (—). The symbols and the lines represent respectively the experimental data and the COSMO-RS prediction calculations.

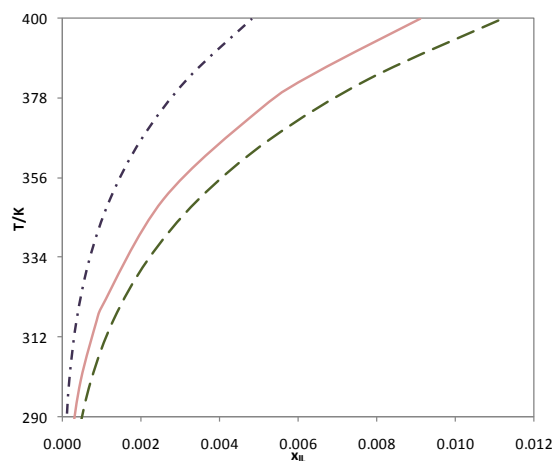


Figure B115 Liquid–liquid phase diagram for $[\text{C}_4\text{mim}][\text{CF}_3\text{SO}_3]^{50}$ (\blacksquare) (– · –), $[\text{C}_4\text{mpyr}][\text{CF}_3\text{SO}_3]^{50}$ (\blacktriangle) (– –) and $[\text{1,3C}_4\text{mpy}][\text{CF}_3\text{SO}_3]^{50}$ (\blacklozenge) (—) with cyclohexane. The symbols and the lines represent respectively the experimental data and the COSMO-RS prediction calculations.

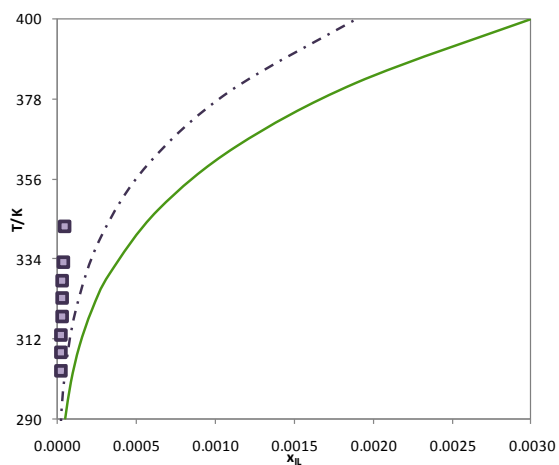


Figure B116 Liquid–liquid phase diagram for $[\text{C}_4\text{mim}][\text{SCN}]^{32}$ (\blacksquare) (– · –) and $[\text{C}_6\text{mim}][\text{SCN}]^{38}$ (\blacklozenge) (—) with cyclohexane. The symbols and the lines represent respectively the experimental data and the COSMO-RS prediction calculations.

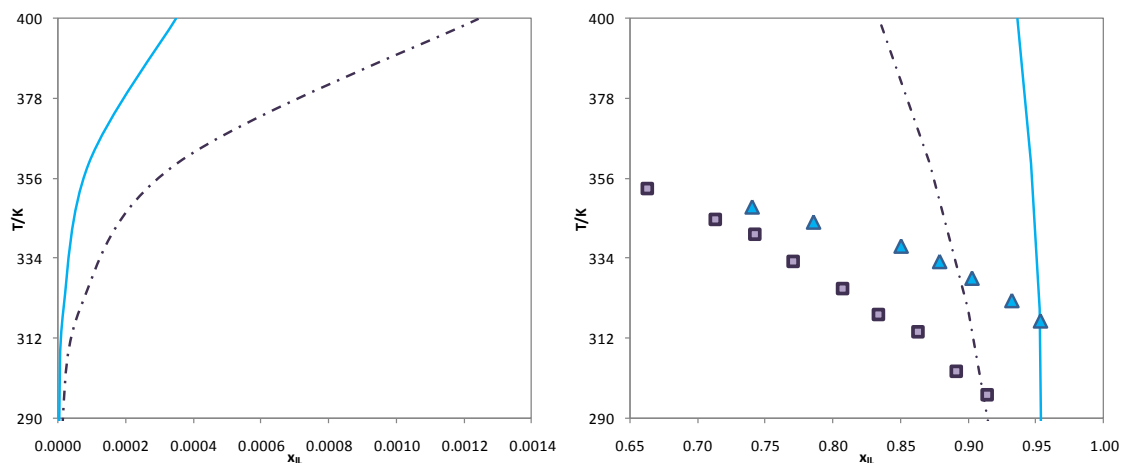


Figure B117 Liquid–liquid phase diagram for $[\text{C}_1\text{mim}][\text{MeSO}_4]$ ³³ (\blacktriangle) (—) and $[\text{C}_4\text{mim}][\text{MeSO}_4]$ ³³ (\blacksquare) (— · —) with cyclohexane. The symbols and the lines represent respectively the experimental data and the COSMO-RS prediction calculations.

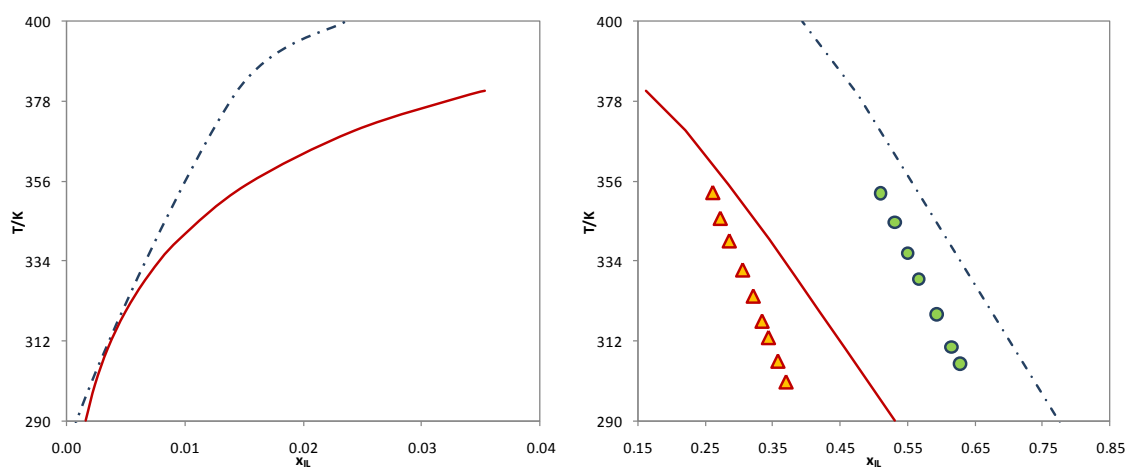


Figure B118 Liquid–liquid phase diagram for $[\text{C}_6\text{H}_{13}\text{OCH}_2\text{mim}][\text{NTf}_2]$ ⁴¹ (\bullet) (— · —) and $[(\text{C}_6\text{H}_{13}\text{OCH}_2)_2\text{im}][\text{NTf}_2]$ ⁴² (\blacktriangle) (—) with cyclohexane. The symbols and the lines represent respectively the experimental data and the COSMO-RS prediction calculations.

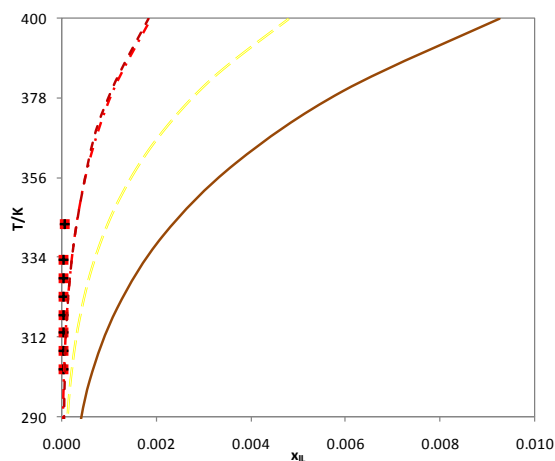


Figure B119 Liquid–liquid phase diagram for $[\text{C}_4\text{mim}][\text{PF}_6]^{51}$ (\diamond) (—), $[\text{C}_4\text{mim}][\text{SCN}]^{32}$ (\blacksquare) (- · -), $[\text{C}_4\text{mim}][\text{CF}_3\text{SO}_3]^{50}$ (\square) (==) and $[\text{C}_4\text{mim}][\text{MDEGSO}_4]^{39}$ (\triangle) (- - -) with cyclohexane. The symbols and the lines represent respectively the experimental data and the COSMO-RS prediction calculations.

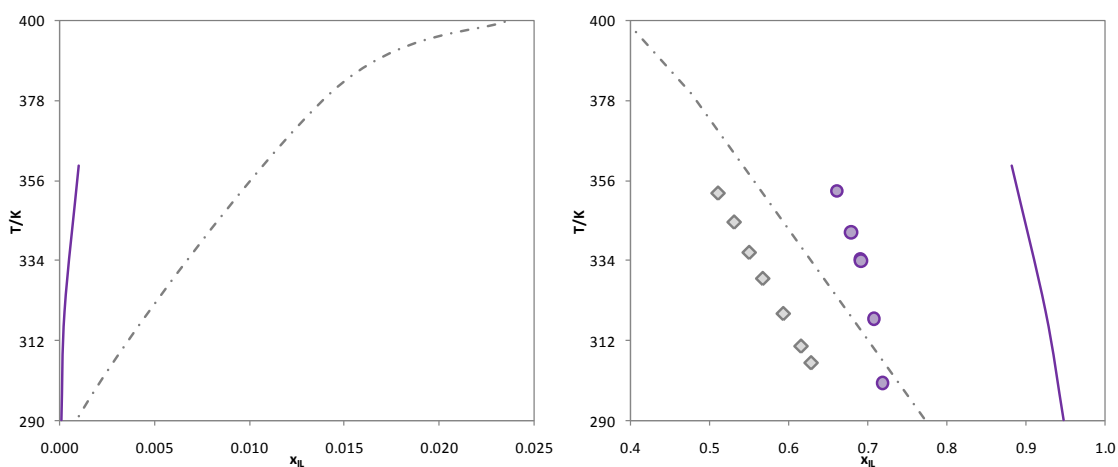


Figure B120 Liquid–liquid phase diagram for $[\text{C}_6\text{H}_{13}\text{OCH}_2\text{mim}][\text{BF}_4]^{41}$ (\bullet) (—) and $[\text{C}_6\text{H}_{13}\text{OCH}_2\text{mim}][\text{NTf}_2]^{41}$ (\diamond) (- · -) with cyclohexane. The symbols and the lines represent respectively the experimental data and the COSMO-RS prediction calculations.

Appendix C

**An Overview of the Liquid-Liquid
Equilibria of Ternary Systems
composed of Ionic Liquid, Aromatic and
Aliphatic Hydrocarbons, and its
Modeling by COSMO-RS**

Table C1 Published LLE experimental data for systems composed of *n*-alkane + aromatic hydrocarbon + ionic liquid, measurement technique, and models already applied.

Nº	Ionic liquid	<i>n</i> -alkane	Aromatic	Experimental procedure	Temperature / K	Model
1.	[C ₁ mim][MeSO ₄] ⁴⁰	<i>n</i> -heptane	toluene	Tie-lines: thermodynamic equilibrium + NMR, GC and overall mass balance ⁴⁰	313.2 ⁴⁰	NRTL ⁴⁰
2.					348.2 ⁴⁰	
3.	[C ₁ mim][NTf ₂] ²³	<i>n</i> -heptane	toluene	Tie-lines: thermodynamic equilibrium + NMR, GC and overall mass balance ²³	313.2 ²³	NRTL ²³
4.	[C ₁ mim][BF ₄] ⁵²	<i>n</i> -heptane	toluene	Tie-lines: thermodynamic equilibrium + GC + density correlation ⁵²	298.15 ⁵²	NRTL ⁵² UNIQUAC ⁵²
5.	[C ₁ mim][P ₁] ⁵²	<i>n</i> -heptane	toluene	Tie-lines: thermodynamic equilibrium + GC + density correlation ⁵²	298.15 ⁵²	NRTL ⁵² UNIQUAC ⁵²
6.	[C ₂ mim][NTf ₂] ^{3, 28}	<i>n</i> -hexane	benzene	Tie-lines: thermodynamic equilibrium + NMR ^{3, 28}	298.15 ^{3, 28, 54, 82}	NRTL ^{28, 54} UNIQUAC ⁵⁴ NRTL-SAC ₈₂
7.					313.15 ²⁸	NRTL ^{28, 54}
8.	[C ₂ mim][NTf ₂] ¹	<i>n</i> -heptane	toluene	Tie-lines: thermodynamic equilibrium + NMR ¹	298.15 ¹	NRTL ¹
9.	[C ₂ mim][NTf ₂] ²³	<i>n</i> -heptane	toluene	Tie-lines: thermodynamic equilibrium + NMR, GC and overall mass balance ²³	313.2 ²³	NRTL ²³
10.	[C ₂ mim][NTf ₂] ¹	<i>n</i> -octane	ethylbenzene	Tie-lines: thermodynamic equilibrium + NMR ¹	298.15 ¹	NRTL ¹
11.	[C ₂ mim][NTf ₂] ⁸	<i>n</i> -octane	<i>o</i> -xylene	Tie-lines: thermodynamic equilibrium + NMR ⁸	298.15 ⁸	NRTL ⁸
12.	[C ₂ mim][NTf ₂] ⁸	<i>n</i> -octane	<i>m</i> -xylene	Tie-lines: thermodynamic equilibrium +	298.15 ⁸	NRTL ⁸

				NMR ⁸		
13.	[C ₂ mim][NTf ₂] ⁸	<i>n</i> -octane	<i>p</i> -xylene	Tie-lines: thermodynamic equilibrium + NMR ⁸	298.15 ⁸	NRTL ⁸
14.	[C ₂ mim][EtSO ₄] ¹³	<i>n</i> -hexane	benzene	Tie-lines: thermodynamic equilibrium + NMR, GC and overall mass balance ¹³	298.2 ¹³	NRTL ¹³ UNIQUAC ¹³
15.					313.2 ¹³	
16.					328.2 ¹³	
17.	[C ₂ mim][EtSO ₄] ³²	<i>n</i> -hexane	benzene	Binodal data: Cloud point method ³² Tie-lines: thermodynamic equilibrium + density correlation ³²	298.15 ³²	NRTL ³² UNIQUAC ³²
18.	[C ₂ mim][EtSO ₄] ⁷	<i>n</i> -hexane	toluene	Binodal data: Cloud point method ⁷ Tie-lines: thermodynamic equilibrium + density correlation ⁷	298.15 ⁷	NRTL ⁷ UNIQUAC ⁷
19.	[C ₂ mim][EtSO ₄] ³⁶	<i>n</i> -hexane	<i>o</i> -xylene	Binodal data: Cloud point method ³⁶ Tie-lines: thermodynamic equilibrium + density correlation ³⁶	298.15 ³⁶	NRTL ³⁶ UNIQUAC ³⁶
20.	[C ₂ mim][EtSO ₄] ³⁶	<i>n</i> -hexane	<i>p</i> -xylene	Binodal data: Cloud point method ³⁶ Tie-lines: thermodynamic equilibrium + density correlation ³⁶	298.15 ³⁶	NRTL ³⁶ UNIQUAC ³⁶
21.	[C ₂ mim][EtSO ₄] ³⁶	<i>n</i> -hexane	<i>m</i> -xylene	Binodal data: Cloud point method ³⁶ Tie-lines: thermodynamic equilibrium + density correlation ³⁶	298.15 ³⁶	NRTL ³⁶ UNIQUAC ³⁶
22.	[C ₂ mim][EtSO ₄] ³²	<i>n</i> -heptane	benzene	Binodal data: Cloud point method ³² Tie-lines: thermodynamic equilibrium + density correlation ³²	298.15 ³²	NRTL ³² UNIQUAC ³²
23.	[C ₂ mim][EtSO ₄] ⁷	<i>n</i> -heptane	toluene	Binodal data: Cloud point method ⁷ Tie-lines: thermodynamic equilibrium + density correlation ⁷	298.15 ⁷	NRTL ⁷ UNIQUAC ⁷

24.	[C ₂ mim][EtSO ₄] ⁴⁰	<i>n</i> -heptane	toluene	Tie-lines: thermodynamic equilibrium + NMR, GC and overall mass balance ⁴⁰	313.2 ⁴⁰	NRTL ⁴⁰
25.					348.2 ⁴⁰	
26.	[C ₂ mim][EtSO ₄] ³²	<i>n</i> -octane	benzene	Binodal data: Cloud point method ³² Tie-lines: thermodynamic equilibrium + density correlation ³²	298.15 ³²	NRTL ³² UNIQUAC ³²
27.	[C ₂ mim][EtSO ₄] ⁷	<i>n</i> -octane	toluene	Binodal data: Cloud point method ⁷ Tie-lines: thermodynamic equilibrium + density correlation ⁷	298.15 ⁷	NRTL ⁷ UNIQUAC ⁷
28.	[C ₂ mim][EtSO ₄] ³²	<i>n</i> -nonane	benzene	Binodal data: Cloud point method ³² Tie-lines: thermodynamic equilibrium + density correlation ³²	298.15 ³²	NRTL ³² UNIQUAC ³²
29.	[C ₂ mim][EtSO ₄] ⁷	<i>n</i> -nonane	toluene	Binodal data: Cloud point method ⁷ Tie-lines: thermodynamic equilibrium + density correlation ⁷	298.15 ⁷	NRTL ⁷ UNIQUAC ⁷
30.	[C ₂ mim][OcSO ₄] ¹⁵	<i>n</i> -heptane	benzene	Binodal data: Cloud point method ¹⁵ Tie-lines: thermodynamic equilibrium + refractive index correlation ¹⁵	298.2 ¹⁵	----
31.	[C ₂ mim][OcSO ₄] ¹⁵	<i>n</i> -hexadecane	benzene	Binodal data: Cloud point method ¹⁵ Tie-lines: thermodynamic equilibrium + refractive index correlation ¹⁵	298.2 ¹⁵	----
32.	[C ₂ mim][CH ₃ SO ₃] ⁵¹	<i>n</i> -heptane	toluene	Tie-lines: thermodynamic equilibrium + NMR ⁵¹	313.2 ⁵¹	NRTL ⁵¹
33.	[C ₂ mim][CF ₃ SO ₃] ⁵¹	<i>n</i> -heptane	toluene	Tie-lines: thermodynamic equilibrium + NMR ⁵¹	313.2 ⁵¹	NRTL ⁵¹
34.	[C ₂ mim][CHF ₂ CF ₂ SO ₃] ⁵¹	<i>n</i> -heptane	toluene	Tie-lines: thermodynamic equilibrium + NMR ⁵¹	313.2 ⁵¹	NRTL ⁵¹
35.	[C ₂ mim][I ₃] ¹⁸	<i>n</i> -heptane	toluene	Tie-lines: thermodynamic equilibrium +	318.2 ¹⁸	NRTL ¹⁸

				NMR, GC and overall mass balance ¹⁸		
36.	[C ₄ mim][NTf ₂] ²⁹	<i>n</i> -hexane	benzene	Tie-lines: thermodynamic equilibrium + NMR ²⁹	298.15 ²⁹	----
37.	[C ₄ mim][NTf ₂] ²³	<i>n</i> -heptane	toluene	Tie-lines: thermodynamic equilibrium + NMR, GC and overall mass balance ²³	313.2 ²³	NRTL ²³
38.	[C ₄ mim][MeSO ₄] ⁴²	<i>n</i> -hexane	benzene	Tie-lines: thermodynamic equilibrium + NMR, GC and overall mass balance ⁴²	298.2 ⁴²	NRTL ⁴² UNIQUAC ⁴²
39.					313.2 ⁴²	
40.					328.2 ⁴²	
41.	[C ₄ mim][MeSO ₄] ⁴⁰	<i>n</i> -heptane	toluene	Tie-lines: thermodynamic equilibrium + NMR, GC and overall mass balance ⁴⁰	303.2 ⁴⁰	NRTL ⁴⁰
42.					328.2 ⁴⁰	
43.	[C ₄ mim][DCA] ¹⁷	<i>n</i> -heptane	toluene	Tie-lines: thermodynamic equilibrium + GC and mass balance ¹⁷	303.15 ¹⁷	NRTL ¹⁷
44.					328.15 ¹⁷	
45.	[C ₄ mim][SCN] ⁵²	<i>n</i> -heptane	benzene	Tie-lines: thermodynamic equilibrium + GC + density correlation ⁵²	298.15 ⁵²	NRTL ⁵² UNIQUAC ⁵²
46.	[C ₄ mim][SCN] ¹⁷	<i>n</i> -heptane	toluene	Tie-lines: thermodynamic equilibrium + GC and mass balance ¹⁷	303.15 ¹⁷	NRTL ¹⁷
47.					328.15 ¹⁷	
48.	[C ₄ mim][PF ₆] ²¹	<i>n</i> -nonane	benzene	Binodal data: Cloud point method ²¹ Tie-lines: thermodynamic equilibrium + density correlation and UV spectrophotometry ²¹	298.15 ^{21, 55}	NRTL ²¹ UNIQUAC ⁵⁵
49.	[C ₄ mim][PF ₆] ²¹	<i>n</i> -nonane	toluene	Binodal data: Cloud point method ²¹ Tie-lines: thermodynamic equilibrium + density correlation and UV spectrophotometry ²¹	298.15 ^{21, 55-56}	NRTL ²¹ ASOG ⁵⁶ UNIQUAC ⁵⁵
50.	[C ₄ mim][PF ₆] ²¹	<i>n</i> -nonane	<i>m</i> -xylene	Binodal data: Cloud point method ²¹ Tie-lines: thermodynamic equilibrium +	298.15 ^{21, 55-56}	NRTL ²¹ ASOG ⁵⁶

				density correlation and UV spectrophotometry ²¹		UNIQUAC ⁵⁵
51.	[C ₄ mim][PF ₆] ²¹	<i>n</i> -undecane	benzene	Binodal data: Cloud point method ²¹ Tie-lines: thermodynamic equilibrium + density correlation and UV spectrophotometry ²¹	298.15 ^{21, 55}	NRTL ²¹ UNIQUAC ⁵⁵
52.	[C ₄ mim][PF ₆] ²¹	<i>n</i> -undecane	toluene	Binodal data: Cloud point method ²¹ Tie-lines: thermodynamic equilibrium + density correlation and UV spectrophotometry ²¹	298.15 ^{21, 55-56}	NRTL ²¹ ASOG ⁵⁶ UNIQUAC ⁵⁵
53.	[C ₄ mim][PF ₆] ²¹	<i>n</i> -undecane	<i>m</i> -xylene	Binodal data: Cloud point method ²¹ Tie-lines: thermodynamic equilibrium + density correlation and UV spectrophotometry ²¹	298.15 ^{21, 55}	NRTL ²¹ UNIQUAC ⁵⁵
54.	[C ₄ mim][BF ₄] ⁵²	<i>n</i> -heptane	toluene	Tie-lines: thermodynamic equilibrium + GC + density correlation ⁵²	298.15 ⁵²	NRTL ⁵² UNIQUAC ⁵²
55.	[C ₄ mim][I ₃] ¹⁸	<i>n</i> -heptane	toluene	Tie-lines: thermodynamic equilibrium + NMR, GC and overall mass balance ¹⁸	318.2 ¹⁸	NRTL ¹⁸
56.	[C ₆ mim][NTf ₂] ²³	<i>n</i> -heptane	toluene	Tie-lines: thermodynamic equilibrium + NMR, GC and overall mass balance ²³	313.2 ²³	NRTL ²³
57.	[C ₆ mim][BF ₄] ³⁷	<i>n</i> -heptane	benzene	Binodal data: Cloud point method ³⁷ Tie-lines: thermodynamic equilibrium + density correlation ³⁷	298.2 ^{37, 55, 57}	NRTL ³⁷ UNIQUAC ⁵⁵ ASOG ⁵⁷
58.	[C ₆ mim][BF ₄] ³⁷	<i>n</i> -dodecane	benzene	Binodal data: Cloud point method ³⁷ Tie-lines: thermodynamic equilibrium + density correlation ³⁷	298.2 ^{37, 55, 57}	NRTL ³⁷ UNIQUAC ⁵⁵ ASOG ⁵⁷
59.	[C ₆ mim][BF ₄] ³⁷	<i>n</i> -hexadecane	benzene	Binodal data: Cloud point method ³⁷ Tie-lines: thermodynamic equilibrium +	298.2 ^{37, 55, 57}	NRTL ³⁷ UNIQUAC ⁵⁵

				density correlation ³⁷		ASOG ⁵⁷
60.	[C ₆ mim][PF ₆] ³⁷	<i>n</i> -heptane	benzene	Binodal data: Cloud point method ³⁷ Tie-lines: thermodynamic equilibrium + density correlation ³⁷	298.2 ^{37, 55-56}	NRTL ³⁷ UNIQUAC UNIQUAC ⁵⁵ ASOG ⁵⁶
61.	[C ₆ mim][PF ₆] ³⁷	<i>n</i> -dodecane	benzene	Binodal data: Cloud point method ³⁷ Tie-lines: thermodynamic equilibrium + density correlation ³⁷	298.2 ^{37, 55-56}	NRTL ³⁷ ASOG ⁵⁶ UNIQUAC ⁵⁵
62.	[C ₆ mim][PF ₆] ³⁷	<i>n</i> -hexadecane	benzene	Binodal data: Cloud point method ³⁷ Tie-lines: thermodynamic equilibrium + density correlation ³⁷	298.2 ^{37, 56}	NRTL ³⁷ ASOG ⁵⁶
63.	[C ₈ mim][NTf ₂] ²⁹	<i>n</i> -hexane	benzene	Tie-lines: NMR for both phases ²⁹	298.15 ²⁹	----
64.	[C ₈ mim][PF ₆] ²²	<i>n</i> -nonane	benzene	Binodal data: Cloud point method ²² Tie-lines: thermodynamic equilibrium + density correlation and UV spectrophotometry ²²	298.15 ²²	NRTL ²²
65.	[C ₈ mim][PF ₆] ²²	<i>n</i> -nonane	toluene	Binodal data: Cloud point method ²² Tie-lines: thermodynamic equilibrium + density correlation and UV spectrophotometry ²²	298.15 ²²	NRTL ²²
66.	[C ₈ mim][PF ₆] ²²	<i>n</i> -nonane	<i>m</i> -xylene	Binodal data: Cloud point method ²² Tie-lines: thermodynamic equilibrium + density correlation and UV spectrophotometry ²²	298.15 ²²	NRTL ²²
67.	[C ₈ mim][PF ₆] ²²	<i>n</i> -undecane	benzene	Binodal data: Cloud point method ²² Tie-lines: thermodynamic equilibrium + density correlation and UV spectrophotometry ²²	298.15 ²²	NRTL ²²

68.	[C ₈ mim][PF ₆] ²²	<i>n</i> -undecane	toluene	Binodal data: Cloud point method ²² Tie-lines: thermodynamic equilibrium + density correlation and UV spectrophotometry ²²	298.15 ²²	NRTL ²²
69.	[C ₈ mim][PF ₆] ²²	<i>n</i> -undecane	<i>m</i> -xylene	Binodal data: Cloud point method ²² Tie-lines: thermodynamic equilibrium + density correlation and UV spectrophotometry ²²	298.15 ²²	NRTL ²²
70.	[C ₈ mim][Cl] ³⁸	<i>n</i> -heptane	benzene	Binodal data: Cloud point method + density correlation ³⁸ Tie-lines: thermodynamic equilibrium + density correlation ³⁸	298.2 ^{38, 55}	NRTL ³⁸ UNIQUAC ⁵⁵
71.	[C ₈ mim][Cl] ³⁸	<i>n</i> -dodecane	benzene	Binodal data: Cloud point method + density correlation ³⁸ Tie-lines: thermodynamic equilibrium + density correlation ³⁸	298.2 ^{38, 55}	NRTL ³⁸ UNIQUAC ⁵⁵
72.	[C ₈ mim][Cl] ³⁸	<i>n</i> -hexadecane	benzene	Binodal data: Cloud point method + density correlation ³⁸ Tie-lines: thermodynamic equilibrium + density correlation ³⁸	298.2 ^{38, 55}	NRTL ³⁸ UNIQUAC ⁵⁵
73.	[C ₈ mim][MDEGSO ₄] ¹⁵	<i>n</i> -heptane	benzene	Binodal data: Cloud point method ¹⁵ Tie-lines: thermodynamic equilibrium + refractive index correlation ¹⁵	298.2 ¹⁵	
74.	[C ₈ mim][MDEGSO ₄] ¹⁵	<i>n</i> -hexadecane	benzene	Binodal data: Cloud point method ¹⁵ Tie-lines: thermodynamic equilibrium + refractive index correlation ¹⁵	298.2 ¹⁵	
75.	[C ₁₀ mim][NTf ₂] ²⁹	<i>n</i> -hexane	benzene	Tie-lines: thermodynamic equilibrium + NMR ²⁹	298.15 ^{29, 54}	NRTL ⁵⁴ UNIQUAC ⁵⁴
76.	[C ₁₂ mim][NTf ₂] ²⁹	<i>n</i> -hexane	benzene	Tie-lines: thermodynamic equilibrium +	298.15 ²⁹	----

				NMR ²⁹		
77.	[C ₂ C ₁ mim][NTf ₂] ⁵³	<i>n</i> -heptane	toluene	Tie-lines: thermodynamic equilibrium + NMR, GC and overall mass balance ⁵³	313.2 ⁵³	NRTL ⁵³
78.	[C ₃ C ₁ mim][NTf ₂] ⁵³	<i>n</i> -heptane	toluene	Tie-lines: thermodynamic equilibrium + NMR, GC and overall mass balance ⁵³	313.2 ⁵³	NRTL ⁵³
79.	[C ₄ C ₁ mim][NTf ₂] ⁵³	<i>n</i> -heptane	toluene	Tie-lines: thermodynamic equilibrium + NMR, GC and overall mass balance ⁵³	313.2 ⁵³	NRTL ⁵³
80.	[amim][NTf ₂] ¹²	<i>n</i> -heptane	toluene	Tie-lines: thermodynamic equilibrium + NMR, GC and overall mass balance ¹²	313.2 ¹²	NRTL ¹²
81.	[(C ₆ H ₁₃ OCH ₂) ₂ im][BF ₄] ⁵	<i>n</i> -hexane	<i>p</i> -xylene	Tie-lines: thermodynamic equilibrium + NMR ⁵	298.15 ⁵	NRTL ⁵
82.	[C ₂ py][EtSO ₄] ³⁰	<i>n</i> -hexane	benzene	Binodal data: Cloud point method ³⁰	283.15 ³⁰	NRTL ³⁰
83.				Tie-lines: thermodynamic equilibrium + density correlation ³⁰	298.15 ³⁰	
84.	[C ₂ py][EtSO ₄] ³⁰	<i>n</i> -heptane	benzene	Binodal data: Cloud point method ³⁰	283.15 ³⁰	NRTL ³⁰
85.				Tie-lines: thermodynamic equilibrium + density correlation ³⁰	298.15 ³⁰	
86.	[C ₂ py][EtSO ₄] ¹⁹	<i>n</i> -octane	benzene	Binodal data: Cloud point method ¹⁹	283.15 ¹⁹	NRTL ¹⁹
87.				Tie-lines: thermodynamic equilibrium + density correlation ¹⁹	298.15 ¹⁹	
88.	[C ₂ py][EtSO ₄] ¹⁹	<i>n</i> -nonane	benzene	Binodal data: Cloud point method ¹⁹	283.15 ¹⁹	NRTL ¹⁹
89.				Tie-lines: thermodynamic equilibrium + density correlation ¹⁹	298.15 ¹⁹	
90.	[C ₂ py][NTf ₂] ⁴	<i>n</i> -hexane	benzene	Tie-lines: thermodynamic equilibrium + NMR ⁴	313.15 ⁴	NRTL ⁴
91.	[C ₂ py][NTf ₂] ³⁵	<i>n</i> -heptane	toluene	Tie-lines: thermodynamic equilibrium + NMR, GC and overall mass balance ³⁵	313.2 ³⁵	NRTL ³⁵

92.	[C ₄ py][NTf ₂] ²⁵	<i>n</i> -heptane	toluene	Tie-lines: thermodynamic equilibrium + NMR, GC and overall mass balance ²⁵	313.2 ²⁵	NRTL ²⁵
93.	[C ₄ py][BF ₄] ¹⁶	<i>n</i> -heptane	toluene	Tie-lines: thermodynamic equilibrium + NMR, GC and overall mass balance ¹⁶	313.2 ¹⁶	NRTL ¹⁶
94.	[C ₆ py][BF ₄] ¹⁶	<i>n</i> -heptane	toluene	Tie-lines: thermodynamic equilibrium + NMR, GC and overall mass balance ¹⁶	313.2 ¹⁶	NRTL ¹⁶
95.	[1,2C ₂ mpy][NTf ₂] ³⁵	<i>n</i> -heptane	toluene	Tie-lines: thermodynamic equilibrium + NMR, GC and overall mass balance ³⁵	313.2 ³⁵	NRTL ³⁵
96.	[1,3C ₂ mpy][EtSO ₄] ¹⁰	<i>n</i> -hexane	benzene	Tie-lines: thermodynamic equilibrium + density and refractive index correlations ¹⁰	283.15 ¹⁰	NRTL ¹⁰
97.					293.15 ¹⁰	
98.					298.15 ¹⁰	
99.					303.15 ¹⁰	
100.	[1,3C ₂ mpy][EtSO ₄] ²⁰	<i>n</i> -hexane	toluene	Binodal data: Cloud point method Tie-lines: thermodynamic equilibrium + density correlation ²⁰	298.15 ²⁰	NRTL ²⁰
101.	[1,3C ₂ mpy][EtSO ₄] ²⁰	<i>n</i> -hexane	ethylbenzene	Binodal data: Cloud point method Tie-lines: thermodynamic equilibrium + density correlation ²⁰	298.15 ²⁰	NRTL ²⁰
102.	[1,3C ₂ mpy][EtSO ₄] ²	<i>n</i> -hexane	<i>o</i> -xylene	Binodal data: Cloud point method Tie-lines: thermodynamic equilibrium + density correlation ²	298.15 ²	NRTL ²
103.	[1,3C ₂ mpy][EtSO ₄] ²	<i>n</i> -hexane	<i>m</i> -xylene	Binodal data: Cloud point method Tie-lines: thermodynamic equilibrium + density correlation ²	298.15 ²	NRTL ²
104.	[1,3C ₂ mpy][EtSO ₄] ²	<i>n</i> -hexane	<i>p</i> -xylene	Binodal data: Cloud point method Tie-lines: thermodynamic equilibrium + density correlation ²	298.15 ²	NRTL ²

105	[1,3C ₂ mpy][EtSO ₄] ^{10, 46}	<i>n</i> -heptane	benzene	Tie-lines: thermodynamic equilibrium + density and refractive index correlations ¹⁰ Tie-lines: thermodynamic equilibrium + NMR ⁷⁷	283.15 ¹⁰	NRTL ¹⁰
106					298.15 ^{10, 46}	
107	[1,3C ₂ mpy][EtSO ₄] ^{34, 46}	<i>n</i> -heptane	toluene	Binodal data: Cloud point method Tie-lines: thermodynamic equilibrium + density correlation ³⁴ Tie-lines: thermodynamic equilibrium + NMR ⁷⁷	298.15 ^{34, 46}	NRTL ³⁴
108	[1,3C ₂ mpy][EtSO ₄] ³¹	<i>n</i> -octane	benzene	Binodal data: Cloud point method ³¹ Tie-lines: thermodynamic equilibrium + density correlation ³¹	283.15 ³¹	NRTL ³¹
109					298.15 ³¹	
110	[1,3C ₂ mpy][EtSO ₄] ³⁴	<i>n</i> -octane	toluene	Binodal data: Cloud point method Tie-lines: thermodynamic equilibrium + density correlation ³⁴	298.15 ³⁴	NRTL ³⁴
111	[1,3C ₂ mpy][EtSO ₄] ³¹	<i>n</i> -nonane	benzene	Binodal data: Cloud point method ³¹ Tie-lines: thermodynamic equilibrium + density correlation ³¹	283.15 ³¹	NRTL ³¹
112					298.15 ³¹	
113	[1,3C ₂ mpy][EtSO ₄] ³⁴	<i>n</i> -nonane	toluene	Binodal data: Cloud point method Tie-lines: thermodynamic equilibrium + density correlation ³⁴	298.15 ³⁴	NRTL ³⁴
114	[1,3C ₂ mpy][NTf ₂] ³⁵	<i>n</i> -heptane	toluene	Tie-lines: thermodynamic equilibrium + NMR, GC and overall mass balance ³⁵	313.2 ³⁵	NRTL ³⁵
115	[1,4C ₂ mpy][NTf ₂] ³⁵	<i>n</i> -heptane	toluene	Tie-lines: thermodynamic equilibrium + NMR, GC and overall mass balance ³⁵	313.2 ³⁵	NRTL ³⁵
116	[1,3C ₁ C ₃ py][NTf ₂] ¹²	<i>n</i> -heptane	toluene	Tie-lines: thermodynamic equilibrium + NMR, GC and overall mass balance ¹²	313.2 ¹²	NRTL ¹²

117	[1,2C ₄ mpy][NTf ₂] ²⁵	<i>n</i> -heptane	toluene	Tie-lines: thermodynamic equilibrium + NMR, GC and overall mass balance ²⁵	313.2 ²⁵	NRTL ²⁵
118	[1,2C ₄ mpy][BF ₄] ³³	<i>n</i> -heptane	toluene	Tie-lines: thermodynamic equilibrium + NMR, GC and overall mass balance ³³	313.2 ³³	NRTL ³³
119	[1,3C ₄ mpy][NTf ₂] ²⁵	<i>n</i> -heptane	toluene	Tie-lines: thermodynamic equilibrium + NMR, GC and overall mass balance ²⁵	313.2 ²⁵	NRTL ²⁵
120	[1,3C ₄ mpy][BF ₄] ^{33, 40}	<i>n</i> -heptane	toluene	Tie-lines: thermodynamic equilibrium + NMR, GC and overall mass balance ^{33, 40}	313.2 ^{33, 40, 55, 57}	NRTL ^{33, 40} UNIQUAC ⁵⁵ ASOG ⁵⁷
121					348.2 ^{40, 55, 57}	NRTL ^{33, 40} UNIQUAC ⁵⁵ ASOG ⁵⁷
122	[1,3C ₄ mpy][DCA] ²⁴	<i>n</i> -hexane	benzene	Tie-lines: thermodynamic equilibrium + GC and mass balance ²⁴	303.15 ²⁴	NRTL ²⁴
123					328.15 ²⁴	
124	[1,3C ₄ mpy][DCA] ²⁴	<i>n</i> -hexane	<i>p</i> -xylene	Tie-lines: thermodynamic equilibrium + GC and mass balance ²⁴	303.15 ²⁴	NRTL ²⁴
125					328.15 ²⁴	
126	[1,3C ₄ mpy][DCA] ¹⁷	<i>n</i> -heptane	toluene	Tie-lines: thermodynamic equilibrium + GC and mass balance ¹⁷	303.15 ¹⁷	NRTL ¹⁷
127					328.15 ¹⁷	
128	[1,3C ₄ mpy][TCB] ²⁶	<i>n</i> -hexane	benzene	Tie-lines: thermodynamic equilibrium + GC and overall mass balance ²⁶	303.2 ²⁶	NRTL ²⁶
129					328.2 ²⁶	
130	[1,3C ₄ mpy][TCB] ²⁶	<i>n</i> -heptane	toluene	Tie-lines: thermodynamic equilibrium + GC and overall mass balance ²⁶	303.2 ²⁶	NRTL ²⁶
131					328.2 ²⁶	
132	[1,3C ₄ mpy][TCB] ²⁶	<i>n</i> - octane	<i>p</i> -xylene	Tie-lines: thermodynamic equilibrium + GC and overall mass balance ²⁶	303.2 ²⁶	NRTL ²⁶
133					328.2 ²⁶	

134.	[1,4C ₄ mpy][NTf ₂] ²⁵	<i>n</i> -heptane	toluene	Tie-lines: thermodynamic equilibrium + NMR, GC and overall mass balance ²⁵	313.2 ²⁵	NRTL ²⁵
135.	[1,4C ₄ mpy][BF ₄] ³⁹	<i>n</i> -hexane	benzene	Tie-lines: thermodynamic equilibrium + NMR, GC and overall mass balance ³⁹	313.2 ^{39, 55, 57}	NRTL ³⁹ UNIQUAC ⁵⁵ ASOG ⁵⁷
136.					333.2 ^{39, 55, 57}	
137.	[1,4C ₄ mpy][BF ₄] ³³	<i>n</i> -heptane	toluene	Tie-lines: thermodynamic equilibrium + NMR, GC and overall mass balance ³³	313.2 ³³	NRTL ³³
138.	[1,4C ₄ mpy][BF ₄] ³⁹	<i>n</i> -octane	ethylbenzene	Tie-lines: thermodynamic equilibrium + NMR, GC and overall mass balance ³⁹	313.2 ^{39, 55, 57}	NRTL ³⁹ UNIQUAC ⁵⁵ ASOG ⁵⁷
139.					348.2 ^{39, 55, 57}	
140.	[1,4C ₄ mpy][BF ₄] ³⁹	<i>n</i> -octane	<i>m</i> -xylene	Tie-lines: thermodynamic equilibrium + NMR, GC and overall mass balance ³⁹	313.2 ^{39, 55, 57}	NRTL ³⁹ UNIQUAC ⁵⁵ ASOG ⁵⁷
141.					348.2 ^{39, 55, 57}	
142.	[1,4C ₄ mpy][BF ₄] ⁶	<i>n</i> -dodecane	propylbenzene	Tie-lines: thermodynamic equilibrium + GC and overall mass balance ⁶	313 ⁶	NRTL ⁸⁴ UNIQUAC ⁸⁴
143.					323 ⁶	
144.					333 ⁶	
145.	[1,4C ₄ mpy][BF ₄] ⁶	<i>n</i> -dodecane	butylbenzene	Tie-lines: thermodynamic equilibrium + GC and overall mass balance ⁶	313 ⁶	NRTL ⁸⁴ UNIQUAC ⁸⁴
146.					323 ⁶	
147.					333 ⁶	
148.	[N _{1(2OH)11}][NTf ₂] ⁴	<i>n</i> -hexane	benzene	Tie-lines: thermodynamic equilibrium + NMR ⁴	313.15 ⁴	NRTL ⁴
149.	[N _{2(2OH)11}][NTf ₂] ²⁷	<i>n</i> -hexane	benzene	Tie-lines: thermodynamic equilibrium + NMR ²⁷	298.15 ²⁷	NRTL ²⁷
150.	[N _{2(2OH)11}][NTf ₂] ²⁷	<i>n</i> -hexane	<i>p</i> -xylene	Tie-lines: thermodynamic equilibrium + NMR ²⁷	298.15 ²⁷	NRTL ²⁷
151.	[N _{2(2OH)11}][NTf ₂] ²⁷	<i>n</i> -hexane	<i>m</i> -xylene	Tie-lines: thermodynamic equilibrium +	298.15 ²⁷	NRTL ²⁷

				NMR ²⁷		
152	[N _{2(2OH)11}][NTf ₂] ²⁷	<i>n</i> -octane	<i>m</i> -xylene	Tie-lines: thermodynamic equilibrium + NMR ²⁷	298.15 ²⁷	NRTL ²⁷
153	[N _{4(2OH)11}][BF ₄] ⁵	<i>n</i> -hexane	<i>p</i> -xylene	Tie-lines: thermodynamic equilibrium + NMR ⁵	298.15 ⁵	NRTL ⁵
154	[N _{6(2OH)11}][BF ₄] ⁵	<i>n</i> -hexane	<i>p</i> -xylene	Tie-lines: thermodynamic equilibrium + NMR ⁵	298.15 ⁵	NRTL ⁵
155	[P _{666 14}][NTf ₂] ³	<i>n</i> -hexane	benzene	Tie-lines: thermodynamic equilibrium + NMR ³	298.15 ³	----

Table C2 Published LLE experimental data for systems composed of cycloalkane + aromatic hydrocarbon + ionic liquid, measurement technique, and models already applied.

Nº	Ionic liquid	cycloalkane	Aromatic	Experimental procedure	Temperature / K	Model
1.	[C ₁ mim][P ₄₄] ⁴¹	cyclohexane	benzene	Tie-lines: thermodynamic equilibrium + NMR, GC and overall mass balance ⁴¹	298.2 ⁴¹	
2.	[C ₁ mim][P ₁₁] ¹⁴	cyclohexane	benzene	Tie-lines: thermodynamic equilibrium + NMR, GC and overall mass balance ¹⁴	298.2 ¹⁴	NRTL ¹⁴
3.					313.2 ¹⁴	
4.	[C ₁ mim][P ₂₂] ¹⁴	cyclohexane	benzene	Tie-lines: thermodynamic equilibrium + NMR, GC and overall mass balance ¹⁴	298.2 ¹⁴	NRTL ¹⁴
5.					313.2 ¹⁴	
6.	[C ₂ mim][EtSO ₄] ⁹	cyclohexane	benzene	Binodal data: Cloud point method ⁹ Tie-lines: thermodynamic equilibrium + density correlation ⁹	298.15 ⁹	NRTL ⁹ UNIQUAC ⁹
7.	[C ₂ mim][EtSO ₄] ¹¹	cyclohexane	ethylbenzene	Binodal data: Cloud point method ¹¹ Tie-lines: thermodynamic equilibrium + density correlation ¹¹	298.15 ¹¹	NRTL ¹¹ UNIQUAC ¹¹
8.	[C ₂ mim][EtSO ₄] ⁹	methylcyclohexane	benzene	Binodal data: Cloud point method ⁹ Tie-lines: thermodynamic equilibrium + density correlation ⁹	298.15 ⁹	NRTL ⁹ UNIQUAC ⁹
9.	[C ₂ mim][EtSO ₄] ⁹	methylcyclohexane	ethylbenzene	Binodal data: Cloud point method ⁹ Tie-lines: thermodynamic equilibrium + density correlation ⁹	298.15 ⁹	NRTL ⁹ UNIQUAC ⁹
10.	[C ₂ mim][EtSO ₄] ⁹	cyclooctane	benzene	Binodal data: Cloud point method ⁹ Tie-lines: thermodynamic equilibrium + density correlation ⁹	298.15 ⁹	NRTL ⁹ UNIQUAC ⁹
11.	[C ₂ mim][EtSO ₄]	cyclooctane	ethylbenzene	Binodal data: Cloud point method Tie-lines: thermodynamic equilibrium +	298.15	NRTL UNIQUAC

				density correlation		
12.	[C ₄ mim][MeSO ₄] ⁵⁰	cyclohexane	toluene	Binodal data: Cloud point method ⁵⁰ Tie-lines: thermodynamic equilibrium + density correlation ⁵⁰	298.15 ⁵⁰	NRTL ⁵⁰ UNIQUAC ⁵⁰
13.	[C ₄ mim][MeSO ₄] ⁵⁰	methylcyclohexane	toluene	Binodal data: Cloud point method ⁵⁰ Tie-lines: thermodynamic equilibrium + density correlation ⁵⁰	298.15 ⁵⁰	NRTL ⁵⁰ UNIQUAC ⁵⁰
14.	[C ₄ mim][MeSO ₄] ⁵⁰	cyclooctane	toluene	Binodal data: Cloud point method ⁵⁰ Tie-lines: thermodynamic equilibrium + density correlation ⁵⁰	298.15 ⁵⁰	NRTL ⁵⁰ UNIQUAC ⁵⁰
15.	[C ₄ mim][TCB] ⁴³	methylcyclohexane	toluene	Tie-lines: thermodynamic equilibrium + GC and overall mass balance ⁴³	293.15 ⁴³	NRTL ⁴³ UNIQUAC ⁴³
16.					313.15 ⁴³	
17.					333.15 ⁴³	
18.	[C ₆ mim][TCB] ⁴³	methylcyclohexane	toluene	Tie-lines: thermodynamic equilibrium + GC and overall mass balance ⁴³	293.15 ⁴³	NRTL ⁴³ UNIQUAC ⁴³
19.					313.15 ⁴³	
20.					333.15 ⁴³	
21.	[1,3C ₂ mpy][EtSO ₄] ⁴⁷	cyclohexane	benzene	Binodal data: Cloud point method ⁴⁷ Tie-lines: thermodynamic equilibrium + density correlation ⁴⁷	298.15 ⁴⁷	NRTL ⁴⁷
22.	[1,3C ₂ mpy][EtSO ₄] ⁴⁷	cyclohexane	toluene	Binodal data: Cloud point method ⁴⁷ Tie-lines: thermodynamic equilibrium + density correlation ⁴⁷	298.15 ⁴⁷	NRTL ⁴⁷
23.	[1,3C ₂ mpy][EtSO ₄] ⁴⁷	cyclohexane	ethylbenzene	Binodal data: Cloud point method ⁴⁷ Tie-lines: thermodynamic equilibrium + density correlation ⁴⁷	298.15 ⁴⁷	NRTL ⁴⁷
24.	[1,3C ₂ mpy][EtSO ₄] ⁴⁹	cyclooctane	benzene	Binodal data: Cloud point method ⁴⁹	298.15 ⁴⁹	NRTL ⁴⁹

				Tie-lines: thermodynamic equilibrium ⁴⁹		
25.	[1,3C ₂ mpy][EtSO ₄] ⁴⁹	cyclooctane	toluene	Binodal data: Cloud point method ⁴⁹ Tie-lines: thermodynamic equilibrium ⁴⁹	298.15 ⁴⁹	NRTL ⁴⁹
26.	[1,3C ₂ mpy][EtSO ₄] ⁴⁹	cyclooctane	ethylbenzene	Binodal data: Cloud point method ⁴⁹ Tie-lines: thermodynamic equilibrium ⁴⁹	298.15 ⁴⁹	NRTL ⁴⁹
27.	[1,3C ₂ mpy][EtSO ₄] ⁴⁴	methylcyclohexane	benzene	Binodal data: Cloud point method ⁴⁴ Tie-lines: thermodynamic equilibrium + density correlation ⁴⁴	298.15 ⁴⁴	NRTL ⁴⁴
28.	[1,3C ₂ mpy][EtSO ₄] ⁴⁴	methylcyclohexane	toluene	Binodal data: Cloud point method ⁴⁴ Tie-lines: thermodynamic equilibrium + density correlation ⁴⁴	298.15 ⁴⁴	NRTL ⁴⁴
29.	[1,3C ₂ mpy][EtSO ₄] ⁴⁴	methylcyclohexane	ethylbenzene	Binodal data: Cloud point method ⁴⁴ Tie-lines: thermodynamic equilibrium + density correlation ⁴⁴	298.15 ⁴⁴	NRTL ⁴⁴
30.	[1,4C ₄ mpy][BF ₄] ⁴⁸	cyclohexane	benzene	Tie-lines: thermodynamic equilibrium + GC density correlation ⁴⁸	303.15 ⁴⁸	----
31.	[1,4C ₄ mpy][BF ₄] ⁴⁸	cyclohexane	toluene	Tie-lines: thermodynamic equilibrium + GC density correlation ⁴⁸	303.15 ⁴⁸	----
32.	[1,4C ₄ mpy][BF ₄] ⁴⁸	cyclohexane	ethylbenzene	Tie-lines: thermodynamic equilibrium + GC density correlation ⁴⁸	303.15 ⁴⁸	----
33.	[1,4C ₄ mpy][BF ₄] ⁴⁸	cyclohexane	o-xylene	Tie-lines: thermodynamic equilibrium + GC density correlation ⁴⁸	303.15 ⁴⁸	----

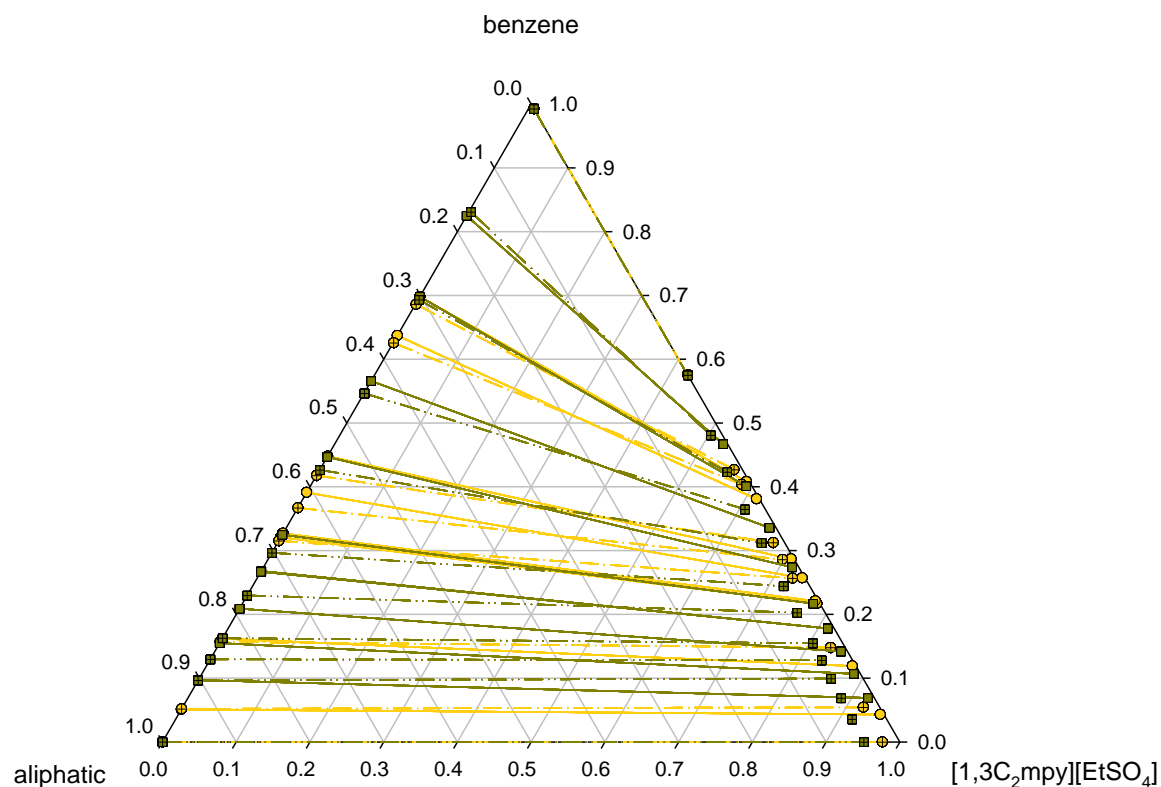
Table C3 Root mean square deviation (RMSD) between the compositions predicted by the COSMO-RS model and the experimental data for the ternary phase diagrams studied.

system aliphatic + aromatic + ionic liquid	RMSD
<i>n</i> -hexane + benzene + [C ₂ mim][EtSO ₄] at 298.15K ³²	1.4
cyclohexane + benzene + [C ₂ mim][EtSO ₄] at 298.15K ⁹	1.9
<i>n</i> -heptane + benzene + [C ₂ mim][EtSO ₄] at 298.15K ³²	1.2
<i>n</i> -octane + benzene + [C ₂ mim][EtSO ₄] at 298.15K ³²	1.5
<i>n</i> -nonane + benzene + [C ₂ mim][EtSO ₄] at 298.15K ³²	1.4
<i>n</i> -hexane + benzene + [1,3C ₂ mpy][EtSO ₄] at 293.15K ¹⁰	1.8
<i>n</i> -hexane + toluene + [1,3C ₂ mpy][EtSO ₄] at 293.15K ²⁰	3.0
<i>n</i> -hexane + ethylbenzene + [1,3C ₂ mpy][EtSO ₄] at 293.15K ²⁰	3.8
<i>n</i> -hexane + <i>o</i> -xylene + [1,3C ₂ mpy][EtSO ₄] at 293.15K ²	2.8
<i>n</i> -hexane + <i>m</i> -xylene + [1,3C ₂ mpy][EtSO ₄] at 293.15K ²	3.1
<i>n</i> -hexane + <i>p</i> -xylene + [1,3C ₂ mpy][EtSO ₄] at 293.15K ²	3.0
<i>n</i> -hexane + benzene + [1,3C ₂ mpy][EtSO ₄] at 283.15K ¹⁰	1.3
<i>n</i> -hexane + benzene + [1,3C ₂ mpy][EtSO ₄] at 298.15K ¹⁰	1.4
<i>n</i> -hexane + benzene + [1,3C ₂ mpy][EtSO ₄] at 303.15K ¹⁰	1.7
<i>n</i> -hexane + benzene + [C ₂ mim][NTf ₂] at 298.15K ³	4.6
<i>n</i> -hexane + benzene + [N ₂ (2OH) ₁₁][NTf ₂] at 298.15K ²⁷	5.1
<i>n</i> -heptane + toluene + [1,2C ₄ mpy][BF ₄] at 313.2K ³³	2.4
<i>n</i> -heptane + toluene + [1,3C ₄ mpy][BF ₄] at 313.2K ³³	4.6
<i>n</i> -heptane + toluene + [1,4C ₄ mpy][BF ₄] at 313.2K ³³	6.4
<i>n</i> -hexane + benzene + [C ₄ mim][NTf ₂] at 298.15K ²⁹	5.4
<i>n</i> -hexane + benzene + [C ₈ mim][NTf ₂] at 298.15K ²⁹	33.5
<i>n</i> -hexane + benzene + [C ₁₀ mim][NTf ₂] at 298.15K ²⁹	33.2
<i>n</i> -hexane + benzene + [C ₁₂ mim][NTf ₂] at 298.15K ²⁹	27.9
<i>n</i> -heptane + toluene + [C ₄ mim][SCN] at 303.15K ¹⁷	4.3
<i>n</i> -heptane + toluene + [C ₄ mim][DCA] at 303.15K ¹⁷	5.8
<i>n</i> -heptane + toluene + [C ₄ mim][MeSO ₄] at 313.15K ⁴⁰	1.2
<i>n</i> -heptane + toluene + [C ₆ mim][PF ₆] at 298.15K ³⁷	4.5
<i>n</i> -heptane + toluene + [C ₆ mim][BF ₄] at 298.15K ³⁷	6.7

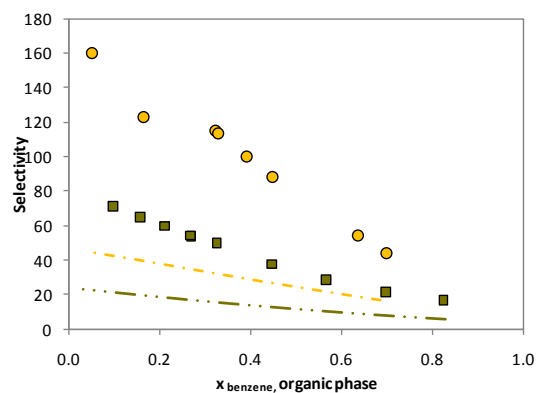
n-hexane + benzene + [C₂mim][OcSO₄] at 298.15K¹⁵

5.6

a)



b)



c)

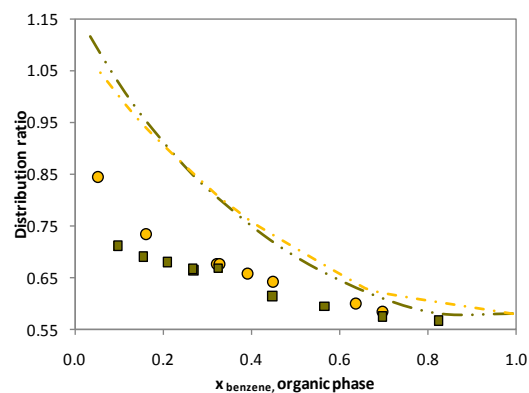
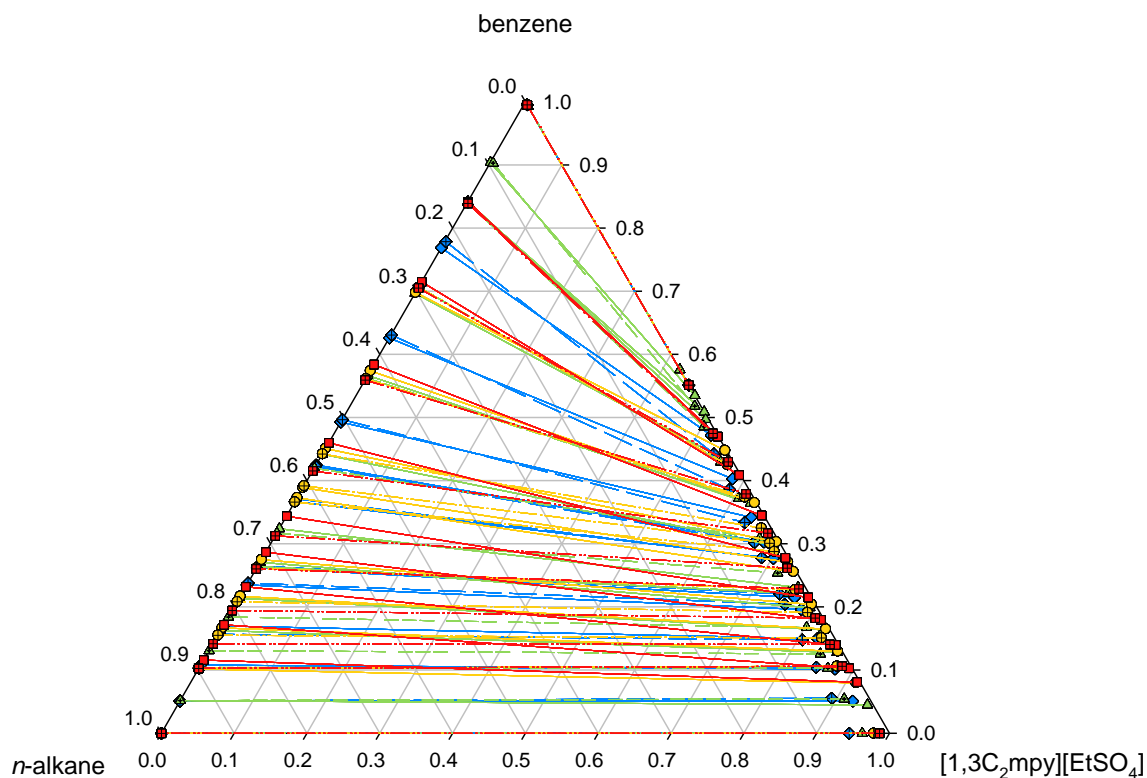
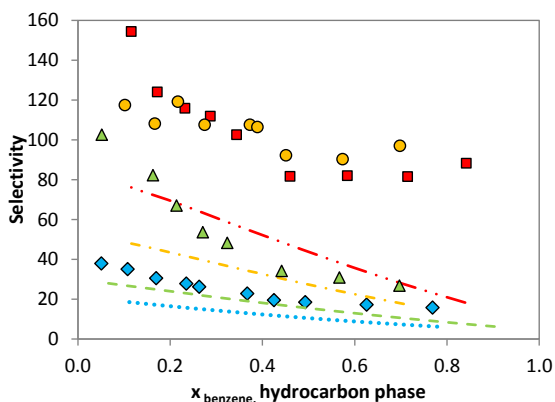


Figure C1 a) Experimental and COSMO-RS predicted tie-lines, b) selectivity and c) distribution ratio for the LLE of the ternary systems *n*-octane + benzene + [1,3C₂mpy][EtSO₄]³¹ (yellow circles, solid line and yellow dotted circles, dot dashed line), and cyclooctane + benzene + [1,3C₂mpy][EtSO₄]⁹ (dark yellow squares, solid line and dark yellow crossed squares, dot-dot dotted line) at 298.15K.

a)



b)



c)

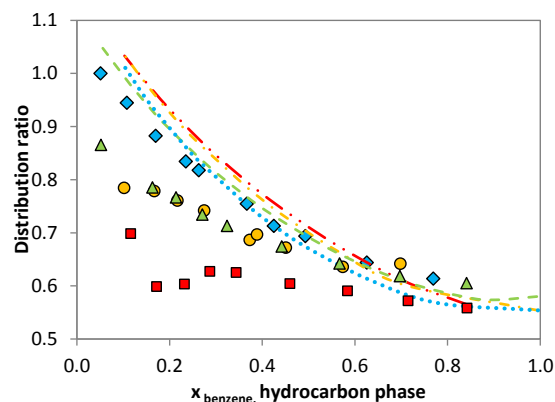
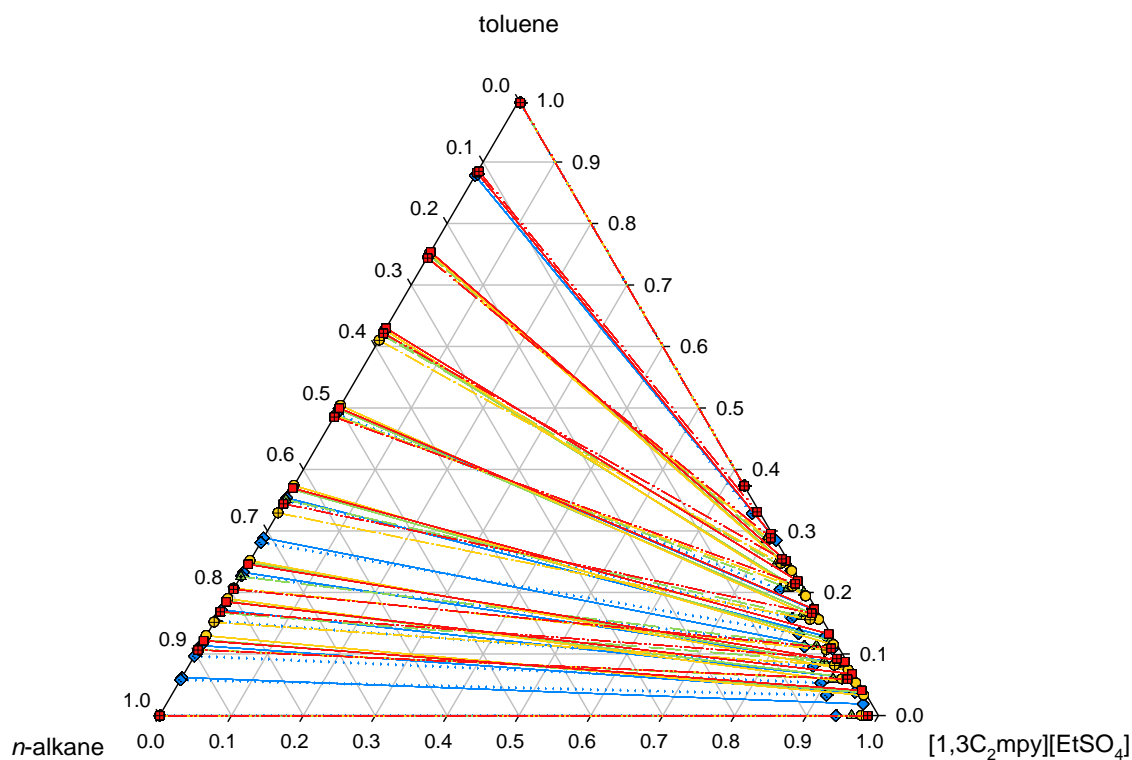
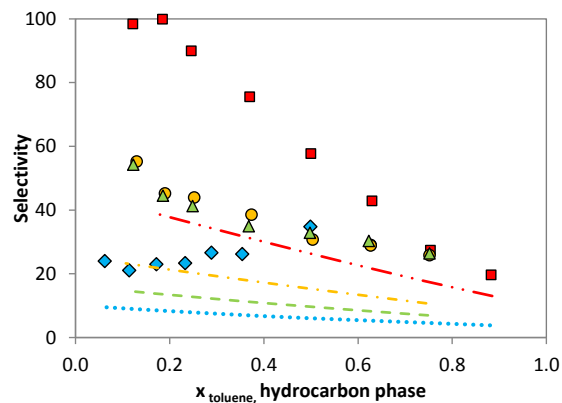


Figure C2 a) Experimental and COSMO-RS predicted tie-lines, b) selectivity and c) distribution ratio for the LLE of the ternary systems *n*-hexane + benzene + [1,3C₂mpy][EtSO₄]¹⁰ (blue diamonds, solid line and blue crossed diamonds, dotted line), *n*-heptane + benzene + [1,3C₂mpy][EtSO₄] (green triangles, solid line and green crossed triangles, dotted line), *n*-octane + benzene + [1,3C₂mpy][EtSO₄] (yellow circles, solid line and yellow crossed circles, dot dashed line) and *n*-nonane + benzene + [1,3C₂mpy][EtSO₄] (red squares, solid line and red crossed squares, dot-dot dashed line) at 298.15K.

a)



b)



c)

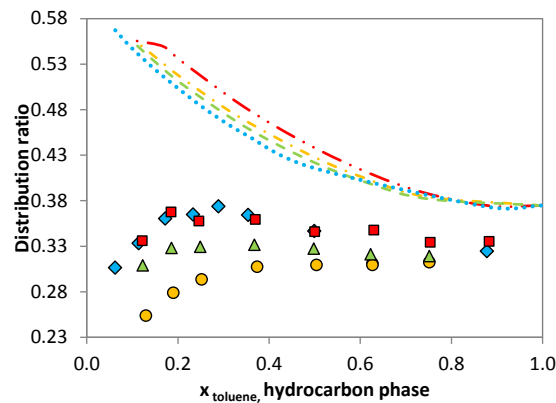
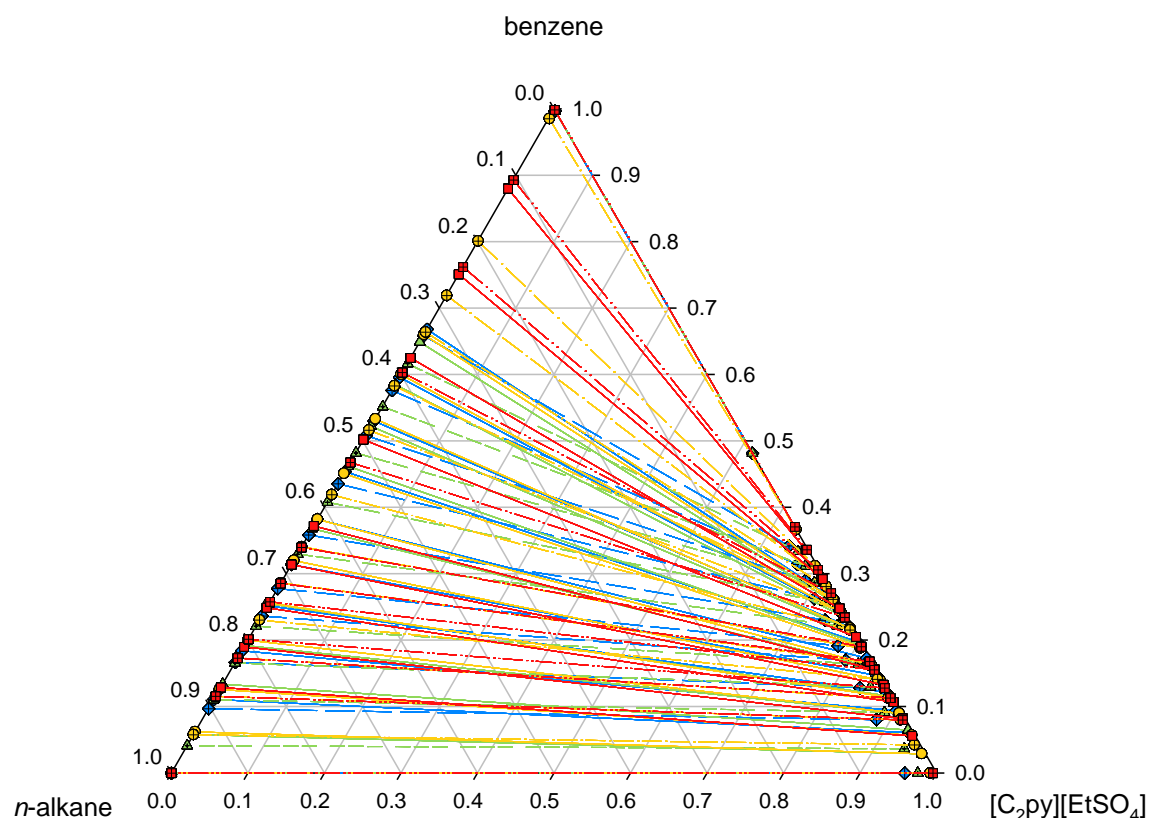
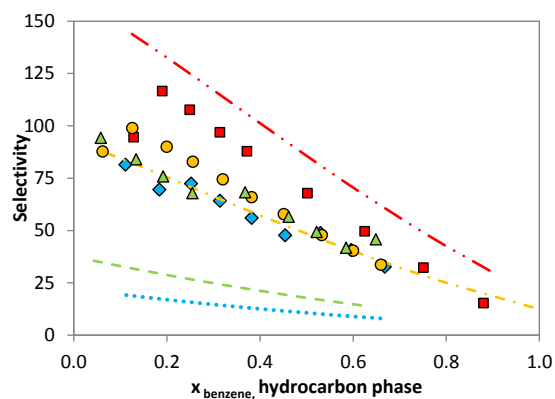


Figure C3 a) Experimental and COSMO-RS predicted tie-lines, b) selectivity and c) distribution ratio for the LLE of the ternary systems *n*-hexane + toluene + [1,3C₂mpy][EtSO₄]¹⁰ (blue diamonds, solid line and blue crossed diamonds, dotted line), *n*-heptane + toluene + [1,3C₂mpy][EtSO₄]¹⁰ (green triangles, solid line and green crossed triangles, dotted line), *n*-octane + toluene + [1,3C₂mpy][EtSO₄]¹⁰ (yellow circles, solid line and yellow crossed circles, dot dashed line), and *n*-nonane + toluene + [1,3C₂mpy][EtSO₄]¹⁰ (red squares, solid line and red crossed squares, dot-dot dashed line) at 298.15K.

a)



b)



c)

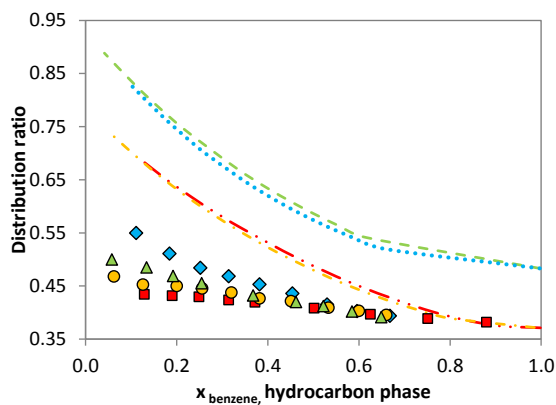
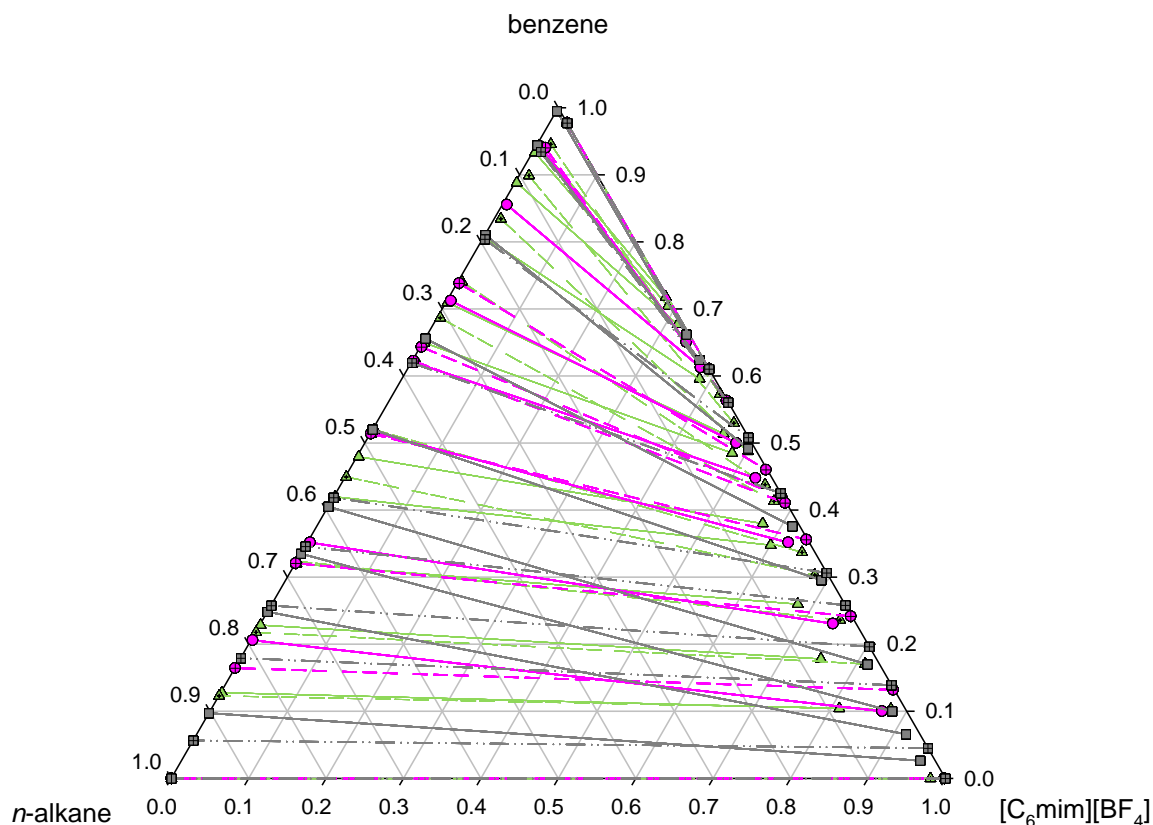
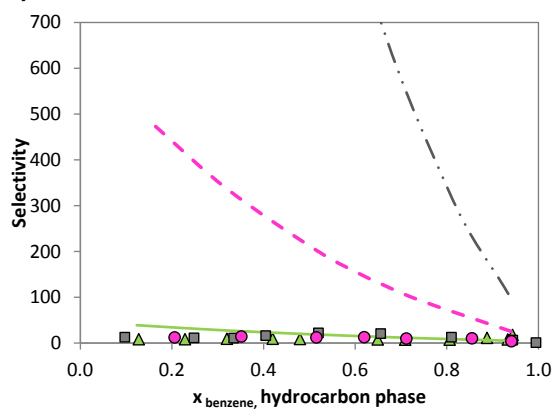


Figure C4 a) Experimental and COSMO-RS predicted tie-lines, b) selectivity and c) distribution ratio for the LLE of the ternary systems *n*-hexane + benzene + [C₂py][EtSO₄]³⁰ (blue diamonds, solid line and blue crossed diamonds, dotted line), *n*-heptane + benzene + [C₂py][EtSO₄]³⁰ (green triangles, solid line and green crossed triangles, dotted line), *n*-octane + benzene + [C₂py][EtSO₄]¹⁹ (yellow circles, solid line and yellow crossed circles, dot dashed line) and *n*-nonane + benzene + [C₂py][EtSO₄]¹⁹ (red squares, solid line and red crossed squares, dot-dot dashed line) at 283.15K.

a)



b)



c)

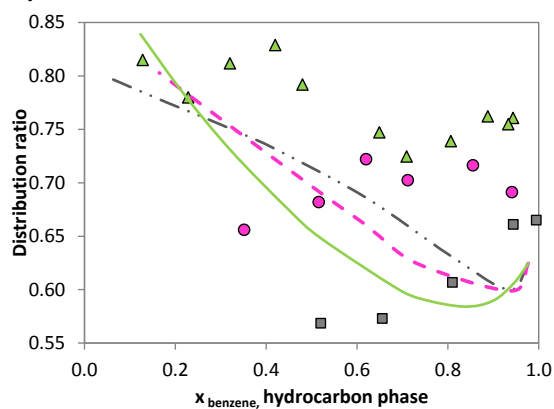
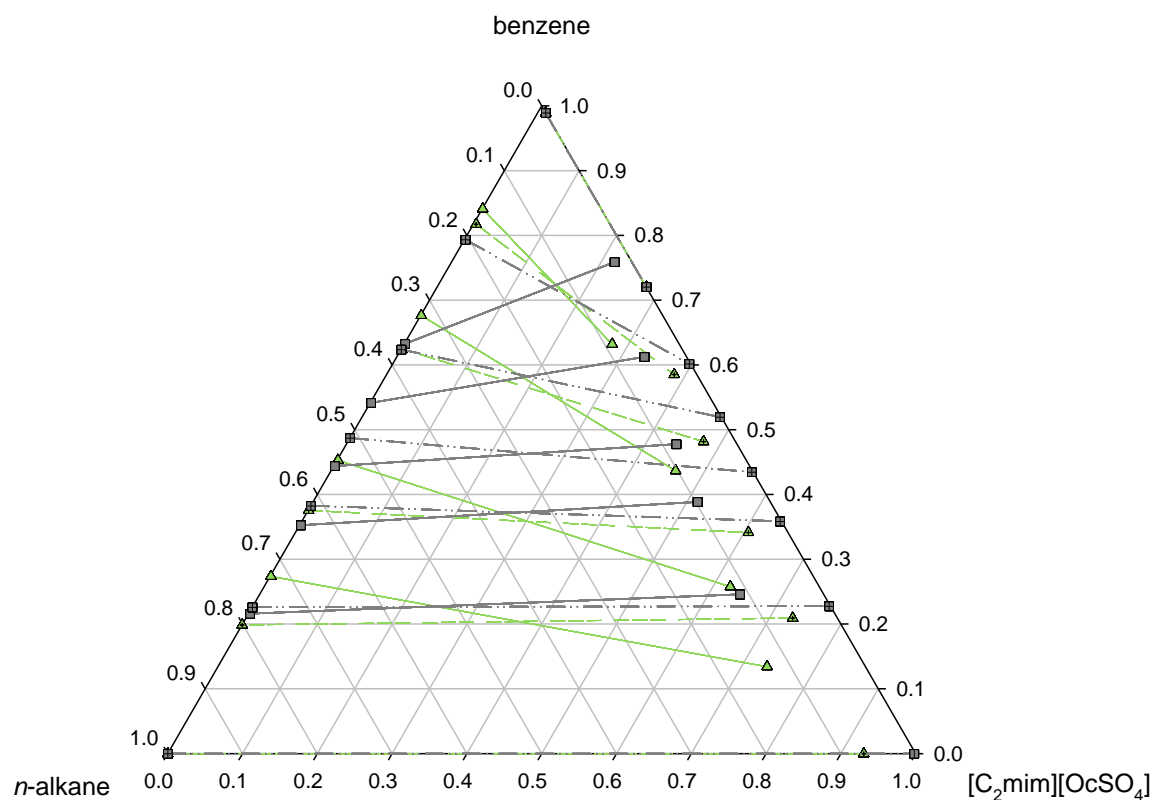
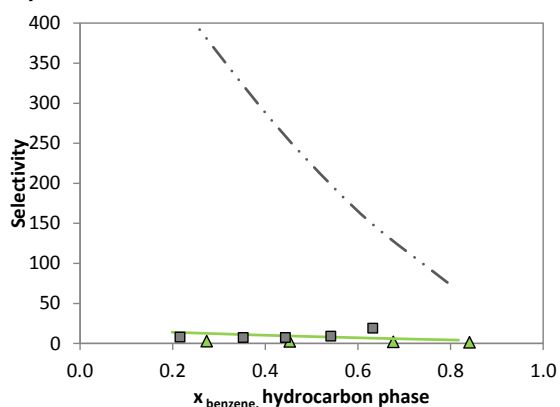


Figure C5 a) Experimental and COSMO-RS predicted tie-lines, b) selectivity and c) distribution ratio for the LLE of the ternary systems *n*-heptane + benzene + [C₆mim][BF₄]³⁷ (green triangle, solid line and green dotted triangle, dotted line), *n*-dodecane + benzene + [C₆mim][BF₄]³⁷ (pink hexagon, solid line and pink dotted hexagon, dashed line), and *n*-hexadecane + benzene + [C₆mim][BF₄]³⁷ (grey square, solid line and grey dotted square, dot-dot dashed line) at 283.15K.

a)



b)



c)

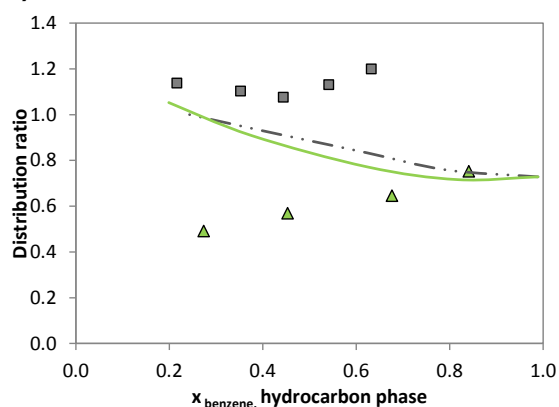
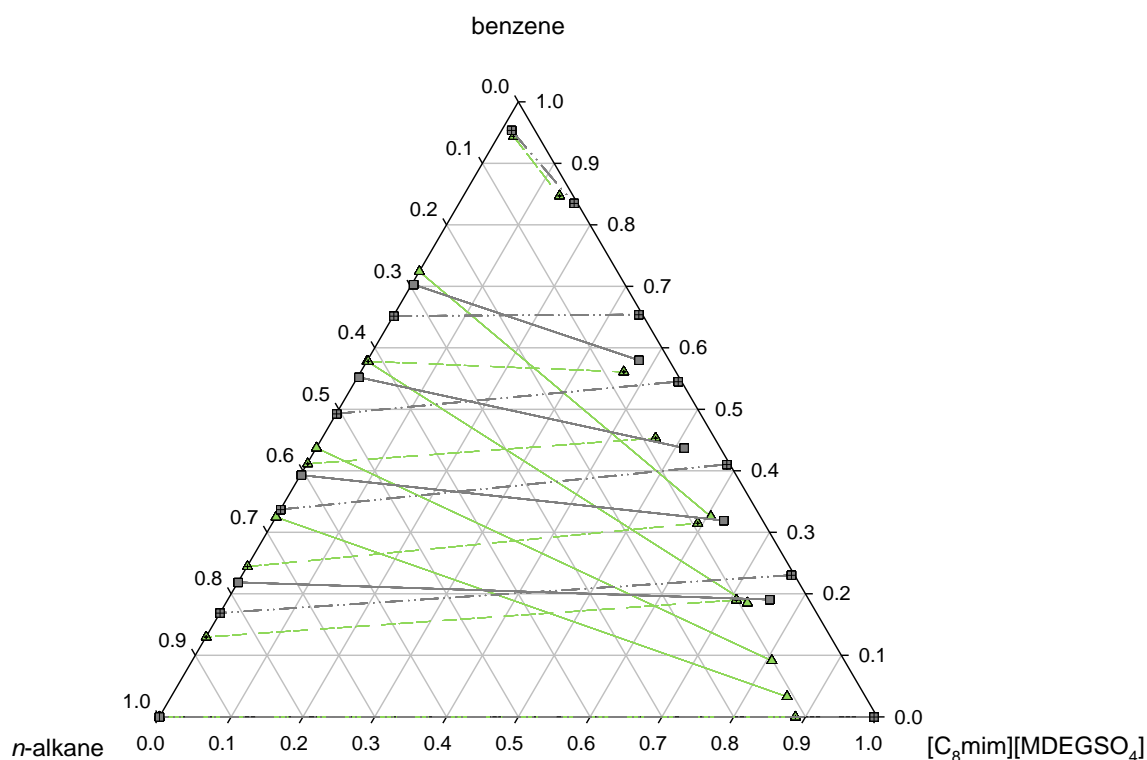
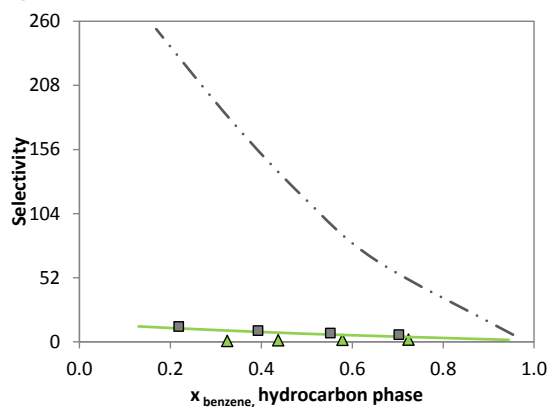


Figure C6 a) Experimental and COSMO-RS predicted tie-lines, b) selectivity and c) distribution ratio for the LLE of the ternary systems *n*-heptane + benzene + $[\text{C}_2\text{mim}][\text{OCSO}_4]^{15}$ (green triangle, solid line and green dotted triangle, dotted line), and *n*-hexadecane + benzene + $[\text{C}_2\text{mim}][\text{OCSO}_4]^{15}$ (grey square, solid line and grey dotted square, dot-dot dashed line) at 298.15K.

a)



b)



c)

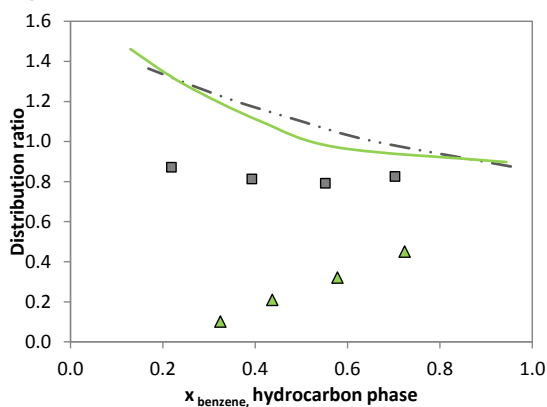
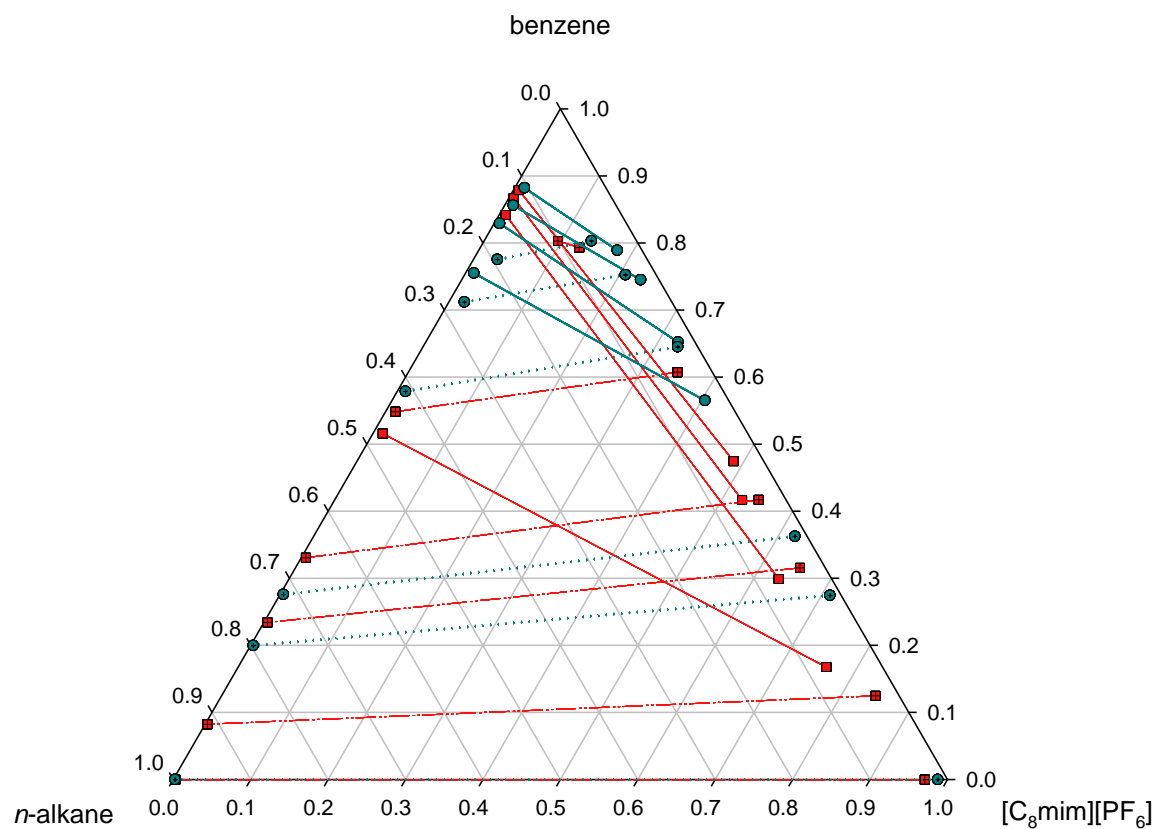
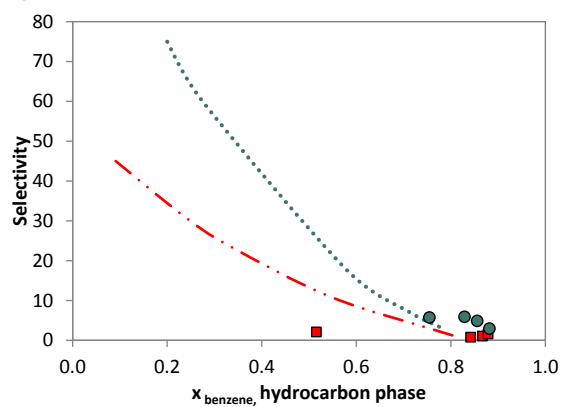


Figure C7 a) Experimental and COSMO-RS predicted tie-lines, b) selectivity and c) distribution ratio for the LLE of the ternary systems *n*-heptane + benzene + $[\text{C}_8\text{mim}][\text{MDEGSO}_4]^{15}$ (green triangle, solid line and green dotted triangle, dotted line), and *n*-hexadecane + benzene + $[\text{C}_8\text{mim}][\text{MDEGSO}_4]^{15}$ (grey square, solid line and grey dotted square, dot-dot dashed line) at 298.15K.

a)



b)



c)

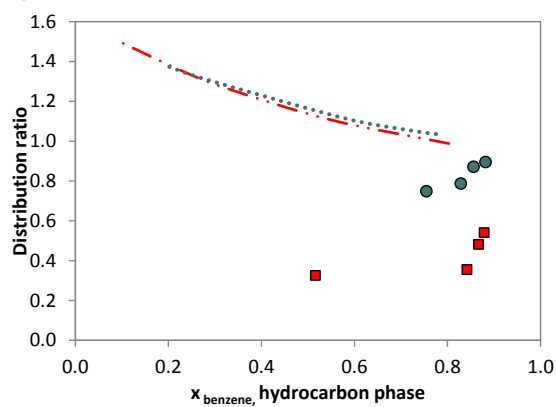
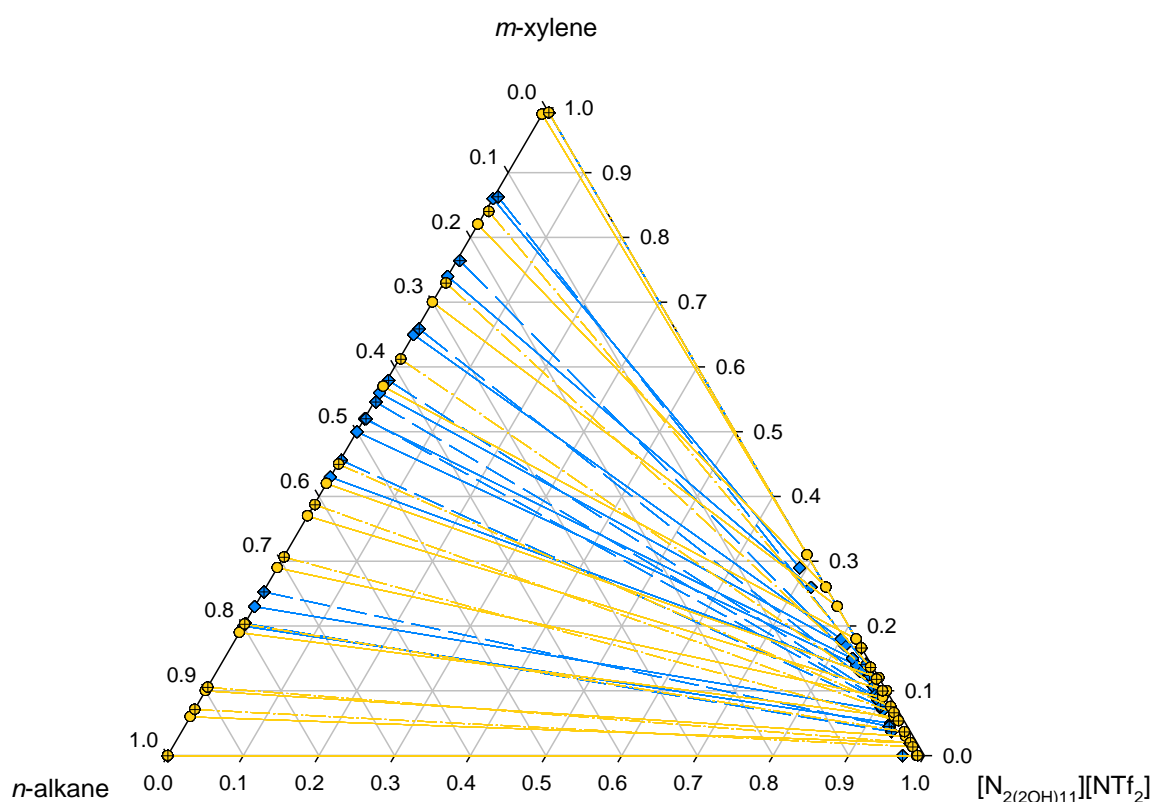
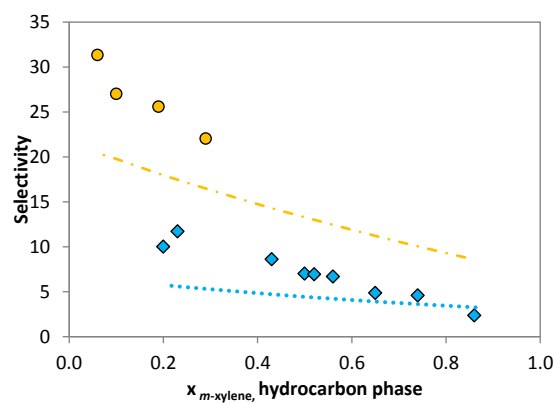


Figure C8 a) Experimental and COSMO-RS predicted tie-lines, b) selectivity and c) distribution ratio for the LLE of the ternary systems *n*-nonane + benzene + $[C_8mim][PF_6]$ ²² (red squares, solid line and red crossed squares, dot-dot dashed line) and *n*-undecane + benzene + $[C_8mim][PF_6]$ ²² (dark cyan circles, solid line and dark cyan crossed circles, dotted line) at 298.15K.

a)



b)



c)

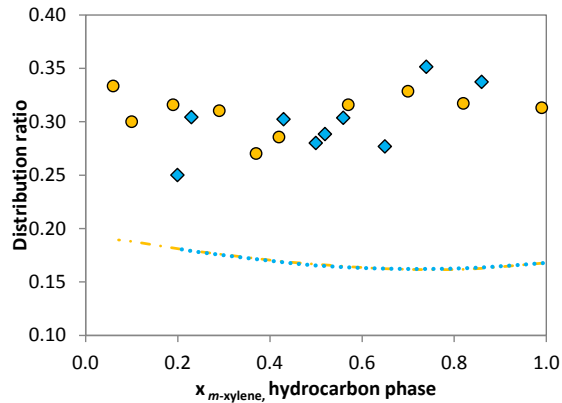
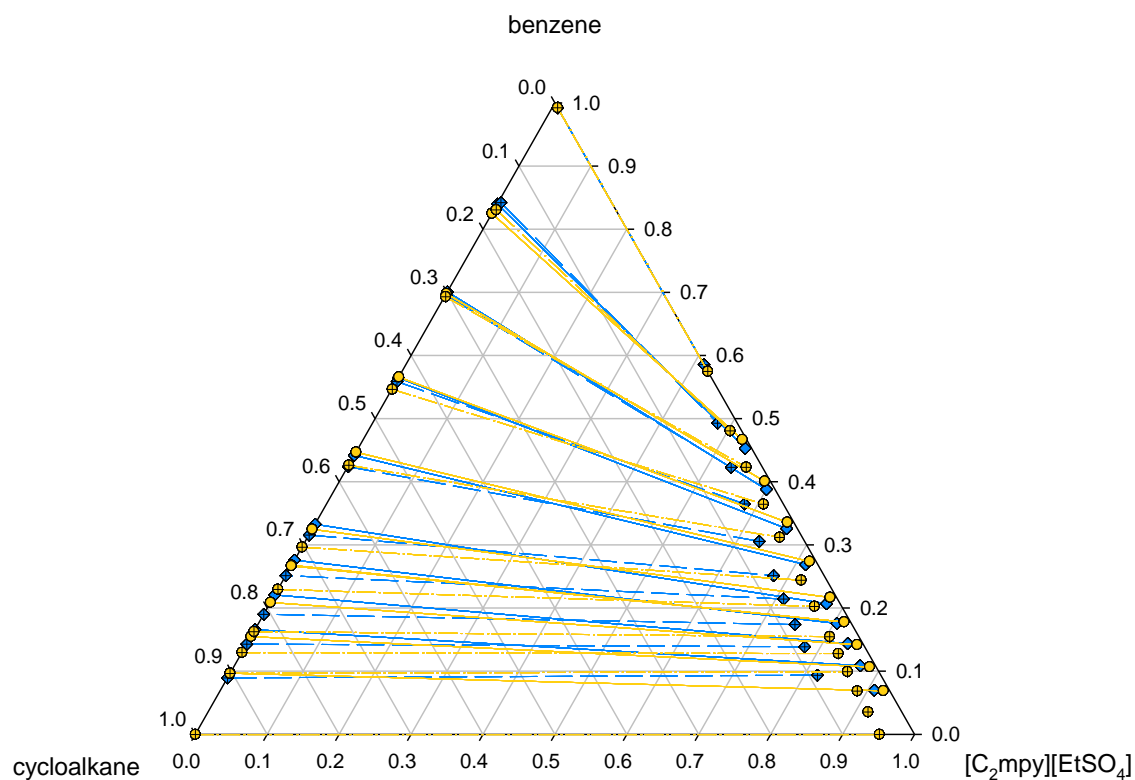
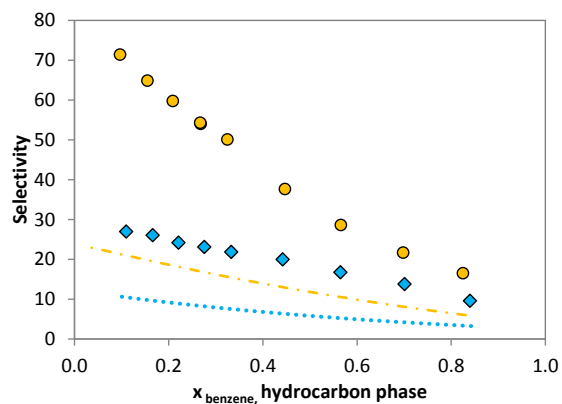


Figure C9 a) Experimental and COSMO-RS predicted tie-lines, b) selectivity and c) distribution ratio for the LLE of the ternary systems *n*-hexane + *m*-xylene + $[\text{N}_{2(2\text{OH})_{11}}][\text{NTf}_2]^{27}$ (blue diamonds, solid line and blue crossed diamonds, dotted line) and *n*-octane + *m*-xylene + $[\text{N}_{2(2\text{OH})_{11}}][\text{NTf}_2]^{27}$ (yellow circles, solid line and yellow crossed circles, dot dashed line) at 298.15K.

a)



b)



c)

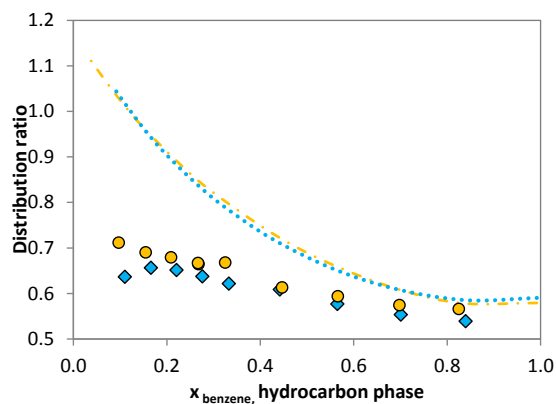
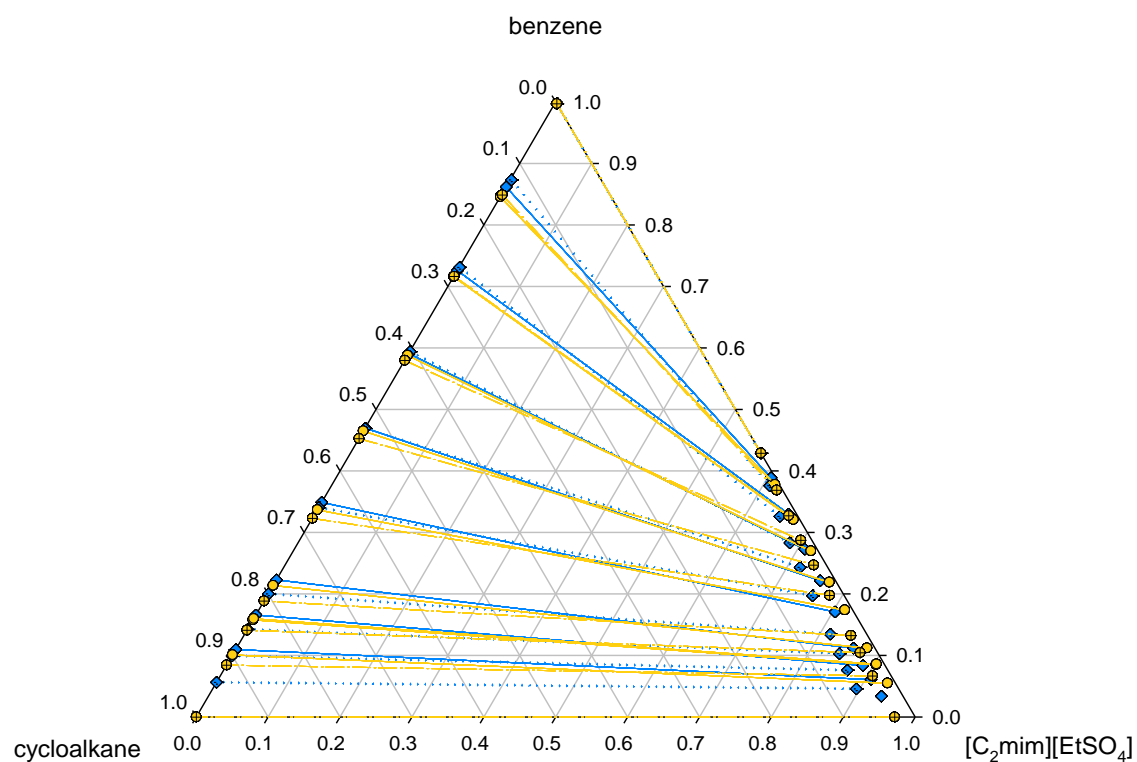
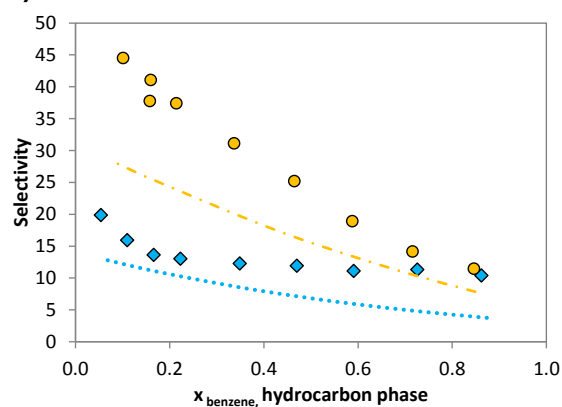


Figure C10 a) Experimental and COSMO-RS predicted tie-lines, b) selectivity and c) distribution ratio for the LLE of the ternary systems cyclohexane + benzene + $[C_2mpy][EtSO_4]$ ⁴⁷ (blue diamonds, solid line and blue crossed diamonds, dotted line) and cyclooctane + benzene + $[C_2mpy][EtSO_4]$ ⁴⁷ (yellow circles, solid line and yellow crossed circles, dot dashed line) at 298.15K.

a)



b)



c)

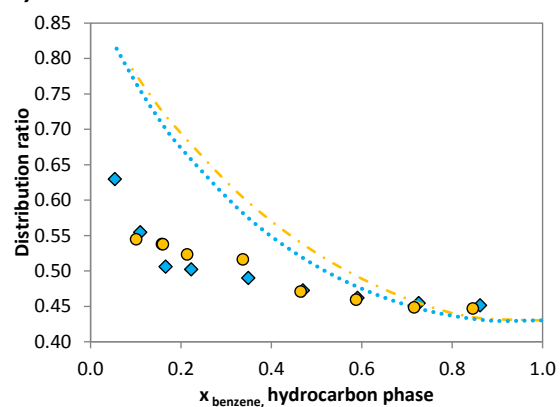
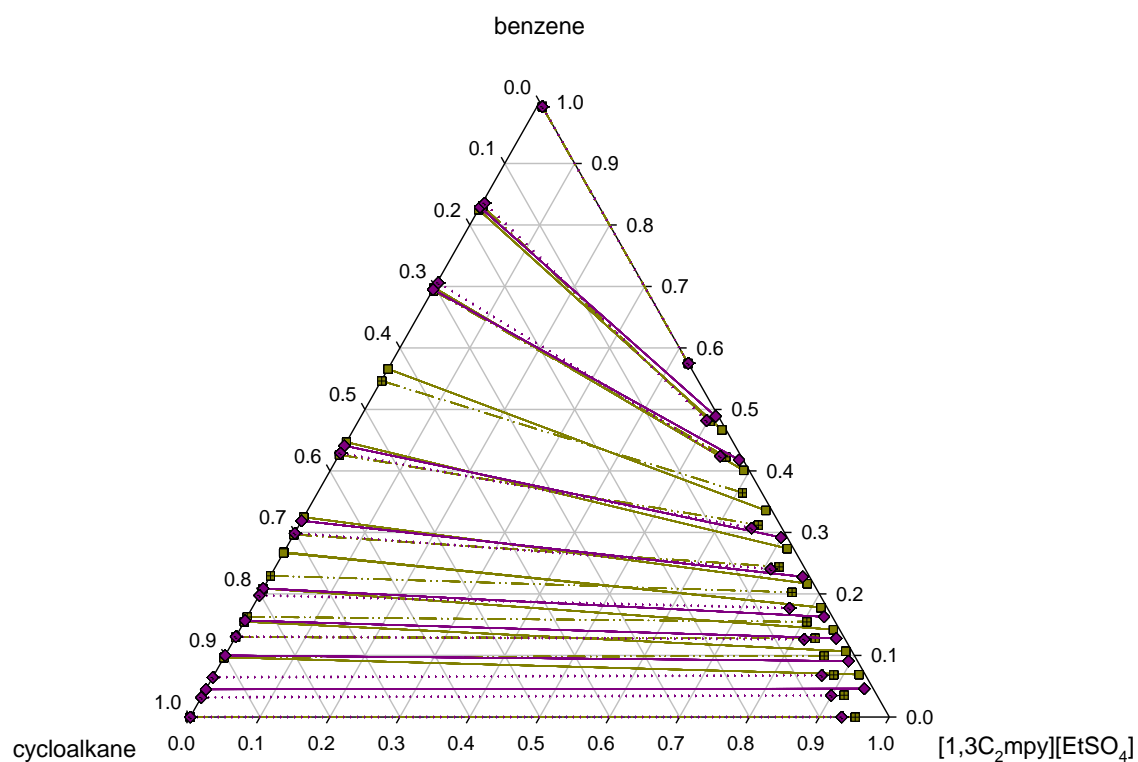
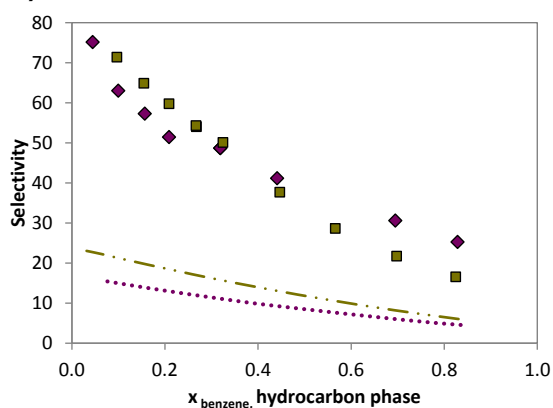


Figure C11 a) Experimental and COSMO-RS predicted tie-lines, b) selectivity and c) distribution ratio for the LLE of the ternary systems cyclohexane + benzene + $[C_2mim][EtSO_4]^9$ (blue diamonds, solid line and blue crossed diamonds, dotted line) and cyclooctane + benzene + $[C_2mim][EtSO_4]^9$ (yellow circles, solid line and yellow crossed circles, dot dashed line) at 298.15K.

a)



b)



c)

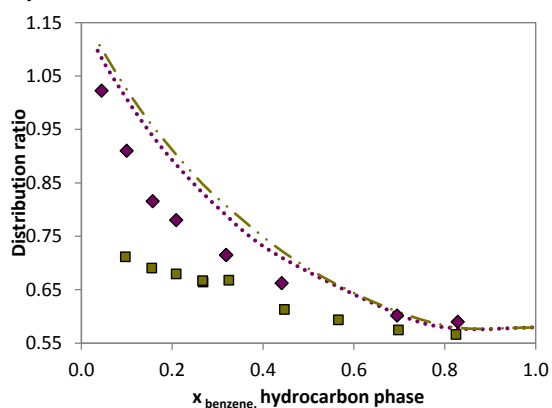
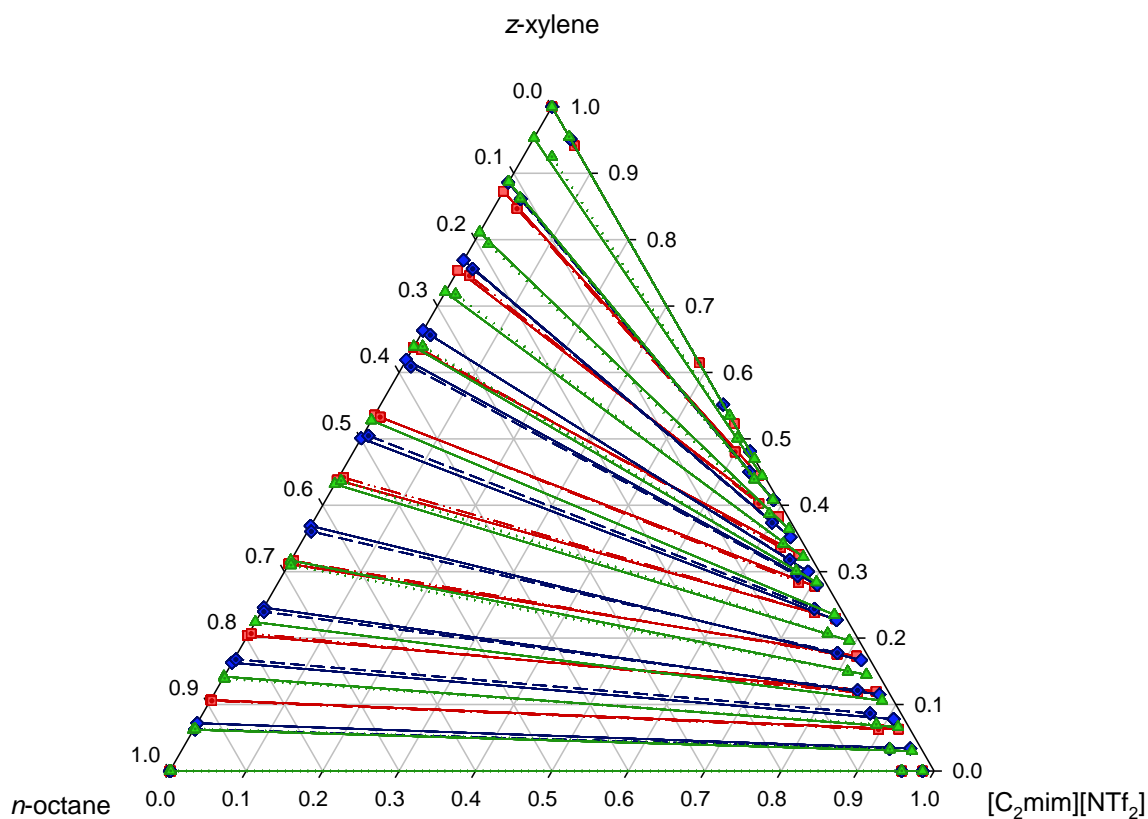
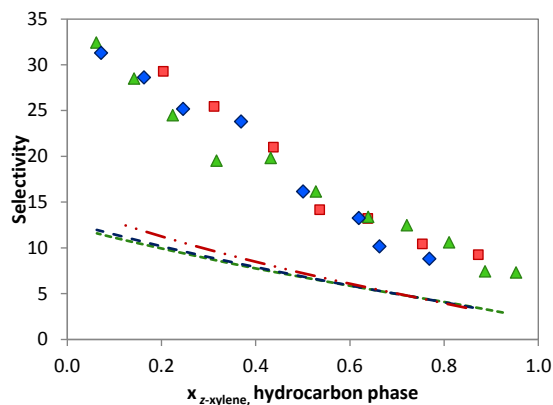


Figure C12 a) Experimental and COSMO-RS predicted tie-lines, b) selectivity and c) distribution ratio for the LLE of the ternary systems cyclooctane + benzene + [1,3C₂mpy][EtSO₄]⁴⁹ (dark yellow squares, solid line and dark yellow crossed squares, dot-dot dotted line), and methylcyclooctane + benzene + [1,3C₂mpy][EtSO₄]⁴⁴ (dark pink diamonds, solid line and dark pink crossed diamonds, dotted line), at 298.15K.

a)



b)



c)

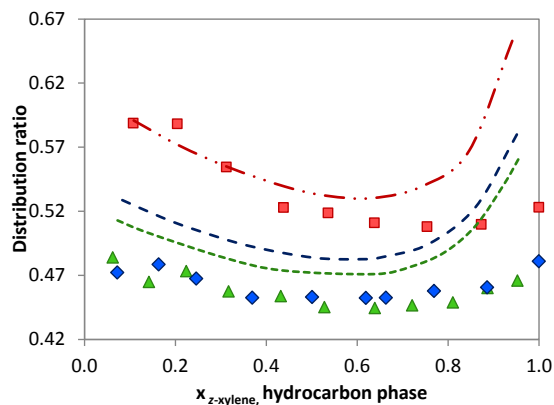
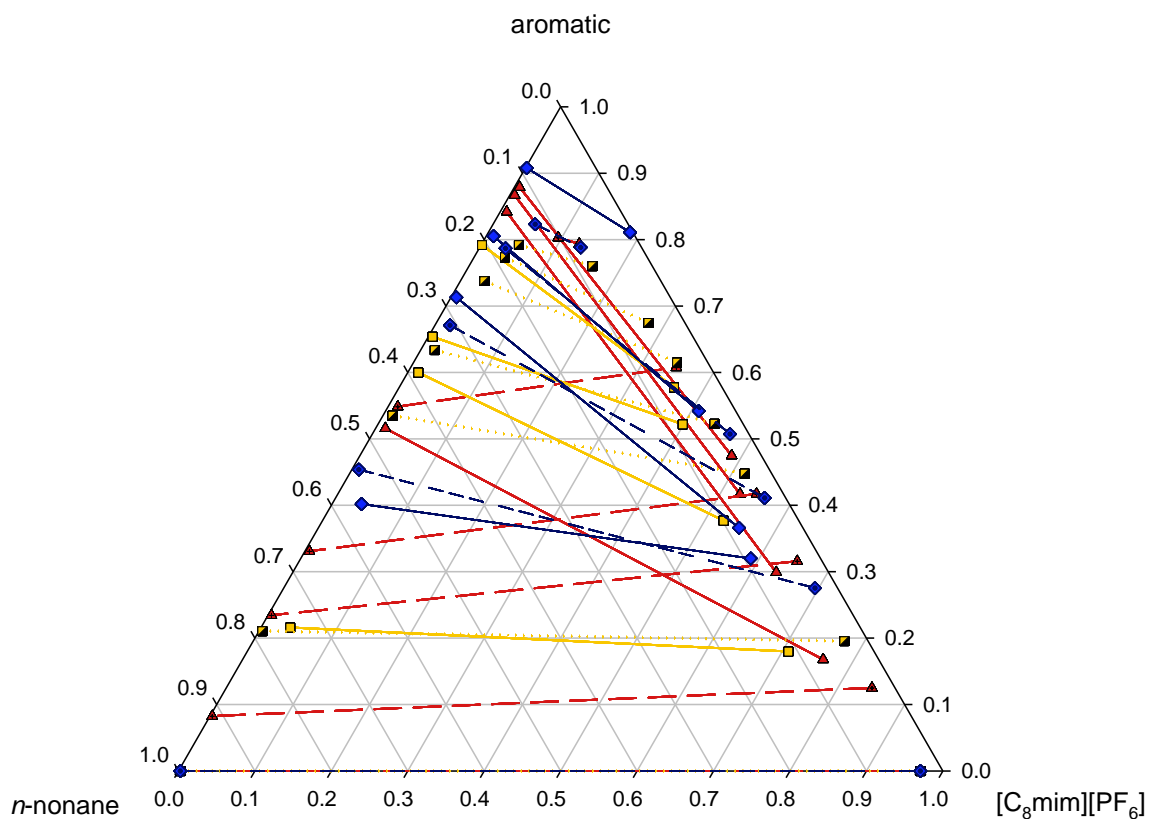
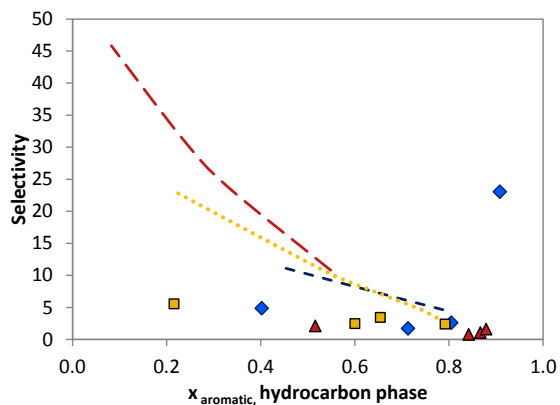


Figure C13 a) Experimental and COSMO-RS predicted tie-lines, b) selectivity and c) distribution ratio for the LLE of the ternary systems n -octane + o -xylene + $[\text{C}_2\text{mim}][\text{NTf}_2]^8$ (red squares, solid line and red dotted squares, dot-dot dashed line), n -octane + m -xylene + $[\text{C}_2\text{mim}][\text{NTf}_2]^8$ (blue diamonds, solid line and blue dotted diamonds, dotted line), and n -octane + p -xylene + $[\text{C}_2\text{mim}][\text{NTf}_2]^8$ (green triangles, solid line and green dotted triangles, dotted line) at 298.15K.

a)



b)



c)

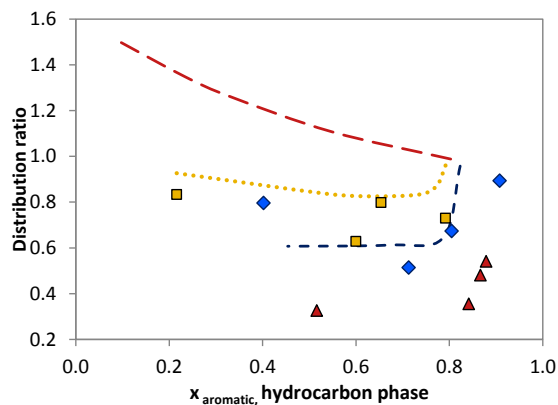
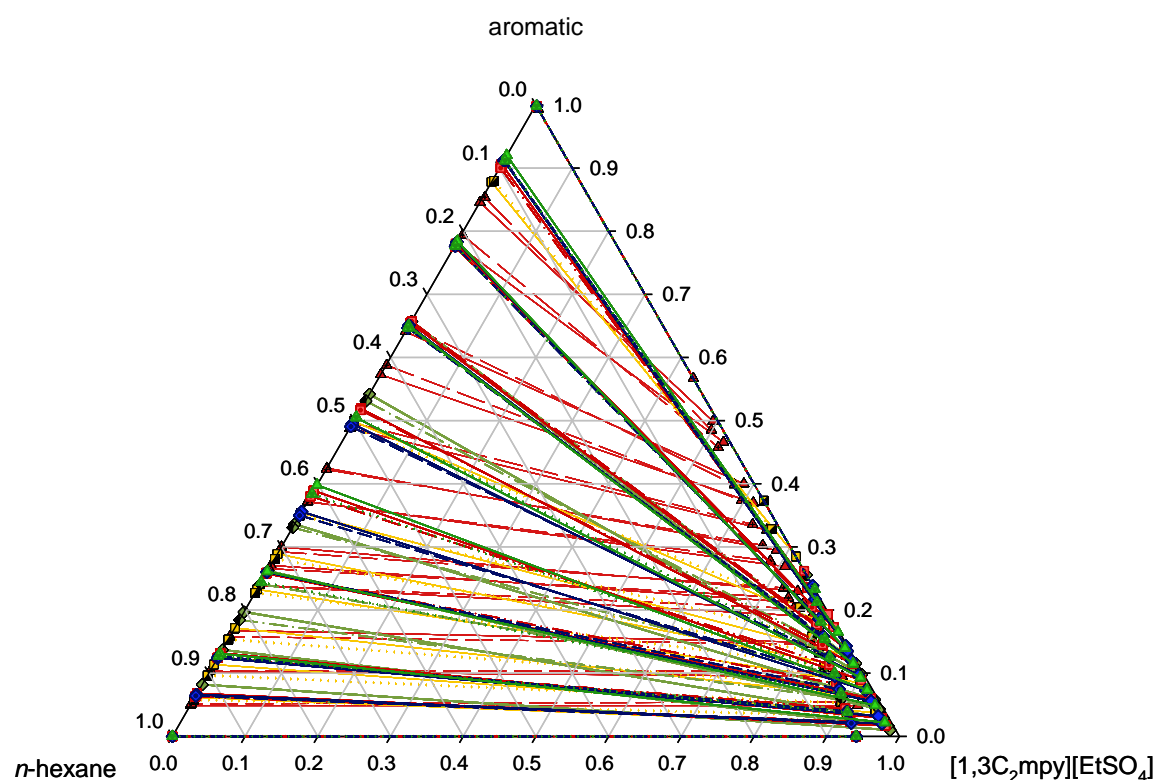
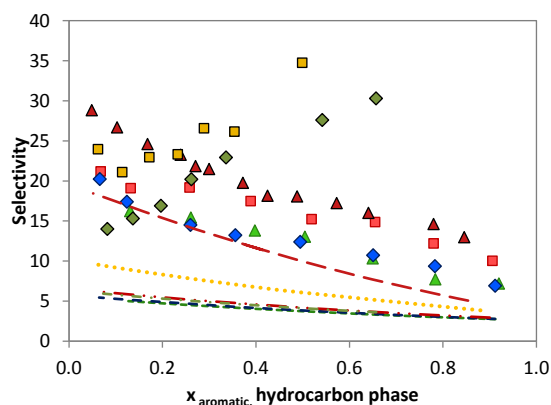


Figure C14 a) Experimental and COSMO-RS predicted tie-lines, b) selectivity and c) distribution ratio for the LLE of the ternary systems n -nonane + benzene + $[\text{C}_8\text{mim}][\text{PF}_6]^{22}$ (red triangles, solid line and red dotted triangles, long dashed line), n -nonane + toluene + $[\text{C}_8\text{mim}][\text{PF}_6]^{22}$ (yellow squares, solid line and yellow semi-filled squares, dotted line), and n -nonane + m -xylene + $[\text{C}_8\text{mim}][\text{PF}_6]^{22}$ (blue diamonds, solid line and blue dotted diamonds, short dashed line), at 298.15K.

a)



b)



c)

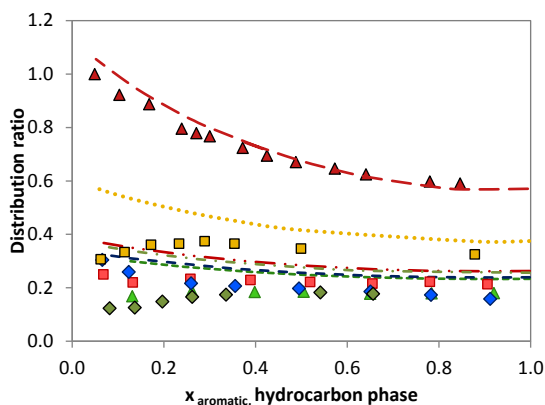
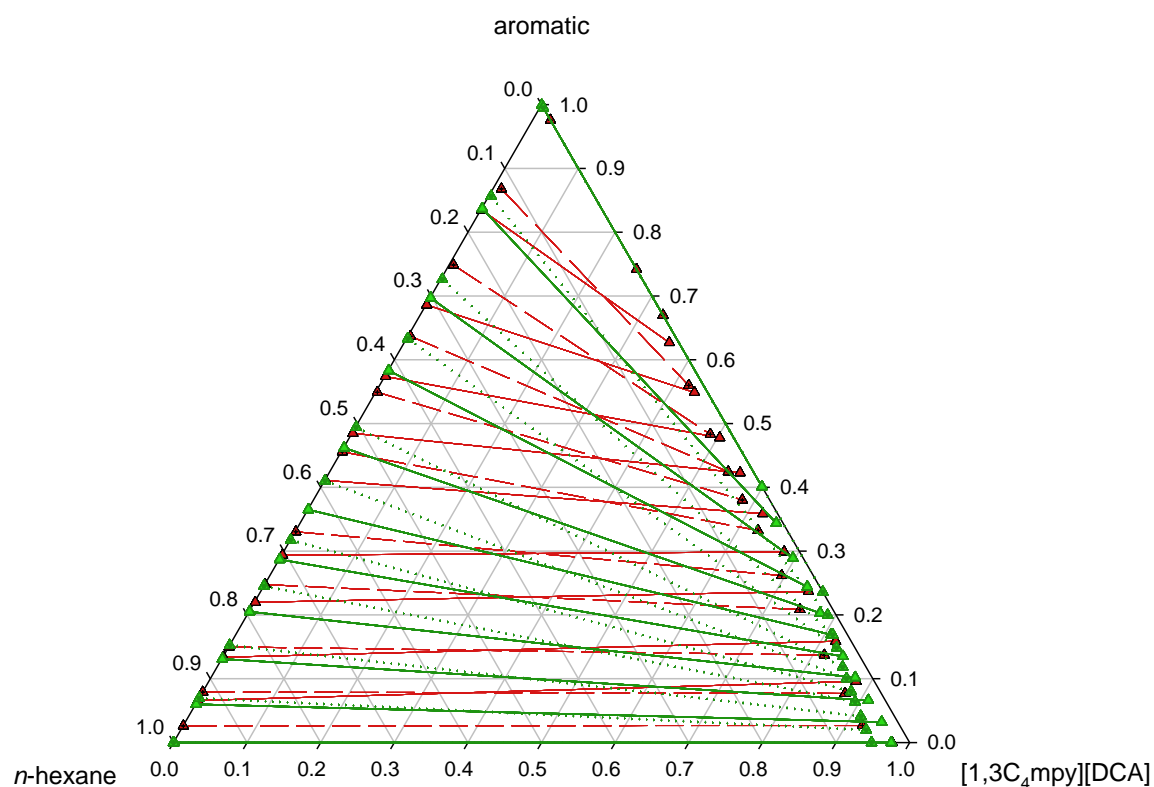
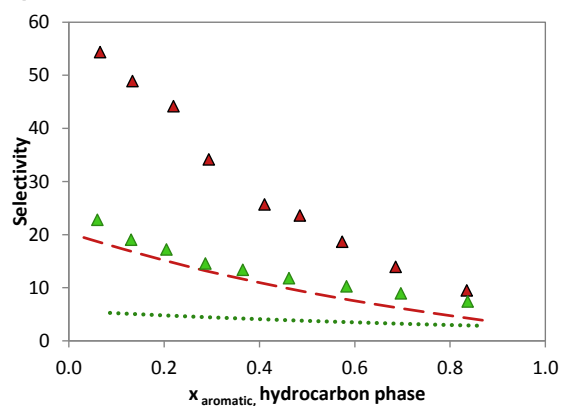


Figure C15 a) Experimental and COSMO-RS predicted tie-lines, b) selectivity and c) distribution ratio for the LLE of the ternary systems *n*-hexane + benzene + [1,3C₂mpy][EtSO₄]¹⁰ (dark red triangles, solid line and dark red dotted triangles, dashed line), *n*-hexane + toluene + [1,3C₂mpy][EtSO₄]²⁰ (yellow squares, solid line and yellow semi-filled squares, dotted line), *n*-hexane + ethylbenzene + [1,3C₂mpy][EtSO₄]²⁰ (dark green diamonds, solid line and dark green semi-filled diamonds, dot dashed line), *n*-hexane + *o*-xylene + [1,3C₂mpy][EtSO₄]² (light red squares, solid line and light red dotted squares, dot-dot dashed line), *n*-hexane + *m*-xylene + [1,3C₂mpy][EtSO₄]² (blue diamonds, solid line and blue dotted diamonds, dotted line), and *n*-hexane + *p*-xylene + [1,3C₂mpy][EtSO₄]² (light green triangles, solid line and light green dotted triangles, dotted line) at 298.15K.

a)



b)



c)

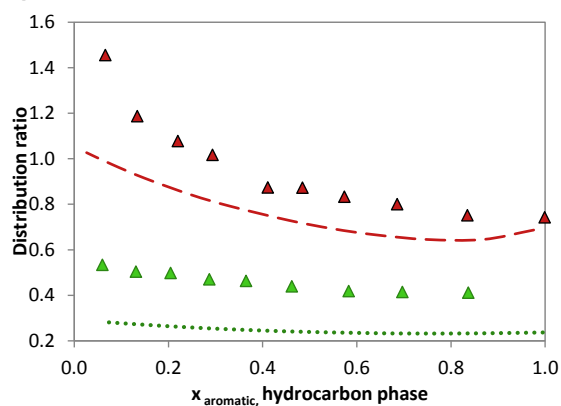
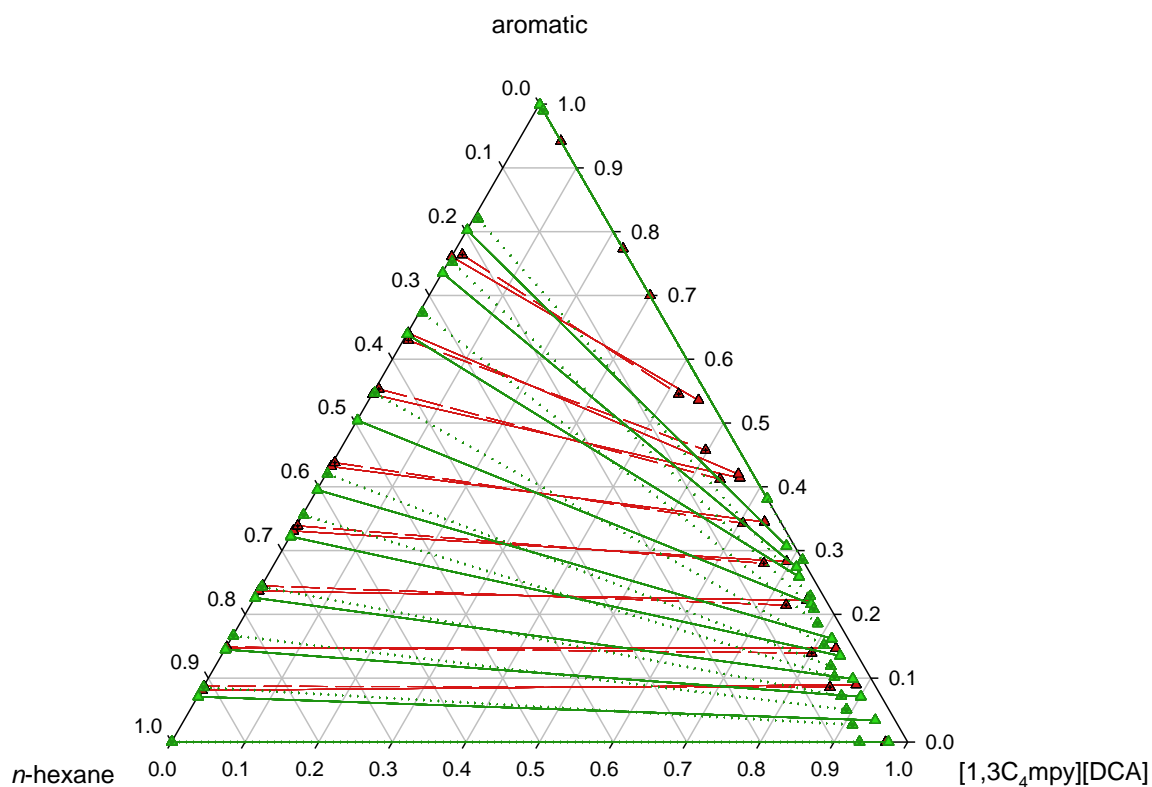
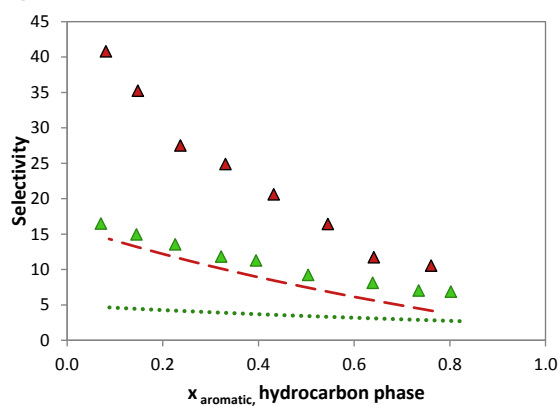


Figure C16 a) Experimental and COSMO-RS predicted tie-lines, b) selectivity and c) distribution ratio for the LLE of the ternary systems *n*-hexane + benzene + [1,3C₄mpy][DCA]²⁴ (red triangles, solid line and red dotted triangles, dashed line), and *n*-hexane + *p*-xylene + [1,3C₄mpy][DCA]²⁴ (green triangles, solid line and green dotted triangles, dotted line) at 303.15K.

a)



b)



c)

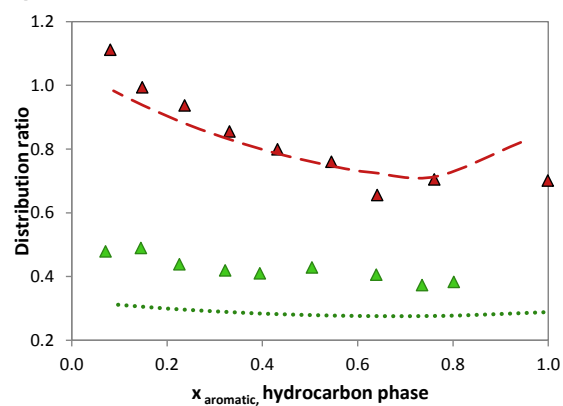
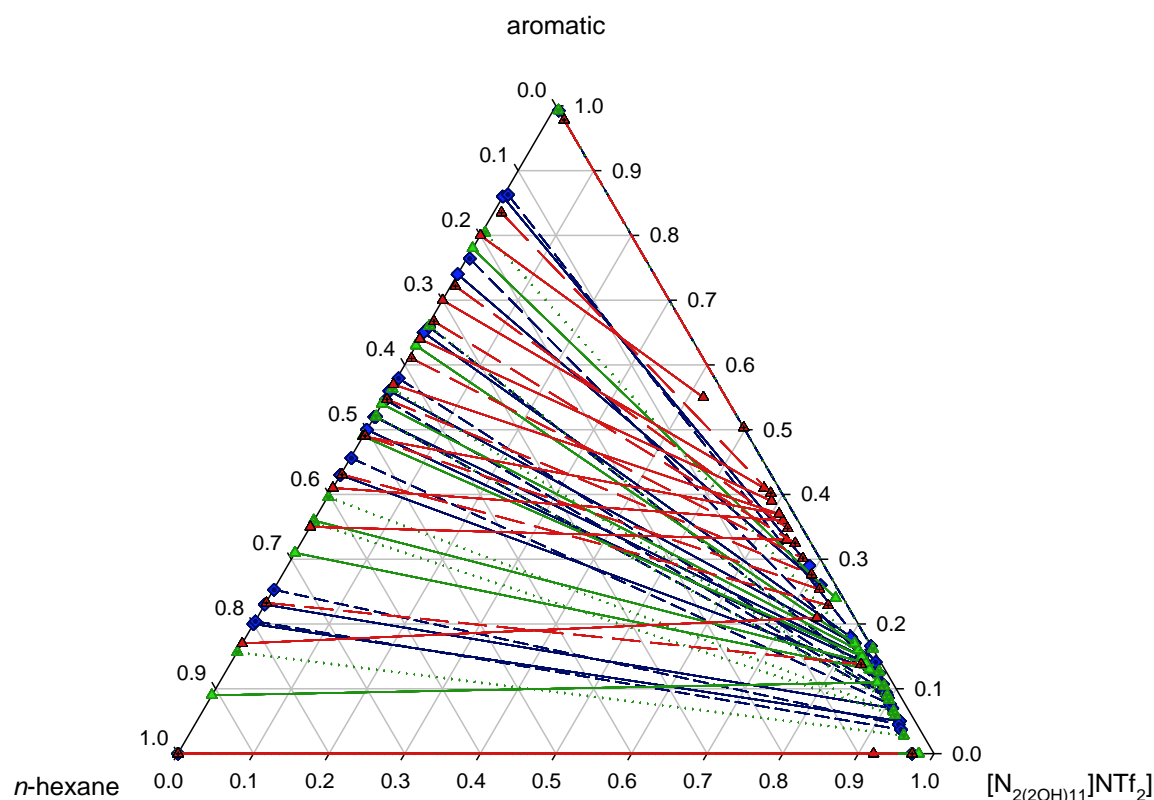
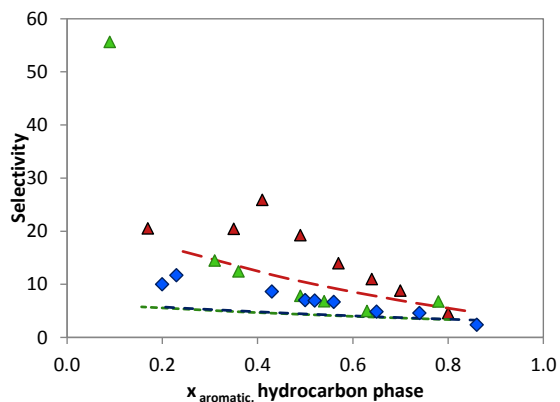


Figure C17 a) Experimental and COSMO-RS predicted tie-lines, b) selectivity and c) distribution ratio for the LLE of the ternary systems *n*-hexane + benzene + [1,3C₄mpy][DCA]²⁴ (red triangles, solid line and red dotted triangles, dashed line), and *n*-hexane + *p*-xylene + [1,3C₄mpy][DCA]²⁴ (green triangles, solid line and green dotted triangles, dotted line) at 328.15K.

a)



b)



c)

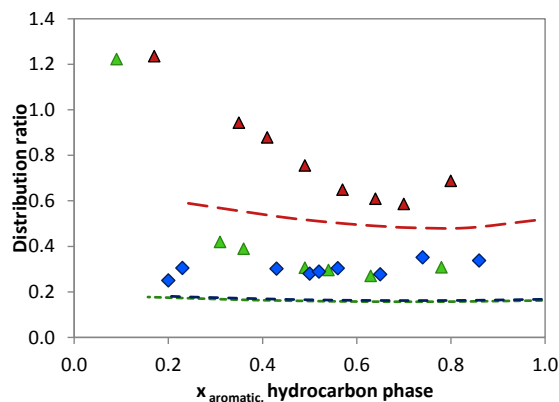
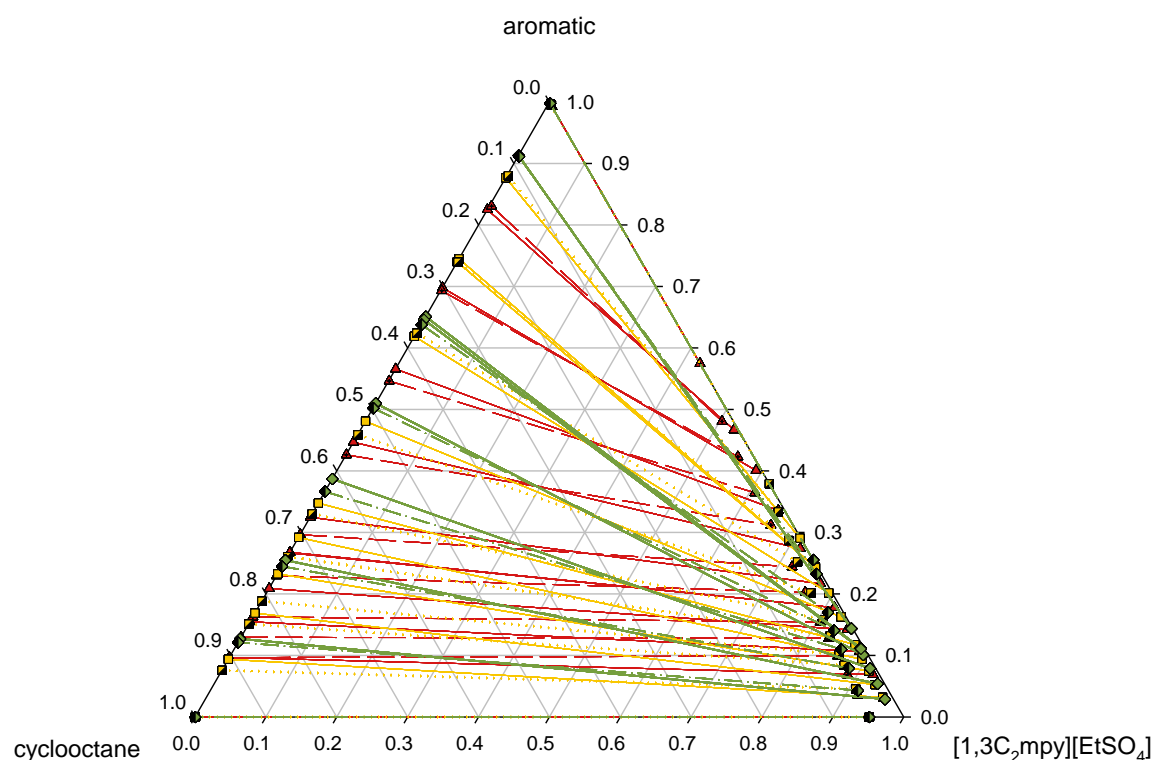
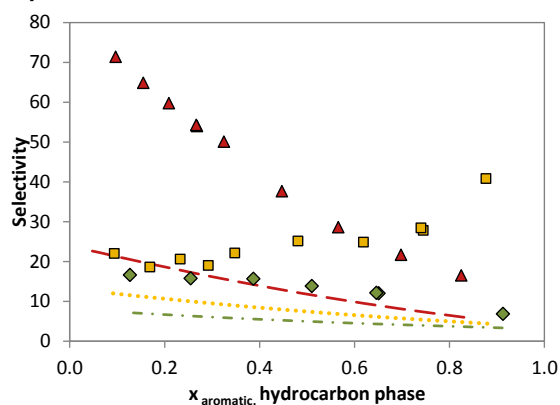


Figure C18 a) Experimental and COSMO-RS predicted tie-lines, b) selectivity and c) distribution ratio for the LLE of the ternary systems *n*-hexane + benzene + $[\text{N}_{2(2\text{OH})_{11}}][\text{NTf}_2]^{27}$ (red triangles, solid line and red dotted triangles, dashed line), *n*-hexane + *m*-xylene + $[\text{N}_{2(2\text{OH})_{11}}][\text{NTf}_2]^{27}$ (blue diamonds, solid line and blue dotted diamonds, dotted line), and *n*-hexane + *p*-xylene + $[\text{N}_{2(2\text{OH})_{11}}][\text{NTf}_2]^{27}$ (green triangles, solid line and green dotted triangles, dotted line) at 298.15K.

a)



b)



c)

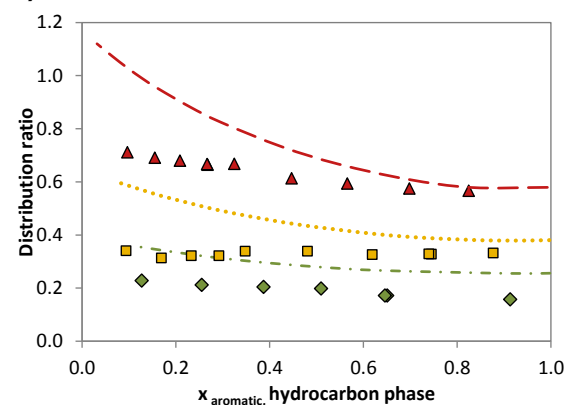
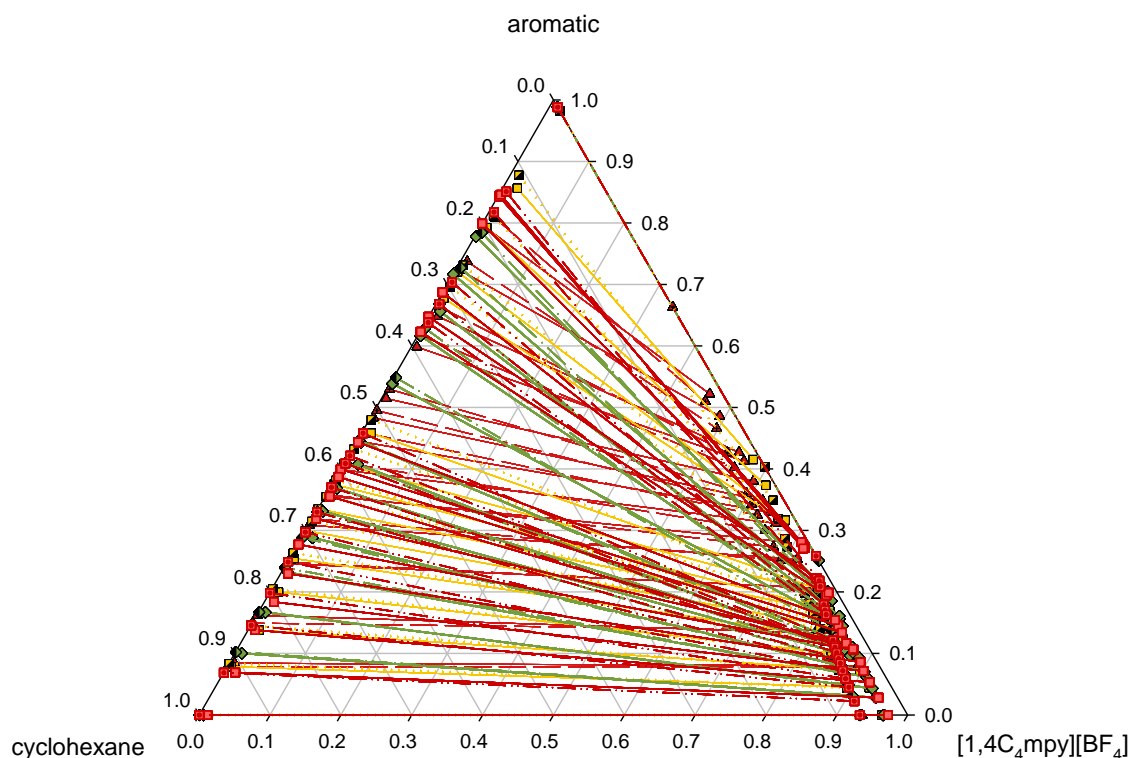
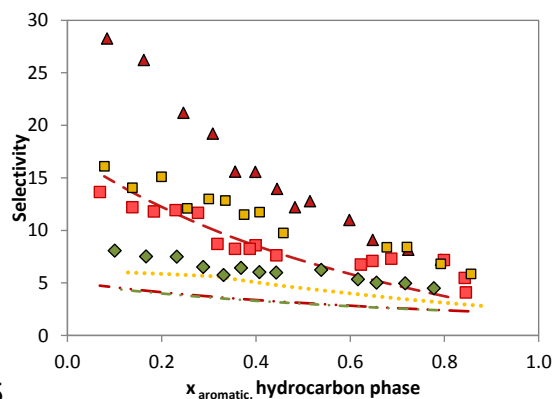


Figure C19 a) Experimental and COSMO-RS predicted tie-lines, b) selectivity and c) distribution ratio for the LLE of the ternary systems cyclooctane + benzene + $[1,3C_2mpy][EtSO_4]^{49}$ (red triangles, solid line and red dotted triangles, dashed line), cyclooctane + toluene + $[1,3C_2mpy][EtSO_4]^{49}$ (yellow squares, solid line and yellow semi-filled squares, dotted line), cyclooctane + ethylbenzene + $[1,3C_2mpy][EtSO_4]^{49}$ (green diamonds, solid line and green semi-filled diamonds, dot dashed line), at 298.15K.

a)



b)



5

c)

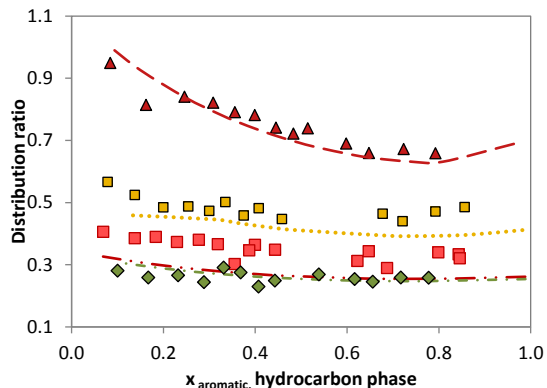
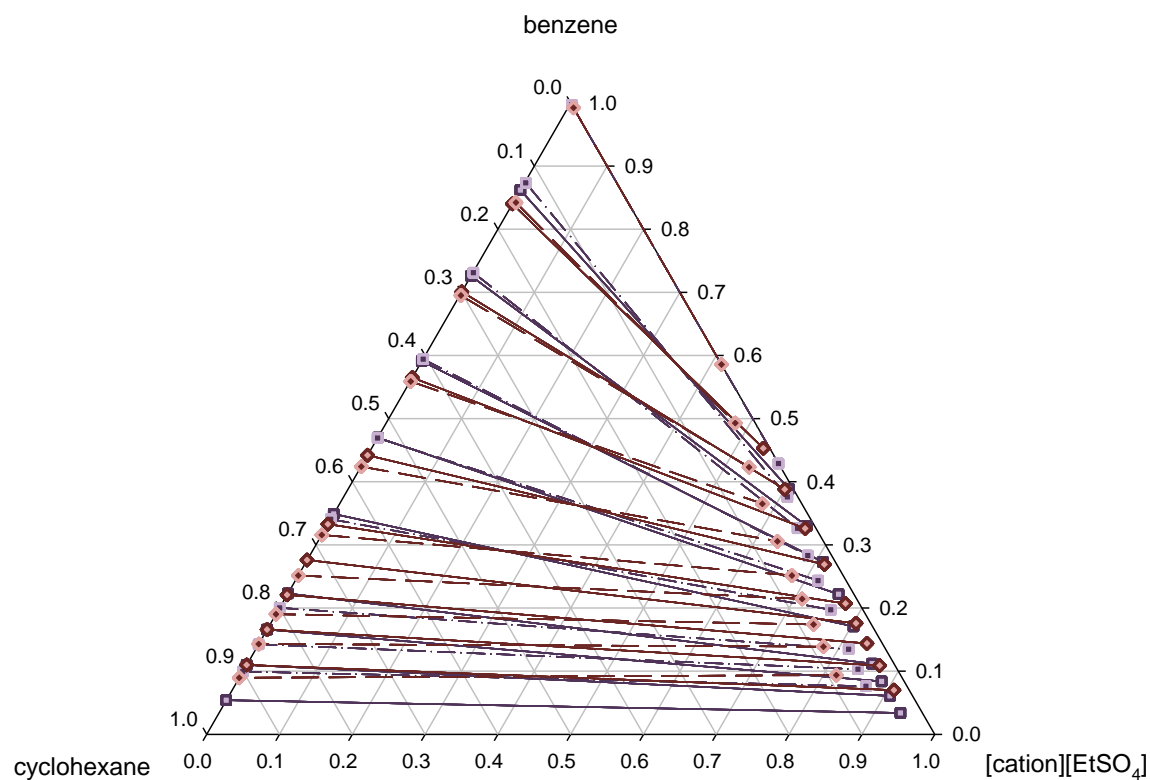
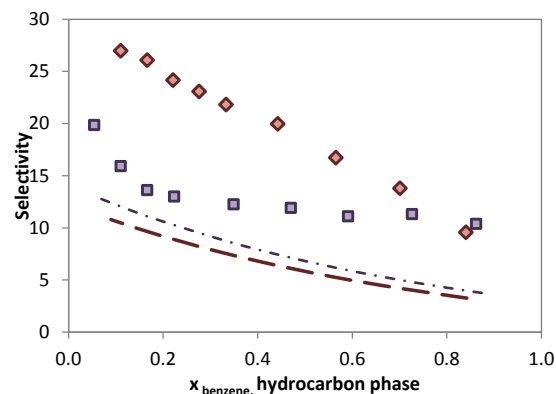


Figure C20 a) Experimental and COSMO-RS predicted tie-lines, b) selectivity and c) distribution ratio for the LLE of the ternary systems cyclohexane + benzene + $[1,4C_4mpy][BF_4]^{48}$ (red triangles, solid line and red dotted triangles, dashed line), cyclohexane + toluene + $[1,4C_4mpy][BF_4]^{48}$ (yellow squares, solid line and yellow semi-filled squares, dotted line), cyclohexane + ethylbenzene + $[1,4C_4mpy][BF_4]^{48}$ (green diamonds, solid line and green semi-filled diamonds, dot dashed line), and cyclohexane + *o*-xylene + $[1,4C_4mpy][BF_4]^{48}$ (red squares, solid line and red dotted squares, dot-dot dashed line) at 298.15K.

a)



b)



c)

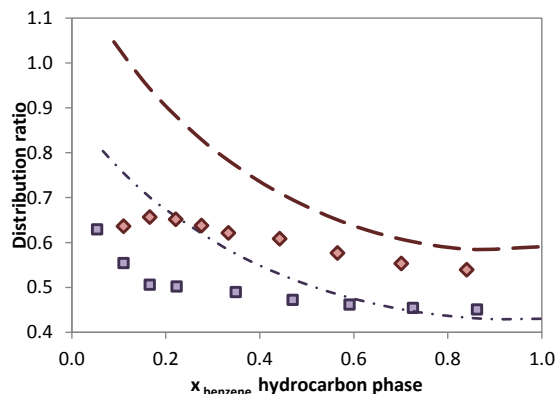
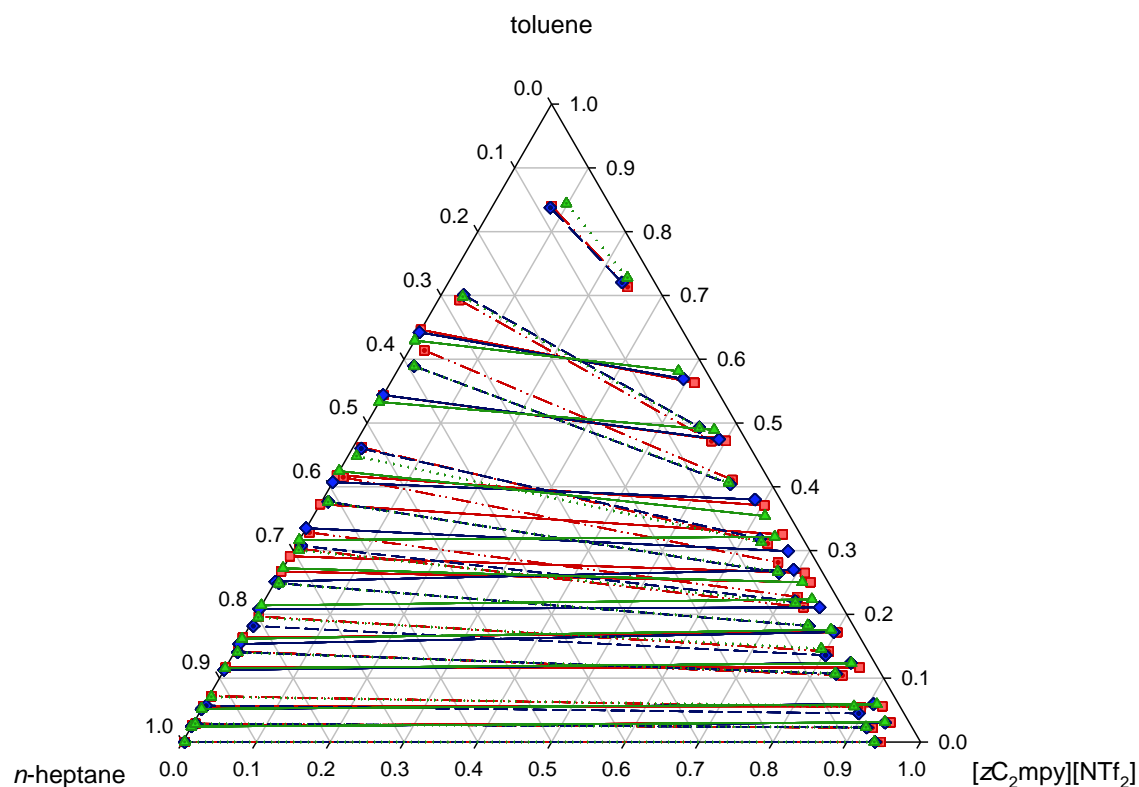
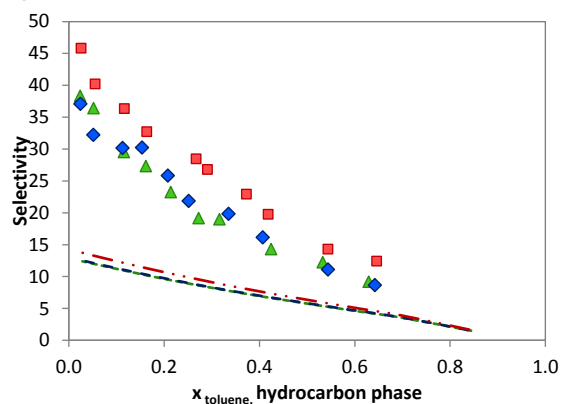


Figure C21 a) Experimental and COSMO-RS predicted tie-lines, b) selectivity and c) distribution ratio for the LLE of the ternary systems cyclohexane +benzene + $[\text{C}_2\text{mim}][\text{EtSO}_4]^9$ (light purple center square, solid line and dark purple center square, dot dashed line) and cyclohexane +benzene + $[\text{C}_2\text{mpy}][\text{EtSO}_4]^{47}$ (light pink center diamonds, solid line and dark pink center diamonds, long dashed line) at 298.15K.

a)



b)



c)

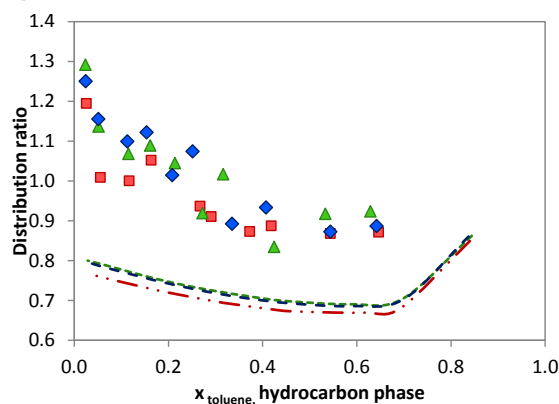
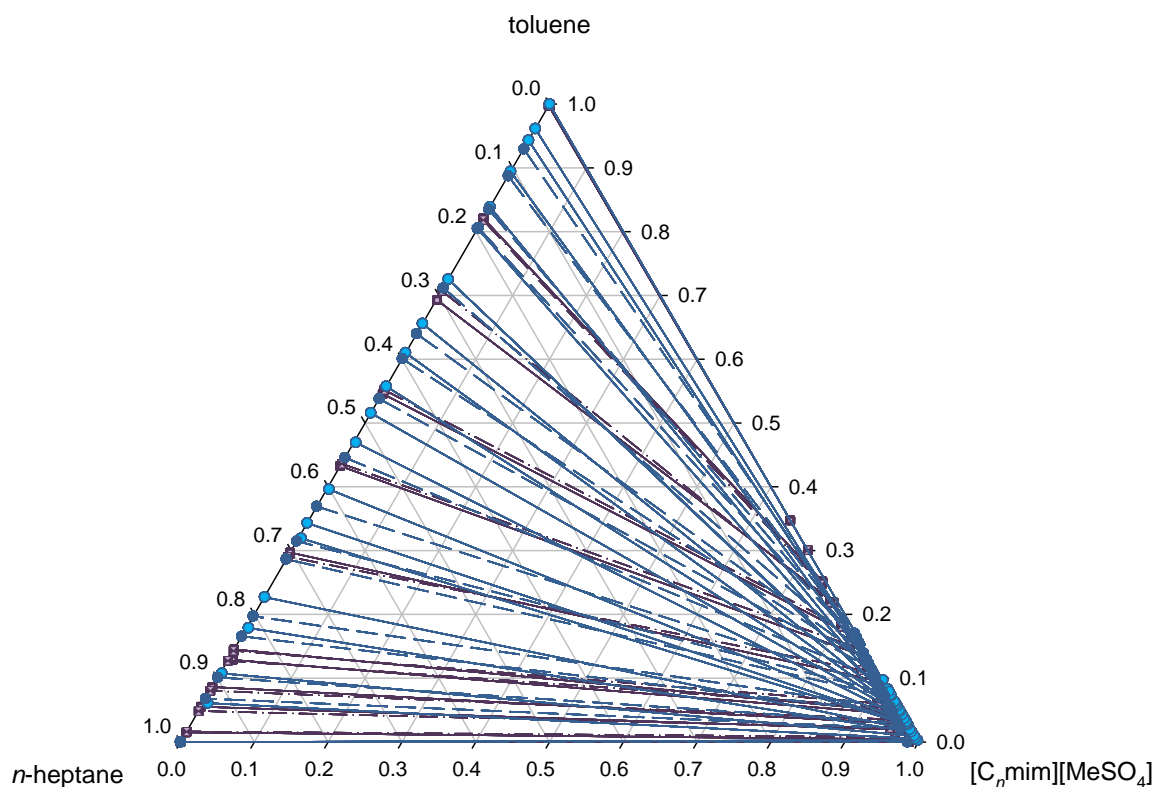
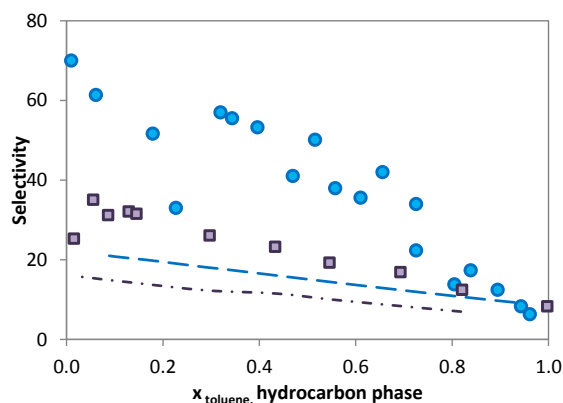


Figure C22 a) Experimental and COSMO-RS predicted tie-lines, b) selectivity and c) distribution ratio for the LLE of the ternary systems *n*-heptane + toluene + [1,2C₂mpy][NTf₂]³⁵ (red squares, solid line and red dotted squares, dot-dot dashed line), *n*-heptane + toluene + [1,3C₂mpy][NTf₂]³⁵ (blue diamonds, solid line and blue dotted diamonds, dashed line), and *n*-heptane + toluene + [1,4C₂mpy][NTf₂]³⁵ (green triangles, solid line and green dotted triangles, dotted line) at 313.2K.

a)



b)



c)

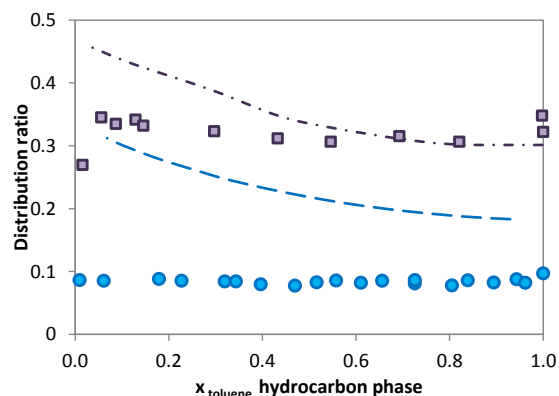
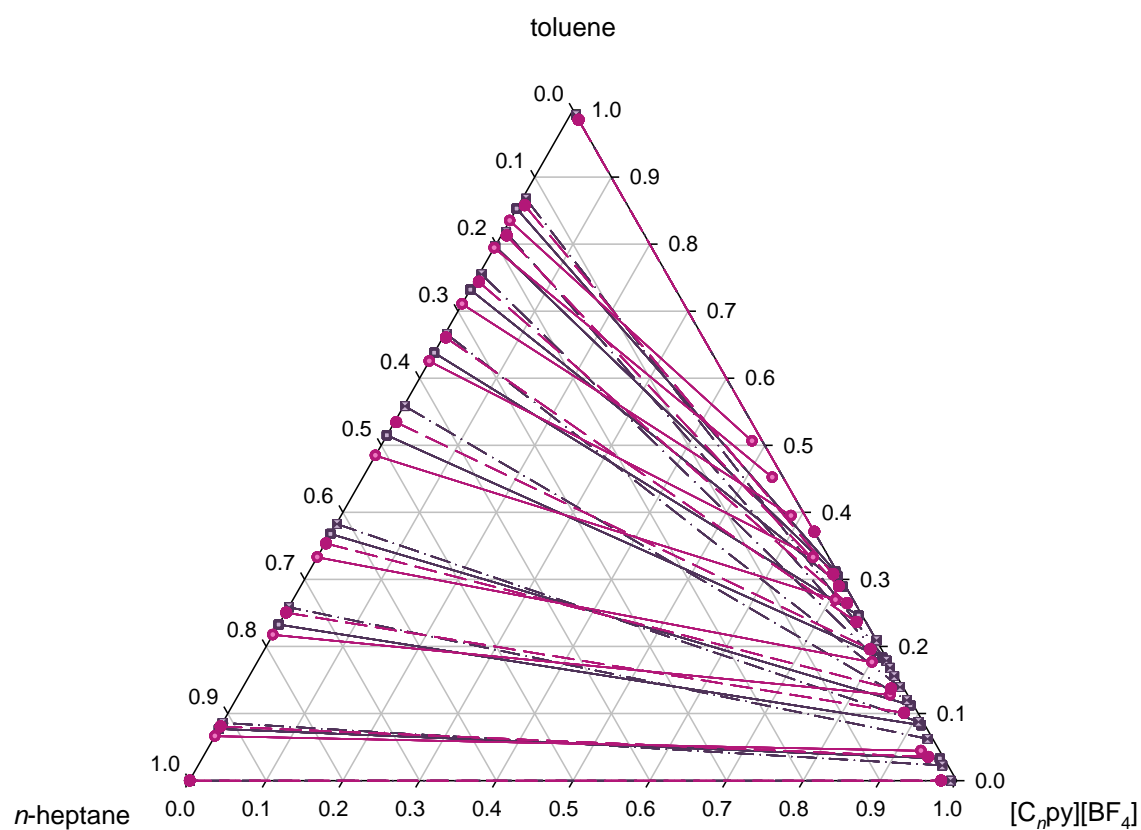
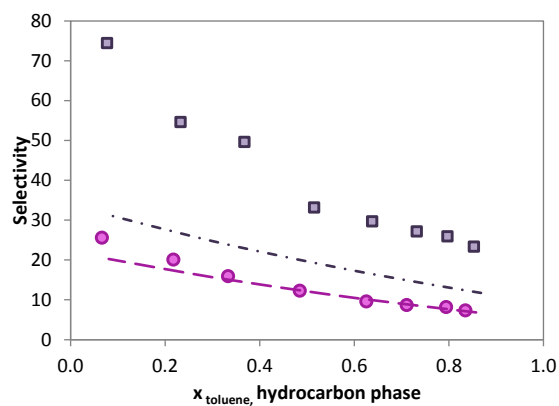


Figure C23 a) Experimental and COSMO-RS predicted tie-lines, b) selectivity and c) distribution ratio for the LLE of the ternary systems *n*-heptane + toluene + $[C_1\text{mim}][\text{MeSO}_4]$ ⁴⁰ (blue circles, solid line and blue hourglass circles, long dashed line) and *n*-heptane + toluene + $[C_4\text{mim}][\text{MeSO}_4]$ ⁴² (purple squares, solid line and purple hourglass squares, dot dashed line) at 313.2K.

a)



b)



c)

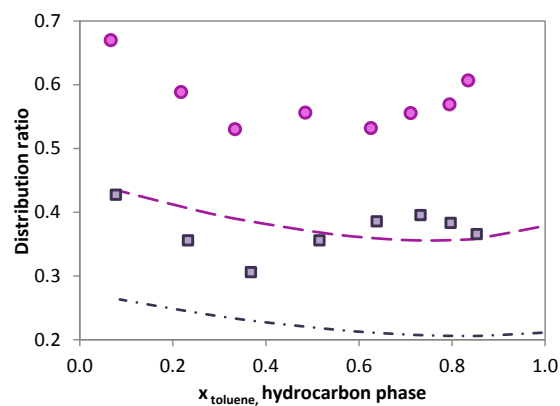
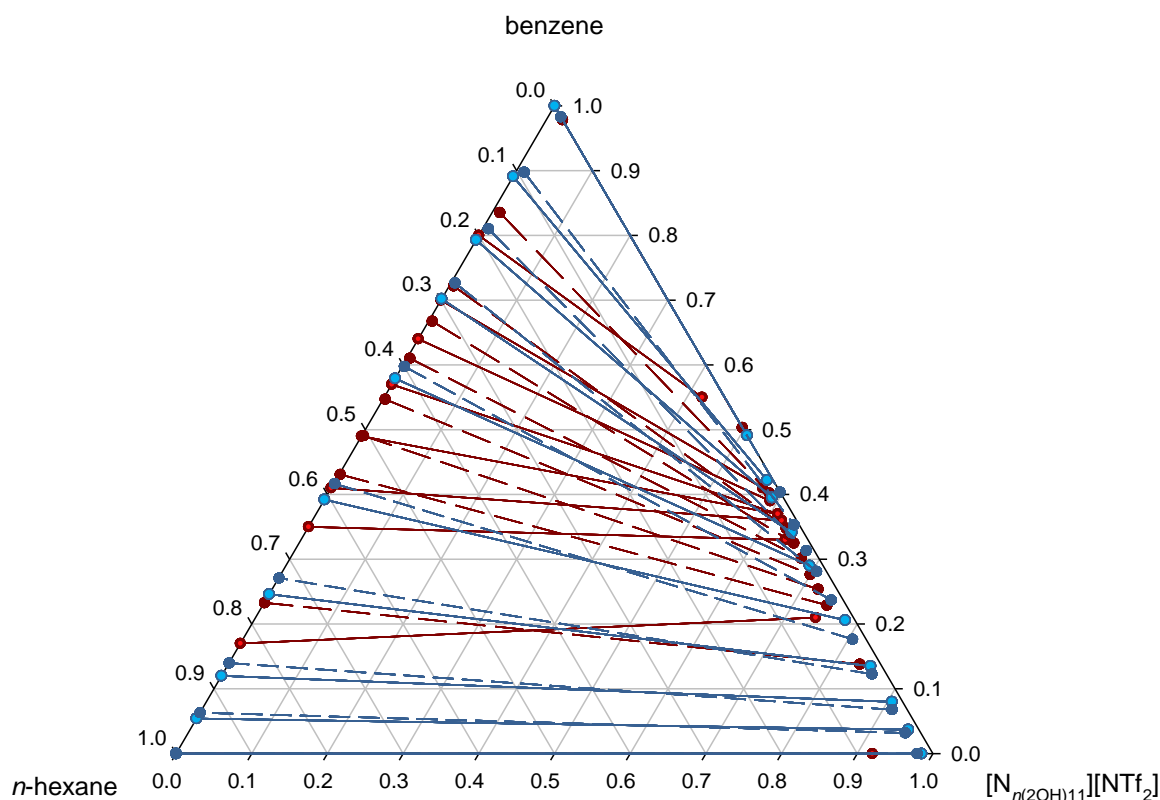
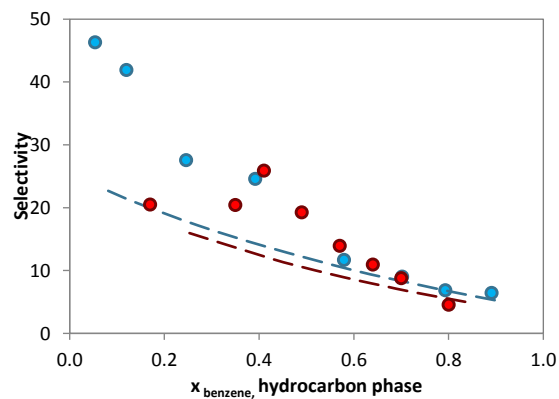


Figure C24 a) Experimental and COSMO-RS predicted tie-lines, b) selectivity and c) distribution ratio for the LLE of the ternary systems n -heptane + toluene + $[C_4py][BF_4]^{83}$ (purple squares, solid line and purple hourglass squares, dot dashed line) n -heptane + toluene + $[C_6py][BF_4]^{83}$ (pink circles, solid line and pink hourglass circles, dashed line), at 313.2K.

a)



b)



c)

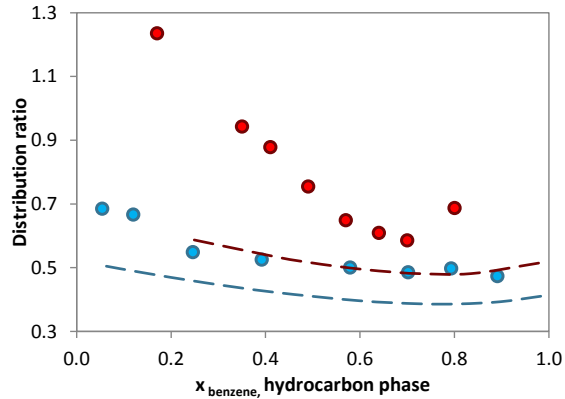
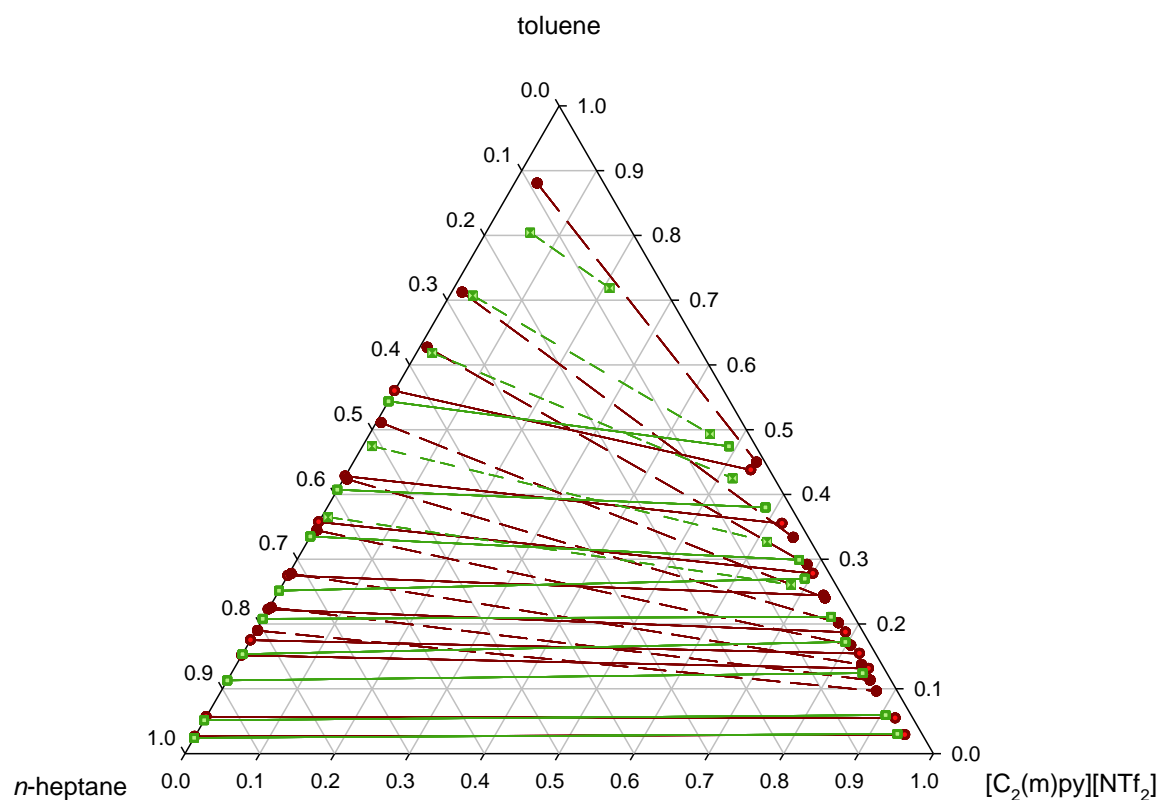
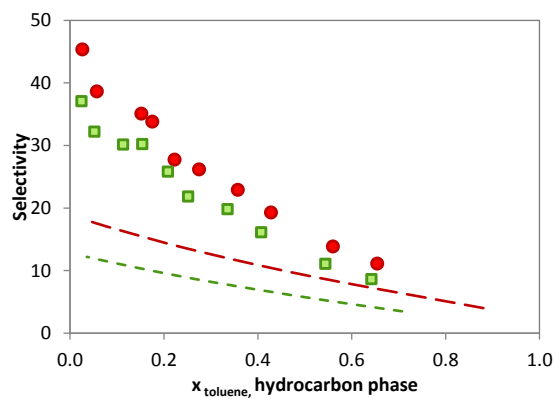


Figure C25 a) Experimental and COSMO-RS predicted tie-lines, b) selectivity and c) distribution ratio for the LLE of the ternary systems n -hexane + benzene + $[N_{1(2OH)11}][NTf_2]^4$ (blue circles, solid line and blue hourglass circles, long dashed line) at 313.2K and n -hexane + benzene + $[N_{2(2OH)11}][NTf_2]^{27}$ (red circles, solid line and red hourglass circles, long dashed line) at 298.15K.

a)



b)



c)

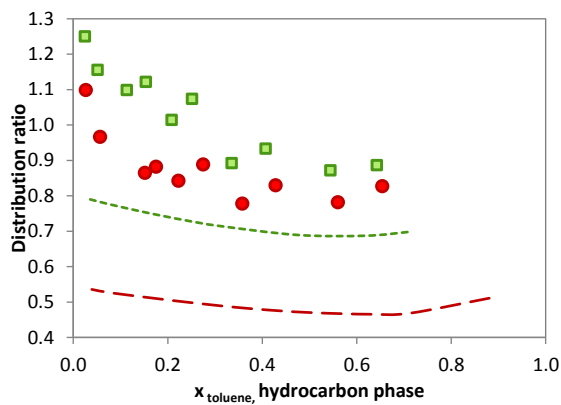
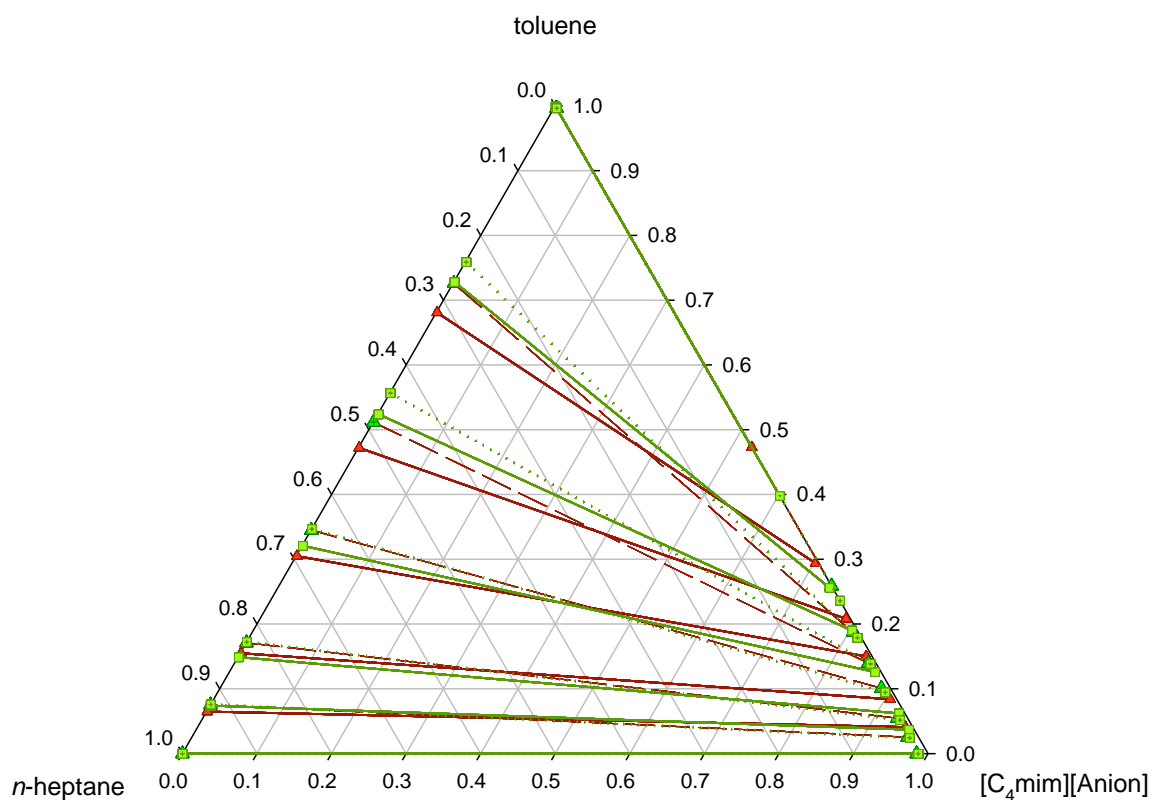
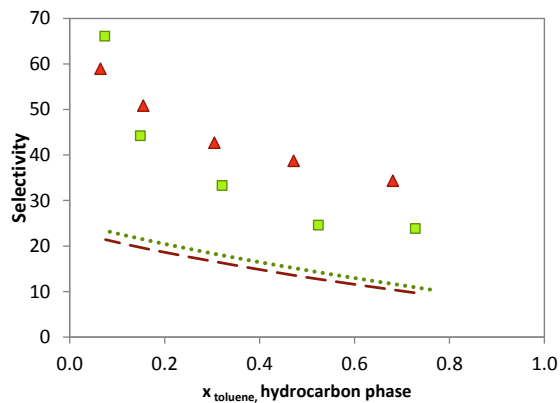


Figure C26 a) Experimental and COSMO-RS predicted tie-lines, b) selectivity and c) distribution ratio for the LLE of the ternary systems n -heptane + toluene + $[C_2py][NTf_2]$ ³⁵ (red circles, solid line and red hourglass circles, long dashed line) and n -heptane + toluene + $[C_2mpy][NTf_2]$ ³⁵ (green squares, solid line and green hourglass squares, short dashed line) at 313.2K.

a)



b)



c)

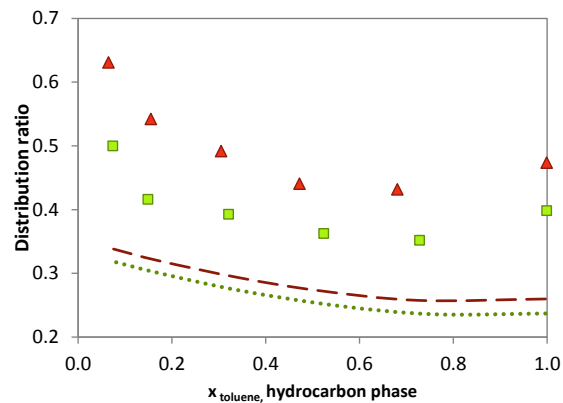
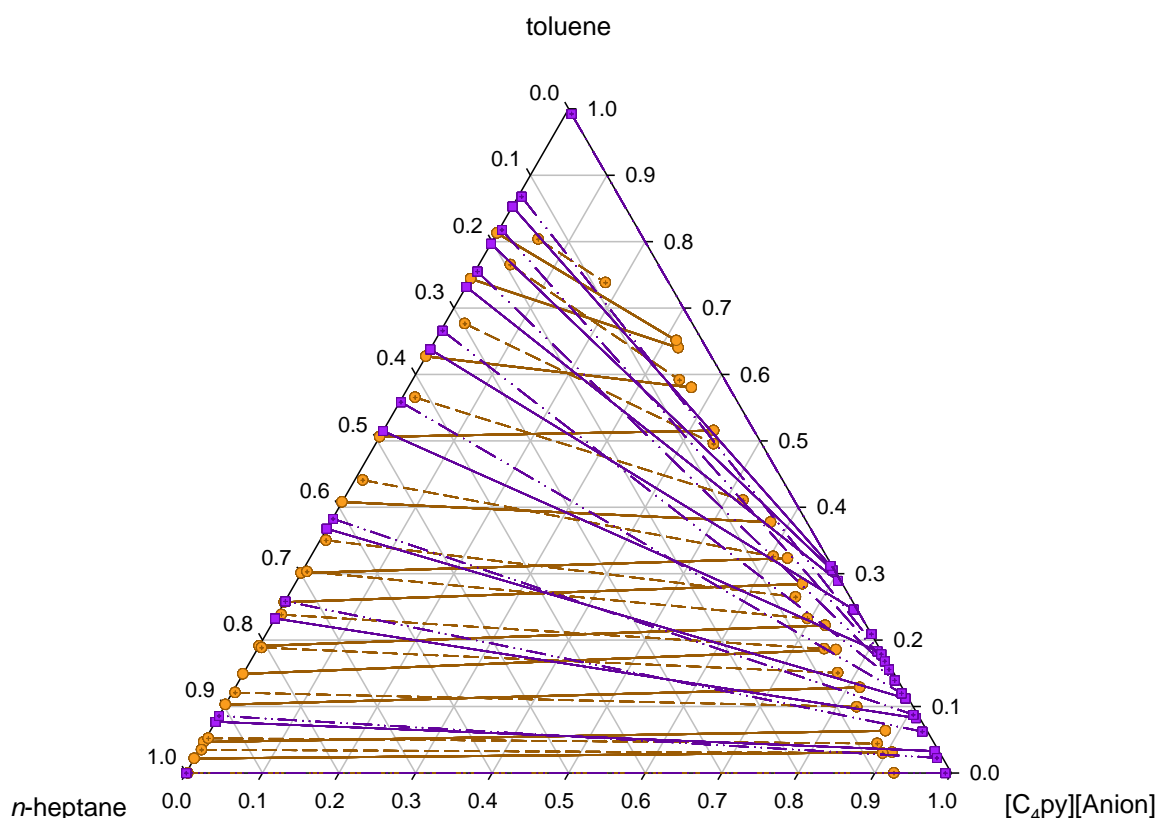
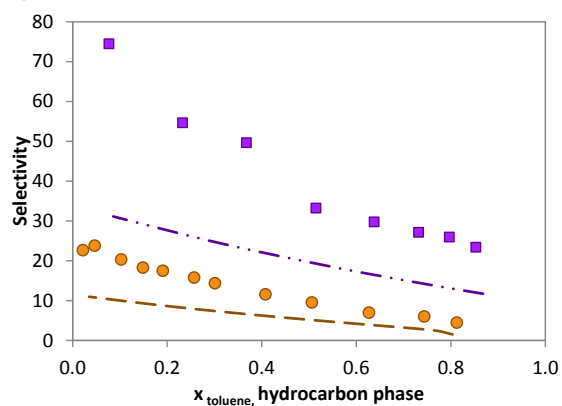


Figure C27 a) Experimental and COSMO-RS predicted tie-lines, b) selectivity and c) distribution ratio for the LLE of the ternary systems *n*-heptane + toluene + [C₄mim][SCN]¹⁷ (green squares, solid line and green dotted squares, dotted line), and *n*-heptane + toluene + [C₄mim][DCA]¹⁷ (red triangles, solid line and red dotted triangles, long dashed line) at 303.15K.

a)



b)



c)

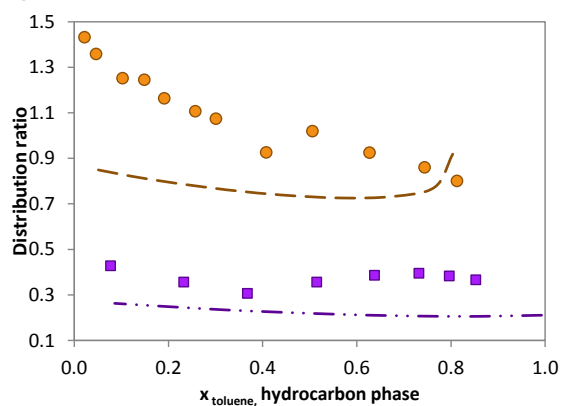
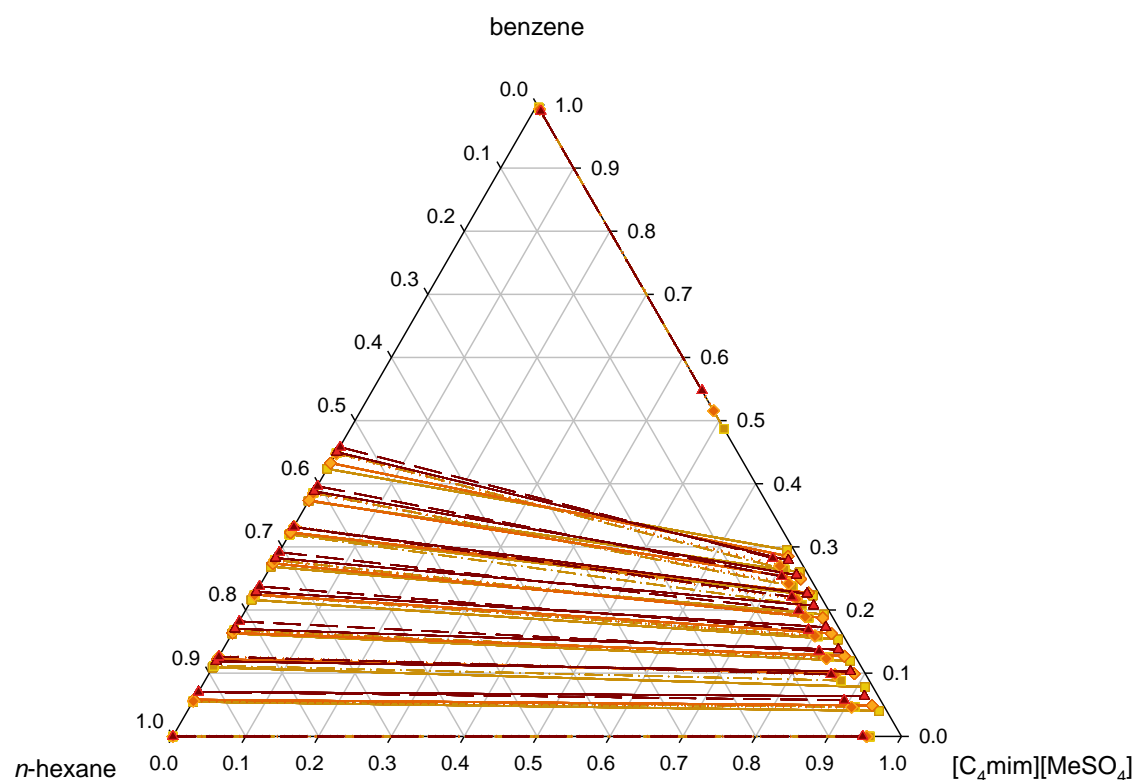
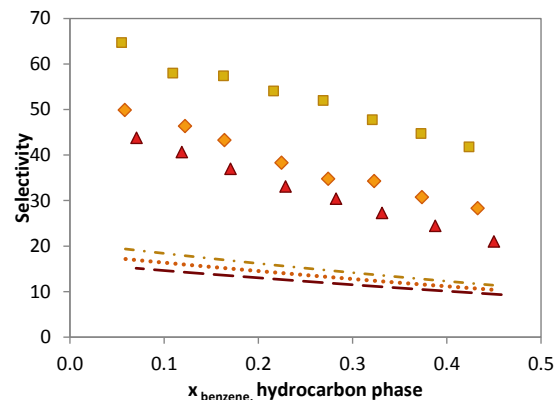


Figure C28 a) Experimental and COSMO-RS predicted tie-lines, b) selectivity and c) distribution ratio for the LLE of the ternary systems n -heptane + toluene + $[C_4py][NTf_2]$ ²⁵ (orange circles, solid line and dark orange dotted circles, long dashed line) and n -heptane + toluene + $[C_4py][BF_4]$ ⁸³ (purple squares, solid line and purple dotted squares, dot-dot dashed line) at 313.2K.

a)



b)



c)

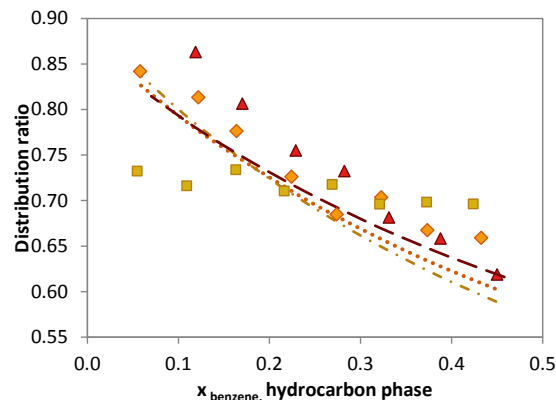
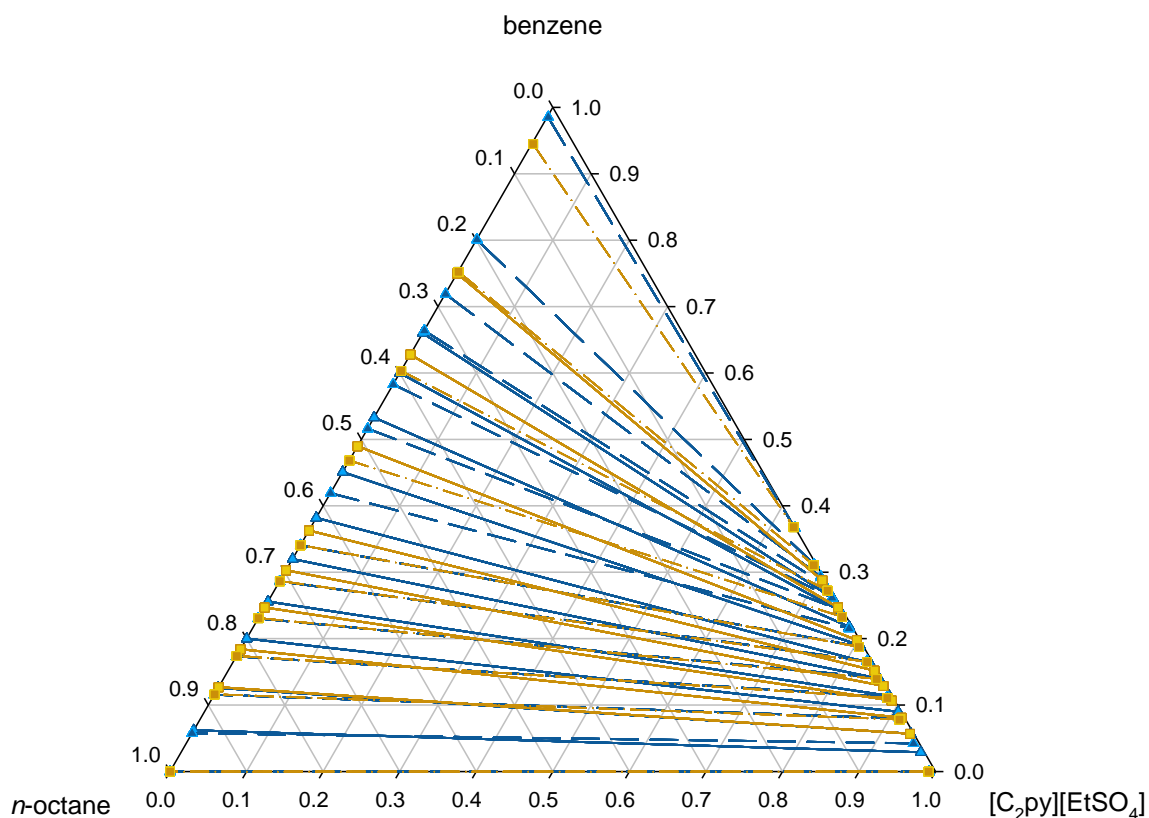
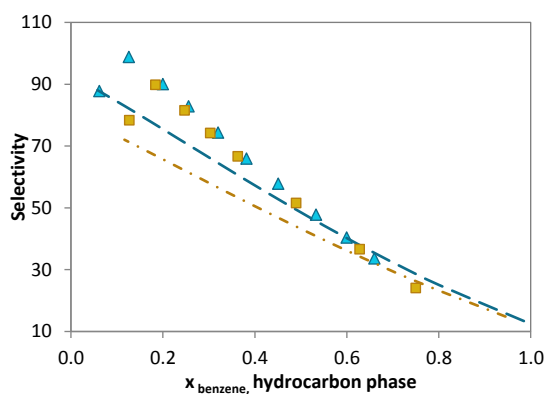


Figure C29 a) Experimental and COSMO-RS predicted tie-lines, b) selectivity and c) distribution ratio for the LLE of the ternary systems *n*-hexane + benzene + [C₄mim][MeSO₄] at temperatures 303.15K (light yellow squares, solid line and dark yellow squares, dot dashed line), 313.15K (light orange diamonds, solid line and dark orange diamonds, dotted line), and 328.15K (light red triangles, solid line and dark red triangles, long dashed line).

a)



b)



c)

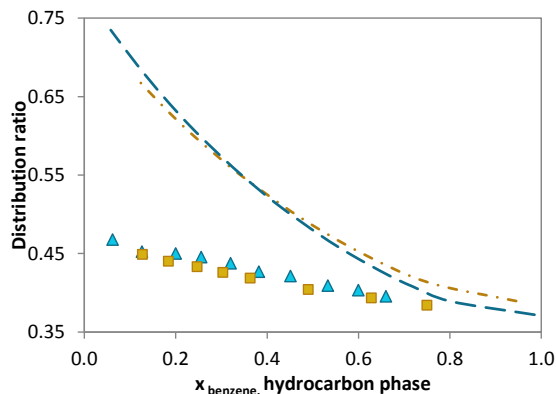
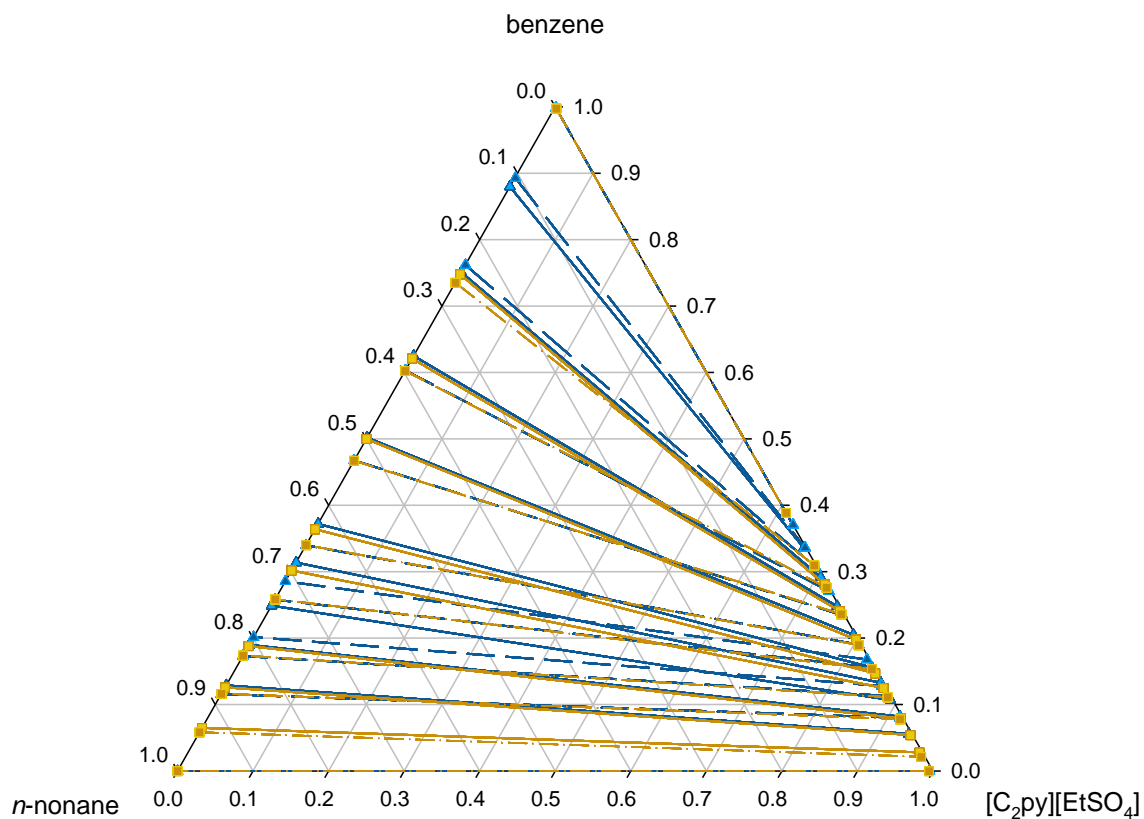
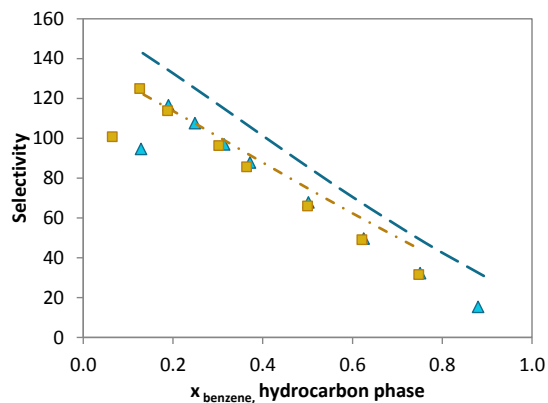


Figure C30 a) Experimental and COSMO-RS predicted tie-lines, b) selectivity and c) distribution ratio for the LLE of the ternary systems *n*-octane + benzene + [C₂py][EtSO₄] at the temperatures 283.15K¹⁹ (light blue triangles, solid line and dark blue triangles, long dashed line) and 298.15K¹⁹ (light yellow squares, solid line and dark yellow squares, dot dashed line).

a)



b)



c)

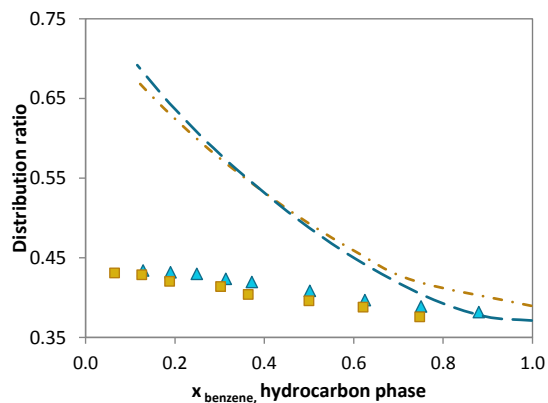
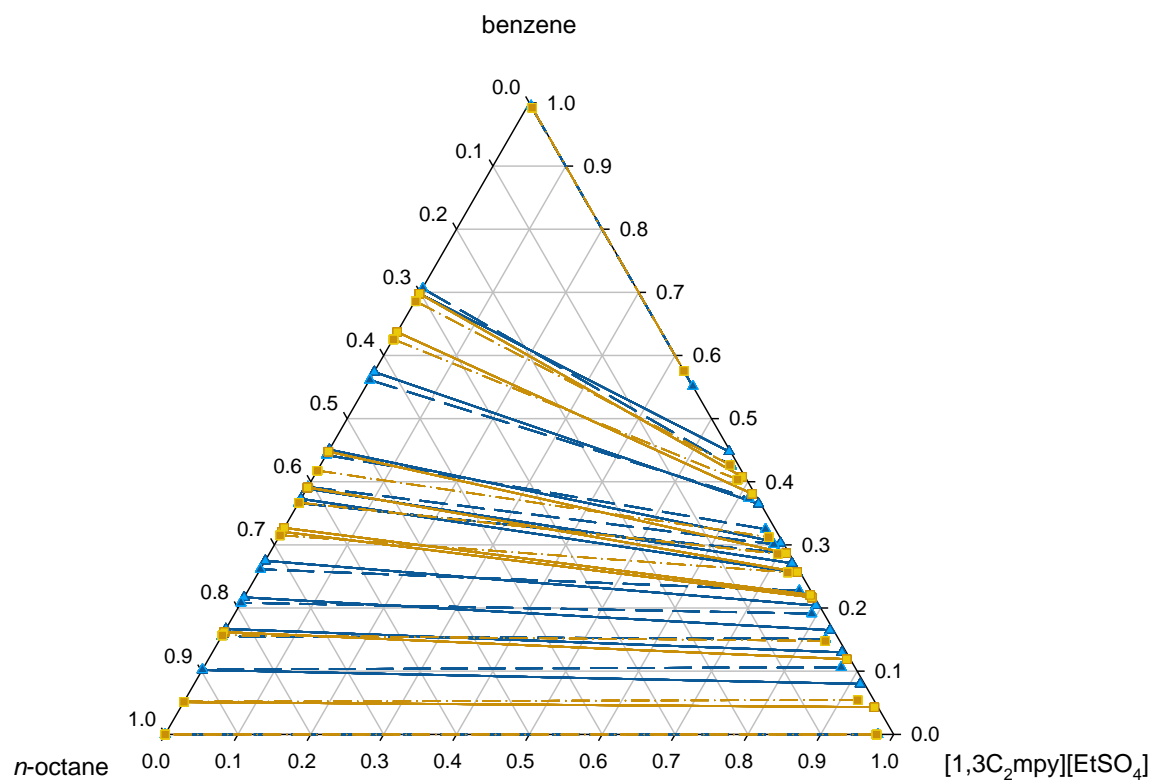
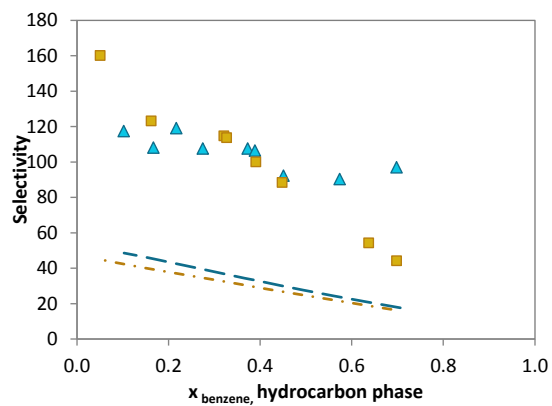


Figure C31 a) Experimental and COSMO-RS predicted tie-lines, b) selectivity and c) distribution ratio for the LLE of the ternary systems n -nonane + benzene + $[C_2py][EtSO_4]$ at the temperatures 283.15K¹⁹ (light blue triangles, solid line and dark blue triangles, long dashed line) and 298.15K¹⁹ (light yellow squares, solid line and dark yellow squares, dot dashed line).

a)



b)



c)

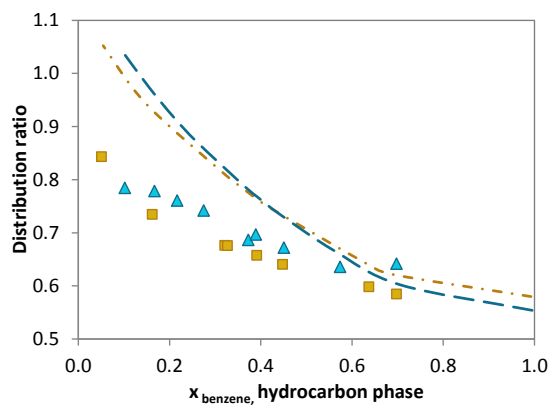
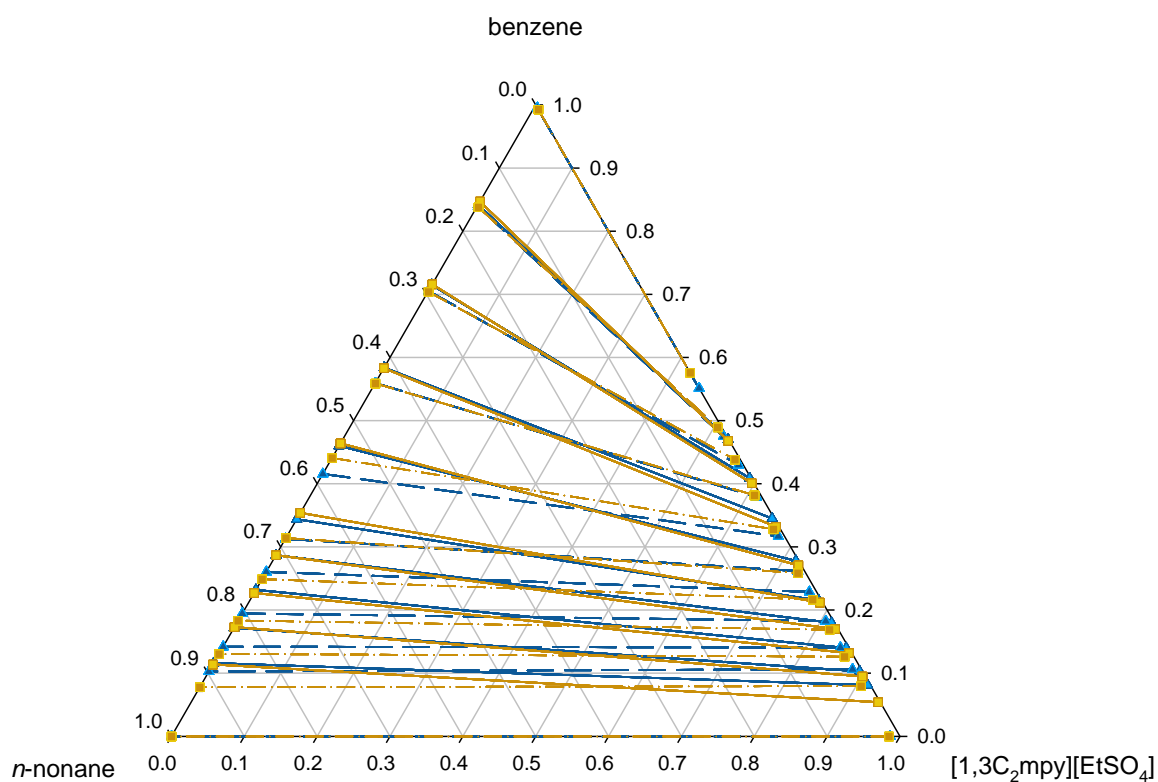
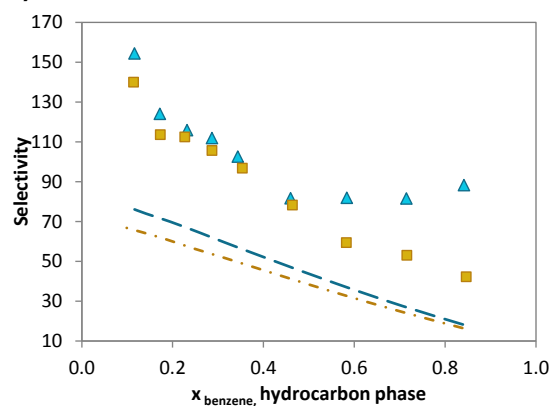


Figure C32 a) Experimental and COSMO-RS predicted tie-lines, b) selectivity and c) distribution ratio for the LLE of the ternary systems *n*-octane + benzene + [1,3C₂mpy][EtSO₄] at the temperatures 283.15K³¹ (light blue triangles, solid line and dark blue triangles, long dashed line) and 298.15K³¹ (light yellow squares, solid line and dark yellow squares, dot dashed line).

a)



b)



c)

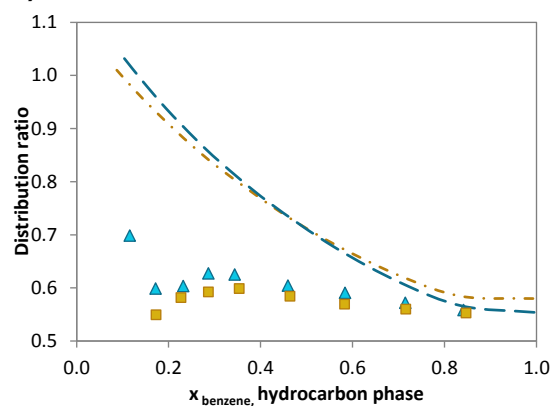
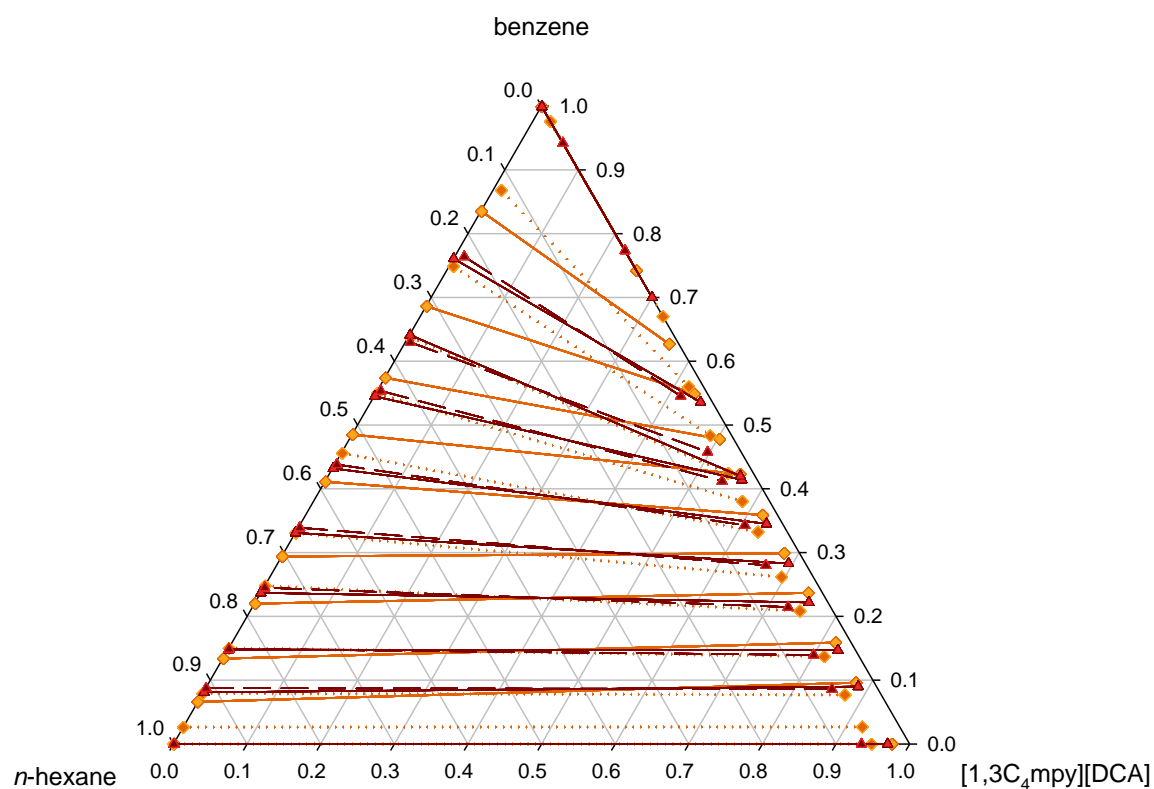
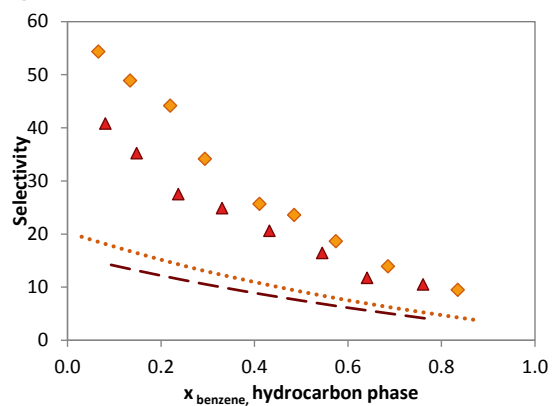


Figure C33 a) Experimental and COSMO-RS predicted tie-lines, b) selectivity and c) distribution ratio for the LLE of the ternary systems *n*-nonane + benzene + [1,3C₂mpy][EtSO₄] at the temperatures 283.15K³¹ (light blue triangles, solid line and dark blue triangles, long dashed line) and 298.15K³¹ (light yellow squares, solid line and dark yellow squares, dot dashed line).

a)



b)



c)

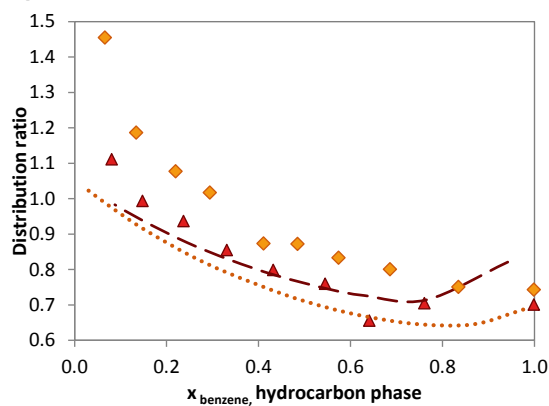
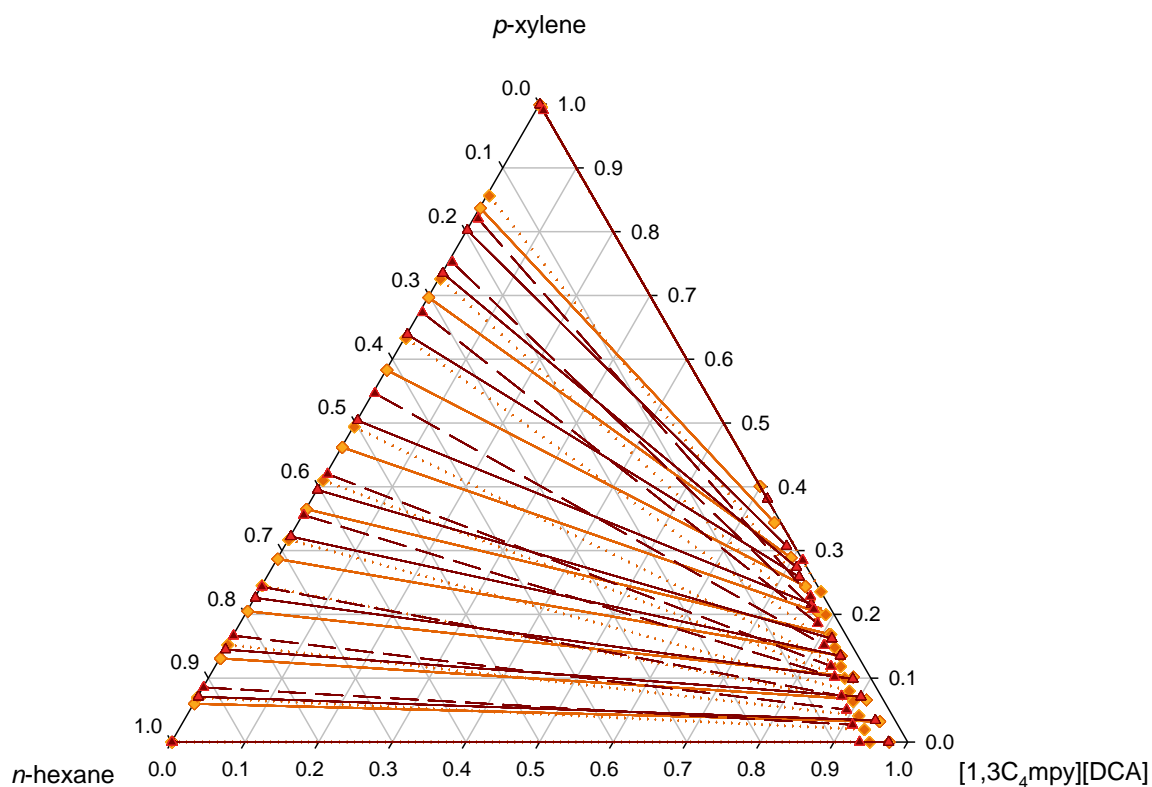
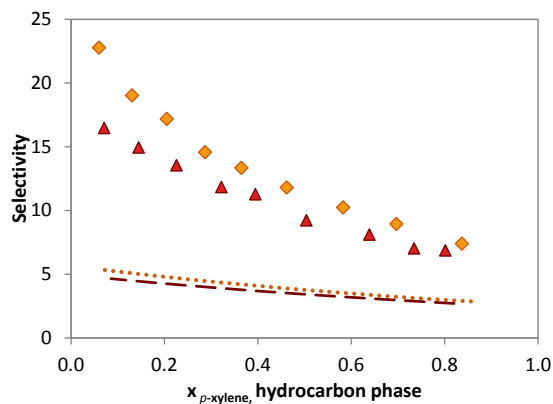


Figure C34 a) Experimental and COSMO-RS predicted tie-lines, b) selectivity and c) distribution ratio for the LLE of the ternary systems *n*-hexane + benzene + [1,3C₄mpy][DCA] at the temperatures 303.15K²⁴ (light orange diamonds, solid line and dark orange diamonds, dotted line) and 328.15K²⁴ (light red triangles, solid line and dark red triangles, long dashed line).

a)



b)



c)

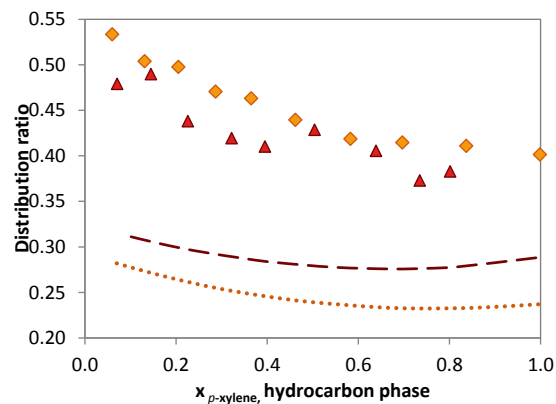


Figure C35 a) Experimental and COSMO-RS predicted tie-lines, b) selectivity and c) distribution ratio for the LLE of the ternary systems n -hexane + p -xylene + $[1,3C_4mpy][DCA]$ at the temperatures 303.15K²⁴ (light orange diamonds, solid line and dark orange diamonds, dotted line) and 328.15K²⁴ (light red triangles, solid line and dark red triangles, long dashed line).

Appendix D

**Ionic Liquids for Mercaptans
Desulfurization:
Experimental Liquid-Liquid Equilibrium
and COSMO-RS Description**

Table D1 Experimental liquid-liquid equilibrium data for the ternary systems composed of ionic liquid (IL) + 1-hexanethiol (RSH) + *n*-dodecane (HC), and respective standard deviation (*ST*).

Initial composition		<i>n</i> -dodecane-rich-phase			Ionic-liquid-rich phase			Distribution ratio
x_{IL}	x_{RSH}	x_{IL}^I	x_{RSH}^I	<i>ST</i>	x_{IL}^{II}	x_{RSH}^{II}	<i>ST</i>	
[C₂mim][MeSO₄] (130.1 ppm H₂O) at 298.2 K								
0.5623	0.0089	0.0000	0.0212	0.0002	0.9994	0.0006	0.0001	0.03
0.5577	0.0247	0.0000	0.0529	0.0006	0.9987	0.0013	0.0001	0.02
0.5557	0.0453	0.0000	0.0989	0.0017	0.9985	0.0015	0.0001	0.02
[C₂mim][CH₃SO₃] (405.2 ppm H₂O) at 298.2 K								
0.5790	0.0069	0.0000	0.0157	0.0003	0.9989	0.0011	0.0002	0.07
0.5765	0.0134	0.0000	0.0291	0.0008	0.9990	0.0010	0.0003	0.03
0.5698	0.0219	0.0000	0.0477	0.0005	0.9984	0.0016	0.0003	0.03
[C₂mim][CF₃SO₃] (305.4 ppm H₂O) at 298.2 K								
0.5367	0.0138	0.0000	0.0144	0.0005	0.9987	0.0013	0.0001	0.09
0.5371	0.0232	0.0000	0.0283	0.0031	0.9979	0.0021	0.0003	0.07
0.5492	0.0072	0.0000	0.0459	0.0006	0.9970	0.0030	0.0002	0.06
[C₂mim][NTf₂] (315.2 ppm H₂O) at 298.2 K								
0.4777	0.0091	0.0000	0.0166	0.0008	0.9978	0.0022	0.0002	0.13
0.4741	0.0157	0.0000	0.0267	0.0018	0.9953	0.0047	0.0006	0.18
0.4669	0.0268	0.0000	0.0456	0.0006	0.9934	0.0066	0.0006	0.15
[C₂mim][BF₄] (523.9 ppm H₂O) at 298.2 K								
0.5931	0.0066	0.0000	0.0168	0.0006	>0.999	<0.0001		0.00
0.5998	0.0127	0.0000	0.0316	0.0012	>0.999	<0.0001		0.00
0.5948	0.0207	0.0000	0.0510	0.0008	>0.999	<0.0001		0.00
[C₄mim][MeSO₄] (80.4 ppm H₂O) at 298.2 K								
0.5231	0.0094	0.0000	0.0198	0.0003	0.9988	0.0012	0.0001	0.06
0.5227	0.0156	0.0000	0.0337	0.0015	0.9986	0.0014	0.0002	0.04
0.5234	0.0251	0.0000	0.0545	0.0008	0.9973	0.0027	0.0002	0.05
[C₄mim][CF₃SO₃] (528.5 ppm H₂O) at 298.2 K								
0.5241	0.0094	0.0000	0.0194	0.003	0.9972	0.0028	0.0003	0.14
0.5318	0.0153	0.0000	0.0309	0.0014	0.9957	0.0043	0.0002	0.14
0.5334	0.0245	0.0000	0.0503	0.0011	0.9938	0.0062	0.0001	0.12
[C₄mim][NTf₂] (245.7 ppm H₂O) at 298.2 K								
0.4277	0.0113	0.0000	0.0175	0.0003	0.9957	0.0043	0.0001	0.25

Appendix D

0.4870	0.0168	0.0000	0.0279	0.0004	0.9934	0.0066	0.0001	0.24
0.4595	0.0284	0.0000	0.0475	0.0003	0.9895	0.0105	0.0005	0.22
[C₂mim][CH₃SO₃] (141 ppm H₂O) at 313.2 K								
0.5813	0.0083	0.0000	0.0194	0.0002	>0.9999	<0.0003		
0.5673	0.0144	0.0000	0.0336	0.0009	0.9985	0.0015	0.0004	0.05
[C₂mim][CF₃SO₃] (31.1 ppm H₂O) at 313.2 K								
0.5417	0.0101	0.0000	0.0211	0.0014	0.9981	0.0019	0.0003	0.09
0.5545	0.0148	0.0000	0.0306	0.0001	0.9972	0.0028	0.0001	0.09
[C₂mpy][CH₃SO₃] (174.8 ppm H₂O) at 298.2 K								
0.5700	0.0073	0.0000	0.0178	0.0002	0.9987	0.0013	0.0003	0.07
0.5611	0.0140	0.0000	0.0308	0.0006	0.9985	0.0015	0.0002	0.05
0.5686	0.0211	0.0000	0.0474	0.0006	0.9978	0.0022	0.0003	0.05
[C₂mpy][NTf₂] (183.9 ppm H₂O) at 298.2 K								
0.4486	0.0095	0.0000	0.0168	0.0004	0.9964	0.0036	0.0003	0.21
0.4490	0.0172	0.0000	0.0268	0.0004	0.9939	0.0061	0.0001	0.23
0.4528	0.0285	0.0000	0.0441	0.0007	0.9915	0.0085	0.0001	0.19
[C₂mpy][CF₃SO₃] (482.7 ppm H₂O) at 313.2 K								
0.5329	0.0094	0.0000	0.0180	0.0007	0.9984	0.0016	0.000	0.09
0.5346	0.0150	0.0000	0.0291	0.0005	0.9966	0.0034	0.0003	0.12
[C₂mim][MeSO₄] (6840.2 ppm H₂O) at 298.2 K								
0.5717	0.0071	0.0000	0.0164	0.0006	0.9987	0.0013	0.0002	0.08
0.5615	0.0139	0.0000	0.0303	0.0006	0.9990	0.0010	0.0001	0.03
[C₂mim][CF₃SO₃] (6583.1 ppm H₂O) at 298.2 K								
0.5468	0.0075	0.0000	0.0150	0.0004	0.9894	0.0016	0.0001	0.10
0.5408	0.0146	0.0000	0.0283	0.0014	0.9803	0.0027	0.0003	0.10

Table D2 COSMO-RS predictive distribution ratio values for the ternary systems constituted by ionic liquid + 1-hexanethiol + *n*-dodecane, with a mole fraction of 1-hexanethiol circa to 0.1 in the *n*-dodecane-rich phase.

Cation Anion	[C ₂ mim] ⁺	[C ₄ mim] ⁺	[C ₆ mim] ⁺	[C ₈ mim] ⁺	[C ₂ C ₂ im] ⁺	[C ₄ C ₄ im] ⁺	[C ₂ mpy] ⁺	[C ₂ mpyr] ⁺	[C ₄ iQuin] ⁺	[C ₄ TZO] ⁺	[Ch] ⁺	[Gu] ⁺	[(C ₁) ₆ Gu] ⁺	[P ₆₆₆₍₁₄₎] ⁺	[OC ₂ (C ₁) ₄ iU] ⁺	[SC ₂ (C ₁) ₄ iU] ⁺
[MeSO ₄] ⁻	0.05	0.07	0.11	0.17	0.07	0.18	0.10	0.16	0.15	0.11	0.01	IP	0.81	0.69	0.42	0.47
[EtSO ₄] ⁻	0.15	0.10	0.15	NP	0.09	0.22	0.11	0.16	0.19	0.14	0.01	IP	0.82	0.68	0.44	0.51
[BuSO ₄] ⁻	0.24	0.15	0.21	NP	0.13	0.31	0.16	0.19	0.26	0.21	0.02	IP	0.82	0.69	0.49	0.56
[OcSO ₄] ⁻	0.19	0.29	0.38	NP	0.26	0.49	0.30	0.32	0.45	0.38	0.06	0.01	0.99	TMP	0.69	0.77
[CH ₃ SO ₃] ⁻	0.12	0.12	0.14	0.18	0.14	0.20	0.20	0.43	0.18	0.17	0.07	1.14	1.28	1.52	0.72	0.82
[CF ₃ SO ₃] ⁻	0.03	0.09	0.16	0.26	0.06	0.25	0.07	0.08	0.19	0.11	IP	0.00	0.52	TMP	0.30	0.32
[(PFBu)SO ₃] ⁻	0.12	0.23	0.35	NP	0.18	0.48	0.19	0.21	0.39	0.24	0.03	IP	0.71	TMP	0.50	0.50
[CH ₃ CO ₂] ⁻	0.09	0.19	0.21	NP	0.22	0.27	0.32	0.64	0.27	0.26	0.15	IP	1.77	1.67	1.01	1.18
[NTf ₂] ⁻	0.12	0.25	0.39	0.54	0.19	0.53	0.19	0.19	0.41	0.26	0.03	0.01	0.58	TMP	0.45	0.44
[PF ₆] ⁻	0.01	0.07	0.16	NP	0.04	0.28	0.04	0.03	0.18	0.07	IP	0.07	0.25	TMP	0.15	0.16
[BF ₄] ⁻	0.01	0.04	0.08	NP	0.03	0.15	0.04	0.06	0.10	0.05	IP	IP	0.42	TMP	0.20	0.22
[N(CN) ₂] ⁻	0.15	0.03	0.07	NP	0.03	0.12	0.03	0.08	0.08	0.05	IP	IP	0.47	TMP	0.22	0.25
[C(CN) ₃] ⁻	0.01	0.04	0.08	NP	0.03	0.14	0.03	0.05	0.09	0.05	IP	IP	0.30	TMP	0.16	0.19
[B(CN) ₄] ⁻	0.01	0.04	0.09	NP	0.03	0.16	0.02	0.05	0.09	0.06	IP	IP	0.23	TMP	0.13	0.15

Obs.: NP – not predicted; TMP – total miscibility predicted; IP – immiscibility predicted.

Table D2 (continuation)

Cation Anion	[C ₂ mim] ⁺	[C ₄ mim] ⁺	[C ₆ mim] ⁺	[C ₈ mim] ⁺	[C ₂ C ₂ im] ⁺	[C ₄ C ₄ im] ⁺	[C ₂ mpy] ⁺	[C ₂ mpyr] ⁺	[C ₄ iQuin] ⁺	[C ₄ TZO] ⁺	[Ch] ⁺	[Gu] ⁺	[(C ₁) ₆ Gu] ⁺	[P ₆₆₆₍₁₄₎] ⁺	[OC ₂ (C ₁) ₄ iU] ⁺	[SC ₂ (C ₁) ₄ iU] ⁺
[TOS] ⁻	0.09	0.14	0.20	NP	0.13	0.29	0.16	0.21	0.25	0.20	0.02	IP	0.85	0.64	0.50	0.57
[DEP] ⁻	0.06	0.21	0.26	NP	0.20	0.35	0.24	0.34	0.32	0.29	0.05	IP	1.30	0.60	0.76	0.88
[DBP] ⁻	0.01	0.33	0.40	NP	0.31	0.51	0.36	0.42	0.48	0.44	0.09	0.01	1.35	0.60	0.88	1.00
[NO ₃] ⁻	0.04	0.05	0.08	NP	0.05	0.13	0.08	0.23	0.10	0.08	0.02	IP	0.94	0.70	0.45	0.51
[FeCl ₄] ⁻	0.15	0.34	0.57	NP	0.24	0.76	0.21	0.17	0.55	0.30	0.05	1.14	0.45	TMP	0.38	0.37

Obs.: NP – not predicted; TMP – total miscibility predicted; IP – immiscibility predicted.

Table D3 COSMO-RS selectivity values for the ternary systems constituted by ionic liquid + 1-hexanethiol + *n*-dodecane, with a mole fraction of 1-hexanethiol circa to 0.1 in the *n*-dodecane-rich phase.

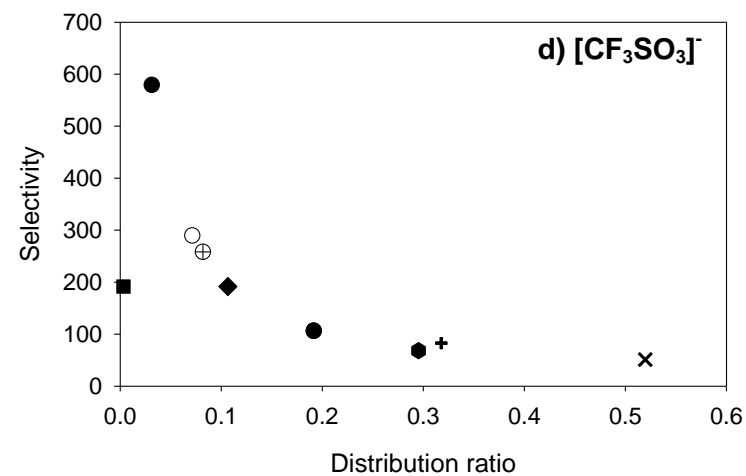
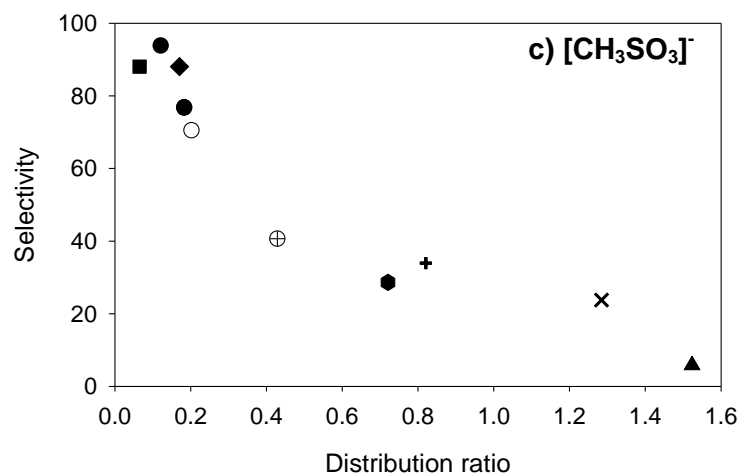
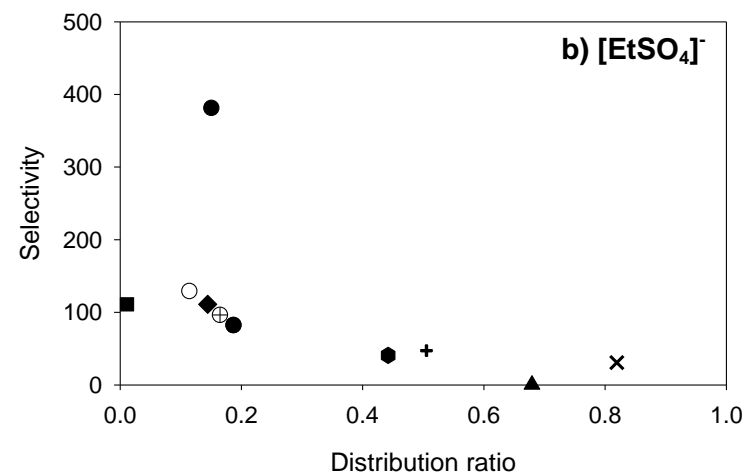
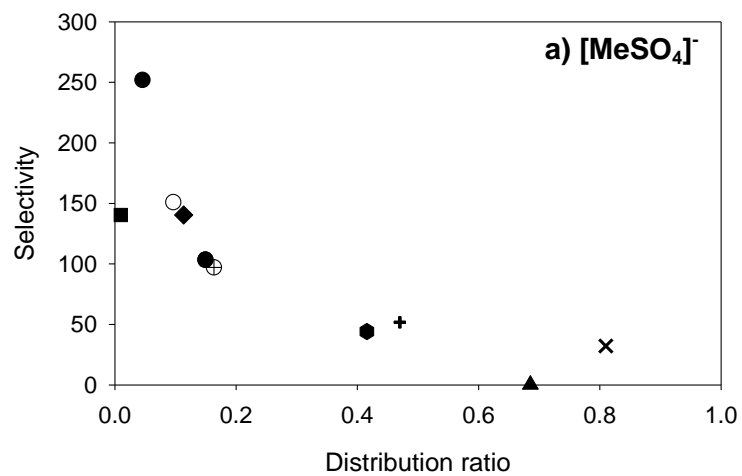
Cation Anion	[C ₂ mim] ⁺	[C ₄ mim] ⁺	[C ₆ mim] ⁺	[C ₈ mim] ⁺	[C ₂ C ₂ im] ⁺	[C ₄ C ₄ im] ⁺	[C ₂ mpy] ⁺	[C ₂ mpyr] ⁺	[C ₄ iQuin] ⁺	[C ₄ TZO] ⁺	[Ch] ⁺	[Gu] ⁺	[(C ₁) ₆ Gu] ⁺	[P ₆₆₆₍₁₄₎] ⁺	[OC ₂ (C ₁) ₄ iU] ⁺	[SC ₂ (C ₁) ₄ iU] ⁺
[MeSO ₄] ⁻	252	168	114	77	174	66	151	97	103	140	644	IP	32	0 - TMP	44	52
[EtSO ₄] ⁻	381	131	90	NP	142	53	129	96	82	111	608	IP	31	0- TMP	41	47
[BuSO ₄] ⁻	48	88	61	NP	99	38	96	85	57	76	436	IP	28	0- TMP	34	40
[OcSO ₄] ⁻	68	44	33	NP	50	22	50	49	32	40	156	312	19	TMP	21	25
[CH ₃ SO ₃] ⁻	94	98	84	66	85	54	71	41	77	88	116	794	24	6	29	34
[CF ₃ SO ₃] ⁻	579	213	113	67	287	59	290	258	107	192	3231	IP	51	TMP	68	83
[(PFBu)SO ₃] ⁻	238	110	66	NP	143	37	150	144	65	109	772	2320	41	TMP	46	59
[CH ₃ CO ₂] ⁻	148	52	46	NP	46	32	41	28	44	50	58	IP	21	6	22	27
[NTf ₂] ⁻	255	108	62	39	146	33	153	149	60	103	916	2936	38	TMP	43	55
[PF ₆] ⁻	1923	418	169	NP	681	75	699	704	154	366	IP	7024	82	TMP	115	134
[BF ₄] ⁻	1097	431	212	NP	527	100	445	275	185	344	IP	IP	51	TMP	82	94
[N(CN) ₂] ⁻	78	221	124	NP	257	65	236	155	114	179	2068	IP	37	TMP	55	63
[C(CN) ₃] ⁻	652	221	113	NP	299	58	307	233	108	178	IP	IP	46	TMP	65	74
[B(CN) ₄] ⁻	656	208	103	NP	297	54	325	228	106	169	2624	IP	48	TMP	65	73

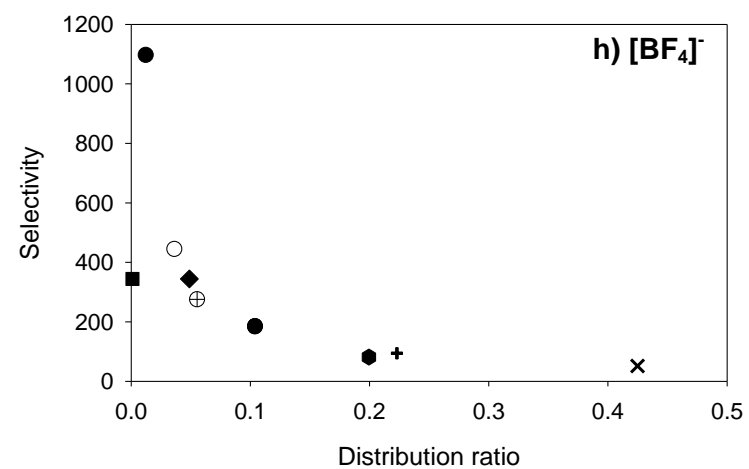
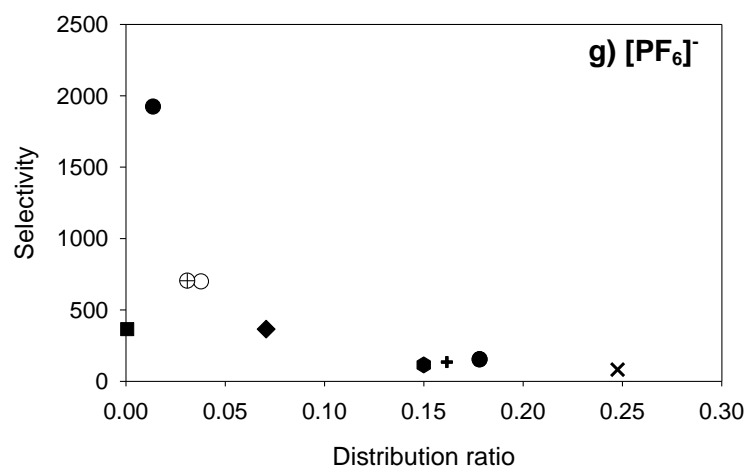
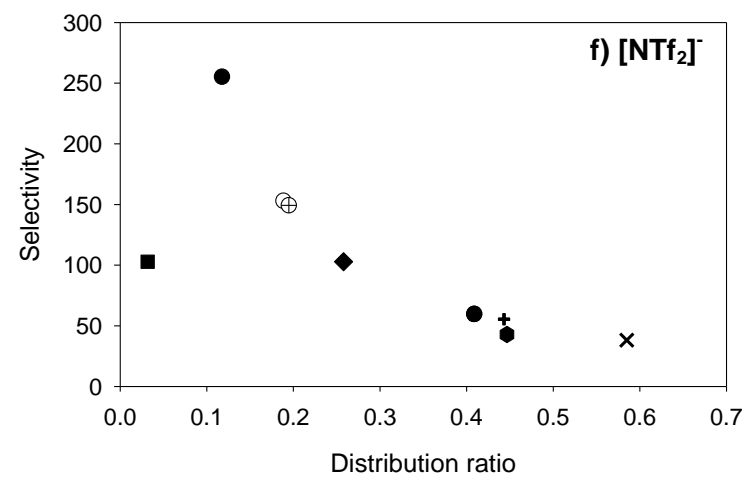
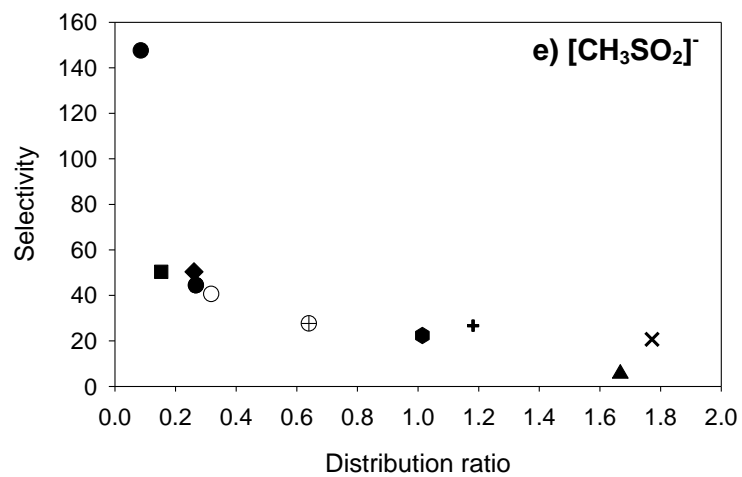
Obs.: NP – not predicted; TMP – total miscibility predicted; IP – immiscibility predicted.

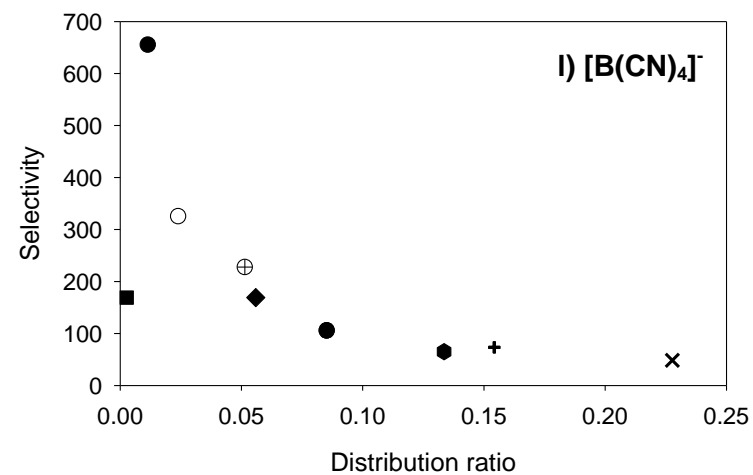
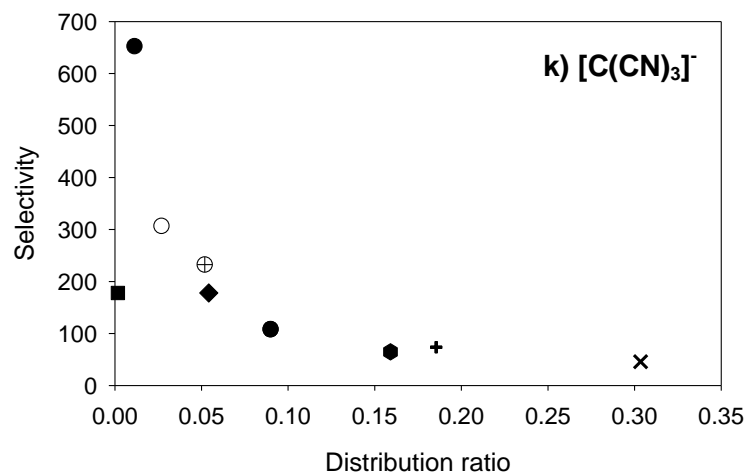
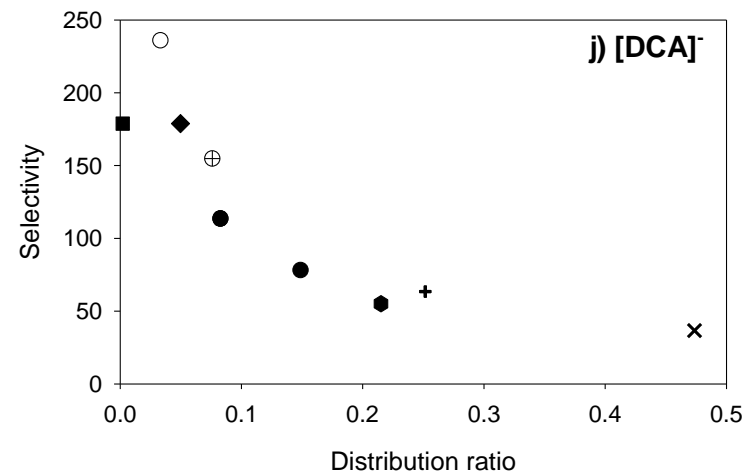
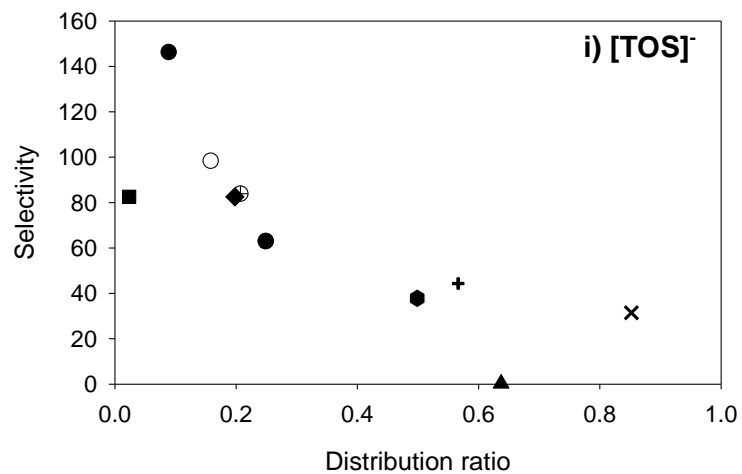
Table D3 (continuation)

Anion \ Cation	[C ₂ mim] ⁺	[C ₄ mim] ⁺	[C ₆ mim] ⁺	[C ₈ mim] ⁺	[C ₂ C ₂ im] ⁺	[C ₄ C ₄ im] ⁺	[C ₂ mpy] ⁺	[C ₂ mpyr] ⁺	[C ₄ iQuin] ⁺	[C ₄ TZO] ⁺	[Ch] ⁺	[Gu] ⁺	[(C ₁) ₆ Gu] ⁺	[P ₆₆₆₍₁₄₎] ⁺	[OC ₂ (C ₁)4iU] ⁺	[SC ₂ (C ₁)4iU] ⁺
[TOS] ⁻	146	93	67	NP	102	42	98	84	63	83	374	IP	31	0- TMP	38	44
[DEP] ⁻	210	57	45	----	60	30	58	50	43	52	165	IP	23	0- TMP	27	31
[DBP] ⁻	483	35	28	----	38	20	38	38	27	33	92	157	18	0- TMP	20	23
[NO ₃] ⁻	233	198	138	----	184	75	147	66	125	165	281	IP	29	0- TMP	40	48
[FeCl ₄] ⁻	381	124	59	----	192	26	210	231	58	127	1627	794	46	TMP	51	66

Obs.: NP – not predicted; TMP – total miscibility predicted; IP – immiscibility predicted.







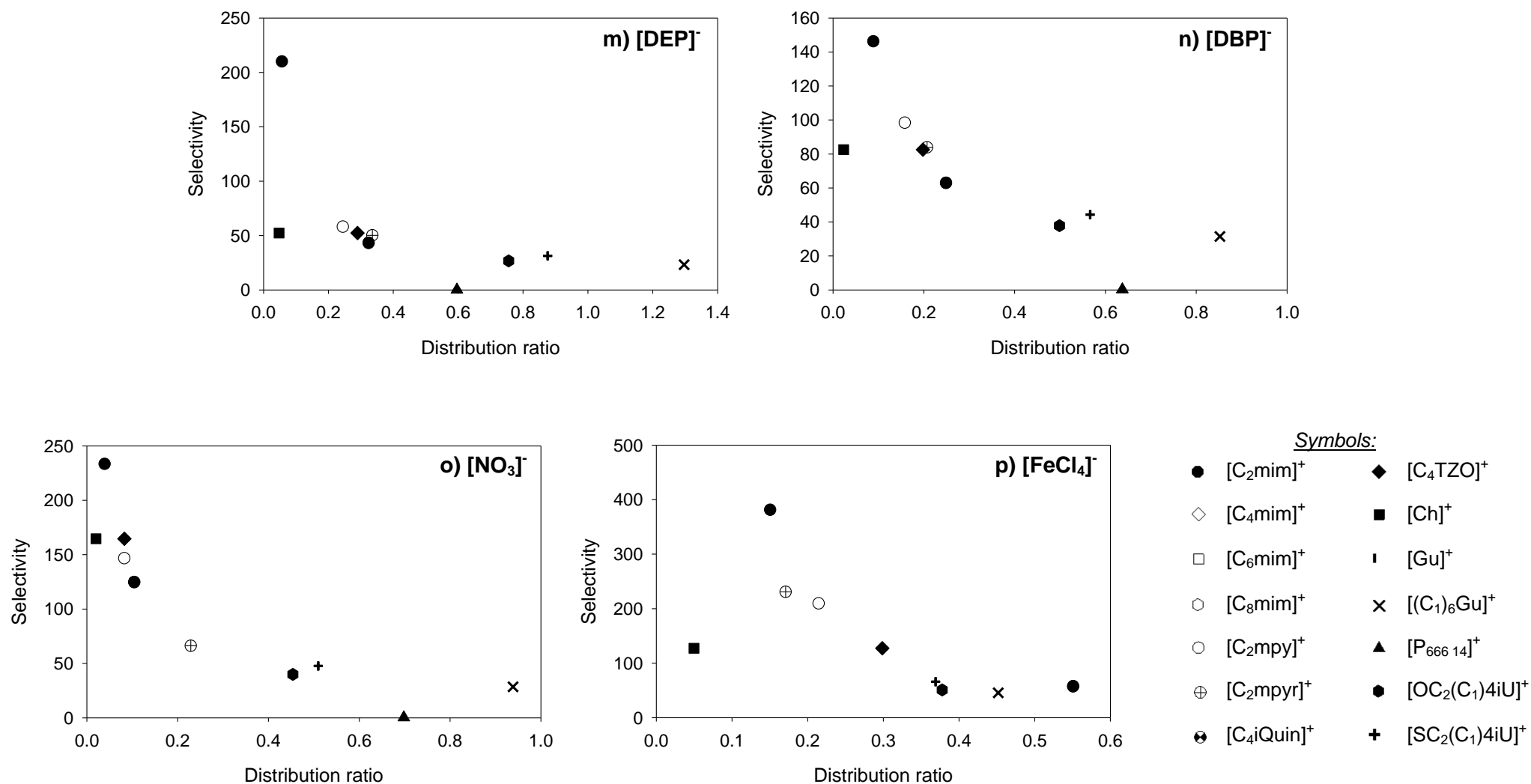
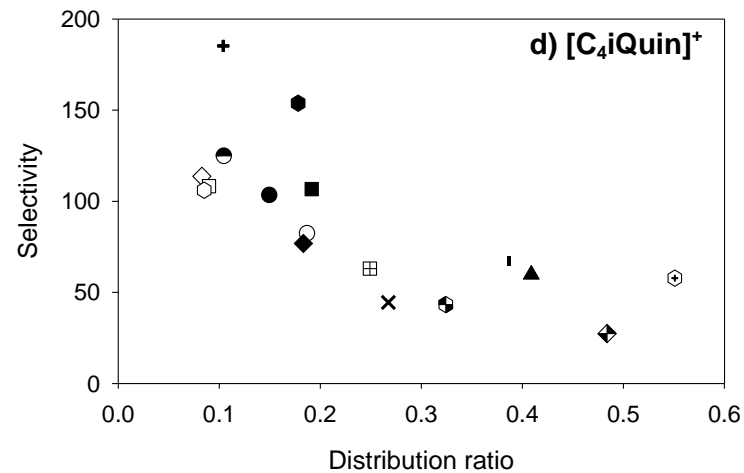
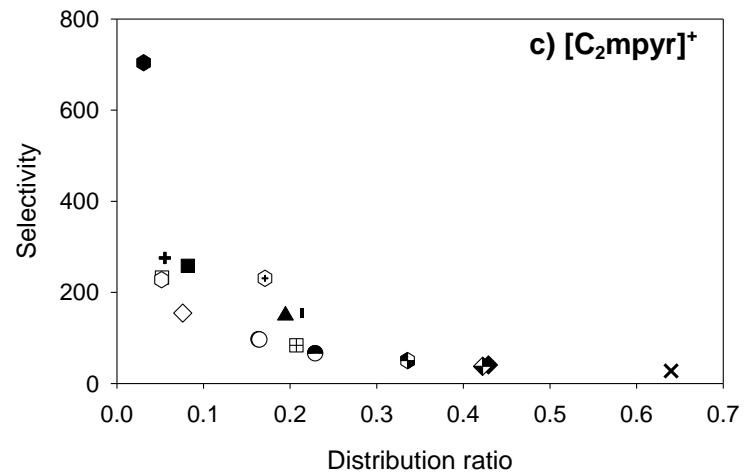
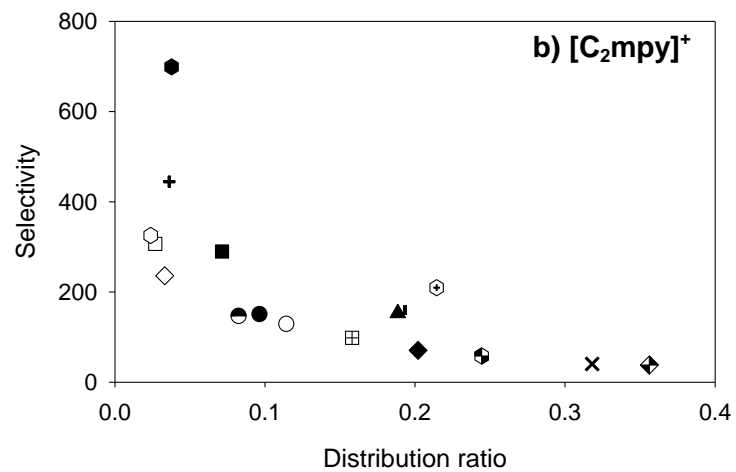
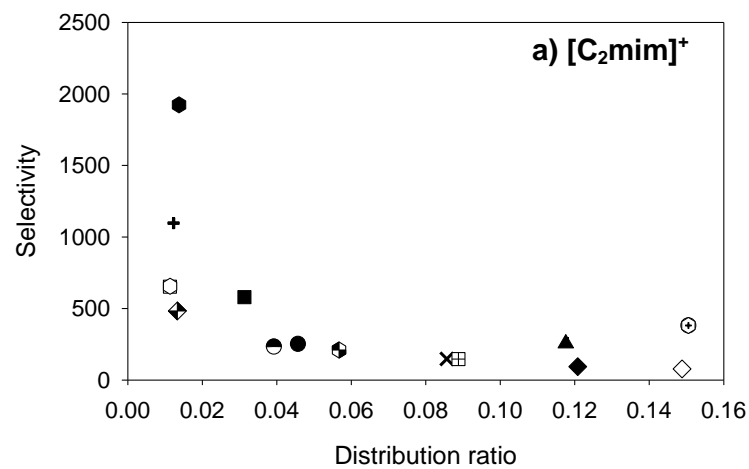
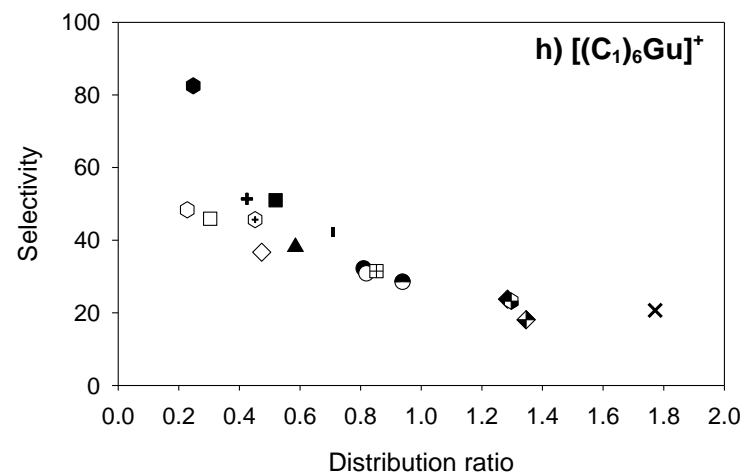
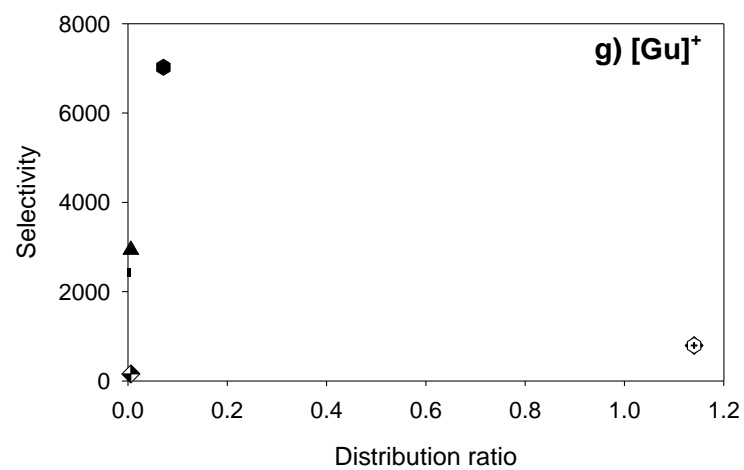
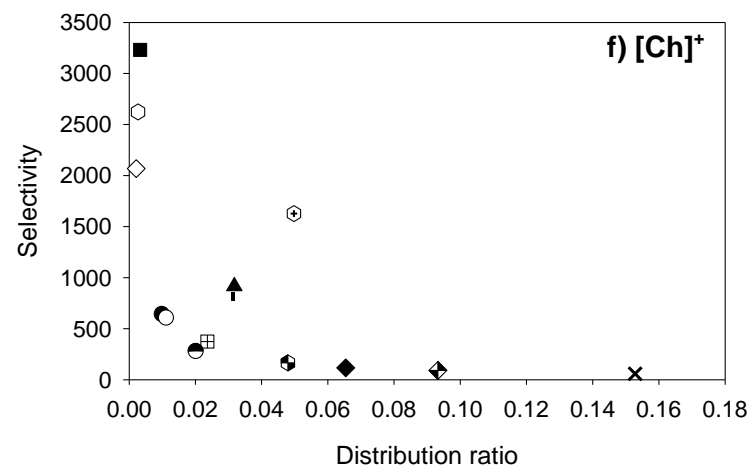
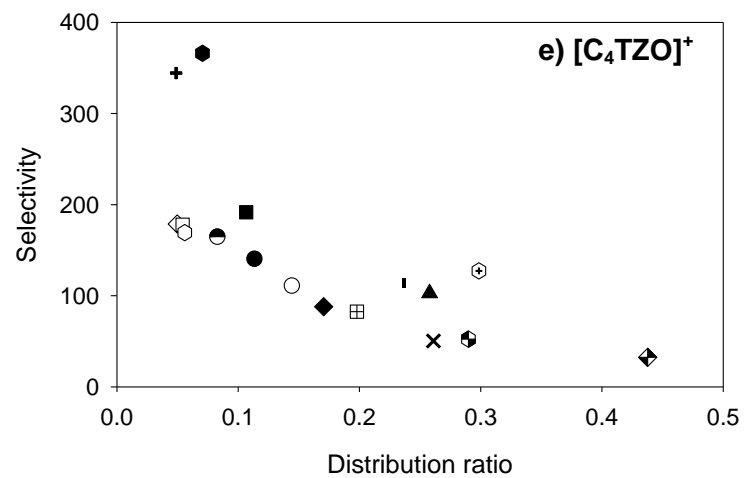


Figure D1 Selectivity versus distribution ratio of 1-hexanethiol in the ternary systems composed of ionic liquids + 1-hexanethiol + *n*-dodecane, at 298.2 K and atmospheric pressure.





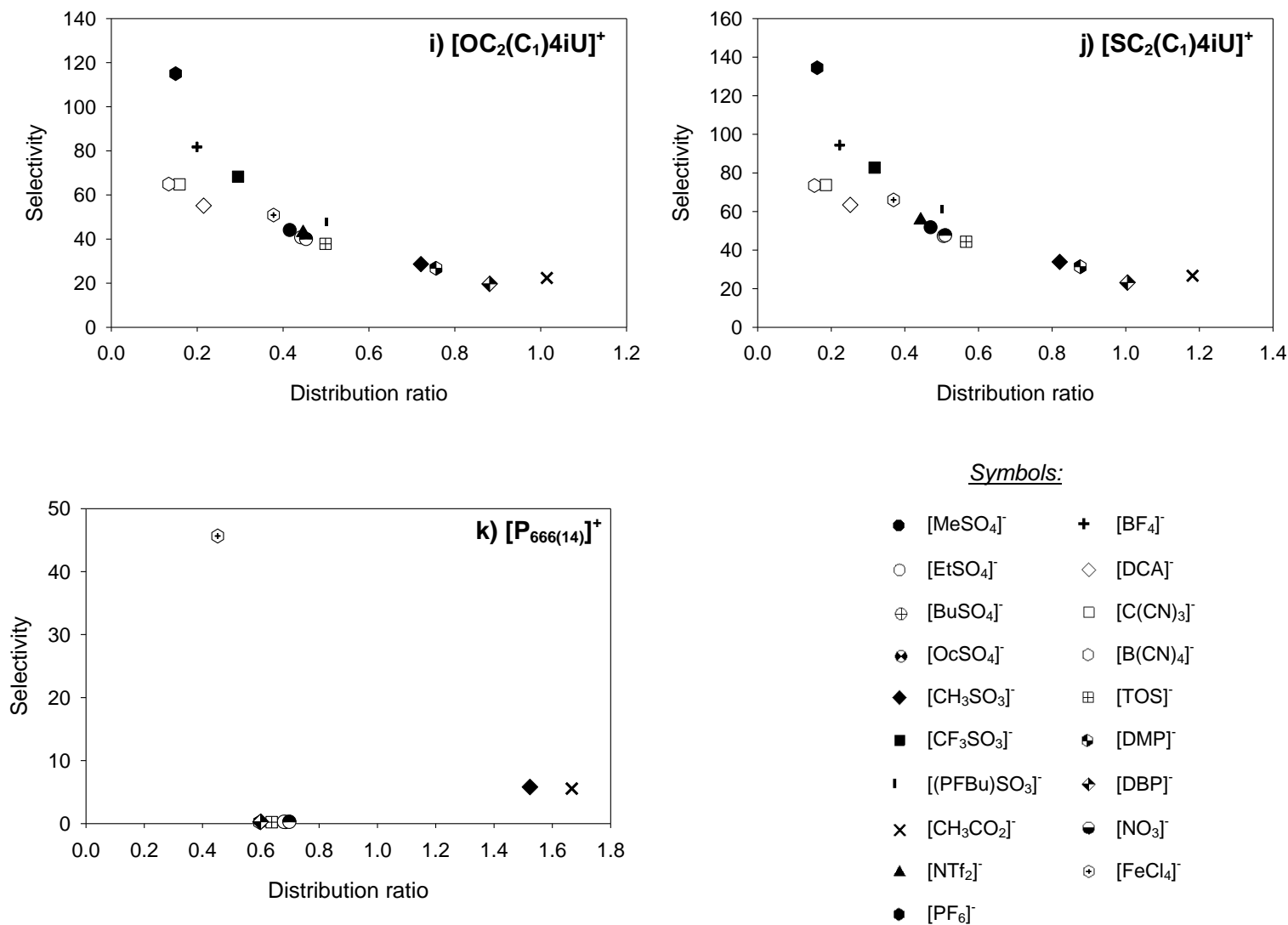


Figure D2 Selectivity *versus* distribution ratio of 1-hexanethiol in the ternary systems composed of ionic liquids + 1-hexanethiol + *n*-dodecane, at 298.2 K and atmospheric pressure.

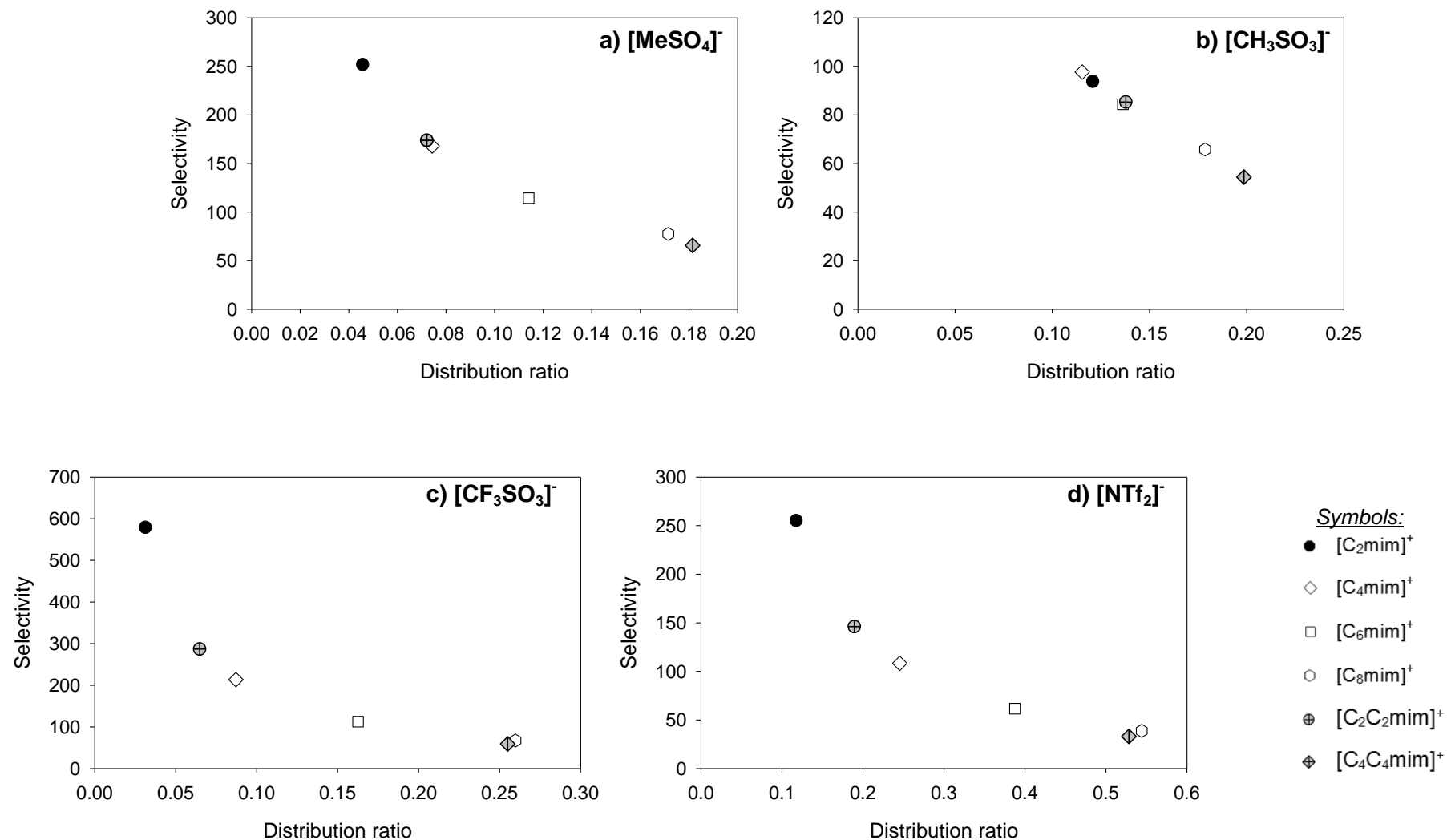


Figure D3 Selectivity versus distribution ratio of 1-hexanethiol in the ternary systems composed of [C_nmim]-based ionic liquids + 1-hexanethiol + *n*-dodecane, at 298.2 K and atmospheric pressure.

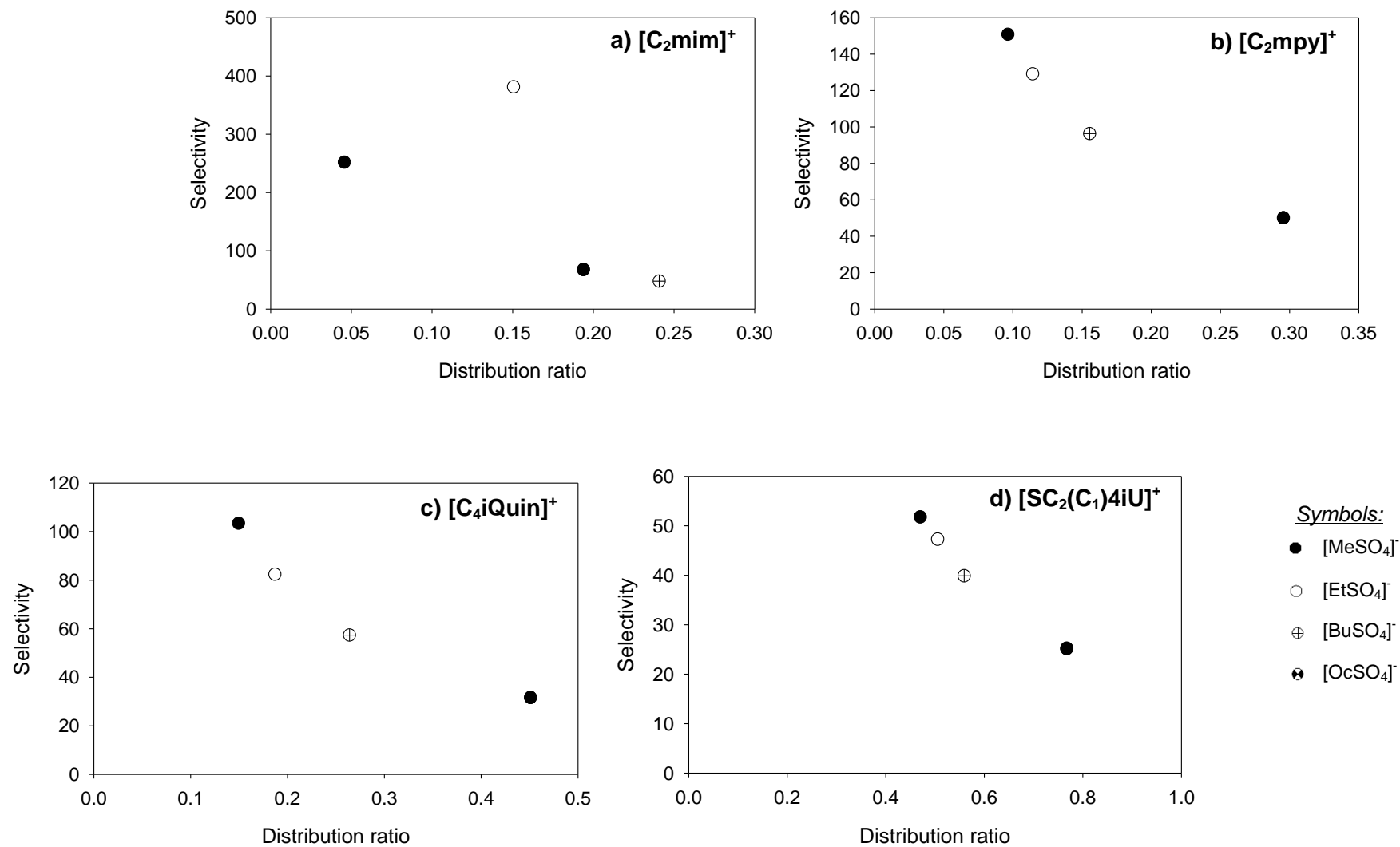


Figure D4 Selectivity *versus* distribution ratio of 1-hexanethiol in the ternary systems composed of [RSO₄]⁻-based ionic liquids + 1-hexanethiol + *n*-dodecane, at 298.2 K and atmospheric pressure.

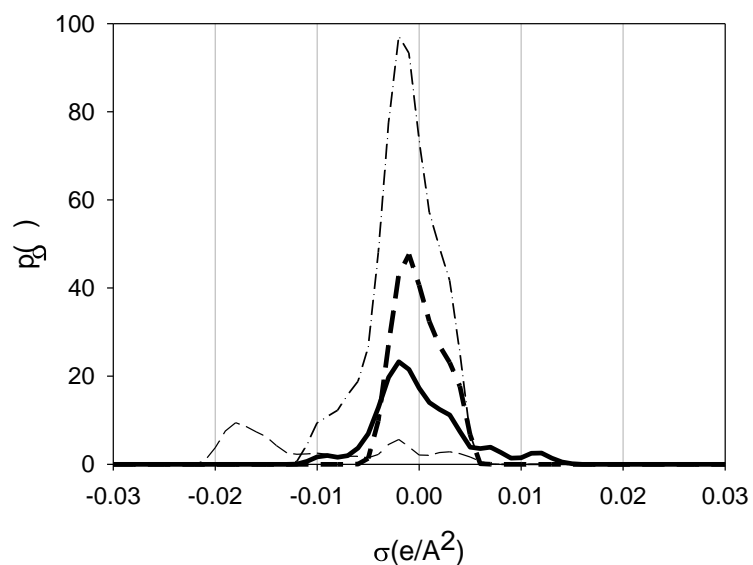


Figure D5 COSMO-RS σ -profiles for the compounds: 1-hexanethiol (solid line), *n*-dodecane (dashed line) and $[P_{666(14)}]^+$ (dot dashed line).

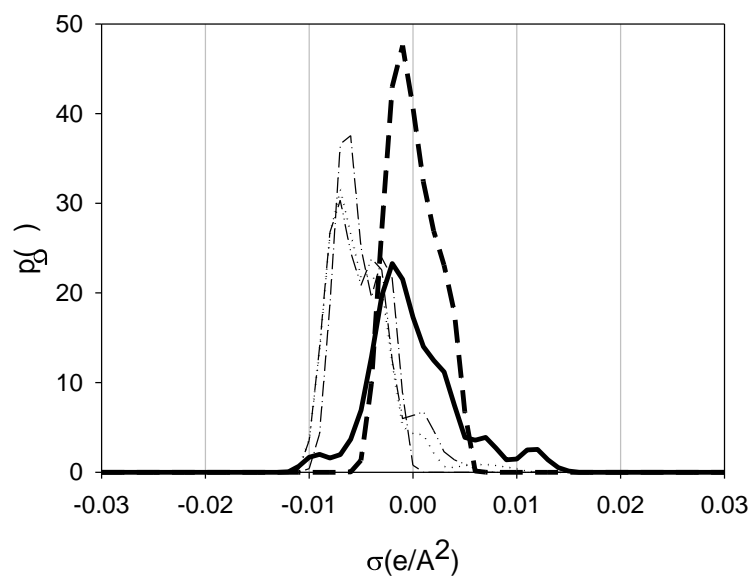


Figure D6 COSMO-RS σ -profiles for the compounds: 1-hexanethiol (solid line), *n*-dodecane (dashed line), and for the ionic liquid cations $[OC_2(C_1)4iU]^+$ (dotted line), $[SC_2(C_1)4iU]^+$ (dot-dot dashed line) and $[(C_1)_6Gu]^+$ (dot dashed line).

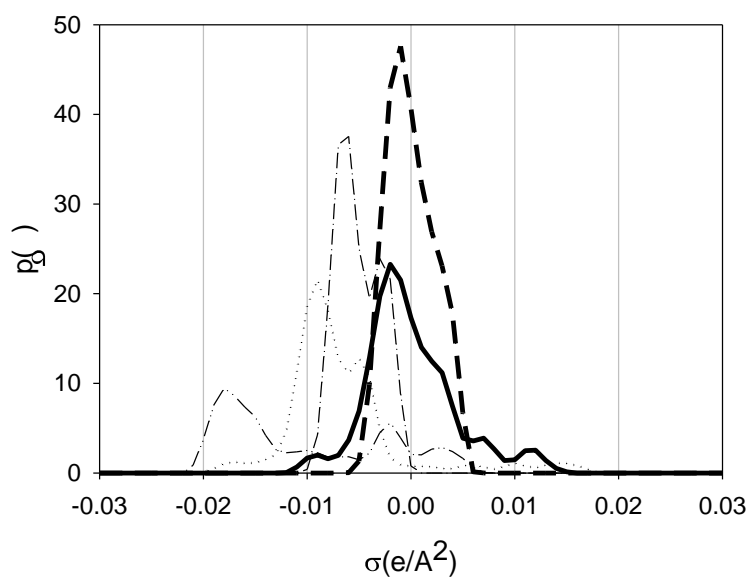


Figure D7 COSMO-RS σ -profiles for the compounds: 1-hexanethiol (solid line), *n*-dodecane (dashed line) and for the ionic liquid cations [Ch]⁺ (dotted line), [Gu]⁺ (dot-dot dashed line) and [(C₁)₆Gu]⁺ (dot dashed line).

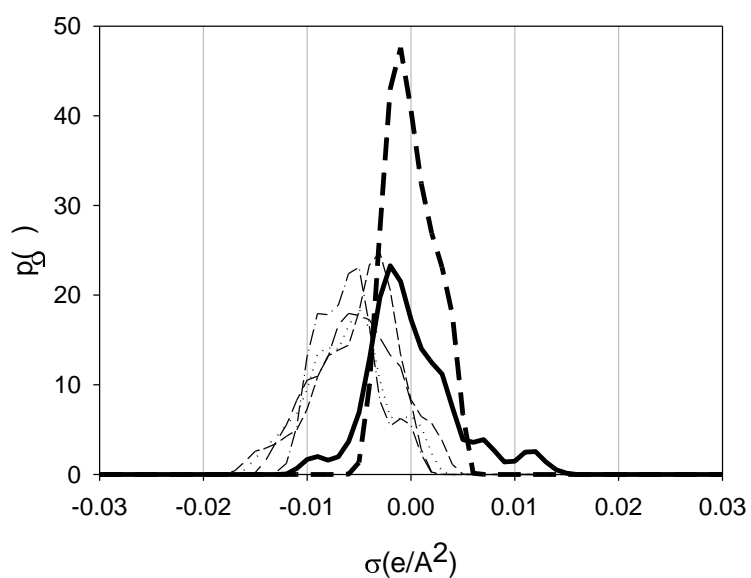


Figure D8 COSMO-RS σ -profiles for the compounds: 1-hexanethiol (solid line), *n*-dodecane (dashed line) and for the ionic liquid cations [C₂mim]⁺ (dotted line), [C₂mpy]⁺ (dot-dot dashed line), [C₂mpyr]⁺ (dot dashed line), [C₄iQuin]⁺ (thin solid line), and [C₄TZO]⁺ (short dashed line).

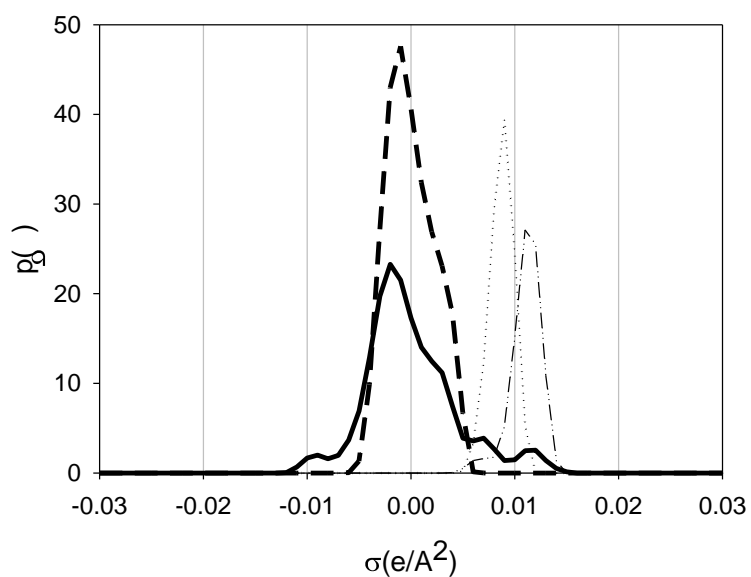


Figure D9 COSMO-RS σ -profiles for the compounds: 1-hexanethiol (solid line), *n*-dodecane (long dashed line), and for the ionic liquid anions $[\text{PF}_6]^-$ (short dashed line) and $[\text{BF}_4]^-$ (dot-dot dashed line).

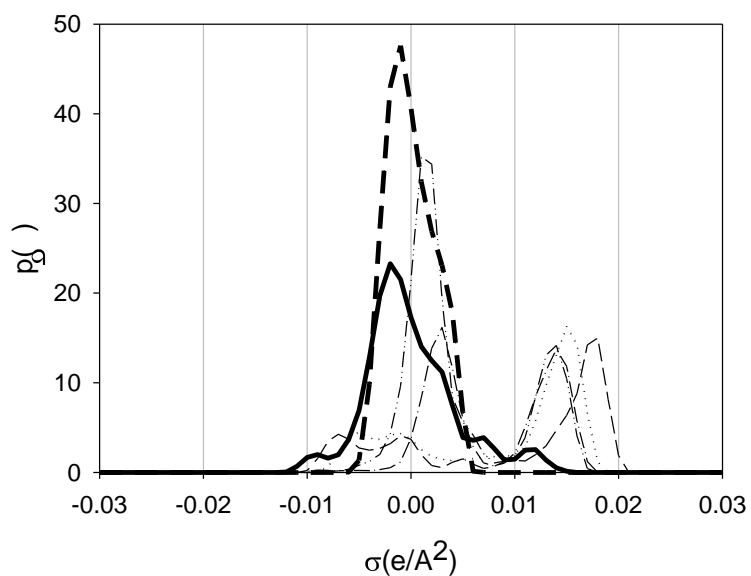


Figure D10 COSMO-RS σ -profiles for the compounds: 1-hexanethiol (solid line), *n*-dodecane (long dashed line) and for the ionic liquid anions $[\text{MeSO}_4]^-$ (dotted line), $[\text{CH}_3\text{SO}_3]^-$ (short dashed line), $[\text{CF}_3\text{SO}_3]^-$ (dot dashed line) and $[(\text{PFBu})\text{SO}_3]^-$ (dot-dot dashed line).

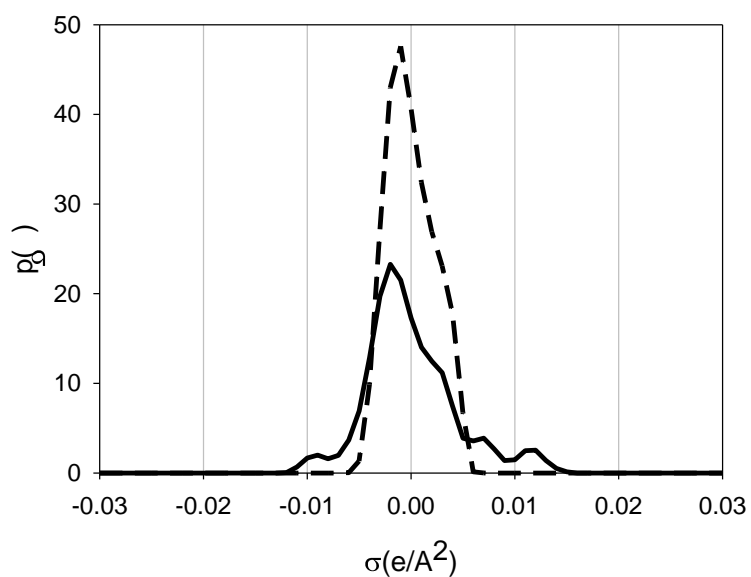


Figure D11 COSMO-RS σ -profiles for the compounds: 1-hexanethiol (solid line), *n*-dodecane (long dashed line) and for the ionic liquid anion $[\text{CH}_3\text{CO}_2]^-$ (thin solid line).

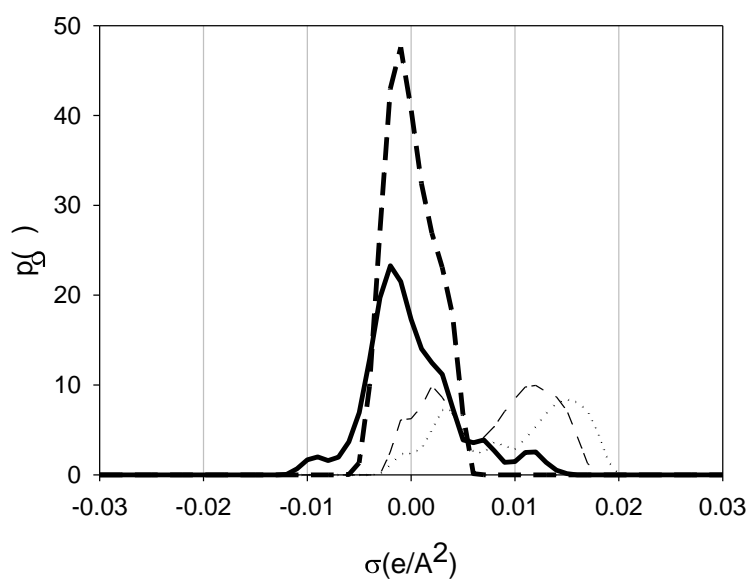


Figure D12 COSMO-RS σ -profiles for the compounds: 1-hexanethiol (solid line), *n*-dodecane (long dashed line), and for the ionic liquid anions $[\text{N}(\text{CN})_2]^-$ (dotted line), $[\text{C}(\text{CN})_3]^-$ (short dashed line) and $[\text{B}(\text{CN})_4]^-$ (thin solid line).

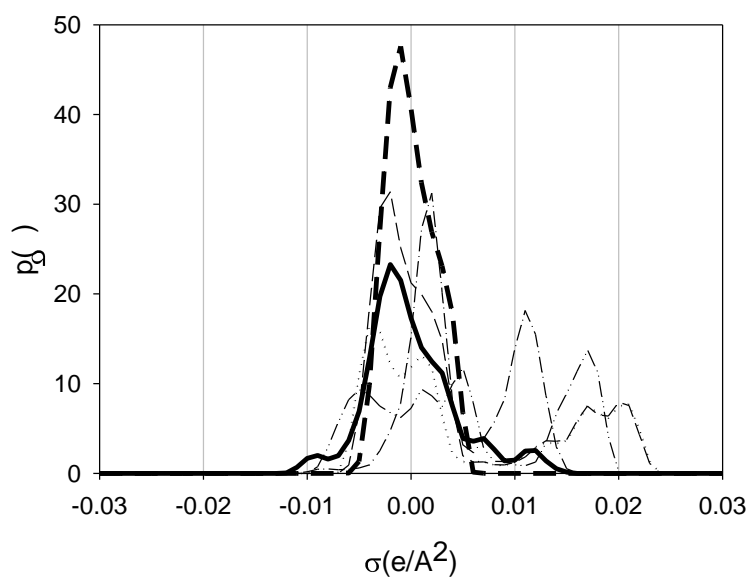


Figure D13 COSMO-RS σ -profiles for the compounds: 1-hexanethiol (solid line), *n*-dodecane (long dashed line), and for the ionic liquid anions [DEP]⁻ (dotted line), [DBP]⁻ (short dashed line), [NTf₂]⁻ (dot dashed line), [TOS]⁻ (dot-dot dashed line) and [FeCl₄]⁻ (thin solid line).

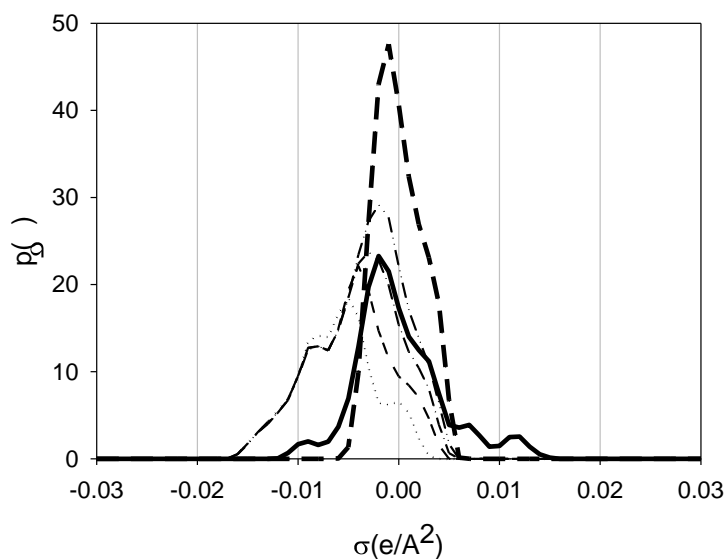


Figure D14 COSMO-RS σ -profiles for the compounds: 1-hexanethiol (solid line), *n*-dodecane (long dashed line), and for the ionic liquid cations [C₂mim]⁺ (dotted line), [C₄mim]⁺ (short dashed line), [C₆mim]⁺ (dot dashed line) and [C₈mim]⁺ (dot-dot dashed line).

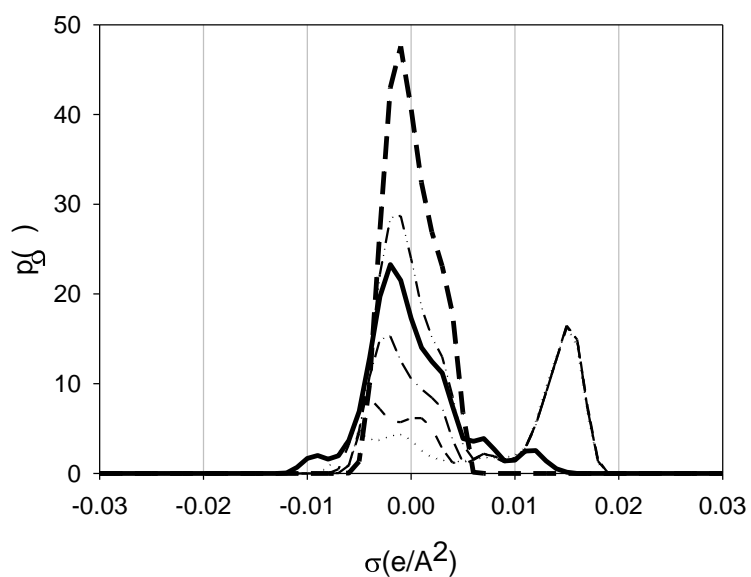


Figure D15 COSMO-RS σ -profiles for the compounds: 1-hexanethiol (solid line), *n*-dodecane (long dashed line), and for the ionic liquid anions [MeSO₄]⁻ (dotted line), [EtSO₄]⁻ (short dashed line), [BuSO₄]⁻ (dot dashed line) and [OcSO₄]⁻ (dot-dot dashed line).

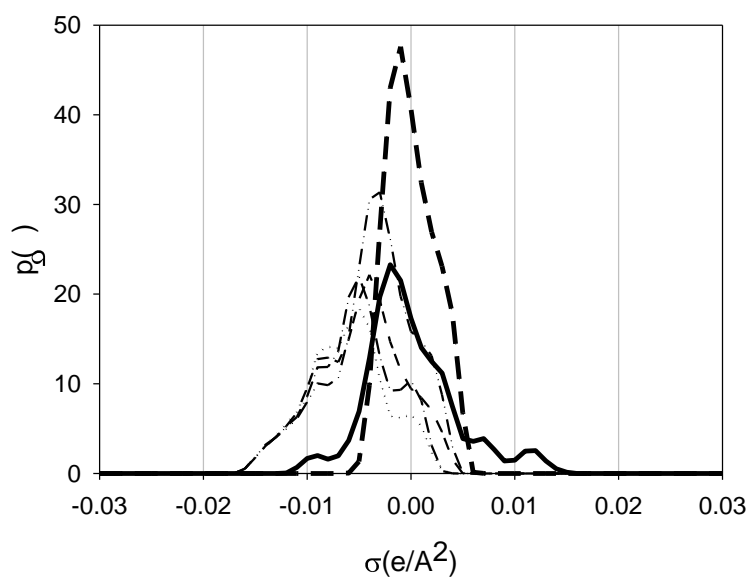


Figure D16 COSMO-RS σ -profiles for the compounds: 1-hexanethiol (solid line), *n*-dodecane (long dashed line), and for the ionic liquid cations [C₂mim]⁺ (dotted line), [C₂C₂im]⁺ (dot dashed line), [C₄mim]⁺ (short dashed line), and [C₄C₄mim]⁺ (dot-dot dashed line).

Table D4 COSMO-RS misfit, hydrogen-bonding and van der Waals energies for the compounds 1-hexanethiol and *n*-dodecane, in the feed model (*n*-dodecane with 2 mol/mol% of 1-hexanethiol) at 298.2 K.

		1-hexanethiol + <i>n</i> -dodecane
1-hexanethiol	E_{MF} (kcal/mol)	1.38795
	E_{HB} (kcal/mol)	-0.00127
	E_{vdW} (kcal/mol)	-9.29809
<i>n</i> -dodecane	E_{MF} (kcal/mol)	0.42834
	E_{HB} (kcal/mol)	0.00000
	E_{vdW} (kcal/mol)	-13.60151

Table D5 a) COSMO-RS misfit, hydrogen-bonding and van der Waals energies for the compounds 1-hexanethiol, *n*-dodecane, and for several [C₂mim]-based ionic liquids combinations in the respective ternary systems at 298.2 K.

		[C ₂ mim] ⁺															
		[MeSO ₄] ⁻	[CH ₃ SO ₃] ⁻	[CF ₃ SO ₃] ⁻	[(PFBu)SO ₃] ⁻	[CH ₃ CO ₂] ⁻	[NTf ₂] ⁻	[PF ₆] ⁻	[BF ₄] ⁻	[N(CN) ₂] ⁻	[C(CN) ₃] ⁻	[B(CN) ₄] ⁻	[TOS] ⁻	[DEP] ⁻	[DBP] ⁻	[NO ₃] ⁻	[FeCl ₄] ⁻
1-hexanethiol	E_{MF} (kcal/mol)	2.55782	2.62863	2.37574	2.26979	2.49283	2.23088	2.42214	2.53459	2.43132	2.38446	2.34889	2.5371	2.51547	2.44307	2.53253	2.23601
	E_{HB} (kcal/mol)	-0.16521	-0.21289	-0.13241	-0.1208	-0.27182	-0.09534	-0.06567	-0.09694	-0.15492	-0.12675	-0.10757	-0.18288	-0.23678	-0.22839	-0.17492	-0.05987
	E_{VDW} (kcal/mol)	-9.17135	-9.19509	-9.0175	-8.83901	-9.22304	-8.85883	-8.9486	-9.05003	-9.10367	-9.07321	-9.03186	-9.18405	-9.19876	-9.20498	-9.14774	-9.47591
<i>n</i> -dodecane	E_{MF} (kcal/mol)	2.81076	2.76034	2.56757	2.36496	2.29493	2.39933	2.80083	2.90318	2.5901	2.58977	2.58188	2.687	2.48027	2.34346	2.72623	2.50145
	E_{HB} (kcal/mol)	0.00000	0.00000	0.00000	0.00000	0.00000	0.00000	0.00000	0.00000	0.00000	0.00000	0.00000	0.00000	0.00000	0.00000	0.00000	0.00000
	E_{VDW} (kcal/mol)	-13.4215	-13.4625	-13.128	-12.7696	-13.4977	-12.8315	-13.0471	-13.2337	-13.376	-13.3183	-13.2504	-13.4307	-13.4628	-13.4769	-13.3946	-13.7419
anion	E_{MF} (kcal/mol)	4.71847	5.38773	3.79905	4.40561	5.14893	4.06777	3.53234	3.68243	3.90759	3.98311	4.14625	6.02923	6.31224	6.98955	3.96031	3.5101
	E_{HB} (kcal/mol)	-2.14734	-3.02229	-1.61431	-1.46247	-4.47742	-0.85255	-0.21034	-0.81124	-2.23068	-1.53068	-1.06666	-2.62202	-3.63538	-3.55814	-2.40153	-0.06841
	E_{VDW} (kcal/mol)	-5.06159	-4.64505	-4.74573	-7.35743	-3.95801	-7.36985	-3.80062	-3.12607	-4.22021	-5.72723	-7.26993	-8.39657	-8.38115	-12.2913	-3.00072	-8.44304
cation	E_{MF} (kcal/mol)	4.07879	4.65995	3.79906	3.76384	5.77313	3.6272	3.63173	3.76317	4.17465	3.89098	3.77035	4.32811	4.9162	4.82531	4.20821	3.59525
	E_{HB} (kcal/mol)	-2.14433	-2.99947	-1.61484	-1.46366	-4.48319	-0.85337	-0.21174	-0.8119	-2.23493	-1.5336	-1.07004	-2.61921	-3.63699	-3.5599	-2.40136	-0.07027
	E_{VDW} (kcal/mol)	-7.427	-7.42934	-7.2923	-7.14139	-7.4704	-7.19208	-7.10358	-7.1735	-7.41464	-7.5087	-7.59999	-7.46009	-7.44199	-7.45221	-7.40665	-8.08254

Table D4 b) COSMO-RS misfit, hydrogen-bonding and van der Waals energies for the compounds 1-hexanethiol, *n*-dodecane and for several [C₄mim]-based ionic liquids combinations in the respective ternary systems at 298.2 K.

		[C ₄ mim] ⁺															
		[MeSO ₄] ⁻	[CH ₃ SO ₃] ⁻	[CF ₃ SO ₃] ⁻	[(PFBu)SO ₃] ⁻	[CH ₃ CO ₂] ⁻	[NTf ₂] ⁻	[PF ₆] ⁻	[BF ₄] ⁻	[N(CN) ₂] ⁻	[C(CN) ₃] ⁻	[B(CN) ₄] ⁻	[TOS] ⁻	[DEP] ⁻	[DBP] ⁻	[NO ₃] ⁻	[FeCl ₄] ⁻
1-hexanethiol	E_{MF} (kcal/mol)	2.51208	2.588	2.33285	2.23333	2.46653	2.19154	2.36801	2.48014	2.39182	2.34307	2.30617	2.49856	2.48521	2.41763	2.48736	2.18937
	E_{HB} (kcal/mol)	-0.16242	-0.21078	-0.12963	-0.11826	-0.27278	-0.09268	-0.06327	-0.09406	-0.15278	-0.12399	-0.10462	-0.18087	-0.23581	-0.22754	-0.17229	-0.0576
	E_{VDW} (kcal/mol)	-9.17364	-9.19611	-9.02775	-8.85659	-9.2232	-8.87549	-8.96126	-9.05714	-9.1068	-9.07848	-9.03973	-9.18589	-9.19975	-9.20567	-9.15104	-9.46854
<i>n</i> -dodecane	E_{MF} (kcal/mol)	2.70504	2.66528	2.46408	2.2752	2.21657	2.30129	2.67197	2.77777	2.491	2.48784	2.47715	2.59596	2.40296	2.27688	2.62013	2.38456
	E_{HB} (kcal/mol)	0.00000	0.00000	0.00000	0.00000	0.00000	0.00000	0.00000	0.00000	0.00000	0.00000	0.00000	0.00000	0.00000	0.00000	0.00000	0.00000
	E_{VDW} (kcal/mol)	-13.4288	-13.4681	-13.1498	-12.8058	-13.5027	-12.8649	-13.0708	-13.248	-13.3844	-13.3295	-13.265	-13.4376	-13.4683	-13.4813	-13.4033	-13.738
anion	E_{MF} (kcal/mol)	4.84949	5.53721	3.88622	4.45355	5.27732	4.09585	3.60067	3.79832	4.02411	4.07399	4.04746	6.14014	6.43104	7.08628	4.10001	3.51222
	E_{HB} (kcal/mol)	-2.08715	-2.95026	-1.56629	-1.41869	-4.40016	-0.82233	-0.20101	-0.78122	-2.18093	-1.48881	-1.6695	-2.55791	-3.55925	-3.48366	-2.34012	-0.06508
	E_{VDW} (kcal/mol)	-5.06376	-4.64673	-4.74576	-7.35766	-3.95905	-7.36589	-3.7972	-3.12315	-4.18251	-5.67929	-5.69764	-8.39809	-8.38407	-12.2953	-2.99884	-8.43639
cation	E_{MF} (kcal/mol)	4.42239	4.97945	4.10907	4.04193	6.00182	3.916	3.98804	4.13128	4.47457	4.20138	4.08731	4.6466	5.19227	5.08333	4.53298	3.90103
	E_{HB} (kcal/mol)	-2.08339	-2.92537	-1.56612	-1.41922	-4.40324	-0.82281	-0.20229	-0.78161	-2.18403	-1.49103	-1.03586	-2.55365	-3.55906	-3.48362	-2.33895	-0.06685
	E_{VDW} (kcal/mol)	-9.39476	-9.40153	-9.22464	-9.02727	-9.44438	-9.08215	-9.03087	-9.12255	-9.34315	-9.42323	-9.49652	-9.42616	-9.41337	-9.42538	-9.36948	-10.0695

Table D4 c) COSMO-RS misfit, hydrogen-bonding and van der Waals energies for the compounds 1-hexanethiol, *n*-dodecane and for several [C₂C₂mim]-based ionic liquids combinations in the respective ternary systems at 298.2 K.

		[C ₂ C ₂ mim] ⁺															
		[MeSO ₄] ⁻	[CH ₃ SO ₃] ⁻	[CF ₃ SO ₃] ⁻	[(PFBu)SO ₃] ⁻	[CH ₃ CO ₂] ⁻	[NTf ₂] ⁻	[PF ₆] ⁻	[BF ₄] ⁻	[N(CN) ₂] ⁻	[C(CN) ₃] ⁻	[B(CN) ₄] ⁻	[TOS] ⁻	[DEP] ⁻	[DBP] ⁻	[NO ₃] ⁻	[FeCl ₄] ⁻
1-hexanethiol	E_{MF} (kcal/mol)	2.5362	2.6166	2.3513	2.2480	2.4961	2.2047	2.3863	2.5020	2.4142	2.3625	2.3238	2.5216	2.5107	2.4400	2.5124	2.2026
	E_{HB} (kcal/mol)	-0.1643	-0.2135	-0.1310	-0.1194	-0.2777	-0.0935	-0.0636	-0.0949	-0.1548	-0.1253	-0.1056	-0.1831	-0.2392	-0.2306	-0.1745	-0.0579
	E_{vdW} (kcal/mol)	-9.1695	-9.1923	-9.0201	-8.8456	-9.2197	-8.8650	-8.9524	-9.0503	-9.1009	-9.0723	-9.0328	-9.1822	-9.1962	-9.2025	-9.1461	-9.4715
<i>n</i> -dodecane	E_{MF} (kcal/mol)	2.7454	2.7084	2.4963	2.3005	2.2525	2.3264	2.7076	2.8175	2.5285	2.5230	2.5104	2.6318	2.4383	2.3078	2.6608	2.4119
	E_{HB} (kcal/mol)	0.0000	0.0000	0.0000	0.0000	0.0000	0.0000	0.0000	0.0000	0.0000	0.0000	0.0000	0.0000	0.0000	0.0000	0.0000	0.0000
	E_{vdW} (kcal/mol)	-13.4212	-13.4611	-13.1355	-12.7849	-13.4965	-12.8454	-13.0552	-13.2362	-13.3755	-13.3198	-13.2542	-13.4306	-13.4620	-13.4758	-13.3947	-13.7384
anion	E_{MF} (kcal/mol)	-2.2798	5.5689	3.8852	4.4594	5.3126	4.0926	3.5800	3.7855	4.0388	4.0819	4.2144	6.1709	6.4797	7.1435	4.1068	3.4953
	E_{HB} (kcal/mol)	4.8618	-2.9437	-1.5676	-1.4207	-4.4096	-0.8231	-0.2004	-0.7792	-2.1926	-1.4955	-1.0373	-2.5552	-3.5568	-3.4817	-2.3397	-0.0648
	E_{vdW} (kcal/mol)	-2.0818	-4.6431	-4.7439	-7.3558	-3.9559	-7.3628	-3.7971	-3.1228	-4.1739	-5.6777	-7.2143	-8.3918	-8.3789	-12.2891	-2.9977	-8.4394
cation	E_{MF} (kcal/mol)	-6.1848	4.7963	3.9021	3.8394	5.8348	3.7034	3.7507	3.9093	4.2933	4.0104	3.8874	4.4528	5.0168	4.9091	4.3389	3.6640
	E_{HB} (kcal/mol)	4.2231	-2.9154	-1.5655	-1.4193	-4.4083	-0.8224	-0.2014	-0.7787	-2.1929	-1.4955	-1.0386	-2.5482	-3.5533	-3.4782	-2.3358	-0.0665
	E_{vdW} (kcal/mol)	-2.0766	-8.3366	-8.1788	-8.0058	-8.3774	-8.0550	-7.9879	-8.0697	-8.2753	-8.3628	-8.4466	-8.3622	-8.3490	-8.3607	-8.3085	-8.9936

Table D4 d) COSMO-RS misfit, hydrogen-bonding and van der Waals energies for the compounds 1-hexanethiol, *n*-dodecane and for several [C₂mpy]⁺-based ionic liquids combinations in the respective ternary systems at 298.2 K.

		[C ₂ mpy] ⁺															
		[MeSO ₄] ⁻	[CH ₃ SO ₃] ⁻	[CF ₃ SO ₃] ⁻	[(PFBu)SO ₃] ⁻	[CH ₃ CO ₂] ⁻	[NTf ₂] ⁻	[PF ₆] ⁻	[BF ₄] ⁻	[N(CN) ₂] ⁻	[C(CN) ₃] ⁻	[B(CN) ₄] ⁻	[TOS] ⁻	[DEP] ⁻	[DBP] ⁻	[NO ₃] ⁻	[FeCl ₄] ⁻
1-hexanethiol	E_{MF} (kcal/mol)	2.56812	2.65707	2.37812	2.27097	2.55431	2.21691	2.39196	2.51908	2.44317	2.38078	2.3344	2.55795	2.55595	2.48246	2.5502	2.20209
	E_{HB} (kcal/mol)	-0.16344	-0.21567	-0.12813	-0.11603	-0.28901	-0.08603	-0.05244	-0.08779	-0.15402	-0.1207	-0.09822	-0.18446	-0.24467	-0.23608	-0.17539	-0.04464
	E_{VDW} (kcal/mol)	-9.16669	-9.18943	-9.01686	-8.84193	-9.21686	-8.86191	-8.94995	-9.04734	-9.09758	-9.06993	-9.03126	-9.17939	-9.1935	-9.19991	-9.14332	-9.47292
<i>n</i> -dodecane	E_{MF} (kcal/mol)	2.80692	2.78081	2.54957	2.34638	2.33271	2.3523	2.7199	2.85287	2.58245	2.55948	2.53238	2.69813	2.5115	2.37568	2.73003	2.41079
	E_{HB} (kcal/mol)	0.00000	0.00000	0.00000	0.00000	0.00000	0.00000	0.00000	0.00000	0.00000	0.00000	0.00000	0.00000	0.00000	0.00000	0.00000	0.00000
	E_{VDW} (kcal/mol)	-13.412	-13.4522	-13.1255	-12.7742	-13.4879	-12.8352	-13.0453	-13.2259	-13.3672	-13.3121	-13.2472	-13.4221	-13.4539	-13.4683	-13.3854	-13.7337
anion	E_{MF} (kcal/mol)	4.95965	5.72623	3.95908	4.54439	5.56662	4.10607	3.54458	3.79552	4.14131	4.12636	4.21426	6.3304	6.70673	6.77531	4.21987	3.438
	E_{HB} (kcal/mol)	-1.62391	-2.31592	-1.2012	-1.07929	-3.46007	-0.62749	-0.16012	-0.61329	-1.62997	-1.10806	-0.76848	-1.98067	-2.77996	-2.75936	-1.81316	-0.05246
	E_{VDW} (kcal/mol)	-5.05175	-4.63606	-4.73955	-7.35285	-3.95058	-7.37388	-3.80316	-3.12874	-4.29837	-5.80806	-7.35597	-8.38186	-8.36953	-8.37635	-2.99643	-8.44461
cation	E_{MF} (kcal/mol)	4.31367	4.94171	3.95532	3.88182	6.06621	3.68146	3.68195	3.91314	4.40497	4.05382	3.87319	4.57345	5.18871	5.07715	4.44881	3.55254
	E_{HB} (kcal/mol)	-1.61858	-2.28887	-1.19882	-1.07767	-3.45629	-0.6266	-0.16084	-0.61229	-1.62973	-1.10777	-0.76903	-1.97347	-2.77457	-2.70644	-1.8088	-0.05373
	E_{VDW} (kcal/mol)	-8.03839	-8.04329	-7.89196	-7.72752	-8.0821	-7.78944	-7.71033	-7.79156	-8.11416	-8.20729	-8.30148	-8.07004	-8.05519	-8.06748	-8.01939	-8.70494

Table D4 e) COSMO-RS misfit, hydrogen-bonding and van der Waals energies for the compounds 1-hexanethiol, *n*-dodecane and for several [C₂mpyr]-based ionic liquids combinations in the respective ternary systems at 298.2 K.

		[C ₂ mpyr] ⁺															
		[MeSO ₄] ⁻	[CH ₃ SO ₃] ⁻	[CF ₃ SO ₃] ⁻	[(PFBu)SO ₃] ⁻	[CH ₃ CO ₂] ⁻	[NTf ₂] ⁻	[PF ₆] ⁻	[BF ₄] ⁻	[N(CN) ₂] ⁻	[C(CN) ₃] ⁻	[B(CN) ₄] ⁻	[TOS] ⁻	[DEP] ⁻	[DBP] ⁻	[NO ₃] ⁻	[FeCl ₄] ⁻
1-hexanethiol	E_{MF} (kcal/mol)	2.64449	2.75561	2.44175	2.32538	2.71243	2.25579	2.42236	2.56943	2.56452	2.47103	2.40346	2.64382	2.66771	2.5874	2.63961	2.22082
	E_{HB} (kcal/mol)	-0.16024	-0.21771	-0.12185	-0.10915	-0.31245	-0.07462	-0.03674	-0.07637	-0.15644	-0.11516	-0.08793	-0.18521	-0.25388	-0.24518	-0.17501	-0.02707
	E_{VDW} (kcal/mol)	-9.16928	-9.19201	-9.01771	-8.84106	-9.21835	-8.86127	-8.95141	-9.04877	-9.08816	-9.06228	-9.02451	-9.18117	-9.19497	-9.20072	-9.1455	-9.4829
<i>n</i> -dodecane	E_{MF} (kcal/mol)	2.96025	2.96755	2.67897	2.45692	2.57036	2.43288	2.78279	2.9575	2.80404	2.73448	2.67085	2.86227	2.70416	2.55542	2.90311	2.44777
	E_{HB} (kcal/mol)	0.00000	0.00000	0.00000	0.00000	0.00000	0.00000	0.00000	0.00000	0.00000	0.00000	0.00000	0.00000	0.00000	0.00000	0.00000	0.00000
	E_{VDW} (kcal/mol)	-13.4416	-13.483	-13.1509	-12.7939	-13.5202	-12.8552	-13.0698	-13.2525	-13.3869	-13.3303	-13.2639	-13.4492	-13.4818	-13.4934	-13.4161	-13.7679
anion	E_{MF} (kcal/mol)	5.13228	6.02818	4.09309	4.70333	6.13348	4.15531	3.49652	3.81179	4.42536	4.33175	4.36603	6.63787	7.17664	7.92015	4.42629	3.37082
	E_{HB} (kcal/mol)	-0.88656	-1.26141	-0.64229	-0.56952	-1.78661	-0.34784	-0.09845	-0.35759	-0.83622	-0.58471	-0.41519	-1.04557	-1.45781	-1.40992	-0.96952	-0.03336
	E_{VDW} (kcal/mol)	-5.05776	-4.64115	-4.73585	-7.33966	-3.95416	-7.33623	-3.78278	-3.11178	-4.06117	-5.52631	-7.00584	-8.38163	-8.38091	-12.2973	-2.98095	-8.43112
cation	E_{MF} (kcal/mol)	4.51679	5.27876	4.08397	3.99521	6.62522	3.67941	3.59569	3.93919	4.57602	4.13131	3.89463	4.8479	5.58978	5.47074	4.70112	3.41421
	E_{HB} (kcal/mol)	-0.88421	-1.23471	-0.64151	-0.56915	-1.7898	-0.34732	-0.09883	-0.35676	-0.83744	-0.58494	-0.41535	-1.04178	-1.45763	-1.41009	-0.9682	-0.03409
	E_{VDW} (kcal/mol)	-7.60087	-7.60689	-7.44978	-7.28307	-7.6434	-7.31765	-7.25035	-7.33646	-7.45128	-7.49029	-7.50838	-7.62433	-7.6195	-7.63455	-7.56392	-8.2199

Table D4 f) COSMO-RS misfit, hydrogen-bonding and van der Waals energies for the compounds 1-hexanethiol, *n*-dodecane, and several [C₄iQuin]-based ionic liquids combinations in the respective ternary systems at 298.2 K.

		[C ₄ iQuin] ⁺															
		[MeSO ₄] ⁻	[CH ₃ SO ₃] ⁻	[CF ₃ SO ₃] ⁻	[(PFBu)SO ₃] ⁻	[CH ₃ CO ₂] ⁻	[NTf ₂] ⁻	[PF ₆] ⁻	[BF ₄] ⁻	[N(CN) ₂] ⁻	[C(CN) ₃] ⁻	[B(CN) ₄] ⁻	[TOS] ⁻	[DEP] ⁻	[DBP] ⁻	[NO ₃] ⁻	[FeCl ₄] ⁻
1-hexanethiol	E_{MF} (kcal/mol)	2.49524	2.58395	2.31434	2.21808	2.49526	2.16492	2.32125	2.44153	2.37962	2.31895	2.27463	2.49308	2.49648	2.43094	2.47615	2.14573
	E_{HB} (kcal/mol)	-0.15844	-0.20994	-0.12406	-0.11259	-0.28312	-0.08376	-0.05184	-0.08518	-0.14925	-0.1167	-0.09511	-0.1796	-0.23903	-0.23084	-0.16989	-0.04475
	E_{VDW} (kcal/mol)	-9.16226	-9.183	-9.02464	-8.86168	-9.20874	-8.8802	-8.96162	-9.05079	-9.09637	-9.07213	-9.03766	-9.17474	-9.1877	-9.19435	-9.14037	-9.45082
<i>n</i> -dodecane	E_{MF} (kcal/mol)	2.65523	2.63608	2.40857	2.22724	2.21662	2.22921	2.55779	2.68482	2.44493	2.42236	2.39685	2.56495	2.39396	2.27327	2.57676	2.27243
	E_{HB} (kcal/mol)	0.00000	0.00000	0.00000	0.00000	0.00000	0.00000	0.00000	0.00000	0.00000	0.00000	0.00000	0.00000	0.00000	0.00000	0.00000	0.00000
	E_{VDW} (kcal/mol)	-13.3985	-13.4355	-13.1349	-12.8081	-13.4694	-12.8649	-13.0586	-13.2243	-13.3566	-13.3069	-13.2485	-13.4095	-13.4391	-13.4539	-13.3734	-13.702
anion	E_{MF} (kcal/mol)	5.06798	5.82944	4.03804	4.57305	5.64017	4.14149	3.64161	3.9259	4.28379	4.24756	4.31248	6.39647	6.75648	7.40978	4.3378	3.4697
	E_{HB} (kcal/mol)	-1.64761	-2.3566	-1.22026	-1.09856	-3.54018	-0.63417	-0.15903	-0.61539	-1.67486	-1.13108	-0.77993	-2.01861	-2.84051	-2.77375	-1.84659	-0.05178
	E_{VDW} (kcal/mol)	-5.05324	-4.63722	-4.74351	-7.36266	-3.95067	-7.37938	-3.80343	-3.12733	-4.26256	-5.78223	-7.3442	-8.38216	-8.36723	-12.271	-3.00338	-8.43935
cation	E_{MF} (kcal/mol)	4.88936	5.47712	4.5043	4.39531	6.48152	4.23172	4.3216	4.54512	5.0064	4.68805	4.52918	5.12042	5.67199	5.54209	4.99597	4.14417
	E_{HB} (kcal/mol)	-1.64572	-2.33229	-1.21939	-1.09825	-3.5421	-0.634	-0.15992	-0.61519	-1.67657	-1.1321	-0.78147	-2.01671	-2.83954	-2.77294	-1.84479	-0.05311
	E_{VDW} (kcal/mol)	-11.2855	-11.296	-11.0924	-10.8654	-11.3393	-10.936	-10.9022	-11.0109	-11.3209	-11.4226	-11.5327	-11.3187	-11.3081	-11.3215	-11.2674	-12.0022

Table D4 g) COSMO-RS misfit, hydrogen-bonding and van der Waals energies for the compounds 1-hexanethiol, *n*-dodecane and several [C₄TZO]-based ionic liquids combinations in the respective ternary systems at 298.2 K.

		[C ₄ TZO] ⁺															
		[MeSO ₄] ⁻	[CH ₃ SO ₃] ⁻	[CF ₃ SO ₃] ⁻	[(PFBu)SO ₃] ⁻	[CH ₃ CO ₂] ⁻	[NTf ₂] ⁻	[PF ₆] ⁻	[BF ₄] ⁻	[N(CN) ₂] ⁻	[C(CN) ₃] ⁻	[B(CN) ₄] ⁻	[TOS] ⁻	[DEP] ⁻	[DBP] ⁻	[NO ₃] ⁻	[FeCl ₄] ⁻
1-hexanethiol	E_{MF} (kcal/mol)	2.51948	2.61493	2.33007	2.22888	2.52753	2.17975	2.34457	2.45981	2.38649	2.32948	2.28846	2.51494	2.52183	2.45148	2.49877	2.16922
	E_{HB} (kcal/mol)	-0.15837	-0.21001	-0.12453	-0.11339	-0.2829	-0.08755	-0.05871	-0.08806	-0.14755	-0.1178	-0.09863	-0.17897	-0.23855	-0.23006	-0.16877	-0.05408
	E_{VDW} (kcal/mol)	-9.2535	-9.27635	-9.10846	-8.93131	-9.3055	-8.95061	-9.04289	-9.13983	-9.18665	-9.15669	-9.11618	-9.25971	-9.27353	-9.27371	-9.23526	-9.54272
<i>n</i> -dodecane	E_{MF} (kcal/mol)	2.69709	2.68342	2.43777	2.24703	2.25982	2.26084	2.60702	2.71956	2.45389	2.43924	2.42221	2.59996	2.43165	2.30329	2.61561	2.32617
	E_{HB} (kcal/mol)	0.00000	0.00000	0.00000	0.00000	0.00000	0.00000	0.00000	0.00000	0.00000	0.00000	0.00000	0.00000	0.00000	0.00000	0.00000	0.00000
	E_{VDW} (kcal/mol)	-13.5289	-13.5699	-13.2512	-12.9005	-13.6083	-12.9592	-13.1731	-13.3513	-13.4844	-13.4261	-13.3587	-13.5306	-13.5619	-13.5671	-13.5088	-13.8298
anion	E_{MF} (kcal/mol)	5.00505	5.74648	3.98252	4.53477	5.4751	4.14245	3.62223	3.86723	4.10297	4.13227	4.25574	6.31751	6.65403	7.31215	4.25165	3.50017
	E_{HB} (kcal/mol)	-1.84166	-2.59387	-1.41562	-1.29327	-3.96493	-0.74268	-0.1713	-0.6775	-2.02181	-1.37784	-0.95414	-2.278	-3.17119	-3.11395	-2.10047	-0.0547
	E_{VDW} (kcal/mol)	-5.13223	-4.70864	-4.8718	-7.55529	-4.01486	-7.54461	-4.02453	-3.32005	-4.31849	-5.80628	-7.32005	-8.48928	-8.46564	-12.3963	-3.04598	-8.67605
cation	E_{MF} (kcal/mol)	4.42465	4.97708	4.06815	3.98046	5.91507	3.85813	3.9478	4.11831	4.38258	4.11507	4.00357	4.62637	5.15366	5.03148	4.51991	3.83612
	E_{HB} (kcal/mol)	-1.83201	-2.55871	-1.40751	-1.28635	-3.94741	-0.73906	-0.17166	-0.67476	-2.01277	-1.37181	-0.95171	-2.26543	-3.15528	-3.09811	-2.08826	-0.05611
	E_{VDW} (kcal/mol)	-9.95109	-9.96147	-9.81672	-9.65174	-10.0066	-9.69	-9.70918	-9.79168	-9.96287	-10.0167	-10.0641	-9.98396	-9.96684	-9.97448	-9.92003	-10.7586

Table D4 h) COSMO-RS misfit, hydrogen-bonding and van der Waals energies for the compounds 1-hexanethiol, *n*-dodecane, and several [Ch]-based ionic liquids combinations in the respective ternary systems at 298.2 K.

		[Ch] ⁺															
		[MeSO ₄] ⁻	[CH ₃ SO ₃] ⁻	[CF ₃ SO ₃] ⁻	[(PFBu)SO ₃] ⁻	[CH ₃ CO ₂] ⁻	[NTf ₂] ⁻	[PF ₆] ⁻	[BF ₄] ⁻	[N(CN) ₂] ⁻	[C(CN) ₃] ⁻	[B(CN) ₄] ⁻	[TOS] ⁻	[DEP] ⁻	[DBP] ⁻	[NO ₃] ⁻	[FeCl ₄] ⁻
1-hexanethiol	E_{MF} (kcal/mol)	2.60191	2.63885	2.43659	2.32733	2.46746	2.30929	2.52881	2.62099	2.5051	2.46997	2.442	2.56009	2.50572	2.43039	2.57084	2.34173
	E_{HB} (kcal/mol)	-0.17205	-0.20837	-0.14636	-0.13613	-0.23904	-0.12801	-0.13104	-0.13415	-0.16043	-0.14264	-0.1337	-0.18162	-0.22161	-0.21381	-0.17633	-0.13691
	E_{VDW} (kcal/mol)	-9.16076	-9.18607	-9.00065	-8.81862	-9.21273	-8.83815	-8.93019	-9.03878	-9.09479	-9.06127	-9.01705	-9.17432	-9.18981	-9.19676	-9.1359	-9.46119
<i>n</i> -dodecane	E_{MF} (kcal/mol)	2.97175	2.88787	2.7544	2.53985	2.45067	2.6084	3.07088	3.13268	2.81949	2.82544	2.82678	2.82131	2.59286	2.4421	2.89407	2.77235
	E_{HB} (kcal/mol)	0.00000	0.00000	0.00000	0.00000	0.00000	0.00000	0.00000	0.00000	0.00000	0.00000	0.00000	0.00000	0.00000	0.00000	0.00000	0.00000
	E_{VDW} (kcal/mol)	-13.4232	-13.4653	-13.1189	-12.7514	-13.4978	-12.8139	-13.039	-13.2367	-13.3745	-13.3143	-13.2433	-13.4313	-13.4637	-13.4777	-13.3952	-13.7401
anion	E_{MF} (kcal/mol)	4.18135	4.69793	3.44853	4.135	4.48896	3.95479	3.42478	3.37919	3.50259	3.72216	4.01903	5.4476	5.60866	6.3138	3.39891	3.56844
	E_{HB} (kcal/mol)	-4.45574	-6.0507	-3.48859	-3.22344	-9.00948	-1.91184	-0.37381	-1.5848	-5.08434	-3.63147	-2.59954	-5.43475	-7.38076	-7.27049	-5.13534	-0.11563
	E_{VDW} (kcal/mol)	-5.05258	-4.64084	-4.73346	-7.33922	-3.95386	-7.29903	-3.77953	-3.10668	-3.85495	-5.32629	-6.82688	-8.37748	-8.37525	-12.2876	-2.97785	-8.42279
cation	E_{MF} (kcal/mol)	4.17859	4.79151	3.99038	4.02714	6.05831	3.87855	3.81648	3.87085	4.31769	4.06136	3.98168	4.50159	5.13873	5.10275	4.33413	3.89132
	E_{HB} (kcal/mol)	-4.91718	-6.3428	-4.15354	-3.93408	-9.25309	-3.07177	-2.19587	-2.80049	-5.54106	-4.33612	-3.60406	-5.77267	-7.62477	-7.50621	-5.54742	-2.16454
	E_{VDW} (kcal/mol)	-6.75697	-6.76227	-6.64448	-6.51865	-6.81512	-6.51242	-6.44719	-6.49378	-6.39994	-6.46689	-6.52313	-6.7857	-6.78155	-6.79658	-6.72613	-7.41486

Table D4 i) COSMO-RS misfit, hydrogen-bonding and van der Waals energies for the compounds 1-hexanethiol, *n*-dodecane and for several [Gu]-based ionic liquids combinations in the respective ternary systems at 298.2 K.

		[Gu] ⁺															
		[MeSO ₄] ⁻	[CH ₃ SO ₃] ⁻	[CF ₃ SO ₃] ⁻	[(PFBu)SO ₃] ⁻	[CH ₃ CO ₂] ⁻	[NTf ₂] ⁻	[PF ₆] ⁻	[BF ₄] ⁻	[N(CN) ₂] ⁻	[C(CN) ₃] ⁻	[B(CN) ₄] ⁻	[TOS] ⁻	[DEP] ⁻	[DBP] ⁻	[NO ₃] ⁻	[FeCl ₄] ⁻
1-hexanethiol	E_{MF} (kcal/mol)	2.11639	2.03394	2.02978	1.97457	1.75147	2.1123	2.51084	2.37507	2.02325	2.12377	2.22384	2.03068	1.8985	1.85998	2.02988	2.45655
	E_{HB} (kcal/mol)	-0.2088	-0.18883	-0.23784	-0.23732	-0.151	-0.28907	-0.33901	-0.27532	-0.22075	-0.25767	-0.29305	-0.18086	-0.16972	-0.16343	-0.20927	-0.37897
	E_{VDW} (kcal/mol)	-9.20553	-9.23391	-9.02508	-8.82395	-9.26126	-8.84204	-8.93574	-9.07072	-9.15098	-9.09837	-9.03289	-9.21882	-9.23433	-9.24033	-9.17547	-9.47976
<i>n</i> -dodecane	E_{MF} (kcal/mol)	1.96436	1.72415	1.88208	1.77452	1.29612	2.11115	2.89086	2.527	1.85845	2.07085	2.29888	1.7875	1.5007	1.4159	1.80516	2.85151
	E_{HB} (kcal/mol)	0.00000	0.00000	0.00000	0.00000	0.00000	0.00000	0.00000	0.00000	0.00000	0.00000	0.00000	0.00000	0.00000	0.00000	0.00000	0.00000
	E_{VDW} (kcal/mol)	-13.5121	-13.5551	-13.1723	-12.7661	-13.5863	-12.8329	-13.08	-13.3161	-13.4568	-13.3783	-13.2811	-13.5124	-13.5447	-13.5559	-13.4789	-13.8042
anion	E_{MF} (kcal/mol)	3.02908	2.63351	2.69364	3.22275	1.51663	4.0995	4.40852	3.56108	2.3975	3.27781	4.15679	3.40877	2.85096	3.23987	2.12964	5.03898
	E_{HB} (kcal/mol)	-11.9346	-15.9356	-9.46581	-8.85181	-20.9829	-5.46498	-1.2023	-4.69198	-13.2642	-9.76455	-7.12996	-14.4911	-18.5269	-18.3262	-12.8471	-0.37916
	E_{VDW} (kcal/mol)	-5.27047	-4.82748	-4.88677	-7.48302	-4.10268	-7.38413	-3.7772	-3.09324	-3.26253	-4.69912	-6.15252	-8.69384	-8.58738	-12.4979	-3.1378	-8.4176
cation	E_{MF} (kcal/mol)	1.61001	1.41351	2.15617	2.38968	2.19348	3.16882	3.74574	2.55695	2.01309	2.47084	3.07087	1.51141	1.60899	1.62588	1.64639	4.74028
	E_{HB} (kcal/mol)	-11.9273	-15.9173	-9.4717	-8.85947	-20.9852	-5.4701	-1.20691	-4.6944	-13.2682	-9.76978	-7.13501	-14.4886	-18.521	-18.3211	-12.8433	-0.38703
	E_{VDW} (kcal/mol)	-4.44248	-4.40938	-4.34991	-4.27084	-4.4567	-4.19419	-4.01518	-3.98321	-3.27436	-3.32847	-3.35514	-4.53953	-4.44303	-4.42998	-4.39135	-4.91719

Table D4 j) COSMO-RS misfit, hydrogen-bonding and van der Waals energies for the compounds 1-hexanethiol, *n*-dodecane and for several [(C₁)₆Gu]-based ionic liquids combinations in the respective ternary systems at 298.2 K.

		[(C ₁) ₆ Gu] ⁺															
		[MeSO ₄] ⁻	[CH ₃ SO ₃] ⁻	[CF ₃ SO ₃] ⁻	[(PFBu)SO ₃] ⁻	[CH ₃ CO ₂] ⁻	[NTf ₂] ⁻	[PF ₆] ⁻	[BF ₄] ⁻	[N(CN) ₂] ⁻	[C(CN) ₃] ⁻	[B(CN) ₄] ⁻	[TOS] ⁻	[DEP] ⁻	[DBP] ⁻	[NO ₃] ⁻	[FeCl ₄] ⁻
1-hexanethiol	<i>E</i> _{MF} (kcal/mol)	2.66467	2.85199	2.43041	2.3095	3.02102	2.20147	2.33509	2.51325	2.5852	2.43912	2.3441	2.70424	2.82566	2.73696	2.68741	2.12964
	<i>E</i> _{HB} (kcal/mol)	-0.15406	-0.22262	-0.11159	-0.09859	-0.36834	-0.05807	-0.01638	-0.05866	-0.1531	-0.10202	-0.07065	-0.18712	-0.27458	-0.26518	-0.17432	-0.00618
	<i>E</i> _{VdW} (kcal/mol)	-9.15763	-9.1759	-9.01714	-8.84966	-9.19624	-8.87054	-8.95611	-9.04303	-9.07068	-9.05385	-9.02291	-9.16877	-9.17854	-9.18507	-9.13333	-9.47716
<i>n</i> -dodecane	<i>E</i> _{MF} (kcal/mol)	2.92044	3.0384	2.58094	2.35483	2.83183	2.25858	2.5387	2.77902	2.74104	2.59216	2.47996	2.88252	2.84318	2.68957	2.89623	2.19047
	<i>E</i> _{HB} (kcal/mol)	0.00000	0.00000	0.00000	0.00000	0.00000	0.00000	0.00000	0.00000	0.00000	0.00000	0.00000	0.00000	0.00000	0.00000	0.00000	0.00000
	<i>E</i> _{VdW} (kcal/mol)	-13.4239	-13.4615	-13.1515	-12.8118	-13.4971	-12.8714	-13.073	-13.24	-13.3686	-13.3197	-13.2605	-13.4327	-13.4623	-13.4747	-13.3982	-13.7555
anion	<i>E</i> _{MF} (kcal/mol)	5.885	7.12321	4.57203	5.09473	7.65404	4.28397	3.595	4.18802	5.08762	4.72429	4.56106	7.56441	8.50295	9.26401	5.2445	3.24328
	<i>E</i> _{HB} (kcal/mol)	-0.03559	-0.07636	-0.02526	-0.02217	-0.0702	-0.014	-0.00427	-0.01485	-0.03133	-0.0223	-0.01615	-0.04459	-0.056	-0.05369	-0.03818	-0.0015
	<i>E</i> _{VdW} (kcal/mol)	-5.04763	-4.62884	-4.73056	-7.33616	-3.94515	-7.35147	-3.78867	-3.118	-4.25934	-5.7134	-7.18486	-8.36692	-8.36323	-12.2754	-2.97799	-8.43282
cation	<i>E</i> _{MF} (kcal/mol)	5.13394	6.05626	4.4459	4.23245	7.44166	3.77316	3.73027	4.32088	5.07197	4.44554	4.06602	5.4653	6.31009	6.10339	5.33481	3.31743
	<i>E</i> _{HB} (kcal/mol)	-0.02438	-0.03303	-0.01758	-0.0154	-0.04596	-0.00995	-0.00317	-0.01074	-0.02101	-0.01533	-0.01129	-0.02737	-0.03762	-0.03594	-0.02629	-0.00114
	<i>E</i> _{VdW} (kcal/mol)	-9.23126	-9.24707	-9.04156	-8.83454	-9.28339	-8.89148	-8.84606	-8.96444	-9.28816	-9.2995	-9.30055	-9.25971	-9.26047	-9.27783	-9.1942	-9.84777

Table D4 k) COSMO-RS misfit, hydrogen-bonding and van der Waals energies for the compounds 1-hexanethiol, *n*-dodecane and several [P₆₆₆₍₁₄₎]-based ionic liquids combinations in the respective ternary systems at 298.2 K.

		[P ₆₆₆₍₁₄₎] ⁺															
		[MeSO ₄] ⁻	[CH ₃ SO ₃] ⁻	[CF ₃ SO ₃] ⁻	[(PFBu)SO ₃] ⁻	[CH ₃ CO ₂] ⁻	[NTf ₂] ⁻	[PF ₆] ⁻	[BF ₄] ⁻	[N(CN) ₂] ⁻	[C(CN) ₃] ⁻	[B(CN) ₄] ⁻	[TOS] ⁻	[DEP] ⁻	[DBP] ⁻	[NO ₃] ⁻	[FeCl ₄] ⁻
1-hexanethiol	<i>E</i> _{MF} (kcal/mol)	2.23742	2.37768	2.07014	2.00389	2.48142	1.92597	1.99655	2.11878	2.19643	2.09512	2.02923	2.28911	2.3773	2.3326	2.23935	1.86288
	<i>E</i> _{HB} (kcal/mol)	-0.13083	-0.1907	-0.0949	-0.08485	-0.31212	-0.05272	-0.02133	-0.05314	-0.13128	-0.08862	-0.06323	-0.16072	-0.23584	-0.22839	-0.14663	-0.01405
	<i>E</i> _{VdW} (kcal/mol)	-9.1956	-9.20692	-9.10588	-8.99	-9.22259	-9.00392	-9.06269	-9.11808	-9.13043	-9.12225	-9.1045	-9.20235	-9.20859	-9.21229	-9.18001	-9.41987
<i>n</i> -dodecane	<i>E</i> _{MF} (kcal/mol)	2.07607	2.16258	1.83085	1.71049	1.96739	1.63971	1.78742	1.95321	1.96531	1.87101	1.79798	2.0875	2.05077	1.97625	2.02831	1.56141
	<i>E</i> _{HB} (kcal/mol)	0.00000	0.00000	0.00000	0.00000	0.00000	0.00000	0.00000	0.00000	0.00000	0.00000	0.00000	0.00000	0.00000	0.00000	0.00000	0.00000
	<i>E</i> _{VdW} (kcal/mol)	-13.4896	-13.515	-13.3133	-13.0782	-13.5425	-13.1183	-13.2552	-13.3644	-13.4509	-13.4191	-13.3816	-13.4943	-13.5147	-13.5211	-13.4744	-13.7189
anion	<i>E</i> _{MF} (kcal/mol)	6.30635	7.43769	4.90321	5.17618	7.59966	4.44326	4.07991	4.78172	5.54096	5.1305	4.91842	7.70539	8.38889	8.9249	5.71435	3.46928
	<i>E</i> _{HB} (kcal/mol)	-0.4772	-0.72307	-0.33468	-0.29639	-1.13151	-0.17229	-0.04634	-0.17679	-0.45927	-0.3033	-0.20752	-0.58909	-0.86386	-0.83547	-0.53125	-0.01535
	<i>E</i> _{VdW} (kcal/mol)	-5.07174	-4.65242	-4.73748	-7.34889	-3.95986	-7.33053	-3.77122	-3.10113	-3.91858	-5.33292	-6.72086	-8.39816	-8.39948	-12.3222	-2.97427	-8.38614
cation	<i>E</i> _{MF} (kcal/mol)	7.69739	8.46707	6.86191	6.54618	9.23997	6.15264	6.38563	6.98535	7.47933	6.94632	6.62113	7.99526	8.54737	8.31623	7.73904	5.77737
	<i>E</i> _{HB} (kcal/mol)	-0.47149	-0.69526	-0.3309	-0.29312	-1.12041	-0.1704	-0.04618	-0.17495	-0.4546	-0.30011	-0.20547	-0.58032	-0.85483	-0.82664	-0.52528	-0.01559
	<i>E</i> _{VdW} (kcal/mol)	-32.3951	-32.4382	-31.9752	-31.4213	-32.501	-31.5082	-31.7385	-31.9897	-32.0897	-32.0553	-31.9808	-32.4091	-32.4418	-32.4638	-32.3354	-33.2166

Table D4 I) COSMO-RS misfit, hydrogen-bonding and van der Waals energies for the compounds 1-hexanethiol, *n*-dodecane, and several [OC₂(C₁)₄iU]-based ionic liquids combinations in the respective ternary systems at 298.2 K.

		[OC ₂ (C ₁) ₄ iU] ⁺															
		[MeSO ₄] ⁻	[CH ₃ SO ₃] ⁻	[CF ₃ SO ₃] ⁻	[(PFBU)SO ₃] ⁻	[CH ₃ CO ₂] ⁻	[NTf ₂] ⁻	[PF ₆] ⁻	[BF ₄] ⁻	[N(CN) ₂] ⁻	[C(CN) ₃] ⁻	[B(CN) ₄] ⁻	[TOS] ⁻	[DEP] ⁻	[DBP] ⁻	[NO ₃] ⁻	[FeCl ₄] ⁻
1-hexanethiol	<i>E</i> _{MF} (kcal/mol)	2.6571	2.81769	2.43524	2.31715	2.90898	2.22089	2.36146	2.5276	2.56377	2.43863	2.35502	2.68324	2.77072	2.68573	2.67001	2.16058
	<i>E</i> _{HB} (kcal/mol)	-0.15273	-0.21756	-0.11168	-0.09903	-0.34667	-0.06045	-0.02027	-0.06131	-0.14868	-0.10167	-0.07225	-0.18336	-0.26459	-0.25561	-0.17098	-0.0103
	<i>E</i> _{VdW} (kcal/mol)	-9.14816	-9.16747	-9.00671	-8.8396	-9.18967	-8.86001	-8.94571	-9.03406	-9.06703	-9.04798	-9.01579	-9.16041	-9.17146	-9.1787	-9.12406	-9.46179
<i>n</i> -dodecane	<i>E</i> _{MF} (kcal/mol)	2.94665	3.02824	2.62857	2.40528	2.75371	2.32951	2.62501	2.84286	2.75211	2.63162	2.53711	2.88893	2.81076	2.65936	2.91175	2.28622
	<i>E</i> _{HB} (kcal/mol)	0.00000	0.00000	0.00000	0.00000	0.00000	0.00000	0.00000	0.00000	0.00000	0.00000	0.00000	0.00000	0.00000	0.00000	0.00000	0.00000
	<i>E</i> _{VdW} (kcal/mol)	-13.4024	-13.4405	-13.129	-12.7905	-13.4763	-12.8496	-13.0519	-13.2203	-13.351	-13.3013	-13.2417	-13.4128	-13.4432	-13.4572	-13.3763	-13.7288
anion	<i>E</i> _{MF} (kcal/mol)	5.60779	6.73437	4.39772	4.95786	7.12453	4.228	3.54052	4.03607	4.82362	4.54898	4.45304	7.23599	8.04123	8.80236	4.94634	3.27356
	<i>E</i> _{HB} (kcal/mol)	-0.18995	-0.28802	-0.13654	-0.12012	-0.37218	-0.07558	-0.0229	-0.08009	-0.16615	-0.11892	-0.08631	-0.21963	-0.30248	-0.29033	-0.20572	-0.00796
	<i>E</i> _{VdW} (kcal/mol)	-5.03883	-4.62233	-4.72591	-7.33424	-3.94053	-7.35362	-3.79354	-3.12204	-4.32247	-5.78056	-7.26401	-8.35931	-8.35222	-12.2595	-2.97606	-8.431
cation	<i>E</i> _{MF} (kcal/mol)	5.10225	5.9833	4.49725	4.32749	7.37051	3.90711	3.85287	4.36563	5.09122	4.517	4.17741	5.44492	6.26549	6.09113	5.29566	3.51562
	<i>E</i> _{HB} (kcal/mol)	-0.18267	-0.25123	-0.13186	-0.11607	-0.35811	-0.07343	-0.02316	-0.07789	-0.16027	-0.11505	-0.08383	-0.20926	-0.29096	-0.2792	-0.19816	-0.00884
	<i>E</i> _{VdW} (kcal/mol)	-9.23088	-9.24511	-9.05048	-8.85335	-9.28413	-8.91448	-8.86214	-8.97337	-9.35507	-9.37977	-9.39968	-9.2645	-9.26006	-9.2779	-9.19722	-9.87774

Table D4 m) COSMO-RS misfit, hydrogen-bonding and van der Waals energies for the compounds 1-hexanethiol, *n*-dodecane and several [SC₂(C₁)₄iU]-based ionic liquids combinations in the respective ternary systems at 298.2 K.

		[SC ₂ (C ₁) ₄ iU] ⁺															
		[MeSO ₄] ⁻	[CH ₃ SO ₃] ⁻	[CF ₃ SO ₃] ⁻	[(PFBu)SO ₃] ⁻	[CH ₃ CO ₂] ⁻	[NTf ₂] ⁻	[PF ₆] ⁻	[BF ₄] ⁻	[N(CN) ₂] ⁻	[C(CN) ₃] ⁻	[B(CN) ₄] ⁻	[TOS] ⁻	[DEP] ⁻	[DBP] ⁻	[NO ₃] ⁻	[FeCl ₄] ⁻
1-hexanethiol	<i>E</i> _{MF} (kcal/mol)	2.639	2.80081	2.41858	2.30282	2.89798	2.20619	2.34197	2.50739	2.55184	2.42562	2.34146	2.66769	2.75817	2.67462	2.65242	2.14343
	<i>E</i> _{HB} (kcal/mol)	-0.15277	-0.21785	-0.11168	-0.09905	-0.34807	-0.06039	-0.02017	-0.06113	-0.14948	-0.10203	-0.07239	-0.18357	-0.26525	-0.25624	-0.17117	-0.01022
	<i>E</i> _{VdW} (kcal/mol)	-9.20896	-9.2287	-9.06785	-8.89665	-9.25151	-8.91729	-9.00769	-9.09694	-9.12712	-9.10631	-9.07249	-9.21657	-9.2275	-9.23035	-9.18782	-9.51594
<i>n</i> -dodecane	<i>E</i> _{MF} (kcal/mol)	2.90451	2.98836	2.58822	2.36997	2.7203	2.29289	2.57839	2.79583	2.71961	2.59803	2.50287	2.8519	2.77806	2.62992	2.86978	2.24359
	<i>E</i> _{HB} (kcal/mol)	0.00000	0.00000	0.00000	0.00000	0.00000	0.00000	0.00000	0.00000	0.00000	0.00000	0.00000	0.00000	0.00000	0.00000	0.00000	0.00000
	<i>E</i> _{VdW} (kcal/mol)	-13.4888	-13.5276	-13.2167	-12.8735	-13.5643	-12.9324	-13.1403	-13.3097	-13.4365	-13.384	-13.3218	-13.4927	-13.5229	-13.5305	-13.4668	-13.8062
anion	<i>E</i> _{MF} (kcal/mol)	5.65259	6.78247	4.42838	4.97106	7.17332	4.23855	3.56735	4.07859	4.8694	4.58275	4.47642	7.27118	8.08333	8.83508	4.9973	3.27767
	<i>E</i> _{HB} (kcal/mol)	-0.20331	-0.30664	-0.14435	-0.12699	-0.39082	-0.08015	-0.02434	-0.08492	-0.17577	-0.12606	-0.0916	-0.23625	-0.3185	-0.30559	-0.21724	-0.00847
	<i>E</i> _{VdW} (kcal/mol)	-5.07189	-4.65004	-4.78561	-7.4414	-3.96253	-7.44687	-3.86273	-3.17121	-4.3036	-5.76839	-7.25074	-8.41097	-8.40111	-12.3254	-2.99171	-8.52321
cation	<i>E</i> _{MF} (kcal/mol)	5.14423	6.01708	4.53064	4.34913	7.38522	3.93238	3.90041	4.41779	5.12012	4.54381	4.20158	5.47898	6.29053	6.11074	5.33427	3.54779
	<i>E</i> _{HB} (kcal/mol)	-0.19557	-0.26943	-0.14088	-0.12397	-0.38502	-0.07805	-0.02381	-0.08266	-0.17216	-0.12317	-0.08939	-0.22425	-0.31246	-0.29983	-0.21229	-0.00843
	<i>E</i> _{VdW} (kcal/mol)	-9.97984	-9.99383	-9.80976	-9.61913	-10.0321	-9.67134	-9.63218	-9.73934	-10.0526	-10.0718	-10.0798	-10.0083	-10.0021	-10.0139	-9.94389	-10.6708